

NUREG/CP-0126  
Vol. 2

Proceedings of the U.S. Nuclear Regulatory Commission

---

---

# Twentieth Water Reactor Safety Information Meeting

Volume 2

- Severe Accident Research
- Thermal Hydraulics

Held at  
Bethesda Marriott Hotel  
Bethesda, Maryland  
October 21-23, 1992

---

---

**U.S. Nuclear Regulatory Commission**

Office of Nuclear Regulatory Research

Proceedings prepared by  
Brookhaven National Laboratory



## NOTICE

These proceedings have been authored by a contractor of the United States Government. Neither the United States Government nor any agency thereof, or any of their employees, makes any warranty, expressed or implied, or assumes any legal liability or responsibility for any third party's use, or the results of such use, of any information, apparatus, product or process disclosed in these proceedings, or represents that its use by such third party would not infringe privately owned rights. The views expressed in these proceedings are not necessarily those of the U.S. Nuclear Regulatory Commission.

Available from

Superintendent of Documents  
U.S. Government Printing Office  
P.O. Box 37082  
Washington D.C. 20013-7082

and

National Technical Information Service  
Springfield, VA 22161

Proceedings of the U.S. Nuclear Regulatory Commission

---

---

# Twentieth Water Reactor Safety Information Meeting

Volume 2

- Severe Accident Research
- Thermal Hydraulics

Held at  
Bethesda Marriott Hotel  
Bethesda, Maryland  
October 21-23, 1992

---

---

Manuscript Completed: March 1993

Compiled by: Allen J. Weiss

Office of Nuclear Regulatory Research  
U.S. Nuclear Regulatory Commission  
Washington, DC 20555

Proceedings prepared by  
Brookhaven National Laboratory



## ABSTRACT

This three-volume report contains 93 papers out of the 108 that were presented at the Twentieth Water Reactor Safety Information Meeting held at the Bethesda Marriott Hotel, Bethesda, Maryland, during the week of October 21-23, 1992. The papers are printed in the order of their presentation in each session and describe progress and results of programs in nuclear safety research conducted in this country and abroad. Foreign participation in the meeting included 10 different papers presented by researchers from CEC, China, Finland, France, Germany, Japan, Spain and Taiwan. The titles of the papers and the names of the authors have been updated and may differ from those that appeared in the final program of the meeting.

**PROCEEDINGS OF THE  
20th WATER REACTOR SAFETY INFORMATION MEETING**

**October 21-23, 1992**

**Published in Three Volumes**

**GENERAL INDEX**

**VOLUME 1**

- **Plenary Session**
- **Advanced Reactor Research**
- **Advanced Passive LWRs**
- **Advanced Instrumentation and Control Hardware**
- **Advanced Control System Technology**
- **Human Factors Research**
- **EPRI's Nuclear Safety Research & Development**

**VOLUME 2**

- **Severe Accident Research**
- **Thermal Hydraulics**

**VOLUME 3**

- **Aging Research Developments**
- **Primary System Integrity**
- **Structural & Seismic Engineering**
- **Earth Sciences**
- **Probabilistic Risk Assessment Topics**

**REGISTERED ATTENDEES (NON NRC)  
20th WATER REACTOR SAFETY INFORMATION MEETING**

D. ADAMONIS  
WESTINGHOUSE  
PO BOX 355  
PITTSBURGH, PA 15239  
USA

J. ALFEO  
GENERAL ELECTRIC - KAPL  
BOX 1072  
SCHENECTADY, NY 12301  
USA

C. ALLISON  
EG&G IDAHO  
PO BOX 1625  
IDAHO FALLS, ID 83415  
USA

H. ALSMEYER  
KERNFORSCHUNGS ZERETRUM  
PO BOX 3640  
KARLSRUHE, W-7500  
GERMANY

R. ARUTYUNYAN  
NSI RUSSIA ACADEMY SCIENCE  
RUSSIA ACADEMY  
MOSCOW,  
RUSSIA

M. AZARM  
BROOKHAVEN NATIONAL LABORATORY  
BLDG. 130  
UPTON, NY 11973  
USA

W. BALZ  
COMM. EUROPEAN COMMUNITIES  
RUE DE LA LOI 200  
BRUSSELS, 1043  
BELGIUM

R. BARI  
BROOKHAVEN NATIONAL LABORATORY  
BLDG. 197C  
UPTON, NY 11973  
USA

J. BASURTO  
ONSNS  
DR BARRAGAN 775  
MEXICO CITY, DF 03220  
MEXICO

D. BEYER  
WESTINGHOUSE  
206 NAVAJO RD  
PITTSBURGH, PA 15241  
USA

S. BHATT  
ELECTRIC POWER RESEARCH INSTITUTE  
3412 HILL VIEW AVE, P.O. BOX 10412  
PALO ALTO, CA 94303  
USA

N. BDXLER  
SANDIA NATIONAL LABORATORY  
P.O. BOX 5800, DEPT. 6422  
ALBUQUERQUE, NM 87185  
USA

S. ADDITON  
TENERA  
7272 WISCONSIN AVE, SUITE 300  
BETHESDA, MD 20814  
USA

P. ALLEN  
AECL TECHNOLOGIES  
2251 SPEAKMAN DR  
MISSISSAUGA, L5K1B2  
CANADA

K. ALMENAS  
U. OF MARYLAND  
COLLEGE PARK, MD  
USA

H. AMARASOORIYA  
SCIENTECH, INC.  
11821 PARKLAWN DR, SUITE 100  
ROCKVILLE, MD 20879  
USA

H. ASCHER  
CONSULTANT  
11916 GOYA DR.  
POTOMAC, MD 20854  
USA

K. BAKER  
BATTELLE HUMAN AFFAIRS RES. CENTERS  
4000 NE 41ST STREET  
SEATTLE, WA 98105  
USA

Y. BANG  
KOREA INST. OF NUCLEAR SAFETY  
PO BOX 16 DAEDUK-DANJI  
TAEJON,  
KOREA

B. BASS  
OAK RIDGE NATIONAL LABORATORY  
P.O. BOX 2008, MS-8056  
OAK RIDGE, TN 37831  
USA

D. BERNFEUTER  
LAWRENCE LIVERMORE NATIONAL LAB  
PO BOX 808, L-196  
LIVERMORE, CA 94550  
USA

S. BHANDARI  
FRAMATOME  
EER, TOUR FIAT  
PARIS-LA DEFENSE, 92084  
FRANCE

W. BINNER  
AUSTRIAN RESEARCH CENTRE  
GOERGENGASSE 30/3  
VIENNA, A-1190  
AUSTRIA

E. BLOCHER  
GILBERT/COMMONWEALTH, INC  
PO BOX 1498  
READING, PA 19603  
USA

M. ALAMMAR  
GPU NUCLEAR CORP.  
PO BOX 15152  
READING, PA 19612  
USA

R. ALLEN  
PACIFIC NORTHWEST LABORATORY  
P.O. BOX 999  
RICHLAND, WA 99352  
USA

A. ALONSO  
UNIVERSITY OF MADRID  
JOSE GUTIERREZ ABASCAL, 2  
MADRID, 28010  
SPAIN

H. ANDRES  
GFS  
SCHWERTNERGASSE 1  
COLOGNE, 5000  
GERMANY

B. ATWATER  
U.S. GEOLOGICAL SURVEY  
UNIV OF WASHINGTON AJ-20  
SEATTLE, WA 98195  
USA

K. BALKEY  
WESTINGHOUSE  
PO BOX 355  
PITTSBURGH, PA 15235  
USA

W. BANKS  
LAWRENCE LIVERMORE NATIONAL LAB  
PO BOX 808  
LIVERMORE, CA 94551  
USA

E. BASSANSKI  
RRC KURCHATOV INSTITUTE  
123182 KURCHATOV SQ 1  
MOSCOW,  
RUSSIA

J. BETLACK  
MPR ASSOCIATES  
1050 CONN. AVE. N.W.  
WASHINGTON, DC 20036  
USA

D. BHARGAVA  
VIRGINIA POWER  
5000 DOMINION BLVD.  
GLEN ALLEN, VA 23060  
USA

B. BISHOP  
WESTINGHOUSE  
PO BOX 355  
PITTSBURGH, PA 15230  
USA

J. BLYTH  
AECS  
270 ALBERT ST.  
OTTAWA, ONTARIO, K1P 5S9  
CANADA

J. BOCCIO  
BROOKHAVEN NATIONAL LABORATORY  
BLDG. 130  
UPTON, NY 11973  
USA

J. BOUTON  
DSIN  
DSIN BP6  
FONTENAY/AUX ROSES, 92265  
FRANCE

M. BRANDYBERRY  
WESTINGHOUSE SAVANNAH RIVER CO.  
PO BOX 616  
AIKEN, SC 29802  
USA

W. BROWN  
BROOKHAVEN NATIONAL LABORATORY  
BLDG. 130  
UPTON, NY 11973  
USA

C. BUCHHOLZ  
GENUCLEAR ENERGY  
175 CURTNER AVE M/C 754  
SAN JOSE, CA 95125  
USA

D. CARROLL  
UNIVERSITY OF FLORIDA  
2440 NW 38TH DR.  
GAINESVILLE, FL 32605  
USA

S. CHAKRABORTY  
SWISS NUCLEAR SAFETY INSPECTORATE  
H5K  
VILLIGAN-H5K, 5232  
SWITZERLAND

T. CHIEN  
ARGONNE NATIONAL LABORATORY  
9700 S. CASS AVE.  
ARGONNE, IL 60439  
USA

G. CICCARELLI  
BROOKHAVEN NATIONAL LABORATORY  
BLDG. 130  
UPTON, NY 11973  
USA

J. CONINE  
GENERAL ELECTRIC - KAPL  
P.O. BOX 1072  
SCHENECTADY, NY 12301  
USA

B. COFFIN  
OAK RIDGE NATIONAL LABORATORY  
P.O. BOX 2008  
OAK RIDGE, TN 37831  
USA

D. DAHLGREN  
SANDIA NATIONAL LABORATORY  
P.O. BOX 5800, DEPT. 6405  
ALBUQUERQUE, NM 87185  
USA

P. DAMERELL  
MPR ASSOCIATES  
1050 CONN. AVE. N.W.  
WASHINGTON, DC 20036  
USA

M. BOHN  
SANDIA NATIONAL LABORATORY  
P.O. BOX 5800  
ALBUQUERQUE, NM 87185  
USA

M. BOWMAN  
BALTIMORE G&E  
CALVERT CLIFFS NUC. POWER PLANT  
LUSBY, MD 20657  
USA

J. BROCHARD  
CEA  
CEA SACLAY  
GIF SUR YVETTE, 91191  
FRANCE

T. BROWN  
SANDIA NATIONAL LABORATORY  
P.O. BOX 5800  
ALBUQUERQUE, NM 87185  
USA

J. BURROWS  
AEA TECHNOLOGY  
SRD. WIGSHAW LANE-CULCHETT  
WARRINGTON, WA34NE  
UK

D. CASADA  
OAK RIDGE NATIONAL LABORATORY  
P.O. BOX 2009  
OAK RIDGE, TN 37831  
USA

C. CHEFFONNEL  
EDF-SEPTEN  
12-14 AVENUE DUTRIEVOZ  
VILLEURBANNE, 69628  
FRANCE

J. CHRISTENSEN  
PACIFIC NORTH-WEST LABORATORY  
P.O. BOX 999  
RICHLAND, WA 99336  
USA

J. CLOSE  
EG&G IDAHO  
P.O. BOX 1625  
IDAHO FALLS, ID 83415  
USA

L. CONNOR  
STS  
3 METRO CENTER-SUITE 610  
BETHESDA, MD 20817  
USA

K. COZENS  
NUMARC  
1776 EYE ST. NW, SUITE 300  
WASHINGTON, DC 20006  
USA

R. DAIL  
APTECH ENGINEERING SERVICES, INC.  
9672 PENNSYLVANIA AVE  
UPPER MARLBORO, MD 20772  
USA

J. DARBY  
SEA  
6100 UPTOWN BLVD., NE  
ALBUQUERQUE, NM 87110  
USA

E. BOUCHERON  
SANDIA NATIONAL LABORATORY  
P.O. BOX 5800, DEPT. 6418  
ALBUQUERQUE, NM 87185  
USA

B. BOYACK  
LOS ALAMOS NATIONAL LABORATORY  
P.O. BOX 1663, MS K551  
LOS ALAMOS, NM 87545  
USA

U. BROCKMEIER  
UNIVERSITY BOCHUM  
UNISTR 150/184/128  
BOCHUM, W4630  
GERMANY

J. BRYSON  
OAK RIDGE NATIONAL LABORATORY  
P.O. BOX 2008  
OAK RIDGE, TN 37831  
USA

A. CAMP  
SANDIA NATIONAL LABORATORY  
P.O. BOX 5800, DEPT. 6412  
ALBUQUERQUE, NM 87185  
USA

J. CATLIN  
BECHTEL POWER CORPORATION  
9801 WASHINGTONIAN BLVD.  
GATHERSBURG, MD 20878  
USA

B. CHEXAL  
ELECTRIC POWER RESEARCH INSTITUTE  
3412 HILLVIEW AVE, P.O. BOX 10412  
PALO ALTO, CA 94303  
USA

T. CHU  
BROOKHAVEN NATIONAL LABORATORY  
BLDG. 130  
UPTON, NY 11973  
USA

R. COLE, JR.  
SANDIA NATIONAL LABORATORY  
P.O. BOX 5800, DEPT. 6418  
ALBUQUERQUE, NM 87185  
USA

S. COOPER  
SCIENCE APPLICATIONS INTERNATIONAL  
1710 GOODRIDGE DR  
MC LEAN, VA 22102  
USA

R. CURTIS  
AECL TECHNOLOGIES  
9210 CORPORATE BLVD, SUITE 410  
ROCKVILLE, MD 20855  
USA

J. DALLMAN  
UNC ANALYTICAL SERVICES  
1700 LOUISIANA BLVD, NE-SUITE 230  
ALBUQUERQUE, NM 87110  
USA

J. DEBOR  
SCIENCE APPLICATIONS INTERNATIONAL  
11251 ROGER BROWN DR.  
RESTON, VA 22090  
USA

S. DESKEVICH  
DUKE POWER CO.  
422 S. CHURCH ST  
CHARLOTTE, NC 28242  
USA

C. DODD  
OAK RIDGE NATIONAL LABORATORY  
P.O. BOX 2008  
OAK RIDGE, TN 37831  
USA

S. DOROFEEV  
KURCHATOV INST.  
KURCHATOV SQ. 1  
MOSCOW,  
RUSSIA

R. DUFLING  
ERIN ENGINEERING AND RESEARCH, INC.  
2175 N. CALIFORNIA BLVD #625  
WALNUT CREEK, CA 94596  
USA

M. ENGINEER  
FLUOR DANIEL  
826 REVERE  
WESTMONT, IL 60559  
USA

P. EWING  
OAK RIDGE NATIONAL LABORATORY  
P.O. BOX 2008, MS-6318  
OAK RIDGE, TN 37831  
USA

N. FARUKHI  
NUMARC  
1776 EYE ST. NW, SUITE 300  
WASHINGTON, DC 20006  
USA

S. FLEGER  
SCIENCE APPLICATIONS INTERNATIONAL  
11251 ROGER BACON DR  
RESTON, VA 22090  
USA

S. FRACHET  
CEA  
CADARACHE  
ST. PAUL-LEZ-DURANCE 13108  
FRANCE

T. FUJIMOTO  
MITSUBISHI  
2-1-1 SHINHAMA ARAI-CHO  
TAKASAGO, HYOGO 676  
JAPAN

O. FURUKAWA  
NUCLEAR ENGINEERING LTD.  
1-3-7 TOSABORI NISHI-KU  
OSAKA, 550  
JAPAN

G. GESSLER  
B&W NUCLEAR SERVICE CO.  
3315 OLD FOREST RD/PO BOX 10935  
LYNCHBURG, VA 24506  
USA

C. GIGGER  
WESTINGHOUSE  
PO BOX 79  
W. MIFFLIN, PA 15122  
USA

S. DINGMAN  
SANDIA NATIONAL LABORATORY  
P.O. BOX 5800, DEPT. 6412  
ALBUQUERQUE, NM 87185  
USA

M. DONOVAN  
HALLIBURTON NUS  
910 CLOPPER ROAD  
GAITHERSBURG, MD 20878  
USA

R. DUFFEY  
BROOKHAVEN NATIONAL LABORATORY  
BLDG. 197C  
UPTON, NY 11973  
USA

J. EAST  
WESTINGHOUSE SAVANNAH RIVER CO.  
1991 CENTENNIAL DRIVE, BLDG. 1  
AIKEN, SC 29803  
USA

H. ESMALI  
ENERGY RESEARCH, INC.  
6290 MONTROSE RD  
ROCKVILLE, MD 20852  
USA

M. FAKORY  
ES TECHNOLOGIES  
8930 STANFORD BLVD.  
COLUMBIA, MD 21045  
USA

M. FELTUS  
PENN STATE UNIV.  
231 SACKETT  
UNIVERSITY PARK, PA 16801  
USA

M. FONTANA  
OAK RIDGE NATIONAL LABORATORY  
P.O. BOX 2009, MS-8063  
OAK RIDGE, TN 37831  
USA

A. FRANKEL  
U.S. GEOLOGICAL SURVEY  
922 NATIONAL CENTER  
RESTON, VA 22092  
USA

M. FUKUDA  
NUCLEAR POWER ENG. CORP.  
3-17-1 TORANOMON, MINATO-KU  
TOKYO, 105  
JAPAN

C. GADDY  
GENERAL PHYSICS CORP.  
6700 ALEXANDER BELL DR.  
CLOUMBIA, MD 21046  
USA

D. GERTMAN  
EG&G IDAHO  
P.O. BOX 1625, MS 2405  
IDAHO FALLS, ID 83415  
USA

T. GINSBERG  
BROOKHAVEN NATIONAL LABORATORY  
BLDG. 130  
UPTON, NY 11973  
USA

S. DOCTOR  
PACIFIC NORTHWEST LABORATORY  
P.O. BOX 999  
RICHLAND, WA 99352  
USA

P. DOFE  
AEA TECHNOLOGY  
WINFRETH TECH. CENTER  
DORCHESTER, DT28DH  
UK

R. DURANTE  
AECL TECHNOLOGIES  
9210 CORPORATE BLVD, SUITE 410  
ROCKVILLE, MD 20850  
USA

Z. ELAWAR  
ARIZONA PUBLIC SERVICES  
PO BOX 52034  
PHOENIX, AZ 85029  
USA

R. EVANS  
NUMARC  
1776 EYE ST. NW, SUITE 300  
WASHINGTON, DC 20006  
USA

K. FARRELL  
OAK RIDGE NATIONAL LABORATORY  
P.O. BOX 2008  
OAK RIDGE, TN 37831  
USA

L. FISCHER  
LAWRENCE LIVERMORE NATIONAL LAB  
PO BOX 808  
LIVERMORE, CA 94550  
USA

C. FORSEBERG  
OAK RIDGE NATIONAL LABORATORY  
P.O. BOX 2008  
OAK RIDGE, TN 37831  
USA

A. FRESCO  
BROOKHAVEN NATIONAL LABORATORY  
BLDG. 130  
UPTON, NY 11973  
USA

P. FULFORD  
HALLIBURTON NUS  
910 CLOPPER ROAD  
GAITHERSBURG, MD 20878  
USA

G. GAUTHIER  
CEA  
BP6  
FONTENAY, 92265  
FRANCE

L. GHAN  
EG&G IDAHO  
P.O. BOX 1625  
IDAHO FALLS, ID 83415  
USA

A. GIRI  
FRAMATOME  
TOUR FIAT CEDEX 16  
PARIS, 92084  
FRANCE

J. GLEASON  
WYLE  
PO BOX 077777  
HUNTSVILLE, AL 35807  
USA

W. GUNTHER  
BROOKHAVEN NATIONAL LABORATORY  
BLDG. 130  
UPTON, NY 11973  
USA

D. HANSON  
EG&G IDAHO  
P.O. BOX 1625  
IDAHO FALLS, ID 83415  
USA

R. HARVEY  
YANKEE ATOMIC  
580 MAIN ST.  
BOLTON, MA 01740  
USA

J. HAWTHORNE  
MATERIALS ENGINEERING ASSOCIATES, INC.  
9700-B MARTIN LUTHER KING HWY.  
LANHAM, MD 20708  
USA

J. HENRY  
CEA  
BP6  
FONTENAY, 92265  
FRANCE

T. HIFONS  
LOS ALAMOS NATIONAL LABORATORY  
P.O. BOX 1663, MS E561  
LOS ALAMOS, NM 87545  
USA

P. HOFMANN  
KERNFORSCHUNGSZERETRUM  
PO BOX 3640  
KARLSRUHE, 7500  
GERMANY

B. HOLMES  
AEA TECHNOLOGY, C/O BNL  
BLDG. 130  
UPTON, NY 11973  
UK

Y. HORIKAWA  
KANSAI ELECTRIC  
1100 17TH ST N.W., SUITE 500  
WASHINGTON, DC 20036  
USA

R. HUDDLESTON  
OAK RIDGE NATIONAL LABORATORY  
P.O. BOX 2009, MS-8112  
OAK RIDGE, TN 37831  
USA

S. HYTEN  
WYLE  
PO BOX 077777  
HUNTSVILLE, AL 35807  
USA

M. ISHII  
PURDUE UNIVERSITY  
PURDUE UNIVERSITY, NUC. ENGINEER  
W. LAFAYETTE, IN 47907  
USA

M. GOMOLINSKI  
CEA  
321 RUE DE CHARENTON  
PARIS, 75012  
FRANCE

G. HACHE  
CEA  
IPSN/DRS/SEMAR B7702  
CEA/ST. PAUL, 13108  
FRANCE

F. HARPER  
SANDIA NATIONAL LABORATORY  
P.O. BOX 5800  
ALBUQUERQUE, NM 87185  
USA

S. HASHIMOTO  
NUCLEAR POWER ENG. CORP.  
3-17-1 TORANOMON - MINATO-KU  
TOKYO, 105  
JAPAN

K. HAYASHI  
NAGOYA UNIVERSITY  
NAGOYA  
AICHI, 464-01  
JAPAN

T. HERNES  
OECD HALDEN REACTOR PROJECT  
PO BOX 173  
HALDEN, N-1751  
NORWAY

L. HOCHREITER  
WESTINGHOUSE  
PO BOX 355  
PITTSBURGH, PA 15235  
USA

C. HOFMAYER  
BROOKHAVEN NATIONAL LABORATORY  
BLDG. 475C  
UPTON, NY 11973  
USA

W. HOPKINS  
BECHTEL POWER CORPORATION  
9801 WASHINGTONIAN BLVD.  
GAITHERSBURG, MD 20878  
USA

J. HOROWITZ  
DUPAGE COMPUTER APPLICATIONS  
8117 NORWOOD CT.  
WOODRIDGE, CT. 60517  
USA

A. HUERTA  
CNSNS  
DR BARRAGAN 779  
MEXICO, DF 03220  
MEXICO

J. IN DE BETOU  
SKI  
BOX 27106  
STOCKHOLM, S10252  
SWEDEN

S. ISKANDER  
OAK RIDGE NATIONAL LABORATORY  
P.O. BOX 2008, MS-6151  
OAK RIDGE, TN 37831  
USA

F. GRIFFIN  
OAK RIDGE NATIONAL LABORATORY  
P.O. BOX 2009, MS-8057  
OAK RIDGE, TN 37831  
USA

F. HAGGAG  
OAK RIDGE NATIONAL LABORATORY  
P.O. BOX 2008  
OAK RIDGE, TN 37831  
USA

E. HARVEGO  
EG&G IDAHO  
P.O. BOX 1625  
IDAHO FALLS, ID 83415  
USA

J. HAUGH  
ELECTRIC POWER RESEARCH INSTITUTE  
3412 HILLVIEW AVE, P.O. BOX 10412  
PALO ALTO, CA 94303  
USA

W. HAZELTON  
CONSULTANT  
218 2ND AVE. SE  
AITKIN, MN 56431  
USA

J. HIGGINS  
BROOKHAVEN NATIONAL LABORATORY  
BLDG. 130  
UPTON, NY 11973  
USA

S. HODGE  
OAK RIDGE NATIONAL LABORATORY  
P.O. BOX 2009, MS-8057  
OAK RIDGE, TN 37831  
USA

C. HOLLIDAY  
NII  
ST. PETERS HOUSE  
LIVERPOOL, L20362  
UK

A. HOPPER  
BATTELLE  
505 KING AVENUE  
COLUMBUS, OH 43235  
USA

T. HSU  
VIRGINIA POWER  
DOMINION BLVD.  
GLEN ALLEN, VA 23060  
USA

C. HYMAN  
OAK RIDGE NATIONAL LABORATORY  
P.O. BOX 2009, MS-8057  
OAK RIDGE, TN 37831  
USA

H. ISBIN  
NSFRIC  
2815 MONTEREY PKWY  
MINNEAPOLIS, MN 55416  
USA

J. JANSKY  
BTB  
07152/41058 GERLINGER ST 151  
LEONBERG,  
GERMANY

K. JHA  
BECHTEL POWER CORPORATION  
9801 WASHINGTONIAN BLVD.  
GAITHERSBURG, MD 20878  
USA

G. JOHNSON  
EG&G IDAHO  
P.O. BOX 1625  
IDAHO FALLS, ID 83415  
USA

E. JONES  
LAWRENCE LIVERMORE NATIONAL LAB  
PO BOX 808, L-190  
LIVERMORE, CA 94550  
USA

T. KAKIUCHI  
MITSUBISHI  
1-1, WADASAKI-CHO, 1-CHOME  
KOBE, HYOGO 652  
JAPAN

T. KASAHARA  
COMPUTER SOFTWARE DEVEL. CO., LTD  
2-4-1 SHIBA KOEN, MINATO-KU  
TOKYO,  
JAPAN

J. KELLY  
SANDIA NATIONAL LABORATORY  
P.O. BOX 5800  
ALBUQUERQUE, NM 87185  
USA

I. KIM  
BROOKHAVEN NATIONAL LABORATORY  
BLDG. 130  
UPTON, NY 11973  
USA

S. KINNERSLEY  
AEA TECHNOLOGY  
WINFRITH TECHNOLOGY CENTRE  
DORCHESTER,  
UK

D. KLEWZ  
ROCHESTER GAS & ELECTRIC  
49 EAST AVE.  
ROCHESTER, NY 14649  
USA

T. KODAMA  
MITSUBISHI  
2-1-1 ARAI-CHO  
TAKASAGO, HYOGO 676  
JAPAN

C. KOT  
ARGONNE NATIONAL LABORATORY  
9700 S. CASS AVE, BLDG. 331  
ARGONNE, IL 60439  
USA

Y. KUKITA  
JAPAN ATOMIC ENERGY RESEARCH INST.  
TOKAI-MURA NAKA-GUN  
IBARAKI-KEN, 319-11  
JAPAN

R. KURTZ  
PACIFIC NORTHWEST LABORATORY  
P.O. BOX 999  
RICHLAND, WA 99352  
USA

Y. JIN  
KOREA ATOMIC ENERGY RESEARCH INST.  
PO BOX 7, DAEDUK-DANJI  
TAEJON,  
KOREA

W. JOHNSON  
BECHTEL POWER CORPORATION  
9801 WASHINGTONIAN BLVD.  
GAITHERSBURG, MD 20878  
USA

N. JONSSON  
ABB ATOM  
ABB ATOM AB  
VISTERAS, S72163  
SWEDEN

J. KARL  
TU MUNICH  
ARCISSTR 21  
8000MUNICH 2,  
GERMANY

D. KEARNAGHAN  
WESTINGHOUSE SAVANNAH RIVER CO.  
1991 CENTENNIAL DRIVE, BLDG. 1  
AIKEN, SC 29803  
USA

B. KERBA  
ONTARIO HYDRO  
700 UNIVERSITY AVE  
TORONTO, ONTARIO M5G1X6  
CANADA

S. KIM  
KOREA ATOMIC ENERGY RESEARCH INST.  
PO BOX 7, DAEDUK-DANJI  
TAEJON,  
KOREA

M. KINOSHITA  
BROOKHAVEN NATIONAL LABORATORY  
BLDG. 197D  
UPTON, NY 11973  
USA

P. KLOEG  
KEMA  
ULTRICHTSEWEG 310  
ARNHEM, 6812AR  
NETHERLANDS

K. KOKE  
OBAYASHI CORPORATION  
4-640, SHIMOKIYOTO  
TOKYO, KIYOSE 204  
JAPAN

J. KROK  
RPI  
RENS. POLYTECH.  
TROY, NY 12180  
USA

C. KULLBERG  
EG&G IDAHO  
P.O. BOX 1625, MS 2405  
IDAHO FALLS, ID 83415  
USA

K. KUJSSMAUL  
MPA-STUTTGAERT  
PFAFFENWALDRING 32  
STUTTGAERT, 7000  
GERMANY

J. JO  
BROOKHAVEN NATIONAL LABORATORY  
BLDG. 130  
UPTON, NY 11973  
USA

A. JONES  
CEC - IISPPRA  
CEC RESEARCH CENTER TP250  
ISPRA (VA), 21020  
ITALY

C. JUPITER  
JUPITER CORP.  
2730 UNIV. BLVD, SUITE 900/WHEATON PL  
WHEATON, MD 20902  
USA

H. KARWAT  
TECH. U. MUNICH  
FORSCHUNGSGELANDE  
GARCHING, W8046  
GERMANY

D. KELLY  
GILBERT/COMMONWEALTH, INC  
P.O. BOX 1498  
READING, PA 19603  
USA

M. KHATIB-RAHBAR  
ENERGY RESEARCH, INC.  
6290 MONTROSE RD.  
ROCKVILLE, MD 20852  
USA

H. KIM  
KOREA INST. OF NUCLEAR SAFETY  
PO BOX 16 DAEDUK-DANJI  
TAEJON,  
KOREA

Y. KITAMURA  
MITSUBISHI  
2-3-8, OTEMACHI, CHIYODA-KU  
CHIYODA-KU, 100  
JAPAN

L. KMETEK  
SANDIA NATIONAL LABORATORY  
P.O. BOX 5800, DEPT. 6418  
ALBUQUERQUE, NM 87185  
USA

K. KORSAH  
OAK RIDGE NATIONAL LABORATORY  
P.O. BOX 2008, MS-6010  
OAK RIDGE, TN 37831  
USA

J. KJEBK  
OAK RIDGE NATIONAL LABORATORY  
P.O. BOX 2009  
OAK RIDGE, TN 37831  
USA

T. KUJE  
HITACHI, LTD.  
1168 MORIYAMA-CHO  
HITACHI-SHI, IBARAKI-KEN 316  
JAPAN

L. LARSON  
WESTINGHOUSE  
PO BOX 79  
W. MIFFLIN, PA 15122  
USA

M. LARSON  
WESTINGHOUSE  
PO BOX 79  
W. MIFFLIN, PA 15122  
USA

J. LEE  
TAIPEI ENERGY  
67 LANE 144 KEELUNG RD., SEC 4  
TAIPEI,  
TAIWAN

R. LINK  
NAVAL SURFACE WARFARE CENTER  
CODE 2814  
ANNAPOLIS, MD 21402  
USA

M. LIVOLANT  
CEA  
CEN/FAR IPSN  
FONTENAY-AUX-ROSES, 92265  
FRANCE

A. LOWE, JR.  
E&W NUCLEAR SERVICE CO.  
PO BOX 10935  
LYNCHBURG, VA 24506  
USA

B. MACDONALD  
GENERAL ELECTRIC-KAPL  
PO BOX 1072  
SCHNECTADY, NY 12301  
USA

C. MARICCHIOLLO  
ENEA DISP  
VIA BRANCATI 48  
ROME, 00148  
ITALY

M. MASSOUD  
BALTIMORE G&E  
CALVERT CLIFFS NUCLEAR POWER PLANT  
LUSBY, MD 20657  
USA

K. MAYERS  
GILBERT/COMMONWEALTH, INC  
P.O. BOX 1498  
READING, PA 19603  
USA

R. McMILLAN  
AEA TECHNOLOGY  
SRD, WIGSHAW LANE, CULCHETH  
WARRINGTON, CHESHIRE WA34NE  
UK

J. MEYER  
SCIENTECH, INC.  
11821 PARKLAWN DR, SUITE 100  
ROCKVILLE, MD 20879  
USA

A. MILLER  
NII  
ST. PETERS HOUSE  
LIVERPOOL, L20 3L2  
UK

K. MOKHTARIAN  
CBI TECHNICAL SERVICES  
1501 N. DIVISION ST.  
PLAINFIELD, IL 60544  
USA

C. LECOMTE  
CEA  
CEN/FAR IPSN  
FONTENAY-AUX-ROSES 92265  
FRANCE

J. LEHNER  
BROOKHAVEN NATIONAL LABORATORY  
BLDG. 130  
UPTON, NY 11973  
USA

M. LINN  
OAK RIDGE NATIONAL LABORATORY  
P.O. BOX 2008, MS-6398  
OAK RIDGE, TN 37831  
USA

R. LOFARO  
BROOKHAVEN NATIONAL LABORATORY  
BLDG. 130  
UPTON, NY 11973  
USA

S. LU  
LAWRENCE LIVERMORE NATIONAL LAB  
P.O. BOX 808, L-196  
LIVERMORE, CA 94550  
USA

I. MADNI  
BROOKHAVEN NATIONAL LABORATORY  
BLDG. 130  
UPTON, NY 11973  
USA

L. MARTENS  
EBASCO SERVICES, INC.  
TWO WORLD TRADE CENTER  
NEW YORK, NY 10048  
USA

T. MATSUMOTO  
HITACHI, LTD.  
1168 MORIYAMA-CHO  
HITACHI-SHI, IBARAKI-KEN 316  
JAPAN

W. McAFEE  
OAK RIDGE NATIONAL LABORATORY  
P.O. BOX 2009  
OAK RIDGE, TN 37831  
USA

J. MENCKE  
CONSUMERS POWER CO.  
1156 OAK HAMPTON ROAD  
HOLLAND, MI 49424  
USA

A. MEYERHEINE  
CEA  
C.E.N. CADARACHE  
CADARACHE, 13  
FRANCE

D. MODEEN  
NUMARC  
1778 EYE ST. NW, SUITE 300  
WASHINGTON, DC 20006  
USA

T. MONTEMARANO  
NAVAL SURFACE WARFARE CENTER  
CODE 2814  
ANNAPOLIS, MD 21402  
USA

J. LEE  
KOREA INST. OF NUCLEAR SAFETY  
PO BOX 16 DAEDUK-DANJI  
TAEJON,  
KOREA

G. LEVOVSKY  
SCIENCE & LIFE MAGAZINE  
82-16 34TH AVE, SUITE 2D  
JACKSON HTS., NY 11372  
USA

H. LIU  
CHINESE EMBASSY  
2300 CONNECTICUT AVE NW  
WASHINGTON, DC 20008  
USA

F. LOSS  
MATERIALS ENGINEERING ASSOCIATES, INC.  
9700-B MARTIN LUTHER KING, JR. HWY  
LANHAM, MD 20708  
USA

W. LUCKAS  
BROOKHAVEN NATIONAL LABORATORY  
BLDG. 130  
UPTON, NY 11973  
USA

B. MAGONDEAUX  
EDF-SEPTEN  
12-14 AVENUE DUTRIEVOZ  
VILLEURBANNE, 69628  
FRANCE

J. MARTINEZ  
CSN SPAIN  
JUSTO DORADO 11  
MADRID, 28040  
SPAIN

B. MAVKO  
J. STEFAN INST.  
JAMOVA 39  
LJUBLJANA, 6111  
SLOVENIA

W. McCURDY  
MPR ASSOCIATES  
1050 CONN. AVE. N.W.  
WASHINGTON, DC 20036  
USA

M. MERLO  
ELECTRIC POWER RESEARCH INSTITUTE  
3412 HILLVIEW AVE, P.O. BOX 10412  
PALO ALTO, CA 94304  
USA

T. MIEDA  
ISHIKAWAJIMA - HARIMA HEAVY INDUST.  
1, SHIN-NAKAHAMA-CHO, ISOGO-KU  
YOKOHAMA, KANAGAWA 235  
JAPAN

M. MODRO  
EG&G IDAHO  
P.O. BOX 1625  
IDAHO FALLS, ID 83415  
USA

D. MORRISON  
MITRE CORP.  
7525 COLSHIRE DRIVE  
MCLEAN, VA 22102  
USA

V. MUBAYI  
BROOKHAVEN NATIONAL LABORATORY  
BLDG. 130  
UPTON, NY 11973  
USA

K. MURATA  
SANDIA NATIONAL LABORATORY  
P.O. BOX 5800, DEPT. 6429  
ALBUQUERQUE, NM 87185  
USA

R. NANSTAD  
OAK RIDGE NATIONAL LABORATORY  
P.O. BOX 2008, MS-6151  
OAK RIDGE, TN 37831  
USA

G. NIEDERAUER  
LOS ALAMOS NATIONAL LABORATORY  
P.O. BOX 1663, MS K557  
LOS ALAMOS, NM 87545  
USA

D. O'CONNOR  
OAK RIDGE NATIONAL LABORATORY  
P.O. BOX 2009  
OAK RIDGE, TN 37831  
USA

H. OHASHI  
UNIVERSITY OF TOKYO  
7-3-1, HONGO, BUNKYO-KU  
TOKYO, 113  
JAPAN

R. ORTON  
PACIFIC NORTHWEST LABORATORY  
P.O. BOX 999, K6-48  
RICHLAND, WA 99352  
USA

L. OTT  
OAK RIDGE NATIONAL LABORATORY  
P.O. BOX 2009  
OAK RIDGE, TN 37831  
USA

W. PENNELL  
OAK RIDGE NATIONAL LABORATORY  
P.O. BOX 2009  
OAK RIDGE, TN 37831  
USA

J. PHILLIPS  
EG&G IDAHO  
P.O. BOX 1625  
IDAHO FALLS, ID 83415  
USA

M. PODOWSKI  
RENS. POLYTECH. INSTITUTE  
RP-DEPT. OF NUCLEAR ENGINEERING  
TROY, NY 12180  
USA

C. PUGH  
OAK RIDGE NATIONAL LABORATORY  
P.O. BOX 2009  
OAK RIDGE, TN 37831  
USA

A. RAO  
GENUCLEAR ENERGY  
175 CURTNER AVE MC 754  
SAN JOSE, CA 95125  
USA

M. MÜHLHEIM  
OAK RIDGE NATIONAL LABORATORY  
P.O. BOX 2009, MS-8065  
OAK RIDGE, TN 37831  
USA

M. NAITO  
TOSHIBA CORPORATION  
8, SHINSUGITA-CHO  
HOKOHAMA, KANAGAWA 235  
JAPAN

D. NAUS  
OAK RIDGE NATIONAL LABORATORY  
P.O. BOX 2009  
OAK RIDGE, TN 37831  
USA

Y. NOMURA  
JAPAN ATOMIC ENERGY RESEARCH INST.  
2-4 SHIRAKATA SHIRANE  
TOKAI-MURA, IBARAKI-KEN 319-11  
JAPAN

J. O'HARA  
BROOKHAVEN NATIONAL LABORATORY  
BLDG. 130  
UPTON, NY 11973  
USA

K. OHFUI  
TOSHIBA ADVANCED SYSTEM CORP  
1-2-4 ISAGO KAWASAKI-KU  
KAWASAKI-SHI, KANAGAWA 210  
JAPAN

M. OSBORNE  
OAK RIDGE NATIONAL LABORATORY  
P.O. BOX 2008  
OAK RIDGE, TN 37831  
USA

F. PANISKO  
PACIFIC NORTHWEST LABORATORY  
P.O. BOX 899  
RICHLAND, WA 99352  
USA

K. PETERSEN  
AMS  
AMS 9111 CROSS PARK DRIVE NW  
KNOXVILLE, TN 37923  
USA

B. PIKUL  
MITRE CORP.  
7525 COLSHIRE DR.  
MCLEAN, VA 22102  
USA

W. PRATT  
BROOKHAVEN NATIONAL LABORATORY  
BLDG. 130  
UPTON, NY 11973  
USA

E. PURVIS  
CONSULTANT  
10105 CLEAR SPRING ROAD  
DAMASCUS, MD 20872  
USA

M. RAVINDRA  
ECE INTERNATIONAL  
18101 VON KARMAN  
IRVINE, CA 92715  
USA

R. MURALIDHARAN  
GENERAL ELECTRIC CO.  
175 CURTNER AVE, M/C 469  
SAN JOSE, CA 95125  
USA

N. NAKAJIMA  
JAPAN ATOMIC ENERGY RESEARCH INST.  
TOKAI-MURA NAKA-GUN  
IBARAKI-KEN, 319-11  
JAPAN

J. NESTELL  
MPR ASSOCIATES  
1050 CONN. AVE. N.W.  
WASHINGTON, DC 20036  
USA

U. NURMSOO  
AECB, C/O ONTARIO HYDRO  
PICKERING NGS OPERATIONS, P.O. BOX 160  
PICKERING, ONTARIO L1V 2R5  
CANADA

S. CH  
ELECTRIC POWER RESEARCH INSTITUTE  
3412 HILLVIEW AVE, P.O. BOX 10412  
PALO ALTO, CA 94303  
USA

M. ORTIZ  
EG&G IDAHO  
P.O. BOX 1625  
IDAHO FALLS, ID 83415  
USA

D. OSETEK  
LOS ALAMOS TECHNICAL ASSOCIATES  
2400 LOUISIANA NE  
ALBUQUERQUE, NM 87110  
USA

F. PAZDERA  
NUCLEAR RESEARCH INSTITUTE  
FEZ  
PRAGUE, 250 68  
CZECHOSLOVAKIA

A. PFEFFER  
BECHTEL POWER CORPORATION  
9801 WASHINGTONIAN BLVD.  
GATHERSBURG, MD 20878  
USA

J. PITTS  
LAWRENCE LIVERMORE NATIONAL LAB  
P.O. BOX 808, L-197  
LIVERMORE, CA 94550  
USA

V. PROKLOV  
KURCHATOV INSTITUTE  
KURCHATOV SQUARE,  
MOSCOW, 123182  
RUSSIA

F. QUINN  
SCIENTECH, INC.  
11821 PARKLAWN DR, SUITE 100  
ROCKVILLE, MD 20879  
USA

W. RETTIG  
U.S. DEPT. OF ENERGY  
785 DOE PL.  
IDAHO FALLS, ID 83401  
USA

L. RIB  
AECL TECHNOLOGIES  
9210 CORPORATE BLVD., SUITE 410  
ROCKVILLE, MD 20850  
USA

M. ROSS  
RPI  
DEPT. OF M.E.  
TROY, NY 12180  
USA

H. RUILE  
TU MUNCHEN  
ARCIS STR.21  
MUNICH,  
GERMANY

R. SANDERS  
OAK RIDGE NATIONAL LABORATORY  
P.O. BOX 2009, MS-8057  
OAK RIDGE, TN 37831  
USA

M. SARRAM  
UNITED ENGINEERS  
30 SOUTH 17TH ST.  
PHILADELPHIA, PA 19101  
USA

R. SCHNEIDER  
ABB COMBUSTION ENGINEERING  
1000 PROSPECT HILL ROAD  
WINDSOR, CT 06095  
USA

D. SCHRAMMEL  
KERNFORSCHUNGSZENTRUM  
WEBER STR  
KARLSNICHE, 7500  
GERMANY

B. SEHGAL  
ROYAL INSTITUTE OF TECHNOLOGY  
NUCLEAR POWER SAFETY  
S10044 STOCKHOLM, S10044  
SWEDEN

P. SEONG  
KOREA ADVANCED INSTITUTE OF SCI.  
373-1, KUSONG-DONG YUSUNG-GU  
DAEJON, 305-701  
KOREA

R. SHARMA  
AMERICAN ELECTRIC POWER  
ONE RIVERSIDE PLAZA  
COLUMBUS, OH 43215  
USA

J. SHEPHERD  
RPI  
DEPT. ME/JEC 2049  
TROY, NY 12180  
USA

K. SHIGAMATSU  
SHIKOKU ELECTRIC POWER CO., INC.  
2-5, MARUNOUCHI  
TAKAMATSU, 260  
JAPAN

E. SILVER  
OAK RIDGE NATIONAL LABORATORY  
P.O. BOX 2009, MS-8065  
OAK RIDGE, TN 37831  
USA

G. ROBINSON  
PENN STATE UNIVERSITY  
231 SACKETT BUILDING  
UNIVERSITY PARK, PA 16802  
USA

E. ROTH  
WESTINGHOUSE  
2061 BEECHWOOD BLVD.  
PITTSBURGH, PA 15217  
USA

H. SAKURAGI  
SHIKOKU ELECTRIC POWER CO., INC.  
6-1-2, MINATO-MACHI  
MATSUYAMA, EHIME 790  
JAPAN

O. SANDERVAAG  
SWEDISH NUCLEAR POWER INSTITUTE  
SEHLSTEDGT 11  
STOCKHOLM, 10252  
SWEDEN

K. SATO  
HITACHI, LTD.  
1-1, SAIWAI-CHO 3-CHOME  
HITACHI-SHI, IBARAKI-KEN 317  
JAPAN

J. SCHNEIDER  
ELECTRIC POWER RESEARCH INSTITUTE  
3412 HILLVIEW AVE, P.O. BOX 10412  
PALO ALTO, CA 94303  
USA

B. SCHWINGES  
GFS  
SCHWERTNERGASSE  
COLOGNE, FRG 5000  
GERMANY

J. SEMANCIK  
WESTINGHOUSE BETTIS LAB  
P.O. BOX 79  
W. MIFFLIN, PA 15122  
USA

S. SETH  
MITRE CORP.  
7525 COLSHIRE DR.  
MC LEAN, VA 22102  
USA

A. SHARON  
QUANTUM TECHNOLOGIES  
2562 BUTTERFIELD ROAD  
OAK BROOK, IL 60521  
USA

R. SHERRY  
GABOR KENTON & ASSOC.  
21733 BRINKMEADOW LANE  
GERMANTOWN, MD 20876  
USA

M. SHINKO  
EMERGENCY RESPONSE TEAM  
24405 CUTSAIL DR.  
DAMASCUS, MD 20872  
USA

F. SIMONEN  
PACIFIC NORTH-WEST LABORATORY  
P.O. BOX 999  
RICHLAND, WA 99352  
USA

M. FOELES  
ABB COMBUSTION ENGINEERING  
1000 PROSPECT HILL ROAD  
WINDSOR, CT 06095  
USA

M. FOUSH  
UNIVERSITY OF MARYLAND  
MATERIALS & NUCLEAR ENGINEERING  
COLLEGE PARK, MD 20742  
USA

J. SALUJA  
VIKING SYSTEMS INTERNATIONAL  
2070 WM. PITT WAY  
PITTSBURGH, PA 15238  
USA

G. SAPONARO  
ENEA-DISP  
VIA V. BRANCATI  
ROME, 00144  
ITALY

R. SCHMIDT  
SANDIA NATIONAL LABORATORY  
P.O. BOX 5800, DEPT. 6423  
ALBUQUERQUE, NM 87185  
USA

J. SCHOTT  
GILBERT/COMMONWEALTH, INC  
P.O. BOX 1498  
READING, PA 19606  
USA

S. SEALE  
INSTITUTE FOR CRUSTAL STUDIES  
U.C.S.B.  
SANTA BARBARA, CA 93106  
USA

Z. SENFU  
NUCLEAR POWER INSTITUTE OF CHINA  
P.O. BOX 436 (5001)  
CHENDU,  
CHINA

W. SHACK  
ARGONNE NATIONAL LABORATORY  
9700 S. CASS AVE, BLDG. 212  
ARGONNE, IL 60439  
USA

I. SHEPHERD  
CEC - IISPPA  
JRC ISPPA 21020  
SPRACUA,  
ITALY

M. SHIBA  
NUCLEAR POWER ENG. CORP.  
3-17-1 TORANOMON  
TOKYO, 105  
JAPAN

L. SIERKIN  
EG&G IDAHO  
P.O. BOX 1625  
IDAHO FALLS, ID 83415  
USA

L. SIMPSON  
AECL TECHNOLOGIES - WHITESHELL LABS  
WHITESHELL LABORATORIES  
PINAWA, MANITOBA RCE10  
CANADA

N. SIJ  
EG&G IDAHO  
P.O. BOX 1625, MS 2405  
IDAHO FALLS, ID 83415  
USA

G. SLOVK  
BROOKHAVEN NATIONAL LABORATORY  
BLDG. 475B  
UPTON, NY 11973  
USA

D. SMITH  
WYLE LABORATORIES  
1841 HILLSIDE AVENUE  
NORFOLK, CA 91760  
USA

B. SPLETZER  
SANDIA NATIONAL LABORATORY  
P.O. BOX 5800, DEPT. 6449  
ALBUQUERQUE, NM 87185  
USA

M. STRAND  
JUPITER CORP.  
2730 UNIV. BLVD.  
WHEATON, MD 20902  
USA

R. STUBBS  
UK NUCLEAR INSTALLATION INSP.  
NII, BAYNARD HSE, CHEPSHOW PLACE  
LONDON, W24TF  
UK

R. SUMMERS  
SANDIA NATIONAL LABORATORY  
P.O. BOX 5800, DEPT. 6418  
ALBUQUERQUE, NM 87185  
USA

J. SURSOCK  
ELECTRIC POWER RESEARCH INSTITUTE  
3412 HILLVIEW AVE, P.O. BOX 10412  
PALO ALTO, CA 94303  
USA

K. SUZAWA  
NUCLEAR POWER ENG. CORP.  
3-17-1 TORANOMON, MINATO-KU  
TOKYO, 105  
JAPAN

J. TAYLOR  
BROOKHAVEN NATIONAL LABORATORY  
BLDG. 130  
UPTON, NY 11973  
USA

G. THOMAS  
LAWRENCE LIVERMORE NATIONAL LAB  
P.O. BOX 808, L-196  
LIVERMORE, CA 94550  
USA

J. TILLS  
JACK TILLS & ASSOCIATES, INC.  
P.O. BOX 549  
SANDIA PARK, NM 87047  
USA

H. TORITA  
NUCLEAR POWER ENG. CORP.  
4-3-13, TORANOMON, MINATO-KU  
TOKYO, 105  
JAPAN

H. SJOVALL  
TVO POWER COMPANY  
SF-27160 OLKILUOTO

FINLAND

A. SMITH  
GILBERT COMMONWEALTH, INC  
P.O. BOX 1498  
READING, PA 19603  
USA

W. SPEKENS  
ATOMIC ENERGY CONTROL BOARD  
270 ALBERT ST.  
OTTAWA, ONTARIO K1P5S9  
CANADA

R. STARCK  
MPR ASSOCIATES  
1050 CONN. AVE. N.W.  
WASHINGTON, DC 20036  
USA

V. STRIZHOV  
NSI RUSSIA ACADEMY SCIENCE  
B. TULSKAYA  
MOSCOW, 113191  
RUSSIA

M. SUBUDHI  
BROOKHAVEN NATIONAL LABORATORY  
BLDG. 130  
UPTON, NY 11973  
USA

J. SUN  
ARGONNE NATIONAL LABORATORY  
9700 S. CASS AVE.  
ARGONNE, IL 60439  
USA

A. SUSLOV  
KURCHATOV INSTITUTE  
KURCHATOV SQUARE,  
MOSCOW, 123182  
RUSSIA

K. TAKUMI  
NUCLEAR POWER ENG. CORP.  
4-3-13, TORANOMON, MINATO-KU  
TOKYO, 105  
JAPAN

Z. TECHY  
INSTITUTE FOR ELECTRIC POWER RESEARCH  
ZRINYI U. 1.  
BUDAPEST, 1051  
HUNGARY

S. THOMPSON  
SANDIA NATIONAL LABORATORY  
P.O. BOX 5800, DEPT. 6418  
ALBUQUERQUE, NM 87185  
USA

T. TIMMONS  
WESTINGHOUSE  
P.O. BOX 355, MS ECE-3-09  
PITTSBURG, PA 15230  
USA

N. TRIKOURIS  
GPU NUCLEAR CORP.  
1 UPPER POND ROAD  
PARSIPPANY, NJ 07054  
USA

G. SLAUGHTER  
OAK RIDGE NATIONAL LABORATORY  
P.O. BOX 2008, BLDG. 4500S  
OAK RIDGE, TN 37831  
USA

O. SMITH  
OAK RIDGE NATIONAL LABORATORY  
P.O. BOX 2008, MS-6010  
OAK RIDGE, NY 37830  
USA

B. SPENSER  
ARGONNE NATIONAL LABORATORY  
9700 S. CASS AVE.  
ARGONNE, IL 60439  
USA

J. STAUDENMEIER  
PENN. STATE UNIVERSITY  
231 SACKETT BLD.  
UNIVERSITY PARK, PA 16802  
USA

E. STUBBE  
TRACEBEL  
AVE. ARIANE7  
BRUSSELS, BELGIUM 1200  
BELGIUM

L. SULLIVAN  
LOS ALAMOS NATIONAL LABORATORY  
P.O. BOX 1663, MS K557  
LOS ALAMOS, NM 87545  
USA

R. SUNDARAM  
YANKEE ATOMIC  
680 MAIN STREET  
BOLTON, MA 01740  
USA

A. SUWABE  
TAISEI CORPORATION  
1-25-1, NISHI-SHINJUKU SHINJUKU-KU  
TOKYO, 163  
JAPAN

M. TANEMURA  
MITSUBISHI  
2-4-1, SHIBAKOEN, MINATO-KU  
TOKYO, 105  
JAPAN

T. THEOFANOUS  
U.C. SANTA BARBARA  
DEPT. OF CHEMICAL ENGINEERING  
SANTA BARBARA, CA 93108  
USA

H. THORNBURG  
ABB COMBUSTION ENGINEERING  
901 S. WARFIELD DR.  
MT. AIRY, MDQ 21771  
USA

W. TONG  
ECE  
18101 VON KARMAN, SUITE 400  
IRVINE, CA 92715  
USA

H. TUOMISTO  
MATRAN VIOMA OY  
P.O. BOX 112  
VANTAA, SF-01601  
FINLAND

S. UENO  
MITSUBISHI  
2-3-6, OTEMACHI, CHIYODA-KU  
TOKYO, 100  
JAPAN

L. VALEO  
WESTINGHOUSE  
P.O. BOX 79  
W. MIFFLIN, PA 15122  
USA

R. VOGEL  
CONSULTANT  
3432 STONERIDGE COURT  
CALABASAS, CA 91302  
USA

C. WAITES  
AEA TECHNOLOGY  
INSPECTION VALIDATION CENTRE  
WARRINGTON, CHESHIRE WA36AT  
UK

B. WALSH  
SCIENCE & ENGINEERING ASSTS. , INC.  
1570 PACHECO, SUITE D-1  
SANTA FE, NM 87501  
USA

R. WATSON  
SANDIA NATIONAL LABORATORY  
P.O. BOX 5800  
ALBUQUERQUE, NM 87185  
USA

K. WHITT  
SOUTHERN NUCLEAR  
40 INVERNESS CENTER PARKWAY  
BIRMINGHAM, AL 35201  
USA

K. WILLIAMS  
SCIENCE APPLICATIONS INTERNATIONAL  
2109 AIR PARK RD S.E.  
ALBUQUERQUE, NM 87108  
USA

K. WINEGARDNER  
PACIFIC NORTHWEST LABORATORY  
P.O. BOX 999  
RICHLAND, WA 99352  
USA

S. WONG  
BROOKHAVEN NATIONAL LABORATORY  
BLDG. 130  
UPTON, NY 11973  
USA

D. WULLAERT  
SCIENCE APPLICATIONS INTERNATIONAL  
12850 MIDDLEBROOK ROAD, STE. 300  
GERMANTOWN, MD 20874  
USA

G. YADIGAROGU  
SWISS FEDERAL INST. OF TECHNOLOGY  
LAB. F. KERntechnik, ETH-ZENTRUM/CLT  
CH-8092 ZURICH,  
SWITZERLAND

T. YAMAMOTO  
JAPAN ATOMIC ENERGY RESEARCH INST.  
2-4 SHIRAKATA SHIRANE  
TOKAI-MURA, IBARAKI-KEN 319-11  
JAPAN

S. URATA  
KANSAI ELECTRIC POWER CO., INC.  
3-3-22, NAKANOSHIMA  
OSAKA, KITA-KU 530  
JAPAN

K. VALTONEN  
FINNISH CENTRE FOR RAD AND NUCL. SAFETY  
P.O. BOX 268  
HELSINKI, SF-00101  
FINLAND

B. VOLKOV  
OKB GIDROPPRESS  
ORDJONIKID ST. 21  
PODOLSK, RUSSIA 142103  
RUSSIA

J. WALKER  
AECL TECHNOLOGIES  
CHALK RIVER LABORATORIES  
DEEP RIVER, ONTARIO KOJ1JD  
CANADA

X. WANG  
ARGONNE NATIONAL LABORATORY  
9700 S. CASS AVE. BLDG. 308  
ARGONNE, IL 60439  
USA

D. WHITEHEAD  
SANDIA NATIONAL LABORATORY  
P.O. BOX 5800, DEPT. 6412  
ALBUQUERQUE, NM 87185  
USA

V. WILLEMS  
GILBERT/COMMONWEALTH, INC  
P.O. BOX 1498  
READING, PA 19603  
USA

J. WILSON  
AEA TECHNOLOGY  
B10-28, HARWELL LABORATORY  
OXFORD, OXFORDSHIRE OX110RA  
UK

S. WINGATE  
HALLIBURTON NUS  
910 CLOPPER ROAD  
GAITHERSBURG, MD 20878  
USA

J. WRIGHT  
MODELING & COMPUTING SERVICES  
39675 CEDAR BLVD.  
NEWARK, CA 94560  
USA

R. WYMAN  
LAWRENCE LIVERMORE NATIONAL LAB  
P.O. BOX 808  
LIVERMORE, CA 94550  
USA

T. YAMADA  
NUCLEAR POWER ENG. CORP.  
4-3-13, TORANOMON, MINATO-KU  
TOKYO, 105  
JAPAN

N. YAMANO  
JAPAN ATOMIC ENERGY RESEARCH INST.  
2-4 SHIRAKATA SHIRANE  
TOKAI-MURA, IBARAKI-KEN 319-11  
JAPAN

T. VACCARO  
GENERAL ELECTRIC - KAPL  
BOX 1072  
SCHENECTADY, NY 12301  
USA

R. VIJAYKUMAR  
ENERGY RESEARCH INC.  
6290 MONTROSE ROAD  
ROCKVILLE, MD 20852  
USA

W. VON RIESEMANN  
SANDIA NATIONAL LABORATORY  
P.O. BOX 5800  
ALBUQUERQUE, NM 87185  
USA

D. WALLACE  
NIST  
KLOPPER RD  
GAITHERSBURG, MD 20899  
USA

Z. WANG  
FAUSKE & ASSOCIATES, INC.  
16W070 83RD ST.  
BURR RIDGE, IL 60517  
USA

R. WHITSEL  
NUMARC  
1776 EYE ST. NW, SUITE 300  
WASHINGTON, DC 20006  
USA

A. WILLEMS  
NUCLEAR ELECTRIC  
BOOTH'S HALL, KNUTSFORD  
CHESHIRE, WA168Q9  
UK

T. WILSON  
LOS ALAMOS NATIONAL LABORATORY  
P.O. BOX 1663, MS K557  
LOS ALAMOS, NM 87545  
USA

M. WITTE  
LAWRENCE LIVERMORE NATIONAL LAB  
P.O. BOX 808  
LIVERMORE, CA 94551  
USA

A. WRIGHT  
OAK RIDGE NATIONAL LABORATORY  
P.O. BOX 2009, MS-8057  
OAK RIDGE, TN 37831  
USA

A. YABUUCHI  
NUCLEAR POWER ENG. CORP.  
4-3-13, TORANOMON, MINATO-KU  
TOKYO, 105  
JAPAN

H. YAMAGATA  
AGENCY OF NATURAL RESOURCES & EN  
1-3-1, KASUMIGASEKI, CHIYODA-KU  
TOKYO, 100  
JAPAN

J. YAMASHITA  
HITACHI, LTD.  
3-1-1, SAIWAI-CHO  
HITACHI-SHI, IBARAKI-KEN 317  
JAPAN

H. YASUI  
TOKYO ELECTRIC POWER CO.  
1901 L STREET N.W. SUITE 720  
WASHINGTON, DC 20036  
USA

M. YUANYOU  
NUCLEAR POWER INSTITUTE OF CHINA  
P.O. BOX 436 (500)  
CHENGDU,  
CHINA

G. ZIGLER  
SCIENCE AND ENGINEERING ASSTS, INC.  
6100 UPTOWN BLVD. NE SUITE 700  
ALBUQUERQUE, NM 87110  
USA

K. YOON  
B&W NUCLEAR SERVICE CO.  
3315 OLD FOREST ROAD  
LYNCHBURG, VA 24501  
USA

T. YUASA  
MITSUBISHI  
2-4-1, SHIBAKOEN, MINATO-KU  
TOKYO, 105  
JAPAN

P. ZMOLA  
C&P ENGINEERING  
5409 NEWINGTON ROAD  
BETHESDA, MD 20816  
USA

R. YOUNGBLOOD  
BROOKHAVEN NATIONAL LABORATORY  
BLDG. 130  
UPTON, NY 11973  
USA

D. ZANOBETTI  
UNIV. OF BOLOGNA  
2 V RISORGIMENTO  
BOLOGNA,  
ITALY

R. ZOGRAN  
MPR ASSOCIATES  
1050 CONN. AVE. N.W.  
WASHINGTON, DC 20036  
USA

**PROCEEDINGS OF THE  
TWENTIETH WATER REACTOR SAFETY INFORMATION MEETING  
October 21-23, 1992**

**CONTENTS - VOLUME 2**

	<u>Page</u>
ABSTRACT .....	iii
GENERAL INDEX .....	v
REGISTERED ATTENDEES .....	vii

**SEVERE ACCIDENT RESEARCH I**

Chairperson: F. Eltawila

Some Results of Steam Explosion Research at UCSB .....	1
T. Theofanous, W. Yuen, S. Angelini, X. Chen (UCSB)	
MACE Core Coolability Test M1B .....	17
M. Farmer, B. Spencer (ANL), B. Sehgal (EPRI)	
Melt Attack and Penetration of Radial Concrete Structures Cooled by Outside Water .....	29
H. Alsmeyer (KfK)	
Results of ORNL VI Series Fission Product Release Tests .....	49
M. Osborne, R. Lorenz (ORNL)	
The Probability of Mark I Liner Attack .....	79
T. Theofanous, H. Yan (UCSB)	

**SEVERE ACCIDENT RESEARCH II**

Chairperson: C. Tinkler

Progress in BNL High-Temperature Hydrogen Combustion Research Program .....	89
G. Ciccarelli, T. Ginsberg, J. Boccio, J. Curtiss, C. Economos, J. Jahelka (BNL), K. Sato (NUPEC)	
Hydrogen Combustion Research at RPI .....	101
J. Shepherd, J. Krok, (RPI)	
Experimental Results of Integral Effects Tests with 1/10th Scale Zion Subcompartment Structures in the Surtsey Test Facility .....	119
M. Allen, M. Pilch, R. Griffith, T. Blanchat (SNL)	
Separate Effect Simulation Experiment on Corium Dispersion in Direct Containment Heating .....	149
M. Ishii, S. Revankar, G. Zhang, Q. Wu, P. O'Brien (Purdue U.)	

## CONTENTS - VOLUME 2 (Cont'd)

	<u>Page</u>
Results of Direct Containment Heating Integral Experiments at 1/40th Scale at Argonne National Laboratory . . . . .	171
J. Binder, L. McUumber, B. Spencer (ANL)	

### SEVERE ACCIDENT RESEARCH III

Chairperson: A. Rubin

Effect of Reactor Vessel Internal Melting Upon Release of BWR Core Debris . . . . .	197
M. Podowski (RPI)	
VICTORIA-Experiments for Hydrogen Distribution in an Ice Condenser Containment . . . . .	229
O. Hongisto, K. Lammila, H. Tuomisto (IVO)	
The Calculation Programme to Prepare the First Phebus FP Test . . . . .	243
A. Mailliat, F. Serre (CEA), A. Jones, I. Shepherd (JRC)	
COPO: Experiments for Heat Flux Distribution From a Volumetrically Heated Corium Pool . . . . .	265
O. Kymäläinen, K.O. Hongisto, J. Antman, H. Tuomisto (IVO), T. Theofanous (UCSB)	
Results From In-Reactor Severe Fuel Damage Tests That Used Full-Length Fuel Rods and the Relevancy to LWR Severe Accident Melt Progression Safety Issues . . . . .	275
F. Panisko, N. Lombardo (PNL)	
Status of ICARE Code Development and Assessment . . . . .	301
G. Hache, R. Gonzalez, B. Adroguer (CEA)	

### SEVERE ACCIDENT RESEARCH IV

Chairperson: R. Lee

VICTORIA-92 and Its Application to the Phebus-FPT0 Test . . . . .	323
N. Bixler, T. Heames, D. Powers (SNL)	
SCDAP/RELAP5/MOD3 Code Development . . . . .	343
C. Allison, L. Siefken, E. Coryell (INEL)	
ESTER - A European Severe Accident Code System . . . . .	363
A. Jones, I. Shepherd (CEC/JRC)	

## CONTENTS - VOLUME 2 (Cont'd)

	<u>Page</u>
MELCOR Verification, Benchmarking, and Applications Experience at BNL . . . . . I. Madni (BNL)	383
Analysis with MELCOR of FPs and Core Materials Release and Transport During Three Accidents in a PWR Plant . . . . . A. Alonso, S. Aleza, J. Fernandez, F. Gonzalez, E. Hontanon, J. Lopez, F. Martin-Fuertes, I. Mas, J. Sanchez (Madrid Polytechnical U.)	401
MELCOR Assessment at SNL . . . . . L. Kmetyk (SNL)	419
<b>THERMAL HYDRAULICS</b> Chairperson: D. Bessette	
Peak Cladding Temperature in LOFT Large Break Transients . . . . . V. Berta, R. Hanson, G. Johnsen, R. Schultz (INEL)	445
Natural Circulation Under Severe Accident Conditions . . . . . D. Pafford, D. Hanson (INEL), V. Tung (Aerospace Corp.), S. Chmielewski (Detroit Edison)	461
PWR Depressurization Analyses . . . . . D. Brownson, C. Dobbe, D. Knudson (INEL)	485
Risk Impact of Two Accident Management Strategies . . . . . S. Dingman, A. Camp (SNL)	511
Identification and Assessment of BWR In-Vessel Severe Accident Mitigation Strategies . . . . . S. Hodge, J. Cleveland, T. Kress, M. Petek (ORNL)	529

# SOME RESULTS OF STEAM EXPLOSION RESEARCH AT UCSB

T.G. Theofanous, W.W. Yuen, S. Angelini and X. Chen  
Center for Risk Studies and Safety  
Department of Chemical and Nuclear Engineering  
University of California, Santa Barbara  
Santa Barbara, CA 93106

## ABSTRACT

The latest results in several fundamental and applied areas of steam explosions research at UCSB are presented. These include: (a) experimental data and PM-ALPHA predictions of premixing under well-controlled conditions, (b) experimental data and interpretations (using the ESPROSE code) of fragmentation kinetics in a simulated steam explosion environment, and (c) integral simulations of premixing and explosion propagation in the KROTOS 1-D facility and in reactor-relevant geometries and conditions. We can conclude that reasonable assessments of energetics for safety purposes are well within reach.

## 1. INTRODUCTION AND OVERVIEW

This is the final presentation on a 3-year research effort in several key aspects of steam explosions carried out at UCSB. This work has been summarized in a soon-to-appear NUREG/CR report (Theofanous et al., 1993); thus, our purpose here is to provide only some highlights. Our experimental/analytical tools are MAGICO/PM-ALPHA and SIGMA/ESPROSE for the premixing and propagation phenomena, respectively.

In the area of premixing, the primary focus is on quantifying the "water depletion phenomenon." This phenomenon refers to the rapid depletion of the mixing zone in water content as a result of boiling and steam carryover. The phenomenon has been quantified for in-vessel explosions with the help of the PM-ALPHA code (Amarasooriya and Theofanous, 1991), and one key aspect of this study was to test the three-fluid aspects of the computation. The MAGICO facility was built for this purpose—the high temperature material in the pour is solid, of a fixed (uniform) particle size. The main experimental challenge was to measure the local water volume fraction transients, and it was met with the development (Angelini et al., 1991; Yan et al., 1992) of a new instrument called FLUTE (for Fluorescence Technique).

In the area of propagation, the SIGMA facility was used to subject single droplets of melt (tin), at temperatures up to 1000 °C, to varying amplitude shock waves, up to 20 MPa. In this way, for the first time, the fragmentation process could be observed under pressure, as in the "reaction" zone of a detonation wave. Fragmentation and mixing (with surrounding water) were obtained from quantitative radiography using Flash X rays. These (fragmentation and mixing) phenomena, and implied thermal interactions, provide the essential feedback in the propagation process, as it develops from an initial trigger to a fully-developed detonation. We conclude that

thermally-driven fragmentation can interact significantly with the hydrodynamic fragmentation mechanisms, depending in a rather complicated manner on both the melt temperature and the shock pressure.

Regarding integral application, especially to reactor geometries, two-dimensionality is a fundamental feature of both premixing and propagation. Accordingly, both PM-ALPHA and ESPROSE employ two-dimensional, three-fluid models. This work culminates with application of these tools to the integral, essentially 1-D experiments in the KROTOS facility, the 2-D premixing experiments in the FARO facility and several in-vessel and ex-vessel reactor cases of interest.

## 2. HIGHLIGHTS ON PREMIXING

The basic concept of the experiment is illustrated in Figure 1. Tens-of-kilograms quantities of mm-sized steel balls are heated to a uniform temperature (up to 1000 °C), then transferred to an intermediate container equipped with a dumping mechanism, and within a few seconds are released into a pool of saturated (atmospheric pressure) water. The pool cross section is rectangular, 40.5 cm on the side. The major experimental parameters are pool depth (15, 25 and 50 cm), particle size (1.5 and 2.4 mm), particle temperature (600 to 1000 °C), pour diameter (12 and 20 cm), and particle entry velocity (corresponding to free fall from 5, 15, and 25 cm, with an initial velocity of 0.72 m/s). The initial velocity was obtained from high-speed movies and found to be independent of particle size or the particle depth in the intermediate container. From this and the measured total mass pour rate, the particle volume fraction at the outlet of the intermediate container could also be obtained as 1.87 and 2.5% for the 2.4 and 1.5 mm particles, respectively. Temperature losses in the intermediate container were minor, and the actual temperature of the particulate just before being released was reported.

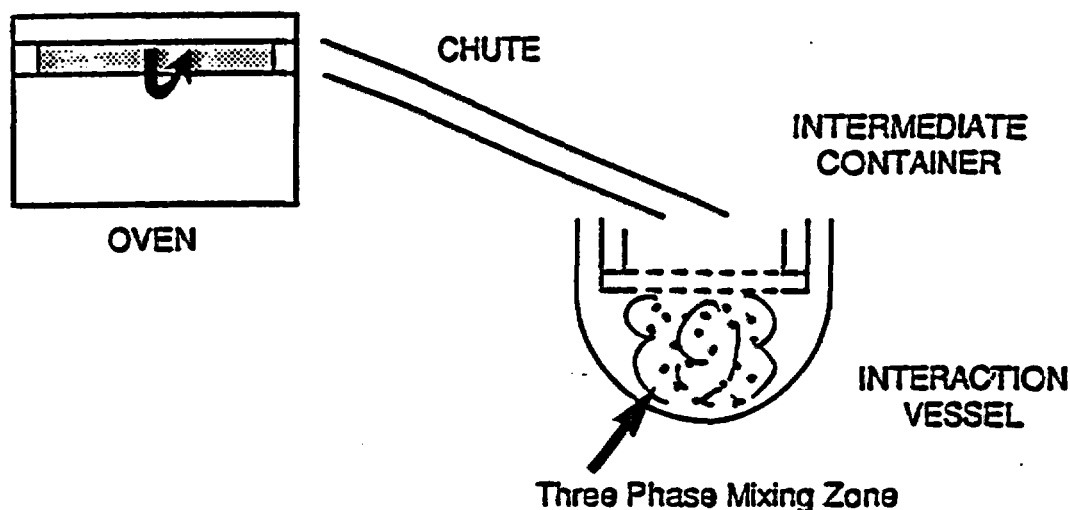


Figure 1. Schematic of the MAGICO experiment.

The actual flow field employed in PM-ALPHA is illustrated in Figure 2. All geometric features and inlet conditions are specified for each experiment, as discussed above, except for the vent openings. Since in the experiment the pool top was completely open to the atmosphere, the only requirement is that these vent openings are chosen of large enough area to avoid any pressurization in the vapor space. Cell sizes are 2.0 cm in the radial direction and 2.5 cm in the axial direction, which gives 10 radial cells and 12-26 axial cells, depending on tank depth and free-fall region. Node size studies showed that this is adequate.

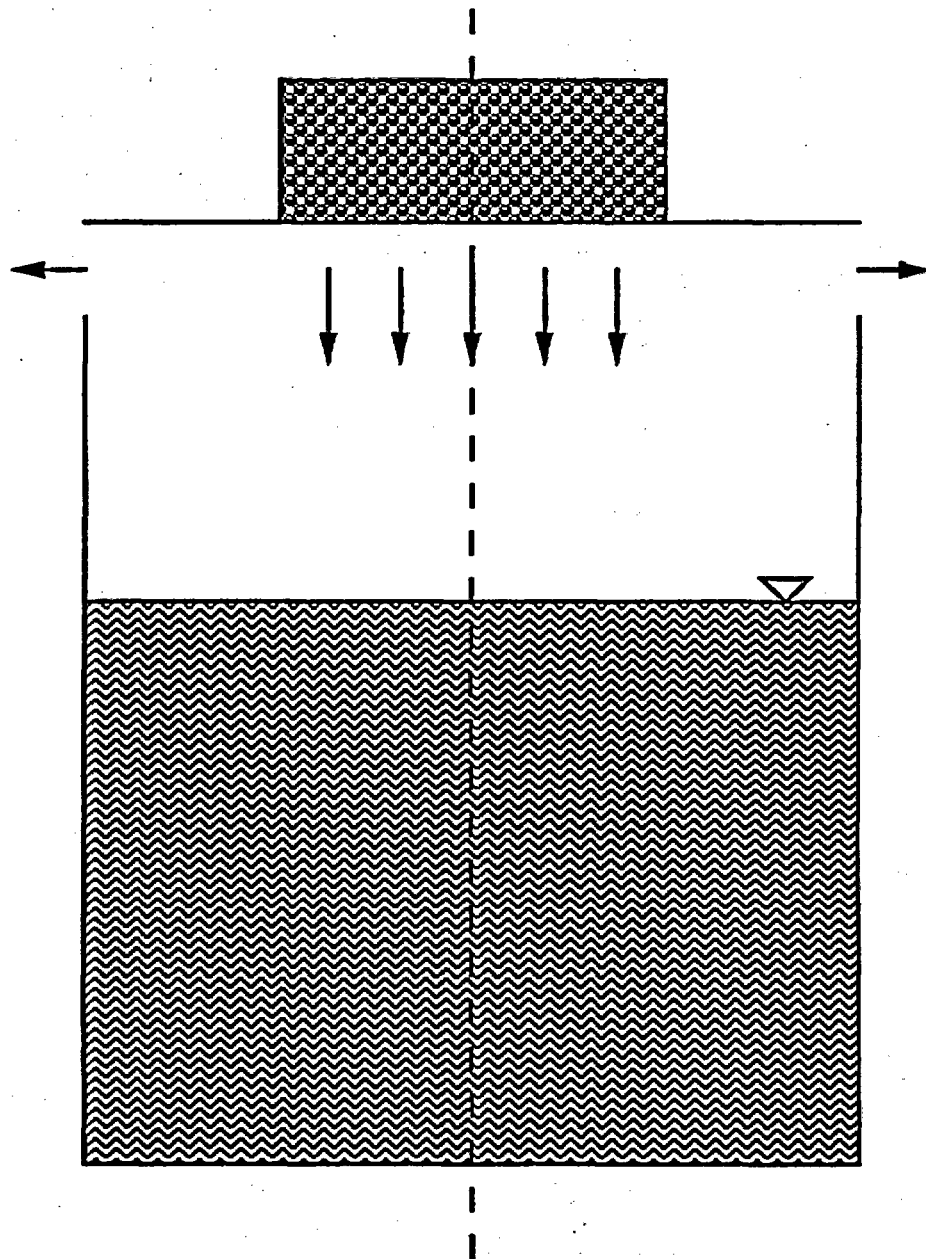


Figure 2. Illustration of the flow field utilized in PM-ALPHA for the interpretation of the MAGICO experiment.

The experimental data consist of mixing-zone-average void fractions obtained from high-speed movies (from the level rise around the mixing zone), and local void-fraction transients using a new instrument, the FLUTE. Both of these quantities can be easily obtained from the results of the PM-ALPHA computations for comparison with the data, and such comparisons have been reported previously (Angelini et al., 1992; Theofanous et al., 1992) with very good agreement. A sample result is illustrated in Figure 3. Also, chordal-average steam volume fractions can be obtained for comparisons with the projection-type information obtained from X-ray radiography, as shown in Figure 4. These comparisons are also very good. Finally, we have also studied the detailed features of the interaction, again with PM-ALPHA (Angelini et al., 1993). The key result here is the identification of a "reversal of water volume flux" phenomenon, which we believe relates to, and explains, an experimentally-found sudden increase in steam generation rate under certain conditions during the premixing transient. Referring to Figure 5, which illustrates this situation as predicted by PM-ALPHA, one can see that in the early stages of the pour, the water in the mixing region is pushed down and to the sides, inducing a motion in the water surrounding it that for the one-half of the flow field depicted in Figure 5 is counterclockwise. At later times, this motion reverses as the mixing region becomes largely void of water and a hydrodynamically unbalanced situation causes the surrounding water to flow into the region, clockwise in Figure 5. We believe that this reversal of water flux causes a strong counter-current melt-water contact and an associated rapid increase in steam generation rates, as illustrated in Figure 6; accordingly, the resulting phenomenon is termed ETHICCA (Energetic Transfer of Heat in a Counter-Current Ambient).

### 3. HIGHLIGHTS ON PROPAGATION

The SIGMA facility is a hydrodynamic shock tube, capable of generating  $\sim 2.5$  millisecond pressure waves in water of amplitude up to 100 MPa. It is equipped with a window for observation, and the instrumentation included pressure transducers, high-speed camera, and a flash X-ray generator. Molten tin drops are generated by a specially-designed inductively heated melt generator that can release high reproducible single drops at any temperature desired, up to 1500 °C. The drops are hit by the shock wave as they fall through water in film boiling; the two events are synchronized so that the interaction zone is within the area of the window at the time selected for observation. At this time, we have results for two shock levels, 6.6 and 20 MPa, and various temperatures of the melt drops up to 1000 °C.

A sample of the fragmentation/mixing morphologies is shown in Figure 7, which led to the concept of microinteractions (Yuen et al., 1992). The idea is that the fragmented melt-drop mass (called debris) is not mixed with the whole quantity of coolant available, but only with that contained in a small zone around the melt drop. As seen in Figure 7, this zone grows and convects with time, and the actual constitutive behavior, necessary to compute the pressure feedback from this interaction in numerical simulations of explosions, can be obtained from the quantitative interpretation of such radiographs (Yuen et al., 1992). As a first attempt to approximate this microinteraction behavior (this is the ESPROSE, a version of the code), we applied ESPROSE such that the computational cells containing the fuel were small enough to contain roughly an equal volume of water (Yuen et al., 1992). In particular, we simulated in this fashion the KROTOS-21 and KROTOS-26 tests run with tin and aluminum oxide melts, respectively (Yuen and Theofanous, 1993). An illustration of the agreement obtained with the experimental data is given in Figure 8. An explicit treatment of the microinteractions (this is

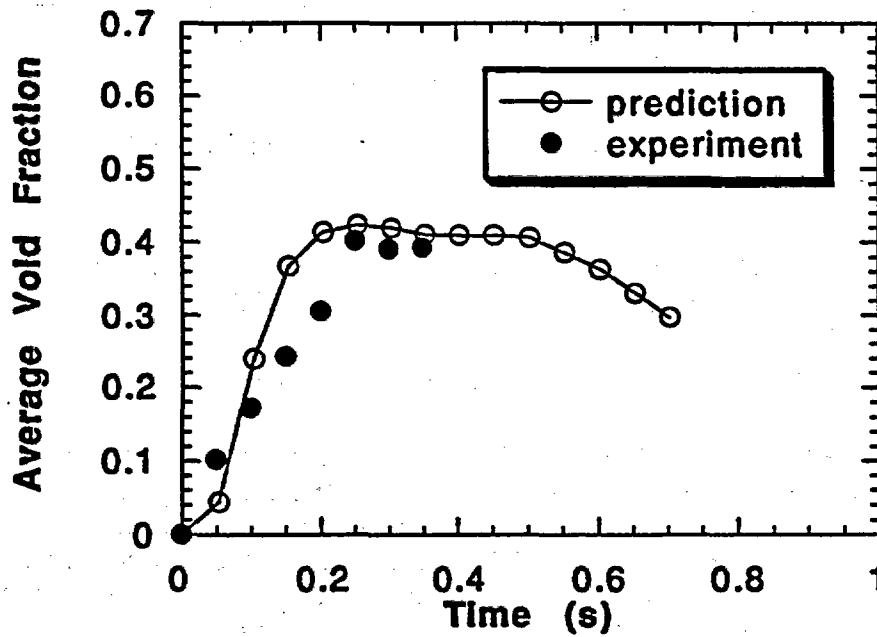
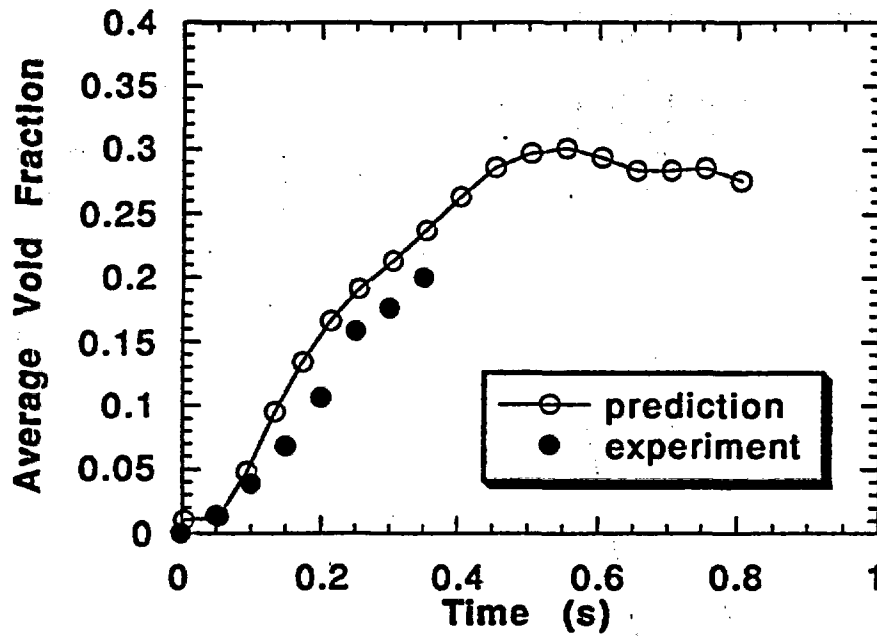


Figure 3. The pool-depth-average (top) and mixing-zone-average (bottom) void fraction transients for run #905 obtained from high-speed movies.

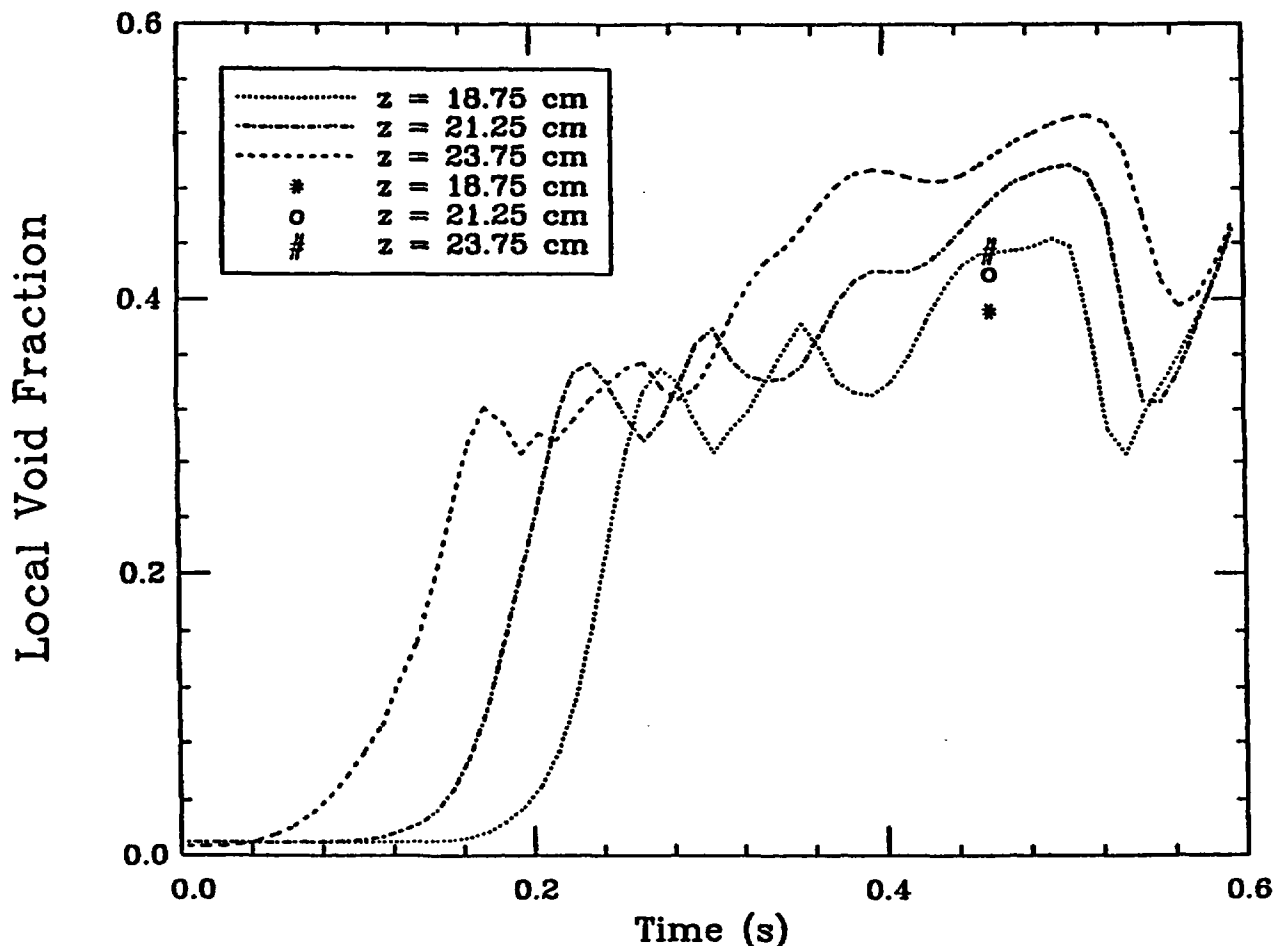


Figure 4. Comparison between prediction and X-ray measurement for run #1005 for cell centered at  $r = 1$  cm and three different heights.

the ESPROSE.m version of the code) and initial results showing a decisive improvement in the quality of simulation can be found in Yuen and Theofanous (1993).

#### 4. HIGHLIGHTS ON REACTOR APPLICATIONS

At this time, we have available results from one in-vessel and two ex-vessel integral pre-mixing/propagation calculations made with reactor geometries. All calculations were run with PM-ALPHA and EXPROSE.a, and they are to be updated when ESPROSE.m results become available. Still, the results are illustrative of the capability, and they do convey clearly the importance of void in the mixing zone and of the two-dimensionality. They also convey clearly the importance of the inertia constraint (pool depth) on the loading developed on the side walls—these would be the cavity or pedestal walls—as can be deduced by comparing the results in Figures 9 and 10 for the 1- and 3-meter pool cases, respectively. These calculations were run with a melt pour through a 0.6 m in diameter hole in the reactor vessel, with initial melt volume fraction of 0.05, accelerated under gravity to 7.4 and 9.7 m/s at the time of entering the 3- and

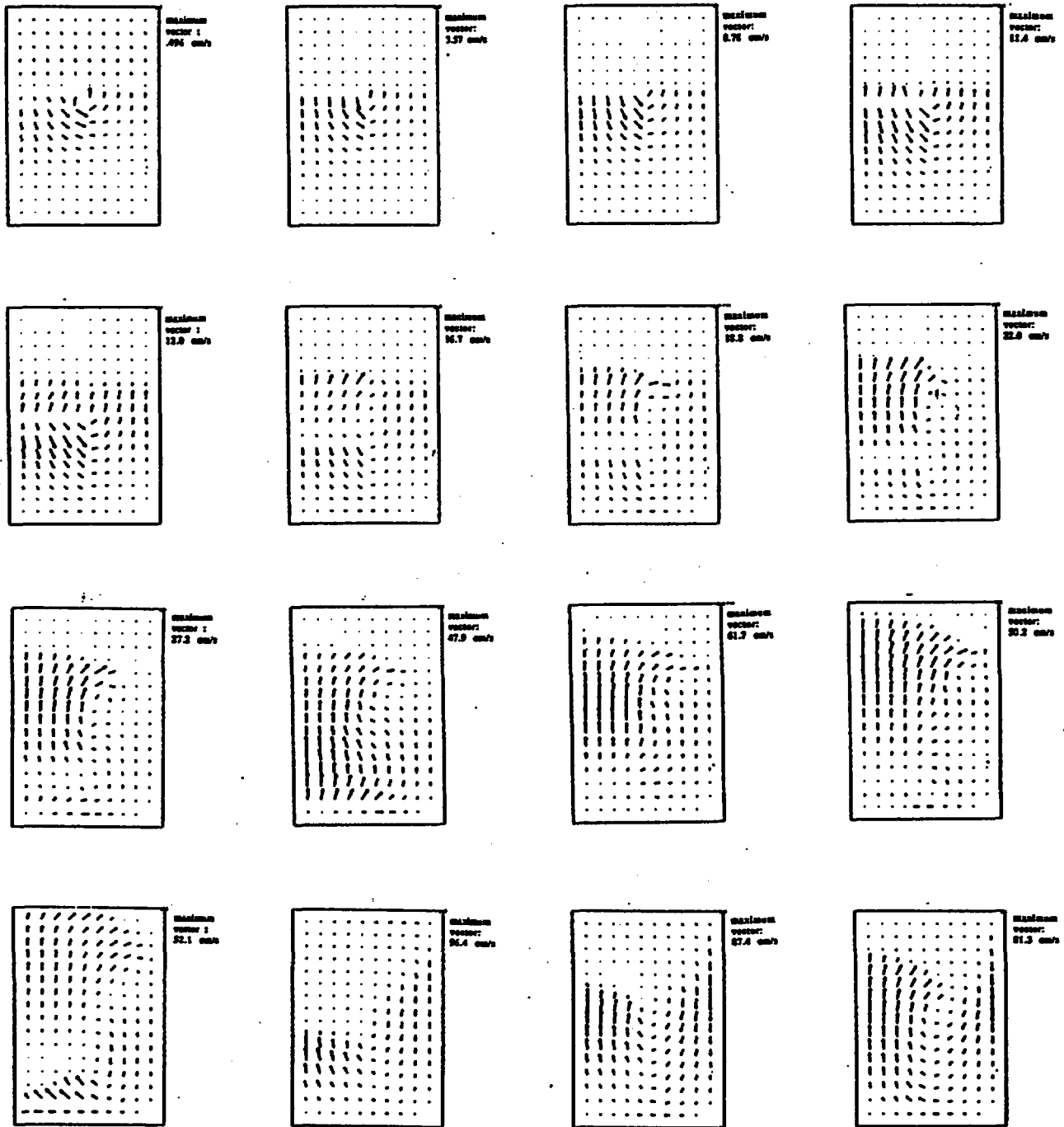


Figure 5. Evolution of water volume flux in numerical simulation of run #702. Upper two rows, times (from impact of balls on the water) are .004 s, .054 s, .104 s, .154 s, .204 s, .254 s, .304 s, .354 s; lower two rows, times (from impact of balls on the water) are .404 s, .454 s, .504 s, .554 s, .604 s, .654 s, .704 s, .754 s.

1-m pool, respectively. The explosion was initiated by a rather strong trigger (one cell containing 100 bar steam, suddenly released), and the development of the pressure field through escalation in the mixing zone, dynamically coupled to the surrounding water, is illustrated in Figures 11 and 12.

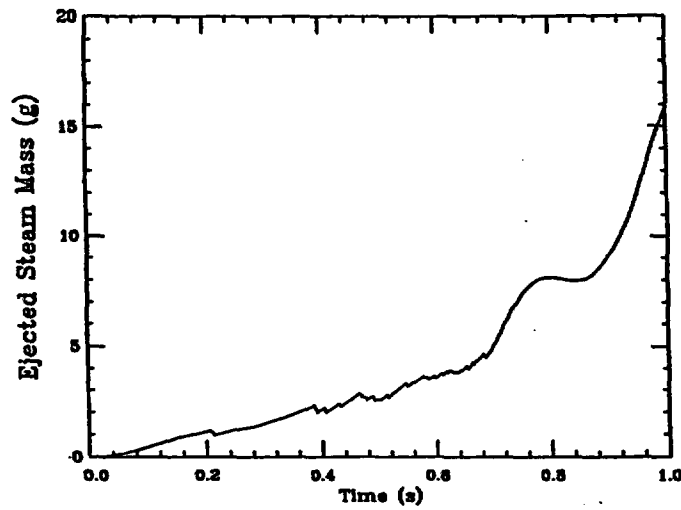


Figure 6. Mass of steam ejected through venting cell in numerical simulation of run #702.

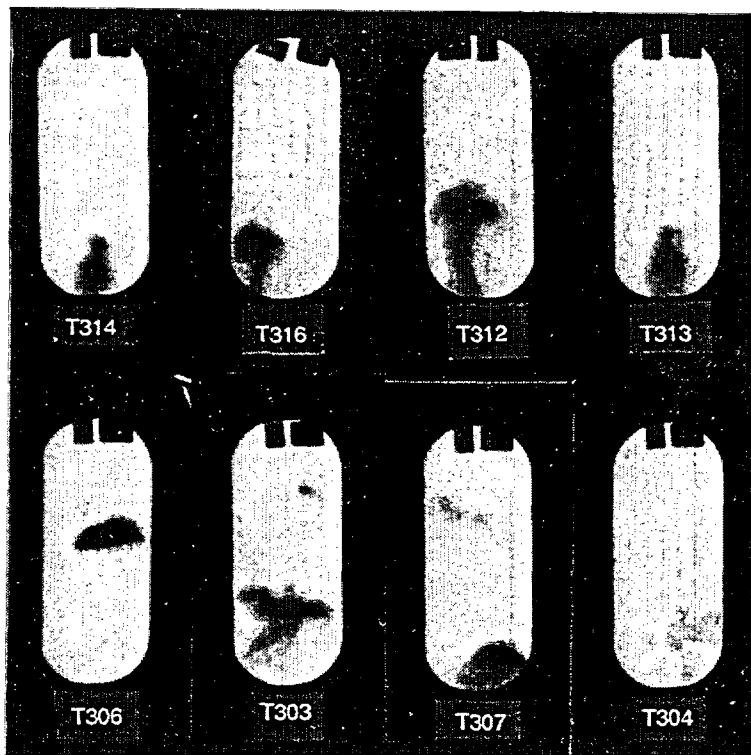


Figure 7. X-ray snapshots from the runs with 200 bar shocks. Tin temperatures of 1000 °C and 670 °C for the top and bottom rows, respectively. Times (in ms) following shock arrival: T314-0.75, T316-0.85, T312-1, T313-1.5, T306-0.75, T303-1, T307-1.5, T304-2.

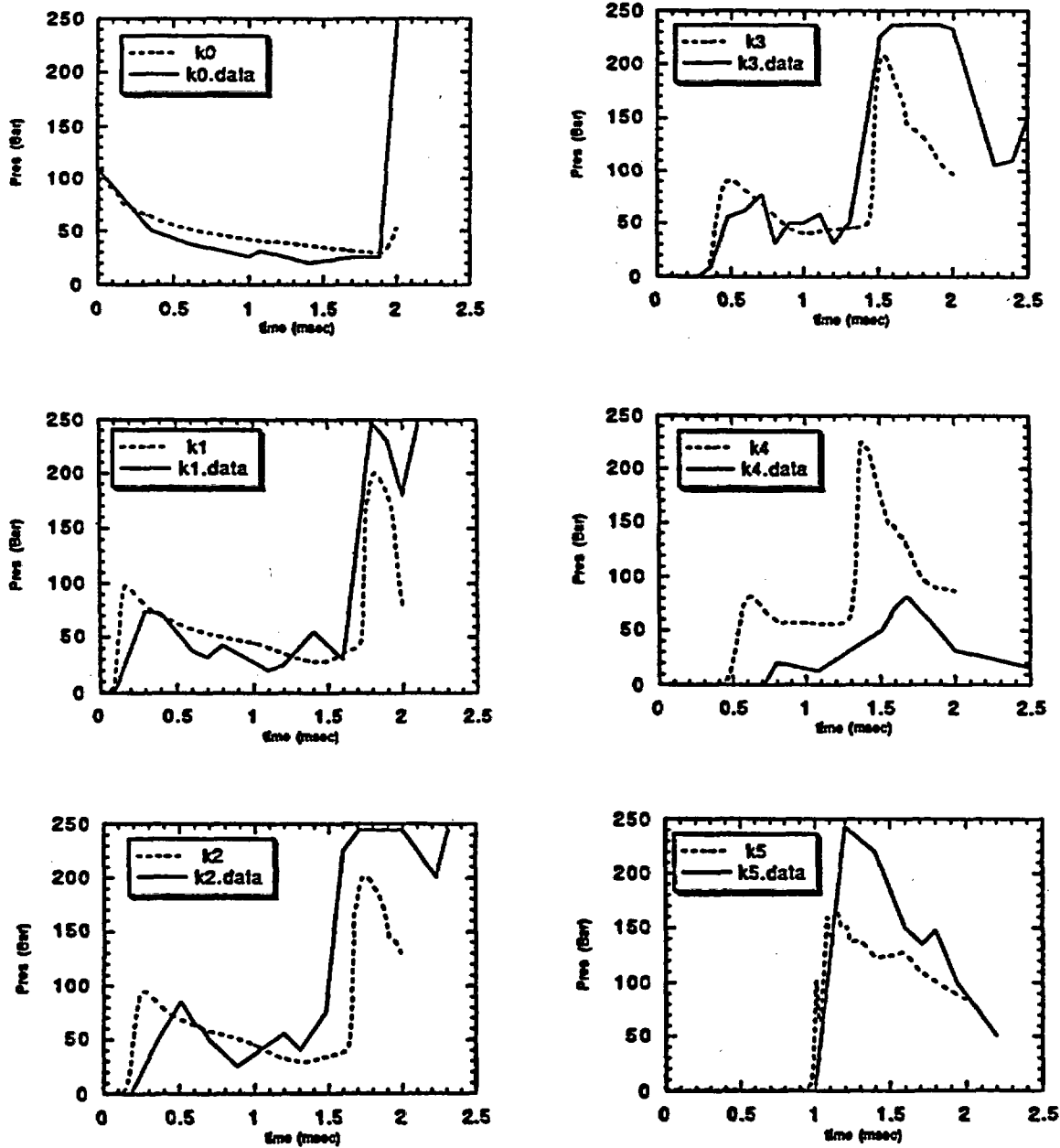


Figure 8. The propagation in KROTOS-26 as calculated by ESPROSE.a, compared to experimental data.

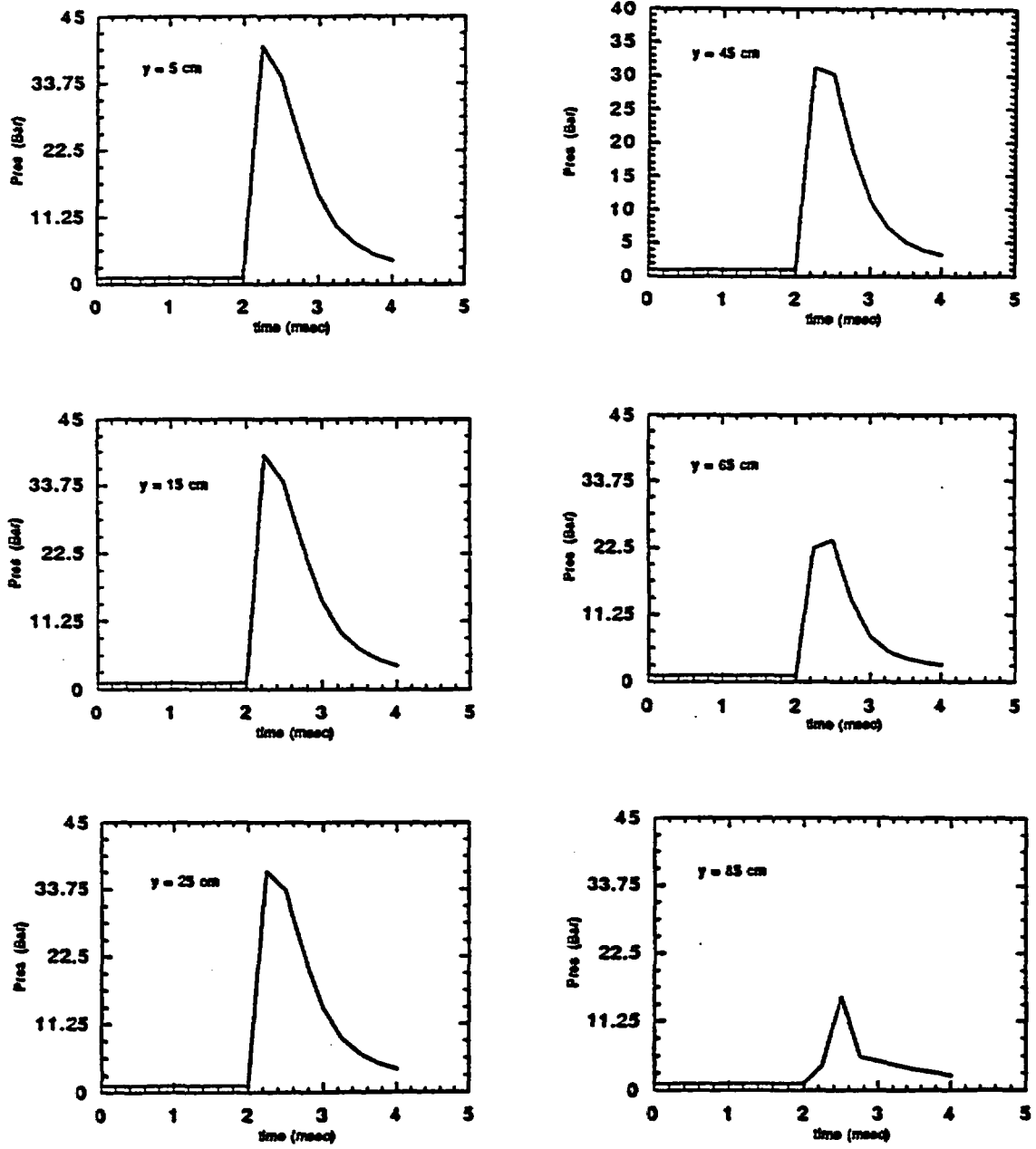


Figure 9. Calculated pressure pulses on the sidewall of the 1-meter pool.

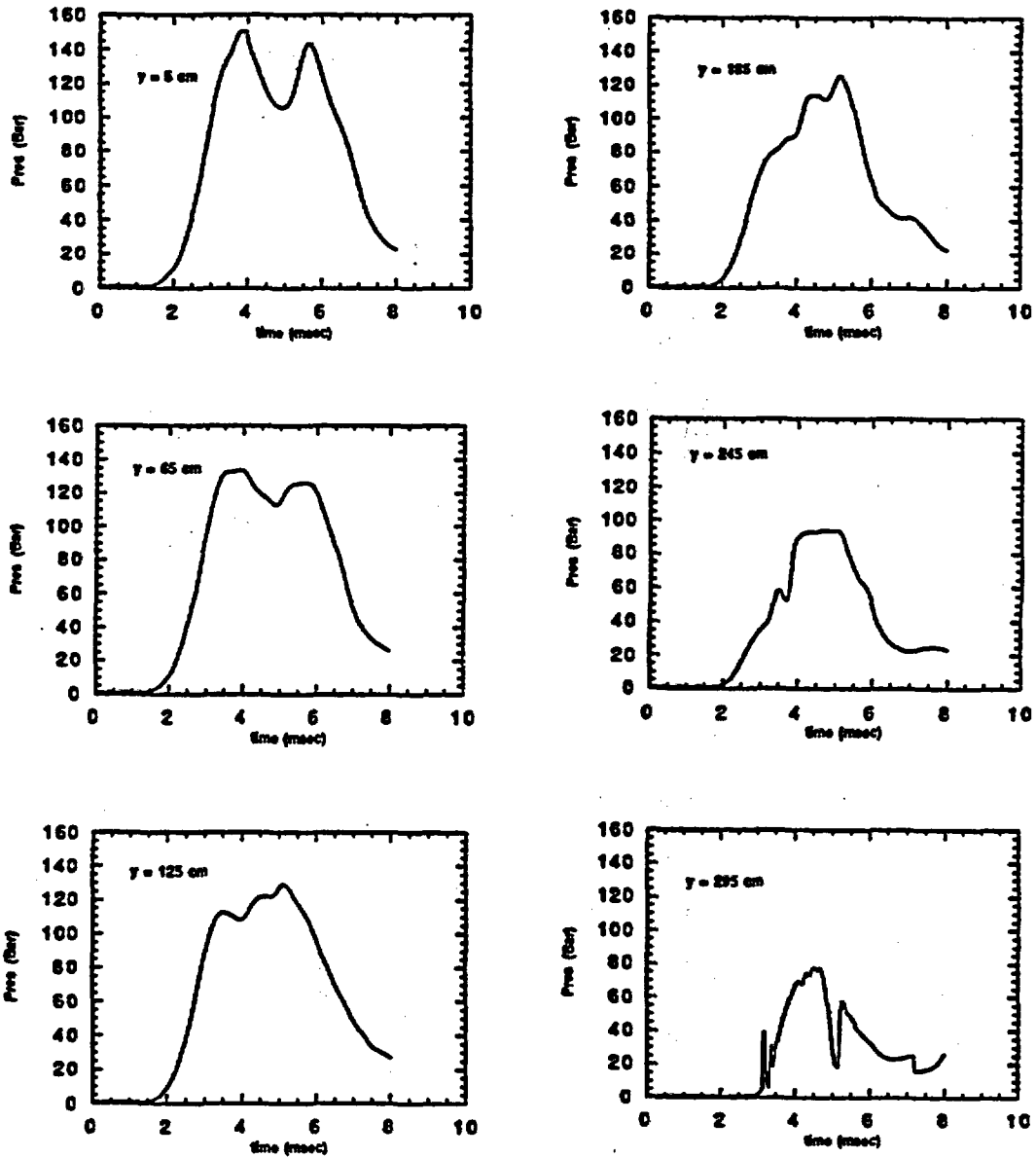


Figure 10. Calculated pressure pulses on the sidewall of the 3-meter pool.

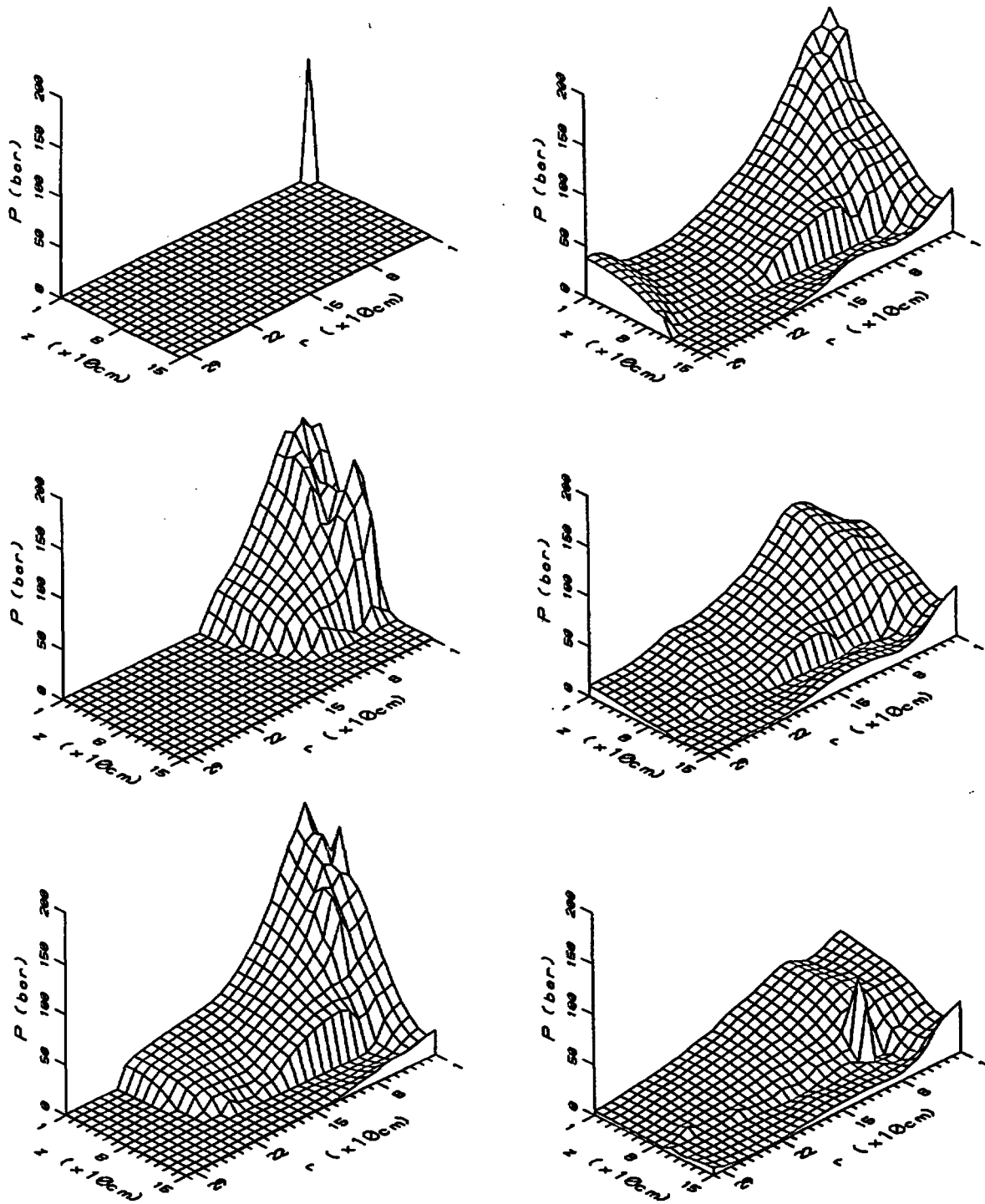


Figure 11. Triggering, escalation and associated pool dynamics, including wave reflection at the walls, for the 1-meter case. ( $f_f = 4$ ,  $f_v = 0.05$ ; plots are made at .8 ms increments starting from top left down at time zero.)

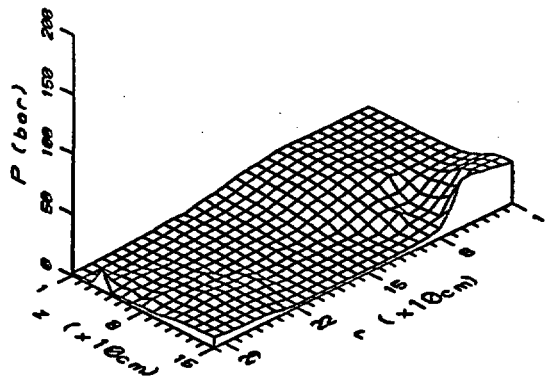
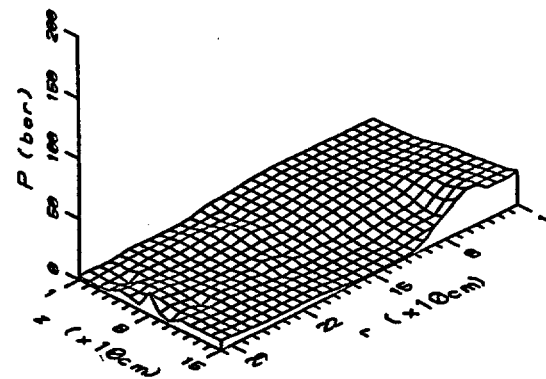
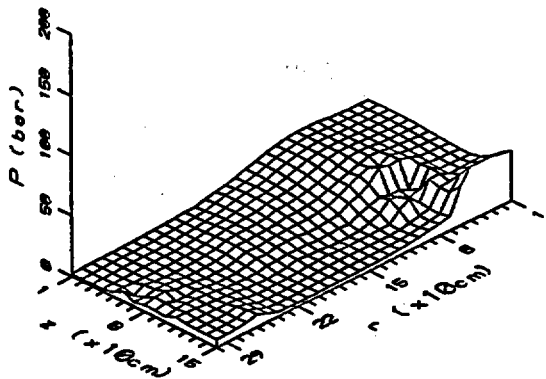
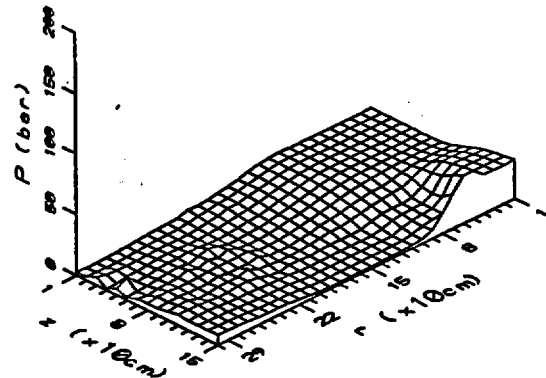
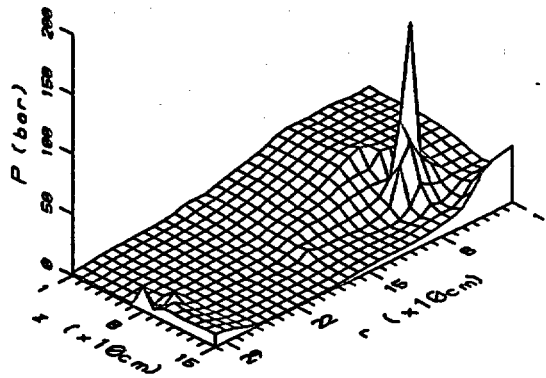


Figure 11. (cont.)

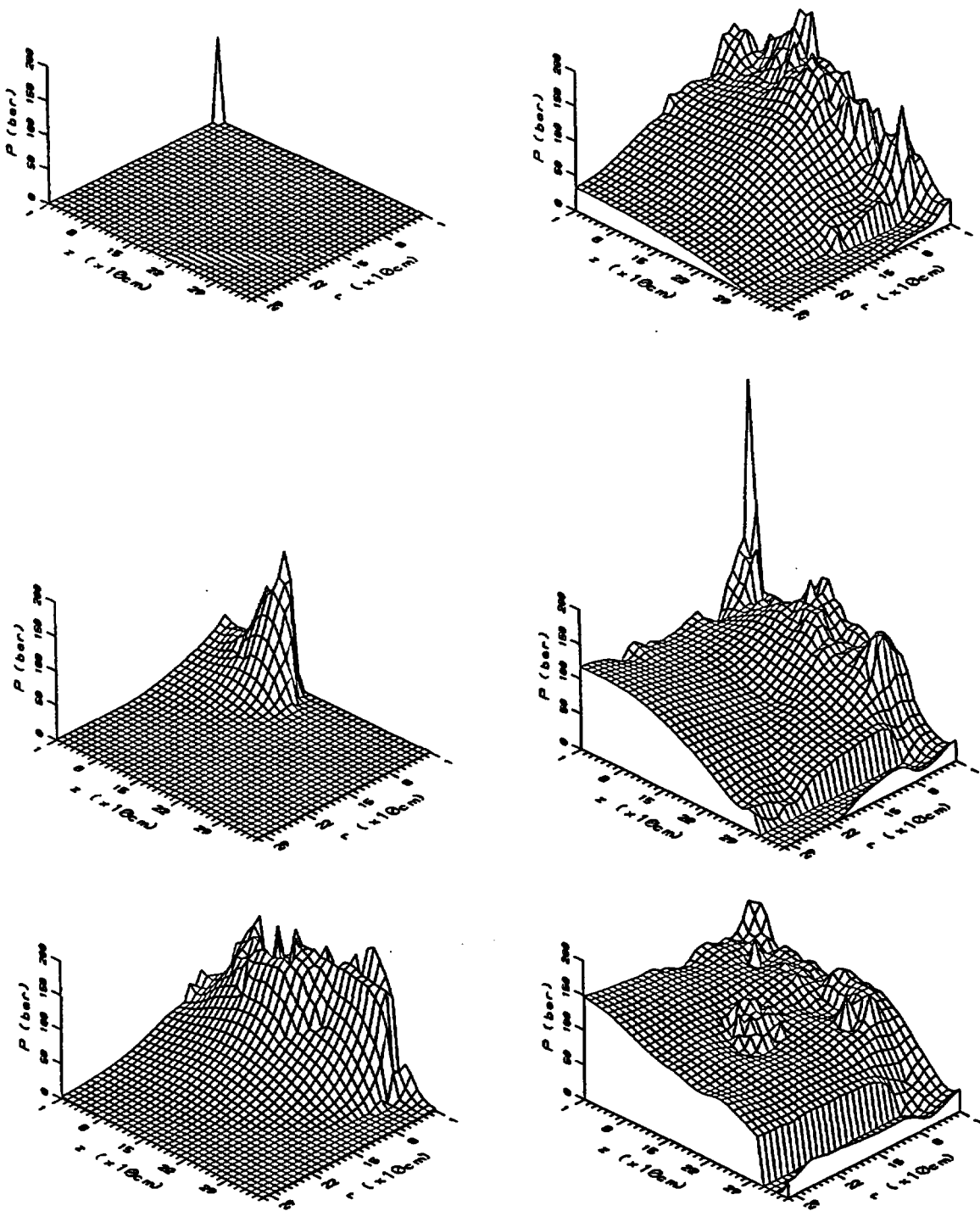


Figure 12. Triggering, escalation and associated pool dynamics, including wave reflection at the walls, for the 3-meter case. ( $f_f = 4$ ,  $f_v = 0.05$ ; plots are made at .8 ms increments starting from top left down at time zero.)

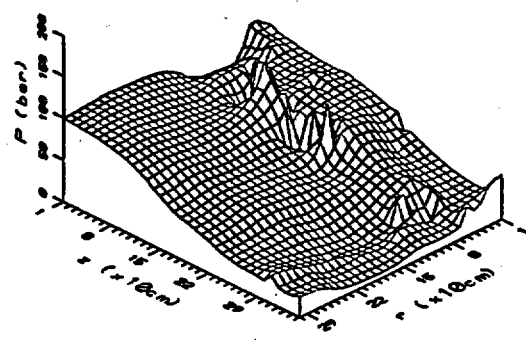
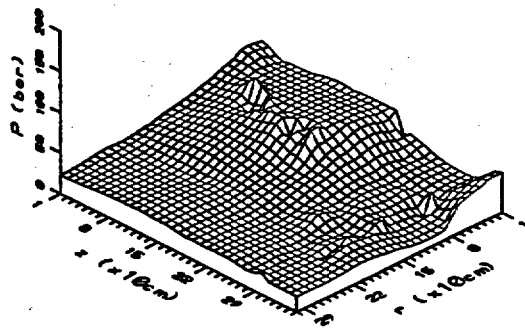
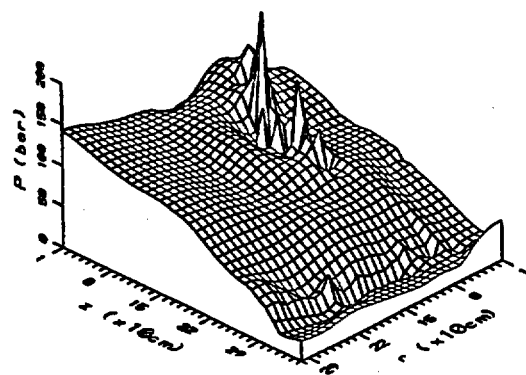
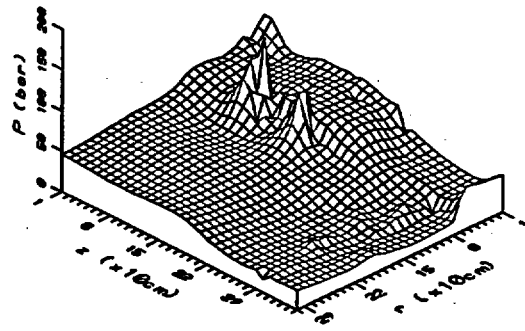
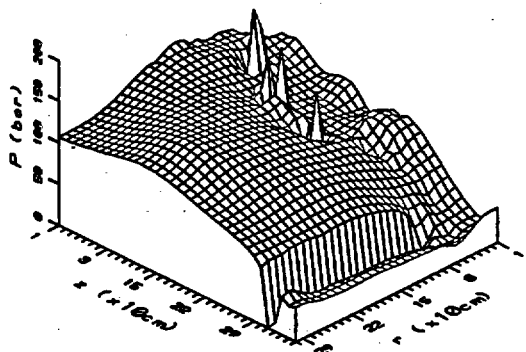


Figure 12. (cont.)

## 5. CONCLUSIONS

- The water depletion phenomenon has been confirmed experimentally and interpreted quantitatively (PM-ALPHA).
- Thermal augmentation of fragmentation kinetics has been found experimentally under conditions relevant to steam explosions (sustained pressure). Characterization of these fragmentation rates and related microinteractions zone is possible through the use of flash X rays.
- Quantitative interpretations of the first data that exhibit supercritical detonations has been possible through the use of the concept of microinteractions and of ESPROSE.a. Illustrative reactor calculations indicate that void in the premixing zone interferes with escalation, and that two-dimensionality is critical to quantify explosion "venting" from water pools.

## ACKNOWLEDGMENTS

This work was supported by the U.S. Nuclear Regulatory Commission under contract No. 04-89-082.

## REFERENCES

1. Amarasooriya, W.H. and T.G. Theofanous (1991) "Premixing of Steam Explosions: A Three-Fluid Model," *Nuclear Engineering & Design* 126, 23-39.
2. Angelini, S., W.M. Quam, W.W. Yuen and T.G. Theofanous (1991) "FLUTE: FLUorescent TEchnique for Two-Phase-Flow Liquid-Fraction Measurements," Proceedings 1991 ANS Winter Meeting, San Francisco, CA, Nov. 1991.
3. Angelini, S., E. Takara, W.W. Yuen and T.G. Theofanous (1992) "Multiphase Transients in the Premixing of Steam Explosions," Proceedings NURETH-5, Salt Lake City, UT, September 21-24, 1992, Vol. II, 471-478.
4. Angelini, S, W.W. Yuen and T.G. Theofanous (1993) "Premixing-Related Behavior of Steam Explosions," CSNI Specialists Meeting on Fuel-Coolant Interactions, Santa Barbara, CA, January 5-8, 1993.
5. Theofanous, T.G., W.W. Yuen, S. Angelini and X. Chen (1992) "Physics of Steam Explosions," Presented to CSARP Meeting, Bethesda, MD, May 4-8, 1992.
6. Theofanous, T.G., W.W. Yuen, S. Angelini, X. Chen, W.H. Amarasooriya and S. Medhekar (1993) "Steam Explosions: Fundamentals and Energetic Behavior," to be published as a NUREG/CR report.
7. Yan, H., W.W. Yuen and T.G. Theofanous (1992) "The Use of Fluorescence in the Measurement of Local Liquid Content in Transient Multiphase Flows," Proceedings NURETH-5, Salt Lake City, UT, September 21-24, 1992, Vol. V, 1271-1278.
8. Yuen, W.W., X. Chen and T.G. Theofanous (1992) "On the Fundamental Microinteractions That Support the Propagation of Steam Explosions," Proceedings NURETH-5, Salt Lake City, UT, September 21-24, 1992, Vol. II, 627-636.
9. Yuen, W.W. and T.G. Theofanous (1993) "The Prediction of 2D Thermal Detonations and Resulting Damage Potential," CSNI Specialists Meeting on Fuel-Coolant Interactions, Santa Barbara, CA, January 5-8, 1993.

**MACE Core Coolability  
Test M1B**

by

**M. T. Farmer and B. W. Spencer  
Engineering Development Laboratories  
Reactor Engineering Division  
Argonne National Laboratory  
Argonne, Illinois 60439**

**B. R. Sehgal\*  
Electric Power Research Institute  
3412 Hillview Avenue  
Palo Alto, CA 94303**

**ABSTRACT**

The Melt Attack and Coolability Experiment (MACE) Program underway at Argonne National Laboratory is addressing the efficacy of water to terminate an accident if it results in a molten corium/concrete interaction (MCCI) in the reactor containment. Large-scale experiments are being conducted involving the addition of water to an MCCI already underway. The experiments utilize prototypic  $UO_2/ZrO_2/Zr$  corium mixtures, and various types of concrete basemats. This paper provides a summary of MACE Core Coolability Test M1B, which investigated the interaction of 416 kg of 70% oxidized PWR corium with a limestone/common sand concrete basemat. Sustained internal heat generation in the melt was achieved through Direct Electrical Heating (DEH); the initial decay heat level corresponded to 350 W/kg  $UO_2$ , which simulates decay heating at about two hours after the accident starts. After a specified depth of concrete erosion, a selected mass of water was added over a selected time interval, with makeup to maintain a constant water level over the melt. The results from the experiment indicate a strong proclivity for water to mitigate the MCCI. In the first several minutes following water addition, the melt temperature was observed to drop by several hundred degrees Kelvin; similar dramatic decreases were seen in the downward erosion and noncondensable gas release rates. After six hours of operation with water present atop the melt, the basemat erosion rate had been reduced to less than 5% of that observed prior to water addition.

\* Nuclear Power Safety, Royal Institute of Technology, S-100 44 Stockholm, Sweden

## INTRODUCTION

The reactor risk studies such as NUREG-1150 have focused attention on sequence specific phenomena pertaining to postulated core melt accident scenarios in light-water reactor systems. One such issue involves the coolability of a molten pool of core materials (corium) accumulated in the vessel lower head or on the concrete basemat of the reactor containment building. The coolability issue pertains to the efficacy of a water layer above the dense corium insofar as removing not only the sensible energy of the corium layer (quench process) but also the fission product decay heat which is a continuous source of internal heat generation. An unsuccessful outcome means that the molten pool would continue its downward migration through the bottom of the reactor vessel and subsequently into the concrete basemat itself. A successful outcome would render the bed quenched and cooled by virtue of heat extracted by water, thereby terminating the accident progression so long as an adequate, continuous supply of water is available. The melt coolability issue has a direct bearing on accident management strategies for current LWRs, as well as accident mitigation design criteria for advanced LWRs.

The elements needed to assess melt coolability under Molten Corium Concrete Interaction (MCCI) conditions are: (a) an understanding of the controlling physical phenomena and parameter ranges (e.g., melt surface state, melt temperature, and water subcooling), (b) models to calculate corium quench and cooling, and (c) a relevant database to validate the quench and cooling models. To date, a limited amount of quenching data using near-prototypic materials has been reported in the literature. The SWISS and WETCOR programs at Sandia National Laboratory (1, 2) provided valuable information on the quenching behavior of both metallic and oxidic melts interacting with concrete. However, the extrapolation of these tests results to the reactor case is limited by the scale of the experiments and the absence of an appreciable fraction of prototypic oxidic melt constituents.

Under sponsorship from the ACE International Consortium, USDOE, USNRC, and EPRI, the Melt Attack and Coolability Experiment (MACE) Program is intended to provide information on the quenching behavior of prototypic oxide melt under MCCI conditions. The experiment philosophy focuses on acceptance and utilization of the database through elimination of scale and material questions (distortions) to the greatest extent possible. Features of the MACE tests include: (1) essential vertical dimensions are full scale (melt and water depths), (2) realistic PWR corium composition, (3) realistic melt temperatures and material properties, (4) realistic MCCI initial conditions, and (5) realistic internal heat generation rates.

This paper summarizes the experiment results from MACE Test M1B, which is the third in a series of large-scale melt coolability experiments performed at Argonne National Laboratory (ANL). Test M1B was performed on April 13, 1992. The experiment investigated the interaction of a 70% oxidized pressurized water reactor (PWR) corium melt with a limestone/common sand concrete basemat in the presence of a water overlayer at nominally atmospheric pressure.

## OBJECTIVES AND APPROACH

The general objectives of the MACE Program are two-fold:

1. determine the ability of water to quench and thermally stabilize a corium melt during the MCCI stage of a postulated ex-vessel severe LWR accident, and
2. enable characterization of the resulting debris for assessment of permanent coolability.

Specifically, the MACE experiments are intended to provide data on the nature and timescale of the melt/water quench process in conjunction with the time-dependent heat transport rates from the melt to the surroundings, i.e., to the overlaying water and the concrete basemat.

The experiment approach for MACE Test M1B was to investigate the interaction of 416 kg of 70% oxidized PWR corium (75 wt.%  $UO_2$ , 16 wt.%  $ZrO_2$ , 3 wt.% Zr, 6 wt.% concrete decomposition products) with a limestone/common sand concrete basemat. Sustained internal heat generation in the melt was achieved through Direct Electrical Heating (DEH); the target decay heat level corresponded to 350 W/kg  $UO_2$ , which simulates decay heating at about two hours after the accident starts. After a specified depth of concrete erosion, a selected mass of water was added over a selected time interval, with makeup to maintain a constant water level over the melt. An instrumented steam condensation system was utilized to measure the time-dependent heat removal rate from corium by the water overlayer. Due to the presence of water in conjunction with the high temperature melt, the experiment was conducted in a highly reinforced containment cell for safety considerations.

## MACE TEST FACILITY

The system for conducting the MACE Tests consists of a test apparatus, a power supply for direct electrical heating of the corium, a water supply system, a steam collection and condensation system, a ventilation system to filter and exhaust the off-gases, and a data acquisition system (DAS). A schematic illustration of the facility is shown in Figure 1. The principal components of the apparatus for containment of the concrete basemat and corium inventory consists of a bottom support plate, three sidewall sections, and an upper enclosure lid. The lower and middle test sections are fabricated from castable  $MgO$ , while the upper section and lid are fabricated from locally obtained limestone/common sand concrete. The overall height of the apparatus is 285 cm. The concrete basemat, located at the bottom of the test section, is heavily instrumented with Type K thermocouples (TCs) to measure downward erosion and heat transfer rates, in addition to high temperature (Type C) TCs in tungsten thermowells to measure MCCI-zone temperatures at a variety of radial and axial locations. The sidewalls of the lower test section are also instrumented with multiple high temperature arrays at various elevations to access heat losses from the MCCI zone to the sidewalls. The initial corium powder charge is placed atop the basemat. The specific loading for MACE Test M1B is shown in Table 1. The charge is in the form of crushed  $UO_2$  pellets (unirradiated) plus particles of  $ZrO_2$  and a typically small amount of concrete decomposition product oxides  $CaO$ ,  $SiO_2$ . Their presence creates a lower, more prototypic melting temperature than

a pure  $UO_2$ - $ZrO_2$  system, and furthermore can be rationalized from consideration of concrete erosion when the melt flows from the breached vessel onto the basemat floor (3). A region of  $UO_2$  crushed pellets is initially heated by tungsten heater elements until electrical conduction is established. The zone initially experiences localized melting, and then eventually grows to encompass nearly all the loaded powders as the DEH power is gradually increased. Zirconium metal intended to participate in the MCCI is incorporated through a distinct layer separating the corium powders from the concrete basemat. The Zr metal is thus the last material to be melted into the charge before concrete ablation begins, thereby precluding premature oxidation of the metal during the powder heatup phase.

A unique operational aspect of the MACE tests has been the use of insertable lance probes which enter the test section through sealed penetrations in the lid of the apparatus. A total of four probes were used in MACE Test M1B; three of these probes were utilized for melt diagnostics, while the fourth was dedicated to an insertable video camera for viewing the melt surfaces after water was added. The three lance diagnostics probes were designed to perform two functions: (i) crust buster mode -- removal of residual powders/crust adhering to the test section sidewalls before water was added, and (ii) crust diagnostics mode -- detect the presence/absence of a crust and also measure the crust surface elevation/temperature after water was added. The first operational mode was motivated by the results of MACE Test M1, in which a partially sintered crust completely covered the melt surface at the time water was added (4). The crust busting mode thus provided the capability for removing unmelted material from atop the melt during the preheat, thereby insuring proper test initial conditions.

At a specified depth of concrete erosion, water addition atop the melt is initiated. As shown in Figure 1, water is delivered from the supply tank to two wiers located at the top of the test section in the walls adjacent to those having the electrodes. Initially, water is added steadily until a 50 cm head is established above the melt layer as recorded by redundant head measuring devices in the test section. Thereafter, water is added intermittently to maintain a 50 +/-10 cm level as boiloff progresses. The vertical dimension of the test section (285 cm) is sized such that roughly the upper one meter would be available for water droplet settling even if the corium and water pools are churn-turbulent owing to the vigorousness of gas sparging. Thermocouples in the test section plenum measure water and cover gas temperatures. Multiple thermocouple arrays embedded in the test section sidewalls above the melt surface monitor the sidewall heatup and quenching behavior. The TC arrays thus allow the net melt/water heat flux to be evaluated from an overall system energy balance which considers the heat transfer contribution from structure above the melt.

A large gas line is present in the top cover to duct dilution gas, noncondensable offgas, and steam to the adjacent quench tank. The quench tank provides a mass of water to condense transported steam and to cool other gases. Condensate spills over and is collected in the overflow tank. The quench tank has a cooling coil to maintain the water inventory in a subcooled state. The cooling coil, quench tank, and overflow tank are instrumented with flowmeters, thermocouples, level sensors, and pressure transducers in order to monitor the transient state of the system and extract the necessary heat balance information. Downstream from the quench tank is a spray tank which performs a redundant quench/gas cooldown function. While adding redundancy, the use of two quench tanks in

series is designed to enhance resolution of the energy transport measurement.

This overcomes the practical difficulty of attempting to make energy transport measurements equivalent to melt-to-water heat fluxes ranging from as high as 5 MW/m<sup>2</sup> during a postulated early bulk cooldown stage to as low as a few hundred or less kW/m<sup>2</sup> depending upon possible crust behavior. Both low and high energy transport rates can be reliably measured with the approach described here.

The argon dilution gas and noncondensable offgas species (CO<sub>2</sub>, CO, H<sub>2</sub>) are cooled to room temperature by transport through the quench tank and spray tank, and exit the system through an exhaust line at the top of the spray tank. The line includes a demister, filter, gas flowmeters, and a gas mass spectrometer which evaluates the time-dependent off-gas composition. The off-gas is released into the exhaust line of the containment cell ventilation system where it flows, further diluted, through a final cleanup system before being released from the building stack.

With the exception of the data acquisition system (DAS), the MACE test apparatus is housed within an explosion-rated containment cell used for a (dismantled) research reactor. The containment cell provides convenient radiological control as well as protection from postulated end-of-spectrum steam explosion and hydrogen behavior effects.

## TEST OPERATIONS

Test Specifications for MACE Test M1B are summarized in Table 2. The target decay heat level, simulated by direct electrical heating (DEH), was 350 W/kg UO<sub>2</sub>, which corresponds to a net power input level of 108 kW for the initial 309 kg UO<sub>2</sub> inventory (see Table 1). Pretest analyses based on the anticipated test operating conditions indicated that melt zone heat losses to the MgO sidewalls would range from ~40 kW at the start of basemat ablation, down to ~20 kW after water was added. Thus, a gross initial power level of 130 kW was adopted for the test, of which 108 kW simulated decay heat, and 22 kW compensated for anticipated sidewall heat losses. The power supply operating mode after water addition into the test section was specified as constant voltage<sup>1</sup> at the voltage level observed just prior to water addition. The two criteria for water addition were established as: (i) ablation of the concrete basemat to a depth of 1.3-2.5 cm, and (ii) the top surface of the corium pool was molten.

Test operations began after the reference covergas flowrate was established and the gas mass spectrometer was calibrated. During the initial heatup phase, all current passed through the tungsten heater elements which were connected to the two sets of electrodes near the top of the corium charge. The temperature of the corium in and around the elements gradually increased until electrical conductance was established. The power was then steadily increased until the

---

<sup>1</sup>The constant voltage operating mode is appropriate with water present since it conserves the specific power density in the melt zone and is independent of melt height participating in the MCCI. This approach is warranted since the DEH technique does not appreciably heat quenched debris. Thus, operation at constant power would lead to unprototypically high power densities should a significant melt quench front develop during the test.

reference 130 kW level was reached at ~2 hours after electrical conductance was first established.

After maintaining the gross power input constant at 130 kW for ~20 minutes, the experiment operators noted that the current was starting to stabilize, implying that the melt zone was approaching equilibrium size at the 130 kW power level. As a result, the power was increased at a rate of ~1 kW/min up to ~190 kW, which was reached ~1 hour prior to the start of concrete ablation. The power was held near this level until the onset of ablation was imminent, at which point it was reduced to the reference 130 kW level. The total duration of the corium preheat was ~6 hours.

During the initial stage of the preheat, overburden collapse exposed the melt surface, which grew laterally as the melt front progressed downward towards the basemat. As time progressed, however, a "skeleton crust" spanning the electrode sidewalls developed above the melt surface. Two attempts were made to dislodge the skeleton crust with the lance probes during the preheat, but neither attempt was successful. As the ablation front reached the zirconium layer atop the basemat,  $H_2$  and CO concentrations increased substantially in the offgas. The view of the melt surface began to deteriorate rapidly as the aerosol production rate increased. The skeleton crust was still visible atop the melt at this time. The view of the melt surface continued to deteriorate, and by the time basemat ablation began the test section had become completely opaque. At this point, the lance probes were inserted in a final attempt to dislodge the skeleton crust. These efforts continued until the probe measurements indicated that the skeleton crust had been dislodged (i.e., elevation measurements indicated that the probe tips had penetrated below the projected melt surface location, and temperatures recorded by the high thermocouples at the probe tips indicated contact with melt). Thus, final preparations for water addition were made, including switching the power supply operating mode from constant power to constant voltage. The addition of water to the test section was initiated at 14.7 minutes into basemat ablation. The water acted to clear the test section plenum of aerosol revealing the corium surface. The lid video camera recorded the continued presence of the skeleton crust with large holes in the south and east quadrants, through which the melt was clearly visible. This observation, in conjunction with posttest examinations, indicate that the skeleton crust did not significantly inhibit initial melt/water contact.

In accordance with test specifications, the power supply operating voltage was held constant at the level observed immediately prior to the water addition until 91 minutes after the start of ablation. At this point the voltage was increased by 8% to account for increased melt resistivity due to the incorporation of concrete decomposition products into the melt. The power supply voltage was then maintained constant until 316 minutes after the start of ablation, at which point the voltage was decreased by 25% simulating a reduction in decay heat level from 350 W/kg  $UO_2$  to 200 W/kg  $UO_2$ . Power was finally turned off to end the test after nearly 6 hours of operation with water atop the melt. The total duration of the experiment was in excess of 12 hours.

## EXPERIMENT RESULTS

The gross electrical input power for MACE Test M1B is shown in Figure 2. The time origin  $t = 0$  in this figure, and in the discussion which follows, represents the start of basemat ablation of the limestone/common sand concrete basemat. In

accordance with test specifications (see Table 2), the gross power level during concrete ablation and prior to water addition was held constant at 130 kW. Just prior to water addition, the power supply operating mode was changed from constant power at the reference 130 kW level, to a constant voltage operating mode. The addition of 125 l of water to the test section at a flowrate of 2 l/s was initiated at 14.7 minutes. Sufficient makeup was provided thereafter to maintain a 50±5/-10 cm water level over the melt. The initial rate of steam generation was very intense, and was a true test of the quench system capability. The quench tank water inventory reached saturation conditions several minutes after initial water addition, and remained so for a time interval of ~4 minutes. During this period, steam condensation occurred in the spray tank. The quench tank reached capacity in less than 30 minutes after initial addition, at which time spillover into the overflow tank began. The initial melt/water heat flux, fully corrected for heat transfer from surrounding structure other than the melt pool itself, was well in excess of saturated water CHF for a long time interval following water addition. This initial intense heat transfer phase, although significantly shorter in duration, was also observed in the MACE Scoping Test (3).

Several other independent and diverse experimental measurements indicate that the energy extraction during the initial melt/water interaction phase had a strong affect on mitigating the MCCI. High temperature (Type C) TCs located at various axial and radial positions within the melt recorded a steep temperature decline of several hundred degrees Kelvin over the first several minutes after water addition.<sup>2</sup> The basemat ablation rate, as calculated from the noncondensable offgas composition and flowrate data recorded by the mass spectrometer (See Figure 1), also fell by more than an order of magnitude in the first several minutes after water was added. Following steep declines, both the melt temperature and ablation rate stabilized at approximately the same time before increasing slightly near  $t = 40$  minutes. These slight upswings preceded an observed ejection of melt into the overlaying water at  $t = 42$  minutes, which lead to a significant but temporary increase in the corium quench rate. As shown in Figure 2, the electric power input was sensitive to the eruptive event, showing a sharp decrease at the onset of the dispersal. As described in Reference (4), periodic melt eruptions with concurrent power drops were observed throughout the Scoping Test; the power drops (at constant voltage) were attributed to loss of conductor (melt) from the electrical path. The same mechanism is felt to be responsible for the post-eruption power drop observed in Test M1B. An important difference between the two experiments is, however, that multiple (i.e., five) eruptive events occurred during the Scoping Test, while a single eruptive event occurred during M1B. The difference is most likely attributable to the variation in decay heat levels between the two experiments (i.e., the Scoping Test was run at 2-4 times the prototypic decay heat power level achieved in M1B).

Following the melt eruptive event, the gross electrical input power, melt temperature, and basemat ablation rate steadily declined over the remainder of the test. This trend is attributable to the fact that the upward heat transfer rate remained very significant in comparison to the electric power input over this time interval. The result was that after six hours of operation with water over the melt, the melt temperature had fallen by many hundreds of degrees

---

<sup>2</sup>Unfortunately, no direct comparison with the MACE Scoping Test results can be made in this regard, owing to a lack of melt temperature data during the initial phase of the melt/water interaction in the Scoping Test (4).

Kelvin, and the ablation rate had been reduced to less than 5% of the level observed prior to water addition. Thus, the initial period of very large heat extraction in conjunction with the substantially long term upwards heat removal rate had the combined effect of substantially mitigating the MCCI in this experiment.

Posttest disassembly of the MIB apparatus revealed the end-of-test debris configuration. The "skeleton crust" observed at the onset of basemat ablation was still present over the melt. This crust material, which was not formed as part of the melt/water interaction, was found to be perforated with three holes made by the lance probes before the melt was flooded, in addition to two holes which appeared to have formed naturally. These observations, in conjunction with the video of the melt surface during the water addition phase of the experiment, confirm that the skeleton crust did not form a significant barrier to melt/water contact. Removal of the skeleton crust revealed the solidified debris surface which participated in the initial melt/water interaction phase. In striking contrast to the Scoping Test (4), the surface was found to be essentially devoid of loose debris formed by eruptive processes. Additional examination indicated that substantial erosion of the west MgO sidewall behind the tungsten electrodes had occurred during the experiment. The effect of the incorporation of the MgO into the melt on the quench process is currently being studied.

#### SUMMARY AND CONCLUSIONS

The Melt Attack and Coolability Experiment (MACE) program is addressing the ability of water to quench and thereby terminate a MCCI. This paper provided a summary of MACE Test MIB, which investigated the interaction of 416 kg of 70% oxidized PWR corium with a limestone/common sand concrete basemat in the presence of a water overlayer. Key findings from this experiment are summarized as follows:

- 1) Initial contact of water with a well sparged, high temperature, prototypic oxide melt was achieved.
- 2) The initial melt/water interaction phase was very vigorous, leading to a decline in melt temperature of several hundred degrees Kelvin and a reduction in basemat ablation rate by over an order of magnitude in the first several minutes after initial water addition.
- 3) After 6 hours operation with water atop the melt, the melt temperature had been reduced by many hundreds of degrees Kelvin, and the ablation rate had fallen to less than 5% of that observed prior to water addition.

Although it is premature to attempt to draw conclusions on melt coolability pertaining to the reactor system based on MIB, the results of the experiment indicate a strong tendency for water to mitigate an MCCI, which has not been shown in any experiment which we are aware of thus far.

## ACKNOWLEDGEMENTS

This work was sponsored by the Advanced Containment Experiments (ACE) international consortium organized by the Electric Power Research Institute. The authors acknowledge the important contributions to the experiments by D. J. Kilsdonk, R. W. Aeschlimann, D. R. Armstrong, D. Bromberek, A. J. Kras, E. Pozzie, and J. F. Weber. The manuscript was prepared for publication by Ms. L. J. Ondracek.

## REFERENCES

1. R. E. Blose, J. E. Gronager, A. J. Suo-Antilla, and J. E. Brockmann, "Swiss: Sustained Heat Metallic Melt/Concrete Interactions with Overlying Water Pools," NUREG/CR-4727, SAND-1546, 1987.
2. E. R. Copus, "Core-Concrete Interactions with Overlying Water Pools," 2nd CSNI Specialist Meeting on Core Debris-Concrete Interactions, Karlsruhe, FRG, April 1-3, 1992.
3. J. J. Sienicki and B. W. Spencer, "The Jet Impingement Stage of Molten Core-Concrete Interactions," OECD CSNI Specialist Meeting on Core Debris/Concrete Interactions, Palo Alto, CA, September 3-5, 1986.
4. B. W. Spencer, et. al., "Results of MACE Tests MO and MI," 2nd CSNI Specialist Meeting on Core Debris-Concrete Interactions, Karlsruhe, FRG, April 1-3, 1992.

# MACE TEST APPARATUS

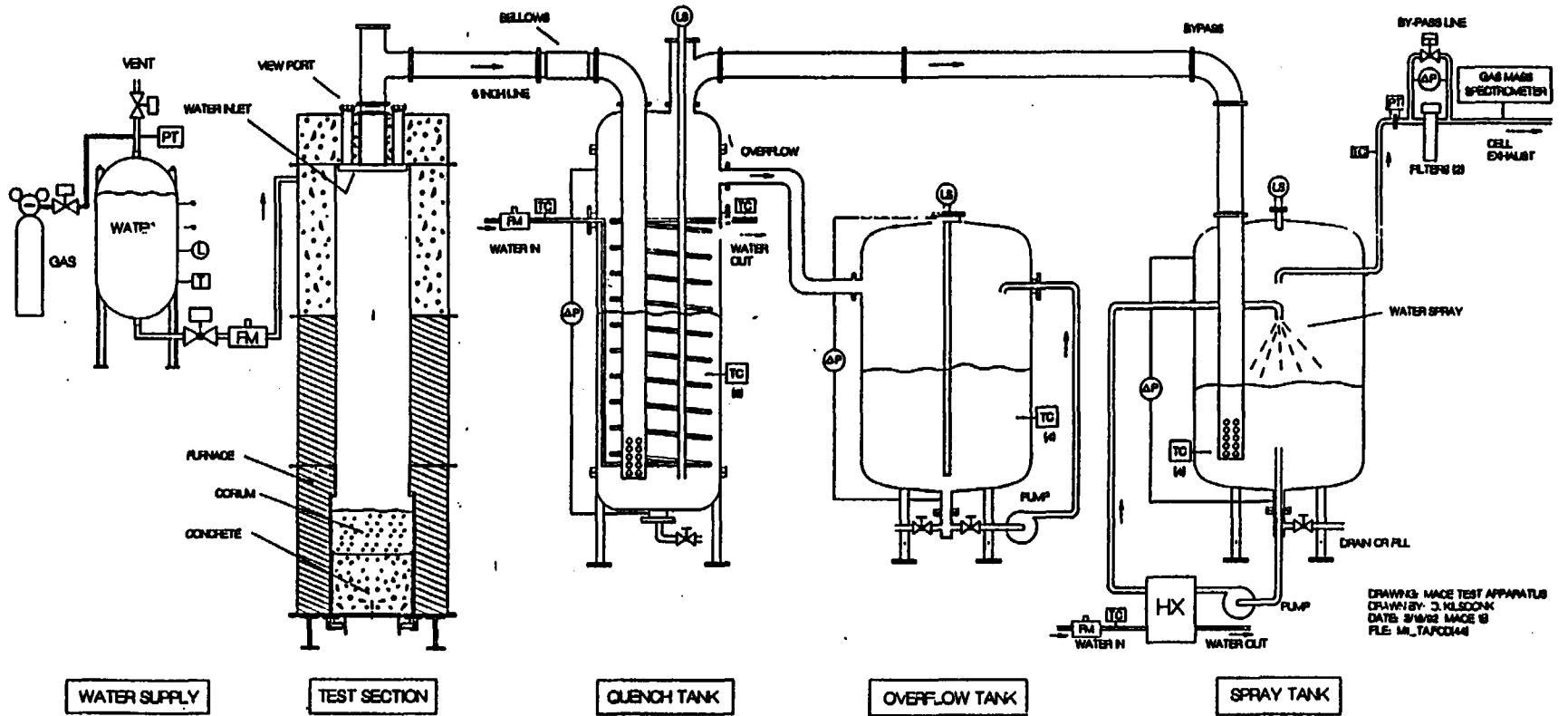


Fig. 1. Schematic Illustration of the MACE Facility

**Table 1. Corium Loading for MACE Test M1B**

Constituent	Mass, kg	Mass %
UO <sub>2</sub>	309.1	74.9
ZrO <sub>2</sub>	65.0	15.5
SiO <sub>2</sub>	13.50	3.3
CaO	12.54	3.0
Zr <sup>1</sup>	13.48	3.3
	412.62	

<sup>1</sup>Present as two layers of rods at the corium powder/concrete interface.

**Table 2. Test Specifications for MACE Test M1B**

Corium	70% Oxidized PWR, 416 kg
Concrete	Limestone/Common Sand
Basemat Dimensions	50 cm x 50 cm
Melt Depth	25 cm
Initial Melt Temperature	2500 K
System Pressure	1 Atmosphere (nominal)
Criteria for Water Addition	1.2-2.5 cm Ablation, and Top Surface is Molten
Initial Inlet Water Flowrate	2 l/s
Makeup Water Flowrate	2 l/s
Sustained Collapsed Water Volume	125 l
Criteria for Makeup	Water Volume <115 l
Inlet Water Temperature	296 K
Power Supply Operation Mode Prior to Water Addition	Constant Power, 130 kW gross
Power Supply Operating Mode After Water Addition	Constant Voltage

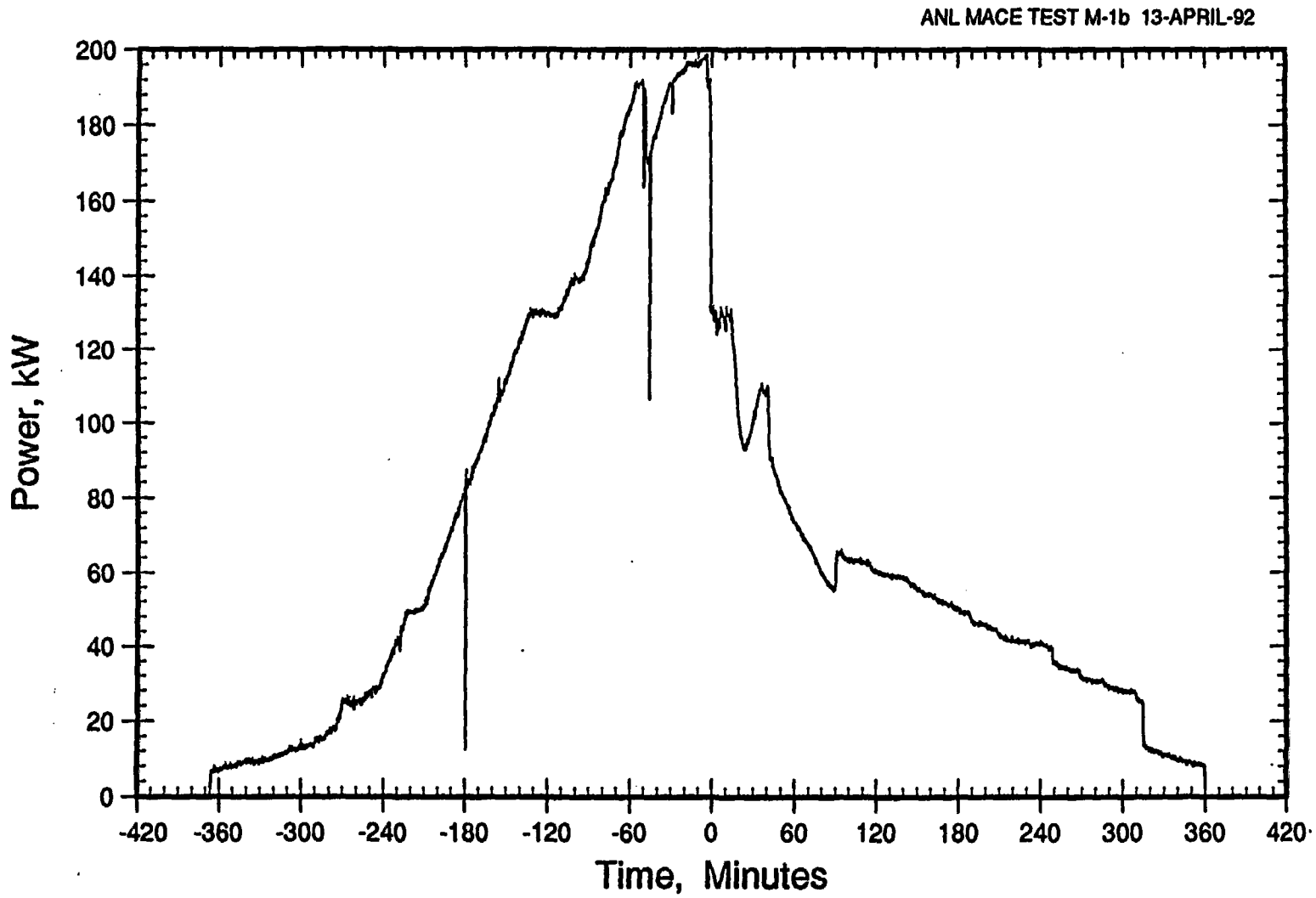


Figure 2. Gross Electrical Input Power for MACE Test M1B.

# Melt Attack and Penetration of Radial Concrete Structures Cooled by Outside Water

H. Alsmeyer

Kernforschungszentrum Karlsruhe  
W-7500 Karlsruhe 1, Germany

## SUMMARY

In the BETA facility two experiments were conducted on the failure of a cylindrical concrete wall which is eroded on the inner side by a heated melt while being cooled outside by stagnant water. No decrease of the radial erosion velocity is observed when the melt front approaches the outer concrete surface and wall failure occurs after the residual wall thickness is reduced to about one centimeter. The melt relocates into the water annulus. Melt/water contact in the second test led to an energetic steam explosion which destroyed the crucible and caused considerable damage of the facility. Applicability of the experimental results for LWR severe accidents is discussed.

## 1. INTRODUCTION

During the late phase of core melt accidents the situation may arise that during the melt attack of the basemat, a vertical concrete wall is eroded from the inner side while the outer side of the wall is in contact with stagnant water. Such a condition may occur in a German standard PWR where the melt is eroding the inner biological shield which on the outside is cooled by the stagnant sumpwater on the containment floor. Therefore, the concrete erosion is a "dry" interaction from the beginning as long as the 85 cm thick concrete shield separates melt and water. Calculations as reported in the German Risk Study Phase 2 [1] predict that the erosion of the cylinder wall after some 8 hours has proceeded so far that failure of the wall might occur. The question arising from this situation is, whether the wall due to cooling by the outside water could form a self stabilizing crucible able to separate effectively melt and water or if, by failure of the wall, a contact of melt and water would occur.

The consequences for the further accident progression would be a continuation of the dry MCCI with a remarkable hydrogen concentration in the gases released from the eroding melt if no water contact should occur. Otherwise, an increase in steam production would accelerate the pressure build-up in the containment. The late contact of melt and water would, however, not lead to coolability of the melt and subsequent stop of concrete erosion as, based on experiments with simulant materials [2], fragmentation of the highly viscous and relatively cold oxidic melt can not be expected for deep pools. For the planning of accident management, the possibility of water contact and resulting steam production are important for the time of containment venting.

## **2. BETA EXPERIMENT V 6.1**

### **2.1 SETUP IN THE BETA FACILITY**

The BETA facility allows simulation of prototypic corium melts in concrete structures which are large enough to allow extrapolation to real reactor geometry with the aid of qualified computer codes. Figure 1 gives a schematic view of the facility with the cylindrical concrete crucible which contains the melt. Decay heat is generated by an induction coil surrounding the crucible. Offgas system and various instrumentation give the necessary experimental information.

To address the problem of the failure mode of the concrete cylinder, a double crucible of siliceous concrete was used in the BETA facility (figure 2). Inner and outer crucible form an annulus which is filled with water to a level corresponding to 350 mm above the initial bottom of the inner crucible. The inner crucible with a wall thickness of 100 mm towards the water annulus, has 380 mm inner diameter and is filled with the metallic and oxidic melt, eroding the concrete. The outer crucible has a wall thickness of 150 mm, outer diameter 1080 mm.

The crucible was constructed in such a way that no mechanical force is acting on the inner crucible, because the weight of the upper crucible is supported by the outer crucible. This simulates a suspended "stress-free" biological shield in contrast to a wall which is loaded by its own weight or additional static forces. Consequently, the realized "stress-free" situation gives the optimum condition for stabilization of the crucible. Any other situation would lead to earlier failure of the cylinder.

The objective of the experiment is the simulation of the wall attack in a real accident after some 8 hours of melt-concrete interaction in the period where failure of the biological shield might occur. Therefore, the 10 cm wall thickness of the inner crucible simulates that portion of the shield which has not yet been eroded and is in contact with the stagnant sumpwater. Consequently, the melt composition and the simulated heat transfer condition imposed by the internal heat generated in the melt must correspond as far as possible, to the accident condition.

The simulated melt consists of 300 kg steel, initially 93.3% Fe, 5% Ni, and 1.7% Cr, and 50 kg oxide with 70%  $\text{Al}_2\text{O}_3$ , 15%  $\text{SiO}_2$ , and 15%  $\text{CaO}$ . The melt is generated externally by a thermite reaction and poured into the crucible where it is mixed up with 25 kg of  $\text{ZrO}_2$  deposited on the bottom of the inner crucible.

In the BETA facility decay heat simulation is by sustained electrical induction heating. As this method heats the metallic melt only, it is somewhat different from the accident situation where the major part of decay heat is generated in the oxidic phase. Indeed, the radial attack of the biological shield in the real accident would be dominated by the oxidic melt progression. Therefore, to allow a representative experimental simulation, the internal heat generation in the BETA test is adjusted to give the same radial heat flux from the melt to the cylinder as in reality 8 hours into the accident situation. With this condition fulfilled, the metallic melt can be used for simulation. The necessary heating rate of 120 kW was determined by WECHSL calculations comparing BETA and accident conditions.

Figure 2 also shows the instrumentation of the inner crucible with 107 thermocouples, which allow the detection of the erosion front in the concrete. This is especially important in the cylinder wall to detect the possible influence of the outside water cooling on melt front progression.

The water in the annulus is introduced through a tube from the lower side of the crucible and is continuously connected to a pressure transducer to register pressure variations when boiling or melt contact would occur. The vapour which would be produced can escape through 3 parallel plastic tubes, 25 mm inner diameter. The water temperature in the annulus is measured by three thermocouples in different heights.

On-line and off-line gas analysis systems are used to identify the rate and composition of gases released from the inner crucible. All gases are fed through the 300 mm inner diameter off-gas line to the environment via a large metal fiber filter.

## 2.2 CONDUCT OF THE EXPERIMENT V 6.1

Precalculations with the WECHSL code have been conducted assuming the planned heating rate of 120 kW in the melt. The calculated cavity shapes are given in Figure 3 for time steps of 240 s. The calculation does not take into account the - unknown - influence of the water jacket, but assumes an adiabatic outer cylinder wall. The calculations predict that radial penetration of the cylinder might occur slightly below the bottom level of the initial inner cavity after some 60 minutes of erosion, caused by the metal phase. However, the simplified assumptions of the calculations do not allow a judgement if radial melt-through would really occur.

The experimental conditions could be maintained throughout the test as planned. The induction heating rate was nearly constant (figure 4), but slightly increased as the radial melt propagation improves the coupling to the induction coil. The time averaged power of 131.5 kW is 9.5% higher than the planned 120 kW until power-off at 2352 s. The initial peak characterizes the early vigorous melt interaction during cool-down in the first 150 s before achieving the steady low temperature of the melt which corresponds to the freezing temperature of steel. Hence, the long term erosion is characterized by the steel melt close to its freezing temperature, probably forming a thin instable crust towards the bottom concrete interface. The upper oxidic melt has a temperature several 100 K lower and forms a stable and relatively cold surface crust which can not be penetrated by the dip-in thermocouple lances.

Axial and radial erosion of the concrete are slowly proceeding after slow-down of the early faster erosion during the first 150 s (figure 5). Then, axial and radial erosion velocity are very similar with 0.027 mm/s erosion rates in the average. For the behavior of the cylinder, the radial erosion is important. The thermocouples detecting the radial erosion front have a distance of 20 mm. Within the scattering of the TC signals no influence of the outer coolant water can be observed, and it is evident that the coolant does effectively not slow down the erosion velocity even when the remaining concrete wall thickness is 10 mm only. At 2352 s (39 min) the melt penetrates into the water, as stabilization of the concrete wall by the coolant water did not occur. It is evident from figure 5, that the local wall thickness at time of cylinder failure did not exceed 8 mm. The first failure by melting evidently did occur in the neighbourhood of the thermocouple in the left part of the crucible whereas due to

some asymmetry of the erosion the remaining wall thickness on the opposite side may still have some 2 cm.

During crucible erosion, the water temperature in the annulus increased with a constant rate of 0.043 K/s from 15°C at 300 s to 90°C at 2050 s, and then subcooled boiling of the water did occur. The constant rate of temperature rise and of steam production throughout the experiment until failure of the cylinder wall shows that the radial heat flux is only little affected when the metal melt approaches the cylinder surface, and confirms the observation of constant radial erosion rates. The heat transferred into the water is 28 kW, corresponding to 21% of the induction heating rate.

Failure of the cylinder wall causes direct contact of the steel melt and water, leading to a characteristic pressure history. Figure 6 gives the pressure in the gas room of the inner crucible (HP-solid line) and in the water annulus (WH-broken line) at the time of cylinder failure. The latter pressure is referred to the initial bottom of the inner cavity as zero level. This pressure starts to increase at 2348 s by faster evaporation. 4 seconds later, relocation of the metallic melt starts as can be seen from the increase of electrical coupling of the induction heating system in figure 3, with the consequence of a stronger increase of the pressure in the annulus. The 3 steam tubes in the annulus are insufficient to release the steam to the atmosphere and the fast pressure increase continues. At 2355 s, there is a strong interaction of melt and water accompanied by a flash to be seen in the crucible. Simultaneously, a gross circumferential failure of the inner cylinder occurs as can be seen from the sectioned crucible in figure 7. It is believed that the circumferential failure of the concrete cylinder is promoted by the higher pressure in the annulus.

The massive contact of melt and water leads to an extremely fast pressure increase to more than 1 bar overpressure for 3 seconds, exceeding the detection limits of the pressure transducers. The 150 kg of water in the annulus are evaporated and ejected through the off-gas line within some 15 s only, leading to a massive steam release to the environment. 200 kg of the 300 kg metal melt relocated into the annulus where it solidified in the form of a compact ring with very little void. No damage occurred to the outer crucible, while the plastic tubes in the annulus were destroyed and some melt was ejected downwards through the tubes. Additionally, an upper sealing of the crucible failed and some minor part of the melt was blown into the experimental hall during the blow-down period.

With the high steam flux from the inner crucible a substantial transport of mostly oxidic melt material and some metallic particles took place downstream through the off-gas system. This caused a damage of the fiber filter where an oxidic "particle" of 1 kg was found. 8.3 kg of finely fragmented metallic particles were collected from the upper part of the facility and the hall. This metallic material evidently has undergone a strong interaction of melt and water while all oxidic particles have greater dimensions typically on the order of some centimeters or more. Therefore it is concluded that the fast pressure built-up is mainly due to the metallic melt fraction while the oxidic particles because of their high viscosity and consequently greater dimensions contribute very little to the fast evaporation.

Sieve analysis of the metallic particles from different locations in the facility are given in figure 8. Comparison with typical size distributions of steam explosion experiments shows that this material underwent a low effectivity steam explosion. From

the upward displacement of some of the particles it is concluded that the peak gas pressure exceeded 4.3 bar.

### 2.3 CONCLUSIONS FROM THE EXPERIMENT V 6.1

The experiment clearly shows that for the conditions realized in the test the water cooling is insufficient to stabilize the melt in the inner crucible. The concrete erosion is not slowing down when the melt front approaches the water annulus because of the poor thermal conductivity of the decomposing concrete. Finally, a stable concrete layer or melt crust is not formed, and melt water contact and relocation of the materials does occur.

For the stability of the concrete cylinder the radial heat flux from the melt to the concrete wall is important. If the same heat flux is realized, the type of melt, oxidic or metallic, is of no more importance. Calculations with the WECHSL code for the experiment and the accident are given in Table. 1. The comparison shows that the heat flux in the experiment and the freezing temperature of the melt meet reasonably well the conditions of the oxidic melt in the accident under consideration. Similarly, the measured erosion velocity in this test with  $0.027 \text{ mm/s} = 9.7 \text{ cm/h}$  meets the desired conditions. Therefore, the result of wall failure is transferable to the accident condition, although in the accident under consideration, because of geometrical reasons, only the oxidic melt would penetrate the cylinder.

Quantity	BETA	Core Melt Accident	
	V 6.1 metal/concrete	oxide/concrete	metal/concrete
radial heat flux, kW/m <sup>2</sup>	112	96	45
radial erosion veloc.*), cm/h	8.6	7.05	3.33
liquidus temperature of melt, K	1788	1849	1768
solidus temperature of melt, K	1778	1512	1758

\*) influence of outside water not taken into account

Table 1: Comparison of Characteristic Quantities for the Erosion as Calculated with the WECHSL Code

The failure of the concrete can be understood from heat conduction estimates. To transfer the radial heat flux to the water without melting, the residual concrete layer must have a thickness  $s$  not exceeding

$$s = k \Delta T / \dot{q} \quad (1)$$

with  $k$  the thermal conductivity of the concrete,  $\Delta T$  the temperature difference over the concrete layer (some 1300 K) and  $\dot{q}$  the heat flux imposed by the melt. With the poor heat conductivity of standard concrete of about  $1 \text{ W/mK}$ , eq. (1) yields a layer thickness on the order of 1 cm. However, the heat conductivity of the concrete layer is still smaller than assumed above, because the high temperature of some 1600 K at

the inner side of the wall causes dehydration of the concrete and increasing porosity with negative effects on conductivity. Consequently, the thermodynamically stable wall thickness may still be lower than 1 cm, a thickness which is mechanically unstable especially under the influence of the extreme temperature gradient. Of course, any mechanical prestress would enhance the failure.

The small influence of heat extraction by the outside water before wall failure is the reason for the relatively good agreement in cavity shape and failure time comparing experiment and WECHSL pretest calculations. Calculated melt-through is at 60 minutes while the observed failure is at 40 minutes. The final cavity shapes just before failure agree reasonably well.

Special consideration must be given to the melt relocation process in relation also to the subsequent BETA test as discussed below.

### **3. BETA EXPERIMENT V6.2**

#### **3.1 SETUP OF THE TEST V 6.2**

The occurrence of the low effectivity steam explosion in BETA test V 6.1 gave rise to considerations how the observed minor steam explosion could be avoided for the given geometry of the double cylinder. It seemed obvious that the steam which developed upon the first penetration of some melt into the annulus, had insufficient flow area to the environment and hence the rising steam pressure contributed to further failure of the inner concrete wall. This caused additional melt water contact and ended with the moderate steam explosion.

The conclusion was that pressure build-up in the annulus should be avoided as far as possible in order to avoid untypical increase of the failure area of the inner concrete crucible and to allow "undisturbed" relocation of the melt into the annulus. This seemed important to quantify the steaming rate when a corium melt in a real accident would submerge the pool of sumpwater.

Consequently, the improved crucible of the next BETA test V 6.2 was fabricated with 6 depressurization channels of 60 mm i.d. (figure 9). The channels allow steam release into the free volume of the inner crucible and from there through the offgas line to the environment. The upper bends of the channels were designed to avoid inflow of melt into the channels early in the test.

The other important conditions of the test, namely geometry, masses and constitution of the melt, and planned induction heating power were the same as in the preceding test. The water level in the annulus was set to 350 mm above the initial bottom of the inner cavity.

#### **3.2 CONDUCT OF THE TEST V 6.2 AND STEAM EXPLOSION**

The erosion process and melt behavior in experiment V 6.2 were very similar to the preceding test. The electrical power input was however some 10% higher and caused a slightly faster radial concrete erosion. The ongoing erosion of the inner crucible wall could be observed throughout the experiment by temperature increase and fail-

ure of the thermocouples which were embedded in the concrete wall. The residual wall thickness at 1893 s (32 min) was 2 cm on the left side and between 1 and 2 cm on the right side of the crucible when the steel melt started to penetrate into the water annulus. The cavity shape at this time is plotted in figure 9 as derived from thermocouple measurements. From calculations with the WECHSL code, wall failure may be expected at 2900 s. The code is slightly underpredicting the radial erosion and overpredicting the downward erosion for the situation under consideration.

The temperature of the melt had dropped from 2205 K at start of the test to temperatures close to the solidification temperature within a few minutes only. The measured temperature of the steel melt (95% Fe, 5% Ni) at the time of crucible penetration was 1670 K determined by two W5Re/W26Re thermocouples slightly extending into the metal melt from the lower concrete surface. This technique is identical to that used in the ANL-ACE experiments. However, from the tabulated values of Fe-Ni freezing temperatures [3] it must be concluded that the bulk temperature of the metal must be higher, close to some 1770 K; otherwise the metal would be solidified. The temperature of the oxidic melt on top of the metal layer was considerably lower probably close to 1600 K. The oxidic melt surface as seen by a video camera was completely dark indicating that a nearly solidified surface was existing at the time of crucible penetration. Melt masses at that time are 300 kg steel plus some 100 kg oxides. The temperature of the 150 kg water in the annulus had reached 93°C, i.e. 7°C below the boiling point.

The penetration of the melt into the annulus at 1893 s led to an almost instantaneous steam explosion which was so strong that it destroyed the crucible and parts of the BETA facility nearby. The transition to the explosion evidently occurred within one cycle time of the data acquisition system which was 0.4 s, namely from 1893.0 s to 1893.4 s. No change is seen before in the pressure of the annulus (figure 10) or in the composition or rate of the gases released from the crucible. The measured electrical heating power which was coupled from the induction coil to the melt can be used to gain information on melt distribution as the coupling efficiency is depending on the geometry of the melt. The power in figure 10 indicates relocation of the melt starting at 1893.0 s and extending to 1893.4 s. As the induction power is switched off automatically before 1893.8 s, no information can be derived from the power history thereafter.

The preceding test V 6.1 had a transition period of 7 seconds from start of melt relocation to rapid pressure escalation as indicated by the rising pressure in the water annulus. This period is reduced to the order of 0.4 s only in the present experiment. The next sampling of the data at 1893.8 s indicates already gross failure of the crucible and some other components of the BETA facility as all measurements in the crucible and nearby give no further information. For example, the pressure transducer for the annulus which is located apart from the crucible shows ambient pressure (corresponding to  $\Delta p = -40$  mbar in figure 10) probably because the connecting tube was already broken. Hence, it is concluded that the main steam explosion and destruction of the crucible occurred close to 1893.4 s. This also corresponds to the rapid inward and outward movement of the offgas tube from 1893.4 to 1894.4 s caused by the displacement of the hood of the crucible and registered by a video camera. As only minimal increase of pressure in the annulus was measured before the explosion it seems evident that the onset of the steam explosion was not influenced by the moderate evaporation and pressure rise in the annulus as was probably the case in test V 6.1.

All available information refers to a spontaneous, self triggered steam explosion in V 6.2.

Nobody was present in the BETA building throughout the test. The operators in the control room heard a substantial detonation and felt vibration of the basement. The gates of the facility were flung open by fast pressure increase inside the building.

The video camera which observed the melt from the top of the crucible with 50 frames per second registered a dark and stable melt surface before the explosion. The start of the explosion first produced a bright flash in the centre of the melt surface visible on two frames, i.e. for 0.04 s. Then the camera was dark for 0.06 s. Subsequently, a diffuse, relatively moderate shine was visible for 0.12 s and then the camera failed. In total, the time period from the first video observation of the explosion until failure of the camera was 0.22 s. Comparison with the optical pyrometer registered by the data acquisition system gives 1893.0 s for the time of the first bright flash. From the video registration it can clearly be excluded that the melt surface in the inner crucible was flushed by any water e.g. through the depressurization channels, until the onset of the explosion. Therefore it is concluded that the explosion originates from the annulus.

Figure 11 gives a view of the destroyed crucible and parts of the facility as seen from the front door. In the foreground the cylindrical part of the crucible is visible which was thrown into the pit under the induction system. The following damages are observed: The outer cylindrical crucible could withstand the explosion because the radial load was mainly taken by the outer protective cylinder of glas-fiber reinforced epoxy which surrounds the concrete structure. The bottom of the crucible was separated from the cylindrical part, and the vertical wall of the inner crucible of 10 cm initial thickness was destroyed completey.

The damages of the facility are due to axial forces mainly, causing the failure of structures above and below the crucible. The bottom of the crucible was pushed downwards, deformed the transport car on which the crucible was located and buckled the pillars of the lifting platform beneath which finally dropped down into the pit. This is the situation depicted in figure 11. The upper hood which connects the free cavern of the crucible with the off gas line (figure 1) is pushed upward by some 50 cm, tearing off the bolts which fastened the hood to a steel platform and partly lifted the offgas line. Collision of the hood with the upper tank for the measurement probes transfered sufficient kinetic energy to the free standing tank of 7800 kg mass that the tank was lifted by 3.3 m and finally fell down on the platform.

Remarkably, the offgas line of 300 mm inner diameter was insufficient to limit the steam pressure in the inner crucible system. Upon failure of the structure the major portion of the steam expanded into the hall of the facility, caused the opening of the gates, and led to some deformation of the ducts for air condition. The steam also transported a substantial amount of finely fragmented melt particles which were deposited throughout the facility. These particles are mostly metallic and are the result of the fragmentation process which the melt underwent during the steam explosion. These particles were sufficiently hot to cause burning of some structure materials of the installation which had to be extinguished by the firemen.

### 3.3 CHARACTERISTICS OF THE STEAM EXPLOSION IN V 6.2

From the damage of the crucible and the facility it is clear that a substantial amount of energy had been involved in the steam explosion. Therefore it was attempted to get further information on the explosion by post test examination.

The mass of finely fragmented particles which were involved in the steam explosion as compared to the mass of coarse or unfragmented melt is an important quantity to judge the energy conversion. From the 300 kg steel plus 100 kg oxide melt present in the crucible at the time of the explosion, only 67 kg of coarse material, mostly metallic, were recovered from the different parts of the facility by very careful inspection. Therefore it is concluded that the rest of the melt, say between 200 and 300 kg was finely fragmented and was distributed with the steam throughout the facility. 25 kg of this material could be collected from the floor of the hall. Samples of this material are analyzed although not necessarily representative for all fine particles. The particles are metallic (Fe), diameter from 5 to 500  $\mu\text{m}$ , and the mass distribution shows a maximum in the range of 200  $\mu\text{m}$  particle diameter [4]. The size distribution is typical for a steam explosion.

Mechanical energy conversion was estimated from two events: (i) From the mechanical energy needed to accelerate the heavy upper tank and taking into account additional dispersion processes for the movement of the crucible hood, the total mechanical energy released in the steam explosion was estimated to 3% of the thermal energy of 300 kg steel melt, i.e. 5 MJ mechanical energy compared to 180 MJ thermal energy. (ii) From the buckling of the pillars of the lower lifting platform the energy conversion was estimated to exceed 1% with an acting pressure in the crucible of 20 bars or more [5]. The estimated efficiencies are in the range of typical steam explosion experiments.

The outer cylinder of the crucible which as mentioned above could withstand the explosion because of the surrounding protection tube, has two characteristic patterns of cracks in the concrete wall: (i) A series of longitudinal cracks from the top to the bottom of the outer cylinder was formed in extension of the depressurization channels. This refers to a symmetrical pressure load on the outer crucible. (ii) A local concentration of cracks in various directions is visible in the south of the outer crucible on the level of the initial bottom of the inner crucible. Additionally, the concrete surface in this area is covered by a thin black layer of iron, partly oxidized indicating an intense contact of melt and concrete. Stress analysis has been carried out for different load assumptions [6] from which the following load sequence of the steam explosion was hypothesized: Upon local melt through of the inner crucible in the south, part of the metal melt relocates into the annulus where a spontaneous steam explosion occurs. This explosion energy produces the local cracks described above under (i) and leads to the implosion of the partly eroded inner crucible wall. Thus, an intense contact and fast mixing of melt and water are possible creating the condition for a second steam explosion in the central region of crucible after a few milliseconds only. This sequence is not contradicting any of the measurements or observations and is a reasonable explanation for the large amount of melt mass and high energy conversion in the explosion.

In conclusion, the observed steam explosion has a typical conversion ratio of a few percent as observed in many laboratory tests [7]. The high portion of melt involved in

the explosion had not been expected before and seems to be the result of the strong confinement of the geometry which increases the probability for intense mixing and multiple explosions. Furthermore, it should be noted that the interaction took place between water and steel. High viscosity oxidic melts would result in less efficient energy conversion [8].

#### 4. CONCLUSIONS

The two BETA experiments which simulate the presence of water behind an eroded concrete wall cover two aspects of the radial melt penetration, namely failure of the wall and subsequent interaction of melt and water.

The experiments simulated the radial attack of a concrete wall with a relatively low heat flux density to the wall corresponding to a core melt accident in a German PWR 8 hours after start of basement erosion. The coolant from the outside water is not sufficient to stabilize the melt in the concrete mainly because of the properties of the concrete. Because of the poor thermal conductivity of the concrete a thermodynamically stable concrete wall would have a thickness of some 10 mm only where the inner concrete surface is at the "melting" temperature of 1600 K and the outer surface has the temperature of the boiling water. This layer is mechanically unstable and penetration of melt into the water and vice versa can occur. This was observed in the two BETA tests and is to be expected for the simulated accident.

The process of melt relocation into the water is strongly influenced by the nature of the melt. In BETA the decay heat simulation technique required the use of a predominantly metallic melt. This in connection with the confined geometry of the BETA crucible led to steam explosions in the tests with minor or considerable energy release, respectively. In contrast, for the accident under consideration the melt which would come into contact with the sumpwater after 8 hours is oxidic, has a low temperature and high silica content which makes the melt highly viscous. For these melts, major energetic steam explosion have a very low probability. Together with the larger volume of the PWR containment, early containment failure by these processes is not expected. On the other hand, the high viscosity of the melt also excludes the transition of the melt into a coolable configuration upon melt-water contact as has been derived from model experiments [2]. Therefore, the downward concrete erosion and moderate steam generation would continue.

The BETA tests refer to the importance of steam explosions for melts which have low viscosity or high metal content. The damage of the facility was caused by an unexpectedly high portion of the melt which took part in the explosion while the conversion ratio to mechanical energy was in the typical range of 1 or 3 percent. The confined geometry of the crucible seems to increase the portion of the interacting melt possibly by the occurrence of multiple explosions or by other very effective premixing processes. Nevertheless, the two BETA experiments show a considerable difference in energy conversion which is probably due to the stochastics of self-triggered steam explosions.

Regarding severe accident conditions with early melt/water contact and high temperature melts, situations may be envisaged where similar contact modes and severe consequences of steam explosions can not be excluded. With this background, further

analyses of steam explosion phenomena are necessary addressing relevant aspects of ex-vessel situations.

### LITERATURE

- [1] Deutsche Risikostudie Kernkraftwerke, Phase B, Verlag TÜV Rheinland, 1990
- [2] Alsmeyer, H., Dres, H., Reimann, M., Stiefel, S.: Modellentwicklung zur analytischen Beschreibung von Kernschmelzunfällen, in: Sicherheitsorientierte LWR-Forschung, Jahresbericht 1987, KfK 4450, p. 113-128
- [3] Hansen, M., Anderko, K., Constitution of Binary Alloys, McGraw-Hill, 1958
- [4] Fröhlich, G., IKE Stuttgart, Personal Communication
- [5] Krieg, R., KfK, Karlsruhe, Personal Communication
- [6] Eibl, J., Schlüter, F.H., University of Karlsruhe, Personal Communication
- [7] Corradini, M.L., Vapor Explosions: A Review of Experiments for Accident Analysis, Nucl. Safety, 32 (2) 1991, p. 337-362
- [8] Zimanowski, B., Fröhlich, G., Bayer, V., Lorenz, V., Beiträge zu hypothetischen Kernschmelzunfällen im LWR aus experimentellen vulkanologischen Studien über Wasserdampfexplosionen, Jahrestagung Kerntechnik, Karlsruhe, 1992, p. 219-222

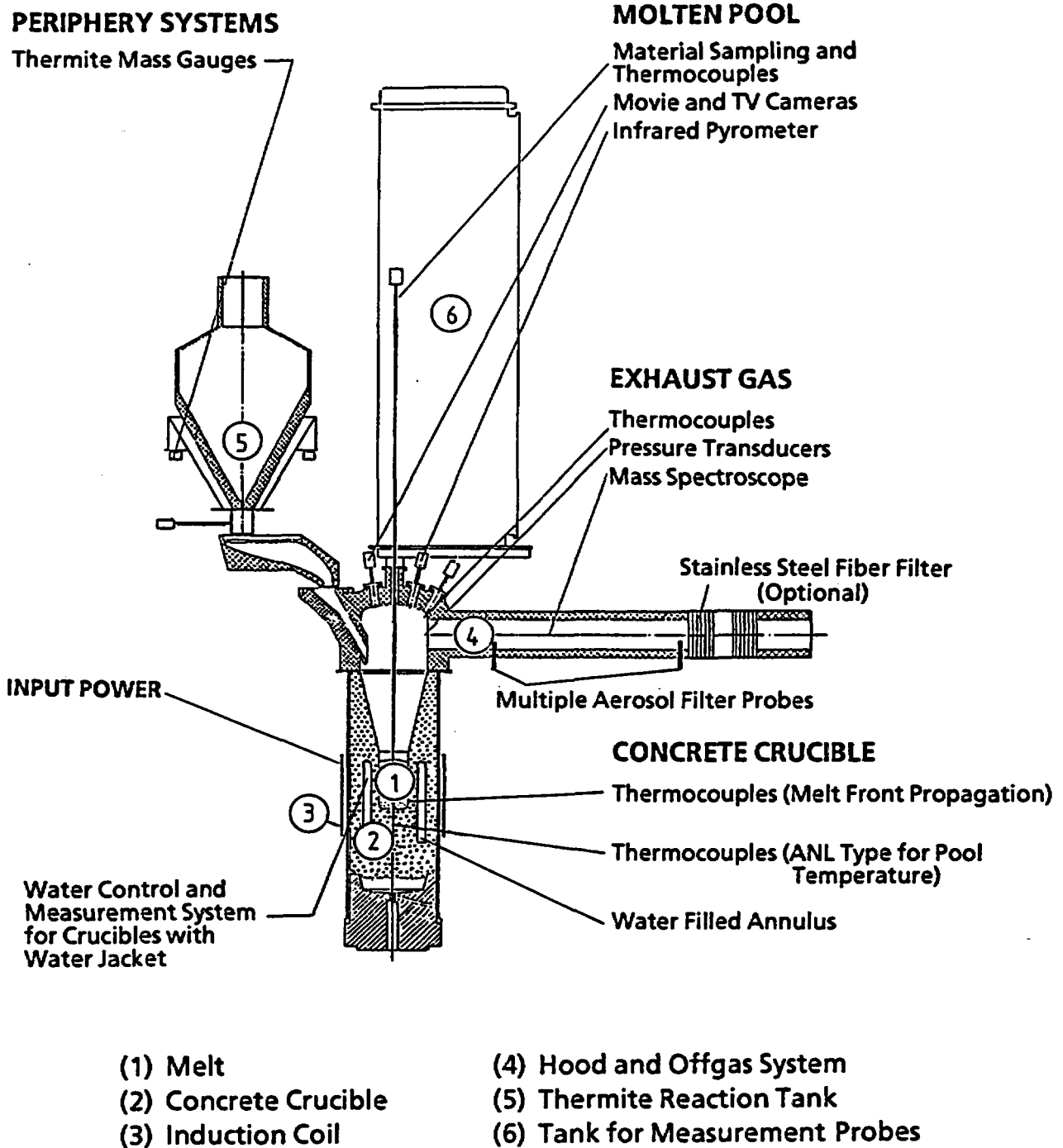


**Figure 1: Schematic View of the BETA Facility in Experiments with Water Contact**

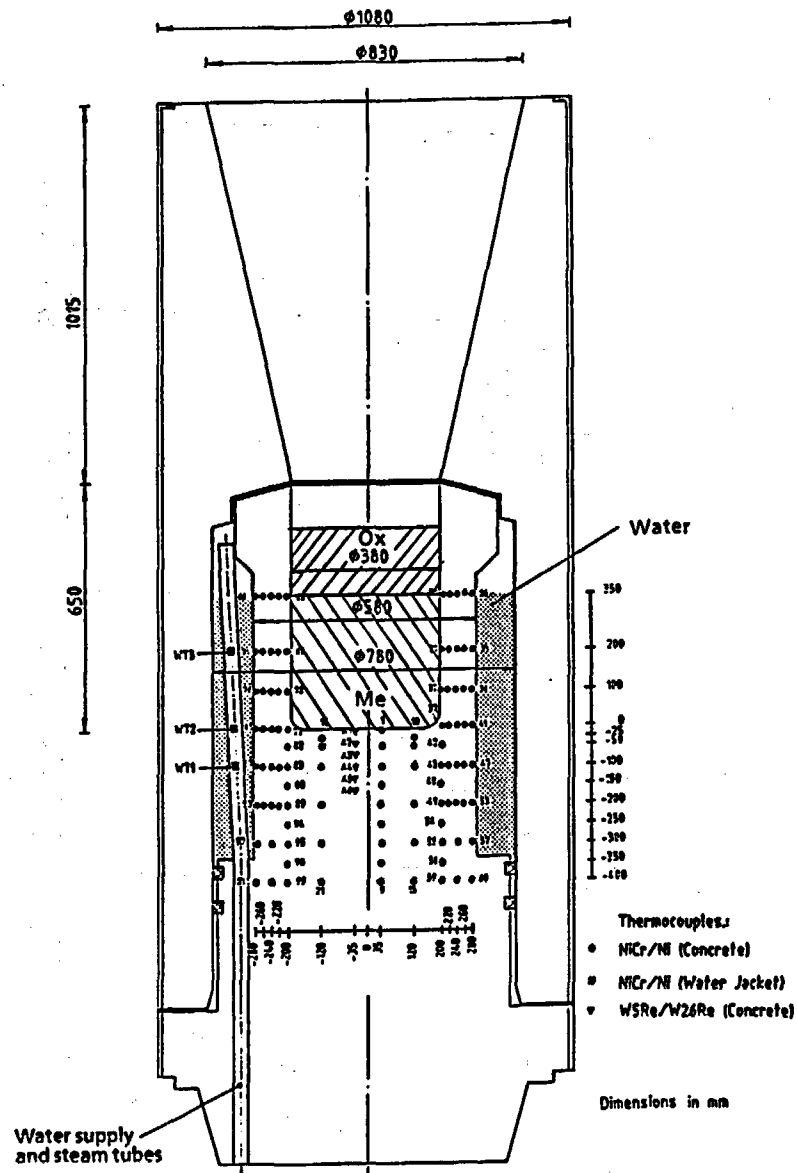


Figure 2: Crucible of BETA Tests V 6.1

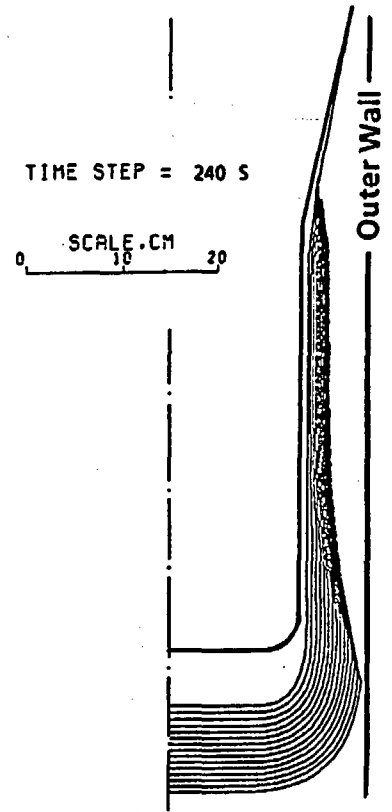


Figure 3: BETA V 6.1: WECHSL Pretest Calculation Calculated Crucible Erosion from 0 - 3600 s

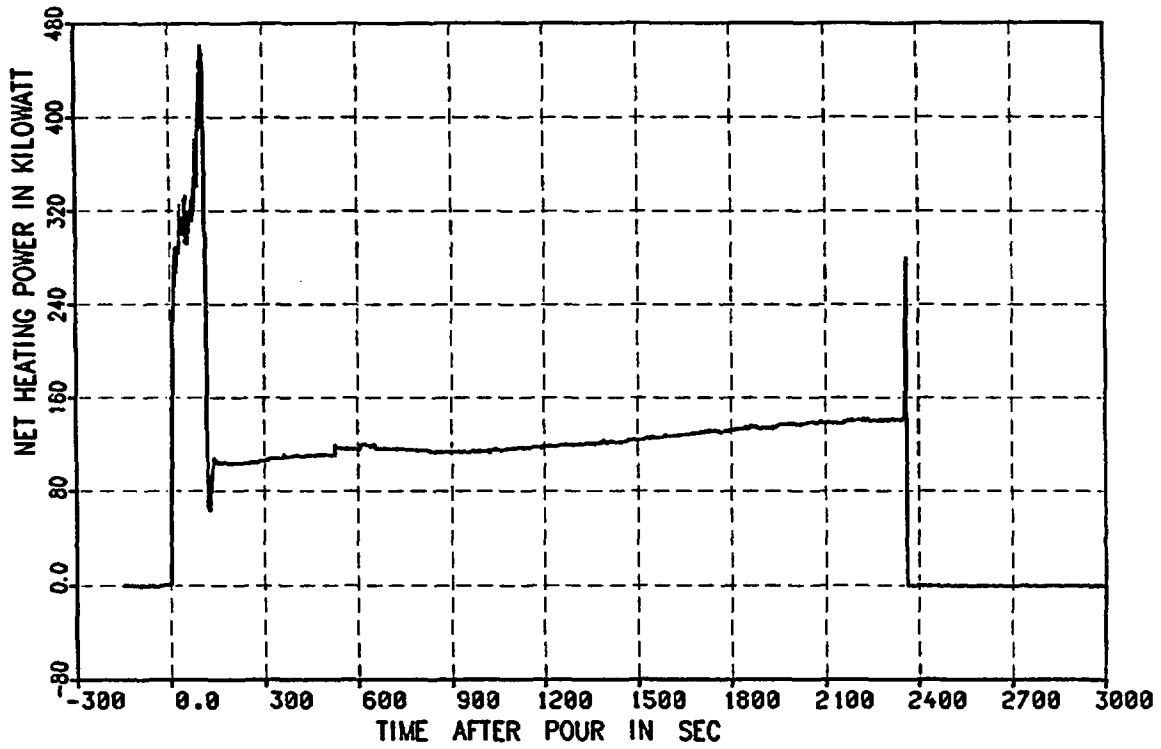


Figure 4: Net Heating Power in BETA V 6.1

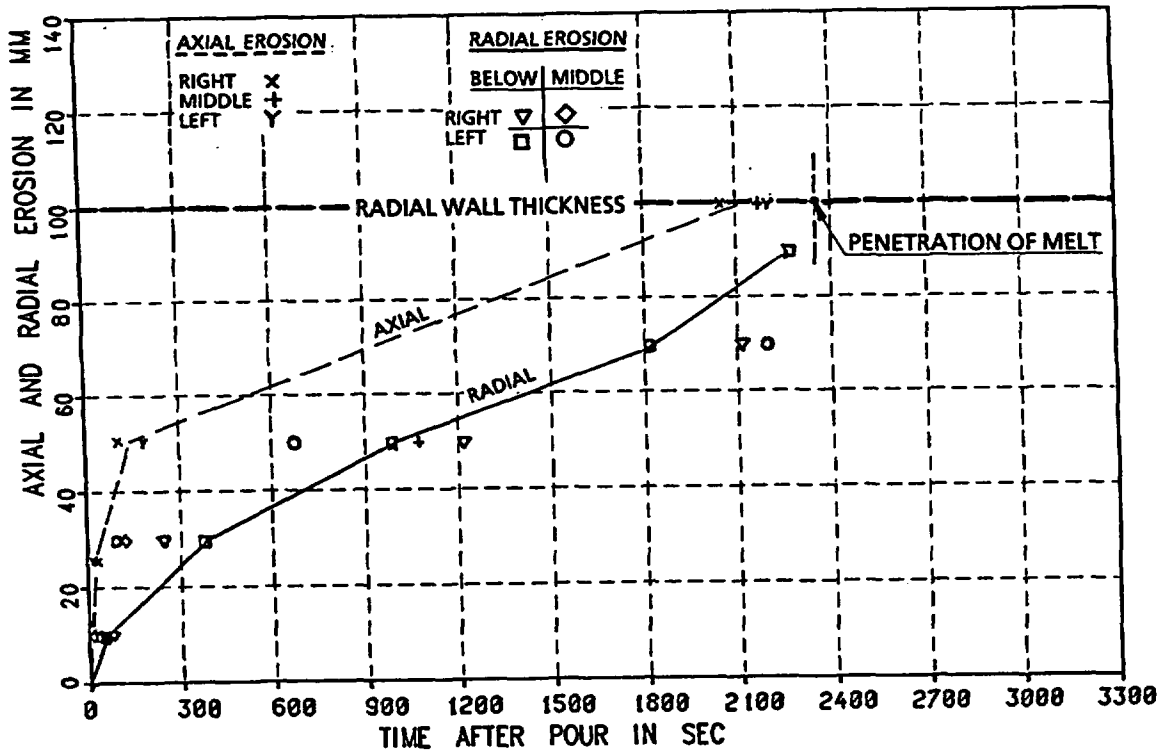


Figure 5: Measured Concrete Erosion in BETA Crucible V 6.1

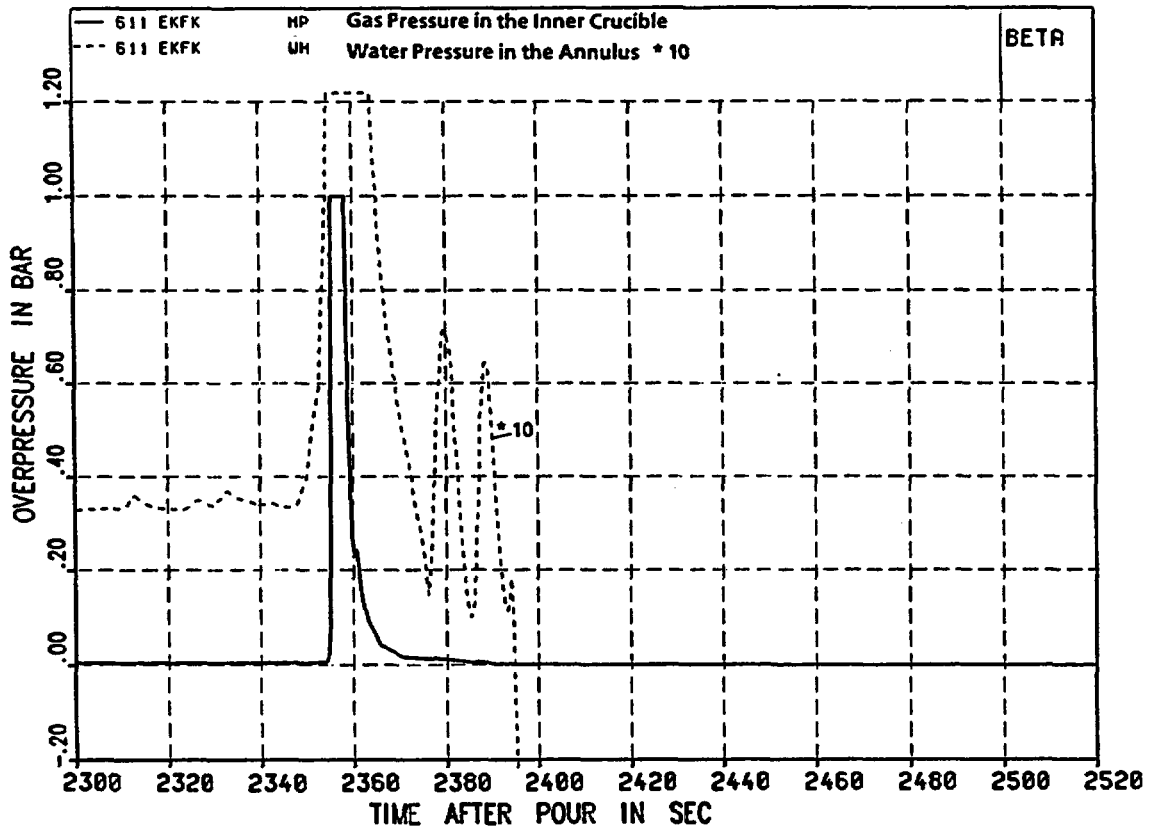


Figure 6: Pressure History of BETA V 6.1 at Time of Melt Penetration

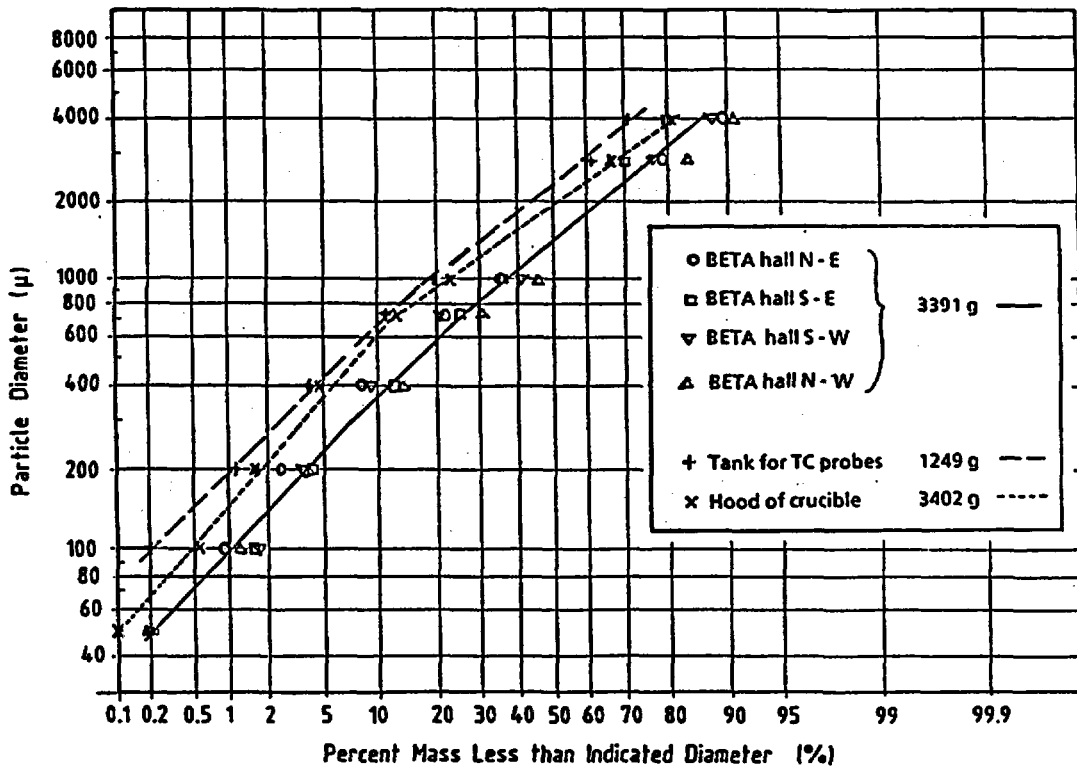


Figure 8: Particle Size Distribution of Metal Fragments in BETA V 6.1

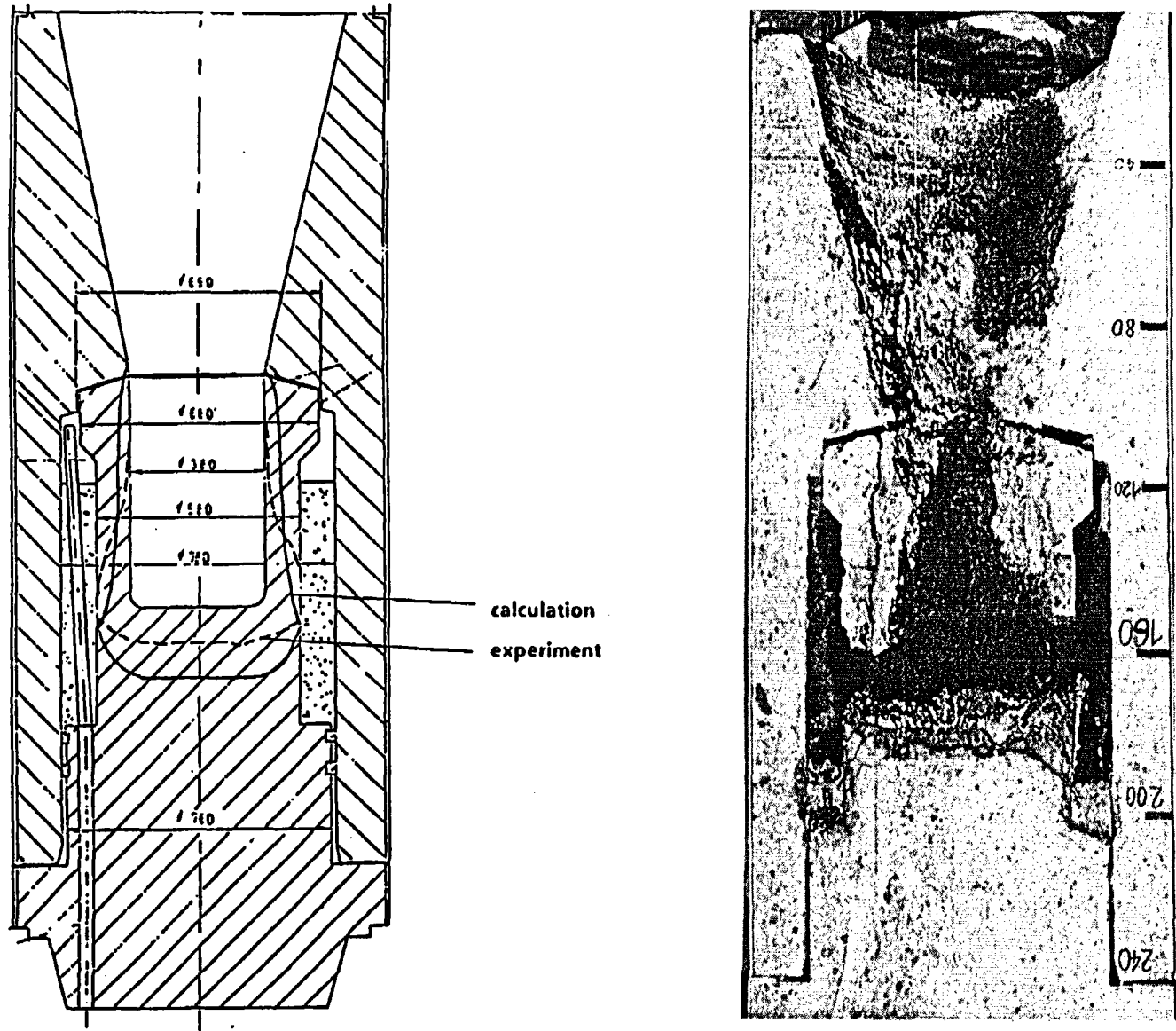


Figure 7: Crucible of BETA Test V 6.1 after the Test

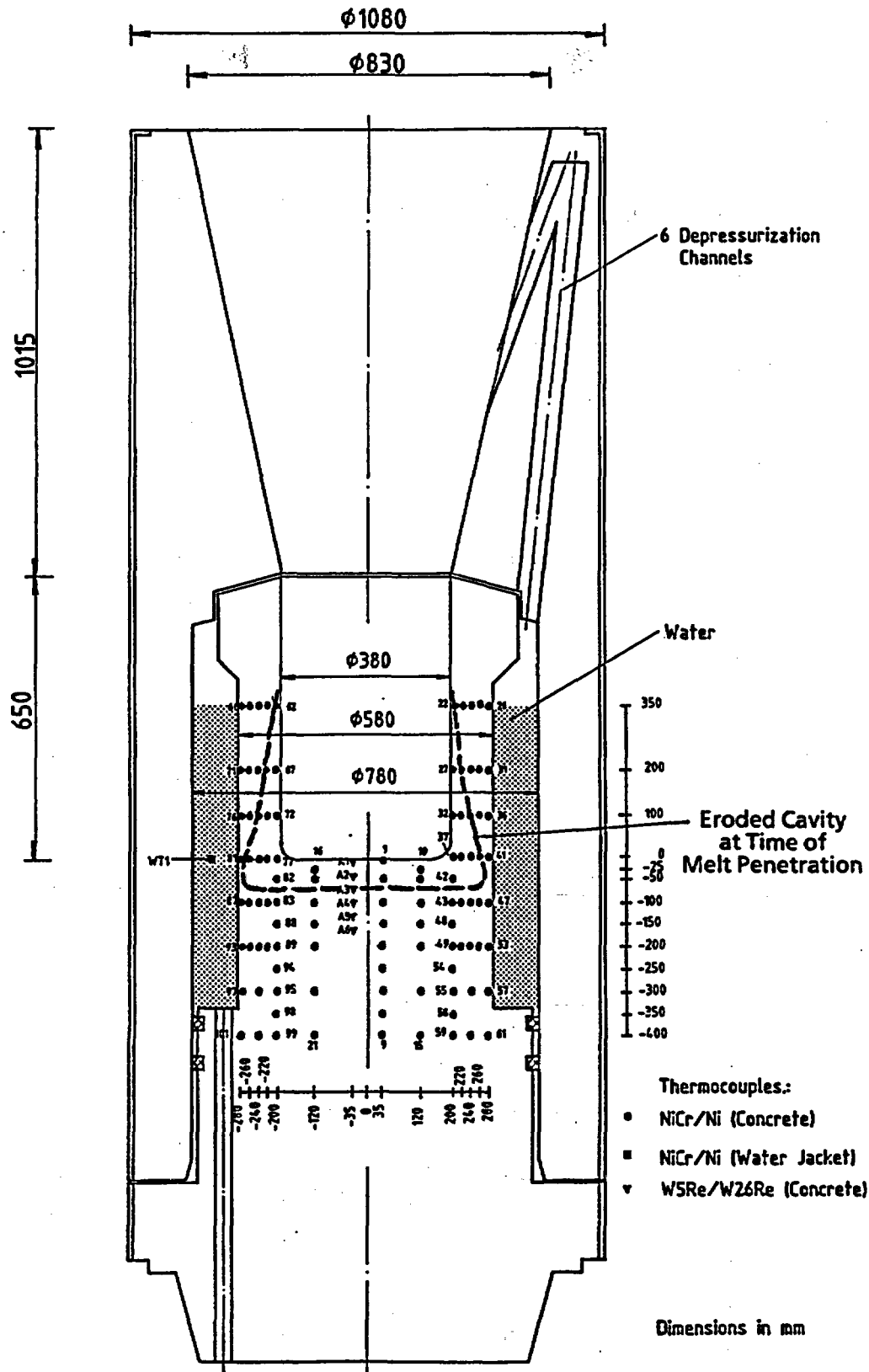


Figure 9: Instrumentation of BETA Crucible V 6.2 and Cavity at Melt Penetration

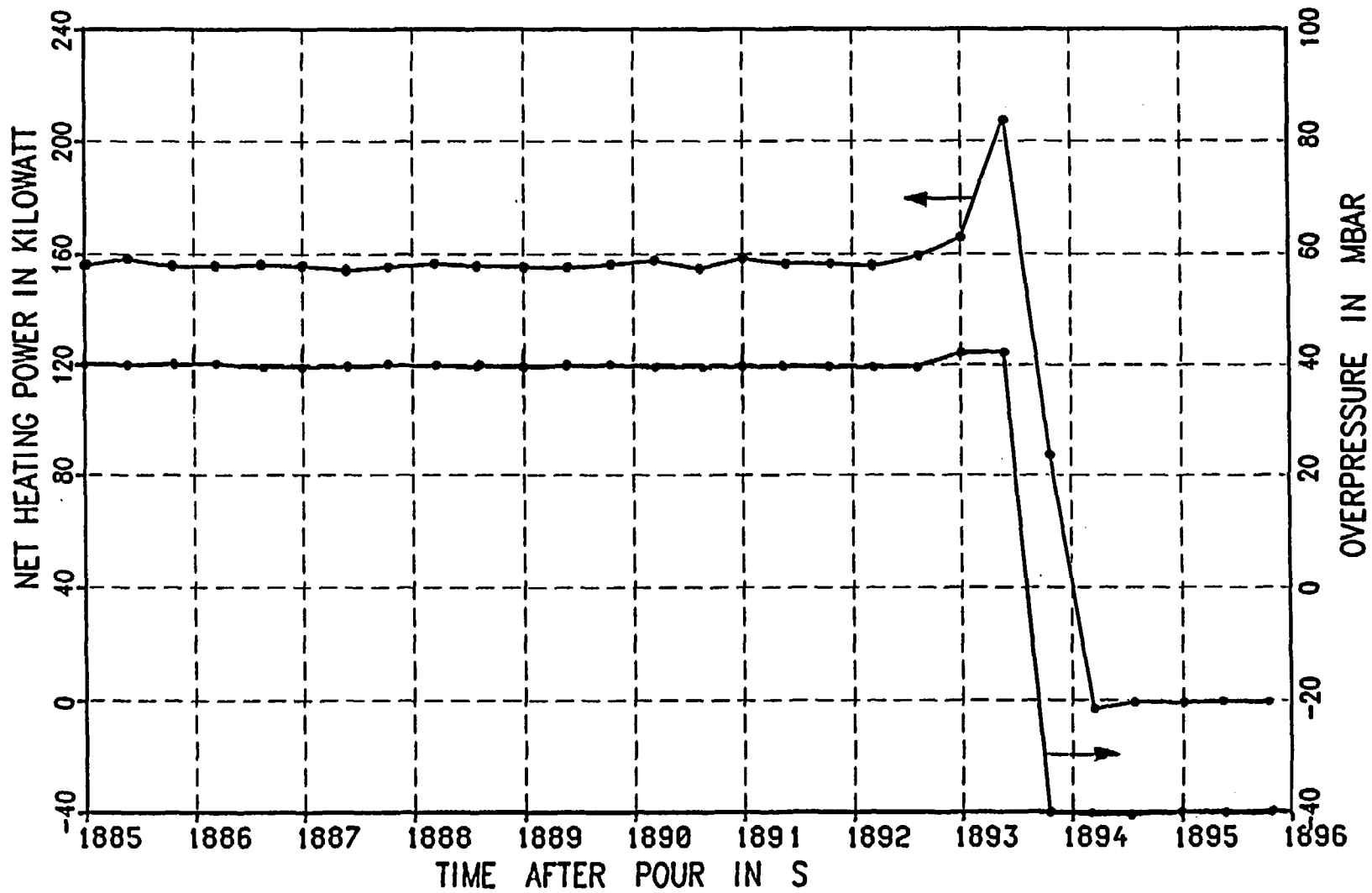
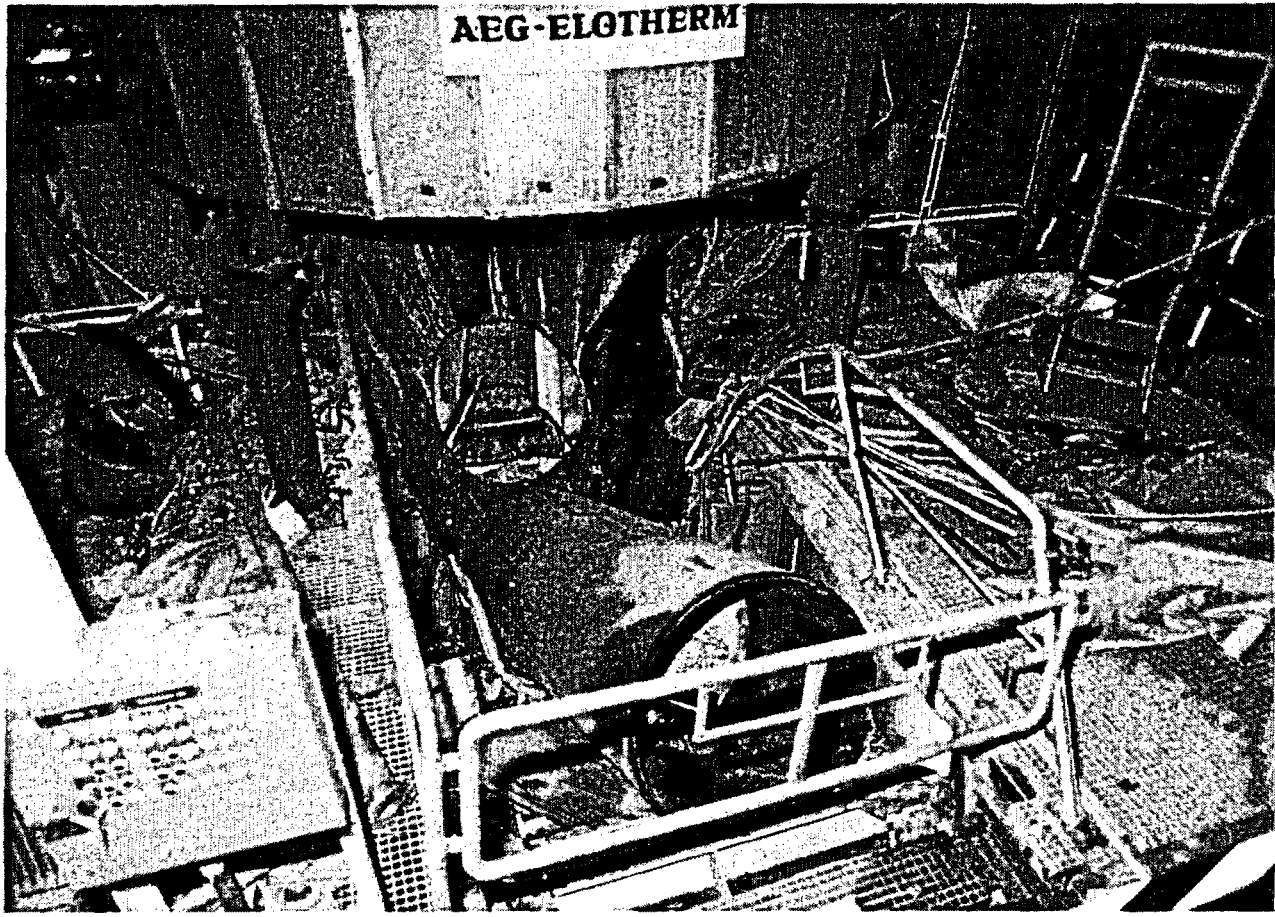


Figure 10: Heating Power in BETA V 6.2 and Overpressure in the Annulus at Melt Penetration



**Figure 11: Destroyed Crucible and Damage of the BETA Facility**

## RESULTS OF ORNL VI SERIES FISSION PRODUCT RELEASE TESTS

M. F. OSBORNE and R. A. LORENZ  
Chemical Technology Division  
Oak Ridge National Laboratory  
Oak Ridge, Tennessee 37831-6221

### INTRODUCTION

The fuel in light-water reactors (LWRs), which generate a significant fraction of our electricity, is designed to retain the highly radioactive fission products that are produced during operation. A variety of high-temperature, severe accident situations, however, both hypothetical and as occurred at TMI-2, may cause fuel damage and result in potentially dangerous releases of these fission products.<sup>1</sup> Therefore, accurate, detailed information about the release and behavior of fission products is required for adequate analysis of reactor safety. To this end, high-burnup Zircaloy-clad  $UO_2$  specimens of commercial LWR fuel have been heated to severe accident temperatures in reactive atmospheres. Such studies, initiated by the Atomic Energy Commission (AEC), have been sponsored by the U.S. Nuclear Regulatory Commission (NRC) at Oak Ridge National Laboratory (ORNL) for many years. The results, particularly those from the most recent HI and VI test series, have provided a significant fraction of the experimental results comprising the data base for computer modeling and consequence analysis for severe reactor accidents. As a part of the NRC Cooperative Severe Accident Research Program, this research project has been recognized by the reactor safety organizations in most developed countries as a major contributor to reactor safety worldwide. The direct participation of visitors from a number of foreign countries in these tests of high-burnup fuel has furthered the international exchange and understanding of our research results.

## EXPERIMENTAL EFFORTS

The major test series and test conditions for these ORNL studies are listed in Table 1. Following three series of tests in the temperature range 775 to 1875 K (500 to 1600°C) in 1976–79, a new induction furnace design was developed to provide uniform heating of a 100- to 200-g fuel specimen to higher temperatures, and the techniques for fission product measurement were expanded and improved.<sup>2</sup> In the HI series, six tests were conducted in steam with the fuel specimen oriented horizontally at temperatures of 1675 to 2275 K (1400 to 2000°C).<sup>3</sup> To investigate the effect of specimen orientation on fuel degradation and fission product release, the furnace was rebuilt to allow the fuel specimen to be mounted vertically during heating. Experiments in the vertical furnace, identified as VI-1 through VI-6, achieved test temperatures of 2000 to 2700 K (1725 to 2425°C).<sup>4</sup> Although these experimental projects at ORNL have emphasized the use of highly irradiated fuel to reduce the uncertainties of radiation effects and as-irradiated fuel conditions, they have been complemented by tests including fission product tracers and simulated high-burnup fuel (HS tests) to provide more information about the behavior of specific fission product species.<sup>5</sup>

The six HI tests showed release fractions in 20-min tests of up to 60% of the volatile fission products — Kr, I, and Cs. In addition, most of the fission product iodine was shown to behave like CsI; only very small fractions of the released iodine were in volatile forms, such as I<sub>2</sub>, HI, and CH<sub>3</sub>I. Furthermore, in the steam atmospheres, most of the fission product cesium was found to behave as CsI and CsOH. A test using radioactive tellurium tracer material in an unirradiated fuel specimen clarified the retention of tellurium in metallic Zircaloy cladding and its rapid release upon approaching complete oxidation of the cladding.<sup>6</sup> Antimony, with its easily measured isotope <sup>125</sup>Sb, was found to behave much like the more difficult to measure, and more hazardous, tellurium. The fact that tellurium decay produces additional radioiodine contributes to its hazardous nature.

In the VI test series, 15-cm-long fuel specimens (~100 g each) were heated in the vertical induction furnace, which is illustrated in Fig. 1. High-temperature ceramics, either  $ZrO_2$  or  $ThO_2$ , surrounded the hot zone, and fibrous  $ZrO_2$  and graphite felt provided good thermal insulation. Thermocouples (W 5% Re vs W 26% Re) and optical pyrometers (both manual and automatic) were used for temperature measurement and control for the times of 20 to 60 min at test temperature. The released material was collected in three sequentially operated collection trains. Each train included a thermal gradient tube (TGT) for deposition of condensible vapors, a package of graded fiberglass filters for collection of aerosols, and heated charcoal cartridges for sorption of any volatile iodine forms that penetrated the filters. A steam condenser and dryer (used in steam tests) and a cooled charcoal trap for fission gas sorption were located further downstream, as shown in Fig. 2. In addition, equipment for on-line measurement of the hydrogen generated by steam oxidation of the Zircaloy cladding was used in steam atmosphere tests. Radiation detectors (NaI) were used for on-line measurement of  $^{85}Kr$  in the cooled charcoal traps and  $^{134}Cs$  and  $^{137}Cs$  on the TGTs and filters. These data, along with all temperatures, were recorded at 1-min intervals.

The fractional release of fission products was determined by gamma spectrometry of the fuel specimen both before and after the test and by direct measurement of the fission products collected on TGTs, filters, and cold traps. The ORIGEN2 computer program was used to calculate the fuel inventories of all fission products and actinides,<sup>7</sup> and techniques other than gamma spectrometry (neutron activation analysis, mass and emission spectrometry, and chemical methods) were used to measure the non-gamma-emitting fission products and actinides. Because all irradiated fuel specimens had decayed at least 5 years, only  $^{134}Cs$ ,  $^{137}Cs$ , and  $^{85}Kr$  could be measured on-line. In posttest analyses  $^{106}Ru$ ,  $^{125}Sb$ ,  $^{144}Ce$ , and  $^{154}Eu$  were measured directly, and, after chemical treatment and separations,  $^{129}I$ , Sr, Te, Ba, Mo, U, and Pu were measured. The high concentrations of  $^{134}Cs$  and  $^{137}Cs$  in all samples complicated handling and limited the precision of some analyses.

## RESULTS AND DISCUSSION

Our tests have indicated that the most important parameters influencing fission product release are temperature, time, and atmosphere, in that order. While fuel characteristics, such as burnup and irradiation history, and test heatup rate appear to influence release, our results are not sufficient to adequately quantify these effects. A summary of the fuel specimen data, test conditions, and release results for the six VI tests is shown in Table 2. In this series, three tests were conducted in steam, two were carried out in hydrogen, and one (VI-6) was heated in hydrogen until the cladding melted and then switched to steam to study the effects of steam oxidation on the  $\text{UO}_2$ . (In addition, varying fractions of hydrogen were present in the steam atmosphere tests as a result of steam oxidation of the Zircaloy cladding.) Three of these tests (VI-1, VI-3, and VI-5) were conducted at two test temperatures of 20 min each. The temperature history and the sequential operation of the three collection trains (A, B, and C) are illustrated in Fig. 3. In addition, the on-line release data for  $^{85}\text{Kr}$  and  $^{134}\text{Cs}$ , recorded at 1-min intervals, are shown. The similar release history for Kr and Cs in this test, which was conducted at 2000 and 2700 K (1725 and 2425°C) in steam, is typical of that observed in all tests. As indicated, the release of these volatile fission products was essentially total within about 10 min at 2700 K in both steam and hydrogen atmospheres.

The different atmospheres (steam and hydrogen) exerted obvious influences on the physical behavior of the fuel. In the three steam tests, the fuel specimens remained upright and generally intact, even after 20 min at 2700 K. The brittle oxidized claddings appeared to provide significant support to the broken  $\text{UO}_2$  and to act as barriers to extensive  $\text{UO}_2$  oxidation by the steam. An example of these effects is illustrated in Fig. 4, illustrating a radial section from test VI-3. Minimal fuel-cladding interaction indicates that the Zircaloy cladding was almost completely oxidized prior to reaching the melting point, ~2050 to 2100 K (1775 to 1825°C). A large radial void was formed by a combination of expansion of the oxidized cladding and evaporation and mass transfer of the  $\text{UO}_2$  away from the hottest region.<sup>3</sup> (Significant deposits found in the collection system verified the

transport of uranium.) In tests heated in hydrogen, however, the Zircaloy cladding was not oxidized but melted and ran down. This molten Zircaloy dissolved some of the  $\text{UO}_2$ , weakening the fuel column and exerting a major influence on the chemistry of the  $\text{UO}_2$  and many fission products.<sup>9</sup> In two of the three tests in hydrogen, the fuel column collapsed to a rubble bed, with the molten cladding at the bottom of the furnace.

Gamma spectrometric analysis of the fuel specimens after the tests provided information about both the physical state of the fuel and the distribution of the fission products. (Pretest gamma scans had shown uniform fission product distributions.) The gamma scans for the fuel from tests VI-3 (2700 K in steam) and VI-5 (2700 K in hydrogen) are compared in Figs. 5 and 6, illustrating the effects of the different atmospheres. As indicated by  $^{144}\text{Ce}$ , the fuel specimen in test VI-3 was uniformly distributed over the original area (see Fig. 5). Also, the other fission products remaining in the fuel (Ru, Cs, and Eu) were uniformly distributed. In test VI-5, however, all distributions were skewed toward the bottom of the furnace (Fig. 6). The large  $^{144}\text{Ce}$  peak shows the concentration of the  $\text{UO}_2$  just below the end of the original fuel location, and similar concentrations of  $^{125}\text{Sb}$ ,  $^{106}\text{Ru}$ , and  $^{154}\text{Eu}$  are apparent also. While Ru and Eu may be associated with the  $\text{UO}_2$  in this region, we believe that the Sb is associated primarily with the Zircaloy cladding and that most of the Te is in this metallic phase also. As observed previously, Sb and Te appear to be released readily from the  $\text{UO}_2$  at high temperatures but are retained in the Zircaloy until it is almost completely oxidized. Based on studies with radioactive tracers, tellurium is believed to be retained in the cladding as zirconium telluride and, following clad oxidation, released as tellurides of tin, a constituent of the Zircaloy cladding, and cesium.<sup>6</sup>

Two groups of fission product elements displayed very different behavior in the different atmospheres. The refractory metals Mo and Ru have very low vapor pressures at the temperatures of our tests, but under oxidizing conditions, relatively volatile compounds may be formed. Hence, the releases of Mo and Ru were higher under oxidizing conditions (i.e., in steam), especially where

significant oxidation of the  $\text{UO}_2$  occurred. In our tests, the volatile forms of these elements are believed to be  $\text{CsMoO}_4$  and  $\text{RuO}_4$ . I. Johnson and C. E. Johnson showed that the  $\text{CsMoO}_4$  forms under these conditions.<sup>10</sup> The behavior of ruthenium has been studied in detail at Chalk River by Iglesias et al., who reported very high releases of ruthenium from small fuel samples at moderate temperatures in air, which oxidizes  $\text{UO}_2$  more readily than steam.<sup>11</sup>

In behavior essentially opposite to Mo and Ru, the elements Sr, Ba, and Eu are more volatile than their oxides, which are the expected forms in steam. Consequently, higher releases of these elements would be expected under reducing conditions (hydrogen) than under oxidizing conditions (steam). As shown in Table 2, almost all of the Kr and Cs was released in tests VI-3 and VI-5, but  $^{125}\text{Sb}$  and  $^{154}\text{Eu}$  behaved quite differently. Antimony release was very high (99%) in steam but only 18% in hydrogen at the same temperature. Measurable releases of Ru (5%) were observed only in the highly oxidizing test VI-3. Conversely, Eu release was barely detectable ( $\sim 0.01\%$ ) in steam but was 57% in hydrogen. The effect of atmosphere on fission product release at three different temperatures is illustrated in Table 3, which shows a small effect on the volatiles (Kr, I, and Cs) but large effects on the other, less volatile elements. Although our data for Sr, Ba, and Mo are limited, all results support the expected behavior for the above two groups of elements.<sup>12</sup>

Although atmosphere (steam or hydrogen) exerted only a small influence on the release of cesium, the dominant physical forms and the mobility were strongly influenced. As shown in Table 4, in steam the amount of cesium collected on filters (aerosol forms) dominated that collected on the TGTs (vapor forms) by a factor of 3. All other tests in steam exhibited a similar ratio. In hydrogen, however, this ratio was approximately reversed; the mass of vapor forms of cesium were much greater than the aerosol forms, suggesting a significant fraction of cesium forms other than  $\text{CsOH}$ , the dominant form found in steam tests. The very reactive nature of  $\text{CsOH}$  is believed to be effective in the formation of aerosols.

Two fission product release models have been used extensively in the analysis and comparison of our results. The fractional release rate model, as described in NUREG-0772,<sup>13</sup> is used in the CORSOR-M code.<sup>14</sup> This simple model has been the generally accepted standard used in the NRC Source Term Code Package for about 10 years.<sup>15</sup> The basic equations for this model are

$$f = 1 - e^{-kt} , \quad (1)$$

and

$$k = -\frac{1}{t} \ln(1-f) , \quad (2)$$

where

$f$  = fraction released;

$k$  = release rate coefficient, which is a function of temperature;

$t$  = time.

Using this model, data are most often compared by plotting  $k$ , the release rate coefficient, vs fuel temperature.

More recently, our release results have been used to develop the ORNL Diffusion Release Model (DRM), which is based on the early work of Booth and Rymer.<sup>16</sup> The latter model assumes single gas atom diffusion across the radii of uniform  $UO_2$  spheres, with release upon reaching the grain boundaries; this model includes the measured (or assumed) average  $UO_2$  grain size. Booth and Rymer derived two equations, to be applied according to the extent of release.

For small releases, where  $Dt/a^2 \leq 0.1$ ,

$$f = 6\sqrt{\frac{Dt}{\pi a^2}} - \frac{3Dt}{a^2} ; \quad (3)$$

and for large releases, where  $Dt/a^2 > 0.1$ ,

$$f = 1 - \frac{6}{\pi^2} \exp\left(\frac{-\pi^2 Dt}{a^2}\right), \quad (4)$$

where

$f$  = fraction released,

$D$  = the diffusion coefficient ( $\text{cm}^2/\text{s}$ ),

$t$  = time (s),

$a$  = the average grain radius (cm).

In using this model for data comparison, we typically plot  $D$ , the diffusion coefficient, vs fuel temperature.

A comparison of the release behavior of Kr and Cs in tests VI-3 (in steam) and VI-5 (in hydrogen), using the CORSOR-M model, is shown in Fig. 7. The individual points were derived from the on-line data collected at 1-min intervals during the tests, and the smooth curves represent the calculated CORSOR-M values. As may be seen, the data are scattered and lie above the CORSOR-M curve at temperatures below  $\sim 1600$  K. The measured data follow the CORSOR-M model well from 1600 to 2000 K, where the 20-min tests periods at constant temperature resulted in declines in the release rates. At higher temperatures, however, the release rates (especially those in steam) lie somewhat below the model. In a comparison of the same test VI-5 data (Fig. 8) using the ORNL DRM, the agreement at temperatures above 1600 K is significantly better, with most of the data lying slightly above the diffusion model curve.

Cesium release data for the first five tests in the VI series are similarly compared with the models in Fig. 9 (CORSOR-M) and Fig. 10 (ORNL DRM). Each point is an average for the collection period A, B, or C. For temperatures  $>2000$  K, all release rate coefficients lie below the CORSOR-M curve, indicating that this model is generally conservative, especially at the higher temperatures (2500 to 2700 K). Conversely, a similar comparison of measured data with the ORNL DRM (Fig. 10) shows better agreement. Only the values from test VI-4 lie consistently above the

curve. Two factors, somewhat different fuel characteristics (higher enrichment, burnup, and irradiation temperature) and a temperature shift during the test (caused by fuel column collapse), are believed to be contributors to these higher diffusion coefficients.

Although not discussed in this paper, other fission product models have been used for correlation of our test data. The FASTGRASS code, developed by Rest at Argonne National Laboratory, is a detailed model which provided good agreement with data from earlier tests in our HI series.<sup>17</sup> The VICTORIA Model, which was developed at Sandia National Laboratories (SNL) and has been reported by Bixler et al.,<sup>18</sup> includes a comprehensive library of possible chemical compounds and reactions. Work at SNL and other laboratories has shown VICTORIA to be similarly applicable for the comparison of data from our VI tests.

## SUMMARY AND CONCLUSIONS

These tests at ORNL have produced extensive data on the release of the volatile fission products from high-burnup LWR fuel under accident conditions. Although the release data obtained for the less-volatile species are less extensive, they contribute to understanding the behavior of less-volatile species and to evaluating the associated hazards. All of these results, including fuel behavior, are summarized in Table 5.

Of particular significance are the results that are most closely related to LWR safety. Almost all of the iodine released in our tests (both the HI and VI series) behaved like CsI, a stable, nonvolatile form. Small fractions, usually <1%, have been collected as volatile forms: I<sub>2</sub>, HI, or organic iodides. This behavior suggests that the volatile fractions result from reaction of CsI with trace impurities in the test apparatus. In the event of air ingress, however, CsI would be oxidized to volatile forms, especially I<sub>2</sub>.

Although the different atmospheres exerted only a small effect on cesium release, they had a significant effect on mobility. Aerosol forms of cesium, which dominate the vapor forms in steam,

are more likely to escape from the reactor primary system and also from the containment than the vapor forms, which are more common under reducing conditions. Consequently, the cesium released under only partial blowdown conditions, where ample water remains to generate steam, would be more mobile than the cesium released under complete blowdown (steam-starved) conditions. With vessel penetration and extensive air ingress, however, the atmosphere would become strongly oxidizing. Even so, the release of cesium vapor forms that had condensed in the cooler regions of the reactor coolant system (RCS) would be delayed for a considerable period and perhaps would be retained indefinitely. In air, however, cesium would occur primarily as oxides, which have similar volatility but are somewhat less reactive than CsOH.

Retention in the metallic cladding of Te and Sb released from the fuel strongly affects the timing of their release from the core, and, as a result, the extent of release to the environment. Rapid, total oxidation of the Zircaloy cladding leads to early release of the Te and Sb. If the Te and Sb are released inside the vessel, large fractions will deposit and be retained in the cooler regions (at temperatures  $\sim 700^{\circ}\text{C}$  or less) of the RCS. Under steam-starved or steam-limited conditions, however, complete oxidation of the Zircaloy would not occur until after vessel meltthrough when air oxidation could effect Te and Sb release ex-vessel. In this case, the Te and Sb, and also the I daughters of the Te, might be more likely to escape to the environment.

High-burnup LWR fuel typically contains  $\sim 1\%$  plutonium as a result of neutron transmutation of the  $^{238}\text{U}$ . These Pu nuclides, because of their shorter-lived alpha decay characteristics, are much more biologically hazardous than U. In our VI tests, the fractional release of Pu has been  $\sim 1$  to  $10\%$  that of U, indicating preferential retention of the Pu, probably as  $\text{PuO}_2$ , in the  $\text{UO}_2$  fuel matrix. This lower fractional release of Pu compared to U reduces the potential hazard of Pu release in a core-melt accident.

Observations of our VI tests in hydrogen indicate that, while extensive fuel-cladding interaction, or "liquefaction", may occur, this physical destruction of the fuel geometry leads to no

large increase in the release of the volatile fission products. The higher release rates for cesium in test VI-4 compared with those of VI-5 (Figs. 9 and 10, respectively) may be related to the earlier collapse of the fuel in test V-4 (at ~2150 K) compared with that in VI-5 (at >2500 K). As noted previously, however, significant increases in some of the less volatile species, notably Sr, Ba, and Eu, may occur. In addition, extensive fuel-cladding interaction, as may occur under reducing conditions, is more likely to cause early flow blockages and a dense rubble bed, thereby accelerating core heatup and resulting in a more severe accident.

#### **ACKNOWLEDGEMENTS**

The authors gratefully acknowledge the valuable contributions of co-workers in conducting these studies: Jack Collins, Jim Travis, and Charlie Webster in the conduct and analysis of experiments in the HI and VI test series; Ed Beahm and Terry Lindemer for technical consultation; Betty Drake for manuscript preparation; and Donna Reichle for editing.

## REFERENCES

1. **Proceedings of the First International Meeting on the TMI-2 Accident**, compiled by S. Langer and W. R. Young, CONF-8510166, U.S. Department of Energy, October 21, 1985.
2. M. F. Osborne, J. L. Collins, R. A. Lorenz, J. R. Travis, and C. S. Webster, *Design, Construction, and Testing of a 2000°C Furnace and Fission Product Collection System*, NUREG/CR-3715 (ORNL/TM-9135), September 1984.
3. M. F. Osborne, J. L. Collins, and R. A. Lorenz, "Experimental Studies of Fission Product Release from Commercial LWR Fuel Under Accident Conditions," *Nucl. Technol.* **78(2)**, 157—69 (August 1987).
4. M. F. Osborne, R. A. Lorenz, and J. L. Collins, "ORNL Studies of Fission Product Release Under LWR Accident Conditions," *Proceedings of the 2nd Workshop on LWR Severe Accident Research at JAERI*, Japan Atomic Energy Research Institute, Tokyo, Japan, March 1992.
5. J. L. Collins, M. F. Osborne, R. A. Lorenz, and A. P. Malinauskas, "Fission Product Iodine and Cesium Release Behavior Under Severe LWR Accident Conditions," *Nucl. Technol.* **81(10)**, 78—94 (1987).
6. J. L. Collins, M. F. Osborne, and R. A. Lorenz, "Fission Product Tellurium Release Behavior Under Severe Light Water Reactor Accident Conditions," *Nucl. Technol.* **77(1)**, 18—31 (April 1987).
7. A. G. Croff, *ORIGEN2 - A Revised and Updated Version of the Oak Ridge Isotope Generation and Depletion Code*, ORNL-5621, Oak Ridge National Laboratory, July 1980.

8. M. F. Osborne, R. A. Lorenz, J. L. Collins, J. R. Travis, C. S. Webster, H. K. Lee, T. Nakamura, and Y.-C. Tong, *Data Summary Report for Fission Product Release Test VI-3*, NUREG/CR-5480 (ORNL/TM-11399), Oak Ridge National Laboratory, June 1990.
9. M. F. Osborne, R. A. Lorenz, J. R. Travis, C. S. Webster, and J. L. Collins, *Data Summary Report for Fission Product Release Test VI-5*, ORNL/CR-5668 (ORNL/TM-11743), Oak Ridge National Laboratory, October 1991.
10. I. Johnson and C. E. Johnson, "Migration of Cesium and Molybdenum in Irradiated Oxide Fuels," *Proceedings of Symposium on Thermodynamics of Nuclear Material*, International Atomic Energy Agency, Vienna, Austria, October 21-24, 1974.
11. F. C. Iglesias, C. E. L. Hunt, F. Garisto, and D. S. Cox, "Ruthenium Release Kinetics from Uranium Oxides," *Proceedings of the ICHMT Conference on Fission Product Transport in Reactor Accidents*, Dubrovnik, Yugoslavia, May 22-26, 1989.
12. M. F. Osborne, R. A. Lorenz, and J. L. Collins, "Atmospheric Effects on Fission Product Behavior at Severe Accident Conditions," *Proceedings of the American Nuclear Society International Topical Meeting on the Safety of Thermal Reactors*, Portland, OR, July 25, 1991.
13. *Technical Bases for Estimating Fission Product Behavior During LWR Accidents*, NUREG-0772, U.S. Nuclear Regulatory Commission, June 1981.
14. M. R. Kuhlman, F. J. Lemicke, and R. O. Meyer, *CORSOR User's Manual*, NUREG/CR-4173 (BMI-2122), Battelle Memorial Institute, March 1985.
15. M. Silberberg, J. A. Mitchell, R. O. Meyer, and C. P. Ryder, *Reassessment of the Technical Bases for Estimating Source Terms*, NUREG-0956, U.S. Nuclear Regulatory Commission, July 1986.

16. A. H. Booth and G. T. Rymer, *Determination of the Diffusion Constant of Fission Xenon in  $UO_2$  Crystals and Sintered Compacts*, CRDC-720, National Research Council of Canada, August 1958.
17. J. Rest, "An Improved Model for Fission Product Behavior in Nuclear Fuel Under Normal and Accident Conditions," *J. Nucl. Mater.* 120, 195 (1984).
18. N. E. Bixler, T. J. Heames, D. A. Powers, and D. A. Williams, "Status of VICTORIA Development and Validation," presented at the USNRC Cooperative Severe Accident Research Program Review Meeting, Bethesda, MD, May 4-8, 1992.

Table 1. Fission product release tests conducted in hot cells at ORNL since 1976

Test prefix <sup>a</sup>	Type of fuel tested	Burnup (MWd/kg)	Number of tests	Temperature range (K)	Test atmosphere <sup>b</sup>
HBU	H. B. Robinson, PWR	30	11	775—1475	Steam, air
HT	H. B. Robinson, PWR	30	4	1575—1875	Steam
BWR	Peach Bottom 2, BWR	10-11	4	1125—1475	Steam
HI	HBR, PB, Oconee PWR and BWR	10-40	6	1675—2275	Steam
HS	Simulated PWR fuel <sup>c</sup>	44	4	1875—2700	Steam
VI	Oconee, BR3, PWR	40-47	6	1975—2700	Steam, hydrogen

<sup>a</sup>Each series of tests was numbered using prefix: HBU, high burnup; HT, high temperature; BWR, boiling-water reactor; HI, horizontal irradiated; HS, horizontal simulant; VI, vertical irradiated.

<sup>b</sup>All test atmospheres included some helium as a noncondensable carrier.

<sup>c</sup>Simulated PWR fuel, supplied by KfK in Germany, was composed of unirradiated UO<sub>2</sub> containing radioactive fission product tracers.

Table 2. Conditions and results for vertical (VI series) fission product release tests

Parameter	Test number					
	VI-1	VI-2	VI-3	VI-4	VI-5	VI-6
<b>Fuel specimen</b>	Oconee	BR3	BR3	BR3	BR3	BR3
Burnup, MWd/kg	40	44	44	47	42	42
In-pile Kr release, %	0.7	~2	~2	~5	~2	~2
<b>Test conditions</b>						
Test temperature, K	2020, 2300 <sup>a</sup>	2300	2000, 2700 <sup>a</sup>	2440	2000, 2720 <sup>a</sup>	2310
Time at temp, min	20, 20	60	20, 20	20	20, 20	60
Atmosphere	Steam	Steam	Steam	Hydrogen	Hydrogen	Hydrogen, steam <sup>b</sup>
<b>Fractional release, %</b>						
<sup>137</sup> Cs	63	67	100	96	100	80
<sup>85</sup> Kr	57	>31	100	85	100	75
<sup>129</sup> I	37	>33	c	71	c	c
<sup>125</sup> Sb	33	68	99	6.4	18	64
<sup>154</sup> Eu	0	0	~0.01	19	57	14
<sup>106</sup> Ru	0	0	5.0	0	0	0

<sup>a</sup>Some tests (VI-1, VI-3, and VI-5) were conducted in two phases, at two different temperatures.

<sup>b</sup>Test VI-6 was heated to 2300 K in hydrogen, then switched to a steam atmosphere.

<sup>c</sup>Analyses incomplete.

Table 3. Release data as function of temperature and atmosphere

Test No.	Maximum temperature (K)	Effective time (min)	Reactive atmosphere	Fission product released (% of inventory)		
				Cs (Kr, I)	Sb (Te)	Eu (Ba, Sr)
VI-3A	2000	34	Steam	22	0	0
VI-5A	2000	33	Hydrogen	31	0	1
VI-2AB	2300	25	Steam	57	49	0
VI-4ABC	2440	31	Hydrogen	96	6.4	19
VI-3ABC	2700	46	Steam	100	99	~0.01
VI-5ABC	2700	31	Hydrogen	100	18	57

Table 4. Comparison of cesium forms collected in steam and hydrogen atmosphere

Location	Atmosphere	Cesium	
		Mass (g)	% of released
<b>Test VI-3</b>	Steam		
Furnace		0.026	10.4
TGTs		0.057	22.9
Filters		0.166	66.7
Total		0.249	100.0
<b>Test VI-5</b>	Hydrogen		
Furnace		0.018	7.7
TGTs		0.142	60.4
Filters		0.075	31.9
Total		0.235	100.0

Table 5. Summary of results

---

- Behavior of volatile fission products (Kr, Xe, I, Cs)
    - Large increases in release rates with temperature
    - Release rates decrease after large fractional releases
    - Usually <1% of released I in filter-penetrating forms
    - Small atmosphere effect on release
    - Large atmosphere effect on Cs forms, transport
  - Behavior of less volatile species (Se, Mo, Ru, Te, Sb, Ba, Eu)
    - Te and Sb are retained by metallic Zircaloy cladding
    - Mo and Ru form more volatile species in steam (oxidizing conditions)
    - Sr, Ba, and Eu are more volatile in hydrogen (strongly reducing molten cladding)
    - Ce and Zr releases are insignificant
  - Fuel behavior
    - In steam, cladding oxidizes and supports fuel
    - In hydrogen, cladding melts, fuel collapses and disintegrates
  - ORNL diffusion release model
    - Simple, single-atom diffusion model reliably predicts release of volatile fission products
-

## **LIST OF FIGURES**

- 1. Vertical fission product release furnace.**
- 2. Vertical fission product release apparatus.**
- 3. Temperature, fission product release, and collection train operating histories for test VI-3.**
- 4. Cross section of fuel specimen from test VI-3 at 10.5 cm above bottom end. Test conditions were 20 min at 2700 K in steam.**
- 5. Distribution of principal fission products in the fuel-furnace tube assembly after test VI-3 in steam.**
- 6. Distribution of principal fission products in the fuel-furnace tube assembly after test VI-5 in hydrogen.**
- 7. Release rate coefficients for krypton (a) and cesium (b) vs temperature in test VI-3 (steam atmosphere) and VI-5 (hydrogen atmosphere).**
- 8. Comparison of diffusion coefficients for  $^{85}\text{Kr}$  and  $^{134}\text{Cs}$  in test VI-5 vs temperature with values calculated by the ORNL Diffusion Release Model.**
- 9. Release rate coefficients for cesium from VI series tests as a function of test temperature, compared with the CORSOR-M model.**
- 10. Diffusion coefficients for cesium from VI series tests as a function of temperature, compared with the ORNL Diffusion Release Model.**

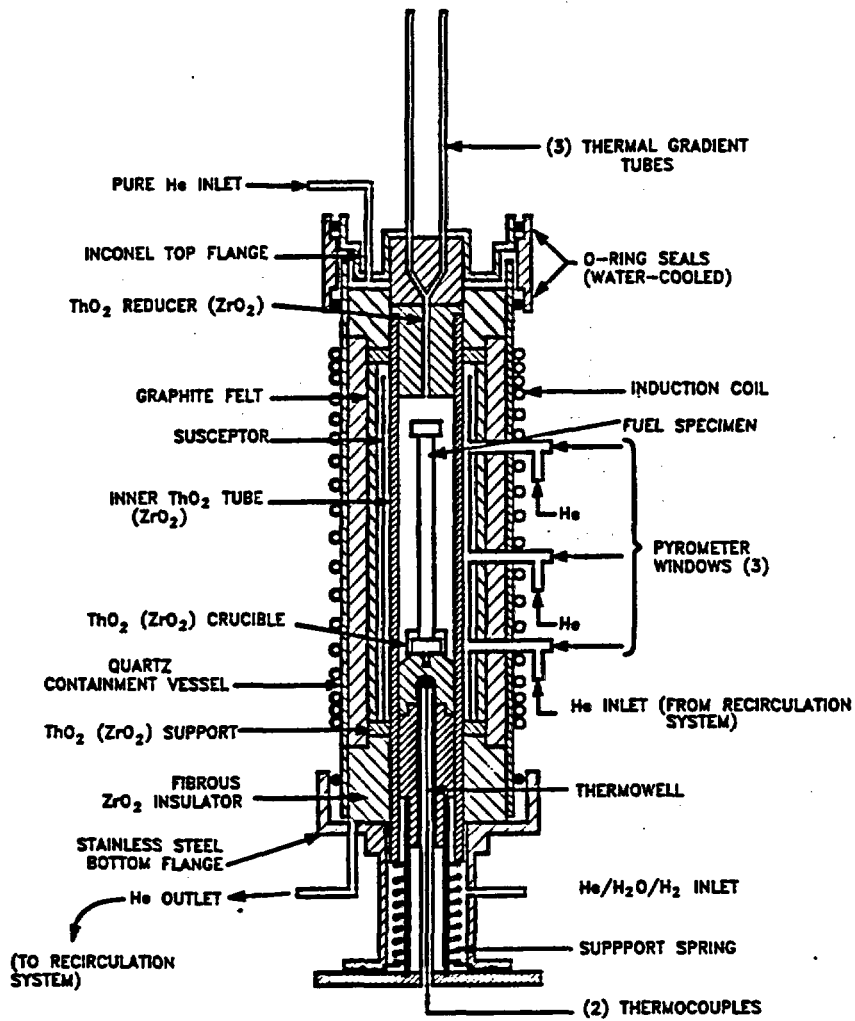


Fig. 1. Vertical fission product release furnace.

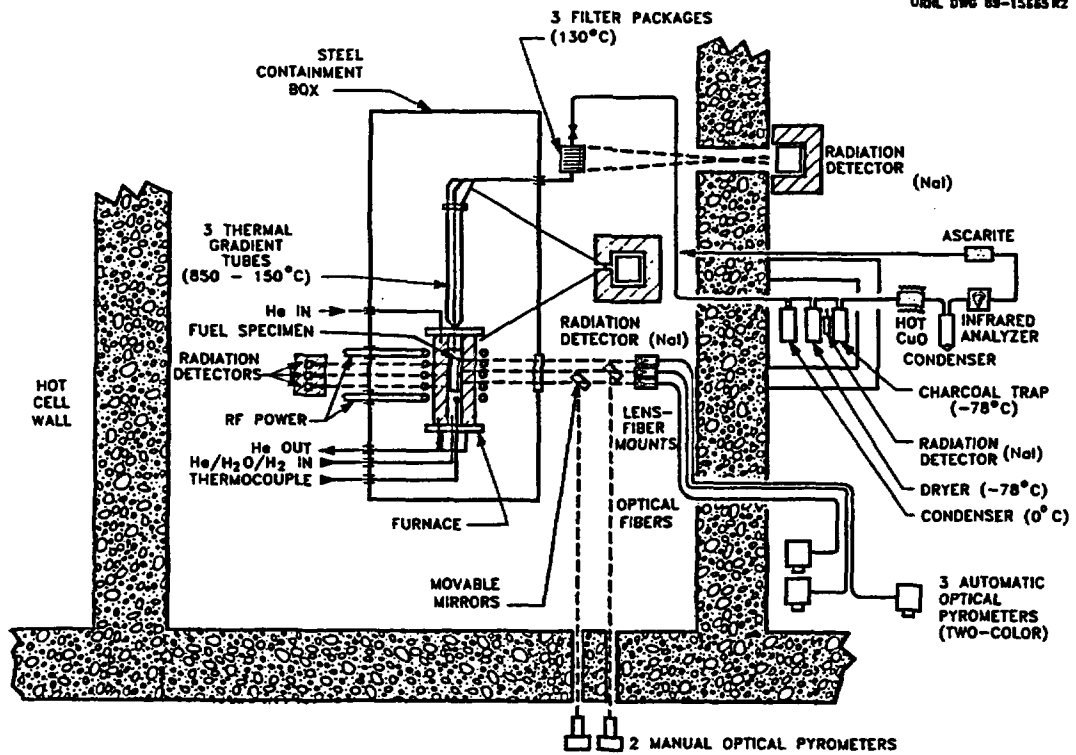


Fig. 2. Vertical fission product release apparatus.

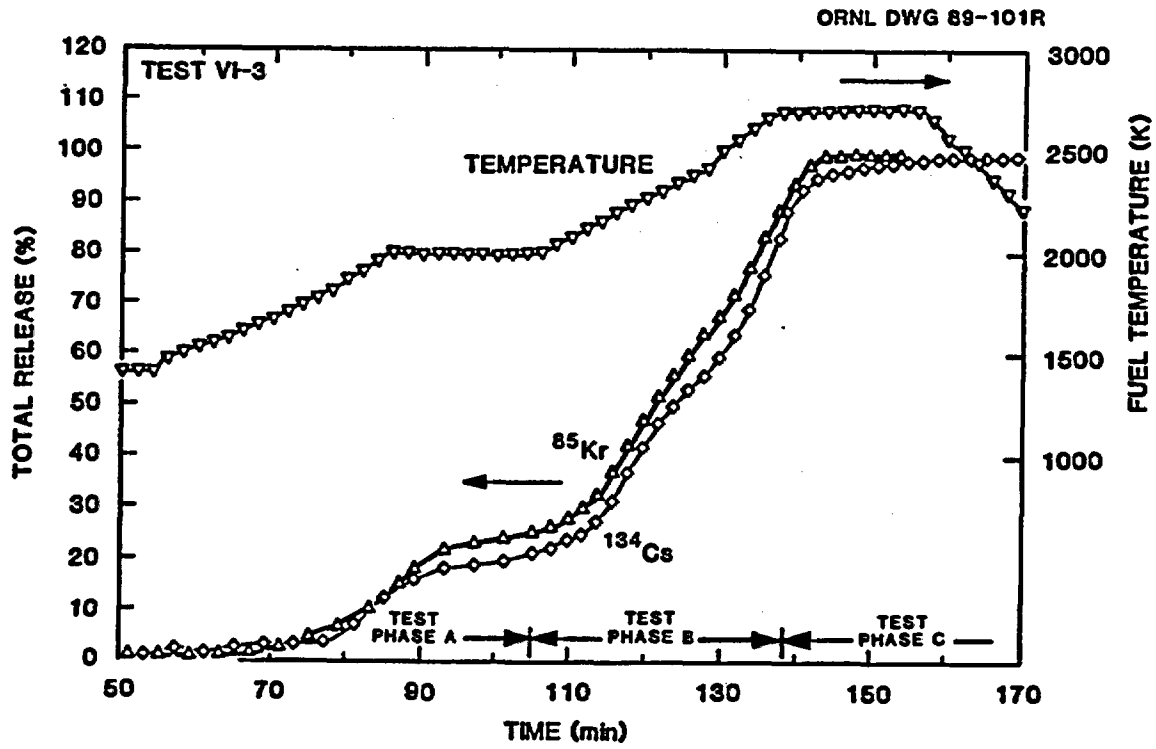
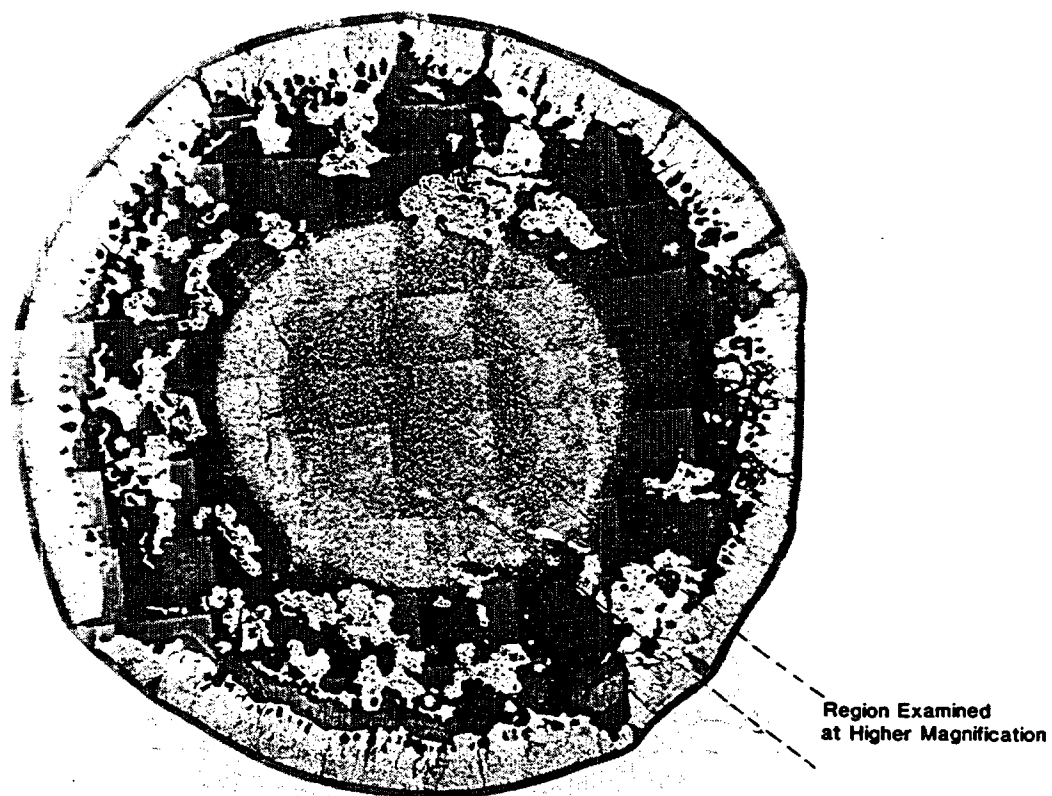


Fig. 3. Temperature, fission product release, and collection train operating histories for test VI-3.



**Fig. 4. Cross section of fuel specimen from test VI-3 at 10.5 cm above bottom end. Test conditions were 20 min at 2700 K in steam.**

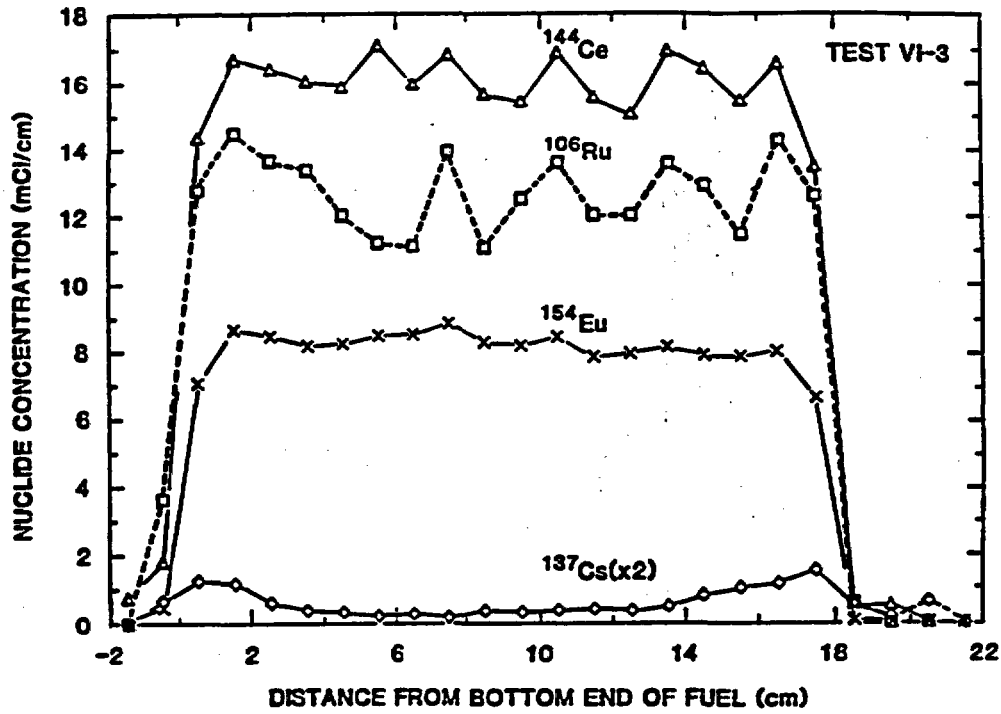


Fig. 5. Distribution of principal fission products in the fuel-furnace tube assembly after test VI-3 in steam.

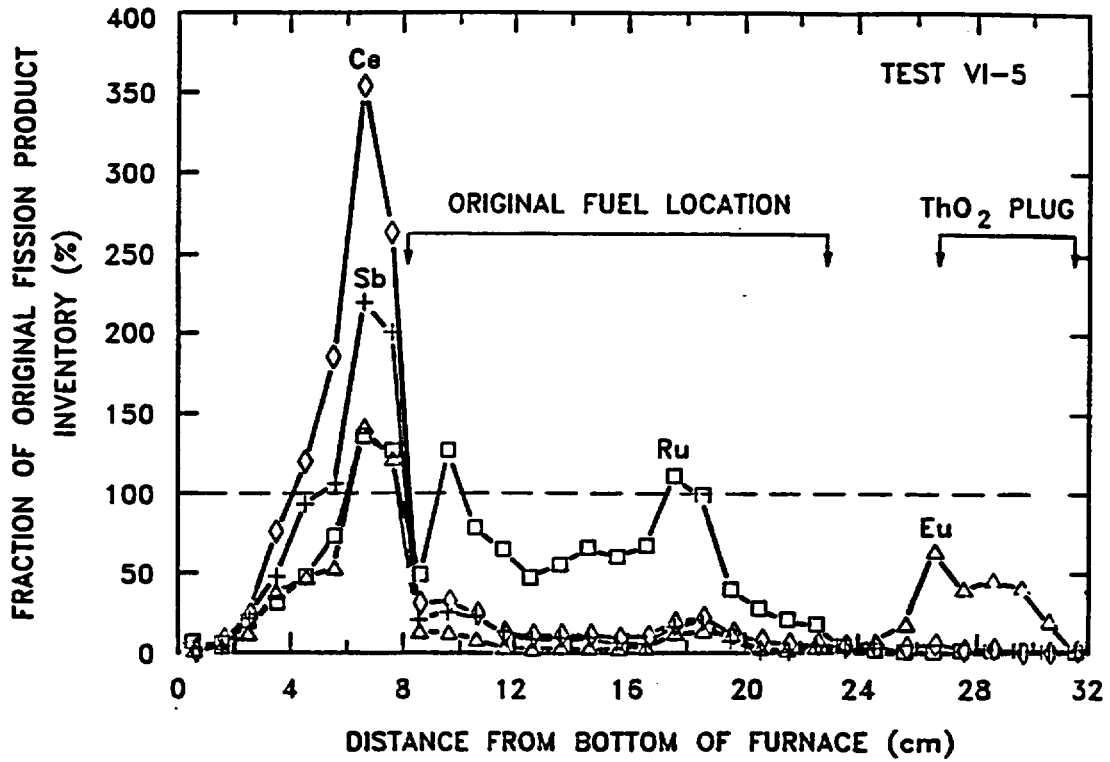


Fig. 6. Distribution of principal fission products in the fuel-furnace tube assembly after test VI-5 in hydrogen.

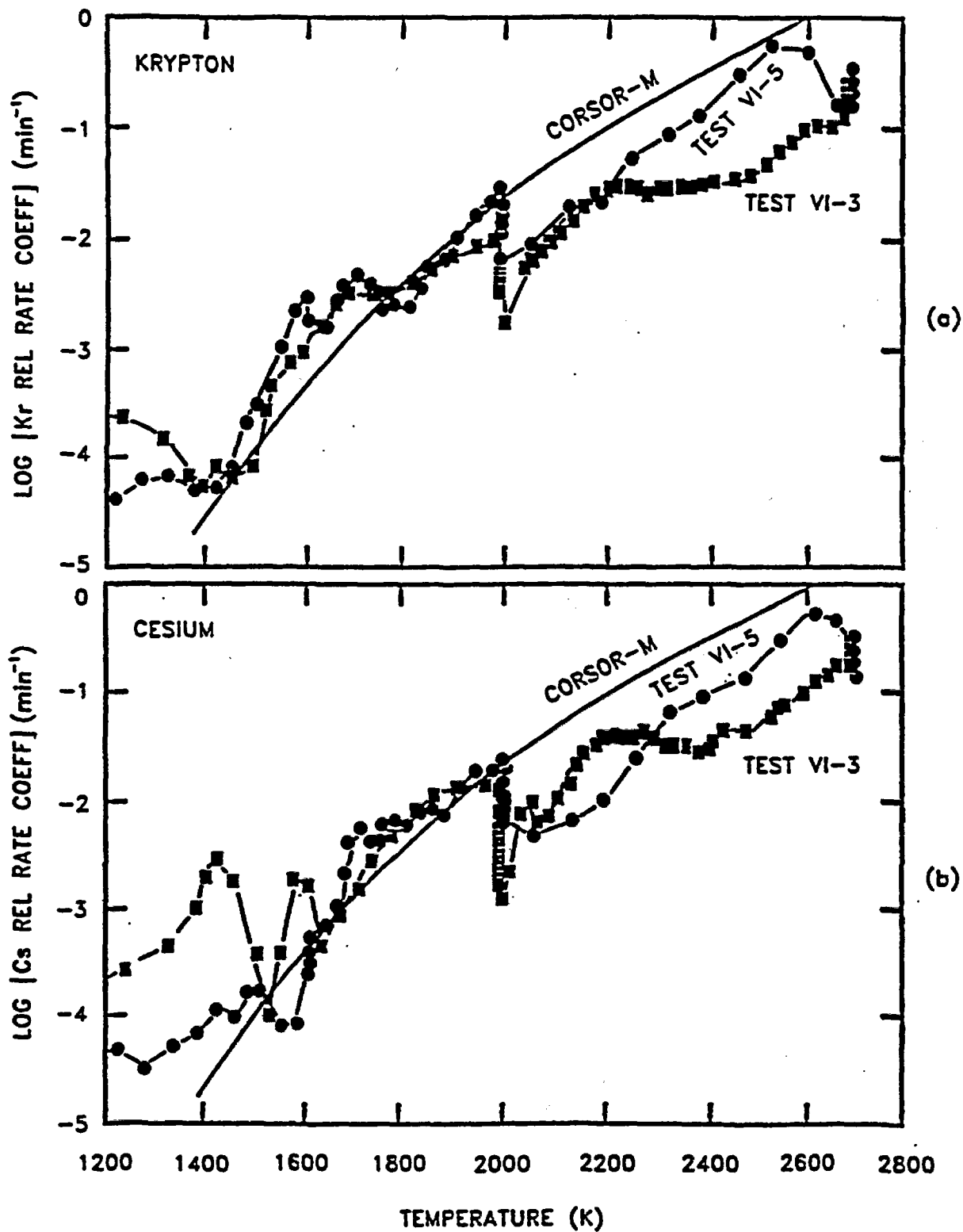


Fig. 7. Release rate coefficients for krypton (a) and cesium (b) vs temperature in test VI-3 (steam atmosphere) and VI-5 (hydrogen atmosphere).

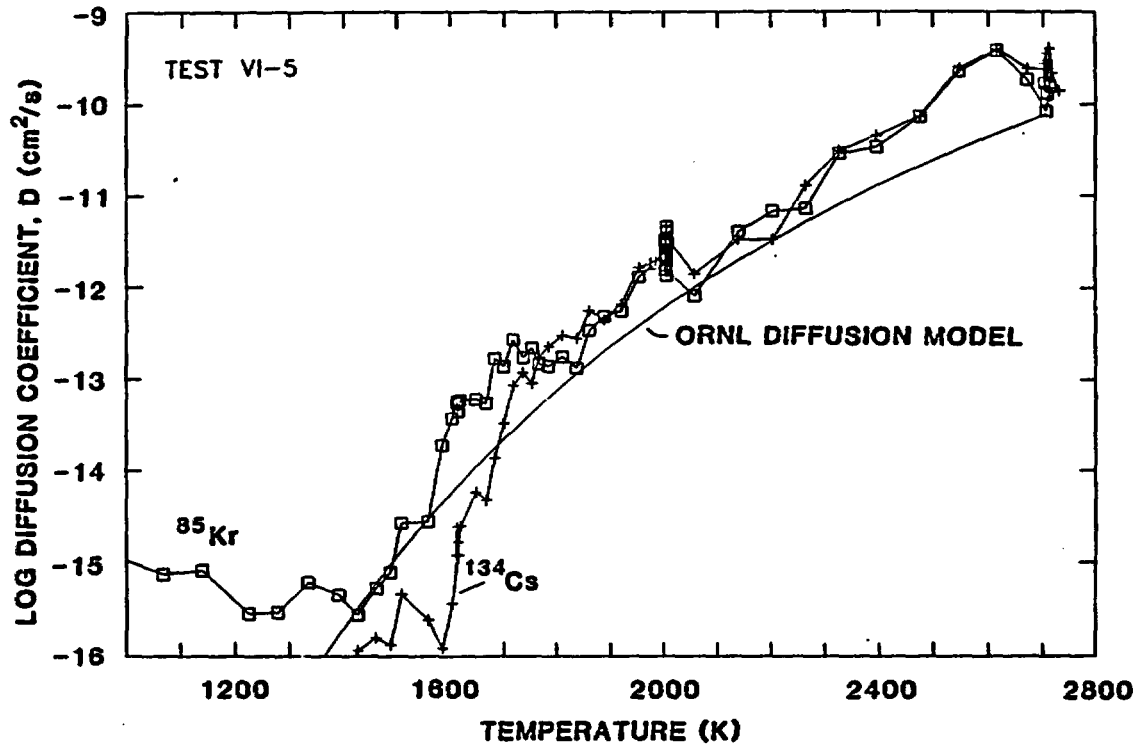


Fig. 8. Comparison of diffusion coefficients for  $^{85}\text{Kr}$  and  $^{134}\text{Cs}$  in test VI-5 vs temperature with values calculated by the ORNL Diffusion Release Model.

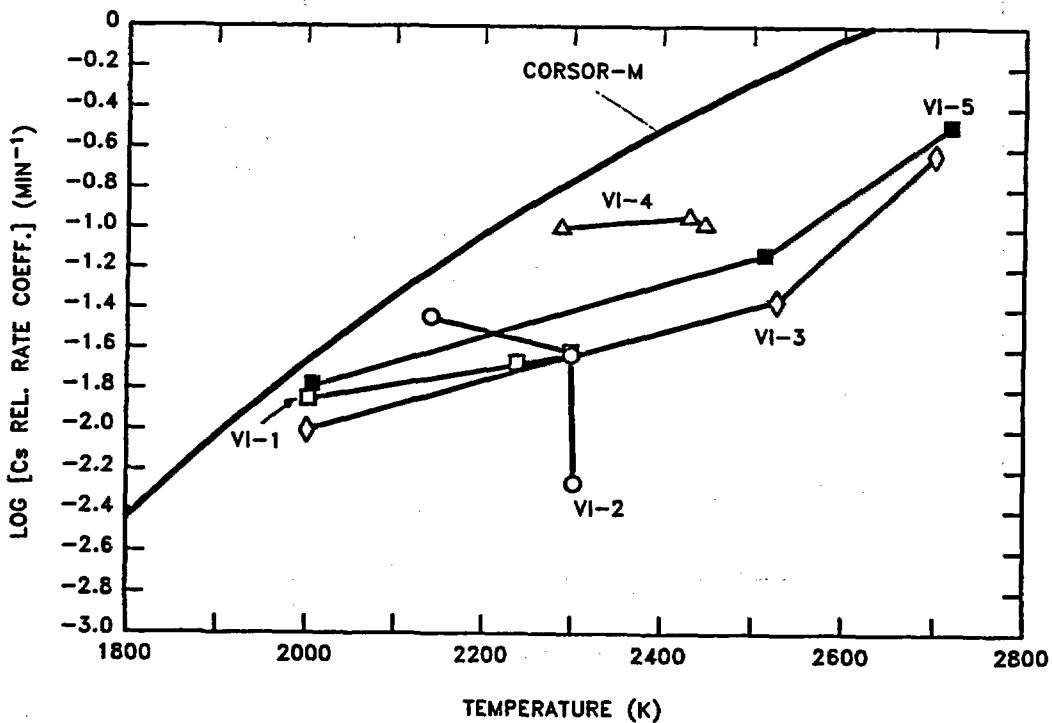


Fig. 9. Release rate coefficients for cesium from VI series tests as a function of test temperature, compared with the CORSOR-M model.

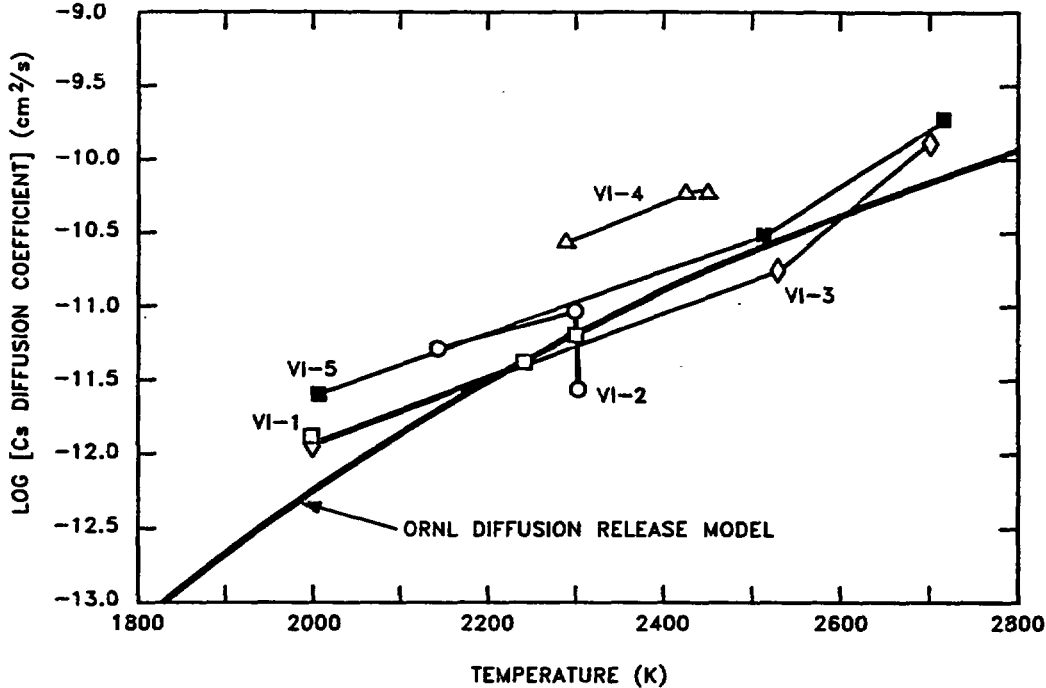


Fig. 10. Diffusion coefficients for cesium from VI series tests as a function of temperature, compared with the ORNL Diffusion Release Model.

# THE PROBABILITY OF MARK-I LINER ATTACK

T.G. Theofanous and H. Yan  
Center for Risk Studies and Safety  
Department of Chemical and Nuclear Engineering  
University of California, Santa Barbara  
Santa Barbara, CA 93106

## ABSTRACT

This paper is a followup to the work presented in NUREG/CR-5423 and constitutes a part of the implementation of the Risk-Oriented Accident Analysis Methodology (ROAAM) employed therein. In particular, it expands the quantification to include four independent evaluations carried out at RPI, ANL, SNL, and ANATECH, Inc. on various portions of the phenomenology involved. The results demonstrate a substantial synergism and convergence which are the essential ingredients for an eventual resolution.

## 1. INTRODUCTION

The Mark-I liner attack problem is well known and it will not be elaborated here. Very briefly, it is concerned with the possibility that the molten corium released from the reactor vessel (in an unmitigated severe accident in a BWR with a Mark-I pressure suppression containment) will come in contact and cause a breach in the containment liner. This liner is the containment pressure boundary, and such a breach would constitute an "early" containment failure. The situation is illustrated in Figure 1. The important phenomenology is sketched in Figure 2, which also notes the key terminology employed in such discussions. The object is to determine the likelihood of such a liner breach (conditional on the occurrence of an unmitigated severe accident), and especially to consider the effect of flooding (by water) of the drywell floor.

A first step toward assessing this likelihood was made in NUREG/CR-5423 (Theofanous et al., 1991). The approach was to decompose the problem in the manner illustrated in Figure 3 and to define several scenarios for consideration in the manner illustrated in Figure 4. The quantification employs a probability scale, and the results, summarized in Figure 5, interpreted by the same scale, indicate that in the presence of water such liner failure is "physically unreasonable."

The key aspect of the ROAAM is that its implementation must be viewed as a "process" of successively refocusing the technical issues until eventual resolution. Resolution is defined when the quantification of each part has reached broad support among the respectively available experts and, in particular, when no serious technical issues remain outstanding. In this particular case, the ROAAM process was initiated by the issuance of Draft NUREG/CR-5423 in January 1990. This draft was distributed to a panel of 19 experts appointed by the NRC for its review—the aim in selecting such an extensive panel was to not leave out anyone with prior experience and expertise in any of the key parts of this problem. During the following six months, the comments were

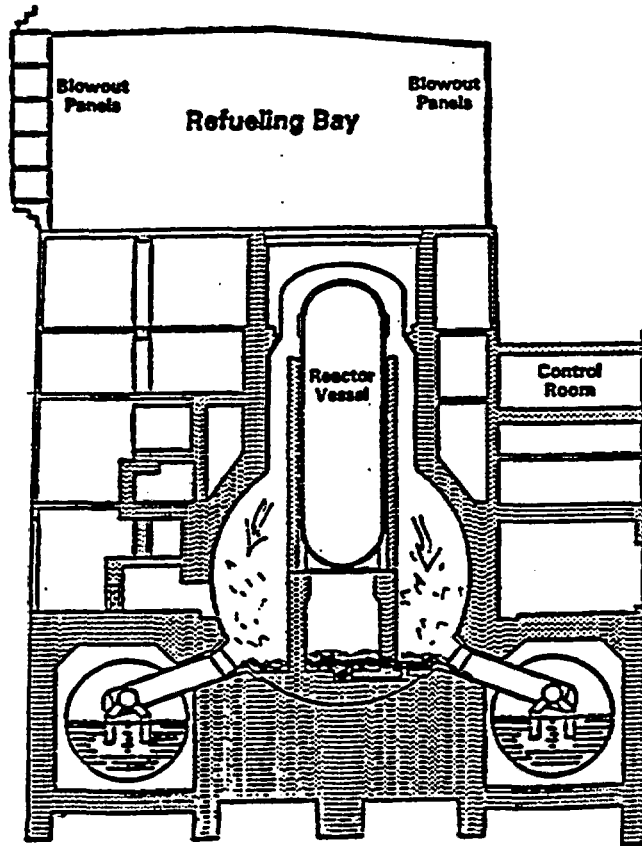


Figure 1. Illustration of the Mark-I liner attack problem.

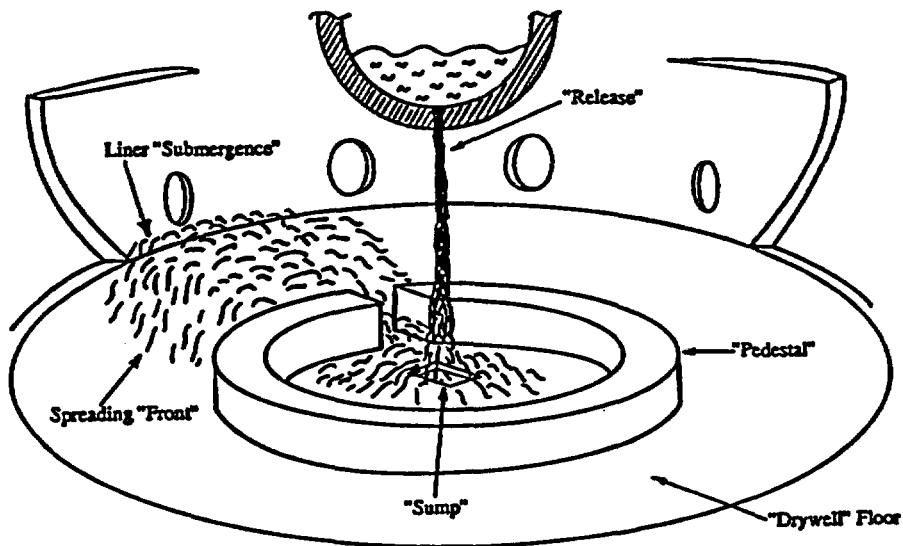


Figure 2. Illustration of the phenomenology involved in the Mark-I liner attack problem.

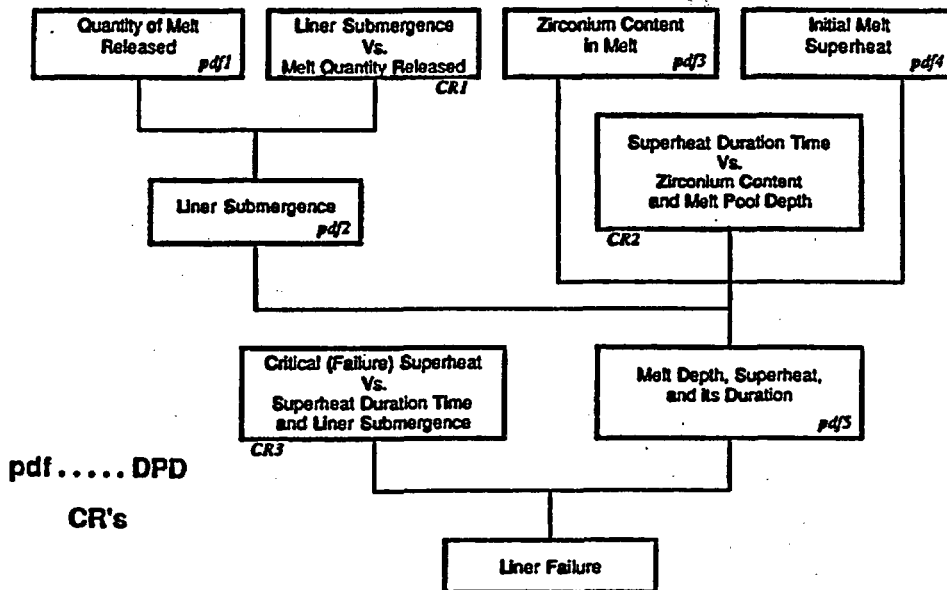


Figure 3. The probabilistic framework for addressing Mark-I liner attack.

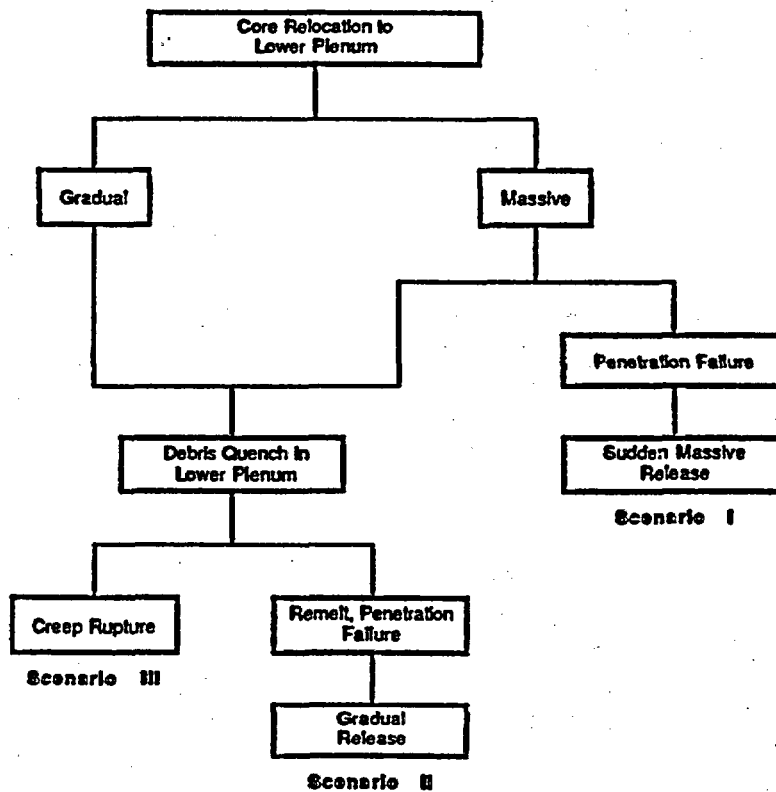


Figure 4. The enveloping, splinter scenarios considered.

	Scenario I	Scenario II
Without Water	1	0.63
With Water	$6 \times 10^{-5}$	or $1.2 \times 10^{-4}$ $3.5 \times 10^{-6}$

Figure 5. The results of quantification in NUREG/CR-5423.

received, the authors provided point-by-point responses to all the comments, and all this material was discussed in a workshop that took place in Harpers Ferry, West Virginia, in the presence of the authors, the review panel, NRC staff, representatives of the ACRS, NSRRC, and the public. As a result of this workshop, four areas requiring further consideration were identified, while the methodology and the specific decomposition (probabilistic framework) essentially received fully support. Four expert groups were formed to pursue these four areas, in a focused manner, and this occurred in oneday meetings during December 1990 and January 1991. The report, NUREG/CR-5423, was issued in August 1991, including appropriate revisions, several additional appendices, and a complete record of reviewers comments (signed), authors responses, a summary of the Harpers Ferry workshop, a closing statement by each one of the experts after the workshop, and a summary of the work, conclusions and the recommendations of each one of the four expert working groups.

Briefly, the four areas and respective recommendations for additional work can be summarized as follows:

**1. Melt Release (Initial) Conditions.** In NUREG/CR-5423, the two main scenarios were defined as releases of mainly metallic (Scenario II) or oxidic (Scenario I) melts, and the concern was that these may not be adequately enveloping. In particular, there was concern that this approach overlooked the possibility of a massive oxidic release, as in Scenario I, but with a very strong metallic component derived from melting of the upper internal (steel) structures. The problem was assigned to the Rensselaer Polytechnic Institute (PRI) for further investigation using the computer code APRIL.

**2. Melt Spreading to the Liner.** In NUREG/CR-5423, the possible range of melt depths against the liner was assessed under the assumption that for Scenario I the behavior is controlled primarily by hydrodynamic effects (Froude number scaled simulant experiments) and for Scenario II primarily by continuity and strong freezing behavior. The concern was that such quantification needed independent inputs with a more complete modelling approach. The problem was assigned to Argonne National Laboratory (ANL) for such evaluation using the computer code MELTSPREAD.

**3. Corium Concrete Interactions.** In NUREG/CR-5423, the corium superheat (temperature in excess of the melt liquidus) was identified as one of the key parameters affecting the

liner thermal loading, and it was determined that for the initial values in the range of interest to this problem, such superheats would decrease to zero rather rapidly. Also, it was concluded that the presence of zirconium and stainless steel and associated exothermic chemical reactions with the concrete decomposition products could not lead to chemical runaways. The assessments were made with the author's own analysis tool, and it was noted that an independent, audit-type evaluation using the state-of-the-art code CORCON-MOD 3 (not yet available, but about to be released) would be quite appropriate. This task was assigned to the CORCON developer, Sandia National Laboratories (SNL).

**4. Liner Failure Criteria.** In NURETH/CR-5423, liner failure was assumed when any part of the liner reached 1500 °C, which is essentially a melt-failure criteria. The authors also carried out an elastic-plastic structural analysis (an ABAQUS finite element model of the whole spherical shell) and concluded that the stiffness of the cold portion of the liner was adequate to prevent catastrophic failure due to loss of strength along the narrow zone in contact with the melt. The remaining concern was whether the liner could be subject to failure at significantly lower temperatures by creep rupture. Fortunately, at the time of the review, the needed high temperature creep data began to become available from a "lower head integrity" program at INEL, and the task was assigned to ANATECH, Inc.

The work in all four areas took place in the mid-1991 to mid-1992 time frame, and at this time, the results of all four reports are available in final form. These final reports incorporate an initial set of comments from the members of the respective working groups, and a final set of comments and respective authors' responses have been made available to the authors of NUREG/CR-5423 for integration into a final quantification and a final report expected in February 1993. This final report is expected to undergo one more peer review by an NRC-appointed panel and to be published, together with these peer review reports, within the next several months. At this time, we can state that all four independent evaluations show substantial synergism and convergence with NUREG/CR-5423 and we, therefore, expect that this final report will be accepted as the final step in the ROAAM resolution process. In this paper we summarize the results of the four independent evaluations and discuss their implications to the overall quantification.

## **2. RESULTS OF THE INDEPENDENT EVALUATION AND DISCUSSION**

### **2.1 Melt Initial Conditions**

The APRIL modelling effort (Podowski and Cho, 1992) paid special attention to representing the upper internal structures and the thermal loading on them due to the flow of highly superheated steam. All calculations produced a gradual relocation behavior (i.e., Scenario II) with an early drain plug failure. The most severe release found involved ~10 m<sup>3</sup> of 95% metallic melt flowing out of the vessel at a rate of 0.66 m<sup>3</sup>/min. This compares very well with the "peak release" Scenario II considered in NUREG/CR-5423, as illustrated in Figure 6. The PRI report (Podowski and Cho, 1992) concluded that the "bounding conditions used in 5423 seem to be adequate."

### **2.2 Melt Spreading to Liner**

The modelling approach and wide scope of phenomena included in MELTSPREAD are indicated in Figure 7. It is noteworthy that, among other verification aspects, the code compares well with the simulant tests reported in NUREG/CR-5423. The results of a large number of parametric and sensitivity studies (Sienicki, Chu and Spencer, 1992) are compared to the

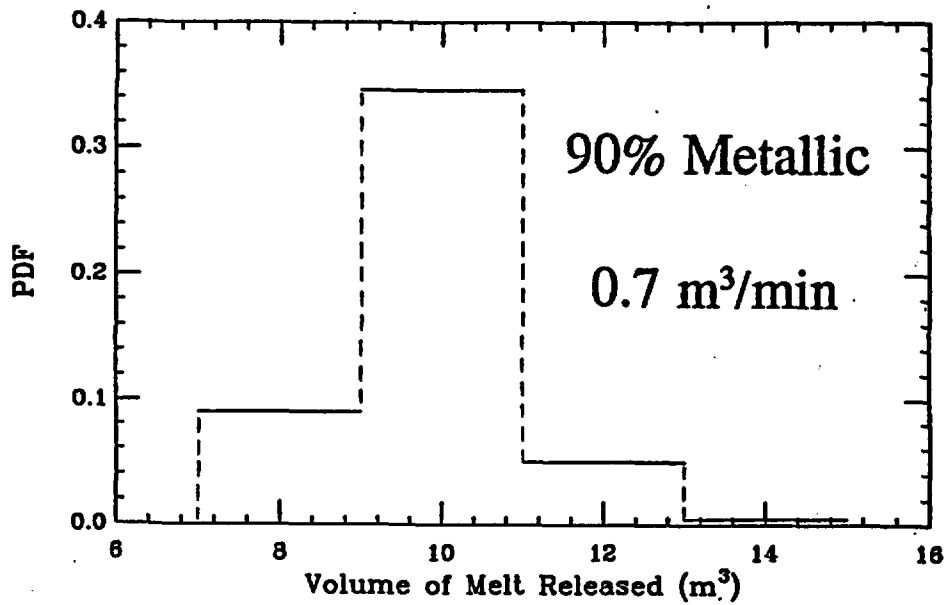


Figure 6. The quantification of release in Scenario II (peak release).

NUREG/CR-5423 quantification in Figures 8 and 9 for Scenario I- and II-type releases, respectively. Clearly, the Scenario I quantification is adequate, while that of Scenario II is grossly conservative. In particular, we see that according to MELTSPREAD the melt does not even reach the liner, except for extremely massive releases of  $\sim 30 \text{ m}^3$ .

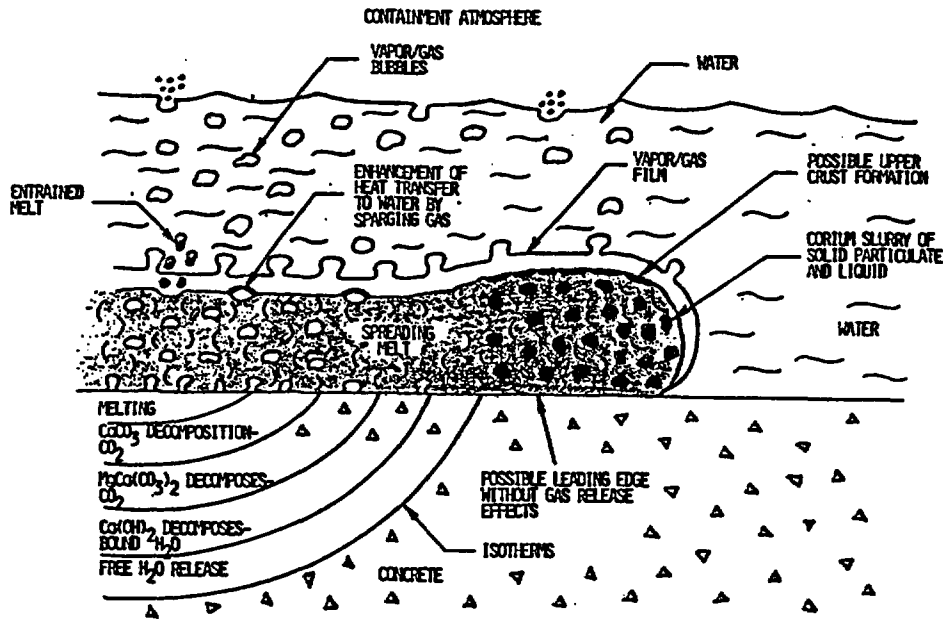


Figure 7. Illustration of the phenomena considered in MELTSPREAD.

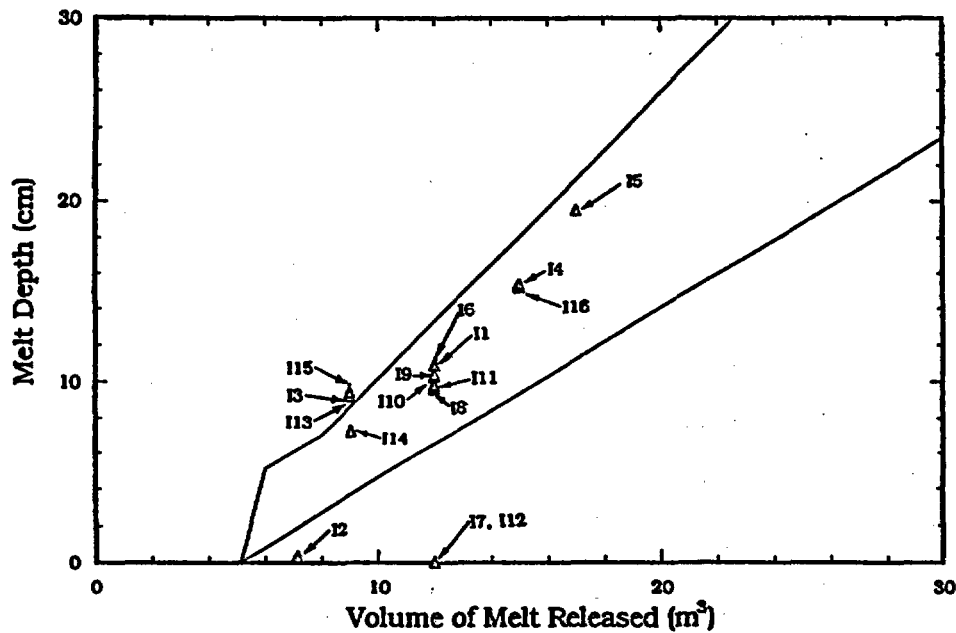


Figure 8. The MELTSPREAD results shown in relation to the original NUREG/CR-5423 quantification for Scenario I.

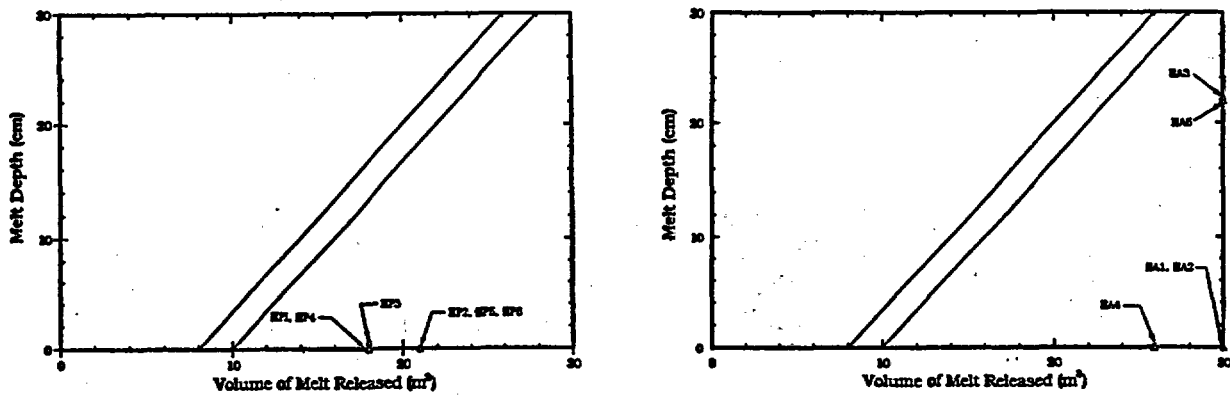


Figure 9. The MELTSPREAD results shown in relation to the original NUREG/CR-5423 quantification for Scenario II.

### 2.3 Duration of Melt Superheat

The Sandia studies in this area (Powers and Heames, 1992) confirmed that the duration of melt superheat scales with the depth of the melt and found the NUREG/CR-5423 quantification in this area rather conservative. This can be seen by the direct comparison of the  $t^*/D$  values computed for 17 audit runs for various permutations of initial melt superheat ( $\Delta T$ ), mass fraction of zirconium in the melt ( $\omega$ ), and melt depth ( $D$ ), in the ranges of interest (for the more limiting Scenario I), as found in Figure 10. Note that the very significant discrepancies appear for the extreme value (0.4) of the  $\omega$  parameter, and the practically uninteresting extremes of very small

depths (2.3 cm) or superheat (10 K). In all other cases (separated out in bold in the figure) the agreement is within about a factor of 2, much better in many cases, but always NUREG/CR-5423 is conservative.

#	$\Delta T$ (K)	$\omega$ (-)	D (cm)	$t^*/D$ (s/cm)	$t^*/D$ -5423 (s/cm)	
1	10	0.05	2.3		<b>0.43</b>	<b>1</b>
2	150	0.05	2.3	1.3	6	
3	10	0.40	2.3		<b>0.4</b>	<b>1</b>
4	10	0.05	20.6	0.3	1	
5	150	0.40	2.3	1.3	16.5	
6	150	0.05	20.6		<b>4.1</b>	<b>6</b>
7	10	0.40	20.6	0.15	1	
8	150	0.40	20.6	1.7	16.5	
9	40	0.14	11.4		<b>1.9</b>	<b>2</b>
10	40	0.40	11.4		<b>1.3</b>	<b>2.5</b>
11	10	0.14	20.6	0.26	1	
12	40	0.14	20.6		<b>1.45</b>	<b>2.0</b>
13	40	0.40	20.6	0.44	2.5	
14	150	0.14	11.4		<b>6.1</b>	<b>8.5</b>
15	75	0.14	11.4		<b>2.63</b>	<b>4.5</b>
16	75	0.14	20.6		<b>4.75</b>	<b>4.5</b>
17	75	0.40	20.6	0.73	5.5	

Figure 10. Summary of the CORCON-MOD 3 results in relation to the quantification employed in NUREG/CR-5423.

#### 2.4 Liner Failure Criteria

The ANATECH work (Castro et al., 1993) fitted a viscoplastic model to the recently obtained high-temperature creep data at INEL, and produced a three-dimensional finite element calculation of the Mark-I shell subject to a thermal loading pattern similar to those found in NUREG/CR-5423. Employing a strain-based failure criterion (~15% local strain) this calculation indicated "rupture" by local creep at a peak temperature of 1260 °C. This failure temperature seems to be supported also by an application of a damage-accumulation criterion modelled according to the Larson-Miller parameter. The mechanism is that local hot spots (an azimuthal zone of a few centimeters in height) at these temperature levels can, under the internal pressure load, creep outward sufficiently to produce local strain in the range of 15 to 20%.

### 3. SYNTHESIS OF THE BY-PARTS QUANTIFICATION

Based on the above, the NUREG/CR-5423 quantification is conservative in all areas, except for the liner failure criteria, where a reduction by 240 °C is indicated. For a Scenario II, this relatively small reduction is overshadowed by the MELTSPREAD results indicating that the melt does not even reach the liner. For Scenario I, the impact of this reduction (ignoring all the conservatisms revealed by the independent quantification) is readily seen from a sensitivity study presented in NUREG/CR-5423 and included here as Figure 11—i.e., a failure probability

increase from  $6 \times 10^{-5}$  to  $4 \times 10^{-3}$ . Accounting just for the conservatism in the time duration of superheat, i.e., using the CORCON-MOD 3 result (in conjunction with a  $1200^\circ\text{C}$  failure criterion) brings the probability back down to  $2 \times 10^{-3}$ . Clearly, for both scenarios the conclusion of NUREG/CR-5423, that in the presence of water liner failure is physically unreasonable, is confirmed.

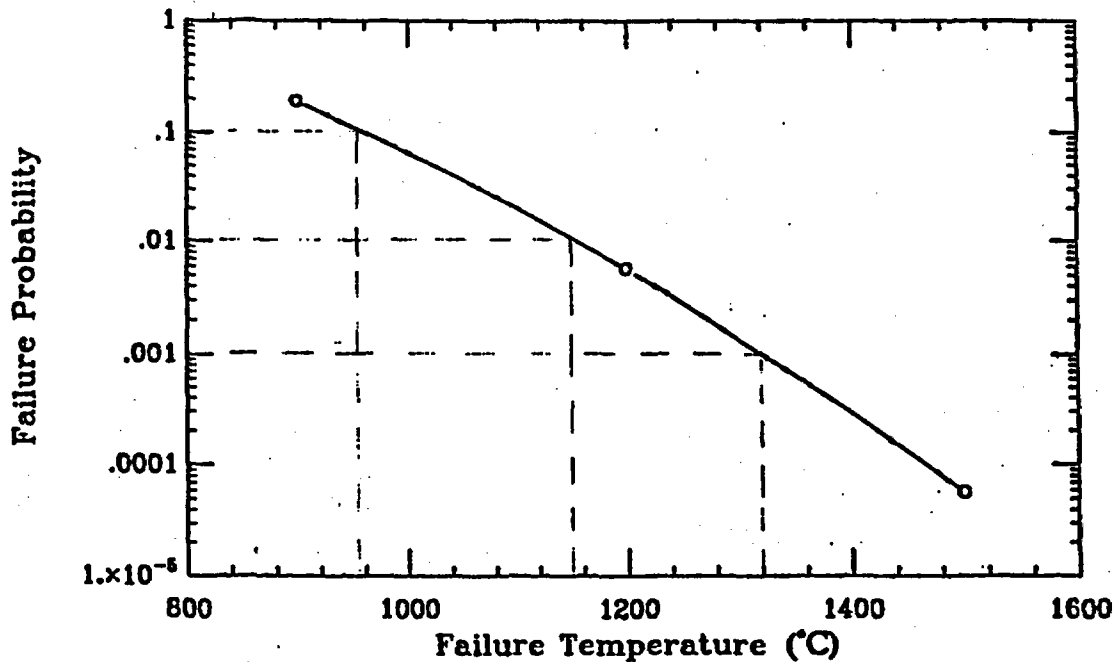


Figure 11. The probability of failure as a function of the liner failure criteria.

#### 4. EXTRAPOLATION TO OTHER MARK-I PLANTS

The original quantification in NUREG/CR-5423, and that discussed above, were for the Peach Bottom NPR. The purpose of this discussion is to provide some initial perspective of the potential extrapolation of these results to the other Mark-I plants. It is emphasized that we did not conduct a detailed plant-specific examination; rather, the discussion is based on data obtained from various sources, and again, it provides for an initial perspective and illustration of how one might go about such a task. This is why the discussion is provided in general rather than in plant-specific terms. In addition, it is noted that based on the results of this work the NRC staff formulated a set of recommended guidelines for use in the individual plant examinations in this area.

Examination of construction data of all Mark-I plants indicates that the pedestal doors are very similar, and that the principal floor dimensions, the drywell floor area, and the sump volumes (except for four cases for which this information could not be found) are equal to or larger than the Peach Bottom values.

Another important design parameter is the downcomer entrance height above the drywell floor. It appears that in two cases this parameter has been reported as zero. We do not know the design details, but both cases need to be examined as to whether they allow the possibility of melt running directly into the downcomer—such an occurrence would almost certainly produce failure. In another case we found a reported height of 23 cm, which is a little less than one-half the Peach Bottom value. Even so, with reference to Figures 8 and 9, used in conjunction

with Scenario I and II releases (as found in NUREG/CR-5423), we conclude that this situation does not present a significant concern with respect to melt overflow into the downcomer(s) or having an adequate degree of cooling of the liner above the melt (internal sprays). This absolute statement is further augmented when we recognize that the plant has about one-half the amount of fuel in the Peach Bottom plant. Then, there are four plants in which this height is ~30 cm; all four are of significantly lower power than the Peach Bottom plant, and for the reasons explained above, we see no particular concerns. In all other plants the height is significantly larger than 40 cm, and again, the Peach Bottom results are applicable.

As a separate issue, we made an attempt to look at the possibility that floor-mounted equipment in the drywell, especially across from the pedestal door, could present any significant obstacles with a significant impact on the melt spreading process. We could learn that this was not the case, but we did not manage to examine the relevant construction details (or any containment) directly for this purpose. Clearly, this is a subject well-suited to the individual plant examinations, and the guidance mentioned above specifically provides for it.

## 5. CONCLUSIONS

The ROAM process applied to the Mark-I liner attack problem is now essentially complete. What remains is to conduct the final peer review and issue the final report. The results confirm the NUREG/CR-5423 conclusion that such failure, in the presence of water in the drywell, is physically unreasonable. This conclusion applies to Peach Bottom, but an initial examination of relevant plant parameters indicates that it may also be applicable to all but two plants. The individual plant examination program has been supplied the relevant guidance, and final conclusions on the other plants must await this detailed plant-specific examination.

## ACKNOWLEDGMENTS

This work was supported by the U.S. Nuclear Regulatory Commission under Contract No. 04-92-055. The cooperation and support of our project manager, Dr. S. Basu, is gratefully acknowledged.

## REFERENCES

1. Castro, J.C., Y.R. Rashid, R.A. Dameron and J.S. Maxwell (1992) "Creep-Rupture Failure in a Mark 1 Containment," ANA-92-0143, ANATECH Research Corp.
2. Podowski, M.Z. and C.S. Cho (1992) "The Effect of Heatup and Meltdown of Reactor Vessel Upper Internals on the Composition of Corium Discharged into the Drywell of BWR Mark-I Containment," Rensselaer Polytechnic Institute Report prepared for Oak Ridge National Laboratory.
3. Powers, D.A. and T.J. Heames (1992) "Audit Calculations with CORCON-MOD 3 of the Duration of Superheat," SAND91-2692, Sandia National Laboratories.
4. Sienicki, J.J., C.C. Chu and B.W. Spencer (1992) "Comparison of MELTSPREAD-I Calculations of Corium Depth Next to the Mark-I Liner with NUREG/CR-5423," Draft Report ANL/RE/LWR 92-5, Argonne National Laboratory.
5. Theofanous, T.G., W.H. Amarasooriya, H. Yan and U. Ratnam (1991) "The Probability of Liner Failure in a Mark-I Containment," NUREG/CR-5423, U.S. Nuclear Regulatory Commission.

PROGRESS IN BNL HIGH-TEMPERATURE HYDROGEN COMBUSTION RESEARCH PROGRAM\*

G. Ciccarelli, T. Ginsberg, J. Boccio, J. Curtiss, C. Economos, J. Jahelka;  
K. Sato<sup>1</sup>

Brookhaven National Laboratory  
Department of Nuclear Energy  
Safety and Risk Evaluation Division  
Upton, NY 11973

ABSTRACT

The objectives of the BNL High-Temperature Hydrogen Combustion Research Program are discussed. The experimental facilities are described and two sets of preliminary experiments are presented. Chemical reaction time experiments have been performed to determine the length of time reactive mixtures of interest can be kept at temperature before reaction in the absence of ignition sources consumes the reactants. Preliminary observations are presented for temperatures in the range 588K-700K. Detonation experiments are described in which detonation cell width is measured as a measure of mixture sensitivity to detonation. Preliminary experiments are described which are being carried out to establish data reproducibility with previous measurements in the literature and to test out and refine experimental methods.

1. INTRODUCTION

Intensive studies of hydrogen combustion phenomena were carried out during the 1980s. Much of this effort was driven by issues related to nuclear reactor safety. The "high-speed" combustion phenomena of flame acceleration, deflagration-to-detonation transition, direct initiation of detonation, detonation propagation, limits of detonation in tubes and channels, transmission of detonations from confined to unconfined geometry and other related phenomena were studied using a variety of gaseous fuel-oxidant systems, including hydrogen-steam-air systems of interest in reactor safety studies. Several reviews are available which document this work [Lee, 1989; Berman, 1986].

---

\*This work was performed under the auspices of the U. S. Nuclear Regulatory Commission.

<sup>1</sup>Visiting Research Engineer, Nuclear Power Engineering Corporation; Tokyo, Japan.

The current understanding of accelerated flames and detonations is based upon a database of gaseous mixtures whose initial conditions generally involved temperatures of 300K and, in some cases, up to 400K [Lee, 1989; Stamps, 1991]. The higher temperature data involved hydrogen-steam-air mixtures of interest to reactor safety studies, where temperatures of concern were in the range of the saturation temperature of water at pressures of 0.1-0.3 MPa. Some severe accident sequences have been postulated that are characterized by the potential existence in containment of premixtures of hydrogen-steam-air mixtures at temperatures greater than 400K and steam fractions of 0.4 or greater [Stamps and Berman, 1988; Yang, 1992]. The objective of the BNL high-speed hydrogen combustion program is to extend the understanding of high-speed combustion phenomena to conditions of high temperature.

The BNL High-Temperature Hydrogen Combustion Research Program is a research effort involving the U. S. Nuclear Regulatory Commission, the Japanese Nuclear Power Engineering Corporation, and BNL. The program addresses the following major technical questions:

- (1) What is the effect of temperature on the inherent sensitivity to detonation of gaseous mixtures of hydrogen, steam, and air as measured via the cell size?
- (2) What is the effect of temperature on the potential for gaseous mixtures to undergo deflagration-to-detonation transition (DDT) in a field of obstacles, and how does venting reduce the potential for DDT?
- (3) What is the effect of temperature on the conditions for hot jet initiation and detonation transmission?
- (4) Do currently available models adequately characterize the detonation phenomena at elevated mixture temperatures?

This paper describes progress made in several basic elements of the program.

## 2. EXPERIMENTAL COMBUSTION APPARATUS

In order to address the high-temperature hydrogen combustion issues, BNL has designed and constructed the Small-Scale Development Apparatus (SSDA) and is in the process of developing the High-Temperature Combustion Facility (HTCF). Table 1 summarizes the major features of the SSDA and the HTCF. The objective of the SSDA is to provide information relevant to the design and operation of the larger HTCF and to provide preliminary data on the effect of temperature on the inherent sensitivity of mixtures of hydrogen, steam, and air to undergo detonation.

The central element of the SSDA is a 4-inch, inner diameter, 20-foot long, stainless steel pressure vessel, capable of being heated to 700K. The central element of the HTCF is a 10.75-inch, inner diameter, 60-foot long, stainless steel pressure vessel, also capable of being heated to 700K. Both vessels are

designed incorporating the quality-control standards of the ASME Boiler Code. This paper focusses on the SSDA.

Figure 1 is a schematic diagram of the test apparatus. The apparatus consists of three major components: (1) the test vessel, (2) the mixing chamber, and (3) the driver section. The SSDA test vessel, whose basic features are described in Table 1, is heated by pads of ceramic-bead insulated, nichrome resistance wire, which cover the vessel wall. The heating system is capable of heating the test vessel to 700K in 3.5 hours with a  $\pm 14K$  spatial uniformity. The maximum allowable working pressure (MAWP) is 1800 psi at 700K. The combustible gas mixture is produced in a 30-liter mixing chamber by the method of partial pressures. The mixture is stirred for two minutes using a rotating impeller in order to ensure proper mixing of the gas constituents. In the cases where steam makes up part of the mixture, the mixing chamber is heated to 422K, and a predetermined amount of liquid water is added. The final pressure in the mixing chamber after heating is 0.3 MPa. During the time that the mixture is being produced in the mixing chamber, the test vessel is being heated and evacuated. The mixing vessel is subsequently depressurized by flowing the test mixture gas into the test vessel. The gas is heated using a radiation-heated tube coil to the desired temperature as it flows from the mixing vessel into the test vessel. The test vessel is charged to a pressure of one atmosphere using the computer control software system.

The SSDA is designed so that it can accommodate a gaseous detonation driver system or a solid explosive driver system. Experiments will be conducted using an acetylene-oxygen gaseous driver system to initiate detonations in the test mixture. Figure 1 schematically represents the driver system on the left side of the diagram, showing the location of the high-voltage discharge system and the acetylene supply tank. Other features of the system include the water reservoir for introduction of water to the mixing chamber for experiments including steam, the vacuum pump, and gas handling valve panel.

Eighteen equally spaced instrument ports are located along the entire length of the test vessel. Detonation pressure is measured using flush-mounted, piezoelectric pressure transducers, with a quoted risetime of 1 microsecond. Flame time-of-arrival is measured with fast response TCs and light sensors (e.g., photodiodes).

### 3. DESCRIPTION OF PRELIMINARY SSDA EXPERIMENTS

#### 3.1 Chemical Reaction Time Experiments

Preliminary experiments are conducted to resolve a basic operational question: After charging the test vessel with reactive mixture at high temperature, how much time is available before the mixture reacts "significantly" in the absence of ignition sources?

Experiments are conducted in which the test vessel is initially evacuated and preheated to the desired temperature. Reactive gas mixtures, created in the mixing vessel, are injected into the test vessel at elevated temperature. No

ignition source is activated. The test vessel pressure and gas temperatures at several locations are monitored for a specified period of time for pressure or temperature excursions as an indication of chemical reaction. After about 30 minutes, an attempt is made to ignite the mixture using a glow plug. If the mixture does ignite, this observation is taken to imply that reactions had not occurred previously. (Gas sampling and chromatography will be used in the future.) Experiments were conducted using stoichiometric (equivalence ratio,  $\phi$ , equal to unity) hydrogen-air mixtures at 0.1 MPa initial pressure. Temperature was varied between 588K-700K.

Typical results are shown in Figures 2 and 3. Figure 2 shows results for a temperature of 588K. The test vessel (TV) and mixing chamber (MC) pressure histories are shown along with gas temperature histories, for thermocouple positions shown in the figure. The pressure profiles show the test vessel being loaded from vacuum. The test vessel pressure shows no sign of rapid combustion. The thermocouple, T2, shows a rapid drop upon introduction of the test mixture. This drop is caused by the temperature drop of the gas as it expands into the evacuated test vessel. No sign of significant temperature rise is observed. These results are interpreted to imply that no significant chemical reaction took place in this experiment. After 30 minutes, the mixture was ignited successfully using the glow plug. Figure 3 presents results for a temperature of 700K. The thermocouple opposite the test vessel gas inlet port, T2, indicates a strong temperature transient. Chemical reaction is believed to have occurred. Additionally, thermocouple T1 also shows a mild change in temperature. Despite the large change in temperature at T2, no significant pressure rise is apparent in the test vessel pressure during the vessel fill time period.

Table 2 summarizes the experimental results. Temperatures were varied and, additionally, the time to fill the test vessel with gas mixture to one atmosphere was varied. The "reaction time" shown was computed by the CHEMKIN computer code [Kee, 1989], a reaction kinetics code which was used to model the chemical reactions and the gas temperature change assuming an adiabatic system and the presence of no bounding metallic walls. The results to date suggest that no "significant" chemical reaction occurred at 588K. At 700K, a burn was observed in all cases, independent of mixture fill time. At 644K, a burn was observed with a short fill time and no burn with a relatively long fill time. The reasons for the observed dependence of the chemical reaction on fill time is not known at this time. It is noted that the observed times to burn initiation are significantly shorter than the reaction times predicted by the CHEMKIN code.

The results obtained to date suggest that at 644K the chemical reactants do not immediately burn off and that the planned experimental program can be conducted with temperatures of at least this magnitude. Additional experiments are planned at 700K with less reactive mixtures.

### 3.2 Inherent Detonability Experiments

The inherent detonability experiments are conducted to measure the characteristic "detonation cell width" as a function of initial mixture composition, pressure, and temperature. The cell width provides a measure of mixture sensitivity. The detonation cell width is measured by the imprint the detonation leaves on a

"smoked foil" [e.g., Lee, 1989]. Prior to an experiment, a 12-inch by 24-inch aluminum sheet is coated with carbon soot and is inserted into the end of the test vessel with the sooted side inward. Measurements of detonation pressure, temperature, and flame trajectory are also measured.

An experiment is reported here which was conducted as part of the SSDA shakedown testing. A stoichiometric ( $\phi=1$ ) mixture of hydrogen-air, initially at 0.1 MPa and 300K, was used. A smoked foil was inserted into the tube prior to the experiment and the test mixture was created in the mixing vessel. The test mixture was then injected into the test vessel. The hydrogen-air test gas was ignited using a high-voltage discharge through a wire fastened across a pair of electrodes. The flame front was tracked through the vessel using a series of photodiodes placed along the axis of the test vessel. The photodiode responses were used to compute the flame velocities in the vessel, shown in Figure 4. The results indicate that the flame accelerated rapidly into a detonation which travelled at the theoretically calculated Chapman-Jouget detonation velocity. Observation of the smoked foil indicated a cell structure with a characteristic transverse scale of approximately 10 mm. No attempt was made to characterize the regularity of the cell structure. This will be done in future work. Previous measurements of cell width for stoichiometric hydrogen-air at 0.1 MPa and 300K were in the range 10 mm - 15 mm [Lee, 1989; Stamps, 1991].

#### 4. SUMMARY

The high-temperature combustion experimental program at BNL has been initiated. Experiments are currently being conducted as part of the shakedown of the Small-Scale Development Apparatus. Preliminary chemical reaction time experiments indicate that stoichiometric hydrogen-air mixtures react, in the absence of ignition sources, at 700K, more rapidly than expected on the basis of reaction kinetics calculations. Preliminary detonation cell width measurements with stoichiometric hydrogen-air at 300K indicate a detonation cell width approximately equal to previous measurements reported in the literature.

#### 5. REFERENCES

1. Berman, M., et al., "A Critical Review of Recent Large-Scale Experiments on Hydrogen-Air Detonations," Nuclear Science and Engineering, 93, 321-347 (1986).
2. Kee, R. J., et al., "CHEMKIN-II: A Fortran Chemical Kinetics Package for Analysis of Gas-Phase Chemical Kinetics," Sandia National Laboratories, SAND89-8001 (September 1989).
3. Lee, J.H.S., et al., "A Summary of Hydrogen-Air Detonation Experiments," Sandia National Laboratories, NUREG/CR-4961, SAND87-7128 (May 1989).
4. Shepherd, J. E., "Chemical Kinetics of Hydrogen-Air-Diluent Detonations," Progress in Astronautics and Aeronautics, 106, Dynamics of Explosions, J.R. Bowen, et al., eds. (1986).

5. Stamps, D. W., et al., "Hydrogen-Air-Diluent Detonation Study for Nuclear Reactor Safety Analyses," Sandia National Laboratories, NUREG/CR-5525, SAND89-2398 (January 1991).
6. Stamps, D. W. and M. Berman, "A Critical Review of High-Temperature Hydrogen Combustion in Reactor Safety Applications," Paper presented at the International Conference on Thermal Reactor Safety, Avignon, France (October 1988).
7. Yang, J. W., "High-Temperature Combustion in LWR Containments Under Severe Accident Conditions," Brookhaven National Laboratory, Technical Report L-1924 1/17/92 (January 1992).

Table 1

## Major Features of Experimental Apparatus

	SSDA	HTCF
Objectives	Solve design and operational questions, chemical reaction time experiments, inherent detonability experiment (cell width measurements)	Inherent detonability experiments, DDT experiments-venting, critical tube experiments, hot jet initiation experiments
Diameter	4 inches inside diameter	10.75 inches inside diameter
Length	20 feet	70 feet
MAWP	1800 psia	1470 psia
Maximum Temperature	700K	700K
Gases	H <sub>2</sub> , Air, O <sub>2</sub> , Steam	H <sub>2</sub> , Air, O <sub>2</sub> , Steam, CO, CO <sub>2</sub>
Diagnostics	Smoked foil, piezoelectric pressure transducers, photodiodes, ion detectors, fast response thermocouples, gas sampling, and gas chromatography	Smoked foil, piezoelectric pressure transducers, photodiodes, ion detectors, fast response thermocouples, gas sampling, and gas chromatography
Control and Data Acquisition	486 PC-clone, high-speed LeCroy digital oscilloscopes	486 PC-clone, high-speed LeCroy digital oscilloscopes

Table 2

## Summary of Chemical Reaction Time Experiments

Temperature K	Computed "Reaction Time" (Chemkin code)*	Gas Mixture Vessel Fill Time**	Results
588	> 3 hours	5s	No burn observed in 30 minutes
644	~ 3 hours	5s	Burn observed during fill time
644	~ 3 hours	25s	No burn observed in 2 minutes
700	1000s	5s	Burn observed during fill time
700	1000s	25s	Burn observed during fill time
700	1000s	90s	Burn observed during fill time

\*Time for mixture temperature to increase by 10 percent (adiabatic system).

\*\*Time to fill the test vessel from vacuum to 0.1 MPa.

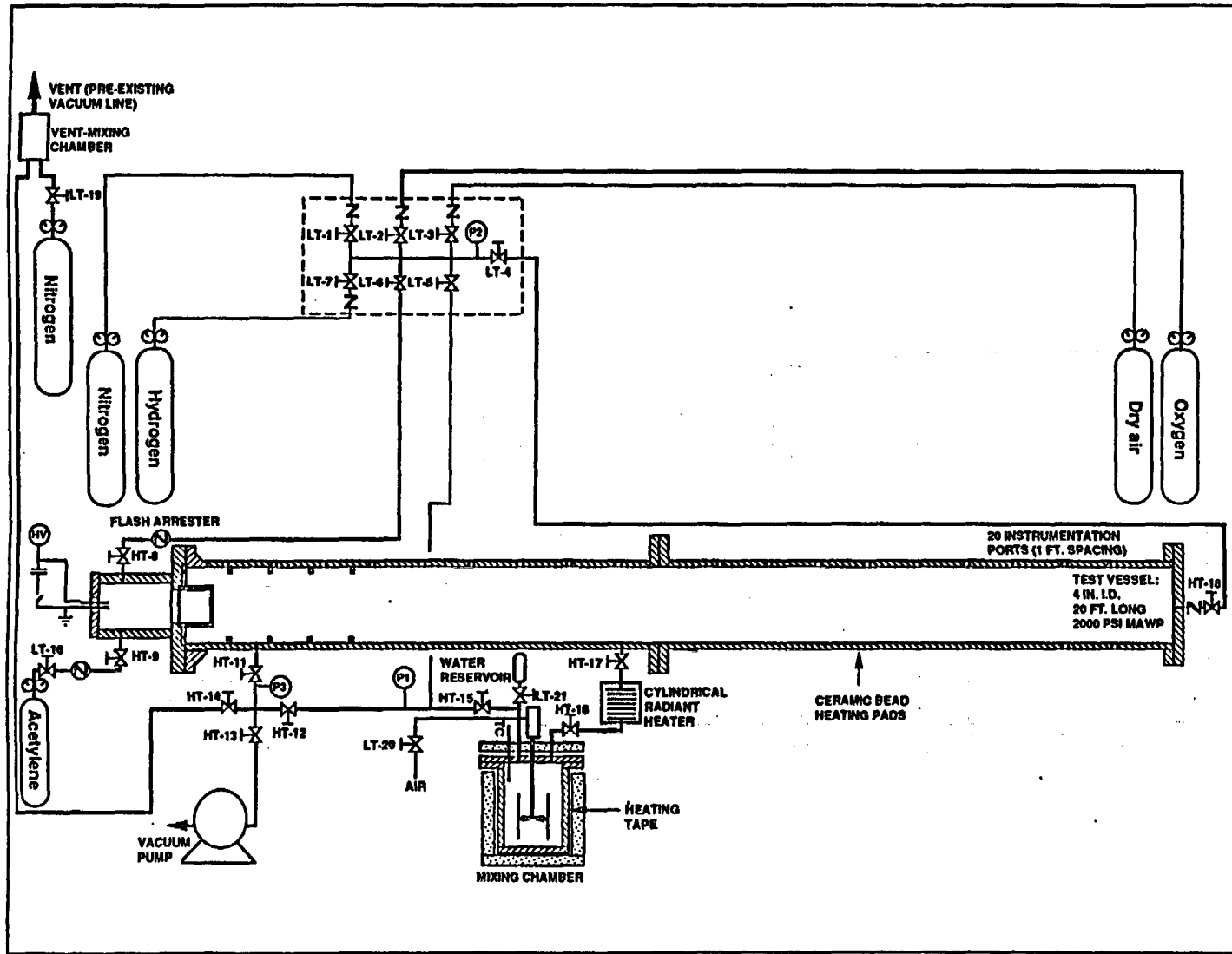
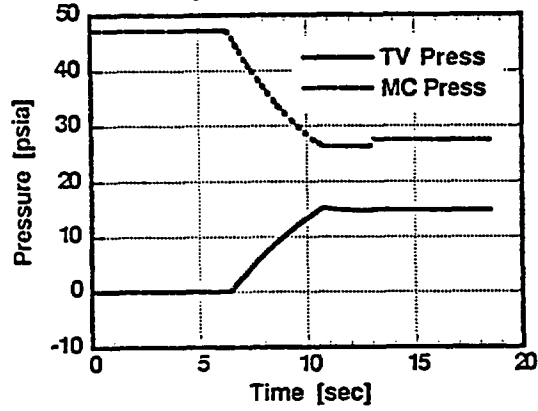


Figure 1 - Schematic Diagram of Small-Scale Development Apparatus

VOX4:  $\phi=1, T_0=588K$ , No Burn during Injection



VOX4:  $\phi=1, T_0=588K$ , No Burn during Injection

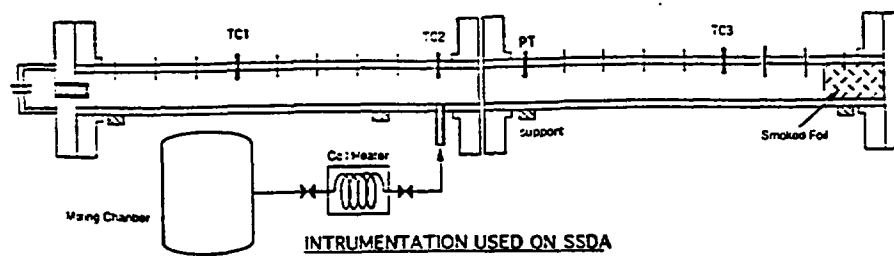
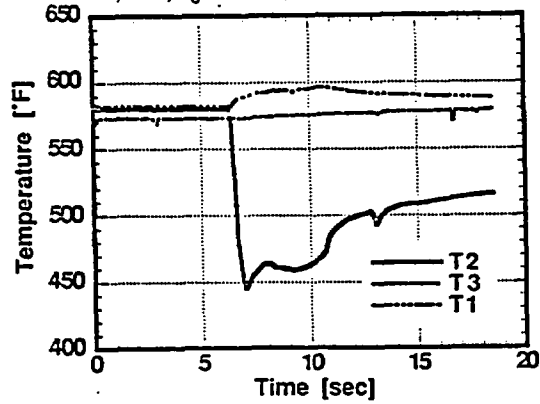
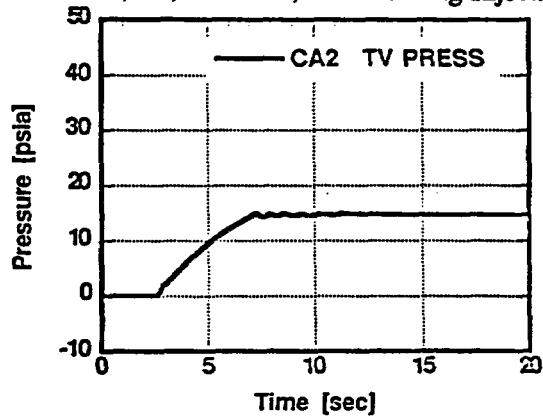


Figure 2 - Pressure and Temperature Resources During Chemical Reaction Time Experiments: Initial Temperature 588K

VOX9:  $\phi=1, T_0=700K$ , Burnt during Injection



VOX9:  $\phi=1, T_0=700K$ , Burnt during Injection

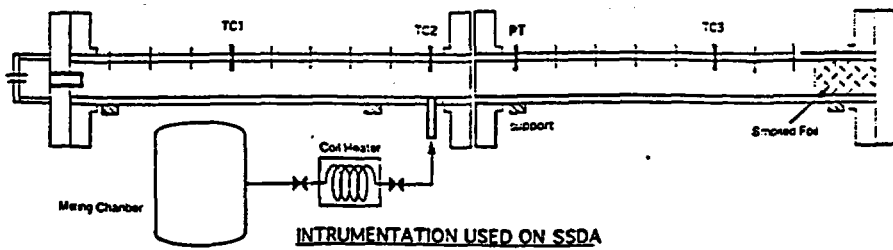
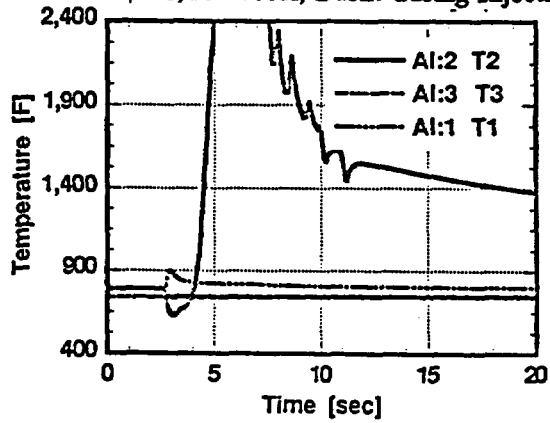


Figure 3 - Pressure and Temperature Resources During Chemical Reaction Time Experiments:  
Initial Temperature 700K

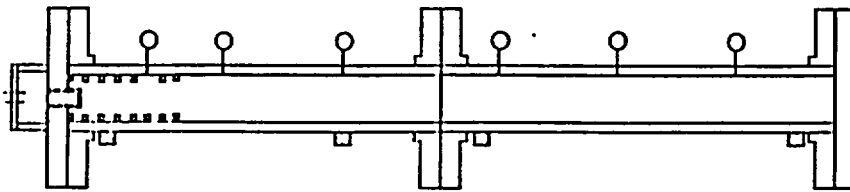
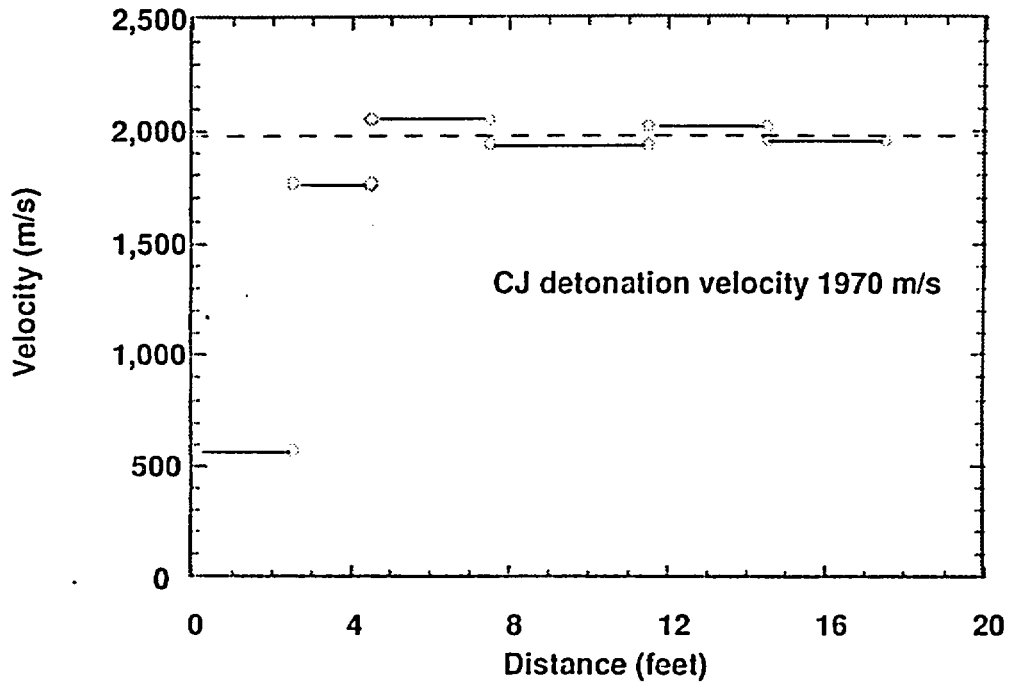


Figure 4 - Flame Acceleration in Stoichiometric Hydrogen-Air

# Hydrogen Combustion Research at RPI

Joseph E. Shepherd  
J. Christopher Krok

Explosion Dynamics Laboratory  
Department of Aeronautical and Mechanical Engineering  
Rensselaer Polytechnic Institute, Troy, New York

Presented at the  
20th Water Reactor Safety Information Meeting  
Bethesda, MD, October 1992

## Introduction

A facility has been constructed at RPI to study hydrogen combustion phenomena related to severe accidents at nuclear power plants. The specific areas of interest are transient diffusion flames, oxidation of near-limit mixtures, and jet initiation of accelerated flames and detonations. These have been identified as key near- and long-term issues in the Revised Severe Accident Research Program (SARP) (1989) set forth by the U. S. Nuclear Regulatory Commission. The RPI experimental facility is designed to examine these problems quickly and systematically by allowing key parameters to be easily changed.

## Facility

This is a small-scale facility, with a total volume of 0.86 m<sup>3</sup>. The basic setup is shown in Figure 1. The experiment is constructed around two identical pressure vessels: the driver and the receiver. The driver is used to generate high-temperature hydrogen-steam jets, while the receiver simulates the containment atmosphere. Both tanks can be filled with various mixtures of hydrogen, oxygen, nitrogen, and air. The hydrogen, oxygen, and nitrogen are supplied by K-type bottles, while air is taken from the house compressed air system. The two vessels have independent filling systems, and mixtures are generated by the method of partial pressures. The vessels are connected through a hydraulically-actuated closure mechanism, which contains the diaphragm, and a test section where the jet is blown into the receiver atmosphere. Both the driver and receiver have independent ignition systems and can be run individually for special tests.

The driver tank is initially filled with a hydrogen-rich mixture of hydrogen-oxygen which is then burned to create the high-temperature mixture of hydrogen and steam. In some tests, particulate dispersions will be added to the initial driver mixture, generating particulate-enhanced jets. The combustion time will depend on the stoichiometry of the mixture, and can be expected to range from 5 to 100 milliseconds. After combustion is complete, 1 to 10 seconds will be required for the driver tank to cool down and vent into the receiver. The venting process begins when the diaphragm ruptures, and by command-rupturing the diaphragm at a specific time, the initial jet conditions can be selected. The diaphragm will be ruptured at a predetermined time after combustion by a solenoid-driven spike. Depending on the driver cool-down time, the jet

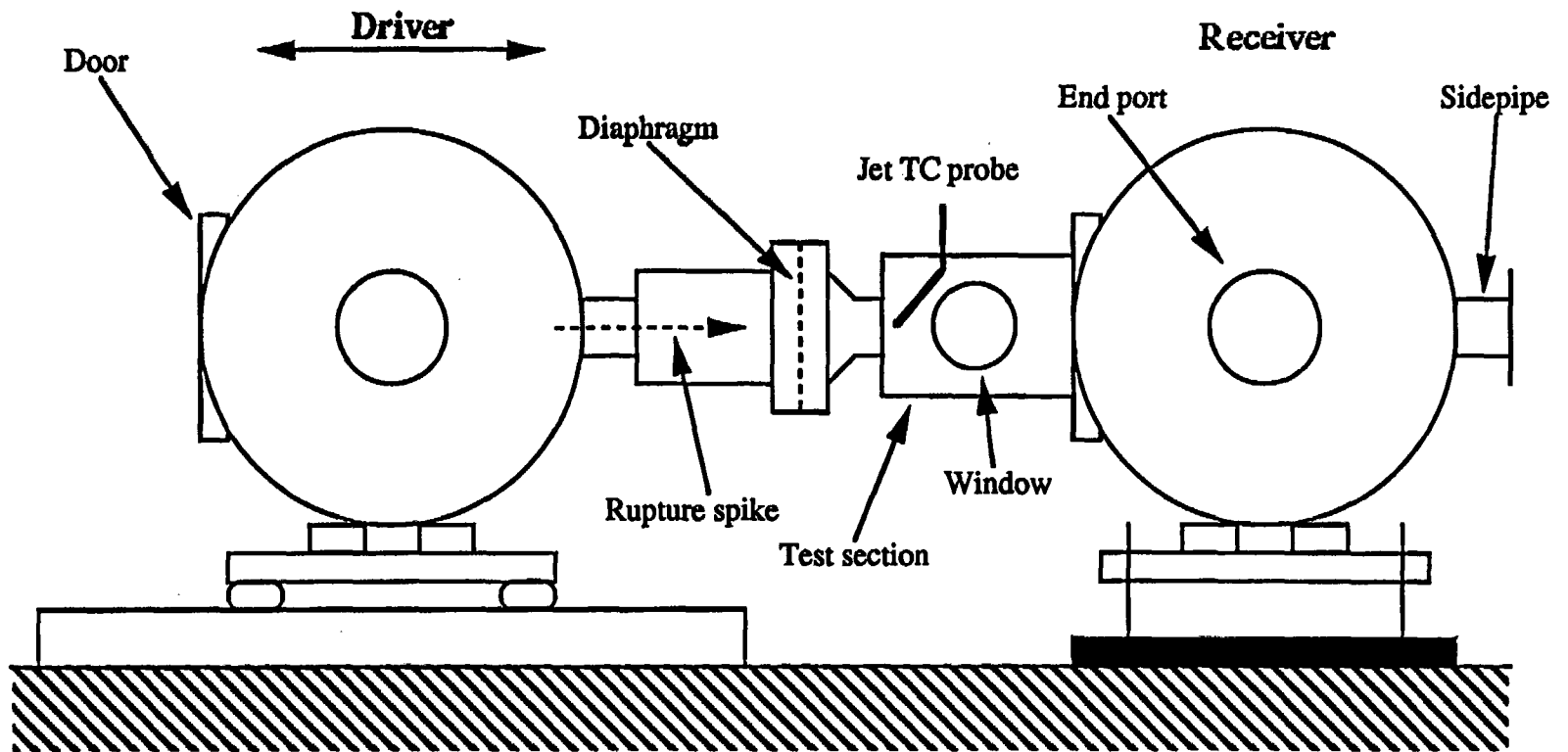


Figure 1: Basic experimental setup, side view. Overall length is approximately 9 ft (2.74 m).

temperature can varied between 400 and 2500 K. Cooler jet temperatures allow radicals to recombine and remove their effect on the combustion process in the receiver.

The driver vents into the receiver through an interchangeable orifice at the end of the test section (see Figure 2). Three orifice diameters are currently available: 1/4-in., 1/2-in., and 1-in. By leaving the orifice out, the 3-in. mounting hole in the test section can act as a large orifice.

The receiver can be filled with mixtures of hydrogen and air, with nitrogen or steam added as a diluent to simulate the high concentrations of steam typically found in reactor containments. The effect of the diluent is to suppress combustion activity, as the gas is inert and serves to absorb energy released by combustion. Without the diluent, all of this energy would be available to sustain the flame. For initial receiver temperatures of 300 K, nitrogen is used to dilute the air. Initial temperatures of 300 to 400 K can be reached by preheating the receiver tank with steam from the building heating supply and maintaining temperature with electrical heaters. Steam can then remain in the receiver as a diluent. Still higher temperatures can be obtained in the receiver by first filling with air, and then adding stoichiometric hydrogen and oxygen which can be burned to generate steam. The nature of this process precludes the study of preexisting hydrogen, of course. Only diffusion flame stability tests will be carried out with the high temperature receivers.

Several types of instrumentation are currently available in the experiment. Instrumentation locations are shown in Figure 3. Both tanks contain Kulite static pressure transducers for measurements in low- to medium-speed combustion. When DDT tests are carried out, these will be supplemented by high-speed PCB dynamic transducers. Both tanks also contain type-K thermocouples. The receiver contains a "thermocouple rake," consisting of a length of stainless steel tubing with six protruding thermocouple beads, spaced on 6-in. centers. This rake lies parallel to and approximately 2.125 inches below the jet axis. The last thermocouple in the rake is 8.5 inches away from the face of the jet orifice. The driver had also contained one of these rakes, but the severe nature of the combustion there eventually destroyed it. The driver now contains a single, heavy-duty type-K thermocouple. The thermocouple wires are jacketed in Nextel insulation and stainless steel braid, and mounted in a length of stainless steel tubing for support and further protection. The thermocouple bead lies near the center of the tank.

One other thermocouple is mounted in the test section and projects down into the center of the jet to measure jet temperatures. This thermocouple is used only in experiments run specifically to measure jet temperature, and is removed at all other times to prevent obstruction of the jet.

Pressure and temperature data are recorded by National Instruments data acquisition equipment and software, installed in a Macintosh IIfx computer.

Optical access to the test section is provided through two 4.5-in. diameter window ports on its sides. A Schlieren system using a high-speed movie camera and a 150 W xenon arc lamp light source is being designed to allow investigation of diffusion flame stability. This system will provide visual evidence of flame lift-off and blowout.

### Planned Tests

Four sets of tests are planned for the RPI experimental facility:

**DF1 series.** This series of tests will examine hot jets venting into cold atmospheres. The receiver will contain gas mixtures at ambient temperature (300 K), with nitrogen as the diluent.

**DF2 series.** These tests are identical to DF1 but will use warm atmospheres in the receiver, which will be heated by steam condensation and electrical heaters. This series will study steam-air-hydrogen mixtures at temperatures of 300 to 400 K.

**DF3 series.** Hydrogen-oxygen combustion in the receiver tank will be used to generate hotter atmospheres than those possible in the DF2 series. The receiver burns will be lean in nature and will contain nitrogen, so as to create steam-air mixtures in the 400 to 1000 K range.

**DF4 series.** This series will add particulate dispersion to the hot hydrogen-steam jets. Particles smaller than 100 microns will be dispersed in the driver tank immediately prior to burning by blowing a strong jet of air into a cup containing the particles. Metal oxides will be used for the

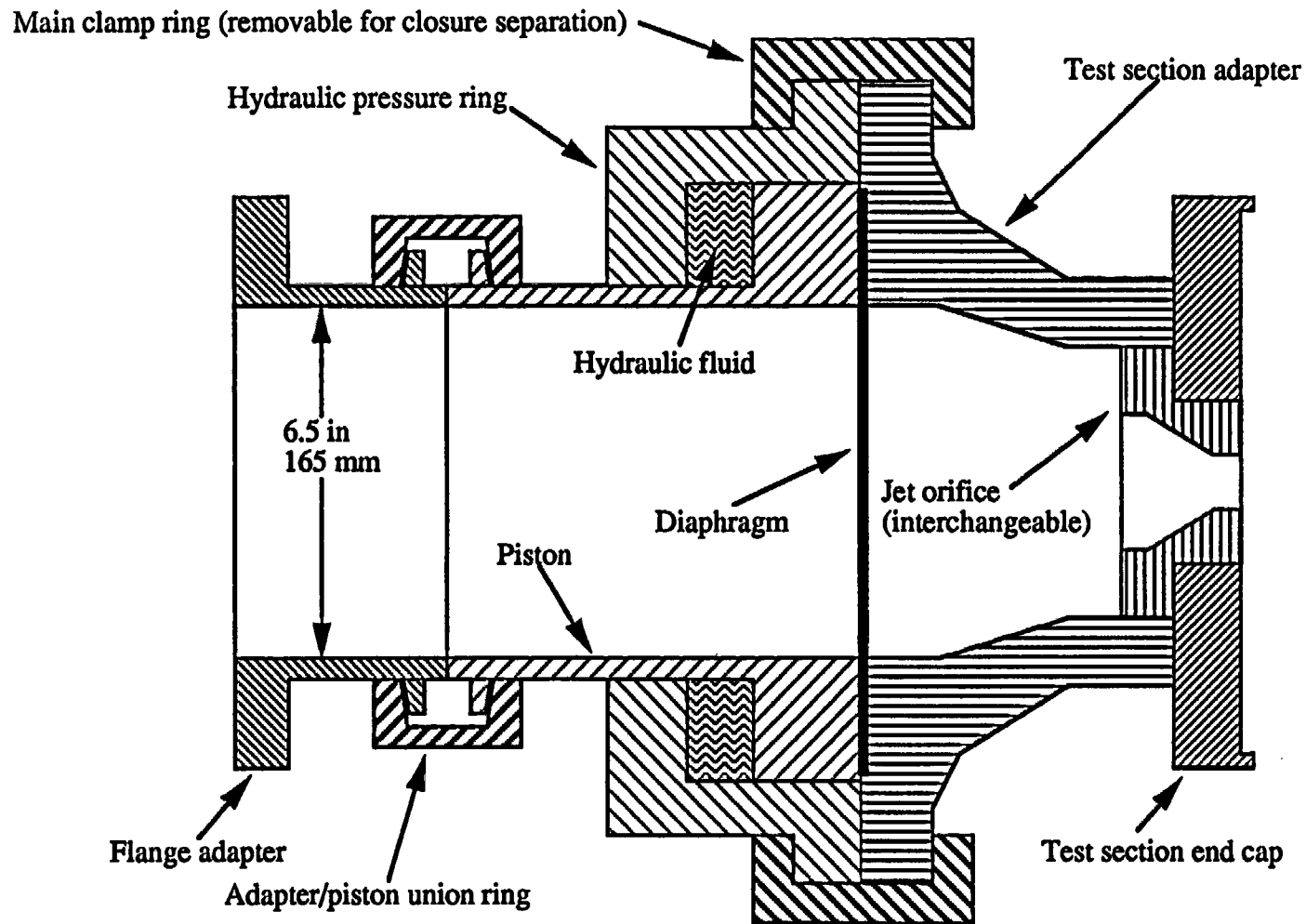


**Figure 2: Cross-sectional view of hydraulic diaphragm closure. All parts are axisymmetric except test section end cap. Hydraulic fluid enters through port in back side of hydraulic pressure ring.**

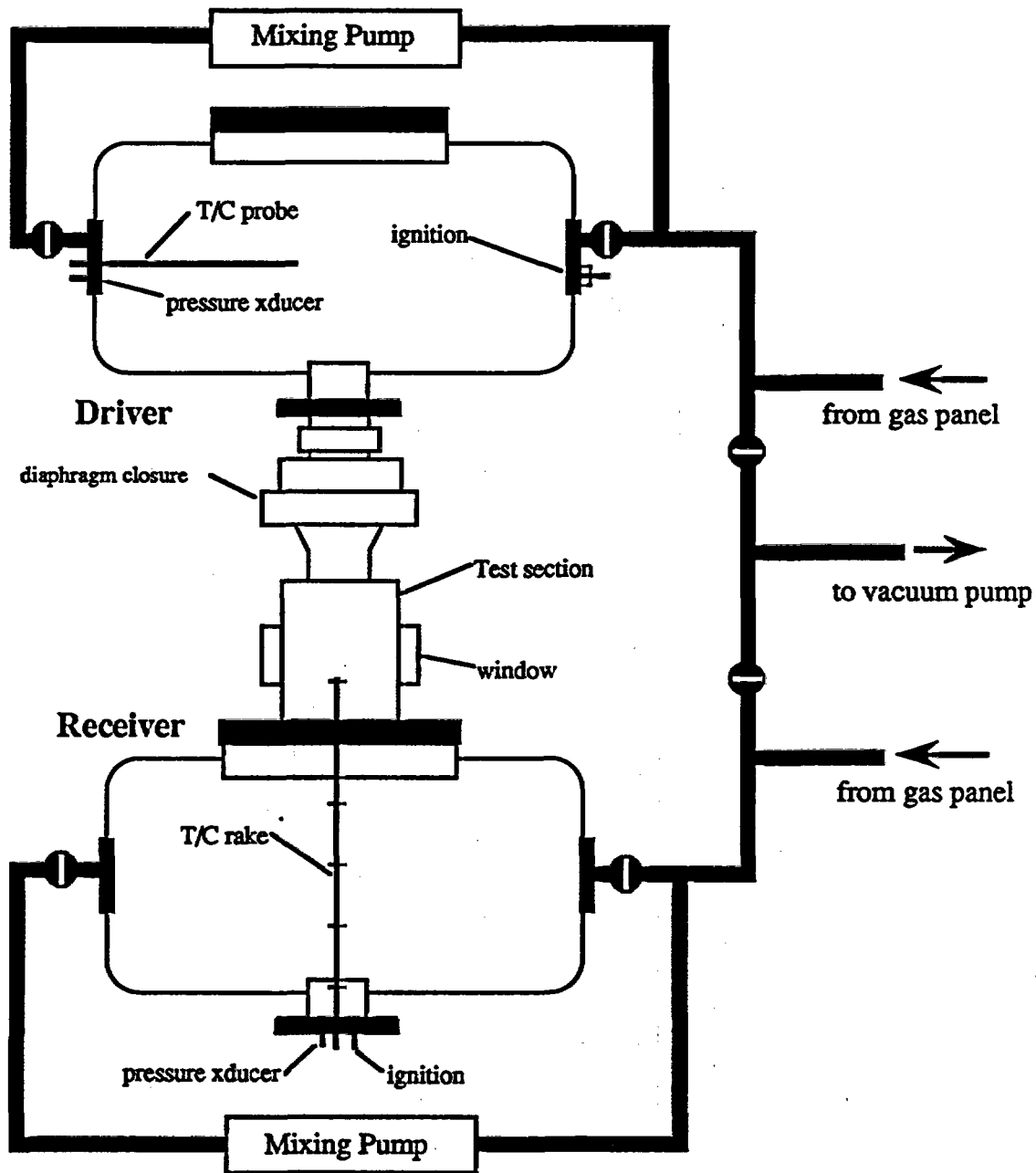


Figure 3: Top view of tanks, showing plumbing and instrumentation locations.

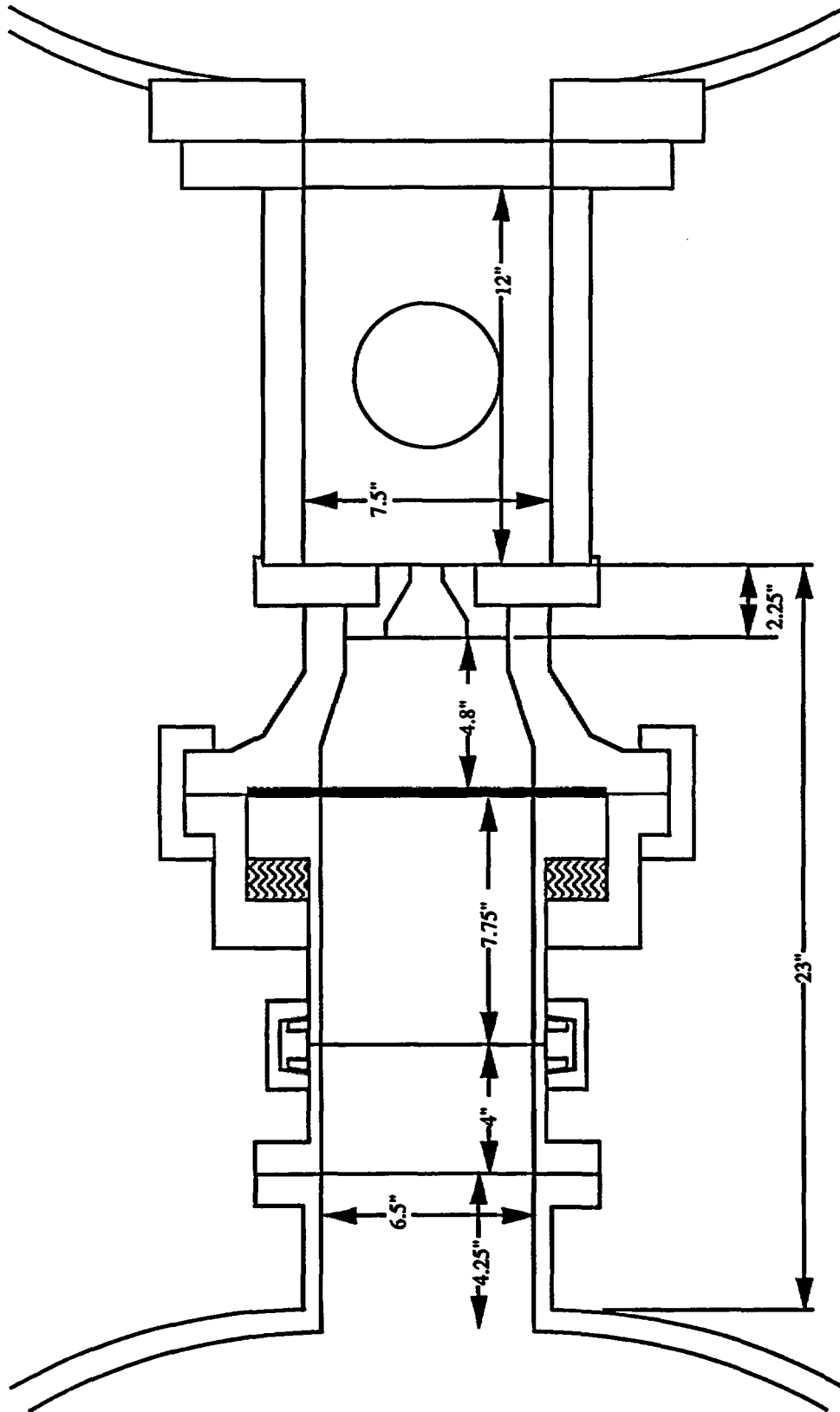
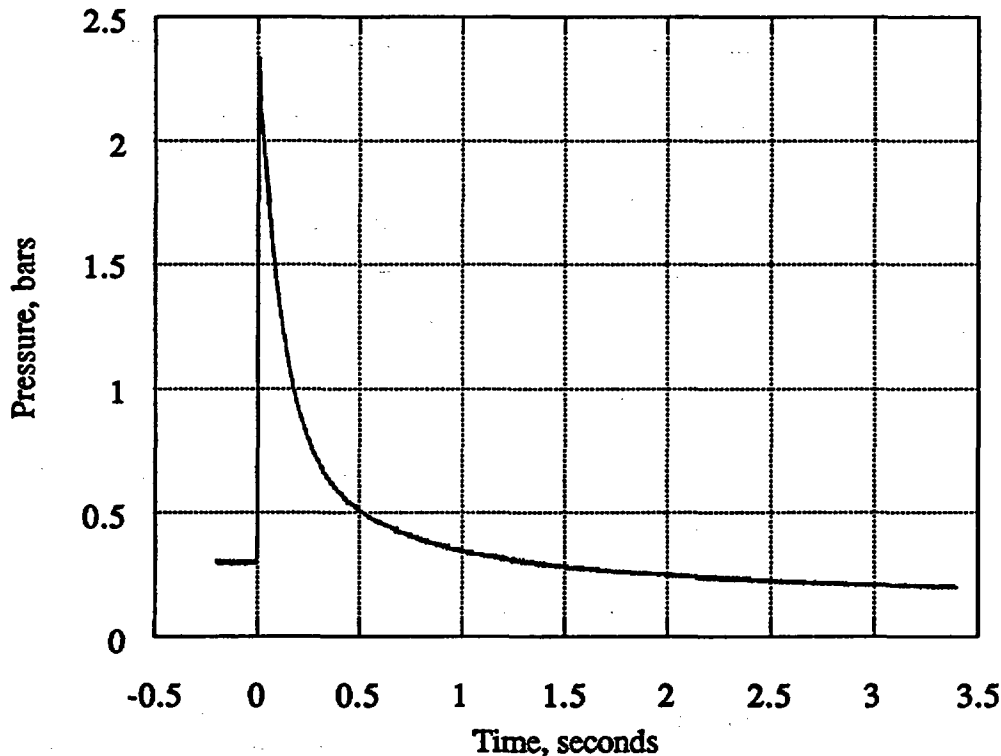


Figure 4: Cross-section of system with basic dimensions.

particulate matter. To simplify these experiments, only ambient temperature atmospheres will be used in the receiver tank.

#### Tests run as of 16 October 1992

**Shakedown tests.** The first set of runs (numbers 1 through 29) used only the driver tank, for systems checkout and cooldown measurements. A variety of minor problems were found in the data acquisition system and control equipment; as a result, 15 valid tests were obtained from these runs. The initial mixtures in these runs used only hydrogen and oxygen, with hydrogen fractions from 30 to 87%. The initial pressure ranged from 0.3 to 1.0 bar, and the initial temperature was ambient (295 to 300 K). A typical cooldown curve is shown in Figure 5. This pressure trace is for an initial mixture of 69% H<sub>2</sub> and 31% O<sub>2</sub> at an initial pressure of 0.262 bar.



**Figure 5: Typical cooldown curve. Initial mixture of 69% H<sub>2</sub> and 31% O<sub>2</sub> at 0.262 bar.**

The peak pressures recorded in these tests were compared with values calculated by STANJAN, a chemical equilibrium code (Reynolds, 1986). The calculations assumed adiabatic, isochoric, complete combustion (AICC). Experimental values all fell within 7% of the calculated ones, and most were within 2%. As expected, the experimental values were lower than the AICC values, due to heat transfer occurring during the burn. These peak pressures are plotted in Figure 6, which also includes the AICC pressure calculated by STANJAN for the full range of H<sub>2</sub>/O<sub>2</sub> mixtures at an initial pressure of 1.0 bar. The triangular points represent initial pressures of 0.8 and 1.0 bar in the experiment.

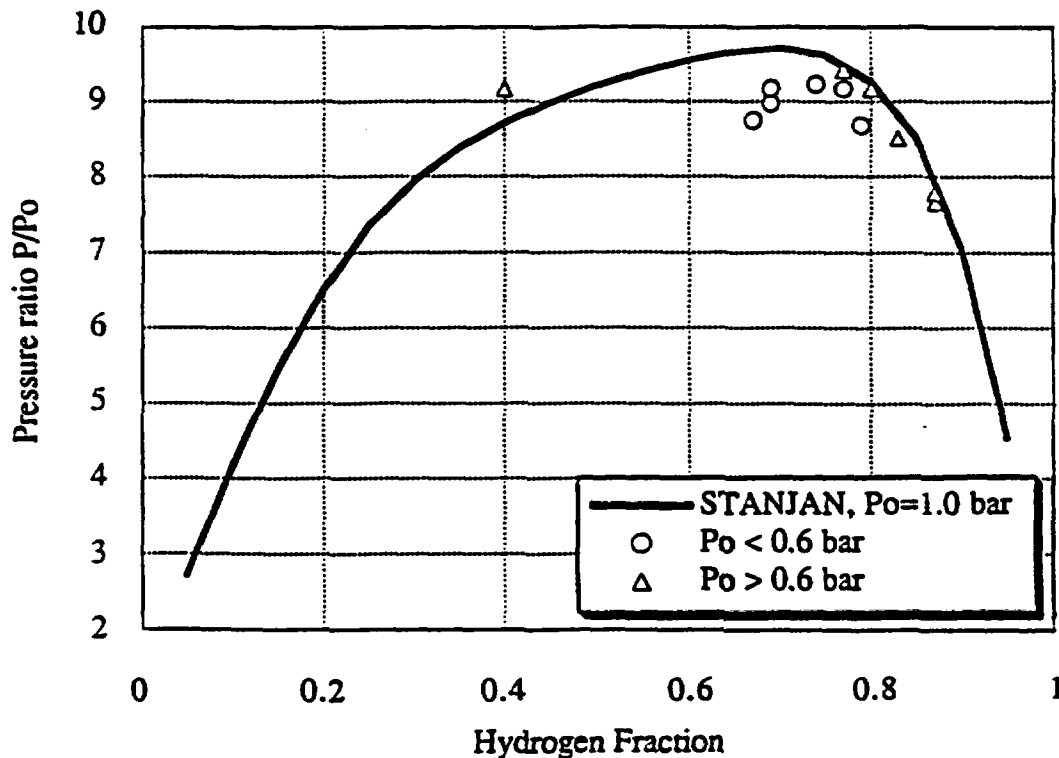


Figure 6: Summary of peak pressures from driver tank shakedown runs, compared to pressures predicted by STANJAN.

**Test series DF1-A.** With both tanks in operation but no diaphragm rupture mechanism or Schlieren system, a subset of the DF-1 test series was run. The purpose of these tests was to examine the influence of jet strength on the lean flammability limit. These tests encompassed runs 30 to 65, with 25 valid tests resulting. In all of the tests, the driver contained an initial mixture of 80% H<sub>2</sub> and 20% O<sub>2</sub>, at an initial pressure of 1 bar and ambient temperature (295 to 300 K). Spark ignition was used to initiate the burn, which required approximately 10ms to complete (time between ignition and peak pressure). The predicted peak pressure and temperature for these initial conditions are 9.1 bar and 3245 K. The measured peak pressure was only 8.6 bar, however; the cause of this is believed to be the thermal protection system installed for the pressure transducers. This system was not in place during the shakedown runs, and the same initial conditions in those tests gave the proper peak pressure.

With no diaphragm rupturing system in place, mylar diaphragms were used. In ambient temperature static pressure tests, these diaphragms were found to rupture at a pressure difference of 1.3 bar. Under the rapid pressure increases and high temperatures of the experiment, these diaphragms are assumed to rupture spontaneously by the time the driver burn completes.

The initial mixture used gives a jet composition of 50% hydrogen and 50% steam. This was vented into the receiver tank through the 1/4-in. and 3-in. orifices. Venting occurred over a 2

second period for the 1/4-in. orifice, while the 3-in. orifice vented the driver in less than 0.1 s. For both orifices, the receiver atmosphere consisted of 4 to 10% hydrogen added to a baseline mixture of 50% nitrogen and 50% air. The receiver atmosphere was at ambient temperature and 1.0 bar of pressure. The receiver mixtures used are listed in Table 1.

Table 1: A-series test matrix for DF-1 subset.

Test	Receiver mixture (volume %)			Receiver burns?	
	Air	N2	H2	1/4-in.	3-in.
A1	(receiver blanked off)			N/A	
A2	0	100	0	N/A	
A3	50	50	0	N/A	
A4	100	0	0	N/A	
A5	45	45	10	Y	Y
A8	46	46	8	Y	Y
A6	47	47	6	N	Y
A7	48	48	4	N	Y

Figure 7 compares expanded pressure traces for the driver tank in tests A1 and A3. In test A1, a non-rupturing (stainless steel) diaphragm is placed in the diaphragm closure, preventing any venting. In that case, heat transfer is the only cause of the pressure decrease after the burn. The A3 test shown in this plot used the 1/4-in. orifice, and the venting process contributes to the pressure loss. In this expanded plot, the pressure traces do not begin to diverge until about 0.125 seconds, indicating that this is the amount of time required for the jet to start, and all of the pressure drop before that is due to heat transfer, as in the A1 test.

Figure 8 is a preliminary examination of diffusion flame stability for the 1/4-in. orifice, showing receiver pressure traces for the A2 and A4 tests. The receiver in the A2 test contains 100% nitrogen, while that in the A4 test contains 100% air. The pressure rise in the A2 case is therefore due to jet pressurization only, with no diffusion flame possible in the inert atmosphere. Figure 8 shows that receiver pressurization is only slightly higher in 100% air, indicating that very little combustion occurs in the receiver. There are two possible reasons for this: First, all of the hydrogen entering the receiver may be burning, but the small size of the orifice may be restricting the flow so much that very little hydrogen enters anyway. Second, the orifice may be too small to produce a stable diffusion flame for these conditions, and the flame may be blowing out (Shepherd, 1985). Completion of the Schlieren system will help determine the correct answer.

Figure 9 demonstrates the effect of preexisting hydrogen in the receiver atmosphere. These and similar results were used to make the conclusions shown in Table 1. The 1/4-in. orifice was used in both tests. The upper plot shows the driver and receiver pressure traces for the A3 test, with no hydrogen in the initial receiver mixture. The pressure increase in the receiver is very small, and is the same as that shown in Figure 8. The lower plot is from the A8 test, with 8% H<sub>2</sub> in the receiver. This time, a deflagration in the receiver mixture is clearly evidenced by the large rise in pressure there. Further experiments determined that 8% was the lowest concentration of hydrogen that could be ignited in the receiver with the 1/4-in. orifice.

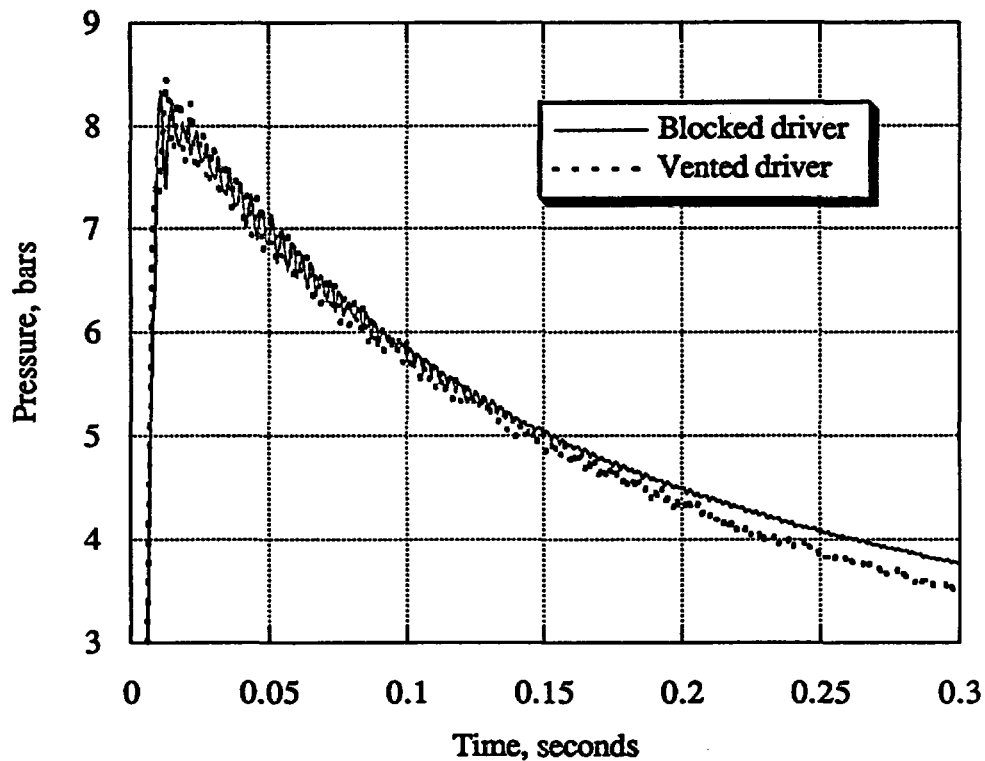


**Figure 7: Expanded pressure traces comparing blocked and vented driver tanks. Blocked driver is from test A1, vented driver is from test A3 with 1/4-in. orifice.**

Figure 10 shows a more direct comparison between burn and no-burn tests, using both pressure and temperature data from the receiver. These plots compare cases A3 and A5 (no H<sub>2</sub> and 10% H<sub>2</sub>), again with the 1/4-in. orifice. The temperature signals are all taken from the #1 thermocouple in the receiver, which is farthest away from the orifice exit. This choice minimizes the effects of the jet on the temperature signal. In these tests, the difference between the deflagrating and baseline (no H<sub>2</sub>) receivers is quite clear. The signals in both pressure and temperature are widely separated.

Results from the 3-in. orifice are presented in Figure 11. These plots compare the signals from the baseline A3 test with those from the A7 (4% H<sub>2</sub>) test. With the 3-in. orifice, it is difficult to tell whether or not a deflagration occurred in the receiver; the effects from the jet alone are very strong. However, the traces from A7 are clearly above those from the baseline test in both pressure and temperature. The peak receiver pressure found in these tests also indicates a deflagration. The peak pressure in the A3 test was 5.86 bars, while that in the A7 test was 6.26 bars. This is well outside the range of experimental variation; the A3 test was run again, and the peak pressure was measured as 5.87 bars.

An additional thermocouple is being installed in a remote location in the driver tank, away from the effects of the jet. This should give a much more distinct difference between deflagrating receivers and those too lean to be ignited by the jet.

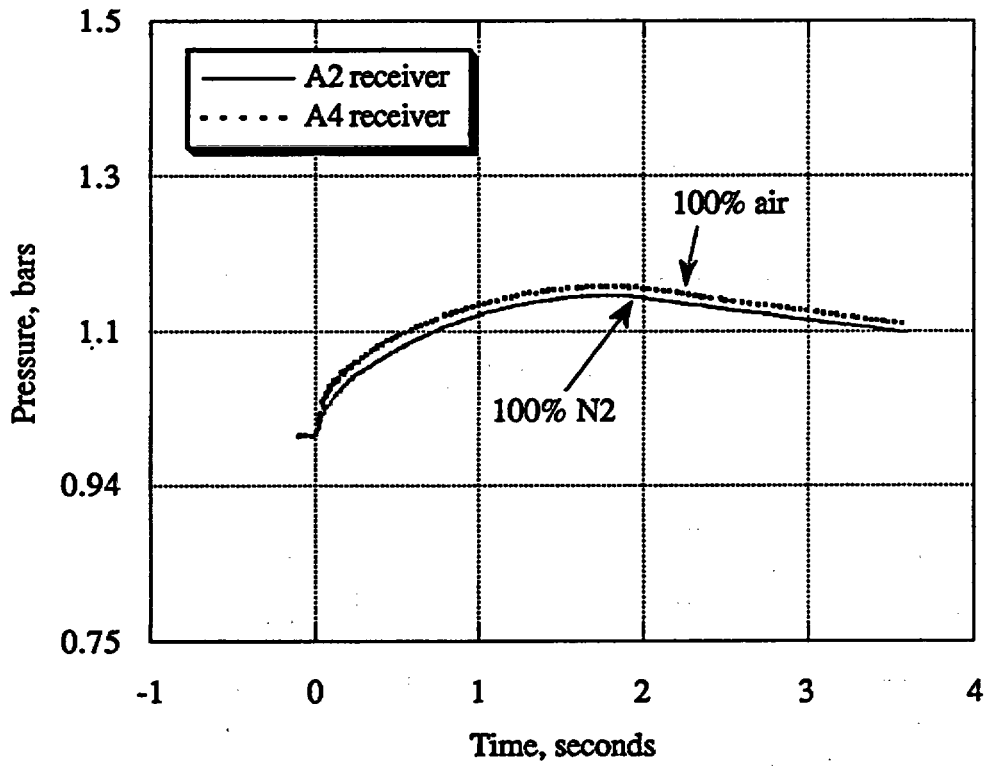


**Figure 8: Receiver pressurization through 1/4-in. orifice, comparing A2 and A4 cases (100% nitrogen and 100% air, respectively)**

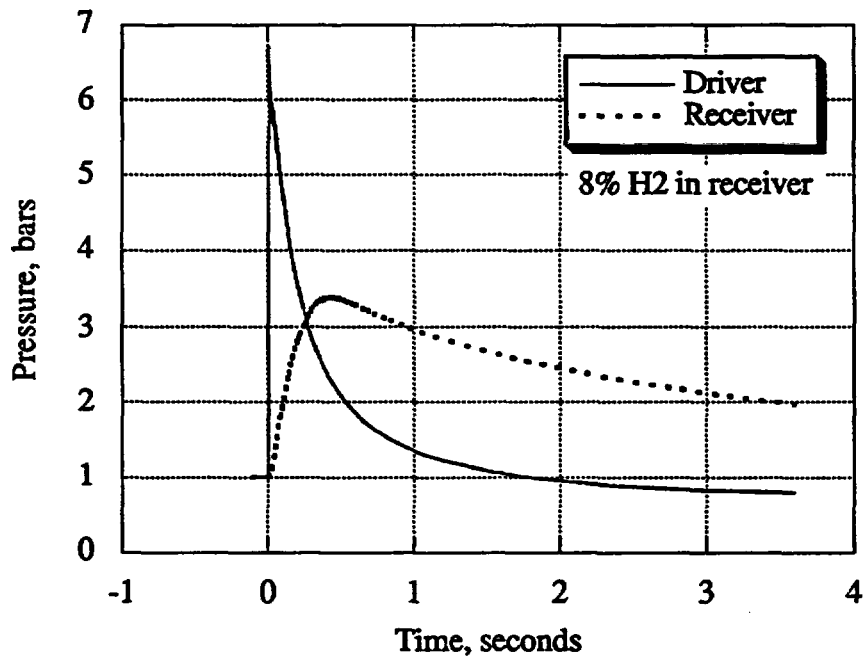
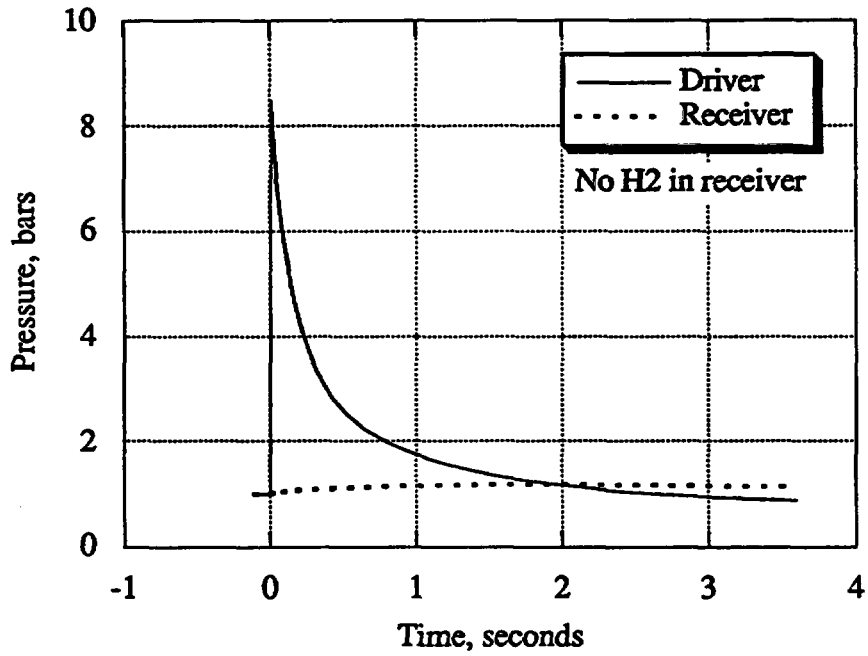


**Figure 9: Comparison of pressure traces for baseline and flammable receivers with 1/4-in. orifice. Upper plot is for test A3, lower is A8.**

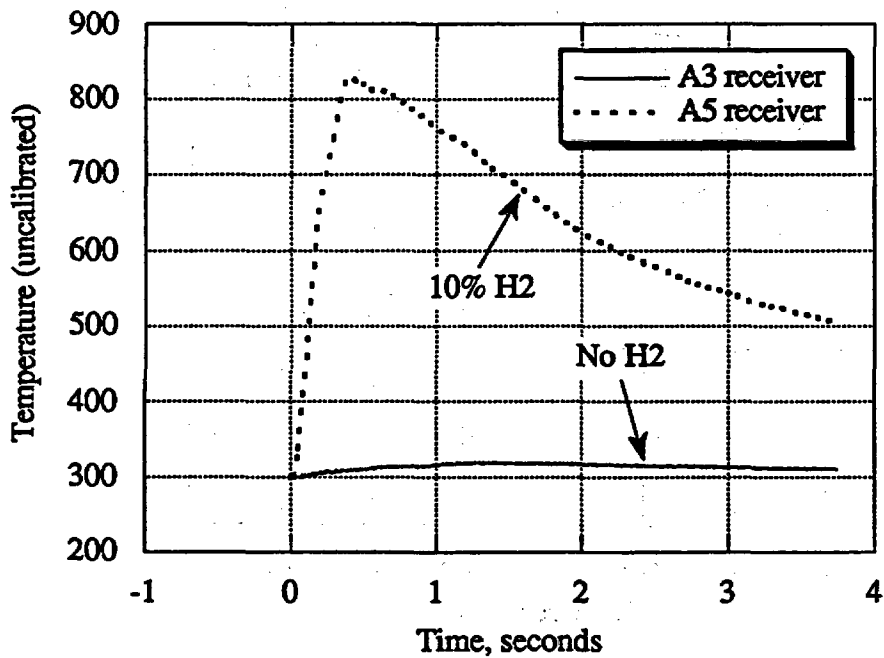
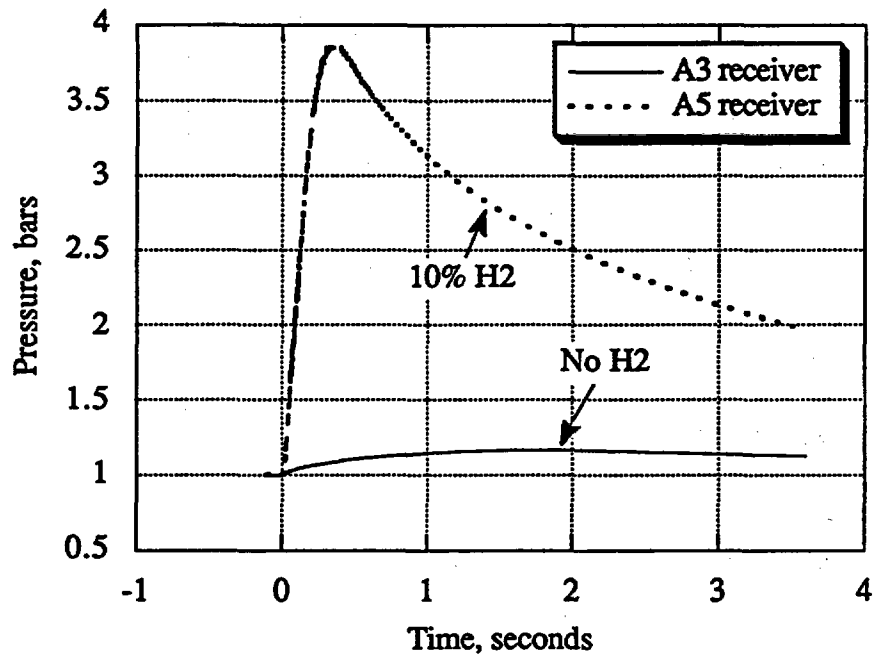


**Figure 10: Direct comparison of flammable (A5) and baseline (A3) cases with 1/4-in. orifice, using both pressure and temperature cases. Deflagration evident in A5.**

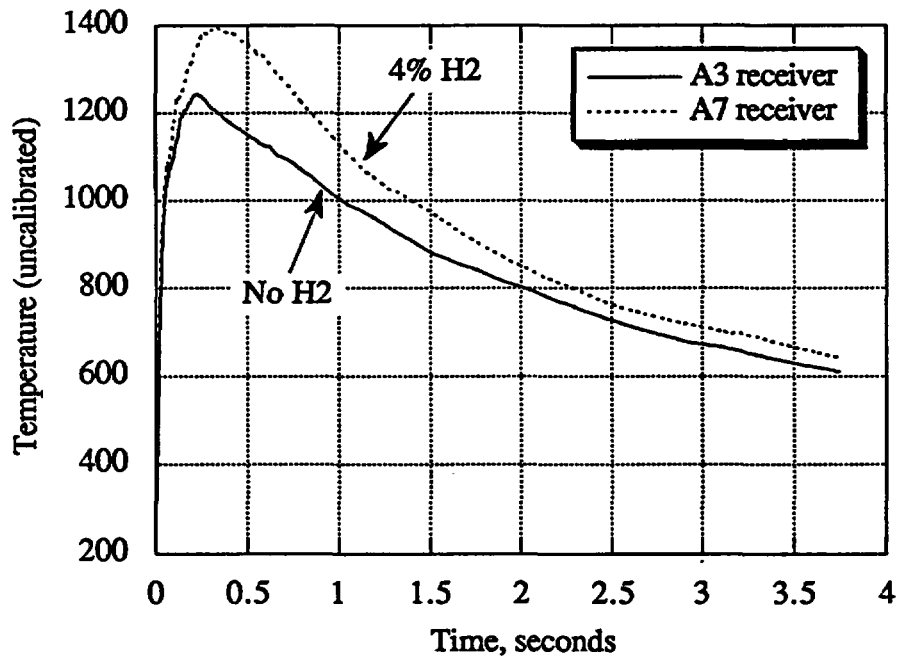
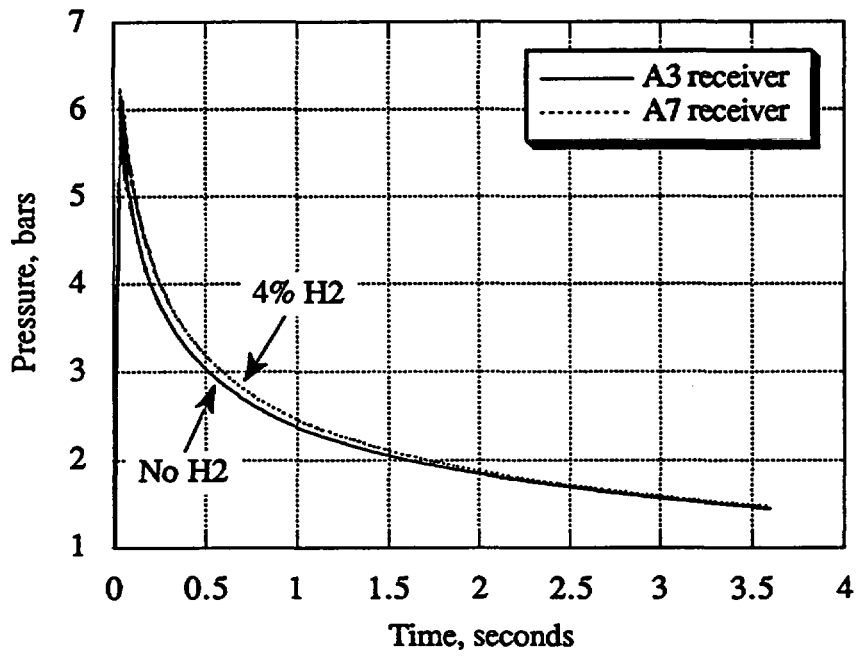


Figure 11: Evidence for deflagration in A7 test with 3-in. orifice.

Another clue that indicates the occurrence of a deflagration in the receiver is the final system pressure. This pressure is read from the Heise gauges after the experiment is run and the driver temperature has fallen below 303 K. The pressure is, of course, the same in both tanks due to the loss of the diaphragm separating them. When the hydrogen burns, it produces water, most of which condenses out. The more hydrogen that burns, the lower the final pressure.

A lower bound on final pressure can be found by balancing the chemical reaction for the two tanks considered as one system. That is, the contents of both tanks are assumed to be placed in one vessel, fully mixed, and burned. The final pressure is found by multiplying the initial pressure by the ratio of the final number of mols in the system to the initial number. The water in the products is at first assumed to be fully condensed, so only nitrogen, hydrogen, and possible oxygen appear in the products. After this calculation, the saturation pressure of water at 303 K (about 0.04 bar) is added to represent the water that still exists as vapor. These values are listed in Table 2, along with the actual final system pressures for the tests run.

Table 2 also includes the percentage of hydrogen in the total system that was burned during each test. The amount of hydrogen combustion shown in each case again considers the entire system as a whole, and the percent combustion possible depends on the overall stoichiometry of the system. The amount of actual combustion was computed from the actual final pressures, again using the concept that the ratio of final to initial pressure is equal to the ratio of final to initial number of mols in the system.

**Table 2: Final system pressures, predicted and actual (bars), and amount of total system hydrogen combusted.**

Test	Receiver	Predicted pressure	Actual, 1/4-in. orifice	Actual, 3-in. orifice	Possible combustion	Actual, 1/4-in.	Actual, 3-in.
A2	N <sub>2</sub>	0.740	0.760	0.762	50%	46.6%	46.6%
A3	N <sub>2</sub> /air	0.583	0.766	0.680	76%	46.6%	60%
A4	air	0.440	0.764	-----	100%	46.6%	-----
A5	10% H <sub>2</sub>	0.598	0.692	-----	65.5%	51.5%	-----
A8	8% H <sub>2</sub>	0.595	0.696	-----	67.4%	52.1%	-----
A6	6% H <sub>2</sub>	0.592	0.754	0.655	69.5%	44.3%	59.7%
A7	4% H <sub>2</sub>	0.589	0.754	0.661	71.6%	44.3%	60.2%

The actual final pressures are all seen to be above the calculated values, and the amount of system hydrogen combusted is always less than the maximum amount possible. The main reason for this is that the gases in both tanks do not fully mix and burn together. The orifice restricts the amount of jet gas that can flow into the receiver and burn there.

As shown in Table 2, the final system pressure in test A2 is the same for both the 1/4-in. and the 3-in. orifices, as the receiver atmosphere is inert and no jet combustion occurs. For the 1/4-in. orifice, no change occurs in tests A3 or A4, indicating that very little if any of the hydrogen in the jet burns. The 3-in. orifice, however, shows a significant drop in final pressure, showing combustion of hydrogen in the jet. For the tests involving preexisting hydrogen, the 1/4-in. orifice shows a lower final pressure in the A5 and A8 tests, but not much change in the A6 and A7 tests. This indicates that a deflagration occurred in the receiver for A5 and A8, but not in A6 or A7. For the 3-in. orifice, the final pressures in both A6 and A7 are significantly lower than that of A3, showing that a deflagration had taken place in those tests. The difference between them is small because the difference in hydrogen concentration in the receiver is small in those tests.

Also shown is that the system as a whole is rich for the baseline A3 case. Adding hydrogen to the receiver in the A5 through A8 tests actually makes the total system richer, resulting in lower percentages of possible hydrogen combustion for these tests, since oxygen is displaced and less hydrogen can be burned. In the actual experiments, however, the two tanks are not completely mixed. For the hydrogen concentrations used, the receiver itself is a lean system. The amount of hydrogen that burns in the driver tank is the same for all cases in the present series, and we believe that the burn is substantially complete before the jet has started up. Also, the results from the A3 tests indicate that not all of the available oxygen in the receiver is consumed. Preexisting hydrogen in the receiver that does burn consumes this remaining oxygen, resulting in final lower pressures. Also, a deflagration in the receiver increases the pressure there, lowering or preventing the further flow of jet gas from the driver. The pressure in the receiver in these cases can even cause reverse flow through the orifice (see Figure 9).

Another short subseries of tests were run to determine the lower flammability limit of the system for weak ignition sources, as a basis of comparison for the jet results. In these tests, both a spark plug and an AC Delco 7G glow plug were used for ignition. If the spark plug failed to ignite the mixture, another try would be made with the glow plug. The leanest mixture that could be ignited by either of these units was 9% hydrogen. An interesting effect was noted in the 8% H<sub>2</sub> test, though. After applying power to the glow plug for several minutes, no ignition occurred, so the system was shut down. Despite the lack of a deflagration, the Heise gauge showed a drop in the system pressure of 10 millibars or so, which was much too large to be attributed to leakage. It appears that some sort of slow combustion took place near the surface of the glow plug, such as would occur in a thermal recombiner. This effect has been seen previously by Lowry et al. (1981).

The lower flammability limit of 9% hydrogen found in this last series of experiments seems high compared to the value of 4% that is frequently cited. This value comes from Bulletin 503 of the Bureau of Mines, by Coward and Jones (1952). It is important to note that this value of 4% was found under a very specific set of test conditions, and was for upward flame propagation only. Furthermore, the upward speed of the flame was due mostly to convection, and small lateral expansion of the flames left much of the hydrogen unburned. A 10% concentration of hydrogen was required before complete combustion occurred in these experiments, and no downward propagation occurred at all for mixtures containing less than 9% H<sub>2</sub>. Horizontal combustion in a tube can occur in 6 to 7% hydrogen, but this is due to the confining effects of the tube. In a large vessel, a flame in these mixtures will still move primarily upward, and slowly spread out. No real horizontal propagation occurs, but the flame is convected sideways due to the gas motion induced by the volume expansion occurring through the flame. When spherical vessels were considered, even some smaller ones required H<sub>2</sub> concentrations of 9% before flame propagation would occur. Considering the large size of the vessel and the weak ignition source in the RPI facility, a lower flammability limit of 9% is perfectly reasonable.

Two additional experiments were run to determine the jet temperatures for the 1/4-in. and 1/2-in. orifices. An attempt was made to measure the temperature of the jet with the 3-in. orifice, but the strength of the jet destroyed the thermocouple assembly. The temperature traces are shown in Figure 12. The peak temperature for the 1/4-in. orifice was 900 K, and that of the 1/2-in. orifice was 1200 K. These temperatures are much lower than the predicted AICC temperature of 3245 K for two reasons: First, the flow is expanding as it passes through the orifice from high pressure (up to 9 bars) down to approximately atmospheric. Estimates of isentropic expansion conditions show that this can be responsible for a 500 to 1000 K drop in temperature, depending on the initial state. Second, the smaller orifices restrict flow and allow the combustion products to transfer heat to the cold steel walls of the closure assembly (Figures 1 through 4).

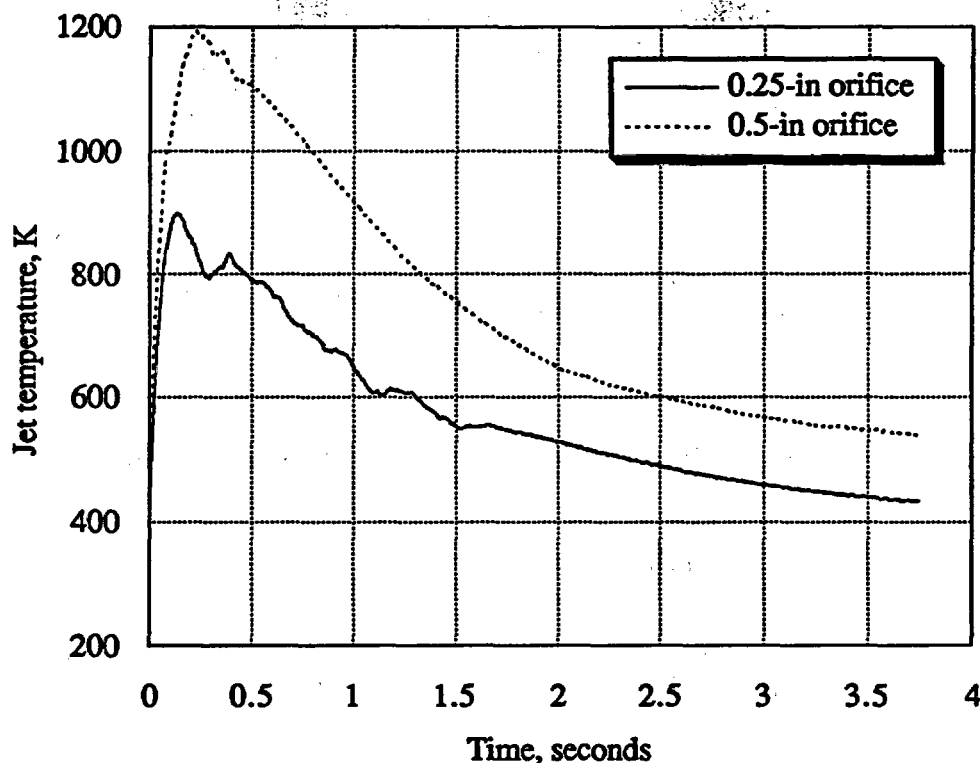


**Figure 12: Jet temperature traces for 1/4-in. and 1/2-in. orifices. Thermocouple mounted 0.5 inches behind orifice exit.**

### Summary and Conclusions

A small-scale facility has been constructed at RPI to study various hydrogen combustion phenomena. The main interests of this research are diffusion flame stability, lean flammability limits, and the possibility of a deflagration-detonation-transition in the containment atmosphere. The experiments utilize a hot combustion-generated jet of hydrogen and steam injected into a diluted hydrogen/air atmosphere, using nitrogen or steam as the diluent. The parameters to be studied in these experiments include the jet velocity, temperature, and composition; particulate effects; and the composition and temperature of the atmosphere. This experiment uses conditions similar to those in other ongoing DCH studies. The facility is presently being used to examine the dependence of the lean flammability limit on the strength of the ignition source.

The A-series of tests run were a subset of the DF-1 test series, venting hot jets of 50% hydrogen and 50% steam into ambient temperature receiver atmospheres. The baseline receiver atmosphere is composed of 50% N<sub>2</sub> and 50% air. It was found that the spark plug, a weak ignition source, could only ignite mixtures containing at least 9% hydrogen. The jet from the 1/4-in. orifice was able to ignite mixtures containing 8% H<sub>2</sub>, and the jet from the 3-in. orifice ignited mixtures as lean as 4%. The information used to determine whether or not a deflagration occurred in the receiver was the peak receiver pressure, the receiver thermocouple signal profiles, and the final system pressure. From the results collected so far, it appears that larger jets are more effective initiators.

The lower flammability limit of the system with the weak ignition source (9% hydrogen) was much higher than the 4% commonly stated. However, Coward and Jones (1952) indicate that the 4% value is only for incomplete, upward propagating combustion. For complete combustion in any direction, the required hydrogen concentration was given as 9 to 10%, corresponding to the value found in the current research.

### **Acknowledgement**

The facility and research described herein are sponsored by the United States Nuclear Regulatory Commission, under contract number NRC-040-91-076. J. C. Krok also thanks the National Science foundation for supporting him through an NSF Fellowship.

### **References**

- Coward, H. F., and G. W. Jones, "Limits of Flammability of Gases and Vapors," Bulletin 503, Bureau of Mines, 1952.
- Lowry, W. E., B. R. Bowman, and B. W. Davis, "Final Results of the Hydrogen Ignitor Experimental Program," NUREG/CR-2486, 1981.
- Revised Severe Accident Research Program Plan*, Division of Systems Research, Office of Nuclear Regulatory Research, U. S. Nuclear Regulatory Commission, NUREG-1365, 1989.
- Reynolds, W. C., *The Element Potential Method for Chemical Equilibrium Analysis: Implementation in the Interactive Program STANJAN, Version 3*, Dept. of Mechanical Engineering, Stanford, CA, January 1986.
- Shepherd, J. E., "Hydrogen-Steam Jet-Flame Facility and Experiments," NUREG/CR-3686, Sandia National Laboratories Report SAND84-0064, 1985.

**Experimental Results of Integral Effects Tests with 1/10th Scale Zion  
Subcompartment Structures in the Surtsey Test Facility**

Michael D. Allen, Martin M. Pilch, Richard O. Griffith, and Thomas K. Blanchat  
Sandia National Laboratories  
P.O. Box 5800  
Albuquerque, NM 87185

**ABSTRACT**

Three Integral Effects Tests (IET-1, IET-3, and IET-6) were conducted to investigate the effects of high-pressure melt ejection on direct containment heating. A 1:10 linear scale model of the Zion reactor pressure vessel (RPV), cavity, instrument tunnel, and subcompartment structures were constructed in the Surtsey Test Facility at Sandia National Laboratories. The RPV was modelled with a melt generator that consisted of a steel pressure barrier, a cast MgO crucible, and a thin steel inner liner. The melt generator/crucible had a hemispherical bottom head containing a graphite limiter plate with a 4-cm exit hole to simulate the ablated hole in the RPV bottom head that would be formed by tube ejection in a severe nuclear power plant accident. The reactor cavity model contained 3.48 kg of water with a depth of 0.9 cm that corresponded to condensate levels in the Zion plant. Forty-three kg of iron oxide/aluminum/chromium thermite were used to simulate molten core debris. The molten thermite in the three tests was driven into the scaled reactor cavity by slightly superheated steam at 7.1, 6.1, and 6.3 MPa for IET-1, IET-3, and IET-6, respectively.

The IET-1 atmosphere was pre-inerted with nitrogen, while the IET-3 atmosphere was nitrogen with  $\approx 9.0$  mole %  $O_2$ . The IET-6 atmosphere was nitrogen with 9.79 mole %  $O_2$  and 2.59 mole % pre-existing hydrogen. In IET-1, approximately 233 g-moles of hydrogen were produced but almost none burned because oxygen was not available. In IET-3, approximately 227 g-moles of hydrogen were produced and 190 g-moles burned. In IET-6, approximately 319 g-moles of hydrogen were produced and 345 g-moles burned.

The peak pressure increases in the IET-1, IET-3, and IET-6 experiments were 0.098, 0.246, and 0.279 MPa, respectively. In IET-3 and IET-6, hydrogen burned in the vent spaces as it was pushed out of the subcompartments into the upper region of the Surtsey vessel. In IET-6, though a substantial amount of pre-existing hydrogen burned, it apparently did not burn on a time scale that made a significant contribution to the peak pressure increase in the vessel.

## 1.0 INTRODUCTION

The Surtsey Test Facility at Sandia National Laboratories is used to perform scaled experiments for the Nuclear Regulatory Commission that simulate hypothetical high-pressure melt ejection (HPME) accidents in a nuclear power plant (NPP). These experiments are designed to investigate the phenomena associated with direct containment heating (DCH). High-temperature, chemically reactive melt is ejected by high-pressure steam into a 1:10 linear scale model of a reactor cavity. Debris is entrained by the steam blowdown into the Surtsey vessel, where specific phenomena, such as the effect of subcompartment structures, water in the cavity, and hydrogen generation and combustion, can be studied.

A series of integral effects tests (IET) was conducted using a 1:10 linear scale model of the Zion Nuclear Generating Station. The first Integral Effects Test (IET-1) [Ref. 1] was conducted with an atmosphere that was almost oxygen free. This virtually eliminated metal/oxygen reactions in the Surtsey atmosphere and preserved the hydrogen produced by steam/metal reactions, so that the total hydrogen production during the HPME event could be accurately measured.

The third Integral Effects Test (IET-3) [Ref. 2] was conducted to replicate the IET-1 test, except that instead of completely inerting the Surtsey atmosphere with nitrogen, the atmosphere was composed of nitrogen and  $\approx 9.0$  mole %  $O_2$ . The goal was to assess the change in the peak pressure due to hydrogen combustion. The sixth Integral Effects Test (IET-6) [Ref. 3] was conducted to examine the effects of pre-existing hydrogen on the peak pressure. In IET-6, the Surtsey vessel atmosphere was composed of 87.1 mole %  $N_2$ , 9.79 mole %  $O_2$ , and 2.59 mole %  $H_2$ . The pre-existing hydrogen in the Surtsey vessel simulated levels that would be produced by partial clad oxidation during the actual core degradation process in a pump seal loss-of-coolant accident.

## 2.0 EXPERIMENT DESCRIPTION

A composite view of the Surtsey vessel, the HPME delivery system, and the subcompartment structures used in the IET experiments is shown in Figure 1. In the IET experiments, 1:10 linear scale models of the Zion reactor pressure vessel (RPV), cavity, instrument tunnel, and subcompartment structures were constructed.

A melt generator (Figure 2) that consisted of a steel pressure barrier, a cast MgO crucible, and a thin steel inner liner modeled the RPV. The melt generator/crucible had a hemispherical bottom head that contained 43 kg of compacted iron oxide/aluminum/chromium thermite to simulate molten core debris. The bottom of the melt generator held a graphite limiter plate with a 4-cm exit hole to simulate the ablated hole in the RPV bottom head that would be formed by tube ejection in a severe NPP accident.

The cavity (Figure 3) used in the IET tests was a 1:10 linear scale model of the Zion reactor cavity designed to withstand internal pressures of 6.9 MPa

with a safety factor of 4. The inclined portion of the instrument tunnel entered the bottom head of Surtsey at a 26-degree angle from vertical, as it does in Zion. A concrete floor was constructed across the Surtsey vessel to support the subcompartment structures. The inclined portion of the instrument tunnel was 2.7 times the correct scaled length of the Zion instrument tunnel exit to match the configuration of a counterpart apparatus at Argonne National Laboratory [Ref. 4].

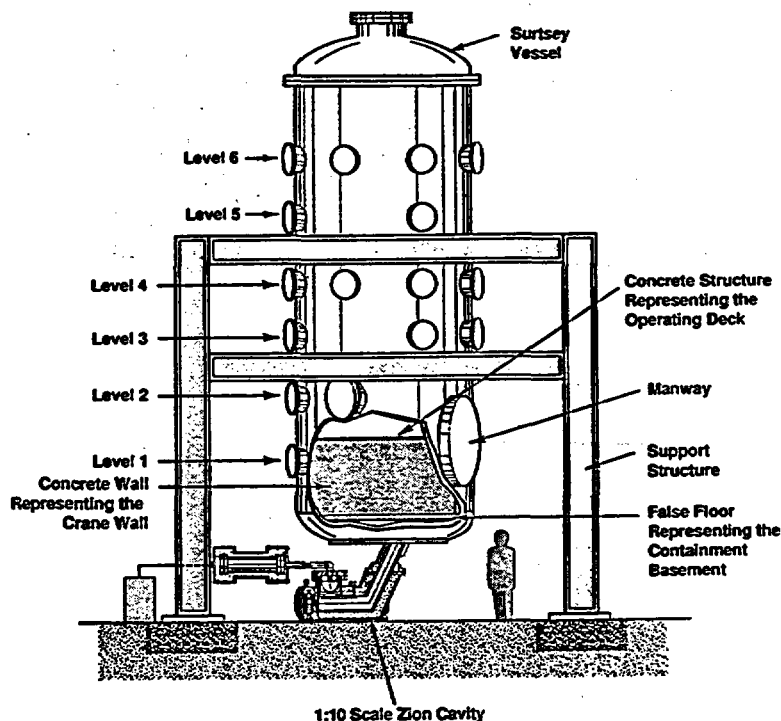


Figure 1. Surtsey vessel, high-pressure melt ejection system, and subcompartment structures used in the IET experiments.

The subcompartment structures (Figure 4) included 1:10 linear scale models of the crane wall, four steam generators, four reactor coolant pumps (RCPs), the seal table opening, the seal table room, the biological shield wall, the refueling canal, the radial beams and the gratings at the RCP deck, and the operating deck. Figure 5 shows an isometric view of the subcompartment structures in Surtsey with a 90-degree section cut out. The freeboard volume inside the subcompartment structures was 4.65 m<sup>3</sup>, and the freeboard volume in the Surtsey upper dome was 85.15 m<sup>3</sup> for a total freeboard volume of 89.8 m<sup>3</sup> in the Surtsey vessel (Table 1). The steam generators, RCPs, and gratings were made of steel and the other structures were constructed of reinforced concrete. All of the structures were painted with an epoxy paint similar to the paint used in NPPs.

The steam accumulator tank was pressurized to  $\approx 6.4$  MPa with superheated steam. After the pressurization sequence, the iron oxide/aluminum/chromium thermite

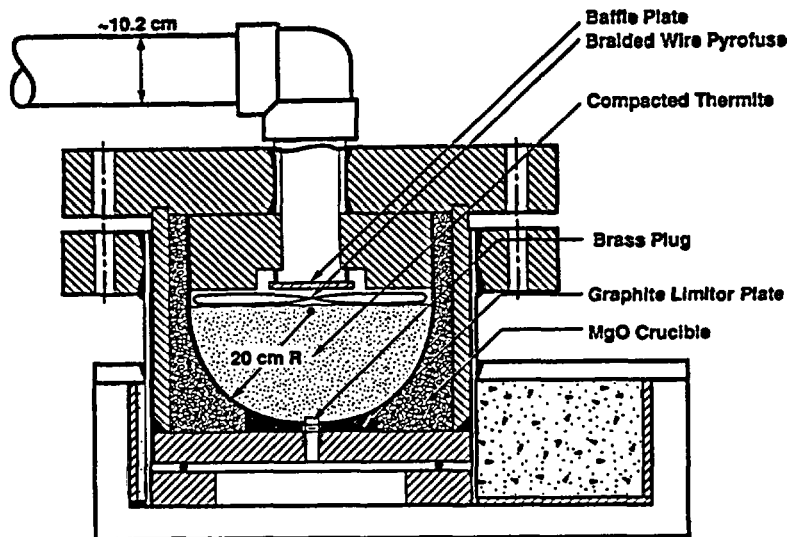


Figure 2. Melt generator and MgO crucible used in the IET experiments.

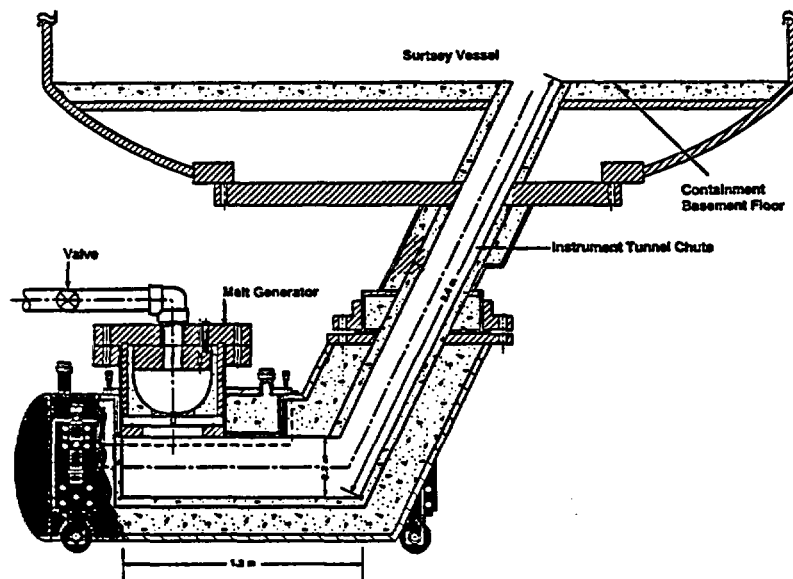


Figure 3. Schematic of the 1:10 linear scale model of the Zion reactor cavity.

mixture was ignited remotely with a braided wire fuse placed on top of the compacted thermite. After the reaction was initiated, the heat generated by the thermite reaction caused the pressure in the crucible to rise. This pressure increase verified that the thermite reaction had started, and signaled the operator to open the valve separating the steam accumulator tank and the molten thermite in the melt generator. This brought superheated steam into contact with the molten thermite. Upon contacting and failing a fusible brass plug at the bottom of the crucible, the molten thermite in the crucible was expelled by high-pressure steam into the cavity.

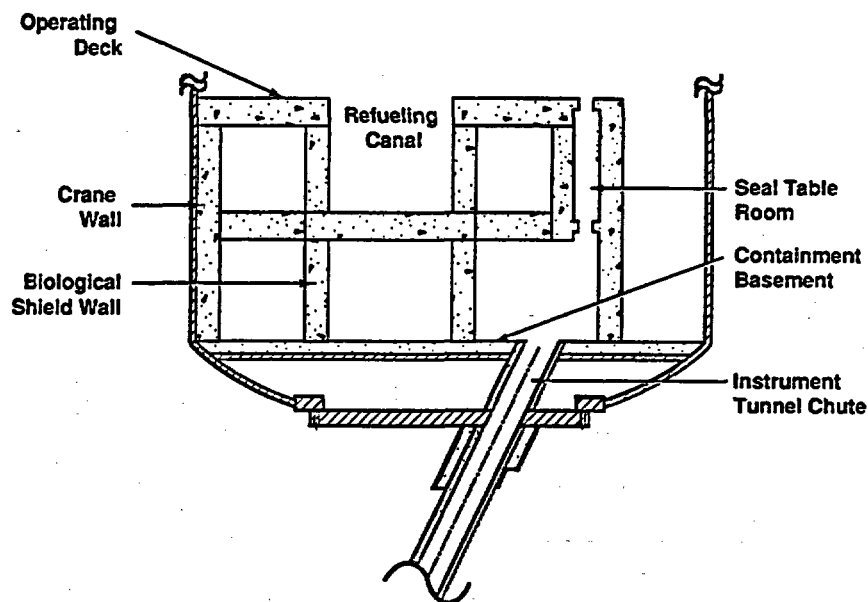


Figure 4. Two-dimensional view of the subcompartment structures inside the Surtsey vessel.

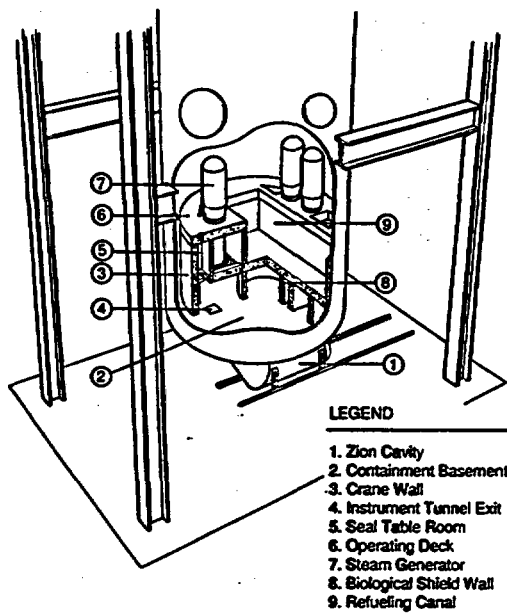


Figure 5. Isometric view of the subcompartment structures inside the Surtsey vessel.

**Table 1**  
Initial conditions for the IET-1, IET-3, and IET-6 experiments.

	IET-1	IET-3	IET-6
Thermite composition (kg)			
- iron oxide	29.26	29.26	29.26
- chromium	4.65	4.65	4.65
- aluminum	9.09	9.09	9.09
Total mass (kg)	43.00	43.00	43.00
Hole diameter (cm)			
- initial	3.50	3.50	3.50
- final	4.04	4.53	3.91
Steam pressure at plug failure (MPa)	7.1	6.1	6.3
Steam temperature at plug failure (K)	600	585	571
Moles of steam driving gas (g·moles)	440	456	505
Cavity water (kg)	3.48 (0.9 cm deep)	3.48 (0.9 cm deep)	3.48 (0.9 cm deep)
Surtsey temperature (K)	295	280	308
Surtsey gas (g·moles)	7323	7291	6961
Initial absolute pressure in Surtsey (MPa)	0.20	0.19	0.198
Initial gas composition in Surtsey (mol. %)	N <sub>2</sub> O <sub>2</sub> H <sub>2</sub> CO <sub>2</sub> Other	99.96 0.03 - - 0.01	90.6 9.0 - - 0.4
Freeboard volume inside subcompartment structures		4.65 m <sup>3</sup>	
Freeboard volume in Surtsey upper dome		<u>85.15 m<sup>3</sup></u>	
Total freeboard volume inside Surtsey		89.8 m <sup>3</sup>	

Zero time for HPME was set by the data acquisition system as the time at which the melt failed the brass plug and entered the cavity. This event was signaled by a photodiode located at the melt plug exit. When the hot melt burst through the brass plug, the intense light emitted from the melt caused the photodiode to emit a signal that was used to mark the initiation of the HPME. The initial conditions of the IET-1, IET-3, and IET-6 experiments are listed in Table 1.

## 2.1 Measurements and Instrumentation

The most significant variables measured in the IET experiments are: (1) the increase in pressure in the Surtsey vessel, (2) the cavity pressure, (3) the number of moles of hydrogen generated by the reaction of metallic debris with steam driving gas and water in the cavity, and (4) the mass of debris recovered from the Surtsey vessel. The instrumentation and techniques used to make these measurements are described in the sections below.

### 2.1.1 Pressure Measurements

Six pressure transducers, two at each level 1, 3, and 5 (Figure 1), were used to measure the pressure in the Surtsey vessel in the IET experiments. These transducers were mounted in tapped holes in instrument penetration ports in the sides of the Surtsey vessel and had their sensing ends protected with steel turnings. Pressure transducers were also used to measure the gas pressure in the accumulator tank, in the crucible above the thermite, in the scaled reactor cavity, in the subcompartment structures, and in the seal table room. These devices were metal-diaphragm, strain gauge-type pressure transducers (Model 141-1, Precise Sensor, Inc., Monrovia, CA). Two additional pressure transducers were used to measure pressure in the scaled reactor cavity. They were embedded in the concrete walls of the round section of the cavity under the melt generator and were piezoelectric-type gauges with a range of 0-6.9 MPa.

### 2.1.2 Temperature Measurements

Following the HPME transient, the gas temperatures in the Surtsey vessel were measured with five aspirated thermocouple assemblies. An aspirated thermocouple assembly consisted of three bare type-K thermocouples mounted in an anodized aluminum tube. One assembly was installed through the instrumentation ports at each level 1, 3, and 5 of the Surtsey vessel. To sample gas from inside the subcompartment structures, a thermocouple assembly was installed through the refueling canal wall just above the radial concrete beam on the same side as the instrument tunnel exit (Figure 5). Another thermocouple assembly was installed through the crane wall projecting into the seal table room. The tubes housing the thermocouples were opened with a solenoid-operated valve that was actuated remotely by a signal from the photodiode under the melt plug immediately after the HPME transient.

The temperature of the driving gas in the steam accumulator tank was measured using two type-K thermocouples that extended through the accumulator shell and were secured in place using pressure-tight fittings. Measurements from these thermocouples were important because the measured temperature and pressure in the accumulator tank were used to calculate the number of moles of steam-driving gas.

### 2.1.3 Gas Composition

Ten pre-evacuated 500-cm<sup>3</sup> gas grab sample bottles were used to collect samples at various times from the vessel at the following locations: a background

sample at level 4 just prior to ignition of the thermite; three gas grab sample bottles located at levels 2, 4, and 6 were opened remotely for 10 seconds at 2 minutes after the HPME; three gas grab sample bottles at levels 2, 4, and 6 were opened manually for 10 seconds at  $\approx 30$  minutes after the HPME; and three gas grab sample bottles that had their inlet inside the subcompartment structures were opened 2 s after the HPME and remained open for 5 s. In addition, two gas grab samples were taken from the cavity following the HPME by opening bottles attached to the cavity; one was opened as the HPME was initiated and remained open for 2 s, and the other was opened at 0.5 s following the HPME and remained open for 2 s. The gas samples were analyzed using gas mass spectroscopy by Battelle Pacific Northwest Laboratories in Richland, WA.

#### 2.1.4 Posttest Debris Recovery

The total mass dispersed into the Surtsey vessel and the mass in specific locations were determined by a very careful posttest debris recovery procedure. The following measurements were made: (1) mass of the molten debris in the cavity and inclined portion of the instrument tunnel; (2) mass on the horizontal surfaces outside the subcompartment structures; (3) mass on the vertical surfaces outside the subcompartment structures; (4) mass recovered from the floor inside the structures; (5) mass recovered from the horizontal surfaces other than the floor inside the structures; (6) mass recovered from the vertical surfaces inside the structures; (7) mass recovered from the doorways inside the structures; (8) mass recovered from the seal table room; (9) mass recovered from the rooms adjacent to the seal table room; and (10) mass recovered from the melt generator/crucible.

### 3.0 EXPERIMENT RESULTS

The experimental results of the IET-1, IET-3, and IET-6 tests [Refs. 1, 2, and 3] are described in this section. These experiments were designed to understand the effect of hydrogen combustion on DCH. The primary variables measured were the Surtsey vessel pressure, cavity pressure, hydrogen production, hydrogen combustion, and posttest debris distribution.

#### 3.1 Blowdown History

Figure 6 shows the blowdown history of the IET-6 experiment, which is typical of the blowdown histories of the other IET experiments. In the experiment, the accumulator tank (volume =  $0.29 \text{ m}^3$ ) was pressurized with superheated steam to  $\approx 6.4 \text{ MPa}$ . The free volume in the crucible and in the 10-cm diameter pipe above the crucible was purged with nitrogen. After the thermite was ignited, the heat from the reaction pressurized the crucible free volume. This signaled the operator to open the valve separating the accumulator and the molten thermite. Figure 6 indicates that in IET-6 steam was in contact with the molten thermite for  $\approx 4.3 \text{ s}$  prior to the HPME. The horizontal line across Figure 6 shows that in IET-6 the steam driving gas pressure at the initiation of the HPME was  $6.3 \text{ MPa}$ . The steam blowdown was complete in  $\approx 4$  seconds.

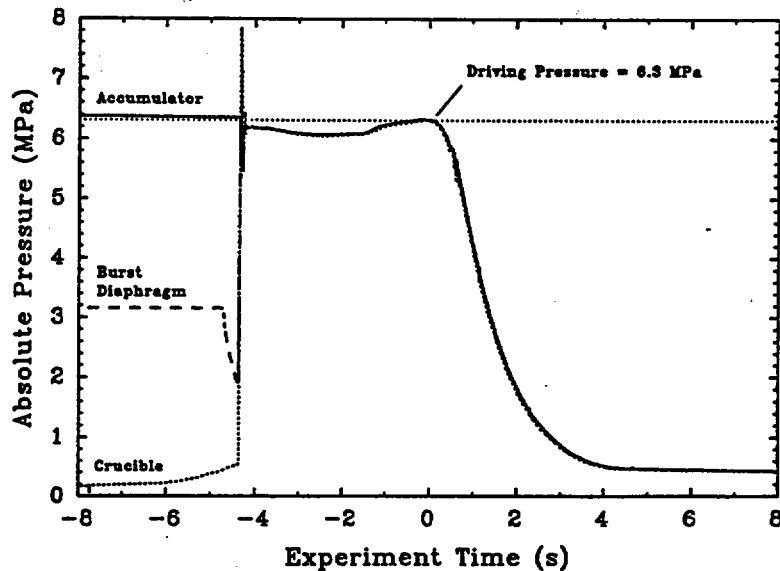


Figure 6. Blowdown history for the IET-6 experiment.

The steam pressure in the accumulator and piping to the crucible at  $t = 0$  was 6.3 MPa, the steam temperature was 571 K, and the total steam volume was  $0.308 \text{ m}^3$ . These data were used to determine the number of moles of steam driving gas using the specific volume of steam from standard thermodynamic tables. The amount of steam driving gas in the IET-6 test was 505 g-moles. The same methodology was used for the other IET experiments.

### 3.2 Pressure Measurements

Pressure transducers were used to measure the pressure increase in the Surtsey vessel, in the cavity, in the seal table room, and in the subcompartment structures caused by the HPME transient. The following sections describe the results of the pressure measurements.

#### 3.2.1 Surtsey Vessel Pressure

Figure 7 shows the absolute pressure measured at level 3 in the Surtsey vessel versus experiment time for IET-1, IET-3, and IET-6. The initial absolute pressure in Surtsey prior to the HPME transient was  $\approx 0.2 \text{ MPa}$  as listed in Table 1. The peak pressure increase without hydrogen combustion in IET-1 was 0.098 MPa. In IET-3, with combustion of hydrogen produced by steam/metal reactions in the HPME, the peak pressure increase was 0.246 MPa. The peak pressure increase in IET-6 with combustion of HPME-produced hydrogen and pre-existing hydrogen was 0.279 MPa. The peak pressure occurred at  $\approx 2.5 \text{ s}$  in all three experiments.

#### 3.2.2 Cavity Pressure

The timing of debris ejection from the cavity into the subcompartment structures is important when analyzing a HPME/DCH event and is best understood

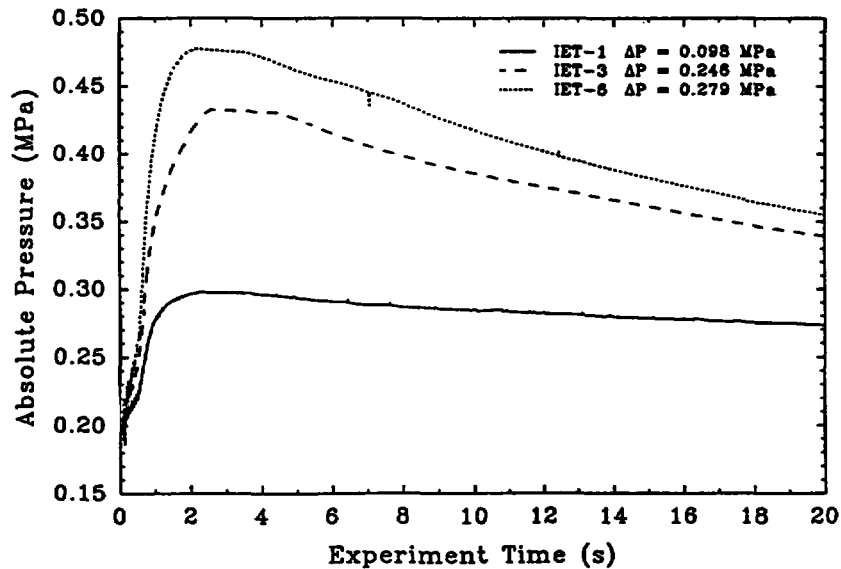


Figure 7. Comparison of the Surtsey vessel pressures measured in IET-1, IET-3, and IET-6 experiments.

by comparing the cavity pressure with the Surtsey vessel pressure. Figure 8 shows the cavity pressure and Surtsey vessel pressure versus experiment time for the IET-1 experiment. This figure shows a relatively small peak just after the HPME began. This peak was caused by gas expansion from hot brass, steel, and thermite entering the cavity. The second peak, which occurred at  $\approx 0.06$  s and had a magnitude of  $\approx 1.4$  MPa, was a relatively small steam explosion. At 0.4 s steam blowthrough occurred and debris was accelerated out of the cavity by the high-velocity steam, which resulted in a higher cavity pressure than Surtsey vessel pressure. The third broad peak, which occurred between 0.4 and 0.8 s, was due to thermite entrainment from the cavity; thus the debris entrainment interval was  $\approx 0.4$  s.

Figure 9 shows the cavity pressure and Surtsey vessel pressure versus time for the IET-3 experiment. This figure shows a relatively small peak in the cavity pressure just after the HPME began. This peak was due to gas expansion caused by hot brass, steel, and thermite entering the cavity. The second peak, which started at  $\approx 0.06$  s and had an absolute pressure of  $\approx 0.46$  MPa, was due to the rapid vaporization of water in the cavity. It did not have a shock wave associated with it and was, therefore, not a steam explosion, as was observed in IET-1. There is previous evidence [Ref. 5] that small steam explosions in the reactor cavity have little effect on the HPME/DCH event. The third broad peak, which occurred between  $\approx 0.4$  and  $\approx 0.75$  s, was due to thermite entrainment from the cavity caused by the steam blowdown; thus the debris entrainment interval lasted  $\approx 0.35$  s. Figure 9 indicates that debris was ejected over the interval between 0.1 and 0.7 s. The rapid vaporization of cavity water apparently created enough force to eject some water and/or debris from the cavity, probably as a slug. Actual entrainment of debris from the cavity by the steam blowdown did not begin until  $\approx 0.4$  s. The debris ejection interval indicated in Figure 9 includes only debris entrainment by the steam blowdown.

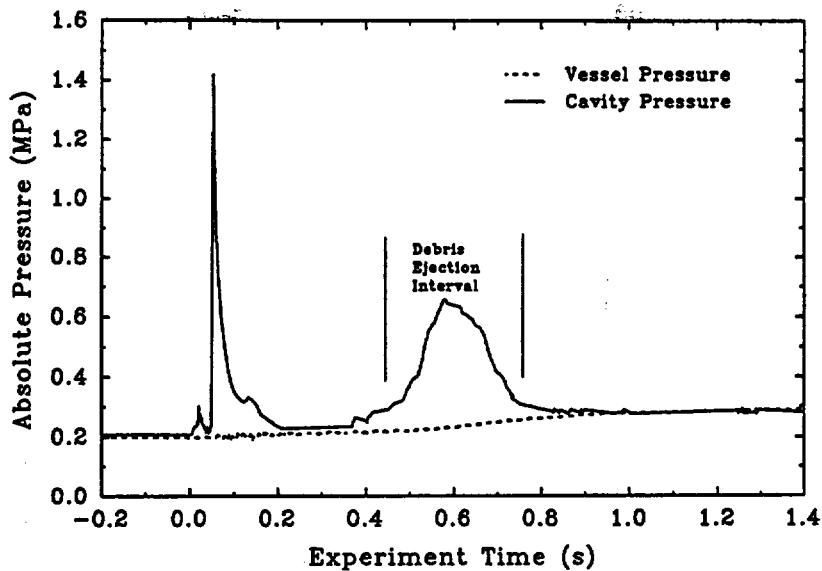


Figure 8. Cavity pressure and Surtsey vessel pressure versus time for the IET-1 experiment.

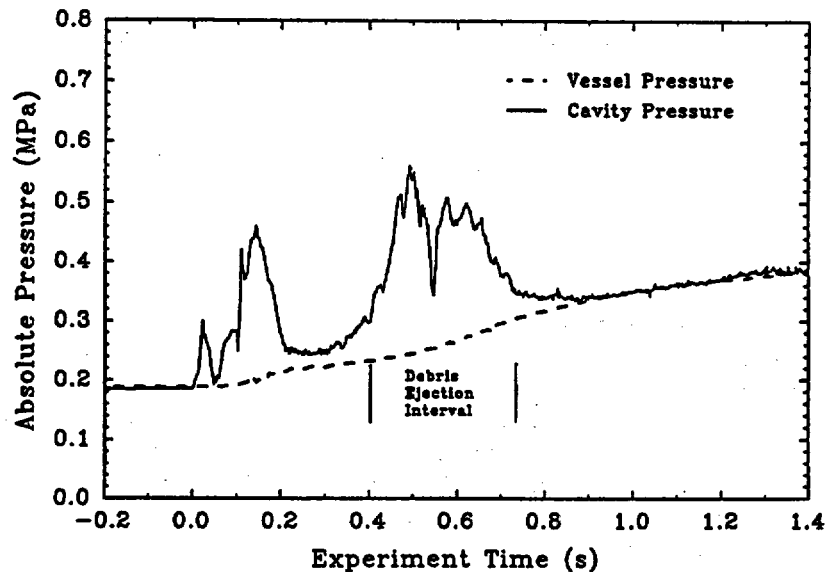


Figure 9. Cavity pressure and Surtsey vessel pressure versus time for the IET-3 experiment.

Figure 10 shows the cavity pressure and Surtsey vessel pressure versus time for the IET-6 experiment. This figure shows a relatively small peak in the cavity pressure just after the HPME began. This pressure peak was caused by efficient gas heating by molten brass, steel, and thermite entering the cavity. The large second peak, which started at  $\approx 0.06$  s and had an absolute pressure of  $\approx 2.45$  MPa, was probably a small steam explosion, similar to the steam explosions observed in IET-1, IET-4, and IET-5 [Refs. 1,6,7]. The

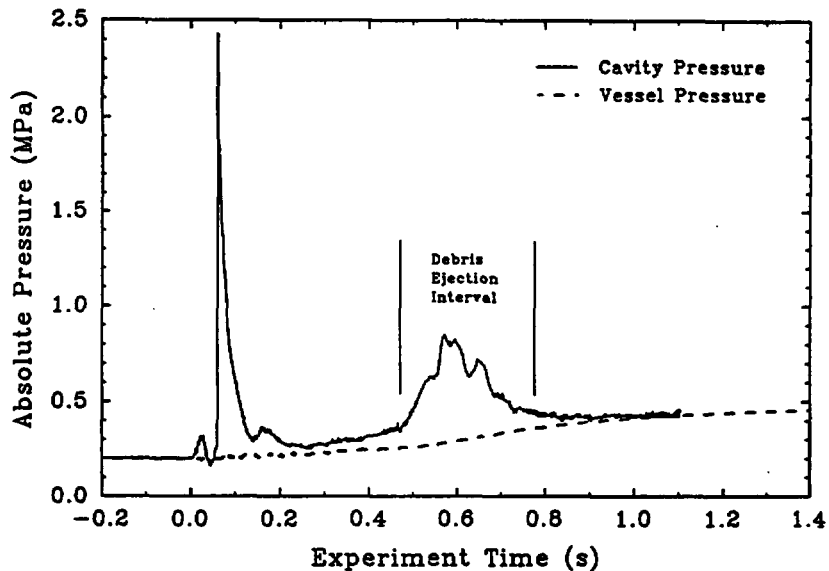


Figure 10. Cavity pressure and Surtsey vessel pressure versus time for the IET-6 experiment.

piezoelectric-type gauges mounted on the east and west cavity walls measured 2.06 MPa and 2.34 MPa, respectively, for the steam explosion peak pressure. The third broad peak, which appears in Figure 10 between  $\approx 0.5$  and  $\approx 0.8$  s, was due to thermite entrainment from the cavity caused by the steam blowdown; thus the debris entrainment interval lasted  $\approx 0.3$  s, whereas steam blowdown lasted  $\approx 4$  s.

### 3.2.3 Pressure Measured Inside the Seal Table Room

Figure 11 shows the pressure measured in the seal table room and the pressure measured in the Surtsey vessel plotted against experiment time for IET-1. Clearly, the pressure measured in the seal table room follows the pressure measured in the cavity (Figure 8). There is a small pressure peak that corresponds to hot thermite entering the cavity. Then there is a large, sharp peak that is probably the result of the steam explosion in the cavity. There is also a broad pressure peak between 0.5 and 0.8 s that corresponds to the debris ejection from the cavity.

In IET-1 the steam explosion in the cavity registered on the pressure transducer in the seal table room. The pressure differential across the seal table room walls caused some damage to the seal table room. The seal table room was separated from the crane wall on one side and also had a large crack in the inner wall. In addition, the concrete plug in the seal table room ceiling was violently ejected into the upper dome of Surtsey.

Figure 12 shows the pressure measured in the seal table room and the pressure measured in the upper dome of Surtsey plotted against time for IET-3. The pressure in the seal table room was greater than the pressure in Surtsey between  $\approx 0.02$  and  $\approx 0.2$  s and between  $\approx 0.4$  and  $\approx 0.7$  s. These intervals

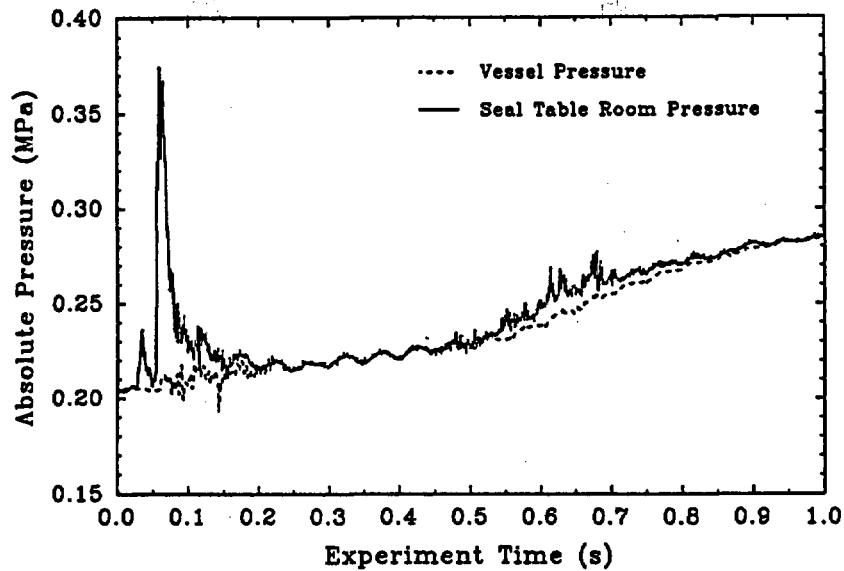


Figure 11. Seal table room pressure and Surtsey vessel pressure versus time in the IET-1 experiment.

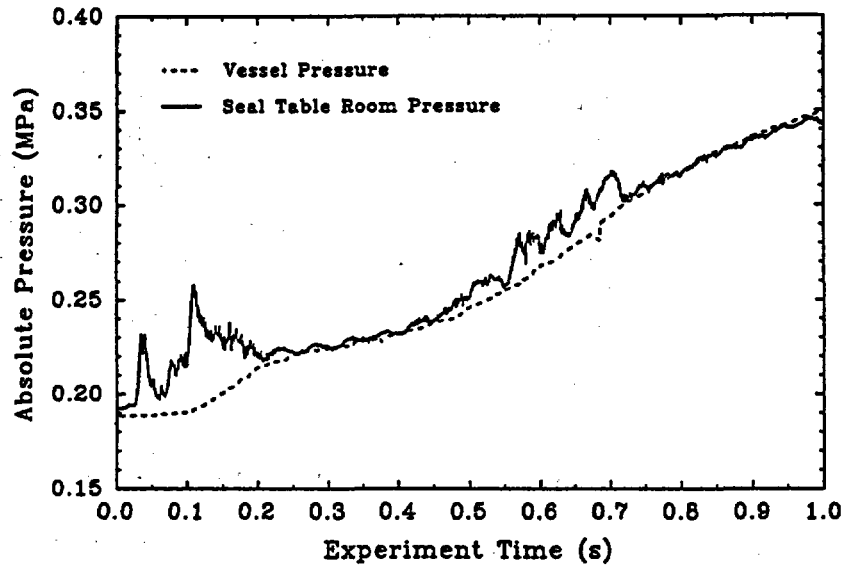


Figure 12. Seal table room pressure and Surtsey vessel pressure versus time in the IET-3 experiment.

correspond respectively to the higher pressures measured in the cavity due to the rapid vaporization of water in the cavity and debris entrainment from the cavity.

Figure 13 shows the absolute pressure measured inside the seal table room and the pressure measured in Surtsey plotted against time for IET-6. The seal table room pressure was positive with respect to the Surtsey vessel pressure

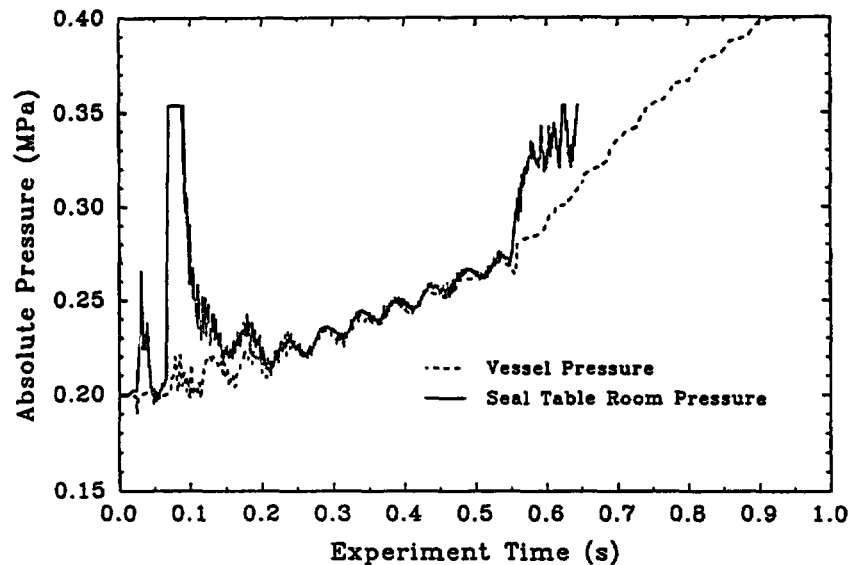


Figure 13. Seal table room pressure and Surtsey vessel pressure versus time in the IET-6 experiment.

from  $\approx 0.03$  to  $0.04$  s, from  $\approx 0.06$  to  $0.2$  s, and from  $\approx 0.55$  s until the transducer overranged. This pressure behavior was also confirmed by a positive seal table room differential pressure. A peak differential pressure of  $0.316$  MPa in the seal table room occurred at  $0.077$  s. This was similar to the seal table room pressure behavior measured in IET-5 [Ref. 7]. The first peak in the seal table room pressure was caused by molten material entering the cavity. The second larger pressure peak was probably caused by a steam explosion. The sensitivity of the seal table room pressure transducer was increased by a factor of two, thus effectively reducing its range from  $0.69$  MPa to  $0.345$  MPa. The transducer overranged between  $0.07$  s and  $0.10$  s.

#### 3.2.4 Pressure Measured Inside the Subcompartment Structures

Pressure data measured inside the subcompartment structures for IET-1, IET-3, and IET-6 showed similar behavior. The fuel coolant interactions (FCIs) that occurred at  $\approx 0.06$  s in these experiments caused the pressure in the subcompartment structure to be higher than the pressure in the upper dome of the Surtsey vessel. The pressure measured inside the subcompartment structures followed the pressure measured in Surtsey after about  $0.1$  s. There was no differential pressure between the structures and Surtsey due to the debris entrainment that occurred between  $0.4$  and  $0.8$  s. Differential pressure across the walls of the structures was caused by the FCIs. All of the pressure transducers showed an oscillatory behavior caused by the FCIs that damped out after approximately  $2$  s. The shock wave from the steam explosion may have caused the Surtsey vessel to resonate.

### 3.2.5 Gas Temperature Measurements

Figure 14 shows the gas temperatures in IET-1 at the Surtsey vessel walls measured with aspirated thermocouples at levels 1, 3, and 5 during the IET-1 experiment. The gas temperatures measured at levels 1 and 3 in the Surtsey vessel were substantially higher than the temperatures measured at level 5. In IET-1, the highest gas temperature was measured at level 3, and the second highest was measured at level 1. The gas temperature was higher at level 3 than at level 1 because there was a direct path for debris ejected from the seal table room to flow past level 3. Level 1 was below the operating deck and thus there was no direct path for debris to flow past the aspirated thermocouple at that level. The gas temperature at level 5, which is relatively high in the vessel, was barely above the ambient temperature. This is an indication that not much debris was ejected into the upper dome of the vessel.

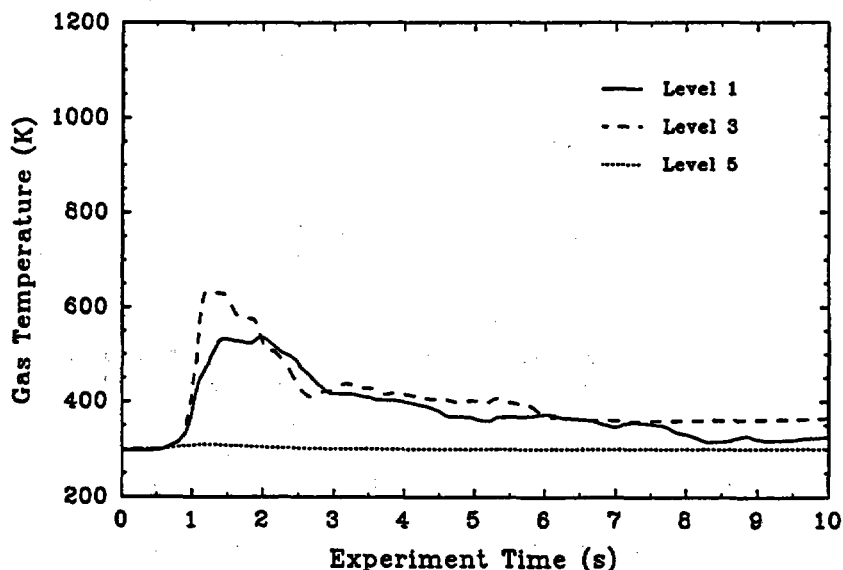


Figure 14. Gas temperatures measured in the upper dome of the Surtsey vessel with aspirated thermocouples in the IET-3 experiment.

Figure 15 shows the gas temperatures measured at the Surtsey vessel walls with aspirated thermocouples at levels 1, 3, and 5 during the IET-3 experiment. The gas temperatures measured at levels 1 and 3 in the Surtsey vessel were substantially higher than the temperature measured at level 5. The highest gas temperature was measured at level 3. Since level 1 is below the operating deck, it is likely that the higher temperature at level 3 was caused by hydrogen burning as it exited the vent spaces above the RCPs. The peak temperature at level 3 in IET-3 was much higher than in IET-1, 1050 K compared to 635 K, and was noticeably shorter in duration. Since no hydrogen burned in IET-1, hydrogen combustion clearly caused the greater magnitude and different shape of the IET-3 temperature peak at level 3. The gas temperature at level 5, which is relatively high in the vessel, was barely above the ambient temperature. This is an indication that not much debris was dispersed into

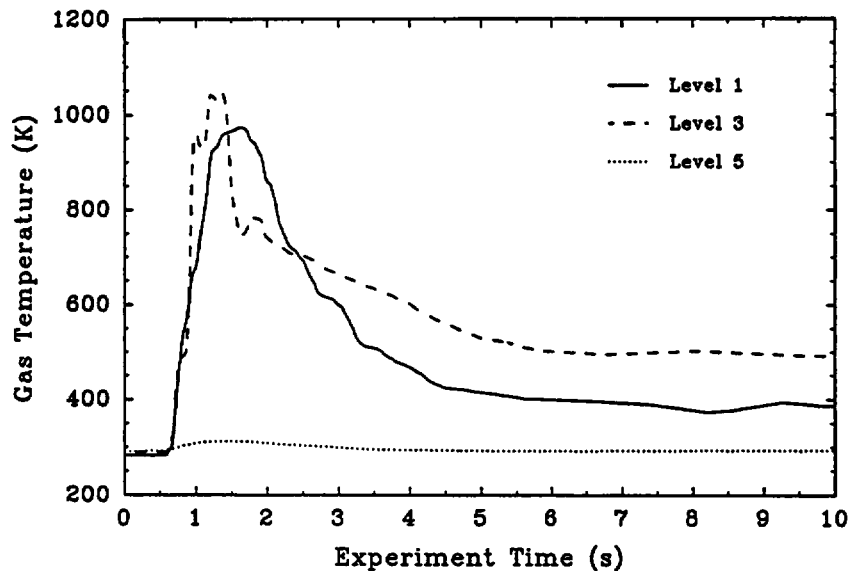


Figure 15. Gas temperatures measured in the upper dome of the Surtsey vessel with aspirated thermocouples in the IET-3 experiment.

the upper dome of the vessel, and that no hydrogen burned at this level. High-speed films of the IET-3 experiment support this explanation.

Figure 16 shows the gas temperatures measured at the Surtsey vessel walls with aspirated thermocouples at levels 1, 3, and 5 during the IET-6 experiment. The peak gas temperatures at level 5 in the Surtsey vessel were substantially lower than the temperatures measured at levels 1 and 3. The peak temperature at level 1 was 1128 K at 1.0 s, and at level 3 was 1033 K at 1.0 s. The aspirated thermocouple temperature at level 5 peaked at 700 K at 4.3 s. The level 5 peak temperature in IET-6 was much greater than the temperatures in either IET-1 or IET-3, probably because of the high driving pressures in the cavity caused by the steam explosion and hydrogen combustion in the upper dome.

Figure 17 shows the gas temperatures inside the subcompartment structures as measured by an aspirated thermocouple in the IET-1, IET-3, and IET-6 experiments. The thermocouple projected through the refueling canal wall just above the radial beam at the RCP deck level, and was on the same side of the refueling canal as the instrument tunnel opening into Surtsey. All three of the type-K thermocouples in the aspirated thermocouple assembly that sampled gas from inside the subcompartment structures showed identical temperature-versus-time curves.

Figure 17 shows three distinct peaks in the gas temperature inside the structures in IET-3 and IET-6. The gas temperature measured with the same aspirated thermocouple in IET-1 only shows two distinct peaks. The first peak in the IET-3 and IET-6 gas temperature curves, which did not show up in the IET-1 data, was probably due to a hydrogen burn inside the subcompartment structures. The second large, broad peak corresponds to debris entrainment

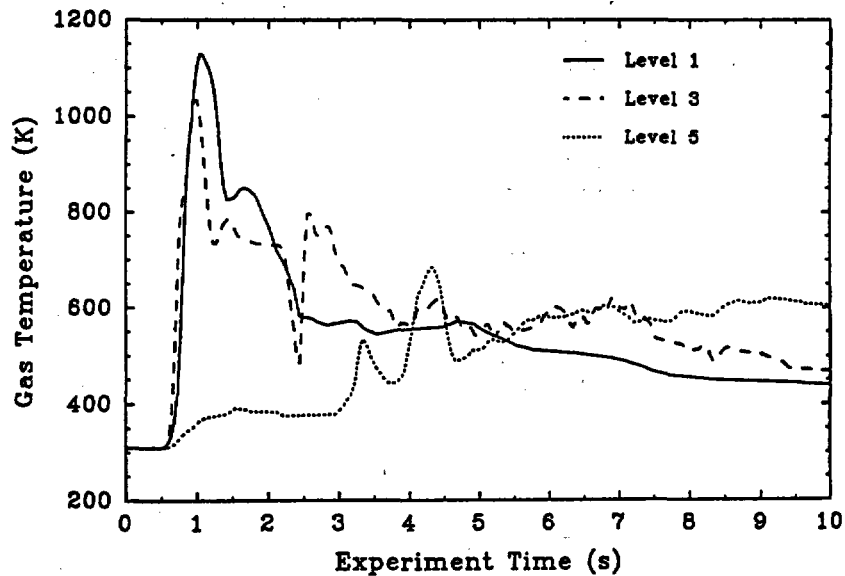


Figure 16. Gas temperatures measured in the upper dome of the Surtsey vessel with aspirated thermocouples in the IET-6 experiment.

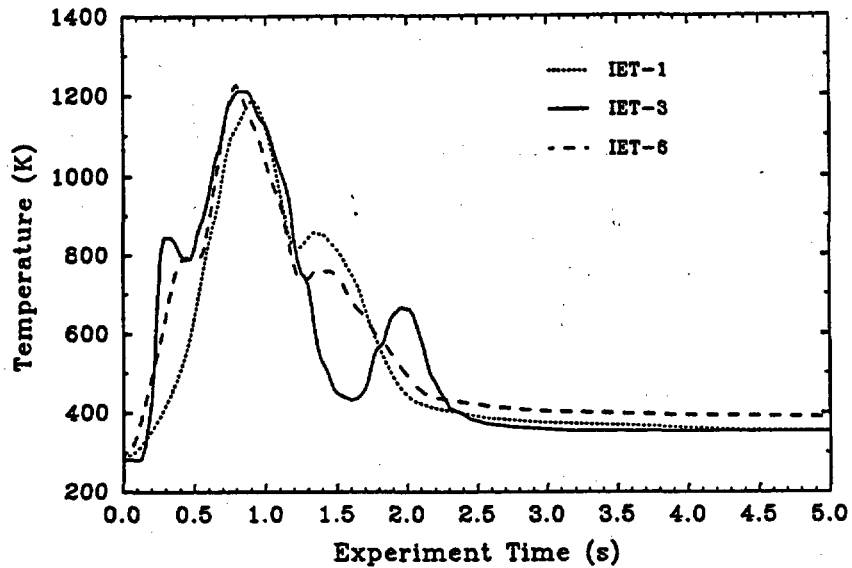


Figure 17. Gas temperatures inside the subcompartment structures measured with an aspirated thermocouple in the IET-1, IET-3, and IET-6 experiments.

from the cavity. The third peak may be due to turbulent mixing of high velocity gas around the backside of the biological shield. This mixing may have caused heating of the gas near the aspirated thermocouple.

Although no hydrogen combustion occurred in IET-1, the peak gas temperatures in the subcompartment structures in IET-1, IET-3, and IET-6 were almost

identical. This indicates that the primary mechanism for heating the subcompartment atmosphere may be debris/gas heat transfer, not hydrogen combustion. The gas temperatures measured in the vent spaces in IET-3 and IET-6 were significantly higher than those measured in IET-1, indicating that hydrogen formed in the cavity or subcompartment structures burned as it was pushed into the air/nitrogen atmosphere in the upper dome of Surtsey.

### 3.2.6 Gas Composition Measurements

Ten gas grab samples were taken from the Surtsey vessel. The locations of the samples, the time at which each grab sample began and its duration, and the hydrogen and oxygen concentrations measured in these gas grab samples are listed in Table 2.

Table 2  
Gas concentrations measured in the IET-1, IET-3, and IET-6 experiments.

Location	Start Time → Duration	IET-1 Species (mole %)		IET-3 Species (mole %)		IET-6 Species (mole %)	
		O <sub>2</sub>	H <sub>2</sub>	O <sub>2</sub>	H <sub>2</sub>	O <sub>2</sub>	H <sub>2</sub>
Background	-20 s → 10 s	0.03	<0.01	9.0	<0.01	9.79	2.59
Cavity	0.0 s → 2 s	0.23	36.5	2.86	41.7	7.82	1.74
Cavity	0.5 s → 2 s	0.04	13.0	2.53	45.8	1.13	74.1
Inside Structures	2 s → 5 s	0.30	20.8	3.41	17.2	3.93	23.5
	2 s → 5 s	0.13	20.9	2.41	24.6	3.64	24.9
Level 2	2 min → 10 s	*	*	*	*	7.49	2.18
Level 2	30 min → 10 s	<0.01	3.10	*	*	7.31	2.21
Level 4	2 min → 10 s	0.05	3.09	*	*	7.42	2.21
Level 4	30 min → 10 s	0.01	3.13	7.71	0.50	7.28	2.21
Level 6	2 min → 10 s	0.01	3.11	*	*	7.48	2.23
Level 6	30 min → 10 s	0.02	3.15	7.70	0.52	7.34	2.20
Mean†		0.03	3.108	7.705	0.52	7.39	2.21
Standard Deviation†		—	0.029	0.007	0.014	±0.09	±0.02

\* This gas grab sample leaked.

† Mean and standard deviations were computed for all of the samples taken outside the subcompartment structures in the Surtsey vessel after the HPME.

Gas grab samples taken from the subcompartment structures in the IET-1, IET-3, and IET-6 experiments indicated that there were high hydrogen concentrations during the HPME transient. Samples taken at 2 s after the HPME ranged from 17.2 mole % H<sub>2</sub> to 24.9 H<sub>2</sub> mole % H<sub>2</sub>. This indicates that the entraining gas in the cavity was a mixture of steam and hydrogen and is important because many analytical entrainment models require the composition of the entraining gas.

Table 3 gives the amounts of pre-existing hydrogen in the vessel, the amounts of hydrogen produced by steam/metal reactions in the HPME, the amounts of hydrogen burned, and the amounts of hydrogen measured posttest at 30 minutes. The measured oxygen and hydrogen concentrations in mole % and amounts of hydrogen produced and combusted in g-moles are plotted versus experiment time in Figures 18 through 21.

**Table 3**  
Amount of gas measured in the IET-1, IET-3, and IET-6 experiments.

	IET-1	IET-3	IET-6
<b>Oxygen (g-moles)</b>			
- Pretest	2	656	681
- Posttest (30 min)	1	610	509
<b>Hydrogen (g-moles)</b>			
- Pretest	0	0	180
- Produced (30 min)	233	227	319
- Burned (30 min)	3	190	345
- Posttest (30 min)	230	37	154
<b>ΔP due to the HPME (kPa)</b>	98	246	279

Figures 18 and 19 show the oxygen and hydrogen concentrations as a function of time in the IET-1, IET-3, and IET-6 experiments. As can be seen from the figures, with the inert atmosphere in IET-1 the oxygen concentration remained close to zero, while the hydrogen concentration increased to about 3.1 mole %. Because of hydrogen recombination, the oxygen concentrations in IET-3 and IET-6 dropped by about 1.3 mole % and 2.3 mole %, respectively, within the first two minutes of the tests.

The IET-1 results shown in Figure 19 indicate that significant amounts of hydrogen can be generated over a relatively short period of time when the hot thermite interacts with high pressure steam. In IET-3, the hydrogen concentration remained smaller than in IET-1 because much of what was produced recombined with oxygen in the containment atmosphere. In IET-6, which had 2.6 mole % of pre-existing hydrogen, the hydrogen concentration actually decreased

as both pre-existing and newly produced hydrogen recombined with oxygen in the containment atmosphere.

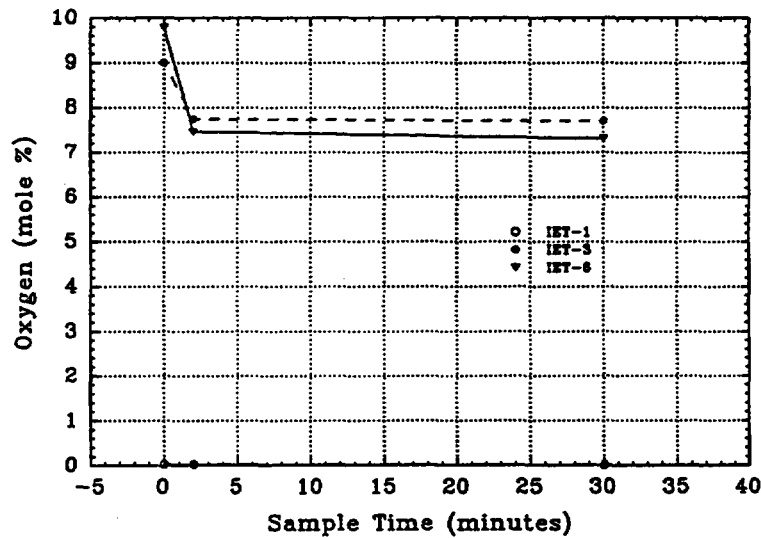


Figure 18. Comparison of the oxygen concentrations versus time for the IET-1, IET-3, and IET-6 experiments.

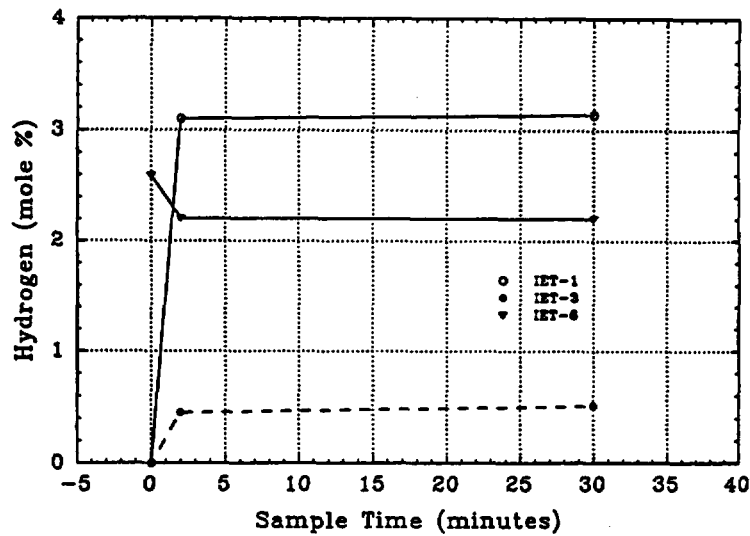


Figure 19. Comparison of the hydrogen concentrations versus time for the IET-1, IET-3, and IET-6 experiment.

Figure 20 shows the rate of hydrogen combustion in the IET-1, IET-3, and IET-6 experiments. The amount of hydrogen combustion was determined by assuming that all oxygen depletion was due to recombination with the hydrogen, and using the stoichiometric chemical reaction for the formation of water. As can be seen in Figure 20, little hydrogen combustion was observed in IET-1. In

IET-3, approximately 184 g-moles of hydrogen had recombined after two minutes. In IET-6, which had 180 g-moles of pre-existing hydrogen, approximately 324 g-moles of hydrogen had recombined after two minutes.

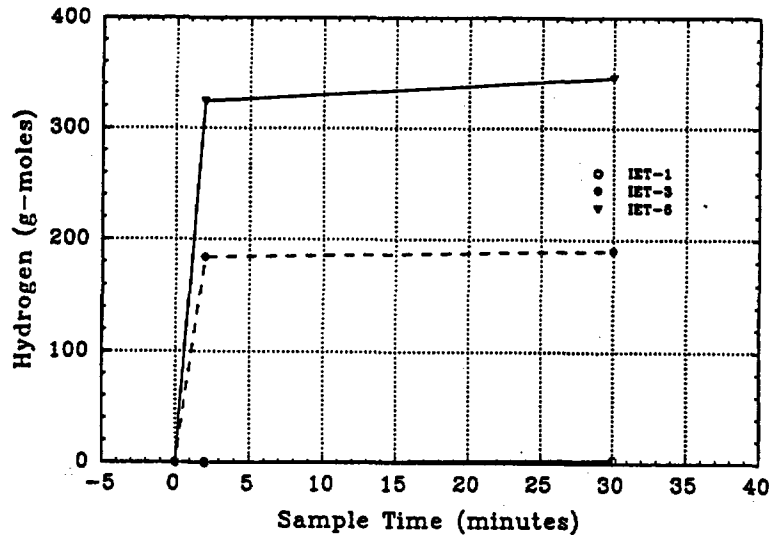


Figure 20. Comparison of hydrogen production versus time for the IET-1, IET-3, and IET-6 experiments.

Figure 21 shows the rate of hydrogen production in the IET-1, IET-3, and IET-6 tests. The hydrogen production amounts were calculated by subtracting the amount of pretest hydrogen from the sum of the posttest hydrogen and the calculated amount of hydrogen that was burned. IET-1 and IET-3 produced approximately the same amount of hydrogen, while IET-6 produced about 25% more than either of those tests. IET-6 may have produced more hydrogen because of the large FCI in the reactor cavity.

### 3.3 Debris Recovery Summary

Table 4 gives the debris recovery summary of the IET-1, IET-3, and IET-6 experiments. The results are reported for four basic locations: (1) from inside the subcompartment structures, (2) from the Surtsey vessel outside the structures, (3) from the cavity and instrument tunnel chute, and (4) from the crucible. The total molten mass available for dispersal into the vessel is usually about 20 percent greater than the initial iron oxide/aluminum/chromium thermite charge due to the melting of the inner wall of the crucible, vaporization of the fusible brass plug, ablation of concrete in the cavity, and oxidation of metallic debris [Ref. 8].

### 3.4 Energy Balance

A single-cell equilibrium model was used to perform an energy balance on the IET experiments [Refs. 1,2,3,6,7], neglecting the presence of water in the cavity. Simple calculations based on the actual IET initial conditions were performed to determine the amount of energy that might be added to the Surtsey

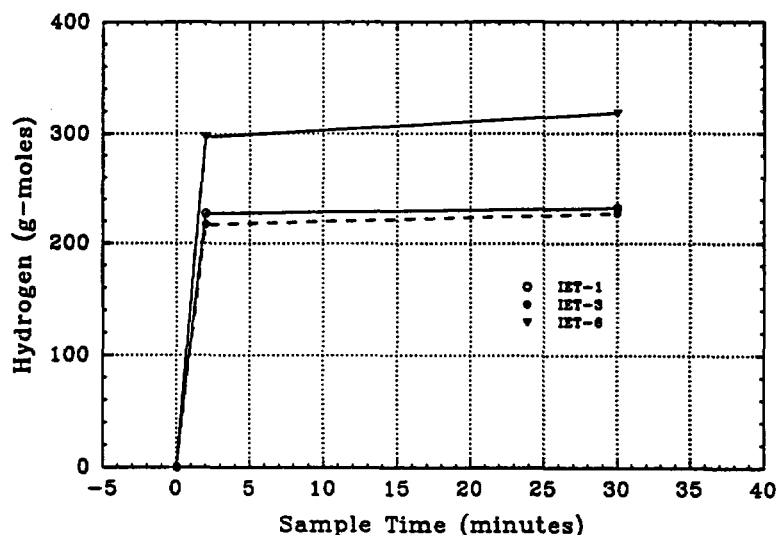


Figure 21. Comparison of hydrogen combustion versus time for the IET-1, IET-3, and IET-6 experiments.

Table 4  
Debris recovery summary for the IET-1, IET-3, and IET-6 experiments.

Mass Balance (kg)	IET-1	IET-3	IET-6
Initial thermite charge, $M_0$ (a)	43.00	43.00	43.00
- Debris inside structures (d)	38.03	31.30	36.60
- Debris outside structures (e)	4.98	3.00	5.87
Total debris recovered from Surtsey	43.01	34.30	42.47
Total debris recovered from cavity and chute (c)	7.06	16.80	8.47
Total debris recovered from crucible (b)	4.54	4.50	2.27
Total mass recovered <sup>1</sup>	54.61	55.60	53.21
<b>Transport Fractions</b>			
Ejected into Cavity $f_{\text{ejct}} = 1-b/a$	0.894	0.895	0.947
Dispersed from Cavity $f_{\text{disp}} = (d+e)/(c+d+e)$	0.859	0.671	0.834
Transported Outside Subcompartment $f_{\text{outs}} = e/(d+e)$	0.116	0.087	0.138
<sup>1</sup> The molten mass available for dispersal into the vessel is usually about 20% greater than the initial iron oxide/aluminum/chromium thermite charge due to melting of the inner wall of the crucible, vaporization of the fusible brass plug, ablation of concrete in the cavity, and oxidation of metallic debris by steam.			

vessel atmosphere by the steam blowdown, exothermic steam/metal chemical reactions, debris/gas heat transfer, and hydrogen combustion. The total amount of energy was used to calculate an upper limit to the possible pressure increase in the Surtsey vessel,  $\Delta P_{\text{equilibrium}}$ . The result could then be compared to the measured peak pressure increase,  $\Delta P_{\text{measured}}$ , to determine the total DCH efficiency,  $\eta = \Delta P_{\text{measured}}/\Delta P_{\text{equilibrium}}$ , in the IET experiments [Refs. 1,2,3,6,7].

The presence of water in the cavity during the IET experiments provided a potential heat sink in the system, since some portion of the thermal and chemical energy in the debris would be used to vaporize the water. In the WC-2 experiment [Ref. 5], the results indicated that less than 15 percent of the water initially present in the cavity was vaporized, despite the fact that the thermite in that experiment contained approximately 5 times the amount of energy necessary to vaporize all of the water that was present. This result suggests that water was ineffective as a heat sink. Furthermore, the HIPS tests with water in the cavity [Ref. 9] suggest that the bulk of the water was ejected prior to debris dispersal. In the IET experiments [Refs. 1,2,3,6,7], the thermite contained approximately 17 times the amount of energy necessary to vaporize all of the water that was present in the cavity. The actual amount of water that was vaporized in the IET experiments cannot be determined from the experimental results, but there was probably very little water vaporized in the cavity.

Derivation of the single-cell model has been documented by Pilch [Ref. 10]. The resulting model is given here. Thermal equilibrium between airborne debris and the containment atmosphere yields a simple, bounding expression for the DCH load,

$$\frac{\Delta U}{U^0} = \frac{\Delta P}{P^0} = \frac{\sum_i \Delta E_i}{U^0(1 + \psi)} \quad (1)$$

where

- $\Delta U$  = total internal energy gained by the containment atmosphere,
- $U^0$  = initial internal energy of the entire containment atmosphere,
- $\Delta P$  = pressure rise in the containment resulting from the DCH event,
- $P^0$  = initial containment pressure,
- $\Delta E_i$  = maximum energy that could be added to the containment atmosphere by the  $i^{\text{th}}$  process, where the  $i$  processes are steam blowdown, debris/gas heat transfer, debris oxidation by steam in an otherwise inert atmosphere, and hydrogen combustion, and
- $\psi$  = heat capacity ratio.

The heat capacity ratio appears because the debris still carries sensible heat that is not available for containment pressurization at thermal equilibrium between airborne debris and the atmosphere. The heat capacity ratio is defined by

$$\psi = \frac{N_d C_d}{(N^0 + N_b) C_v} \quad (2)$$

where

- $N_d$  = number of g-moles of debris participating in DCH,  
 $C_d$  = molar heat capacity of debris,  
 $N^0$  = number of gas g-moles initially in the containment,  
 $N_b$  = number of gas g-moles added to the containment by RCS  
 blowdown, and  
 $C_v$  = molar heat capacity of the containment atmosphere.

The g-moles of debris participating in DCH can be expressed in terms of the initial charge of thermite by

$$N_d = f_{\text{eject}} f_{\text{disp}} \frac{M_d^0}{MW_d} \quad (3)$$

where

- $f_{\text{eject}}$  = fraction of the initial charge that is ejected from  
 the melt generator to the cavity,  
 $f_{\text{disp}}$  = fraction of the melt ejected into the cavity that is  
 subsequently dispersed into the containment,  
 $M_d^0$  = initial (mass) charge of thermite, and  
 $MW_d$  = the effective molecular weight of thermite, 0.0631  
 kg/g-mole.

Table 4 lists all the information necessary to complete this calculation.

Blowdown of the steam accumulator adds both mass and energy to the containment atmosphere. The maximum amount of energy that the accumulator can contribute to Surtsey pressurization is given by

$$\Delta E_b = \frac{P_{\text{acc}}^0 V_{\text{acc}}}{\gamma - 1} \left[ 1 - \frac{P^0}{P_{\text{acc}}^0} \right], \quad (4)$$

where

- $P_{\text{acc}}^0$  = equilibrium pressure of the accumulator/melt generator  
 system just prior to plug failure,  
 $V_{\text{acc}}$  = total free volume of the accumulator and melt generator, and  
 $\gamma$  = ratio of specific heats.

The term preceding the brackets represents the total internal energy of the accumulator, while the bracketed term represents the fraction of this total that is convected into the containment.

Molten debris dispersed from the reactor cavity carries both latent and sensible heat that can be transferred to the atmosphere. The maximum energy source associated with debris thermal energy,

$$\Delta E_t = N_d \Delta e_t \quad , \quad (5)$$

is equal to the amount of dispersed debris,  $N_d$ , times the specific molar internal energy of the debris,  $\Delta e_t$ , which has a value of 0.147 MJ/g-mole for thermite.

The energy source due to debris oxidation,

$$\Delta E_r = N_d \Delta e_r \quad , \quad (6)$$

is equal to the amount of debris participating in DCH times the specific molar oxidation energy of the debris. Assuming all the metals react with steam, the specific molar oxidation energy,  $\Delta e_r$ , has a value of 0.054 MJ/g-mole for thermite.

The energy source due to hydrogen combustion is

$$\Delta E_{H_2} = N_{H_2, \text{tot}} \Delta e_{H_2} = (N_{H_2, \text{pre}} + U_{H_2} N_d) \Delta e_{H_2} \quad (7)$$

where

$N_{H_2, \text{pre}}$	=	g-moles of pre-existing hydrogen in the containment atmosphere prior to the DCH event,
$U_{H_2}$	=	the effective stoichiometric coefficient for debris oxidation, 0.892 g-moles- $H_2$ /g-mole-debris, and
$\Delta e_{H_2}$	=	the specific combustion energy for hydrogen, 0.242 MJ/g-mole- $H_2$ .

The second term in the brackets,  $U_{H_2} N_d$ , represents the total number of g-moles of hydrogen that can be produced by the complete oxidation of the metallic constituents of the dispersed debris. There is sufficient steam in the accumulator and water in the cavity to achieve complete oxidation of debris.

The initial internal energy of the atmosphere is computed from

$$U^0 = N^0 C_v T^0 \quad (8)$$

where

$T^0$	=	initial temperature of the Surtsey atmosphere.
-------	---	--

Table 5 summarizes the energy balance for the IET-1, IET-3, and IET-6 experiments. The thermal (latent and sensible heats) and chemical energy (debris oxidation) are computed for the dispersed thermite mass only. The calculated efficiencies of the IET-1, IET-3, and IET-6 experiments are 25.5, 40.0, and 33.6 percent, respectively.

#### 4.0 HYDROGEN FLAMMABILITY

An important issue in HPME sequences is the contribution of hydrogen combustion to the peak containment pressure. Hydrogen that is produced by

**Table 5**  
**Energy balance for the IET-1, IET-3, and IET-6 experiments.**

Term	IET-1 Value	IET-3 Value	IET-6 Value	Description
$\Delta E_b$	5.45 MJ	5.19 MJ	5.36 MJ	Blowdown energy
$\Delta E_l$	83.7 MJ	58.2 MJ	76.2 MJ	Latent and sensible heat
$\Delta E_c$	31.9 MJ	23.2 MJ	30.2 MJ	Chemical energy from debris oxidation
$\Delta E_{H_2}$	0 MJ	97.7 MJ	151.3 MJ	Hydrogen combustion
$C_d$	70.75 J/g-mole-K	70.75 J/g-mole-K	70.75 J/g-mole-K	Heat capacity of debris
$C_a$	24.2 J/g-mole-K	24.2 J/g-mole-K	24.2 J/g-mole-K	Heat capacity of atmosphere
$\psi$	0.219	0.156	0.212	Heat capacity ratio
$U^o$	51.7 MJ	49.8 MJ	51.8 MJ	Internal energy of atmosphere
$P^o$	0.20 MPa	0.19 MPa	0.198 MPa	Initial pressure of atmosphere
$\Delta P$	0.38 MPa	0.608 MPa	0.831 MPa	Calculated pressure rise
$\eta$	25.5 %	40%	33.6%	DCH efficiency

steam/metal reactions in the cavity and subcompartments, along with any pre-existing hydrogen in the containment atmosphere, may recombine with oxygen in the subcompartments or upper dome. The extent of hydrogen combustion in a HPME event can be estimated using a hydrogen/oxygen/nitrogen flammability chart, such as the one presented in Figure 22 [Ref. 11].

Figure 22 shows that the initial atmospheric conditions in the IET-6 experiment are outside of the envelope of flammable concentrations. This implies that global combustion of the hydrogen in the containment atmosphere will not occur. However, it is possible that the atmospheric conditions in the subcompartments and upper dome during the HPME event may change sufficiently to permit hydrogen combustion. For example, higher gas temperatures will decrease the flammable concentration of hydrogen and, therefore, increase the possibility that global combustion of hydrogen will occur. This is illustrated in Figure 22 by showing the flammability limit at 473 K.

Although global hydrogen combustion was unlikely under the conditions in these experiments, hydrogen apparently burned as a jet as it exited the subcompartments and entered the upper dome atmosphere. Gases displaced from the subcompartments into the upper dome initially had the composition of the ambient atmosphere. As the HPME proceeded, hydrogen produced by steam/metal reactions apparently enriched the hydrogen concentration in the jet, though the relative portions of oxygen and nitrogen remained the same. A line has been drawn in Figure 22 from a 100 percent hydrogen concentration to the ambient conditions in the IET-6 experiment. The line therefore represents all possible jet concentrations, and clearly indicates that hydrogen combustion

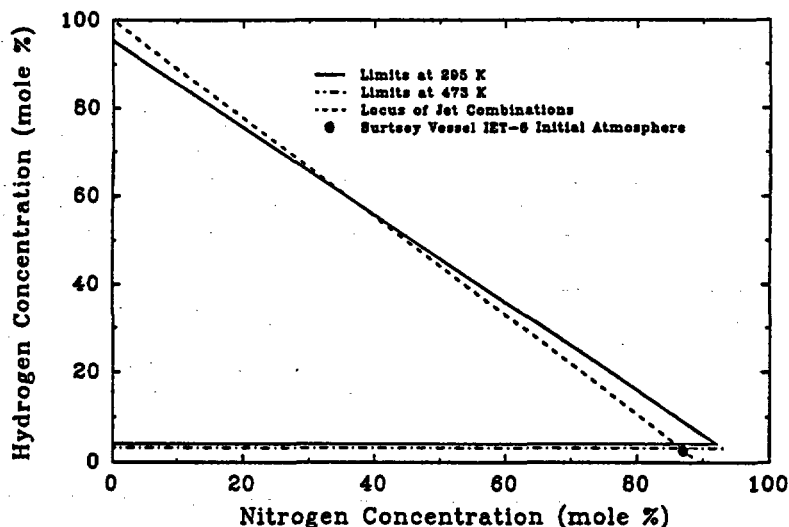


Figure 22. Upward propagation limit for hydrogen/oxygen/nitrogen mixtures.

could occur within the jet as it entered the upper dome. Clearly, the experimental results indicate that hydrogen produced by steam/metal reactions during the HPME burned as it entered the upper dome, but the pre-existing hydrogen did not undergo global combustion even though dispersed molten debris represented a significant ignition source.

#### 5.0 SUMMARY AND CONCLUSIONS

Table 6 summarizes the results of the IET-1, IET-3, and IET-6 tests. In the IET experiments, 43 kg of molten iron oxide/aluminum/chromium thermite was ejected by slightly superheated steam through a hole in a graphite limiter plate into a 1:10 linear scale model of the Zion reactor pressure vessel, cavity, instrument tunnel, and subcompartment structures. Steam blowthrough entrained the molten debris into the Surtsey vessel.

The primary difference in the three IET experiments, besides some minor variations in the initial driving pressure and mass of steam, was in the atmospheric composition in the cavity and the Surtsey vessel. The IET-1 atmosphere was pre-inerted with nitrogen, the IET-3 atmosphere contained about 9.0 mole %  $O_2$ , and the IET-6 atmosphere contained both 9.79 mole %  $O_2$  and 2.59 mole % pre-existing hydrogen. In IET-1, no hydrogen could burn because oxygen was not available. In IET-3, about 80 percent of the hydrogen that was produced by steam/metal reactions burned in the Surtsey vessel. In IET-6, some of the hydrogen that was produced by steam/metal reactions and some of the pre-existing hydrogen also burned.

**Table 6**  
**Summary of the results of the IET-1, IET-3, and IET-6 experiments.**

	IET-1	IET-3	IET-6
Driving pressure at plug failure (MPa)	7.1	6.1	6.3
Moles of H <sub>2</sub> O driving gas (g-moles)	440	456	505
Cavity water (g-moles)	193	193	193
Ablated hole diameter (cm)	4.04	4.53	3.91
Total debris dispersed into Surtsey (kg)	43.0	34.3	42.5
Hydrogen (g-moles)			
- Pretest	0	0	180
- Produced (30 min)	233	227	319
- Burned (30 min)	3	190	345
- Posttest (30 min)	230	37	154
ΔP due to the HPME (kPa)	98	246	279

A comparison of the results of the IET-1, IET-3, and IET-6 experiments yields several important conclusions:

- 1) The similarity in the peak gas temperatures in the subcompartment structures in all three experiments indicates that the primary mechanism for heating the subcompartment atmosphere may be debris/gas heat transfer, not hydrogen combustion.
- 2) High gas temperatures in the vent spaces of IET-3 and IET-6 (and video analyses) indicate that hot jets of hydrogen produced by debris oxidation in the cavity and subcompartment structures burned as a diffusion flame as it was pushed into the air/nitrogen atmosphere in the upper dome of Surtsey. The hydrogen combustion contributed significantly to containment pressurization.
- 3) A comparison of IET-3 with IET-6 indicates that as much as 50 percent of the pre-existing hydrogen in IET-6 burned, but did not contribute significantly to the peak pressure increase. The pre-existing hydrogen appeared to burn on a longer time scale than the HPME event.
- 4) Despite the fact that nearly twice as much hydrogen burned in IET-6 than in IET-3, the peak pressure increases were very close: 0.246 in IET-3 and 0.279 in IET-6. Clearly, the energy released by the additional hydrogen combustion in IET-6 did not occur on a short enough time scale to have a significant impact on the peak pressure in the Surtsey vessel.

## ACKNOWLEDGMENTS

This work was sponsored by the United States Nuclear Regulatory Commission and performed at Sandia National Laboratories, which is operated for the U.S. Department of Energy under contract number DE-AC04-76DP00789.

## REFERENCES

1. M.D. Allen, M. Pilch, R.O. Griffith, R.T. Nichols and T.K. Blanchat, Experiments to investigate the effects of 1:10 scale Zion structures on direct containment heating (DCH) in the Surtsey test facility: The IET-1 and IET-1R tests. SAND92-0255, Sandia National Laboratories (July 1992).
2. M.D. Allen, M. Pilch, R.O. Griffith, D.C. Williams and R.T. Nichols, The third integral effects test (IET-3) in the Surtsey Test Facility. SAND92-0166, Sandia National Laboratories (March 1992).
3. M.D. Allen, T.K. Blanchat, M. Pilch and R.T. Nichols, An integral effects test in a Zion-like geometry to investigate the effects of pre-existing hydrogen on direct containment heating in the Surtsey test facility: The IET-6 experiment. SAND92-1802, Sandia National Laboratories (July 1992).
4. J.L. Binder, Quick look data report on the integral effects test #2 in the Corexit facility at Argonne National Laboratory. Argonne National Laboratory (1992).
5. M.D. Allen, M. Pilch, R.O. Griffith and R.T. Nichols, Experiments to investigate the effect of water in the cavity on direct containment heating (DCH) in the Surtsey test facility: The WC-1 and WC-2 tests. SAND91-1173, Sandia National Laboratories (March 1992).
6. M.D. Allen, T.K. Blanchat, M. Pilch and R.T. Nichols, The effects of condensate levels of water on direct containment heating (DCH) in Zion-like geometry: The fourth integral effects test (IET-4) conducted in the Surtsey test facility. SAND92-1241, Sandia National Laboratories (September 1992).
7. M.D. Allen, T.K. Blanchat, M. Pilch and R.T. Nichols, Experimental results of an integral effects test in a Zion-like geometry to investigate the effect of a classically inert atmosphere on direct containment heating: The IET-5 experiment. SAND92-1623, Sandia National Laboratories (November 1992).
8. M.D. Allen, M. Pilch, R.T. Nichols and R.O. Griffith, Experiments to investigate the effect of flight path on direct containment heating (DCH) in the Surtsey test facility: The limited flight path (LFP) tests. NUREG/CR-5728, SAND91-1105, Sandia National Laboratories (October 1991).

9. W.W. Tarbell, M. Pilch, J.W. Ross, M.S. Oliver, D.W. Gilbert and R.T. Nichols, Pressurized melt ejection into water pools. NUREG/CR-3916, SAND84-1531, Sandia National Laboratories (March 1991).
10. M. Pilch, Adiabatic equilibrium models for direct containment heating. SAND91-2407C, presented at the 19th Water Reactor Safety Information Meeting, Washington, DC (October 1991).
11. R. K. Kumar, Flammability limits of hydrogen-oxygen-diluent mixtures. Journal of Fire Sciences, Vol. 3, (July/August 1985).

**Separate Effect Simulation  
Experiment on Corium Dispersion  
in Direct Containment Heating**

by

**M. Ishii, S.T. Revankar, G. Zhang, Q. Wu and P. O'Brien  
School of Nuclear Engineering  
Purdue University**

The present research at Purdue addresses the most important factor in assessing the direct containment heating in severe accidents. The degree of corium dispersion has not only the strongest parametric effect on the containment pressurization but also the highest uncertainty in predicting it. In view of this, a separate effect test program on the corium dispersion mechanisms in the reactor cavity and the subcompartment trapping mechanisms was initiated in spring of 1992 at Purdue under the direction of the Nuclear Regulatory Commission. Four major objectives of this corium dispersion study are: (1) to perform a detailed scaling study using the newly proposed step-by-step integral scaling method, then to evaluate existing models for entrainment, particle size and trapping, (2) to perform carefully designed simulation experiments using water-air and woods metal-air in a 1/10 linear scale model, (3) to develop reliable mechanistic models and correlations for corium dispersions, which can be used to predict corium jet disintegration, entrainment, drop size, liquid film carry over, and subcompartment trapping, and (4) to use the models to perform stand alone calculations for typical prototypic conditions. The combination of water-air and woods metal-air as working fluid will give a unique data base over broad parametric ranges which can be used together with the integral test results to develop reliable models and correlations.

## **1. STEPWISE INTEGRAL SCALING METHOD**

Specific scaling criteria focused on key phenomena and important mechanisms are developed by the step-by-step integral scaling method described below. This particular scaling method is then applied to the corium dispersion problem in the reactor cavity during the DCH.

### **1.1 Identification of System**

The first step is to identify the system and initial and boundary conditions for the problem. This is followed by the selection of the major subsystems and identification of the interfacial conditions between them. Then the scaling study is carried out for each subsystem separately.

## 1.2 Identification of Subsystem Phenomena and Sequence of Analysis

The second step is to identify the key transfer processes and potentially important mechanisms. These should be ranked in terms of the relative importance and order of events. The possible bifurcation phenomena and feedback mechanisms should be also identified. The bifurcation phenomena highlights the changes in transfer mechanisms whereas the feedback mechanisms focus on the coupling effects between different transfer processes. Based on the above study, the sequence of the scaling study in terms of the transfer processes and mechanisms is determined.

## 1.3 Step-by-Step Scaling Analysis

The actual scaling analysis is carried out by starting from the most dominant process and considering the various mechanisms which can cause that transfer process. The step-by-step approach is used here by considering only one mechanism at a time. The analysis should start from the subsystem boundary and upstream event. First, the most possible mechanism is chosen. The integral rate process equations, integral balance equations and boundary conditions are identified for a particular mechanism together with the transition criteria for the mechanism. The first set of scaling criteria are obtained by nondimensionalizing the integral response from the balance equations or the rate equations.

The next step is carried out by considering the second mechanism. The transition criterion between the first and second mechanisms should be evaluated if the bifurcation is possible. Also the coexistence of the first and second mechanisms should be considered. In this case the relative importance between them is evaluated using the scaling parameters. It is also important to obtain the characteristic time constant for each mechanism. It will give an estimate of the time required to complete the transfer process within the subsystem by that particular mechanism.

By continuing the above step-by-step scaling analysis, a whole set of scaling criteria, transition criteria and characteristic time constants are obtained for the most dominant transfer process. If the other processes are considered to be important, the similar steps are repeated.

## 1.4 Evaluation of Relative Importance

Following the above approach, it is possible to evaluate the relative importance of various effects and mechanisms between the prototype and the scale-down or simulant system.. For this purpose the scaling criteria and time constants are used. In order to obtain quantitative results, it is necessary to give initial and boundary conditions for both systems. Using these, the actual values of the scaling parameters and time constants are calculated. Then the similarity as well as the scale distortions between the systems are analysed. It is essential that the model system should produce dominant phenomena and key mechanisms that are similar to those expected in the prototype. From this requirement, the desirable experimental conditions for scale-down model or simulant model can be developed. When the uncertainty for the dominant mechanism

in the key transfer process is large, the separate effect test focusing on that particular phenomenon is indicated. It is also noted that the experimental data from the model system are indispensable to test the underlining assumptions and physical models used to develop the scaling criteria.

## 2. SCALING STUDY OF CORIUM DISPERSION IN DCH

The stepwise integral scaling method explained above is applied to the corium dispersion in the reactor cavity in DCH. Thus the subsystem is the reactor cavity with the reactor vessel break as the upstream boundary. The previous studies for the DCH problem indicated that the most significant factor affecting the containment heating and pressurization was the degree of the molten corium dispersion. This is because the heat transfer and chemical reactions which may lead to the containment overpressurization are basically proportional to the available surface area of the molten corium.

Therefore, for the scaling study the corium dispersion is taken as the most important phenomenon to be studied in detail in the reactor cavity. For the molten corium dispersion and corium transport, the following four mechanisms are critical.

- i) Corium discharge and corium jet disintegration
- ii) Liquid corium spread-out upon impact of the jet or droplet
- iii) Liquid mass transport due to inertia, pressure and shear force
- iv) Entrainment and drop formation by streaming gas

These are studied by using the step-by-step integral scaling method and starting from the upstream event.

### 2.1 Initial Corium Jet Break-up

The molten corium jet can disintegrate into droplets after the discharge from the reactor vessel break. The corium discharge can be in a form of a single phase jet or two-phase jet due to the depressurization or punch through of the gas flow over the liquid corium surface in the reactor vessel. Several possible mechanisms and jet disintegration length are discussed below. The comparison of the jet disintegration length with the height below the reactor vessel gives the base to determine whether the molten corium disintegrates before impinging on the floor or not. Obviously, if the break-up length,  $L_B$ , is much smaller than the height, then it is expected that the jet disintegrates into small droplets during the vertical downward motion below the break. Hence it is important to know the break-up length.

**2.1.1 Single Phase Jet Breakup.** The single phase liquid jet can break-up in two major modes depending on the relative velocity between the liquid and gas phases, Obot and Ishii [1].

**2.1.1.1 Jet Surface Hydrodynamic Instability.** Obot and Ishii [1] showed that for a

relatively small gas Weber number range given by

$$We_{gr} \equiv \frac{\rho_g v_r^2 D_J}{\sigma} < 3.5 \quad (1)$$

the jet break up length  $L_B$  is given by

$$\frac{L_B}{D_J} = 595 \sqrt{\frac{\mu_f v_{ff}}{\sigma}} \quad (2)$$

where  $v_r$ ,  $v_{ff}$  and  $D_J$  are the relative velocity, jet velocity and jet initial diameter.

2.1.1.2 Jet Surface Break-up due to Relative Motion. When the relative velocity is high,  $We_{gr} > 3.5$ , the break-up length can be significantly reduced [1] and is given by

$$\frac{L_B}{D_J} = 1110 \sqrt{\frac{\mu_f v_{ff}}{\sigma}} (We_{gr})^{-0.5} \quad (3)$$

These correlations indicate that the capillary number  $\frac{\mu_f v_{ff}}{\sigma}$  and gas Weber number scale the jet break-up. The time constant is  $L_B/v_{ff}$ .

2.1.2 Two-phase Jet Break-up. When the jet consists of two phases due to either the gas blow through or gas generation the effect of the void fraction should be considered, Denten and Ishii [2]. In this case

$$\frac{L_B}{D_J} = 595 \sqrt{\frac{\mu_f j_J}{\sigma}} \left[ 1 - \frac{\alpha_J}{0.854} \right]^{1.22} \quad (4)$$

for

$$We_{gr} = \frac{\rho_g j_J^2 D_J}{\sigma} < 3.5 \quad (5)$$

where  $j_J \equiv \alpha_J v_{gJ} + (1 - \alpha_J) v_{fJ}$ . Here  $\alpha_J$  and  $v_{gJ}$  are the void fraction and gas velocity at the jet discharge point. For higher relative velocity,  $We_{gr} > 3.5$

$$\frac{L_B}{D_J} = 1110 \sqrt{\frac{\mu_f j_J}{\sigma}} (We_{gr})^{-0.5} \left[ 1 - \frac{\alpha_J}{0.854} \right]^{1.22} \quad (6)$$

These correlations indicate that the existence of void accelerates the jet disintegration significantly.

2.1.3 Jet Break-up Droplet Diameter. The second phenomenon of importance for the corium jet disintegration is the resultant droplet size. For the DCH problem the droplet size is the key in determining the degree of chemical reaction, heat transfer and corium transport. In the following, the droplet size from the disintegrating jet is discussed in terms of the primary jet disintegration and subsequent droplet disintegration. The correlations given below are applicable both for the single and two-phase jet disintegration. By modifying the annular droplet size correlation of Kataoka, Ishii and Mishima [3] the mean droplet size in the disintegrated jet flow is given by De Jarlais, Ishii and Linehan [4] by

$$d = 0.028 \frac{\sigma}{\rho_g v_r^2} (Re_j)^{1/2} \left[ \frac{\rho_g}{\rho_f} \right]^{1/3} \quad (7)$$

and the maximum size is given from the maximum log normal distribution as  $d_{\max} = 3.13d$ . This criterion roughly corresponds to the Weber number criterion of 12.

**2.1.4 Secondary Disintegration of Jet Droplet.** When the jet disintegrates, the initial droplet size is given by the above correlation. However, often these initial droplets can be relatively large and may not be stable. The droplets from the jet can further disintegrate under two conditions. These are

- (i) Existence of Extremely High Gas Turbulence such as Shock Waves
- (ii) Exceeding of Spherical Limit

During the molten corium discharge phase, the first mechanism is unlikely. Under extreme conditions such as the sudden exposure of droplets to shock waves, the disintegration Weber number can be as low as 2 or 3. However, the condition around the disintegrated jet before the gas blow down phase does not meet such extreme gas turbulences requirement. The second mechanism indicates that if the initial droplet size given by the above correlation far exceeds the spherical stable drop size limit, then droplets will further disintegrate to reach this stability limit. The spherical limit is given by

$$d_{sl} = 4 \left[ \frac{2\sigma}{g \Delta \rho} \right]^{1/2} \left[ N_{\mu g} \right]^{1/3} \quad (8)$$

where the gas viscosity number,  $N_{\mu g}$  is defined by

$$N_{\mu g} = \frac{\mu_g}{\left[ \rho_g \sigma \sqrt{\sigma / g \Delta \rho} \right]^{1/2}} \quad (9)$$

## 2.2 Corium Drop or Jet Impingement Phenomena

In the above, the criteria for the jet break-up length and resultant droplet size are discussed. The next phenomenon of interest is the vertical impingement of the intact jet or the disintegrated jet in the form of droplet flow. The main question here is whether the impinging liquid mass spreads out coherently over the cavity wall or bounces back into the cavity space. The phenomena after the drop or jet impingement at the cavity floor can be scaled by the impact Weber number defined by

$$We_{im} = \frac{\rho_f v_j^2 d}{\sigma} \quad (10)$$

where  $d$  is the drop or jet diameter.

For  $We_{im} > 80$ , the drop or jet will spread out as a liquid film due to large inertia overcoming the surface tension effect to recover. When  $We_{im} < 30$ , the droplets bounce back after the impingement, Bolle and Moureau [5].

### 2.3 Corium Spread Out Over Cavity Wall

Under a prototypic condition the above criterion for the corium spread out is most likely satisfied. Then it is important to know the thickness and velocity of the molten corium film. For this purpose, several different length scales for the film thickness are considered below. From the continuity relation, and assuming that the magnitude of the velocity remains constant during the impingement, the initial film thickness  $\delta_i$  at the vicinity of the impingement point is given by

$$\frac{\delta_i}{D_j} = 0.25 \quad (11)$$

The order of the lower limit of the corium film thickness is estimated by the symmetric spread of the liquid film with the constant liquid film velocity. The length scale for the extent of the film spread is taken as the hydraulic diameter of the cavity,  $D_h$ . Then

$$\delta_{\min} = \frac{D_j^2}{4 D_h} \quad (12)$$

It is noted that instead of  $D_h$ , other length scale may be used here, however for the present study  $D_h$  is satisfactory.

The maximum thickness is obtained by assuming the entire corium mass accumulated on the floor. Thus

$$\delta_{\max} = \frac{M_{cor}}{\rho_f A_f} \quad (13)$$

where  $M_{cor}$  and  $A_f$  are the total corium discharge mass and cavity floor area.

Another reference film thickness can be obtained by assuming that the all molten corium spreads over the entire cavity surface. In this case

$$\delta_c = \frac{M_{cor}}{\rho_f A_w} = \frac{M_{cor}}{\pi \rho_f D_h L_c} \quad (14)$$

where  $A_w$  and  $L_c$  are the cavity wall area and cavity length.

### 2.4 Estimate of Cavity Conditions

In order to evaluate the molten corium dispersion in the reactor cavity, it is necessary to specify the global cavity conditions in terms of the liquid and gas flows. These parameters can be estimated from the geometry and boundary conditions.

In the above, several length scales for the corium film thickness have been obtained. Typical values for these are calculated in table I by considering the following reference conditions.

In the following analysis, the typical film thickness of  $\delta_f = \delta_i$  is assumed over the entire cavity wetted perimeter. Then from the continuity condition, the film velocity is given by

$$v_f = \frac{D_j^2 v_{fj}}{4 D_h \delta_f} \quad (15)$$

The film Reynolds number is defined by

$$R_{ef} = \frac{\rho_f j_f D_h}{\mu_f} = \frac{4 \rho_f \delta_f v_f}{\mu_f} \quad (16)$$

If the film is only on the floor of the cavity, the velocity  $v_f$  and  $R_{ef}$  should be about  $\pi$  times the values given above. Because of the relatively high initial film velocity (in the order of 40 m/s), the liquid corium can climb up the side walls and may even cover the ceiling of the cavity. The actual values should be somewhere between them.

The gas flow conditions are estimated along the analysis proposed by Henry [6]. By assuming the choked flow for the gas discharge following the corium discharge, the pressure at the throat is given by

$$p_t = 0.6 p_v \quad (17)$$

and the choked flow velocity by

$$v_{gt} = \sqrt{\frac{RT}{M_w}} \quad (18)$$

>From the ideal gas at the isothermal condition

$$\rho_{gt} = 0.6 \rho_v \quad (19)$$

The unlimited isothermal expansion can give the maximum velocity of twice the discharge velocity. The cavity gas initial velocity before entrainment can be given from the continuity relation and the cavity pressure. Thus

$$v_{gc} = \frac{0.6 p_v}{p_{co}} \left[ \frac{A_v}{A_c} \right] \left[ \frac{RT}{M_w} \right]^{0.5} \quad (20)$$

where  $A_v$  and  $A_c$  are the vessel break area and cavity flow area.  $p_{co}$  is the cavity initial pressure. This equation indicates that the cavity gas velocity is a strong function of the cavity pressure.

## 2.5 Flow Regime in Cavity

When the molten corium spreads out in the reactor cavity, three different two-phase flow regimes are possible. These are stratified wavy flow, slug flow and annular flow. In order to identify the most possible flow regime, the transition criteria between these regimes are examined. The onset of slugging from horizontal stratified wavy flow is given by the following form (Wallis and Dobson [7]; Mishima and Ishii [8]; Taitel and Dukler [9]):

$$v_r \geq 0.5 \sqrt{\Delta \rho g h_g / \rho_g} \quad (21)$$

In the Taitel and Dukler correlation, the constant of 0.5 is replaced by a function of the void fraction which approaches unity as the relative film thickness becomes smaller.

The transition to annular flow either from the stratified wavy or slug flow is determined by the entrainment process. Thus if the gas (or relative) velocity exceeds the onset of entrainment velocity, the entrainment of wave crests or liquid slugs occurs. In case of slug flow, this leads to the elimination of liquid slugs. Since the part of entrained droplets are deposited on the wall surface, the onset of entrainment leads to the formation of annular flow with liquid wetting the whole surface. However, due to the gravity effect it is expected that the liquid film thickness at

the cavity floor is much larger than those at the side wall and ceiling. The criterion for the annular flow transition is discussed below in terms of the entrainment process.

## 2.6 Corium Entrainment and Droplet Size

The most likely flow regime in the cavity is the film flow. In this case the droplet entrainment becomes the most important mechanisms to disperse the molten corium mass. The onset of entrainment, entrainment rate and entrained droplet size are discussed below. The onset of entrainment criteria is given (Ishii and Grolmes [10]) by

$$\frac{\mu_f v_r}{\sigma} \sqrt{\frac{\rho_g}{\rho_f}} \geq N_\mu^{0.8} \quad (22)$$

where the viscosity number is defined as

$$N_\mu \equiv \frac{\mu_f}{(\rho_f \sigma \sqrt{\alpha / (g \Delta \rho)})^{1/2}} \quad (23)$$

The entrainment rate from the film is given (Kataoka and Ishii, 1982) by

$$\frac{\varepsilon D_h}{\mu_f} = 6.6 \times 10^{-7} (Re_f We)^{0.925} \left[ \frac{\mu_g}{\mu_f} \right]^{0.26} \quad (24)$$

where

$$Re_f = \frac{\rho_f j_f D_h}{\mu_f}, \quad We = \frac{\rho_g j_g^2 D_h}{\sigma} \left[ \frac{\Delta \rho}{\rho_g} \right]^{1/3} \quad (25)$$

Here  $D_h$  is the hydraulic diameter of the cavity. The initial drop size is

$$d = 0.028 \frac{\sigma}{\rho_g v_r^2} Re_f^{-1/6} Re_g^{2/3} \left[ \frac{\rho_g}{\rho_f} \right]^{-1/3} \left[ \frac{\mu_g}{\mu_f} \right]^{2/3} \quad (26)$$

However subsequent disintegration may occur if

$$We_d \equiv \frac{\rho_g (v_g - v_{fd}) 2d}{\sigma} > 12 \quad (27)$$

It is noted that drop size can be as small as  $We_d = 1.7 - 2.5$  if very high gas turbulence exists. Under the reactor cavity condition, the criterion of the Weber number at 12 is more likely than the later criterion. Furthermore, for the droplet to disintegrate beyond the initial entrainment drop size, a sufficient interaction time should exist between drops and the gas flow.

## 2.7 Various Time Constant

Several time constants are important to the analysis of the corium dispersion in the reactor cavity. These are listed below.

$$\text{Corium Discharge Time } \tau_{cd} = \frac{M_{cor}}{\pi \rho_f D_j^2 v_{ff} / 4}$$

$$\text{Primary System Blow Down Time } \tau_{pr} = \frac{V_{pr}}{0.6 \pi D_j^2 v_{gt} / 4}$$

$$\text{Corium Film Transport Time } \tau_f = \frac{L_c}{v_f}$$

$$\text{Corium Entrainment Time } \tau_e = \frac{\delta_f \rho_f}{\epsilon}$$

The latter two time constants are particularly important in determining the dominant transport mode of the corium out of the reactor cavity.

### 3. DISCUSSION OF RESULTS

The above scaling study is applied to the following typical reference conditions, see table I.

Cavity geometry	:Zion
Reactor Vessel Break Size	:35 cm diameter
Molten Corium Mass	:54 tons
Vessel Pressure	:7 MPa (1000 psia)
Cavity Pressure	:0.2 MPa (30 psia)

Relative to the above prototypic conditions, several models and simulation experiments are considered. At full scale and full pressure, a water-air system which simulates the molten corium-steam system is considered. For the 1/10 linear scale-down model, the following cases are considered for sample calculations.

Corium-Steam	(full pressure, 7 MPa)
Thermite-Steam	(full pressure, 7 MPa)
Water-Air	(reduced pressure, 1.4 MPa, (200 psia) - to 0.1 MPa)
Wood Metal-Air	(reduced pressure, 1.4 MPa, (200 psia) - to 0.1 MPa)

The break size for the liquid discharge is geometrically scaled, thus it is 3.5 cm diameter. However, in order to see the parametric effects of the gas flow as well as to compensate for the reduced pressure in the vessel, several enlarged flow area for the gas jet with the increment of twice, three times, five times and seven times are considered in the sample calculations, see table I.

#### 3.1 Prototypic Case

When the reference conditions are applied to the phenomenological models used in the scaling study, the following results are obtained. The molten corium discharge at the velocity of 40 m/s. The disintegration length for the single and two-phase jets are 9 m and 2.3 m respectively. Thus the corium jet tends to disintegrate before reaching the floor of the cavity in the case of two-phase flow. The void fraction of 0.5 is used for this prediction. Since the jet velocity is high, the second mode of disintegration due to the relative motion is applicable. The resultant droplet mean diameter is 6.2 mm with the maximum size of 19.5 mm. The ultimate spherical limit is 1.3 mm.

The value of the impingement Weber number far exceeds the spreading limit of 80. Thus both the coherent jet and droplets spread out upon impingement to the floor and form a corium liquid film rather than bouncing back and form a dispersed droplet flow. This indicates that most of the mass that is discharged as a jet and mostly disintegrated into droplets reforms a coherent liquid film upon impingement to the floor. Therefore, for the corium dispersion in the cavity, the liquid film entrainment becomes the most important mechanism. The duration of the entrainment depends on the liquid film residence time in the cavity. Hence the liquid film motion and transport out of the cavity is also important.

For estimating the film motion, the film thickness and velocity are essential. Several reference values for the film thickness are given below.

Initial Thickness	$\delta_i = 8.8$ cm
Minimum Thickness	$\delta_{\min} = 1.23$ cm
Maximum Thickness	$\delta_{\max} = 20$ cm
Whole Wall Static Spreading	$\delta = 4.3$ cm

The initial film velocity is very high at 40 m/s. Furthermore, complicated three dimensional motion and mixing due to the geometry of the cavity is expected. Because of these, some of the liquid can climb up the side walls and may even flow over the ceiling of the cavity. In the subsequent analysis, a typical film thickness of 8.8 cm is assumed over the entire cavity wetted perimeter. This value is chosen in view of the initial thickness and the average between the minimum thickness and whole wall static spreading thickness. The corresponding average film velocity is 5.5 m/s in the axial direction from the continuity relation. The actual flow should have a very complicated three dimensional pattern. If most of the liquid flows only over the cavity floor then the velocity is about 15 m/s. With the film velocity of 5.5 m/s, the film residence time is in the order of 4 seconds. The jet discharge time for 54 tons of the molten corium from the 35 cm break is about 1.6 sec.

When the liquid starts to flow as a film, three different regimes are possible as discussed previously. The stratified to slug flow transition criterion gives the required gas velocity of 300 m/s, which is about twice the expected gas velocity. However, the more important transition is that to the annular flow, which is determined by the entrainment process. As shown below, for the case of the sample calculation the onset of entrainment velocity is exceeded by the expected gas

velocity. Hence these two transition criteria indicate that the most possible flow regime in the cavity is the annular flow with thicker film at the bottom of the cavity and thinner film at the sides and ceiling.

The entrainment of liquid from the film is governed by the relative velocity and film Reynolds number. The minimum relative velocity required for the onset of the entrainment is given by  $v_r$  in Table I. The steam velocity in the cavity of 192 m/s far exceeds this onset of entrainment velocity of 89 m/s at the assumed cavity pressure of 0.2 MPa. Thus significant entrainment of the film into droplets is expected. The calculated entrainment rate is 12.6 g/cm<sup>2</sup>sec. At this rate, the characteristic time constant is 5.3 seconds. This value should be compared with the film residence time of 3.6 seconds. The two characteristic time constants indicate that the film transport and entrainment mechanisms are in the same order of magnitude. A little less than one half of the molten corium is expected to be entrained by the streaming gas and the remaining mass discharged from the cavity to the lower compartment as a liquid film.

The mean droplet size from the entrainment is 3.9 mm, which is rather large. The subsequent disintegration due to the relative motion between the droplets and gas flow may be possible. When the free stream gas velocity and Weber number of 12 to 2 are used, the droplet stability criterion gives a diameter of about 0.6 to 0.1 mm. The very high entrainment rate shown above will certainly slow down the gas flow, specially in the boundary layer region, since the entrainment process and subsequent acceleration of droplets require considerable momentum transfer from the gas to liquid. When the onset of entrainment gas velocity is used as a mean gas velocity in the droplet boundary layer, the criterion gives the droplet the size of 2.4 to 0.4 mm. Thus it is expected that the size of droplets is in the range of 0.4 to 3.9 mm.

The significant effects of the cavity pressure on the gas velocity and the entrainment process should be noted. For example, if the cavity pressure is 0.3 MPa or 1.5 times the pressure in the sample calculation, the entrainment rate is reduced by a factor of two. The corresponding characteristic time for entrainment is 10 seconds, which is much larger than the film residence time of 3.6 seconds. In that case the corium dispersion is considerably reduced.

The break size has also very strong effects on the corium dispersion. The sample calculations are carried out by assuming the diameter of the break to be 35 cm. The increase in the break size shortens both the corium and gas discharge time. However, the most important effect is on the cavity gas velocity. For example, a twice larger diameter for the break leads to four times larger gas velocity and nearly four times larger entrainment rate. In that case, the entrainment becomes the dominant corium transport process.

### 3.2 Scaled Experiments

It should be also emphasized that the above results are obtained from the existing phenomenological models based on experimental data far from the prototypic DCH conditions. Most of the data base are obtained in standard air-water systems with a relatively small hydraulic diameter of

1 to 2 cm. Only the onset of entrainment criterion has a relatively larger data base with  $D_h$  ranging from 1 to 15 cm. Hence there is a great uncertainty in predicting the corium dispersion in the DCH problem. Two main reasons for this deficiency are:

- (1) Mechanism of corium dispersion are not well understood.
- (2) Large uncertainty in the scale-up capability of the available droplet entrainment correlations.

In view of these, well scaled and focused separate effect experiments on the corium dispersion phenomena may be required. These separate effect experiments should be focused on understanding of the mechanisms of the liquid dispersion and establishing data base which can be used to develop phenomenological models applicable to prototypic conditions. For this purpose several scaled down experiments and simulation experiments are evaluated as a demonstration of the bottom-up scaling method. The results are summarized and compared to the hypothetical prototypic conditions in table I.

In the sample calculations, four different cases are considered. The most important phenomena of liquid entrainment and droplet size are discussed below.

i) Corium-Steam (1/10 scale, full 7MPa pressure)

The entrainment rate is  $1.78 \text{ g/cm}^2\text{s}$  and the droplet size is 1.23 mm. The entrainment rate is roughly 1/7 of the prototypic case, thus the entrainment time is 4 sec, which is comparable to the realistic case. The liquid film transport velocity is essentially the same, at 5.5 m/s, thus the film transport time is reduced by a factor of 10 which is the linear scale rate. Hence the relative significance of the entrainment is reduced by a factor of 7 in this system. This is a significant scale distortion. The droplet size is reduced by a factor of 3. In comparison the system dimension is reduced by a factor of 10. Thus there is a scale distortion in the surface area by a factor of 3.

ii) Water-Air (1/10 scale, reduced pressure 1.4 MPa, 5 times break area for gas)

The entrainment rate is  $3.3 \text{ g/cm}^2\text{s}$  and the droplet size is 0.11 mm. The entrainment rate is about 1/4 of the prototypic case, and the entrainment time is 0.27 sec. Here the smaller density of the water has a very strong effect. The entrainment time is reduced by a factor of 15. The liquid film transport velocity is 7 m/s, which is comparable to the prototype. Hence the film transport time is reduced by a factor of 12.5. Therefore, the ratio of the entrainment time to the transport time is distorted by a factor of only 1.2. The entrainment is slightly accelerated in this system, but overall the agreement is good. The droplet size is reduced by a factor of 35. In comparison the system dimension is reduced by a factor of 10. However, this distortion can be eliminated if the break area for the gas is two times the scaled value. In this case the droplet size is 0.36 mm, which is about 1/10 of the realistic case. Then the geometrical scales are well matched between the system scale and the internal scale (droplet size).

iii) Wood Metal-Air (1/10 scale, reduced pressure 1.4 MPa, 5 times break area for gas)

The entrainment rate is  $2.7 \text{ g/cm}^2\text{s}$  and the droplet size is 0.71 mm. The entrainment rate

is roughly 1/5 of the prototypic case. The corresponding entrainment time is 2.55 sec., which is comparable to the reactor case. The liquid transport velocity is 2.5 m/s, hence the liquid film transport time is reduced by a factor of 5. Therefore, the ratio of the entrainment time to the transport time is increased by a factor of 2. This implies that the relative importance of the entrainment is reduced. The droplet size is reduced by a factor of 5, which should be compared to the linear system scale down factor of 10. Hence the internal surface area is reduced relative to the system surface area by a factor of 2. It is noted that this system behavior is similar to the 1/10 scale corium-steam system. Furthermore, by reducing the break area for gas flow, the droplet size can be increased to about 2.5 mm, which is much closer to the physical dimension of the droplet in the reactor case than that in the water-air system.

The above sample calculations demonstrate the usefulness of the bottom-up scaling method in evaluating various possible experimental conditions. It is noted, however, the numbers obtained for various parameters are based on the best available phenomenological models and correlations. As mentioned above, the data base for these correlations at the prototypic conditions is missing. Hence the verification of both the phenomena and correlations at conditions similar to the reactor conditions is necessary. Furthermore, the present discussion has been limited to the hydrodynamic effects in the corium dispersion. The effects of water in the cavity or the solid materials in the molten corium have not been addressed here. Both of these effects can have a significant influence on the corium dispersion phenomena. These should also be evaluated by further researches. However, the methodology of the bottom-up scaling and its effectiveness in analyzing the key phenomena are clearly demonstrated.

#### 4. SEPARATE EFFECT EXPERIMENT FOR CORIUM DISPERSION

The schematic of the experimental facility is given in Figure 1 and the cross sectional view of the test cavity is given in Figure 2. Three 0.9 m<sup>3</sup> air tanks at 200 psia supply the compressed air. This is connected to the liquid holding tank as well as to gas discharge nozzle. The gas discharge timing is controlled by a solenoid valve to coincide with the time when the liquid discharge is completed. The cavity is made of the polycarbonate material enforced by steel beams such that flow visualization is possible. The subcompartment is made of wood structure. It has viewing windows especially near the exit port of the cavity for the observation of film carry-over and disintegration phenomena. The subcompartment has a deflector plate whose angle of attack and the projected area on the fluid stream can be changed.

The gas and liquid velocities at key points are measured by hot film anemometers. The locations of the hot film probes are rotated in several similar experiments to get full information on velocity distributions. The amount of entrained droplet flow and droplet sizes are measured by several isokinetic sampling probes. The Thermal-hydraulic and Reactor Safety Laboratory has recently developed the isokinetic sampling probe to measure the droplet entrainment rate and droplet size distribution. For droplet size distribution, the droplets are collected into a oil bath and the CDC pictures of the suspensions are obtained. Using digital image processing system

these pictures are analyzed with a software developed at the laboratory. The equipment facility for measurement of entrainment rate and droplet size distribution and typical droplet size distribution measured in horizontal 2 inch pipe with water entrained by air flow is shown in Figure 3. The liquid film thickness is measured by several conductivity probes. The laboratory has the facility for measurement of liquid film thickness using ac and dc signal conductivity probes.

The system pressures are measured by four pressure transducers. In cases of the woods metal-air experiments, the system will be preheated. The liquid film at the end of the cavity is collected in the subcompartment and the collection tank. In addition to these, high speed photography and movies are made to quantify the flow visualization results.

The following list summarizes various parameters measured and the instruments.

Data	Instrument
Jet velocity ( $v_{ff}$ )	Pitot static probe
Liquid film thickness ( $\delta_f$ )	Conductivity probe
Liquid film velocity ( $v_f$ )	Hot film anemometer (liquid)
Cavity air velocity ( $j_g$ )	Hot film anemometer (gas)
Entrainment Droplet Size ( $d$ )	Isokinetic sampling probe
Entrainment rate ( $\epsilon$ )	Entrainment thimble
Pressure ( $P_c$ )	Pressure transducer
Temperature ( $T_c$ )	Thermocouple
Carry-over film liquid	Film collection tank
Carry-over entrained liquid	Entrained liquid collection tank
Flow visualization	High speed still (using 2-3 $\mu$ s strobo)

In order to establish the technical basis for the reliable DCH models based on the present scaling analysis the following separate effect experiments will be performed.

#### a) Cavity Entrainment

The following test matrix and procedures are formulated such that they encompass the range of conditions associated with high pressure corium ejection accidents including system pressure and reactor pressure vessel hole size. The test runs are divided into water-air (1st year) and woods metal-air (2nd year) experiments. The gas flow rate is the major parameter to be varied. The flow area for gas is changed from the geometric similarity case (3.5 cm ID opening) to several times of that area. The break size and the amount of the liquid will be also changed in lesser degree. Two different break sizes of 2 and 3.5 cm ID are used.

For the water-air system, the tests are carried out in two modes,

- 1) Transient blow-down mode ( 200 psia max.)
- 2) Continuous blow-down at low pressure (50-100 psia).

Several experiments are run at same conditions with different hot-film probe locations in order to map the velocity distributions for gas and liquid with the minimum equipment cost.

For the woods metal-air experiments, corresponding simulation test are run only for the transient blow down cases. The system requires preheating and cleaning because of the metal characteristics.

#### (b) Film Disintegration Experiments

Droplet sizes generated by the film disintegration are expected to be quite different from droplet entrainment. For the ejected liquid film, the droplets are generated essentially by the jet disintegration mechanism. In such a case the droplet size for the film ejection has a dimension similar to the film thickness. This implies that the system scale effects are very significant for the droplet generated by the film ejection. Therefore it is utmost important to measure the droplet size independently of entrained droplets. For this purpose, the droplet sizes due to film ejection are measured by isokinetic sampling probe and high speed photography near the exit of the cavity over the same pressure and flow conditions used in the cavity entrainment experiments.

#### (c) Subcompartment Trapping

Two types of experiments are carried out for the subcompartment trapping phenomena for both water-air (1st year) and woods metal-air (2nd year): these are 1) with deflector plate and 2) without deflector plate. These experiments will provide data base for diffusion controlled and trajectory controlled entrainment mechanism at various operating conditions.

### 5. SUMMARY AND CONCLUSIONS

The present research addresses the most important factor in assessing the direct containment heating which is one of the near term goals of the revised SARP of the NRC. The degree of the corium dispersion has not only the strongest parametric effect on the containment pressurization but also the highest uncertainties in predictions. If the corium is highly dispersed and the resulting droplet size to be very small, then the risk to the containment is indeed very high.

The preliminary scaling and modeling study carried out for this proposed research indicates that the entrainment rate is not very high. The amount of molten corium carried out from the cavity as a liquid film is about equal to the amount of entrainment. Furthermore, the entrained droplet mean size is relatively large. The subcompartment plays a major role by entrapping a large fraction of dispersed corium. All these indicate that the molten corium is not highly dispersal. If the applicability of the model and scale-up capability are proven, it may be easily demonstrated that the risk from DCH is negligibly low.

### ACKNOWLEDGEMENT

The authors would like to express their sincere appreciation to Drs. R. Lee, C. E. Tinkler and F. Eltawila of NRC for their valuable discussions and support to this project. This work was

performed under the auspices of the U. S. Nuclear Regulatory Commission.

## NOMENCLATURE

$A_C$	reactor cavity flow area	$N_\mu$	viscosity number based on liquid
$A_f$	cavity flow area	$N_{\mu g}$	viscosity number based on gas
$A_V$	vessel break area	$P_t$	break throat pressure
$A_W$	cavity whole wall area	$P_v$	vessel pressure
$d$	droplet diameter	$R$	universal gas constant
$d_{max}$	maximum droplet diameter	$Re_f$	Reynolds number of film
$d_{sl}$	spherical limit droplet diameter	$Re_j$	Reynolds number of jet
$D_h$	cavity hydraulic diameter	$T$	temperature
$D_j$	discharge jet diameter	$v_{fj}$	liquid jet velocity
$g$	gravity	$v_{gt}$	gas discharge throat velocity
$h_g$	height above corium film	$v_r$	relative velocity
$j_f$	liquid volumetric flux	$V_{pr}$	volume of primary system
$j_j$	total volumetric flux of jet	$We$	Weber number of entrainment
$L_B$	jet break-up length	$We_d$	droplet Weber number
$L_c$	cavity total length	$We_{gr}$	gas Weber number based on relative velocity
$M_{cor}$	total corium mass discharged	$We_{im}$	impact Weber number
$M_W$	gas molecular weight		

## Greek Letters

$\alpha_j$	jet void fraction
$\Delta\rho$	density difference
$\delta_c$	corium thickness from whole wall static spreading
$\delta_i$	initial corium film thickness
$\delta_{min}$	minimum corium film thickness
$\delta_{max}$	maximum corium film thickness
$\delta_f$	corium film thickness in cavity
$\epsilon$	entrainment rate
$\mu_f$	viscosity of liquid
$\mu_g$	viscosity of gas
$\rho_f$	density of liquid
$\rho_g$	density of gas
$\sigma$	surface tension

## REFERENCES

1. N.T. Obot and M. Ishii, Two-phase Flow Regime Transition Criteria in Post Dryout Region Based on Flow Visualization Experiments, *Int. J. Heat Mass Transfer* **31**, (1989) 2559-2570.
2. J.G. Denten and M. Ishii, Flow Visualization Study of Post Critical Heat Flux Region for Inverted Bubbly, Slug and Annular Flow Regime, NUREG/CR-5171, ANL-88-27, (1988).
3. I. Kataoka, M. Ishii, and K. Mishima, Generation and Size Distribution of Droplet in Annular Two-phase Flow, *J. Fluid Eng.* **105**, (1983) 230-238.
4. G. DeJarlais, M. Ishii, and J. Linehan, Hydrodynamic Stability of Inverted Annular Flow in Adiabatic Simulation, *J. of Heat Transfer* **108**, (1986) 84-92.
5. L. Bolle and J.C. Moureau, Spray Cooling of Hot Surfaces, *Multiphase Science and Technology 1* (Edited by G.F. Hewitt, J.M. Delhay and N. Zuber), (1982) 1-98.
6. R. Henry, An Evaluation of Fission Product Release Rates During Debris Dispersal, *Proc. ANS International Topical Meeting - Probability, Reliability and Safety Assessment 1*, April 2-7 (1989) 375-383.
7. G.B. Wallis and J.E. Dobson, The Onset of Slugging in Horizontal Stratified Air-Water Flow, *Int. J. Multiphase Flow* **1**, (1973) 173-183.
8. K. Mishima and M. Ishii, Theoretical Prediction of Onset of Horizontal Slug Flow, *J. Fluids Engineering*, **102**, (1980) 441-445.
9. Y. Taitel and A.E. Dukler, A Model for Predicting Flow Regime Transition in Horizontal and Near Horizontal Gas-Liquid Flow, *AIChE J.*, **22**, (1976) 47-55.
10. M. Ishii and M.A. Groloms, Inception Criteria for Droplet Entrainment in Two-phase Concurrent Film Flow, *AIChE*, **21**, (1975) 308-318.
11. I. Kataoka and M. Ishii, Mechanism and Correlation of Droplet Entrainment and Deposition in Annular Two-phase Flow, NUREG/CR-2885, ANL-82-44, (1982).

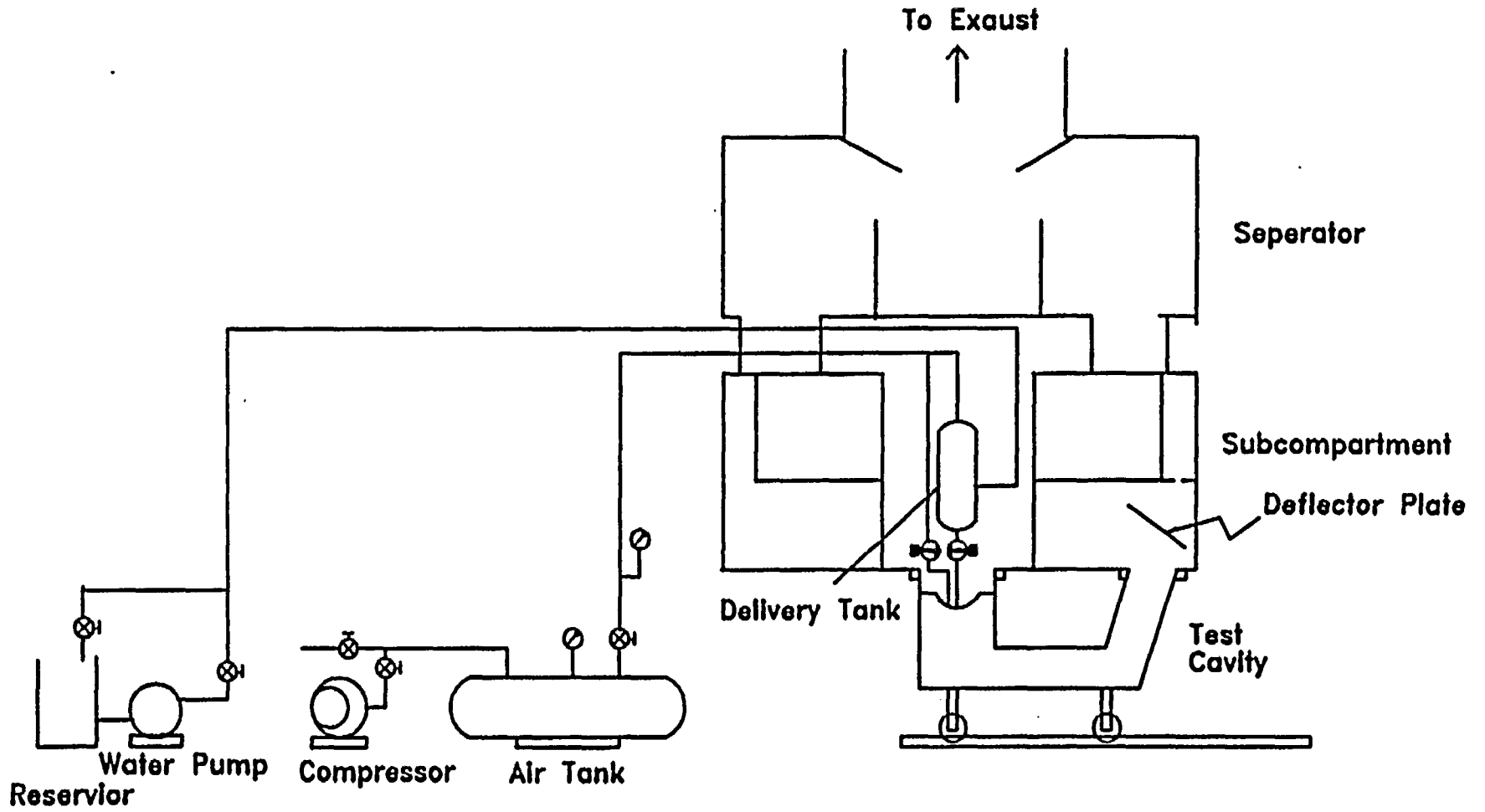


FIGURE 1. Purdue DCH Experimental Facility

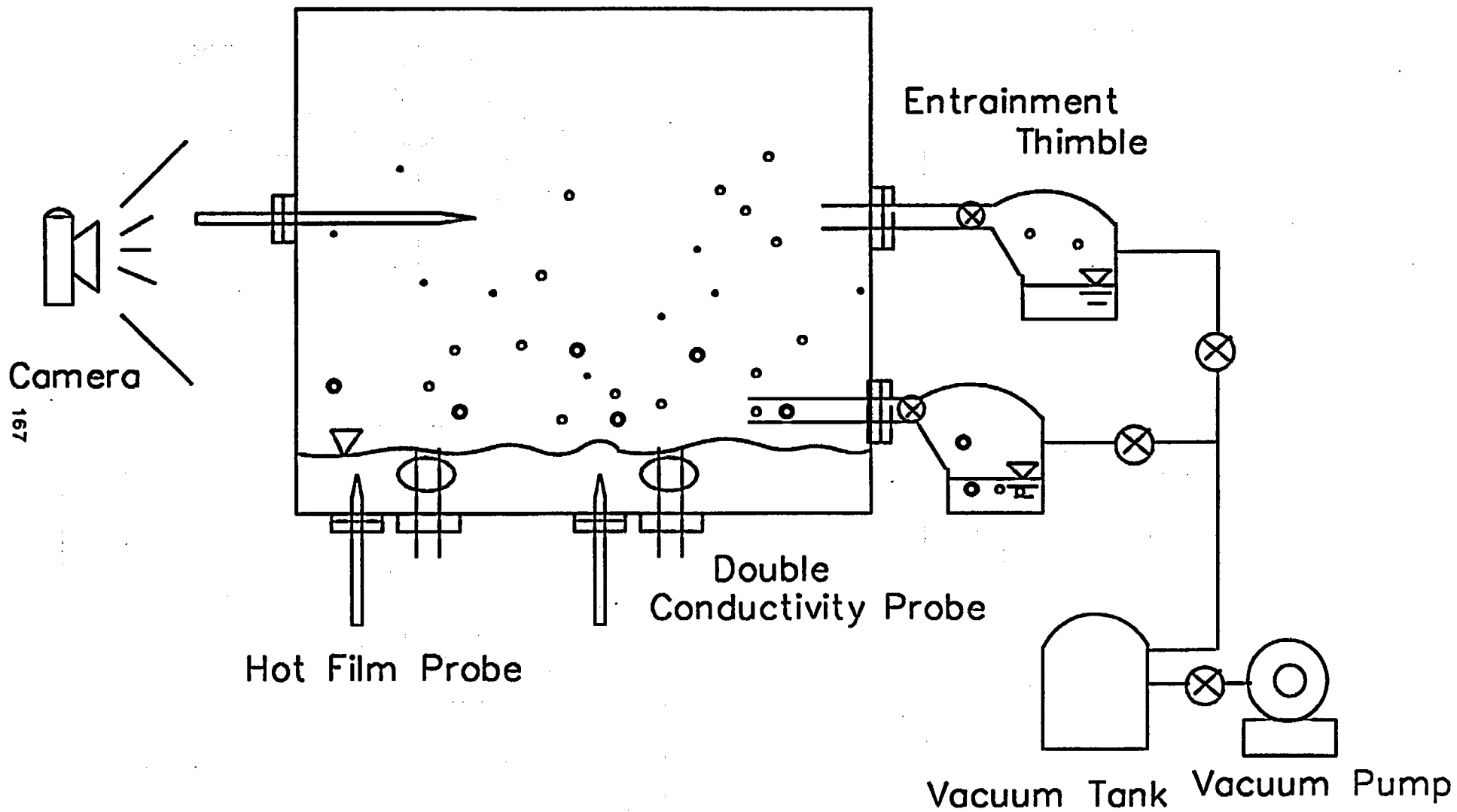
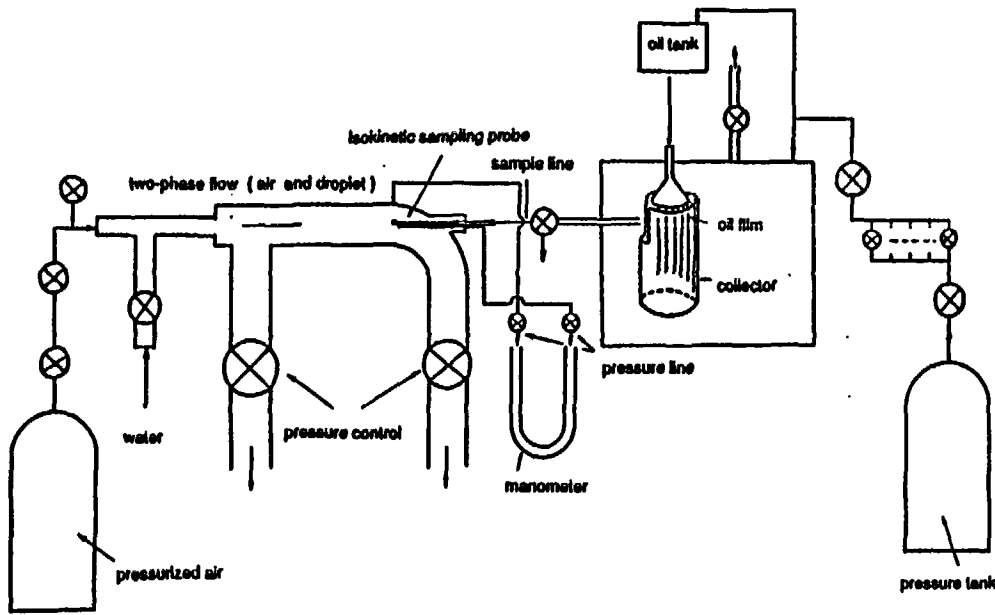


FIGURE 2. Cross sectional view of test cavity



Isokinetic Sampling System

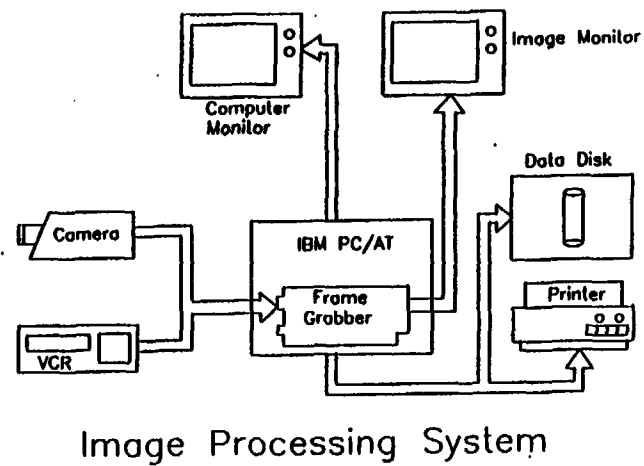
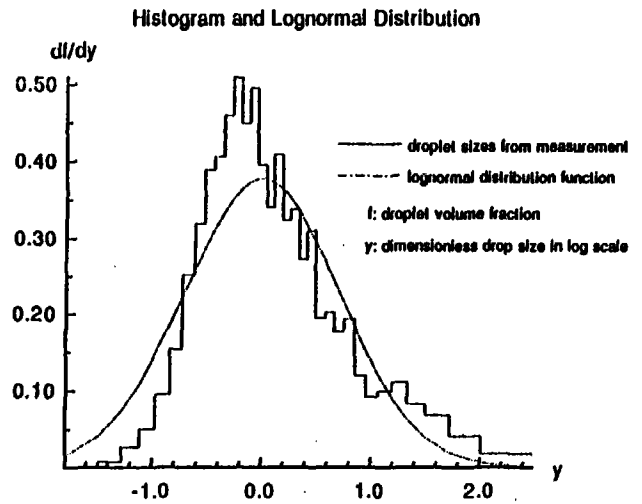


Image Processing System

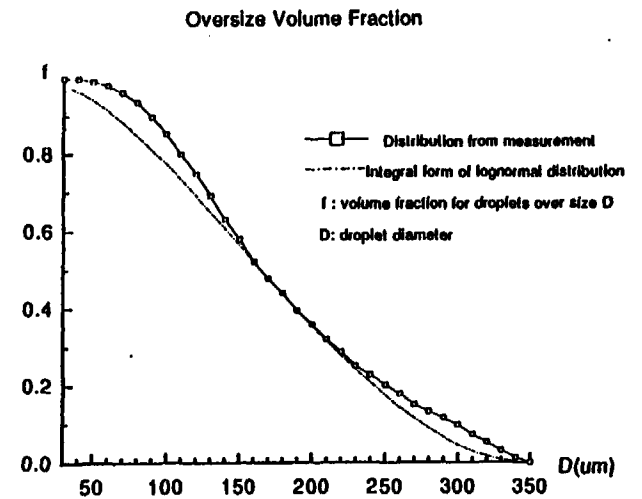


FIGURE 3. Droplet Size Measurement System and Typical Measurement Data

## SAMPLE CALCULATION FOR VARIOUS PARAMETERS IN CORIUM DISPERSION

Tab.1 Jet Disintegration and Impingement ( $D_j=0.35m, 54t$ )

	V <sub>fj</sub> (m/s)	L <sub>b1</sub> (m)	L <sub>b2</sub> (m)	d (mm)	d <sub>max</sub> (mm)	d <sub>sl</sub> (mm)	B	W <sub>egr</sub>	We <sub>im</sub> (e04)
ZION-S2d, 1/1	39.6	9.1	2.3	6.2	19.5	1.3	0.18	330	7.7
ZION-S2d, 1/10	39.6	2.9	0.7	2.0	6.2	1.3	0.18	330	2.4
SNL/IET-1,1R, 1/10	52.4	1.7	0.4	1.0	3.1	1.8	0.18	91	1.3
ANL/IET-1RR, 1/40	52.4	0.9	0.2	0.5	1.6	1.8	0.18	23	0.64
PURDUE/WATER, 1/10	50.0	0.8	0.2	0.1	0.3	1.6	0.69	1500	0.34
PURDUE/WMETAL,1/10	17.7	2.4	0.6	2.9	9.1	1.2	0.09	25	1.6

Tab.17 Film Spreading ( $D_j=0.35m, 54t$ )

	d <sub>ti</sub> (cm)	d <sub>tmin</sub> (cm)	d <sub>tmax</sub> (cm)	d <sub>tcavi</sub> (cm)	V <sub>f</sub> (m/s)	Ref (E05)
ZION-S2d, 1/1	8.75	1.23	19.65	4.27	5.54	33.72
ZION-S2d, 1/10	0.88	0.12	1.96	0.43	5.54	3.37
SNL/IET-1,1R, 1/10	0.88	0.12	2.37	0.35	7.34	3.44
ANL/IET-1RR, 1/40	0.22	0.03	0.72	0.09	7.55	0.91
PURDUE/WATER, 1/10	0.88	0.12	1.96	0.43	7.00	2.55
PURDUE/WMETAL,1/10	0.88	0.12	1.94	0.42	2.47	3.01

Tab. 18 Entrainment ( $D_j=0.35m, 54t$ )

	V <sub>g</sub> (m/s)	V <sub>r</sub> (m/s)	E(g/c m <sup>2</sup> s)	t (s)	d (mm)	d <sub>max</sub> (mm)	d <sub>we</sub> (mm)	d <sub>cr</sub> (mm)	Reg (E06)	We (E06)
ZION-S2d, 1/1	191.9	88.93	12.6	5.33	3.90	12.2	0.58	.096	22.2	1.3
ZION-S2d, 1/10	191.9	88.39	1.78	3.77	1.23	3.86	0.58	.096	2.21	.13
SNL/IET-1,1R, 1/10	217.6	63.43	2.33	1.64	0.78	2.43	0.29	.048	2.34	.19
ANL/IET-1RR, 1/40	230.2	63.43	0.84	1.17	0.36	1.12	0.26	.043	0.62	.053
PURDUE/WATER,1/10 D <sub>j</sub> =3.50cm	31.8	16.13	0.16	5.54	0.91	2.84	1.18	.196	0.50	.040
4.95	63.6	16.13	0.59	1.48	0.36	1.13	0.23	.038	1.00	.160
6.06	95.4	16.13	1.25	0.70	0.21	0.66	0.093	.015	1.50	.359
7.00	127.2	16.13	2.13	0.41	0.14	0.45	0.050	.008	2.01	.638
7.83	159.1	16.13	3.22	0.27	0.11	0.33	0.031	.005	2.51	.997
8.57	190.9	16.13	4.51	0.19	0.08	0.26	0.021	.004	3.01	1.436
PURDUE/WMETAL,1/10 D <sub>j</sub> =3.50cm	34.70	56.78	0.14	50.1	NO	NO	NO	NO	0.42	.014
4.95	69.3	56.78	0.51	13.9	2.42	7.56	1.18	.197	0.83	.055
6.06	104.0	56.78	1.07	6.56	1.41	4.40	0.51	.085	1.25	.123
7.00	138.7	56.78	1.82	3.86	0.96	3.00	0.29	.047	1.67	.219
7.83	173.3	56.78	2.74	2.55	0.71	2.23	0.18	.030	2.08	.341
8.57	208.0	56.78	3.84	1.82	0.56	1.75	0.13	.021	2.50	.492

## RESULTS OF DIRECT CONTAINMENT HEATING INTEGRAL EXPERIMENTS AT 1/40TH SCALE AT ARGONNE NATIONAL LABORATORY

by

J. L. Binder, L. M. McUmbler and B. W. Spencer  
Engineering Development Laboratories  
Reactor Engineering Division  
Argonne National Laboratory  
Argonne, IL 60439

### ABSTRACT

A series of integral tests have been completed that investigate the effect of scale and containment atmosphere initial composition on Direct Containment Heating (DCH) phenomena at 1/40 linear scale. A portion of these experiments were performed as counterparts to integral experiments conducted at 1/10th linear scale at Sandia National Laboratories. The tests investigated DCH phenomena in a 1/40th scale mockup of Zion Nuclear Power Plant geometry. The test apparatus was a scaled down version of the SNL apparatus and included models of the reactor vessel lower head, containment cavity, instrument tunnel, lower subcompartment structures and the upper dome. A High Pressure Melt Ejection (HPME) was produced using steam as a blowdown gas and iron-alumina thermite with chromium as a core melt simulant. The results of the counterpart experiments indicated no effect of scale on debris/gas heat transfer and debris metal oxidation with steam. However, the tests indicated a slight effect of scale on hydrogen combustion, the results indicating slightly more efficient combustion with increasing scale. The experiments demonstrated the effectiveness of the subcompartment structures in trapping debris exiting the cavity and preventing it from reaching the upper dome. The test results also indicated that a 50% air - 50% steam atmosphere prevented hydrogen combustion. However, a 50% air - 50% nitrogen did not prevent hydrogen combustion in a HPME with all other conditions being nominally the same.

### INTRODUCTION

Risk studies of U. S. nuclear power plants have focused attention on low probability, beyond design basis, severe accidents. These accidents involve a core melt, relocation to the vessel lower head, failure of the lower head, and release to the containment. The release of the molten core material (corium) to the containment can produce thermal or pressure loadings that pose a threat to the integrity of the containment. Of interest here is a corium release in a PWR while the vessel is at elevated pressure. In such a case the corium will be forcibly ejected into the containment cavity. An event of this type is termed a High Pressure Melt Ejection (HPME). The fundamental question is: Will the HPME cause an energy transfer to the containment atmosphere large enough to produce a pressure load that threatens the containment integrity? The transfer of energy

to the containment atmosphere is termed Direct Containment Heating (DCH).

The sources and mechanisms for direct containment heating will be described below. There are four sources of energy to the containment atmosphere. The first is the addition of the blowdown gasses (steam and hydrogen) from the reactor coolant system (RCS) to the containment. The mass of gas in the RCS is typically an order of magnitude less than the mass of gas in the containment. Therefore, the blowdown source of energy to the containment is negligible. The transfer of the corium thermal energy to the containment, debris/gas heat transfer, is a second source of energy. The blowdown of the primary system gasses into the cavity will fragment and disperse the corium out of the cavity into the containment. In general this source of energy will be large for HPME's. However, it is expected that the efficiency of this debris/gas heat transfer will increase with debris flight path. The presence of many lower compartment structures in the containment building can trap debris, reducing the flight path and consequently lead to significant mitigation of the debris/gas heat transfer. A second mitigation of the debris/gas heat transfer can occur due to quenching of the debris by water in the containment or cavity. It should be noted that debris quenching by water will lead to vaporization and the addition of gas moles to the containment atmosphere. Water vaporization is, therefore, a source of energy to the containment. However, the net effect of debris quenching is an energy sink. The third source of energy to the containment is the release of chemical energy in the corium via metal oxidation reactions with steam or oxygen. This energy source may be significant if the corium released from the vessel contains a significant fraction of "reactive" metal. In the prototype case this reactive metal is zirconium which readily has exothermic reactions with steam or oxygen at high temperatures. The corium may also contain significant amounts of metal iron; however, the oxidation reactions with iron are only slightly exothermic. Therefore, iron oxidation does not present a significant energy source. The oxidation of the metal is expected to occur mainly in the cavity where highly fragmented melt is intimately mixed with high velocity steam exiting the primary system. The fourth source of energy to the containment is the combustion of hydrogen. There may be three sources of hydrogen in the containment. Hydrogen may be in the containment pre-existing to the HPME due to in-vessel zirconium oxidation and then subsequent release from the primary system to the containment. In vessel oxidation also leads to hydrogen in the blowdown gasses which is a second source of hydrogen to the containment. The third source of hydrogen is the metal steam reactions during the debris dispersal phase of the HPME and blowdown. Hydrogen combustion may be a significant source of energy, possibly the dominant one, to the containment.

The NRC has been sponsoring a research program to resolve the DCH issue. An important part of this effort is an integral effects testing program. In general the objective of this program is assess the effects of scale on DCH phenomena. This is being accomplished by performing integral and counterpart experiments in two different facilities. Experiments at 1/40th linear scale are being conducted at Argonne National Laboratory and at 1/10th linear scale at Sandia National Laboratories. The more specific objective of the counterpart testing is to simulate the fundamental interrelated processes and effects of a HPME. The experiments incorporate melt ejection from the vessel, high pressure blowdown of primary system, entrainment and sweepout of debris from the cavity, transport and trapping in the lower containment subcompartments, oxidation of metallic constituents in the melt, combustion of hydrogen, and vaporization of water in

the containment. The experiments employed the geometry of the Zion Nuclear Power Plant (NPP). These tests provide important data in order to validate system level codes. In addition the experiments will be used to evaluate scaling methodologies proposed by the SASM group and SNL.

This paper reports on the ANL experiments. The specific objective of the experiments was to conduct integral DCH tests applying the SNL scaling methodology using a 1/40th scale mockup of the SNL 1/10th scale facility. Useful counterparts to the SNL tests have been insured by employing linear geometric scaling to the greatest extent feasible. The facility includes models of the vessel lower head, cavity, subcompartments and containment dome. In addition operating conditions were matched to the greatest extent possible to minimize sources of difference in the results, other than the scale distortions. Measurements in the tests are made of the primary system pressure history, the cavity and containment pressure responses, gas temperatures, debris disposition, hydrogen production and oxygen depletion.

The integral tests at ANL have addressed several questions. The first and most important relates to the effect of scale on DCH phenomena. Comparison of test results between ANL and SNL have indicated little effect of scale on debris gas/heat transfer and metal-steam oxidation/hydrogen production. The scale effects on hydrogen combustion are somewhat more unclear. However, the results indicate a small marginal increase in hydrogen combustion, with an increase in scale from 1/40th to 1/10th. The ANL tests have also addressed the question of whether steam in the containment atmosphere will inert hydrogen combustion. Tests were run comparing 50% inerting of air by nitrogen or steam in the containment. The results indicated that steam was effective in inerting the hydrogen combustion while the nitrogen was not. The ANL tests have also addressed questions regarding the debris sweepout from the cavity. Gas temperature measurements indicate that the blowdown gasses and the melt nearly thermally equilibrate during the cavity sweepout. This process alone significantly contributes to the measured pressure response of the containment. The ANL tests have also addressed the question of over what time scale is hydrogen produced during HPME. Gas sample analyses have indicated that significant hydrogen is produced in the cavity during the sweepout process. This occurs on the time scale of the blowdown. The hydrogen results from steam oxidation reaction with the "reactive" metal in the melt. However, data indicates that hydrogen is produced on time scale well after the blowdown. This hydrogen may be produced from slow reactions with "non-reactive" iron. The effectiveness of the subcompartment structures in trapping debris was also addressed in these experiments. The results here indicate that only 5-10% of the debris ejected from the vessel is transported to the upperdome.

#### DESCRIPTION OF THE EXPERIMENTS

The first step in specifying the experiments was the selection of the NPP and the accident sequence. The selected NPP is the Zion Nuclear Power Plant. The accident is precipitated by a station blackout, followed by a pump seal LOCA. The core melts and relocates to the vessel lower head. The HPME is begun by a failure of an instrument tube penetration.

Table 1 provides a summary of the specified reference initial and boundary conditions for the NPP, SNL and ANL scales. For convenient comparison of the ANL

and SNL dimensions to the NPP, columns are given with the equivalent full scale value. The hole diameter in the experiments were scaled to the final hole calculated hole diameter in the NPP because ablation of the hole during the melt ejection could not be scaled properly. The composition of the containment atmosphere was the main parameter varied in the tests.

The driving pressure specification in the test was dictated by a pump seal LOCA as 6.2 MPa. The only significant area of geometric distortion in the experiments was the scaled volume of primary system. Due to facility limitations the SNL volume is approximately 18.2% underscaled with respect to the ANL RCS volume.

The core melt simulant used was produced by an iron/alumina thermite with the addition of chromium. The chromium does not participate in the thermite reaction, however, it adds a "reactive" metal to the simulant. The chromium will oxidize with steam similar to zirconium. Therefore, it is considered a good substitute. The same thermite and chromium powders were used in both the ANL and SNL tests. Due to non-uniformities in the iron oxide powder used in the thermite the reaction was non-stoichiometric and resulted in 1.4 mass% of the simulant containing aluminum. Further details on this can be obtained in Allen et al (1991). The excess aluminum adds additional "reactive" metal. The temperature of the simulant at ejection has been measured in the SNL facility by two-color pyrometers as 2550 K. This is 230 degrees of superheat with respect to the melting point of the alumina. The specific enthalpy of the simulant at 2550 K is 2.8 MJ/kg compared to 1.15 MJ/kg for the prototype melt at 2600 K. The specific metal-steam oxidation energy is 1.20 MJ/kg for the simulant and 1.22 MJ/kg for the prototype melt. The mass of hydrogen produced per mass of melt oxidized by steam is 0.0318 and 0.0156 for the simulant and prototype respectively. This data includes the iron oxidation. The density of the simulant melt is 4000 kg/m<sup>3</sup>, approximately one-half of the oxidation prototype melt.

The scaling rationale for selecting the initial simulant melt mass was based on preserving the ratio of total melt energy input, including oxidation and hydrogen combustion energy, to the containment volume between the prototype and experiment. In effect this matches the maximum expected pressure increase from a single cell adiabatic calculation. Details on this calculation is given in the results. Applying this approach resulted in the specification of 0.71 kg of melt ejected in the ANL experiments.

The ANL experiments were conducted in the Corium EX-Vessel Interaction (COREXIT) facility.

A schematic of the experiment apparatus is shown in Figure 1. Major components of the facility include an explosion resistant containment cell, a 1.51 m<sup>3</sup> expansion vessel (EV) and a high pressure steam boiler. The expansion vessel stands approximately 3.4 meters high and is 0.76 meters in diameter. The vessel is trace heated and insulated. It can accommodate a steam atmosphere.

The steam delivery system consists of an accumulator volume representing the primary system volume, and a pneumatically actuated ball valve designed for high pressure steam. The accumulator, valve, and all piping in the steam delivery system are heated and insulated.

The Zion cavity model was designed and built from drawings supplied by the SNL DCH team. A schematic of the cavity is shown in Figure 2. Bolted on top of the pipe body is a saddle piece, referred to as the top cap, which contains the melt generator and injector (MGI). The cavity keyway is elongated by a transition chute which connects the cavity to the bottom of the expansion vessel. The elongation is required in order to allow room for the melt generator to fit underneath the expansion vessel. Thus, the keyway, is elongated by 1.7 times its correctly scaled length. The melt generator is shown in Figure 3. The melt generator also includes a baffle plate in order to diffuse the steam jet entering from the accumulator.

The model of the Zion subcompartment structures is shown schematically in Figure 4. The model is a scaled down version of the model used in the SNL test. Prominent features which are modeled include the seal table room, refueling canal, biological shield wall, reactor coolant pumps, steam generators, floor grating and operating deck floor. The walls and floors are constructed from concrete and mortar. The structure has been painted with epoxy paint. The model was built up from the lower flange of the expansion vessel. The perimeter of the model is defined by a circular concrete wall which simulates the crane wall in the plant. The walls and floors are held together by 1/4" threaded rods. Seals are made at various joints with high temperature RTV silicon rubber.

Table 2 details the type and location of instrumentation that was recorded during the test. All pressure measurements were taken with strain gauge type transducers. Temperature measurements were made with type K thermocouples at various locations. The thermocouples in the subcompartment model were bare junction. The thermocouples located in the expansion vessel were also bare junction. Cavity gas temperatures were measured by an aspirated thermocouple assembly. The assembly consists of a bare-junction tungsten rhenium thermocouple, shielded by 1/4" stainless steel tube. The tube has a slot cut in the end to draw gas through and over the junction. The flow area through the slot equals the cross sectional flow area of the tube. The TC junction is set back away from the slot. The tube is inserted into the cavity through a hole in the wall near the cavity exit. The end of the tube is connected to a solenoid valve which vents the assembly to a gas bottle. The solenoid valve is opened from 0 to 0.5 seconds after the start of the HPME. The start of the high pressure melt ejection is signalled by a twisted pair of varnished copper wires located just below the brass melt plug. When melt is ejected it contacts the wires, vaporizing the varnish and making an electrical connection between the two wires. This signal actuates the automatic gas sampling system. Gas composition measurements were made by use of gas grab sample bottles. All sample bottles are evacuated prior to the test. The disposition of the thermite melt was measured after the test. The recovery was typically made by vacuuming the debris from each specific location of interest. The debris is maintained in sealed plastic bags. Particle sizing, when possible, was carried out with a sonic sifter.

Test operations are begun by preheating the apparatus to the correct initial temperatures. If called for by the test, water is added to the cavity. The EV is then pressurized to the initial condition. The steam generator is brought to the test specified pressure. The accumulator is pressurized with steam from the boiler to the test specification.

The test is begun by starting the data acquisition and then depressing a start

button which activates a timer. This applies power to the ignitor assembly which starts the thermite reaction. The reaction proceeds downward until it encounters a burn wire located above the melt plug. This actuates the opening of the steam valve. The valve opening time is typically 100 milliseconds. At some time after the steam introduction the thermite reaction reaches the brass plug in the melt generator and fails the plug. This starts the high pressure melt ejection and is signalled by the burn wire under the plug. The burn wire signal starts a timer which actuates the automatic gas sample bottles. At specified times after the melt ejection gas samples are also taken manually.

## EXPERIMENTAL RESULTS

Table 3 summarizes the initial conditions for the six Integral Effects Tests (IET) completed. A brief description of each test and the rationale for selecting the conditions of each of the test is summarized below.

IET-1R and IRR were counterpart to the SNL IET-1 and IR tests. These tests contained nitrogen inerted containment atmospheres to allow a separate measurement of the hydrogen produced in the metal oxidation by the blowdown steam. IET-1R was repeated in IET-1RR for two reasons. First the application of the steam to melt generator was mistimed with the failure of the brass plug and the melt was partially ejected under low pressure conditions. Secondly, the blowdown time of the accumulator (primary system) was elongated due to vaporization of significant amounts of condensate in the system.

The IET-3 test was counterpart to SNL IET-3. The initial conditions for IET-3 were nominally the same as IET-1RR with the exception of the containment atmosphere. The initial atmosphere composition was 50 mole percent air and 50 mole percent nitrogen. Hydrogen produced in the metal steam reactions can combust with the oxygen in the atmosphere.

IET-6 was counterpart to SNL IET-6. This test further changed the atmosphere composition by adding pre-existing hydrogen. The amount of hydrogen added was consistent with the levels produced by approximately 50 % in-vessel zirconium oxidation during the core degradation process.

IET-7 was not run counterpart to any specific SNL test. This initial conditions in this test were nominally the same as IET-3 with the exception of the initial containment pressure which was reduced by one half. This test was motivated to test the effect of the ratio of the initial driving pressure to the initial containment pressure. This has been identified as an important scaling group in the CLCH model of Theofanous (1992).

The IET-8 test was not run counterpart to any specific SNL test. This test nominally repeated the same initial conditions of IET-6 with the exception of the containment atmosphere. This test used steam instead of nitrogen. This represents a more realistic state of the containment during a pump seal LOCA.

Table 4 summarizes the results of all the tests. The driving pressure in these tests vary from 5.7 to 6.7 MPa. Figure 5 shows a typical pressure history in the vessel obtained in the experiments. Figure 6 shows the mass flow rate of steam exiting the vessel. This result indicates that the HPME in the experiments is

characterized initially by the ejection of melt and steam simultaneously. This is followed by a period of single phase steam ejection starting at approximately 0.22 seconds. Similar results were obtained in all of the experiments.

Figure 7 plots the containment pressure response obtained in all of the experiments. It is noted that the largest increase was obtained in the test containing pre-existing hydrogen, IET-6. The second and third largest increases were obtained in IET-3 and 7 were the containment atmospheres were partially inerted with nitrogen. The lowest increases were obtained in the fully inerted IET-IRR and the partially steam inerted IET-8.

Figure 8 shows a typical pressure response of the cavity in the tests. Also plotted is the containment pressure and the output of a photodiode positioned at the cavity exit. The photodiode outputs a signal when the luminescent melt is present at the cavity exit. This indicates that the pressure difference between the cavity and containment is associated with the sweepout of the melt from the cavity. Figure 9 plots the temperature of the gasses exiting the cavity in IET-3 as measured by the aspirated thermocouple assembly located near the cavity exit. This measurement indicates the high heat transfer rates that occurs between the melt and blowdown gasses during the cavity sweepout period. The cavity sweepout is also characterized by the significant conversion of the blowdown steam to hydrogen. This is indicated the analysis of gas grab samples taken in the cavity during the sweepout period. The results of cavity gas grab sample analysis for all tests showed 30 to 60 mole % hydrogen. These samples were taken from 0 to 0.5 seconds after the start of the HPME.

In addition to the gas samples taken in the cavity, many gas samples were taken in the upperdome. All of these samples were taken nominally at the same elevation and at different radial locations near the vessel walls. In tests IET-1 through 3 samples were taken at one and 7.5 minutes after the HPME. Three samples were taken at each time. The samples were found to be very consistent and the results were averaged to obtain the vessel atmosphere composition post test. In IET-6 through 8 gas samples were also take at 30 seconds after the HPME. These samples indicated lower hydrogen and greater oxygen concentrations that those samples taken at later times. Table 5 summarizes the results of gas sample measurements. These data have a significant impact on the interpretation of hydrogen production and combustion in the experiments. This will be expanded on in detail in the following section of the paper.

Table 6 summarizes the debris disposition for the ANL IET tests. The distribution of the debris was consistent in all the tests. It is noted that there was nearly complete ejection of the melt (over 90 %) from the melt generator in all tests. The sweepout fraction from the cavity varied from 69 to 79 percent in all of the tests. The data indicates that of the debris swept out of the cavity, nearly 90 percent of it is trapped within the subcompartment. Of the debris retained in the subcompartment 20 to 30 percent of it is trapped in the seal table room. All of the debris retained in the cavity is present as an evenly dispersed crust on the walls and the floor.

The size of the debris particles is an important piece of information. However, it is difficult to characterize the size after the test. The debris retained in the subcompartment is typically present as re-agglomerated particles. Therefore, it is difficult to characterize their size. Only the debris that is transported

to the upper dome appears to solidify at the size that is produced by the HPME. Table 7 summarizes that results of a sonic sifting analysis of the debris found outside the subcompartment.

A meaningful way to compare tests at different scales or with different initial conditions is on the basis of the measured pressurization efficiency,  $\eta$ . This is defined as

$$\eta = \frac{\Delta P_{\text{exp}}}{\Delta P_{\text{max}}}, \quad (1)$$

where  $\Delta P_{\text{EXP}}$  is the peak pressure increase measured in the upperdome and  $\Delta P_{\text{MAX}}$  is the maximum expected pressure increase based on a single cell adiabatic equilibrium calculation. Pilch and Allen (1991) have developed in detail a single cell equilibrium model for calculating the bounding pressure increases due to a HPME. This was the basis for the scaling rationale used to select the initial melt mass. The maximum pressure increase results from the contributions of the four energy sources to the containment. It gives a bounding estimate because it makes the following assumptions. All of the debris that is ejected from the vessel into the cavity is assumed to participate and fully equilibrate with the containment atmosphere. It assumes all of the metal in the melt to oxidize in steam to the extent that steam is available. All of the hydrogen produced in these reactions is burned to the extent that oxygen is available. Finally it does not account for the mitigating effects of water in the cavity in the containment. The efficiency calculation was carried out for the ANL integral tests and the results are shown in Table 8.

In the next section the experiment results are discussed and interpreted in the context of what insight has been gained into understanding and resolving the DCH issue.

## DISCUSSION OF RESULTS

The principal question that motivated this integral effects testing program is; What are the effects of scale on DCH phenomena? Considerable insight has been gained into answering this question. Table 9 compares the results obtained in the three ANL-SNL counterpart tests. The table give columns on the actual measured quantities and also columns on the values scaled up to full size for convenient comparison. Several important points can be noted from this table. The only significant distortion in the initial conditions was the total g-moles of steam in the blowdown gas. The measured maximum pressure increase in the containment was smaller in the larger scale for the inerted 1R tests. However, the maximum pressure increase for the non-inerted 3 and 6 tests was greater in the larger scale. The total amount of hydrogen produced in the test was comparable with no test varying by more than 20%. The percentage of hydrogen burned in IET 6 and 7 also appear comparable. It should be noted that these calculations are based on the long time gas sample data, that is samples taken well after the HPME. However, data taken on a shorter time scale in IET-6, 7 and 8, show less hydrogen production and oxygen depletion than the later data. The calculation of the hydrogen production assumed that all of the change in oxygen is due to hydrogen combustion. This may be in error because the oxygen may also directly react with metal in the melt. This point will be elaborated on in

further detail below. The data on the distribution of the debris after the test are also quite similar. No significant distortion in the sweepout fraction or the transport to the upperdome is indicated with scale. Experiments in both scales demonstrate the effectiveness of the subcompartment structures in trapping debris. The calculated pressurization efficiency for the counterpart tests indicated a larger efficiency for the inerted tests and smaller efficiencies for the non-inerted test when the small scale is compared to the large scale.

From this data, two observations can be made on the effect of 1/40th versus 1/10th linear scale on DCH phenomena. Tests with inerted containment atmospheres, where debris/gas heat transfer and exothermic metal/steam reactions are the only significant energy sources, did not produce any significant difference in containment load with scale. In fact the 1/40th scale ANL test produced a higher pressure load, 150 kPa compared to 110 kPa in the 1/10th SNL scale, and higher efficiency, 31.3% compared to 25.8%. This leads to the first observation that the processes controlling debris/gas heat transfer and debris oxidation is not scale dependent. In contrast with the inerted test, the non-inerted tests yielded higher containment loads in the larger scale. This results lead to a second observation that the efficiency of hydrogen combustion increases with scale. This is tentative. It is strongly dependent on the interpretation of the gas sample data.

The observation that the debris/gas heat transfer and oxidation processes are scale independent arises from data indicating that the cavity sweepout is the controlling mechanism for these processes. The sweepout of the melt by the high velocity blowdown gasses leads to a high degree of mixing in the cavity. This efficient mixing process leads to nearly complete oxidation of the "reactive" metals in the melt and nearly complete thermal equilibration of the melt and blowdown steam. This is supported by measurements of the gas temperature exiting the cavity, Figure 9, and the large hydrogen concentrations found in the cavity gas samples. When the melt is ejected from the cavity into the lower subcompartments the majority, 90 to 95 percent, is trapped by structure where it can no longer efficiently transfer energy to the containment atmosphere. Thus, the cavity interaction becomes the dominant process by which the melt energy is transferred to the containment. This situation is only expected to hold for geometries where the lower compartment structures are effective in trapping the majority of the debris and significantly reducing the effective flight path of debris exiting the cavity. In the limiting case where the containment pressure rise is obtained only by the heat up of the blowdown gasses, the time rate of change of the containment pressure is given by

$$\frac{dP}{dt} = \dot{m} \frac{C_v (\gamma - 1)}{V_{cont}} T \quad (2)$$

where the  $\dot{m}$  is the blowdown rate of the accumulator and  $T$  is temperature of the gas exiting the cavity. Figure 10 gives the results of the calculation for the blowdown rate obtained in IET-8 with various assumed temperatures exiting the cavity. This is a good comparison because hydrogen combustion was inerted in this test. Similar results are found for IET-1R and 1RR which were inerted by nitrogen. Here gas temperatures from 1500 to 2000 K gives order of magnitude agreement with containment pressure increase. Cavity gas temperatures from 1400 to 1900 K have been measured in the ANL tests. This gives an indication to the role that the cavity sweepout process plays in controlling the energy transfer

to the containment in the ANL tests.

The effects of scale on the cavity sweepout process is somewhat unclear. However, due to the similarity of the sweepout fraction and hydrogen production data between the ANL and SNL tests, it can be inferred that the efficiency of the cavity energy transfer process is roughly scale independent. Therefore, the measured containment loads in the inerted tests were similar.

The observations on the effects of scale on the debris/gas heat transfer process can be summarized as follows. The cavity sweepout process is characterized by large heat transfer rates between the blowdown steam and melt. This leads to a large increase in temperature of the blowdown gas. This process is roughly scale independent. When the subcompartment structures are effective in reducing the flight path and trapping debris ejected from the cavity, the cavity interaction becomes the controlling process for debris/gas heat transfer and metal oxidation. Since this process is scale independent the measured containment loads are independent of scale for inerted tests.

The effects of scale have been minimal on the debris/gas heat transfer and metal oxidation in the counterpart tests. However, there appears to be some scale effects on hydrogen combustion. The data in Table 9 indicate a larger containment pressure loads and higher efficiencies in the larger scale experiments. However gas sample analyses show similar hydrogen production and combustion amounts as indicated in Table 9. In addition the increases in pressure rise in the non-inerted tests relative to the inerted test does not fully account for the amount of hydrogen the gas sample analyses indicates being burned. This is true for tests in both scales.

In IET-6, 7 and 8, gas sample measurements were made also at 30 seconds after the start of the HPME. These measurements indicated that the concentration of hydrogen and oxygen was changing well after the HPME. Figures 11 and 12 show the number of gram-moles of hydrogen and oxygen in the containment atmosphere as a function of time elapsed from the start of the HPME for IET-6 and 8. The physical significance of the plots is open to interpretation, however, the following explanation is plausible.

In the case of IET-6, there was visual evidence of a hydrogen burn that occurred on the timescale of the blowdown. This evidence was obtained by video cameras in the upper dome looking down on the subcompartment structures. The burn occurred as hydrogen produced in cavity exited, passed through the subcompartment and up into the upper dome. The duration of the burn was on the order of 0.2 seconds and commenced just after the start of the HPME. Thus, the visual evidence indicated a burn of hydrogen as a plume exiting the cavity that scaled with the blowdown time. However, the data in Figure 11 show the continued depletion of oxygen and increase of hydrogen well after the blowdown. Extrapolating the oxygen data back to time zero yields a depletion of approximately 1.8 gram-moles of oxygen on the time scale of the blowdown or sweepout. This would correspond to the combustion of 3.6 gram-moles of hydrogen on the time scale of the sweepout. This is consistent with 4.0 gram-moles of hydrogen produced in the inerted IET-1RR test. The data in Figure 11 shows a continued slight increase in  $H_2$  and decrease in  $O_2$  well after the HPME. This can be attributed to the long time oxidation of iron in the melt by both steam and oxygen. There is no indication that any of the pre-existing  $H_2$  burned in IET-6.

The results obtained in IET-6 is contrasted with results obtained in IET-8. The conditions for these two tests were comparable with the exception of steam in the containment atmosphere in IET-8 as opposed to nitrogen in IET-6. In IET-8 there was no visual evidence indicating a hydrogen burn in IET-8 as was obtained in IET-6. The data in Figure 12 indicates very little depletion of  $O_2$  on the sweepout time scale. However, there is a large increase in the hydrogen moles due to oxidation of metal in the melt by steam. This predominately occurred in the cavity, during sweepout, as in all other tests. The data shows the total depletion of one gram-mole of oxygen over a long time scale. This can be attributed to the further oxidation of iron in the melt.

These results show that the apparent discontinuity of the measured pressure increases in the tests and the amount of hydrogen burned, as indicated by long time gas samples can be explained. However, tests with more samples in time should be performed in order to clarify this issue. The findings here may also explain the apparent affects of scale that have been obtained in the non-inerted tests. It is possible that the hydrogen combustion is more efficient at larger scale. Tests run at both scales with gas samples at increased times will help to clarify this issue.

### CONCLUSIONS

A series six of integral experiments have been completed that investigate DCH phenomena in Zion Nuclear Power Plant geometry at 1/40th scale. Three experiments, IET-1RR, 3 and 6, were counterpart to 1/10th scale integral experiments at SNL. These tests directly addressed issue of scale effects on DCH phenomena. In addition tests were conducted that investigated the effect containment atmosphere initial condition by decreasing the initial pressure in IET-7 and partially inerting with steam in IET-8. The following major conclusions are drawn from these tests:

- 1) There is little effect of scale on debris/gas heat transfer and debris oxidation. In these tests the majority of debris swept out of the cavity was trapped in the lower subcompartments. In these cases the transfer of thermal energy from the debris is confined to the cavity region during sweepout.
- 2) The lower subcompartment structures were effective in trapping 90 to 95 percent of the debris that exited the cavity.
- 3) The efficiency of hydrogen combustion increased with increasing scale in the counterpart experiments. However, when measured by the actual containment pressure load, this effect is small. Complete quantification of scale effect on hydrogen combustion cannot be made at this time due to some open questions which require resolution. There remains a question with regards to the time scale of hydrogen production and combustion. Tentative data from the ANL tests indicate significant amounts of hydrogen being produced and oxygen being depleted well after the HPME. In addition the fraction of the pre-existing hydrogen which burns remains unanswered. More experiments are required in order to resolve the hydrogen burn question.

- 4) A decrease in the initial containment pressure from 0.2 to 0.1 MPa did not produce a significant change in the containment loading. The pressurization efficiency was approximately the same while the pressure increase was less due to the lower atmosphere heat capacity in the lower pressure test.
- 5) The effect of a more prototypic atmosphere composition was investigated in the IET-8 test. In this test the initial containment atmosphere contained 50 percent steam and 50 percent air. The steam was effective in preventing the combustion of the hydrogen compared to the IET-3, 6 and 7 tests which contained initially 50 percent air and 50 percent nitrogen.

#### ACKNOWLEDGEMENTS

The work was sponsored by the Nuclear Regulatory Commission under FIN #2266. The authors acknowledge the important contributions made to the experiments by D. Wesel. The manuscript was prepared by L. J. Ondracek.

#### REFERENCES

1. Allen, M. D., M. Pilch, R. T. Nichols, and R. O. Griffith, "Experiments to Investigate the Effect of Flight Path on Direct Containment Heating (DCH) in the Surtsey Test Facility," NUREG/CR-5728, 1991.
2. Pilch, M. and M. D. Allen, "A Scaling Methodology for Direct Containment Heating with Application to the Design and Specifications of an Experiment Program for Resolving DCH Issues," SAND 91-2784, 1991.

Table 1. Summary of Specified Reference Initial and Boundary Conditions

	Zion NPP	SNL (1/10)	ANL (1/40)	SNL (FS)	ANL (FS)
Melt Mass, kg	54,000	43	0.71	45,000	45,400
Composition, Mass Fraction	61% UO <sub>2</sub> , 15% Zr, 24% SSt	52% Fe, 11% Cr, 3% Al, 34% Al <sub>2</sub> O <sub>3</sub>		-----	-----
Temperature, K	2600 K	2500 K		-----	-----
RPV Gas Composition	Steam	Steam	Steam	-----	-----
Pressure, MPa	17.0 (6.2*)	6.2	6.2	-----	-----
Volume, m <sup>3</sup>	360.0	0.345	6.1x10 <sup>-3</sup>	345	368
Hole Dia, cm	Initial 2.54 Final 35.0	3.5	0.89	35.0	35.0
Containment Free Vol, m <sup>3</sup>	77,000	89.8	1.51	89,800	91,100
Pressure, MPa	0.20	0.20	0.20	-----	-----
Composition, Mol%	50% air, 46.0% Steam, 4.0 H <sub>2</sub>	Varied	Varied	-----	-----
Temperature, K	373	300	300	-----	-----
Cavity Water, kg	2600	3.48	0.057	3480	3480
Depth, cm	6.7	0.9	0.23	9.0	9.0
Containment Water, kg		71	1.18	71,000	71,000
Depth, cm		1.5	0.38	15.0	15.0

\* Pump seal LOCA initiated by station blackout.

Table 2. Instrumentation

Channel No.	Type <sup>(1)</sup>	Range	Location/Purpose
1	Current/Continuity	0-50 mV	Ignition signal and start of HPME
2	Thermocouple	0-485°C	Accumulator Gas Temperature
3	"	"	" " "
4	Pressure Transducer	0-1500 psig	Accumulator Pressure
5	"	"	" "
6	Continuity	0-1.5 V	Signal to Open Steam Valve
7	Pressure Transducer	0-1500 psig	MGI Pressure
8	"	"	" "
9	"	0-100 psig	Cavity Pressure
10	Thermocouple	0-485°C	Cavity Floor Temperature
11	"	"	" " "
12	Photocell	0-1 V	Cavity Window/Measure Melt Ejection
13	Thermocouple	0-1233°C	Seal Table Room Gas Temperature
14	Microswitch	0 - 6 V	Valve Open Signal
15	Pressure Transducers	0 - 125 psia	EV Pressure
16	"	"	" "
17	Thermocouple	0 - 1233°C	Subcompartment Gas Temperature
18	"	"	" " "
19	"	"	" " "
20	"	"	" " "
21	Pressure Transducer	0 - 100 psig	EV Pressure
22	"	"	" "
23	"	"	" "
24	Thermocouple	0 - 485°C	Refueling Canal Temperature
25	"	"	EV Temperature H = 0.79 m
26	"	"	" " H = 1.22 m
27	"	"	" " H = 1.63 m
28	"	"	" " H = 1.83 m
29	Pressure Transducer	0 - 100 psig	Aspirated TC Assembly Pressure
30	Thermocouple W-Re, Base	0 - 2300°C	Cavity Gas Temperature
31	Thermocouple	0-485°C	EV Temperature H = 2.13 m
32	"	"	" " H = 2.59 m

<sup>1</sup> All Thermocouples are bare bead type K unless otherwise noted.

Table 3. Initial Conditions for ANL Fe/Al<sub>2</sub>O<sub>3</sub>-Cr Tests.

	IET-1R	IET-1RR	IET-3	IET-6	IET-7	IET-8
D <sub>N</sub> , cm	0.89	1.3	1.1	1.1	1.1	1.1
P <sub>o</sub> , MPa	6.2	6.7	5.7	6.6	6.1	6.5
g-moles Steam	8.55	9.84	8.43	9.65	8.88	9.36
P <sub>co</sub> , MPa	0.2	0.2	0.2	0.2	0.1	0.2
T <sub>co</sub> , K	308	318	318	315	318	477
EV Atm, Mole %						
N <sub>2</sub>	99.9	99.9	88.8	87.5	89.9	37.4
O <sub>2</sub>	0.0026	0.12	10.8	9.9	10.1	7.7
H <sub>2</sub> O	-0	-0	-0	-0	-0	50.0
H <sub>2</sub>	-0	-0	-0	2.0	-0	3.9

Table 4. Summary of Results from ANL 1/40 Scale Tests

	IET-1R	IET-1RR	IET-3	IET-6	IET-7	IET-8
P <sub>o</sub> , MPa	6.2	6.7	5.7	6.6	6.1	6.5
ΔT <sub>P-a, s</sub> <sup>(1)</sup>	-0.6	0.22	0.28	0.29	0.81	0.42
Ejected Melt Mass, kg	0.81	0.79	0.75	0.69	0.71	0.70
Blowdown Duration, s (P/P <sub>o</sub> = 0.1)	3.20	0.61	1.00	0.76	0.82	0.82
Blowdown Steam, g-moles	8.55	9.84	8.43	9.65	8.88	9.36
Initial EV Pressure, MPa	0.2	0.2	0.2	0.2	0.1	0.2
Initial EV Atmosphere Composition, mole%						
H <sub>2</sub>	-0	-0	-0	2.0	-0	3.9
O <sub>2</sub>	0.0026	0.12	10.8	9.9	10.1	7.7
N <sub>2</sub>	99.9	99.9	88.8	87.5	89.9	37.4
Δ P <sub>max, cavity</sub> , kPa	920	550	200	480	430	290
Δ P <sub>max, dome</sub> , kPa	170	150	190	250	166	133

- 1 Elapsed time from pressurization of melt generator to onset of melt ejection.
- 2 An unknown amount of debris was lost from this region during the recovery procedures.

Table 5. Summary of Gas Sample Measurements for ANL IET-1, 1R, 1RR, 3 and 6

Gas	IET-1	IET-1R	IET-1RR	IET-3	IET-6		IET-7		IET-8	
Background/Initial Conditions										
N <sub>2</sub> (mol %)	99.4	99.9	99.9	88.8	87.5		89.4		37.3	
H <sub>2</sub>	<0.01	<0.01	<0.01	<0.01	2.0		±0.01		3.8	
O <sub>2</sub>	0.5	0.0026	0.12	10.8	9.9		10.1		7.7	
CO <sub>2</sub>	0.0048	0.004	0.011	0.011	0.013		0.021		0.5	
CO <sub>1</sub>	<0.01	<0.006	<0.005	<0.02	<0.01		<0.01		0.2	
H <sub>2</sub> O	0	0	0	0	0	0	0	0	50.0	
Mean Concentrations in Upper Dome					a	b	a	b	a	b
N <sub>2</sub>	97.1	96.0	95.5	88.3	88.0	88.3	88.2	88.0	29.1	30.0
H <sub>2</sub>	1.28	3.14	3.36	0.965	2.6	2.2	2.7	2.0	8.3	4.8
O <sub>2</sub>	0.46	0.094	0.13	9.23	8.1	8.3	6.8	8.0	5.5	6.1
CO <sub>2</sub>	0.33	0.19	0.18	0.677	0.53	0.51	---	---	1.0	0.28
CO	0.64	0.48	0.70	0.18	0.17	0.13	---	---	1.4	1.0
H <sub>2</sub> O	0	0	0	0	0	0	0	0	54.0	57.5

- a) Mean of samples taken at 1 and 7.5 minutes.
- b) Means of samples taken at 30 seconds.

Table 6. Summary of Debris Disposition

Location	IET-1R	IET-1RR	IET-3	IET-6	IET-7	IET-8
A. Initial Thermite Mass	820.0	820.0	820.0	713.0	713.0	713.0
B. Recovered from MGI	4.0	43.3	67.3	30.3	4.0	11.8
C. Recovered from Cavity and Chute	197.1	260.8	232.2	262.7	153.7	179.3
D. Seal Table Room	*	148.9	163.1	167.9	113.6	158.7
E. Remaining Subcompartment Structures	511.1	358.2	428.2	339.6	448.9	405.3
F. Total Retained in Subcompartment = D+E	551.1	507.1	591.3	507.5	562.5	564.0
G. Outside Structures	87.7	114.6	37.8	81.3	26.2	22.6 <sup>(1)</sup>
H. Total Recovered = B + C + F + G	799.9	925.8	928.6	881.8	746.48	804.5
Percent Increase (H-A)/A × 100%	-2.5	12.9	13.2	23.0	4.7	12.8
Fraction Ejected Into Cavity (A-B)/A	0.995	0.947	0.918	0.966	0.994	0.984
Fraction Sweepout of Cavity (F+G)/(C+F+G)	0.752	0.705	0.734	0.691	0.793	0.766
Fraction Transported out of Subcompartment F/(F+G)	0.147	0.184	0.060	0.138	0.045	0.0385

<sup>1</sup> An unknown amount of debris was lost during the vacuuming procedure.

Table 7. Particle Size

Test	Driving Pressure, MPa	Hole Size, mm	D, mm
1R	6.2	11	700
1RR	6.7	13	458
3	5.7	11	1009
6	6.6	11	1044
7	6.1	11	400

Table 8. DCH Pressurization Results

	IET-1RR	IET-3	IET-6	IET-7	IET-8
a) Experiment peak pressurization in cavity region, kPa	550	200	480	430	290
b) Experiment peak pressurization in done region, kPa	150	190	250	166	133
c) Theoretical maximum pressurization (adiabatic), kPa	479	904	1106	813	1108
d) DCH Efficiency = $\frac{(b)}{c} \times 100$	31	21	23	20	13

Table 9a. Counterpart Test-1R

	ANL	SNL	ANL(FS)	SNL(FS)
$P_o$ , MPa	6.7	6.3	6.7	6.3
$M_d$ , kg	0.79	38.37	45,800	38,400
Blowdown Time, s	0.61	3.42	23.92	34.2
Blowdown Steam, g-moles	9.84	477	593,000	477,000
$P_{co}$ , MPa	0.2	0.2	0.2	0.2
$T_{co}$ , K	318	290	318	290
EV atmosphere, mole %				
$N_2$	99.9	99.8	99.9	99.8
$O_2$	0.12	0.19	0.12	0.19
$H_2$	-0	-0	-0	-0
$\Delta P_{max, cavity}$ kPa	550	265	550	265
$\Delta P_{max, cont}$ kPa	150	110	150	110
% Sweepout	70.5	67.0	70.5	67.0
% Dispersed to Upper Dome	18.4	10.5	18.4	10.5
$H_2$ Pre-Existing, moles	0	0	0	0
$H_2$ Produced <sup>1</sup> , g-moles	4.0	223	241,00	223,000
$O_2$ Depleted <sup>1</sup> , g-moles	0	0	0	0
DCH Efficiency, %	31.3	25.8	31.3	25.8
Percentage of $H_2$ Burned	0	0	0	0

<sup>1</sup> Based on mean of gas sample measurements at 1 and 7.5 minutes.

Table 9b. Counterpart Test 3

	ANL	SNL	ANL(FS)	SNL(FS)
$P_o$ , MPa	5.7	6.1	5.7	6.1
$M_d$ , kg	0.7	38.5	42,200	38,500
Blowdown Time, s	1.00	3.05	39.2	30.5
Blowdown Steam, g-moles	8.43	456	508,000	456,000
$P_{co}$ , MPa	0.2	0.19	0.2	0.19
$T_{co}$ , K	318	290	318	290
EV atmosphere, mole %				
$N_2$	88.8	90.6	88.8	90.6
$O_2$	10.8	9.0	10.8	9.0
$H_2$	-0	-0	-0	-0
$\Delta P_{max, cavity}$ kPa	200	370	200	370
$\Delta P_{max, cont}$ kPa	190	246	190	246
% Sweepout	73.5	61.7	73.5	61.7
% Dispersed to Upper Dome	6.0	8.8	6.0	8.8
$H_2$ Pre-Existing, moles	0	0	0	0
$H_2$ Produced <sup>1</sup> , g-moles	4.65	223	280,00	223,000
$O_2$ Depleted <sup>1</sup> , g-moles	1.75	9.3	106,000	93,000
DCH Efficiency, %	21.0	31.2	21.0	31.2

Table 9c. Counterpart Test 6

	ANL	SNL	ANL(FS)	SNL(FS)
$P_o$ , MPa	6.6	6.3	6.6	6.3
$M_d$ , kg	0.69	40.7	41,600	40,700
Blowdown Time, s	0.761	3.2	29.8	32.0
Blowdown Steam, g-moles	9.65	505	582,000	505,000
$P_{co}$ , MPa	0.2	0.2	0.2	0.2
$T_{co}$ , K	318	308	318	308
EV atmosphere, mole %				
$N_2$	87.5	87.1	87.5	87.1
$O_2$	9.9	9.8	9.9	9.8
$H_2$	2.0	2.6	2.0	2.6
$\Delta P_{max, cavity}$ kPa	480	1020	480	1020
$\Delta P_{max, cont}$ kPa	250	279	250	279
% Sweepout	69.1	83.4	69.1	83.4
% Dispersed to Upper Dome	13.8	13.8	13.8	13.8
$H_2$ Pre-Existing, moles	2.28	1800	138,000	180,000
$H_2$ Produced, g-moles	4.89	308	295,00	308,000
$O_2$ Depleted <sup>1</sup> , g-moles	2.11	168	127,000	168,000
DCH Efficiency, %	22.6	28.1	22.6	28.1

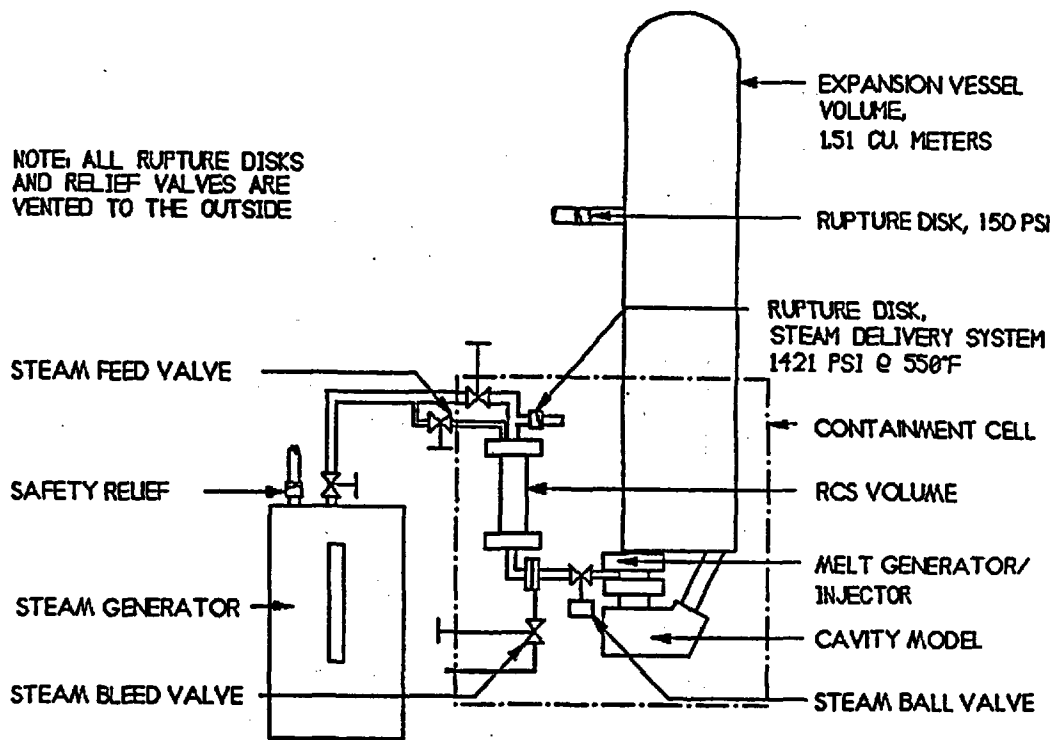


Figure 1. COREXIT Facility.

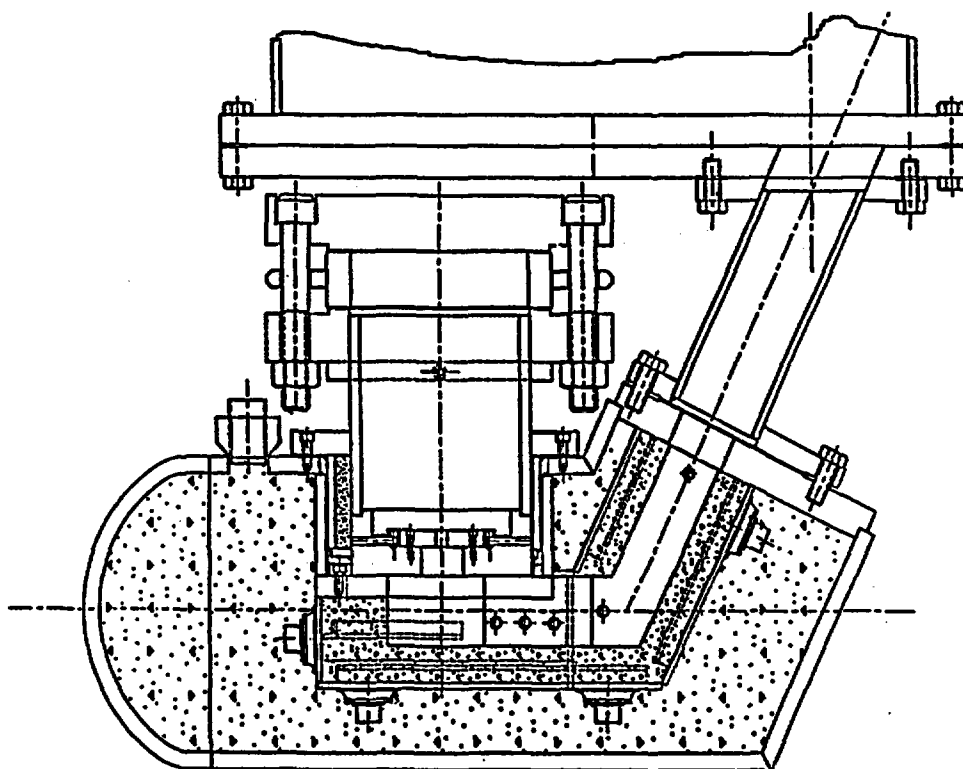


Figure 2. Zion Cavity Model.

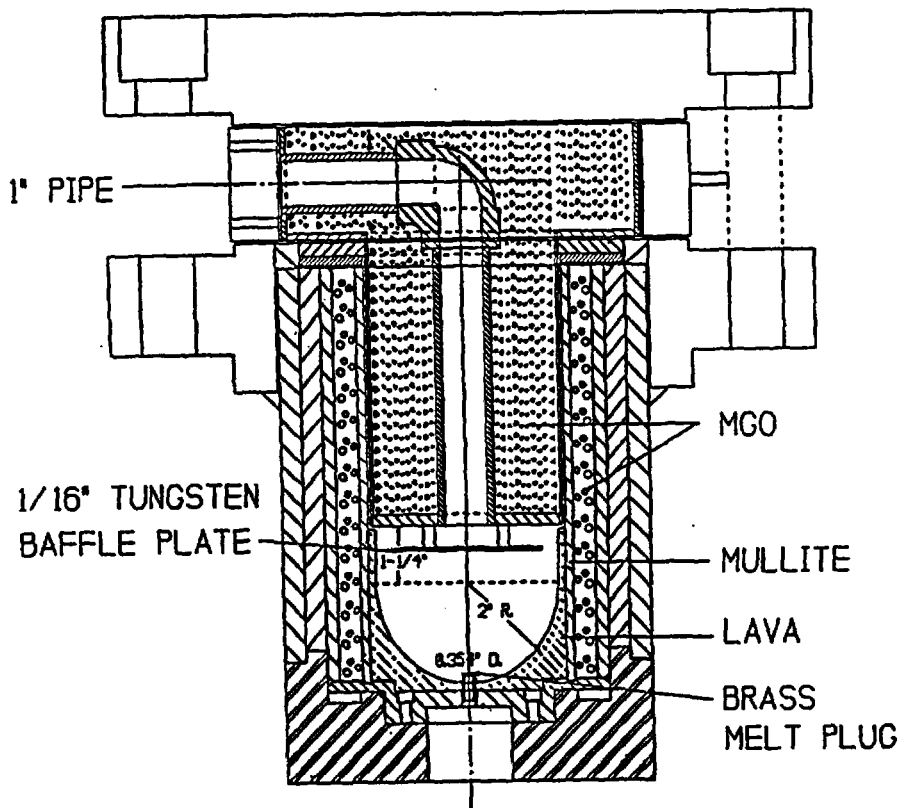


Figure 3. Schematic of Melt Generator and Injector (MGI).

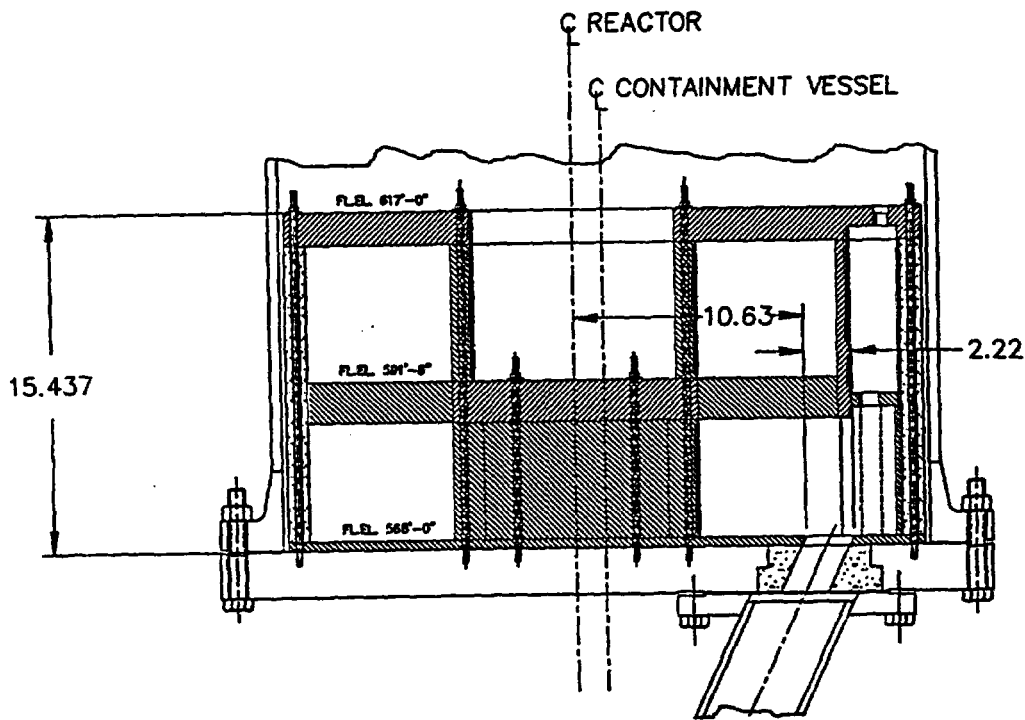


Figure 4. Schematic of the Subcompartment model.

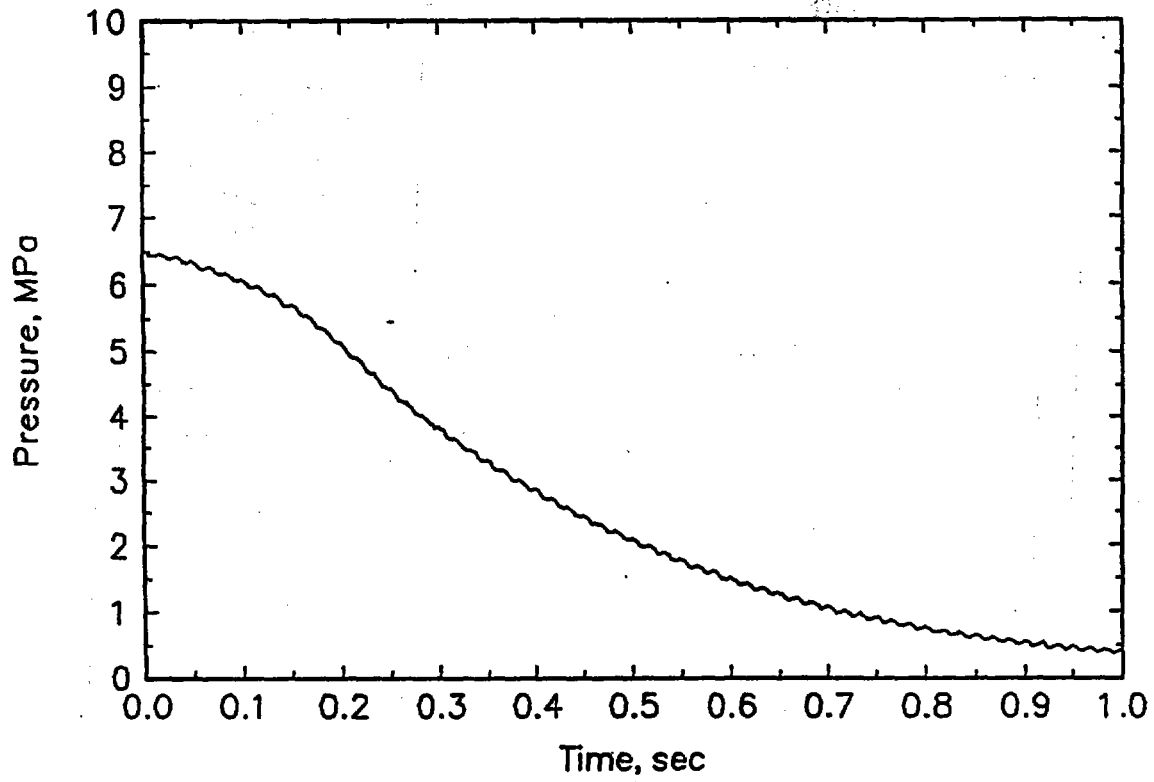


Figure 5. IET-8 Blowdown History.

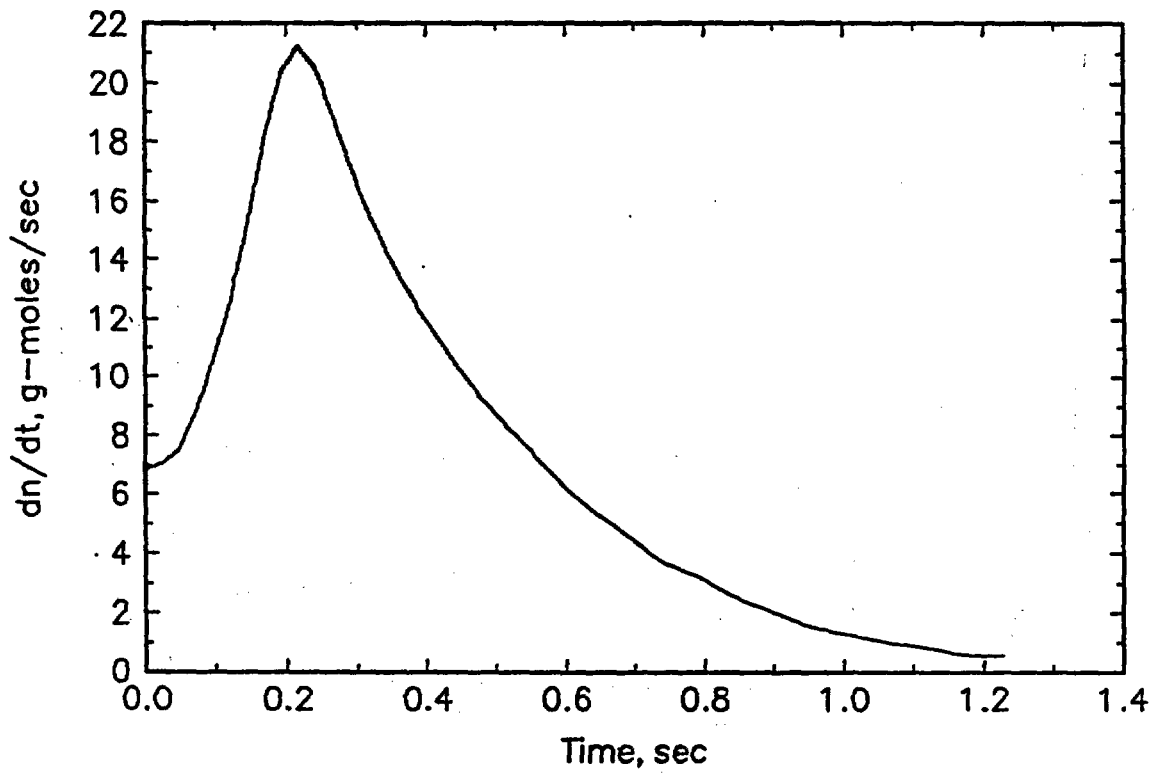


Figure 6. IET-8 RCS Blowdown Rate.

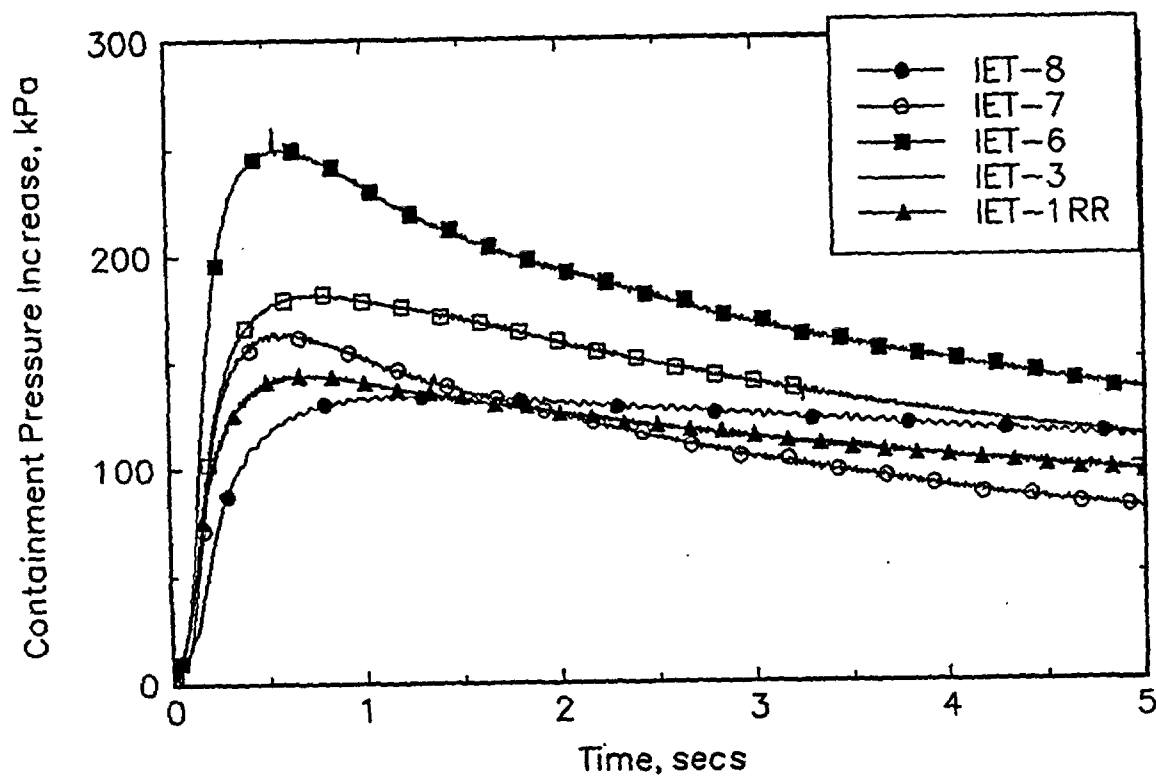


Figure 7. ANL IET Results.

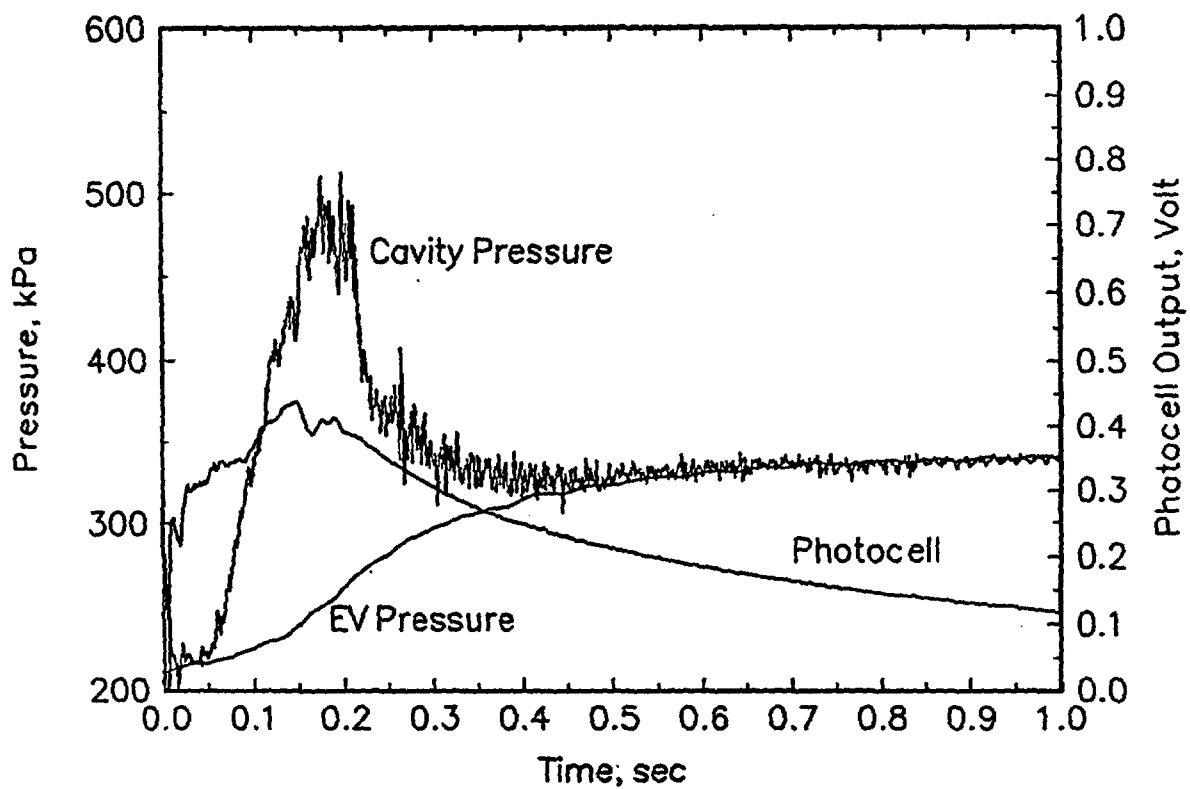


Figure 8. IET-8 Cavity Pressure and Photocell Output.

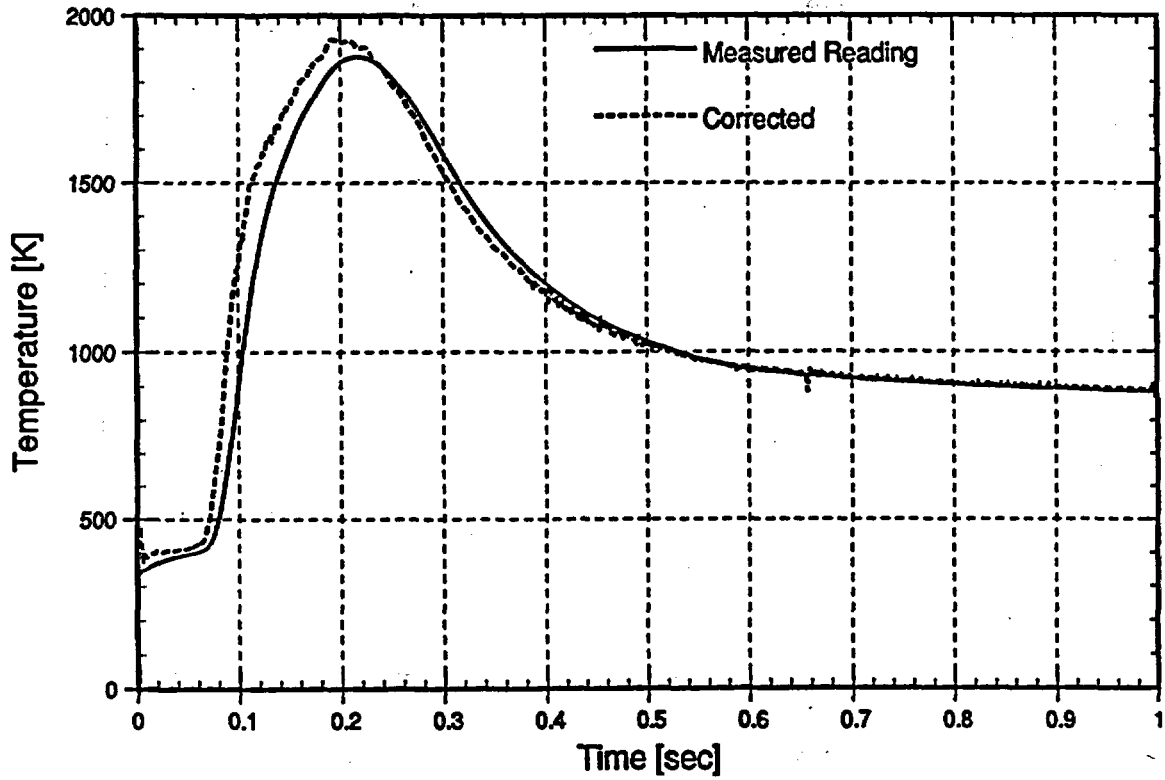


Figure 9. Cavity Gas Temperature Obtained in the IET-3 Test.

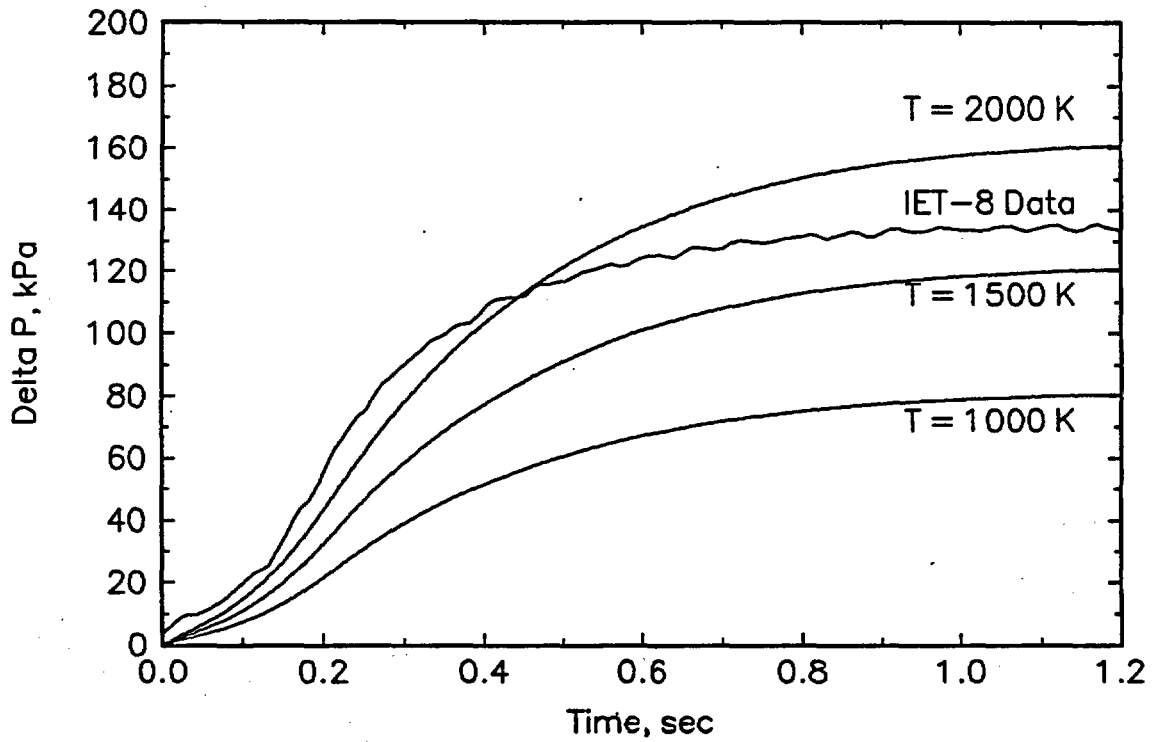


Figure 10. Comparison of IET-8 Containment Pressure with Prediction by Blowdown Gas Heatup.

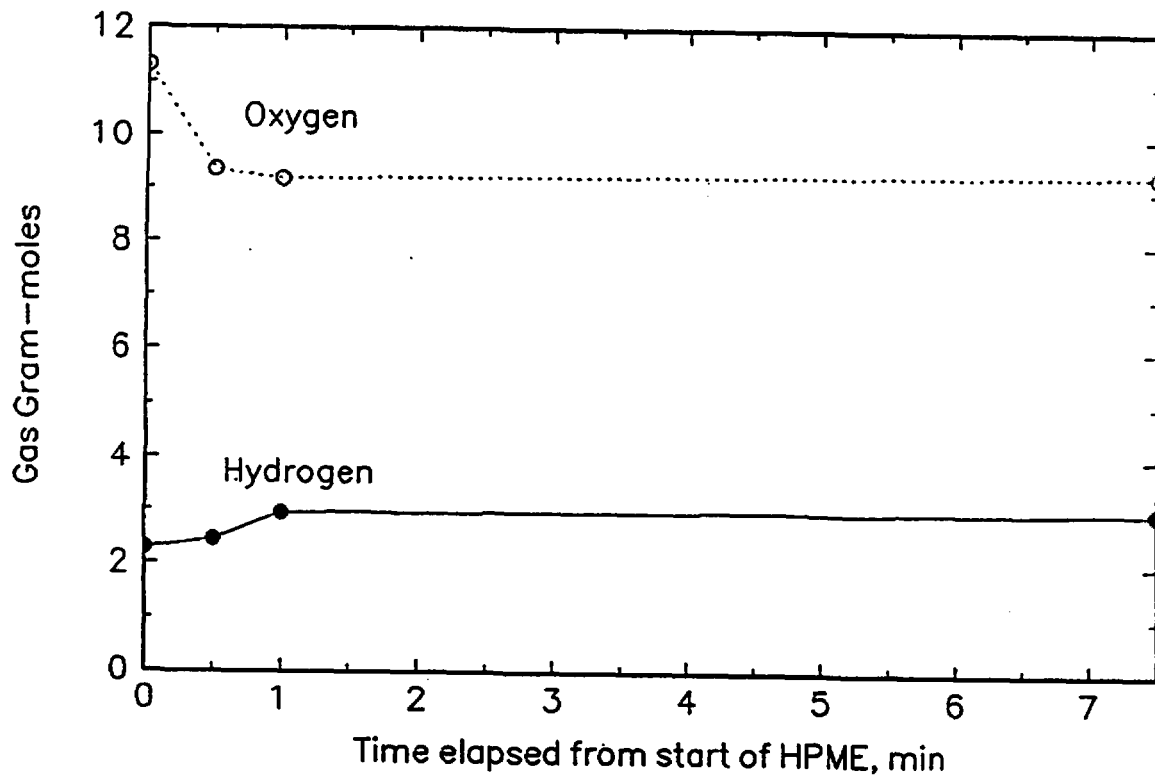


Figure 11. Number of Oxygen and Hydrogen Moles in IET-6.

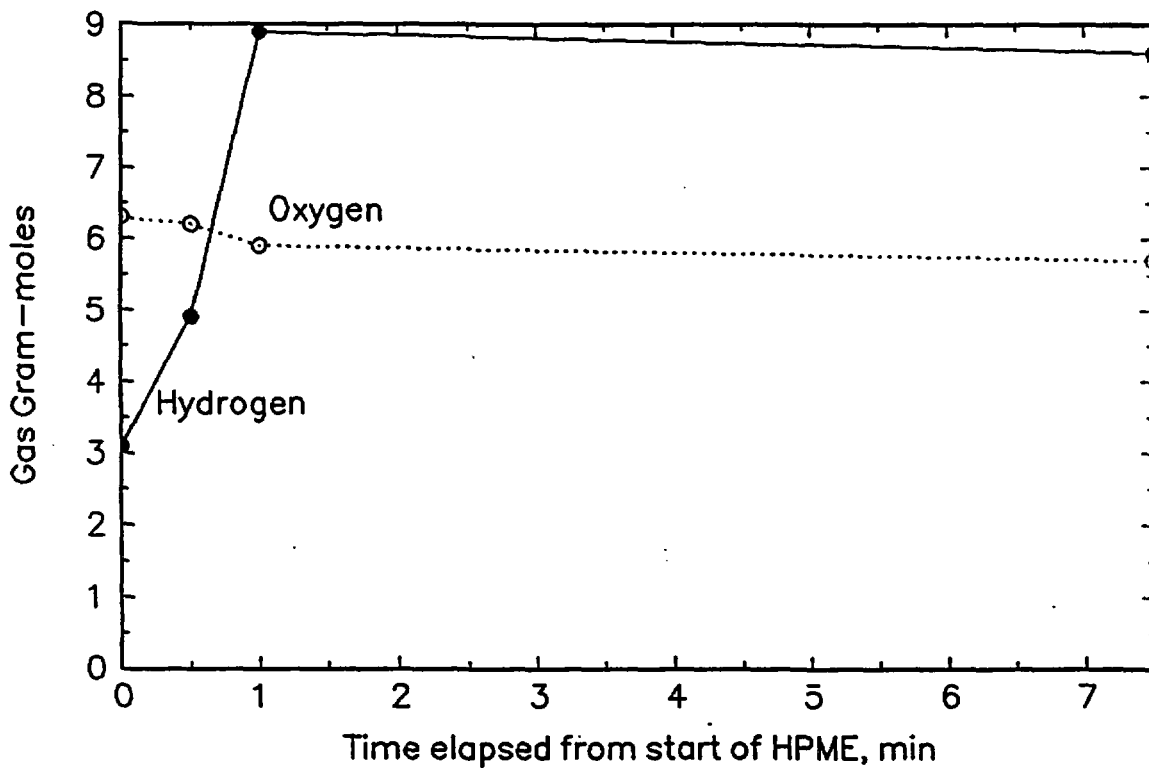


Figure 12. Number of Oxygen and Hydrogen Moles in IET-8.

# EFFECT OF REACTOR VESSEL INTERNAL MELTING UPON RELEASE OF BWR CORE DEBRIS

Michael Z. Podowski

Department of Nuclear Engineering & Engineering Physics  
Rensselaer Polytechnic Institute  
Troy, New York 12180-3590, USA

## ABSTRACT

One of the important issues in the analysis of accident consequences in BWRs and with MARK-I containments is concerned with the possibility of drywell liner failure as a result of attack by hot corium spreading over the drywell floor. The probability of failure strongly depends on the composition of corium released from the reactor pressure vessel [Theofanous et al., 1990].

The objective of the present work was to perform numerical analyses in which the effect of heat transfer from a degraded & partially molten reactor core towards the upper internals (upper shroud, standpipes, steam separator & dryer) in a BWR reactor pressure vessel (RPV) would be accounted for, and the resultant failure and melting of these structures, on the composition of corium released to the drywell following RPV failure. The calculations for this study were performed using the APRIL.MOD3 computer code, and the Peach Bottom BWR was used a reference power plant with MARK-I containment.

## I. INTRODUCTION

The propagation and consequences of severe reactor accidents are governed by several factors of a different nature, including both deterministic and stochastic processes. The state-of-the-art in the modeling of accident phenomena varies considerably with the stage of accident. The initial phase of core heatup has been investigated quite extensively before, including both analyses and experiments. As a result, numerical predictions for this phase (in particular, prior to core degradation) agree quite well with the existing experimental data. However, when an advanced phase of core heatup and meltdown is reached, deterministic models become much less reliable due to the increasing randomness of potential failure mechanisms of the reactor system pressure boundaries and of the resultant corium spreading. In particular, the above applies to estimating the composition of corium attacking the drywell liner in MARK-I containments.

In the analysis of MARK-I liner failure performed by Theofanous et al. [1990], two basic corium release scenarios have been examined. In one of them a predominantly oxidic corium was assumed, and corium containing mainly metallic phase was considered in the other. The results shown in the above-mentioned report indicate that in either case the probability of liner failure is very low. A common factor in both cases was the assumed low superheat of molten corium. The reasoning behind using  $T_{sup} = 70^{\circ}\text{C}$  as the upper limit for melt superheat was that (especially in the case of high-temperature oxidic corium) the heat transfer between the corium and the reactor vessel would result in the lower head failure, and the subsequent melt release, thus preventing any substantial superheating of the molten corium.

A considerably different situation might occur if the composition of corium at the time of RPV failure was intermediate between the values used in the two scenarios (Scenario-I and Scenario-II) examined by Theofanous et al. [1990]. Namely, if the corium is composed of similar fractions of both oxidic and metallic phases, the latter constituent (in particular, steel) may reach a significantly higher superheat than that used in NUREG-5423, even if the average corium temperature remains unchanged. The question is if there exist hypothetical BWR accident sequences which may lead to the in-vessel formation of a substantial amount of mixed oxidic-metallic corium which could be released onto the drywell floor after RPV failure.

Possible severe accident scenarios in BWRs, which bear the potential of producing a large amount of molten steel mixed with molten (partially at least)  $\text{UO}_2$ , are those resulting in the failure and melting of the upper vessel internals. The specific events leading to the release of significant quantities of steel, are still unclear.

The purpose of the present work was to investigate accident sequences in a typical BWR with MARK-I containment which may lead to the heatup, failure, and subsequent melting, of the steam separator/dryer complex inside the reactor pressure vessel. The analysis was performed using the APRIL.MOD3 severe accident computer code. In addition, scoping calculations were performed to assess the effect of heat radiation to the upper structures on the heatup and melting of these structures, and to verify the APRIL results.

## II. OVERVIEW OF THE APRIL.MOD3 CODE

APRIL is a computer code developed at Rensselaer Polytechnic Institute under the sponsorship of Oak Ridge National Laboratory (originally, as a subcontract of the US NRC project) and Empire State Electric Energy Research Corporation (ESEERCO). Some of the features of APRIL.MOD3 which make this code a useful tool for the present analysis, are:

- APRIL has been developed especially for BWRs, and contains many mechanistic modes of phenomena not accounted for in other codes, such as: gradual relocation of molten materials and their refreezing in contact with cold structures, channel blockage and crust remelting, and heatup and possible failure of the steam separator/dryer complex.

- Several models in APRIL have been validated against detailed experimental data, including those taken at Rensselaer and elsewhere. In particular, recently completed comparisons against the SANDIA DF-4 and KfK CORA-16/17 experiments have shown excellent agreement between the APRIL calculations and experimental results.

- APRIL.MOD3 has a built-in restarting option, which allows for modifying input parameters during the calculations. This is very useful when parametric analyses are to be performed of various user-specified parameters and different accident conditions (such as the status of selected safety systems).

The APRIL code, and APRIL.MOD3 in particular, has been extensively documented, including reports on model description and testing [Koh et al., 1985; Kim et al., 1988; Lahey & Podowski, 1990], an APRIL.MOD3 user manual [Cho et al., 1991], and the reports showing the results of model validation against experimental data.

The results of APRIL.MOD3 code comparison exercises so far confirm the validity of the modeling assumptions used and consistency of the overall modeling concept. In comparison with other severe accident analysis codes, APRIL.MOD3 yields results which can be judged, according to the existing state of the art, as realistic but containing some degree of conservatism. In particular, APRIL.MOD3 was compared against the results [Abramson and Komoriya, 1988] of other severe accident codes such as: STCP, MARCH/RMA, and MAAP 3.0. Details concerning the results of this comparison can be found in [Podowski et al., 1989] and [Lahey & Podowski, 1990].

The modeling concepts in APRIL.MOD3 which are important for the present work include, in particular, the following:

- (1) Melting of various core materials and melt relocation inside the core, and from the core onto the lower core plate, and into the lower plenum,
- (2) Heatup, failure, and melting of the upper vessel internals, and the relocation of molten steel through a degraded core.

The above-given models are summarized below. Additional information can be found in [Koh et al., 1985], [Kim et al., 1988], and [Lahey & Podowski, 1990].

The core model in APRIL.MOD3 uses a two-dimensional (in axial and radial directions) nodalization scheme. In each node the following core structures are accounted for: fuel (UO<sub>2</sub> pellets), cladding, canisters, and control rods. During the initial phase of core heatup and oxidation, the nodal temperatures of each structure are calculated separately. When either the temperature of control rods, cladding, or canister walls, reaches the melting temperature of the respective material (stainless steel or zircaloy), the time-dependent mass replaces temperature as a state variable. The formation, and propagation, of rubble bed inside the core may result in a gradual, radially-dependent, reduction in the core height.

The specific in-core phenomena modeled in the APRIL code include: 2-D heat transfer between individual core components as well as between the core and surrounding structures, heat convection to the coolant in both the covered and uncovered portions of the core, oxidation of the fuel cladding, channel walls, and control blades, fuel buckling (used as a criterion for rubble bed formation), slumping of the canisters and control blades, melting of individual core components, the formation of a eutectic mixture of fuel and molten zircaloy, molten material relocation and refreezing, channel blockage and the resultant flow redistribution.

The core model is coupled with the model of in-vessel thermal-hydraulics. Various flow configurations inside the vessel are accounted for, including the formation of a natural circulation loop between the hot (fully uncovered) core and the relatively cold downcomer regions. The in-vessel model provides the core model with boundary conditions such as the gas/steam mixture inflow temperature, system pressure, and the temperature of surrounding structures.

A model of particular importance for the present analysis is concerned with the heatup and possible melting of the upper in-vessel structures (upper shroud head, standpipes, steam separators, and steam dryers). The shroud-head/steam-separator assembly consists of a domed base on top of which is welded an array of standpipes with a multi-stage steam separator located on the top of each standpipe. The entire assembly, made of stainless steel, rests on the top guide grid and forms a cover for the core outlet plenum region. The steam dryer assembly is mounted in the reactor vessel above the shroud-head/steam-separator assembly. Since, in the case of an accident, the upper shroud head may be directly exposed to a high-temperature core, the combined effects of radiation from the core and convective/radiative heat transfer from the hot steam/gas mixture in the upper plenum, may increase the shroud temperature to failure point. When the weakened shroud head cannot support the mass above it, the upper structures may collapse onto the core (except for the steam dryer which has a separate support system). The molten steel from these structures may penetrate the hot and partially molten core and flow into the lower plenum and, following lower head failure, into the containment.

In the APRIL.MOD3 code, a lumped-parameter energy equation is used to calculate the average temperature of each structure separately. These equations account for heat transfer modes such as: heat radiation from the top of the core, combined heat convection/radiation from/to the steam/gas mixture (both on the core and downcomer sides), Heat conduction between the neighboring structures, and direct heating due to the deposition of fission products. The failure of the shroud head is calculated by comparing the actual weight-induced stress against the temperature-dependent ultimate tensile strength of stainless steel. After the failure, the upper shroud head, together with the standpipes and steam separators, is assumed to relocate downwards and rest on the top of the core. When the temperature of any given structure reaches the melting point of stainless steel, the respective energy balance is used to calculate the melting rate of the structure's material.

### III. SCOPE OF WORK

As was mentioned in Section II, the specific purpose of this work was to use the APRIL.MOD3 code to determine if a significant amount of metals might be mixed with the liquid oxides formed in the core during a BWR severe accident. Specifically, APRIL.MOD3 has been employed to analyze the consequences of a hypothetical short-term station blackout accident in one unit of the Peach Bottom power plant. The input parameters concerning the accident sequence of reference were identified based on the conditions used before at ORNL for the BWR SAR calculations of a short-term station blackout at Peach Bottom. These conditions were set up according to the emergency procedures guidelines (EPG) for the Peach Bottom BWRs. In addition, parametric calculations were performed using APRIL.MOD3 in which the effect of selected input parameters on the progression of melting was quantified. The various accident simulations included calculations in which the following parameters were changed:

- (a) radiative heat transfer between the degraded core and the upper structures (steam separator/dryer complex) in the reactor pressure vessel (RPV),
- (b) CRD hydraulic system (CRDHS) flow rate,
- (c) timing of RPV failure,
- (d) axial power distribution.

The effect of radiative heat transfer was tested by using a multiplication factor in the expression in APRIL.MOD3 calculating the radiative power exchanged between the top of the core and the upper structures. Specifically, the base-case calculations were compared against the results in which the radiation heat transfer from the core was

reduced to 10% its original value. The purpose of this study was to quantify the uncertainties associated with the emissivities of the various materials in the reactor vessel, modeling simplifications in regard to the view factors for radiation, etc. The rationale behind considering only cases of reduced radiative power was that the base-case calculations already indicated that radiation may play a significant role in the heatup and melting of the upper structures.

It was assumed in the calculations that the only core cooling (if any) was via the CRDHS flow. In particular, the no-flow situation was considered so that the possibility could be examined of the upper structure heatup via radiation only. In addition, calculations were performed including a 60 g/min. CRDHS flow in order to test the impact of two competing effects on the progression of the in-vessel heatup and melting.: (a) the role of CRDHS flow as heat sink and, since the added small amount of water is insufficient to cool the reactor, the effect of enhanced-evaporation-induced oxidation.

The amount and composition of melt released into the containment depend on the mode of reactor pressure vessel failure. Because of the complexity of the phenomena governing melt relocation and the resultant lower head failure, substantial uncertainties are inherently present in any analytical/numerical predictions of the timing of RPV failure. In the present calculations the APRIL.MOD3 code predicts a local failure of the lower head due to the drain plug meltdown when, following the lower core plate failure, molten fuel is released into the lower plenum. In order to test the sensitivity of calculated melt release into the containment to the timing of RPV failure, two accident scenarios were considered in addition to the original APRIL.MOD3 predicted sequence. In one of them, the RPV failure was delayed by approximately 20 min., and by about one hour in the other, both relative to the basic case.

In order to parametrically test the effect of different pre-accident conditions, in particular the reactor operation time prior to the accident, calculations were performed for two different axial power distributions in the core. Namely, in addition to the power distribution obtained from the project sponsor, in which a typical end-of-life (highly nonuniform, bottom-peaked) power distribution was used, the APRIL.MOD3 code was also run for a situation simulating the other end of possible axial power profiles, in which a uniform axial decay heat generation rate was assumed.

In addition to changing the parameters described above, additional calculations were also performed to quantify the effect of ADS on the progression of reactor meltdown. Since high-pressure accident sequences are not the subject of the present investigations (only low pressure melt ejections were considered in the MARK-I liner attack analysis by Theofanous et al. [1991]), the main purpose of the APRIL.MOD3 calculations for such situations was to confirm that this code properly captures the effect of in-vessel conditions prior to the failure on the parameters of melt released to the containment after the failure.

Since the primary objective of the present study was to check the impact of upper structures melting on the amount and composition of melt released into the containment, it was deemed important to obtain an independent confirmation concerning the correctness of the results of APRIL.MOD3 calculations. For this purpose, calculations using a stand-alone model were performed in order to estimate the amount of heat radiated from the top of the degraded BWR core to the upper vessel internals and the resultant heatup and melting rate of these structures.

#### IV. DESCRIPTION OF SITUATIONS ANALYZED

The input data to APRIL.MOD3 included the plant geometry and pre-accident operating conditions as well as some parameters concerning the accident sequence. The latter included, in particular, the decay heat power curve used before in BWRSAR calculations (see Fig. 1) and the prescribed timing of selected events, as shown in Table 1.

The above-mentioned data were used to develop an input file for the APRIL.MOD3 code, which will be referred to as the base case (Case 1 in Table 2). Later, selected modifications in the input parameters were introduced in order to investigate the various parametric effects discussed in Section III. The specific cases analyzed are also summarized in Table 2.

#### V. STAND-ALONE MODEL OF HEAT RADIATION BETWEEN DEGRADED CORE AND RPV UPPER INTERNALS

In order to obtain an independent verification of the APRIL.MOD3 model of heat transfer between the core and the upper vessel internals, a stand-alone model has been developed to calculate the heatup (and melting) rate of the upper structures exposed to the combined effects of heat radiation from the top of the degraded core and from the gas (steam/hydrogen mixture) heated when passing through the uncovered and partially molten core. Among others, this model was used to check the sensitivity of the calculated rate of heat transfer to the temperature of the top of the core and to the assumed emissivities of solid surfaces and the gas.

In the model, a three body enclosure is considered, including two solid surfaces exchanging thermal radiation and a participating gas filling the space between these surfaces. As shown in Fig. 2, the lower surface represents the top of the degraded core and the upper surface represents the shroud head.

Using the network shown in Fig. 3, the radiative heat transfer between the elements of the enclosure shown in Fig. 2 can be modeled by the following equations:

$$\frac{E_{b,c} - J_c}{R_c} + \frac{J_s - J_c}{R_{c-s}} + \frac{E_g - J_c}{R_g} = 0 \quad (1)$$

$$\frac{E_s - J_s}{R_s} + \frac{J_c - J_s}{R_{c-s}} + \frac{E_g - J_s}{R_g} = 0 \quad (2)$$

$$\frac{E_g - J_c}{R_g} + \frac{E_g - J_s}{R_g} = 0 \quad (3)$$

where  $E_b = \sigma T^4$  is the black body emissive power of a surface at a temperature,  $T$ ,  $J$  is the radiosity,  $R$  is the resistance to radiation, and the subscripts  $c$ ,  $s$ , and  $g$  refer to core, shroud head and gas, respectively.

It has been assumed in Eqs.(1)-(3) that the view factor from the core to the shroud head is equal to unity (which is true if the top of the core is treated as a flat surface). The same values have been used for the view factors between the gas and each of the solid surfaces.

The resistances of the solid surfaces can be expressed as

$$R_c = (1 - \epsilon_c) / \epsilon_c \quad (4)$$

$$R_s = (1 - \epsilon_s) / \epsilon_s \quad (5)$$

the gas resistance is given by (assuming that the gas is nonreflective)

$$R_g = 1 / \epsilon_g \quad (6)$$

and the resistance for heat radiation directly between the core top and the shroud head is

$$R_{c-s} = 1 / (1 - \epsilon_g) \quad (7)$$

where  $\epsilon_c$ ,  $\epsilon_s$ , and  $\epsilon_g$ , are the emissivities of the respective materials.

Solving Eqs.(1)-(3) for  $J_c$ ,  $J_s$ , and  $E_g$ , yields

$$J_c - J_s = (E_c - E_s) / \{1 + [(2R_g)^{-1} + (R_{c-s})^{-1}](R_c - R_s)\} \quad (8)$$

$$E_g - J_s = -(E_g - J_c) = (J_c - J_s) / 2 \quad (9)$$

Eqs.(8) and (9) can be used to evaluate the heat flux received by the shroud head,

$$q_s'' = (E_c - E_s) / R_{eff} \quad (10)$$

where

$$R_{eff} = [(R_{c-s})^{-1} + (2R_g)^{-1}]^{-1} + R_c + R_s \quad (11)$$

For a given area of the shroud head,  $A_s$ , the total heat rate received by the shroud head is

$$q_s = q_s'' A_s \quad (12)$$

Eq.(12) has been used to parametrically estimate the thermal power received by the shroud head for various temperatures of the top of the core and various emissivities of the solid surfaces and the gas. The results are discussed in the next Section.

## VI. RESULTS OF CALCULATIONS

The results of APRIL.MOD3 calculations for Case 1 are shown in Figures 4 through 9. Complete results for all the cases listed in Table 2 are given by Podowski and Cho [1992]. The timing of the main events calculated for Case 1 is shown in Table 3.

The APRIL.MOD3 results were also used to evaluate the amount of and composition of corium released into the containment and to show the effect of heat transfer to the upper structures. The basic parameters characterizing melting of the upper structures and corium delivery to the containment are shown in Figure 10 and Tables 4 through 11.

The corium release results shown in Tables 4-11 are based on averaging the values obtained for two bounding cases. The upper bound case assumes that the entire mass of corium in the lower plenum is released into the containment at the time of vessel failure. On the other hand, the lower bound case assumes that corium (metallic phase) released to the lower plenum prior to the vessel failure freezes in contact with the water in the plenum, so that only the metals melted after the failure can be released into the containment. Since any specific predictions of the amount of melt at the time of vessel failure would be very uncertain, averaging between these two most extreme

situations was deemed to be the best approach to obtain realistic estimates of the corium release into the containment. Nevertheless, the results of the two bounding calculations are also shown in Tables 4-11.

As can be seen in Fig. 10(also, see Fig. 6), the APRIL.MOD3 calculated melting rates of the shroud head and steam dryer are about 7.4 kg/s and 8.4 kg/s, respectively, whereas the average melting rate of the standpipes and steam separator is about 28.5 kg/s and for a short time increases to a 100 kg/s range. Both the higher average value of the standpipes & steam separator and, in particular, the narrow peak observed at approximately 195 min., are due to the enhanced heat convection following melt discharge into the water pool in the lower plenum. The evaporation of water increases the steam flow rate and, therefore, the convective heat transfer coefficient to the upper structures, whereas the simultaneous oxidation of the remaining zircaloy in the core increases the steam/gas mixture flowing from the degraded core towards the upper regions of the reactor vessel. It is important to notice that (see Table 3) this accelerated melting occurs after the failure of the reactor pressure vessel.

In order to verify the APRIL.MOD3 predictions concerning the heatup and melting of the in-vessel upper structures, the model discussed in Section VI was used to obtain parametric estimates of the heat rate received by these structures and of their melting rates. Specifically, the effective resistance for heat radiation between the core upper surface and the upper structures (see Eq. 11) was calculated for various assumed values of the emissivities of the solid surfaces and the gas. The results of these calculations are shown in Table 12.

Table 12 covers a broad range of emissivities. Whereas the actual emissivity of stainless steel (at room temperature) varies from 0.16 (type 301 polished) to 0.39 (type 347, cleaned), after repeating heating and cooling the emissivity of various types of steel may substantially increase (to 0.57 at 230 °C) [Ozisik 1985]. Hence, it is not unrealistic to anticipate the emissivity of the top surface of the degraded reactor core to be about 0.5.

Based on the above discussion, an effective resistance for radiation,  $R_{\text{eff}} = 5$  (see Table 12), was used in Eq.(12) to obtain estimates of the heating rate of the upper structures. In these calculations, the structure temperature was taken as the melting temperature of steel (1,783°K) and the heat radiation area from the degraded core was assumed to be 10 m<sup>2</sup> (which corresponds to a diameter of 3.57 m, or 11'8"). The calculations were performed for various assumed temperatures of the top surface of the degraded (and partially molten) core, are shown in Table 13.

The results given in Table 13 clearly indicate that the combined effects of heat radiation directly from the core and from the flowing gas produce a significant heatup rate of the upper structures. It is interesting to notice that the time needed to completely

melt the shroud head (the mass of which was 15,000 kg in the present calculations) would be only about 57 min. (from the moment when the shroud temperature reached the steel melting temperature) if the core surface temperature stayed close to the zircaloy melting temperature (1,853°C), and less than 22 min. if the core temperature was 2,200°C.

Even though the present estimates are based on several simplifying assumptions (in particular, they do not include the effect of convective heat transfer from the steam/gas mixture, which may become significant during the periods of high flow rate combined with increased oxidation-induced in-core heatup of the mixture), its results are consistent with the APRIL.MOD3 predictions. This can be readily seen by comparing the results in Table 13 against the rates of upper structure melting shown in Fig. 4 and Table 4.

## VII. CONCLUDING REMARKS

The APRIL.MOD3 code has been used to simulate the progression of core meltdown during short-term station blackout accidents in a typical BWR/4 reactor with MARK-I containment. The particular input deck for the APRIL calculations was prepared based on the Peach Bottom data and the postulated pre-accident conditions and ADS actuation timing similar to those used before in BWR SAR calculations. In addition to the reference accident scenario, several APRIL.MOD3 runs were performed in order to test the sensitivity of results to various input parameters and modeling assumptions and to quantify some of the major uncertainties in the modeling of severe accident phenomena.

In addition, stand-alone parametric calculations were performed which confirmed the order of magnitude of the APRIL-calculated melting rates of the upper vessel internals due to heat radiation from the degraded and partially molten reactor core.

The obtained results can be summarized as follows:

1. The depressurization of the reactor pressure vessel when the core is already partially uncovered leads to a sudden and complete core dryout. As a result of this, the water level drops below the lower core plate, which in turn minimizes the evaporation rate from the pool and practically stops oxidation of the metallic core constituents. Consequently, the decay heat power becomes the only source of energy, and the core heatup process is much slower compared to the scenario without RPV depressurization.
2. The gradual heating of the entire core (central zones first) prevents a substantial crust formation and channel blockage, so that molten materials

(zircaloy and steel, in particular) are released onto the lower core plate and, after the plate failure, into the lower plenum.

3. The almost-adiabatic mode of core heatup results in a relatively uniform (axially) temperature increase in the core, especially - in its upper regions. With the increasing corium temperature the effect of heat radiation from the top of the core becomes more significant and the heatup of the top-most regions slows down compared with the other upper and central parts of the core.

4. The heat radiation from the top of the core substantially contributes to the heatup of the upper vessel internals (steam separator/dryer complex). It should be pointed out, however, that the temperature increase of the shroud head, standpipes and steam separator is controlled by two inter-related processes: direct heat radiation from the top of the core and a combined heat radiation/convection from the hot gas flowing from the core upwards. As long as the evaporation of water from the pool in the lower plenum is very low, the direct surface-to-surface radiation has a dominant effect. This situation changes dramatically when the core melting progresses to the extent that the lower core plate fails and molten corium is released into the lower plenum. The resultant evaporation, and the associated oxidation of the remaining zircaloy, increase the temperature of the steam/hydrogen mixture at core exit. The energy transfer from the gas to the upper structures via radiation and convection becomes an important (or even dominant) factor in the heatup of the latter. During this phase of an accident, the thermal power received by the upper structures may become very high, resulting in fast melting of large quantities of steel.

5. Due to the complexity of geometry involved and the material properties which can only be roughly estimated, the modeling of heat radiation in a degraded core is inherently associated with substantial uncertainties. Hence, it was deemed important that the effect of radiation be parametrically tested in the present study. Specifically, two cases were investigated using the APRIL.MOD3 code. In one of them, the radiation model in APRIL was used in its original form. In the other, the direct radiation from the core towards the upper structures was reduced by a factor of ten. Whereas the observed differences in the results were consistent with the anticipated trends, the overall molten mass of the upper structures experienced only a moderate change. This can be explained by the fact that during the phase of intensive heatup and melting of the steam separator/dryer complex the most important mode of heat transfer into the structures is via heat convection/radiation from the steam flowing from the core towards the steam separator (the steam/gas flow rate is enhanced by a closed-loop natural circulation formed inside the vessel ('core'-'steam separator'-downcomer'-lower plenum'-'core')). It is important to mention that this result of

APRIL.MOD3 calculations agrees well with the parametric estimates performed using a separate stand-alone model described in Section VI.

6. The composition of corium released from the reactor pressure vessel into the drywell depends on the time of vessel failure. In the calculations performed in this study, APRIL.MOD3 predicted an early local failure of the lower head penetrations (in particular, of the lower head plug). In such a case, the mass of molten  $\text{UO}_2$  at the time of RPV failure is relatively small. The amount of corium released immediately after the failure, and the associated rate of release, depend on two major factors: (a) the amount of molten metals in the lower plenum at the time of failure, and (b) the rate of in-vessel melting immediately after the failure. In the present analysis, two bounding cases have been considered for each calculated accident progression sequence. In one of them the pre-failure melt was assumed to be completely solidified, in the other - in the liquid form. In both cases, the predictions show that the melt released from the vessel during the initial time period after the failure (varying from 10 to 15 min) was predominantly metallic. The results for both cases have been subsequently used to obtain average release rates for each scenario (Cases 1 through 8). The total initial release in the base case (Case 1) was 35,000 kg (less than  $5\text{m}^3$ ) of 94% metallic corium, at a rate of  $0.5\text{ m}^3/\text{min}$ . The maximum total initial release was obtained in Case 7: 71,000 kg ( $9.9\text{ m}^3$ ) of 95% metallic corium at a rate of  $0.66\text{ m}^3/\text{min}$ . On the other hand, the highest content of oxidic phase during the period of initial release was 13% (Case 3), but the associated total release and release rate were only 53,000 kg ( $7.3\text{ m}^3$ ) and  $0.5\text{ m}^3/\text{min}$ , respectively. For a comparison, the major assumptions in NUREG/CR-5423 [Theofanous et al., 1990] were: in Scenario I -  $12.5\text{ m}^3$  of 90%+ oxidic corium at a rate of  $0.5 - 4.0\text{ m}^3/\text{min}$ ; Scenario II -  $14\text{ m}^3$  of corium containing 10% of oxidic phase released at a rate of  $0.7\text{ m}^3/\text{min}$ .

7. Since the core heatup process after the RPV failure and lower plenum dryout is due to the decay heat only, the rates of corium melting and melt release into the containment are much lower than during the initial period after failure. During this time, however, the composition of corium gradually changes and its oxidic fraction increases. In the base case, the highest percent of oxidic phase in the corium being released from the RPV (after about 5 hrs. from the beginning of accident) was 25%, but the melt flow rate was only  $0.16\text{ m}^3/\text{min}$ . Of all the scenarios with system depressurization (Cases 1-7) the highest content of oxide during a late release phase was about 50% at a rate of less than  $0.15\text{m}^3/\text{min}$ .

8. In order to see the effect of RPV failure time on the composition and rate of the corium released into the containment, calculations were performed in

which the originally-calculated failure time was delayed. As can be seen in Appendices III and IV, and in Tables 6 and 7, whereas the calculated: initial releases, release rates, and oxide content, of corium tend to grow with the increasing failure time, the observed changes are relatively slow and the conclusions drawn in regard to the base case remain valid even if the reactor vessel does not fail until about 4 hrs. after the beginning of core uncovering.

9. A similar conclusion applies to the results of calculations in which the effect was tested of axial power profile in the core.

10. Whereas the calculations for various options of a short-term station blackout accident with system depressurization performed according to the current accident management procedures gave similar results and led to similar conclusions concerning the anticipated composition and amount of melt released into the MARK-I containment, the calculation performed for a high pressure accident scenario (ie, without ADS) indicates that the accident consequences in the latter case would be significantly different. As the results shown in Appendix VIII and Table 11 indicate, in the case without depressurization the core meltdown process accelerates, and the corium released into the containment may contain a larger fraction of the oxidic constituent than in any other cases investigated in this work. This, in turn, confirms the importance of including vessel depressurization in BWR accident management strategies.

### Final Conclusions

1. The objective of the present study was to analyze the effect of heat transfer from a degraded and partially molten BWR core towards the upper internals in the reactor pressure vessel, and of the resultant melting of these structures, on the composition of corium released into the drywell following vessel failure. The numerical simulations for this study were performed using the APRIL.MOD3 computer code, with the Peach Bottom BWR as a reference power plant with Mark-I containment. The accident conditions analyzed assumed system depressurization via ADS performed according to the Peach Bottom emergency procedure guidelines (EPG).
2. Scenario-I in the NUREG/CR-5423 report assumes the release of a large amount of mainly oxidic corium over a short period of time. Practically speaking, such a release is possible only when a molten debris pool is formed inside the core. If water is still available in the vessel, the heat transfer from the bottom, sides and top of the molten region may be sufficient to form a crust confining the pool but insufficient to cool down the melt. The melting and heatup processes may continue for a long time, so that the accumulated melt may eventually amount to a substantial fraction of the total fuel inventory in the core (see the TMI accident).

It should be mentioned here that the phenomena of corium solidification and crust/molten-corium-pool formation are modeled in APRIL.MOD3. However, according to the APRIL.MOD3 predictions reported in the present study, following system depressurization via ADS the water level in the BWR reactor vessel quickly falls below the bottom of the core, and even below the lower core plate. As a result of this, the core heatup process occurs rather uniformly, and the various molten materials gradually relocate along the lower portions of the core and fall into the water in the lower plenum (prior to reactor vessel failure) or are released into the containment (after vessel breach). Naturally, the melting process is enhanced by the heat of oxidation reaction between the metallic Zircaloy in the core and steam from melt quenching in the lower plenum. Hence, if the corium release onto the reactor vessel lower head directly leads to vessel failure (which is the case in both the NUREG/CR-5423 Scenario-I and the present simulations), the APRIL.MOD3 predicted release of molten oxidic corium into the containment is much smaller than the maximum Scenario-I-postulated value in NUREG/CR-5423.

3. Heat radiation from the core and combined convective/radiative heat transfer from the hot steam/gas mixture may have a very significant effect on the heatup and melting of the upper structures (steam separator/dryer complex) and, consequently, may add a large amount of molten steel to the molten debris accumulated on the reactor vessel lower head. Hence, the molten steel is likely to dominate the composition of corium released after vessel failure. The contribution of the oxidic phase may substantially increase during the long-term release through the vessel breach, but the volumetric flow rate of the melt at that time is expected to be small. On the other hand, it can be readily deduced from the results of the present study that if the melting of the upper structures was not accounted for, the composition of corium released onto the containment floor would be significantly different (the fraction of oxidic constituents would be much higher, although the metallic phase could still account for as much as 50%). At the same time, however, the release rates would be lower by at least one order of magnitude compared to the current results of APRIL.MOD3 simulations.
4. It is widely recognized that the modeling of core meltdown phenomena in existing severe accident codes (including APRIL.MOD3) is still associated with substantial uncertainties. Examples include: spatial effects of heat transfer (in particular, heat radiation) and heatup in a degraded core, eutectic interactions and the resultant changes in material properties, the effect of core geometry deformation and local steam availability on the extent of Zircaloy oxidation, melt coolability, core blockage, etc. Nevertheless, the results of the present analysis indicate that even if the calculated oxidic debris releases were substantially increased (i.e. by 50% or more), the overall melt release should still stay below the bounding conditions used in NUREG/CR-5423. It should be stressed here that this conclusion applies only to BWR core meltdown accidents with timely

system depressurization. According to the statement of work, the present study was specifically directed towards the analysis of such a class of severe accidents.

## VIII. REFERENCES

Abramson, P. and Komoriya, H., "BWR Source Term Codes Comparison", ESEERCO Report EP 86-19, 1988.

Cho, C.S., Jia, H., Kim, S.K., Lahey, R.T., Jr. and Podowski, M.Z., "APRIL.MOD3 User Manual", Rensselaer Polytechnic Institute, 1991.

Kim, S.H., Kim, D.H., Koh, B.R., Pessanha, J., SiAhmed, El-K., Podowski, M.Z., and Lahey, R.T., Jr., "The Development of APRIL.MOD2 - A Computer Code for Core Meltdown Accident Analysis of Boiling Water Nuclear Reactors", NUREG/CR-5157, 1988.

Lahey, R.T., Jr. and Podowski, M.Z., "Degraded BWR Core Modeling; APRIL.MOD3 Severe Accident Code", ESEERCO Report, EP84-4, 1990

Ozisik, M.N., "Heat Transfer; A Basic Approach", McGraw-Hill Book Company, New York, 1985.

Podowski, M.Z., Lahey, R.T., Jr and Burger, J.M., "The Analysis of Core Meltdown Progression in BWRs", Proceedings of the Fourth International Topical Meeting on Nuclear Reactor Thermal- Hydraulics, Karlsruhe, FRG, 1989.

Theofanous, T.G., Amarasooriya, W.H., and Ratnam, U., "The Probability of Liner Failure in a MARK-I Containment", NUREG/CR-5423, 1990.

TABLE 1

Main events in short-term station blackout accident scenario at Peach Bottom, used as input in the APRIL.MOD3 simulations of core meltdown progression

Event	Time from the beginning of calculation [min]
1. Reactor scram after loss of offsite power	- 35
2. Beginning of core uncovering (swollen level falls below top of core)	0
3. ADS system actuation	45

TABLE 2

Cases studied in the parametric analysis of corium composition during short-term station blackout at Peach Bottom

CASE	Heat Radiation to RPV upper structures	CRDHS Flow Rate [gal/min]	ADS	Power Distribution	Time of RPV Failure
1	100%	0	yes	ref.	$T_{calc}^{(*)}$
2	10%	0	yes	- " -	- " -
3	100%	60	yes	- " -	- " -
4	10%	60	yes	- " -	- " -
5	10%	0	yes	- " -	$T_{calc}+20min$
6	10%	0	yes	- " -	$T_{calc}+60min$
7	10%	0	yes	uniform	$T_{calc}$
8	10%	0	no	ref.	$T_{calc}$

(\*)  $T_{calc}$  is the RPV failure time predicted by the APRIL.MOD3 code.

TABLE 3

APRIL.MOD3-calculated main events in a short-term station blackout  
 accident at Peach Bottom.

CASE 1.

Event	Time from the beginning of calculation [min]
Reactor scram after loss of offsite power	- 35
Beginning of core uncovering (swollen level falls below top of core)	0
ADS system actuation	45
Melting of zircaloy begins	114
Melting of Control blades begins	117
Relocation begins of molten steel onto lower core plate	129
Beginning of zircaloy relocation onto lower core plate	153
Lower core plate fails	154
Shroud head reaches melting point	155
Beginning of UO <sub>2</sub> relocation into lower head	169
Reactor vessel fails	173
Fast melting of upper structures begins	182

TABLE 4  
Summary of APRIL.MOD3 results for Case 1.

Time of RPV failure	173 min.			
Melting of RPV upper structures				
Melting of RPV upper structures	Duration of high melting period, $t_m$ [min]			36
	Average melting rate during $t_m$ [kg/s]			28.5
	Total molten mass during $t_m$ [kg]			62,000
Corium release to the containment				
Time interval	0 to 10 min after RPV failure	during 10 min interval at highest release rate of oxidic phase		
Total mass released to the containment [kg]	35,000 (45,000 <sup>a</sup> , 21,000 <sup>b</sup> )	12,000		
Total volume released to the containment [m <sup>3</sup> ]	4,8 (6.5 <sup>a</sup> , 3.1 <sup>b</sup> )	1.6		
Rate of release [m <sup>3</sup> /min]	0.48 (0.65 <sup>a</sup> , 0.31 <sup>b</sup> )	0.16		
Composition of corium released onto drywell floor [% mass]	metal	oxide	metal	oxide
	94	6	75	25
	(92 <sup>a</sup> , 96 <sup>b</sup> )		(8 <sup>a</sup> , 4 <sup>b</sup> )	

(a) and (b), respectively, refer to the upper and lower bounds of mass released.

TABLE 5  
Summary of APRIL.MOD3 results for Case 2.

Time of RPV failure	174 min.											
Melting of RPV upper structures												
Melting of RPV upper structures	Duration of high melting period, $t_m$ [min]	30										
	Average melting rate during $t_m$ [kg/s]	36										
	Total molten mass during $t_m$ [kg]	65,000										
Corium release to the containment												
Time interval	0 to 10 min after RPV failure	during 10 min interval at highest release rate of oxidic phase										
Total mass released to the containment [kg]	44,000 (53,000 <sup>a</sup> , 34,000 <sup>b</sup> )	22,000										
Total volume released to the containment [m <sup>3</sup> ]	6.4 (7.7 <sup>a</sup> , 5.0 <sup>b</sup> )	2.9										
Rate of release [m <sup>3</sup> /min]	0.64 (0.77 <sup>a</sup> , 0.50 <sup>b</sup> )	0.29										
Composition of corium release onto drywell floor [% mass]	<table style="width: 100%; border-collapse: collapse;"> <tr> <td style="width: 50%; text-align: center;">metal</td> <td style="width: 50%; text-align: center;">oxide</td> </tr> <tr> <td style="text-align: center;">97</td> <td style="text-align: center;">3</td> </tr> <tr> <td style="text-align: center;">(98<sup>a</sup>, 96<sup>b</sup>)</td> <td style="text-align: center;">(2<sup>a</sup>, 3<sup>b</sup>)</td> </tr> </table>	metal	oxide	97	3	(98 <sup>a</sup> , 96 <sup>b</sup> )	(2 <sup>a</sup> , 3 <sup>b</sup> )	<table style="width: 100%; border-collapse: collapse;"> <tr> <td style="width: 50%; text-align: center;">metal</td> <td style="width: 50%; text-align: center;">oxide</td> </tr> <tr> <td style="text-align: center;">82</td> <td style="text-align: center;">18</td> </tr> </table>	metal	oxide	82	18
metal	oxide											
97	3											
(98 <sup>a</sup> , 96 <sup>b</sup> )	(2 <sup>a</sup> , 3 <sup>b</sup> )											
metal	oxide											
82	18											

(a) and (b), respectively, refer to the upper and lower bounds of mass released.

TABLE 6  
Summary of APRIL.MOD3 results for Case 3.

Time of RPV failure	172 min.			
Melting of RPV upper structures				
Melting of RPV upper structures	Duration of high melting period, $t_m$ [min]			40
	Average melting rate during $t_m$ [kg/s]			21
	Total molten mass during $t_m$ [kg]			50,000
Corium release to the containment				
Time interval	0 to 15 min after RPV failure	during 10 min interval at highest release rate of oxidic phase		
Total mass released to the containment [kg]	53,000 (70,000 <sup>a</sup> , 35,000 <sup>b</sup> )	12,000		
Total volume released to the containmen [m <sup>3</sup> ]	7.3 (9.7 <sup>a</sup> , 4.9 <sup>b</sup> )	1.4		
Rate of release [m <sup>3</sup> /min]	0.49 (0.65 <sup>a</sup> , 0.33 <sup>b</sup> )	0.14		
Composition of corium released onto drywell floor [% mass]	metal 87 (91 <sup>a</sup> , 83 <sup>b</sup> )	oxide 13 (9 <sup>a</sup> , 17 <sup>b</sup> )	metal 55	oxide 45

(a) and (b), respectively, refer to the upper and lower bounds of mass released.

TABLE 7  
Summary of APRIL.MOD3 results for Case 4.

Time of RPV failure	173 min.			
Melting of RPV upper structures				
Melting of RPV upper structures	Duration of high melting period, $t_m$ [min]			40
	Average melting rate during $t_m$ [kg/s]			26.5
	Total molten mass during $t_m$ [kg]			64,000
Corium release to the containment				
Time interval	0 to 15 min after RPV failure		during 10 min interval at highest release rate of oxidic phase	
Total mass released to the containment [kg]	62,000 (68,000 <sup>a</sup> , 55,000 <sup>b</sup> )		11,000	
Total volume released to the containment [m <sup>3</sup> ]	8.5 (9.3 <sup>a</sup> , 7.6 <sup>b</sup> )		1.3	
Rate of release [m <sup>3</sup> /min]	0.56 (0.62 <sup>a</sup> , 0.50 <sup>b</sup> )		0.13	
Composition of corium released onto drywell floor [% mass]	metal	oxide	metal	oxide
	91	9	72	28
	(92 <sup>a</sup> , 90 <sup>b</sup> )		(8 <sup>a</sup> , 10 <sup>b</sup> )	

(a) and (b), respectively, refer to the upper and lower bounds of mass released.

TABLE 8  
Summary of APRIL.MOD3 results for Case 5.

Time of RPV failure	194 min.		
Melting of RPV upper structures			
Melting of RPV upper structures	Duration of high melting period, $t_m$ [min]	30	
	Average melting rate during $t_m$ [kg/s]	36	
	Total molten mass during $t_m$ [kg]	64,000	
Corium release to the containment			
Time interval	0 to 10 min after RPV failure	during 10 min interval at highest release rate of oxidic phase	
Total mass released to the containment [kg]	70,000 (98,000 <sup>a</sup> , 41,000 <sup>b</sup> )	6,000	
Total volume released to the containment [m <sup>3</sup> ]	8.0 (12.7 <sup>a</sup> , 5.3 <sup>b</sup> )	0.7	
Rate of release [m <sup>3</sup> /min]	0.80 (1.27 <sup>a</sup> , 0.53 <sup>b</sup> )	0.07	
Composition of corium released onto drywell floor [% mass]	metal	oxide	metal
	94	6	48
	(96 <sup>a</sup> , 92 <sup>b</sup> )	(4 <sup>a</sup> , 8 <sup>b</sup> )	52

(a) and (b), respectively, refer to the upper and lower bounds of mass released.

TABLE 9  
Summary of APRIL.MOD3 results for Case 6.

Time of RPV failure	234 min.			
Melting of RPV upper structures				
Melting of RPV upper structures	Duration of high melting period, $t_m$ [min]			30
	Average melting rate during $t_m$ [kg/s]			36
	Total molten mass during $t_m$ [kg]			65,000
Corium release to the containment				
Time interval	0 to 10 min after RPV failure		during 10 min interval at highest release rate of oxidic phase	
Total mass released to the containment [kg]	59,000 (117,000 <sup>a</sup> , 0.0 <sup>b</sup> )		11,000	
Total volume released to the containment [m <sup>3</sup> ]	8.0 (16.0 <sup>a</sup> , 0.0 <sup>b</sup> )		1.2	
Rate of release [m <sup>3</sup> /min]	0.8 (1.6 <sup>a</sup> , 0.0 <sup>b</sup> )		0.12	
Composition of corium released onto drywell floor [% mass]	metal	oxide	metal	oxide
	100	0	50	50
	(100 <sup>a</sup> , -- <sup>b</sup> )		(0 <sup>a</sup> , -- <sup>b</sup> )	

(a) and (b), respectively, refer to the upper and lower bounds of mass released.

TABLE 10  
Summary of APRIL.MOD3 results for Case 7.

Time of RPV failure	207 min.			
Melting of RPV upper structures				
Melting of RPV upper structures	Duration of high melting period, $t_m$ [min]		30	
	Average melting rate during $t_m$ [kg/s]		36.5	
	Total molten mass during $t_m$ [kg]		66,000	
Corium release to the containment				
Time interval	0 to 15 min after RPV failure		during 10 min interval at highest release rate of oxidic phase	
Total mass released to the containment [kg]	71,000 (95,000 <sup>a</sup> , 47,000 <sup>b</sup> )		13,000	
Total volume released to the containment [m <sup>3</sup> ]	9.7 (13.2 <sup>a</sup> , 6.1 <sup>b</sup> )		1.5	
Rate of release [m <sup>3</sup> /min]	0.66 (0.90 <sup>a</sup> , 0.41 <sup>b</sup> )		0.15	
Composition of corium released onto drywell floor [% mass]	metal	oxide	metal	oxide
	95	5	57	43
	(97 <sup>a</sup> , 93 <sup>b</sup> )		(3 <sup>a</sup> , 7 <sup>b</sup> )	

(a) and (b), respectively, refer to the upper and lower bounds of mass released.

**TABLE 11**  
**Summary of APRIL.MOD3 results for Case 8.**

Time of RPV failure	116 min.			
<b>Melting of RPV upper structures</b>				
Melting of RPV upper structures	Duration of high melting period, $t_m$ [min]			13
	Average melting rate during $t_m$ [kg/s]			53.5
	Total molten mass during $t_m$ [kg]			42,000
<b>Corium release to the containment</b>				
Time interval	0 to 10 min after RPV failure	during 15 min interval at highest release rate of oxidic phase		
Total mass released to the containment [kg]	59,000 (76,000 <sup>a</sup> , 42,000 <sup>b</sup> )	23,000		
Total volume released to the containment [m <sup>3</sup> ]	8.1 (10.8 <sup>a</sup> , 5.3 <sup>b</sup> )	2.3		
Rate of release [m <sup>3</sup> /min]	0.81 (1.10 <sup>a</sup> , 0.53 <sup>b</sup> )	0.15		
Composition of corium released onto drywell floor [% mass]	metal 92 (94 <sup>a</sup> , 90 <sup>b</sup> )	oxide 8 (6 <sup>a</sup> , 10 <sup>b</sup> )	metal 5	oxide 95

(a) and (b), respectively, refer to the upper and lower bounds of mass released.

TABLE 12

Effective resistance of the upper structures for heat radiation from the core & hot gas.

Thermal Emissivity			Effective Resistance for Radiation
Core Surface	Upper Shroud	Gas	
0.5	0.5	0.2	3.1
0.5	0.5	0.8	3.7
0.5	0.3	0.2	4.4
0.5	0.3	0.8	5.0
0.5	0.2	0.2	6.1
0.5	0.2	0.8	6.7
0.3	0.2	0.2	7.4
0.3	0.2	0.8	8.0

TABLE 13

Heating and melting rates of the upper in-vessel structures for various temperatures at the top of the core.

Temperature of the top of the core	Heating rate of the upper structures	Steel melting rate
[K]	[MW]	[kg/s]
3073	9.0	33.8
2773	5.6	20.8
2473	3.1	11.6
2125	1.2	4.4

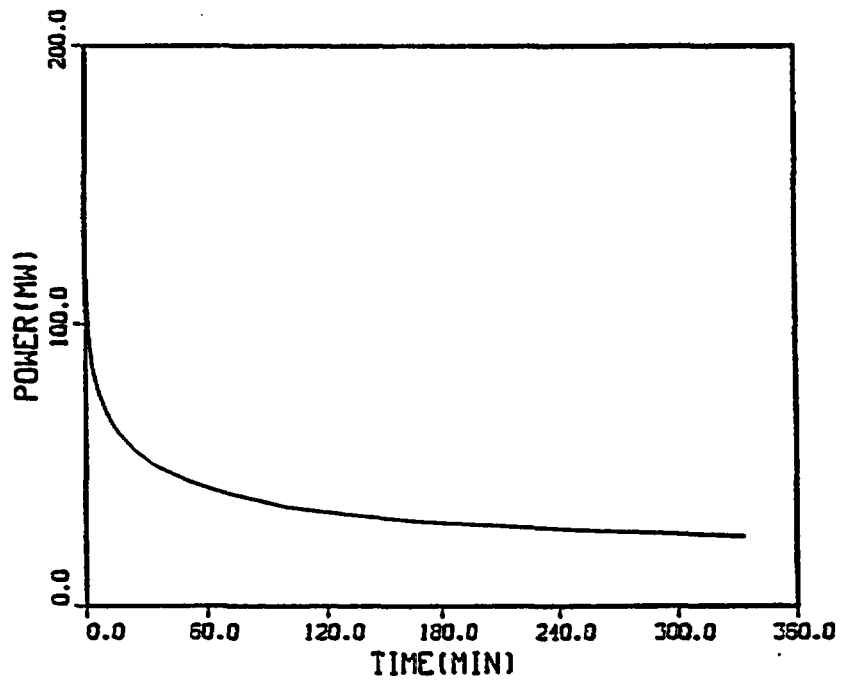


Figure 1. Decay heat power used in the APRIL.MOD3 simulation of a short-term station blackout accident at Peach Bottom.

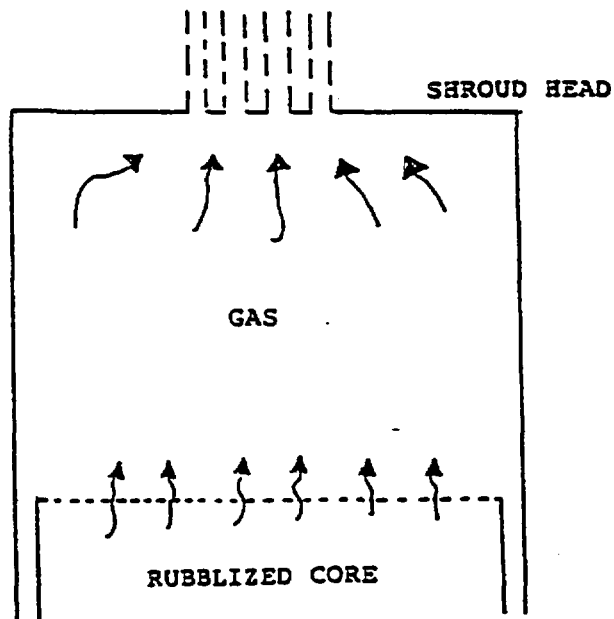


Figure 2. A schematic of the geometry used in the stand-alone model of radiative heating of the upper in-vessel structures.

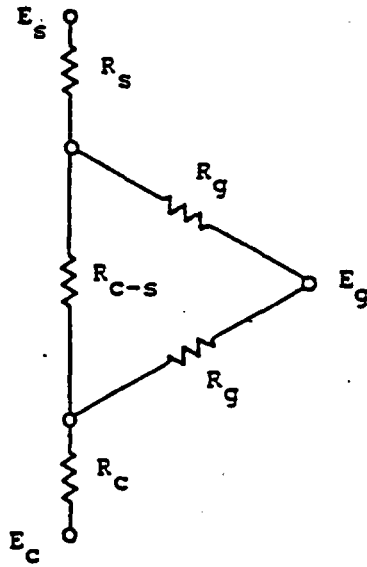


Figure 3. Radiation network for the model in Figure 2.

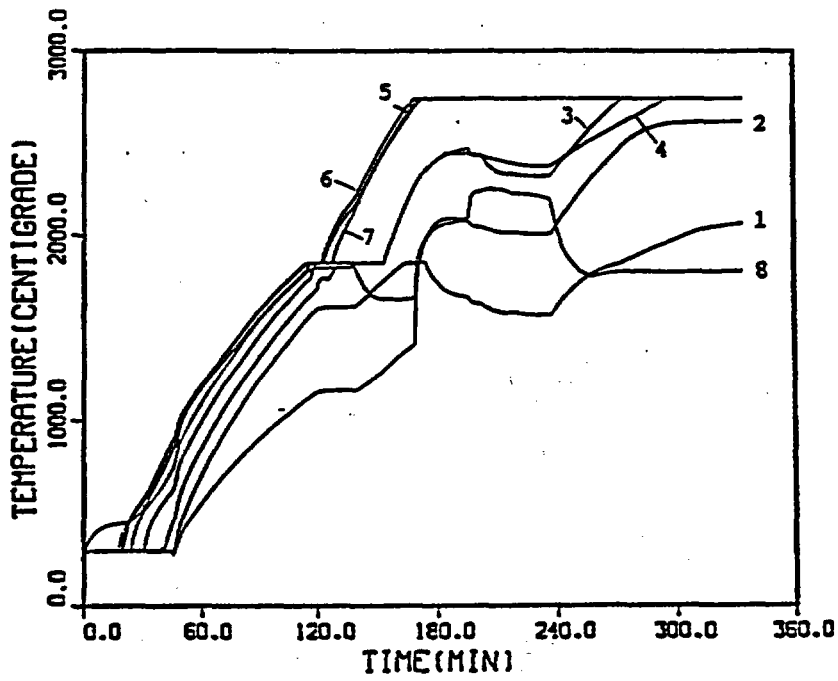


Figure 4. Nodal fuel temperatures in the central radial zone for Case 1 scenario. 1 - bottom axial node, 8 - top axial node.

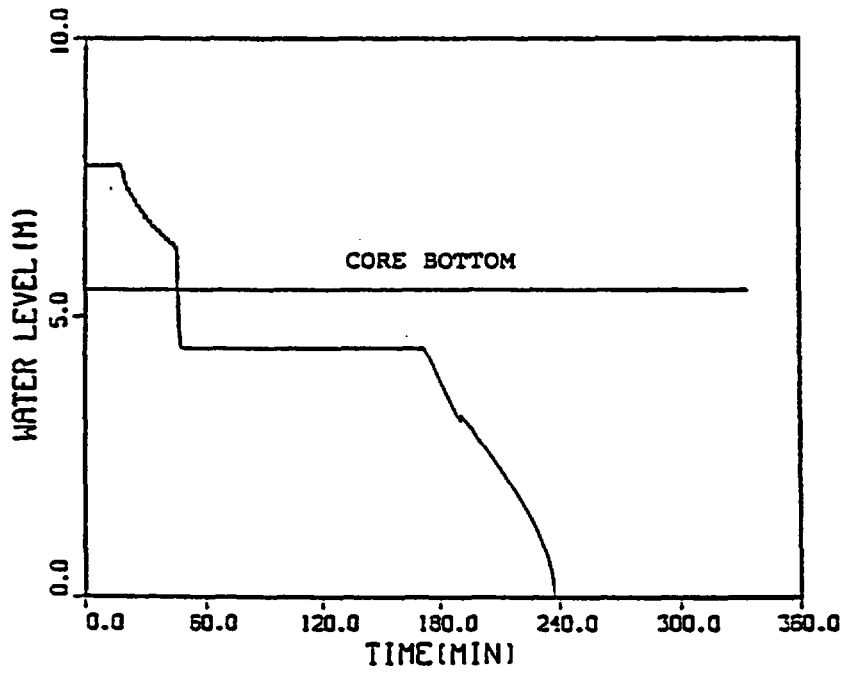


Figure 5. Water level in the reactor vessel for Case 1 scenario.

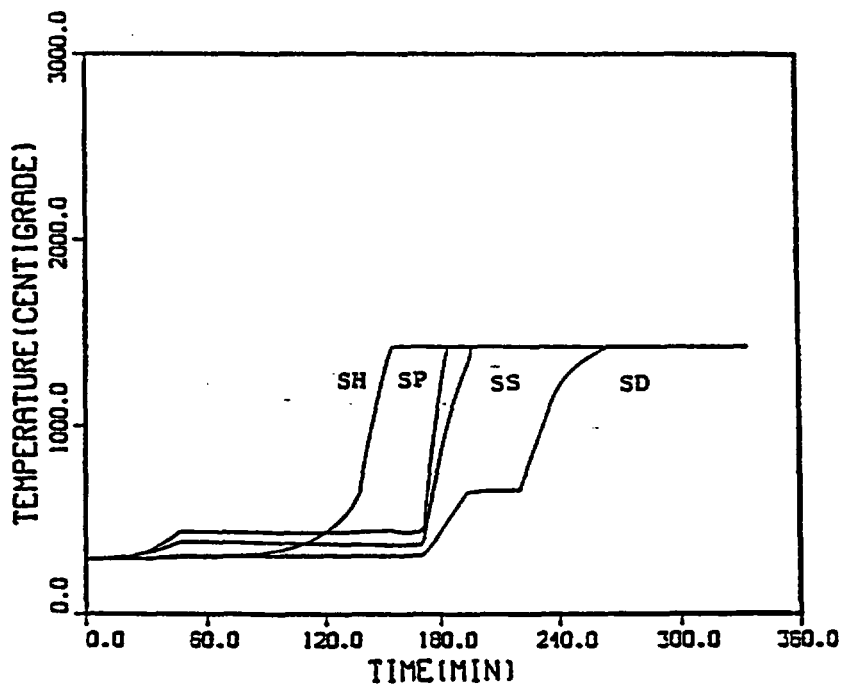


Figure 6. Temperature of the upper structures for Case 1 scenario. SH - shroud head, SP - stand pipes, SS - steam separator, SD - steam dryer.

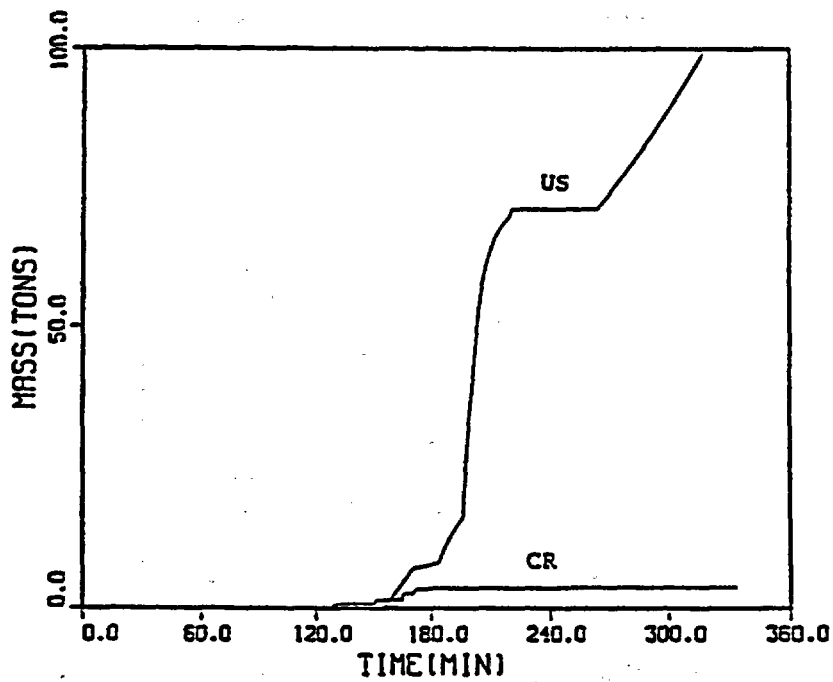


Figure 7. Molten mass of steel from control blades and upper structures for Case 1 scenario. CR - control rods, US - upper structures.

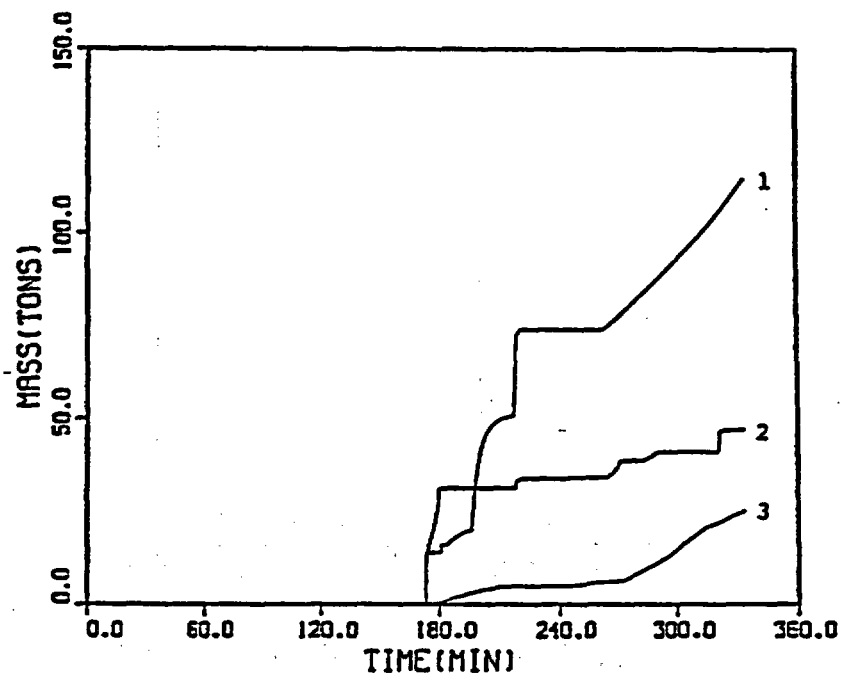


Figure 8. Mass of corium in the containment; upper bound calculation for Case 1 scenario. 1 - steel, 2 - zircaloy, 3 - UO<sub>2</sub>.

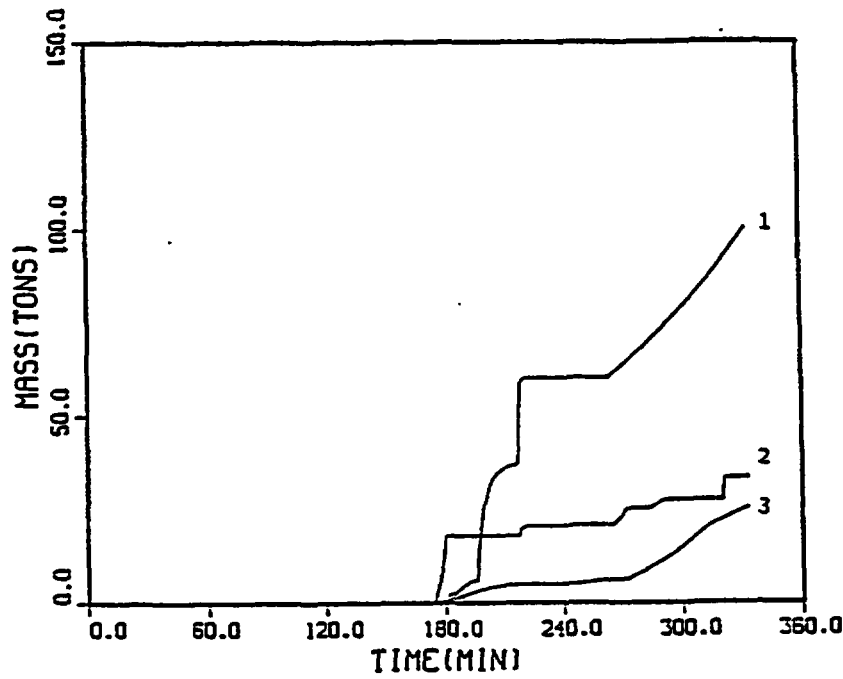


Figure 9. Mass of corium in the containment; lower bound calculation for Case 1 scenario. 1 - steel, 2 - zircaloy, 3 - UO<sub>2</sub>.

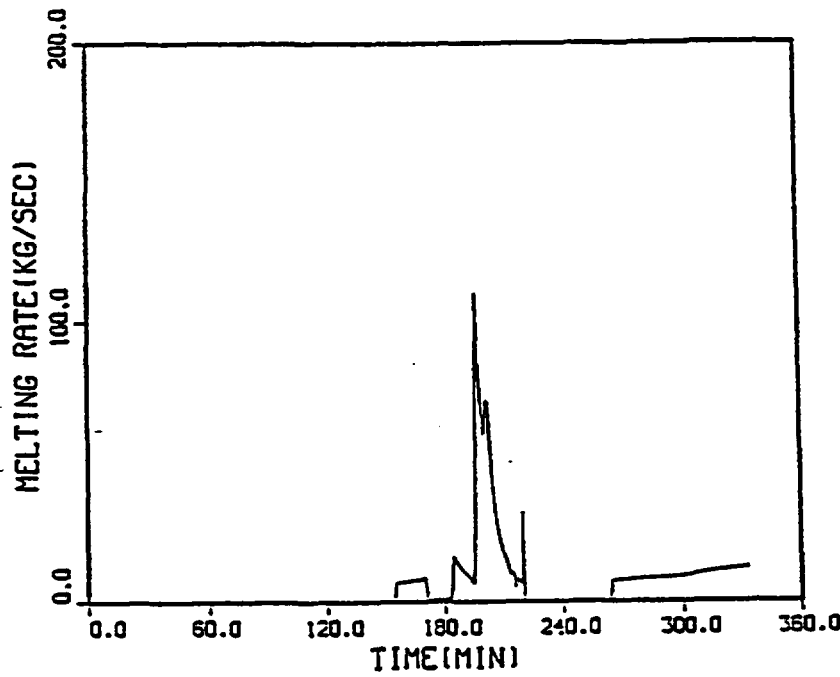


Figure 10. Melting rate of the upper vessel structures for the basic case (Case 1).

# **VICTORIA - EXPERIMENTS FOR HYDROGEN DISTRIBUTION IN AN ICE CONDENSER CONTAINMENT**

Olli Hongisto, Kari Lammila and Harri Tuomisto  
Imatran Voima Oy  
P.O.Box 112, SF-01610 Vantaa  
Finland

## **ABSTRACT**

The VICTORIA facility has been constructed for studying the Loviisa Ice Condenser Containment thermal-hydraulics during small break LOCA and severe accidents. The results from Test Phase 1 have given plenty of valuable information on how the ice condenser and the facility behave and presently this knowledge is being used in code verification process and in planning the future tests in which the long term behaviour of the facility will be studied together with the containment inside and outside spray systems and in planning the final stage of the test program, in which the hydrogen distribution in the ice condenser containment will be studied.

## **1. INTRODUCTION**

The Loviisa NPP, owned and operated by Imatran Voima Oy (IVO), is a unique combination of the nuclear technologies from east and west with the Soviet VVER-440 reactor and the ice condenser containment (ICC). The Loviisa ICC is a double containment in which the pressure boundary of the containment is the free standing cylindrical pressure vessel with a dome inside the secondary containment. The containment design pressure is 0.17 MPa, and estimated ultimate failure pressure 0.325 MPa. The ice condenser is divided in the Loviisa NPP into two separate sections in contrary to a single ice section in the US and Japanese ice condenser containments. The other significant differences in the Loviisa ICC, compared to the US and Japanese ICC's, are that the total volume of the containment is much bigger, i.e it is of the size of dry containment, there are no air return fans for mixing the atmosphere of the whole containment and the external spray system of the containment steel shell have been installed at Loviisa.

Based on an assumed "hydrogen design-basis accident", potential hydrogen burns were studied at the beginning of the 1980's, assuming 75% of zirconium in contact with fuel to react with steam. As result of these studies, a system for deliberate hydrogen ignition was installed in 1982. The igniter system consists of about 70 glow plugs, which are powered from the emergency diesel generators /1/.

Finnish Nuclear Regulatory Guides (Finnish Centre for Radiation and Nuclear Safety, 1987) require that the containment should maintain its integrity also during severe accidents. This is also the focus of severe accident management at Loviisa /2/. In a consistent approach to severe accident management (SAM) at the Loviisa nuclear power plant /3/ one of the main idea is to demonstrate absence of energetic events. In case of a core melt it is expected due to specific features of the VVER core that the molten material relocates gradually from the core region to the lower part of

the reactor vessel. Since the reactor vessel would be submerged into water melting from the ice condensers during accident conditions, our aim is to show that the corium can be retained indefinitely on the lower head. Gradual relocation of the core and in-vessel coolability eliminate a number of potentially significant containment challenges due to melt interaction (i.e., FCI, CCIs, DCH). The only concern left is a major hydrogen combustion event in the containment atmosphere. To confirm homogeneity in the containment atmosphere compositions under all relevant accident sequences and plant damage states and to confirm igniter capability to consume the relevant (but bounding) rates of hydrogen releases by combustion at concentrations very near the ignition limit are therefore the most important technical issues. For this purpose a linearly-scaled test facility (VICTORIA) of the Loviisa containment was built. The test results of the facility together with scaling analyses are expected to demonstrate absence of significant stratification of atmosphere in the containment.

## **2. THE VICTORIA FACILITY**

### **2.1 The facility description**

The VICTORIA facility (see Figure 1) is a scale model of Loviisa ICC with linear scaling 1:15, which gives a volume scaling 1:3375. The model and the Loviisa ICC are geometrically similar. All the structures that are made of concrete inside the Loviisa containment have been made of concrete inside the model, too. The structures of the model are designed and constructed so that the layout of the model containment is easy to modify and there is an access to practically all the measurement locations. All the large steel equipment inside the containment, i.e. the primary circuit piping, steam generators, pressurizer and pressure vessel, are modelled as dummy elements into the model compartments.

Instead of modelling the pressure boundary of the test facility in the same way as it is in Loviisa NPP, the secondary containment was chosen as the boundary in order to control and minimize the heat losses to the environment. The model containment has been insulated from all sides, including top and bottom. The lower compartment of the model can be heated to actual operating conditions with the built-in preheating system.

The ice condenser model was built so that one of the ice condenser sections at a time can be moved into or out from the model. The section consists of four levels of ice handling baskets (total of 12 baskets in one section). In one basket there are 15 lattice cases, and in each of them there are 6 ice batons. The opening and closing of the ice condenser doors, i.e. lower inlet doors, intermediate and top deck doors, as well as the by-passes of the doors and the ice condenser have been modelled, too.

The design of the facility allows also the modelling of other containment safety systems, such as containment spray, steel shell external spray and sump water recirculation.

When scaling the test facility /4/ due regard was given to the work of Prof. Karwat. In his work he stresses several important physical phenomena and other aspects, such as test procedures, test facility geometry, the interpretation and extrapolation of the results, which all should be carefully taken into consideration.

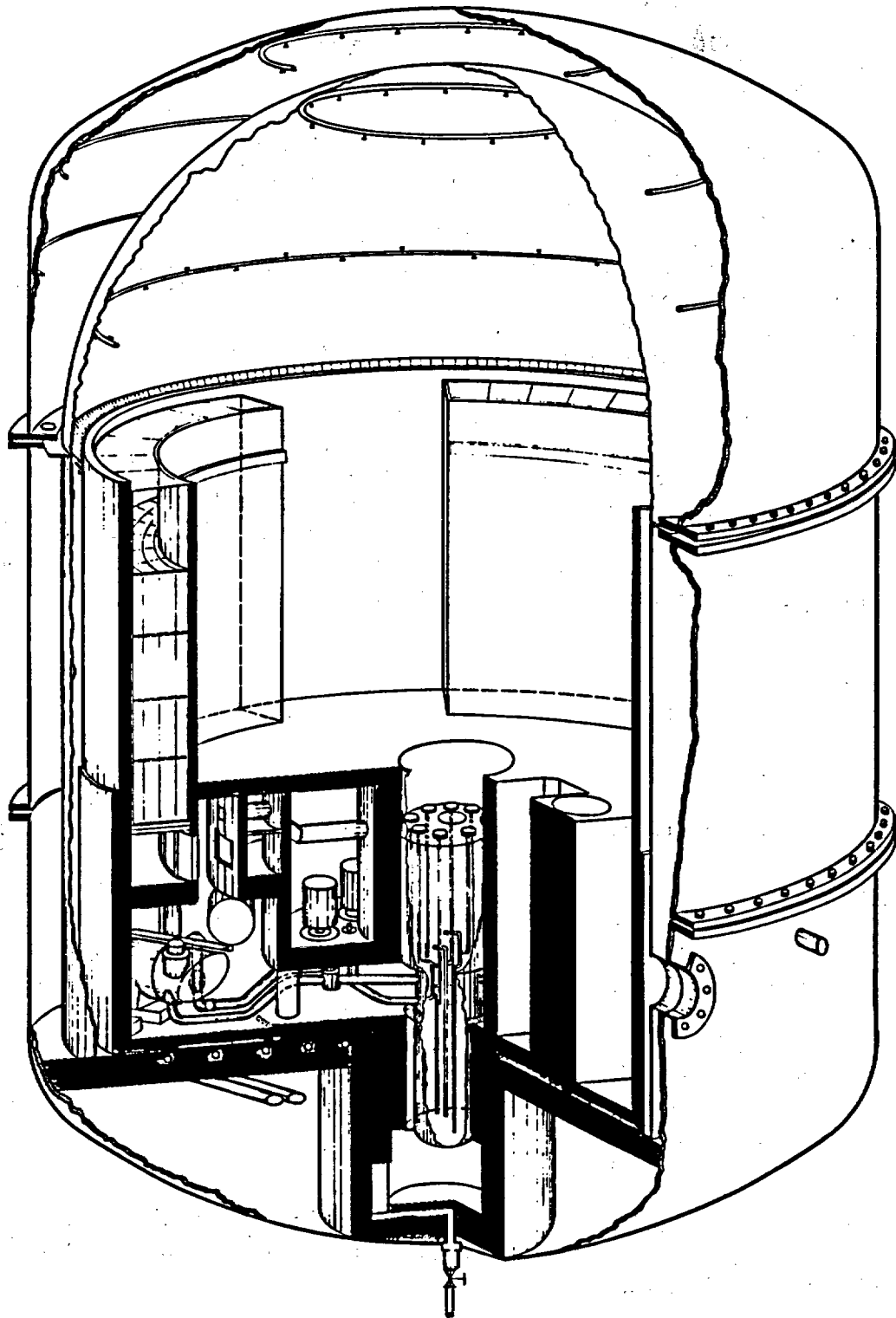


Figure 1. The VICTORIA facility

## 2.2 Instrumentation and measurements

The instrumentation comprises of data acquisition and process control systems. The data acquisition system is based on a 386-processor micro computer with two PC TO S-NET -adapters and S-NET network to IMP (Isolated Measuring Pods) data collectors in which the collection is controlled by the computer program. The IMP based measuring system has many advantages. The system is very flexible and the IMPs are well protected for use in difficult environment. The system can be built very large, up to 1000 channels, and still all the channels can be recorded once a second. The real time information is shown on screen by either graphical or numerical presentation. The data is stored to the hard disk of the computer during the experiment. The four processes of the facility i.e. steam flow and hot water flow to the break, containment spray and recirculation of the sump water, are regulated each through process controller, control valve and flow measurement. The external spray mass flow rate is kept constant, when used, and it is measured by rotameter.

In the data acquisition system there are 380 measurement channels. Temperature is measured inside the facility in 290 different points, out of which 126 are in the ice condenser, 65 are in the structures or in the insulations and 99 are measuring the temperatures of the atmosphere. Temperatures outside the facility are measured in 10 different locations. Pressures (total pressure, pressure difference between compartments, water level height) are measured in 7 and humidities are measured in 10 different locations. The local gas velocities in the upper compartment are measured with a fiber-optics laser-doppler anemometer system (LDA), equipped with an industrial robot for maneuvering.

## 3. EXPERIMENTAL PROGRAM AND TEST MATRIX OF TEST PHASE 1

### 3.1 Experimental program

The experimental program can be divided into three separate phases, which have their own specific objective. In the first phase the melting of the ice and the ice condenser behaviour are studied during a SBLOCA or a small steam line break. These experiments are used also to verify the results of the previous ice condenser experiments /5/. Especially the influence of the ice condenser doors (lower inlet doors, intermediate deck doors and top deck doors) is studied as well as the effect of the door by-passes. The quantity of heat transferred to lower compartment structures and its effects on ice melting are also studied carefully. The second phase of the test program concentrates in the long-term behaviour of the ice condenser containment, also during severe accidents. In these experiments the effect of the external spray system is of great interest. Hydrogen distribution experiments, which are the final objective of the test program, will be done in the third phase. Two previous phases serve as fundamental steps to understand the facility behavior before running into the integral experiments with all aspects modelled.

It has not been deemed necessary to prepare a definite test matrix for these experiments, because it has been considered beneficial to analyse the previous experiments before the decision of the following experiments should be done.

### 3.2 Test matrix of Test Phase 1

A 20 cm<sup>2</sup> hot leg break was selected as the base case for the energy and mass release of water and steam. In all of the experiments conducted in Test Phase 1 (see Table 1) the water (enthalpy  $\approx$  460 kJ/kg) and the steam (enthalpy  $\approx$  2700 kJ/kg) releases were identical, except in three experiments (13, 21 and 22), in which the objective of the experiment was defined in more detail. The Froude-scaled break experiment, in which the release rates are a factor of  $\sqrt{13}$  times higher than those obtained from volumetrical scaling and the time scale was reduced by the same factor, was conducted in order to clarify and confirm the scale effects of the important parameter groups. In those two experiments, in which the amount of heat transferred to the lower compartment structures and the consecutive amount of ice melted were studied in more detail, the energy and mass injected into the facility was only in form of steam at the rate of 10 g/s.

NUMBER	TITLE OF THE EXPERIMENT	ENERGY RELEASES
04	BASE CASE	20 cm <sup>2</sup> hot leg break
05	BASE CASE	20 cm <sup>2</sup> hot leg break
06	ALL DECK BY-PASSES CLOSED	20 cm <sup>2</sup> hot leg break
07	ALL INLET DOORS OPEN	20 cm <sup>2</sup> hot leg break
08	BASE CASE	20 cm <sup>2</sup> hot leg break
10	TWO INLET DOORS OPEN	20 cm <sup>2</sup> hot leg break
11	SOME DECK DOORS OPEN	20 cm <sup>2</sup> hot leg break
12	ALL DECK DOORS OPEN	20 cm <sup>2</sup> hot leg break
13	FROUDE-SCALED BREAK	factor of $\sqrt{13}$
15	BASE CASE (LDA)	20 cm <sup>2</sup> hot leg break
16	BASE CASE (LDA)	20 cm <sup>2</sup> hot leg break
17	BASE CASE (LDA)	20 cm <sup>2</sup> hot leg break
19	PARTLY INSULATED LOWER	20 cm <sup>2</sup> hot leg break
20	PARTLY INSULATED LOWER	20 cm <sup>2</sup> hot leg break
21	CONSTANT STEAM RELEASE	10 g/s of steam
22	CONSTANT STEAM RELEASE	10 g/s of steam
24	ALL ICE CONDENSER DOORS OPEN	20 cm <sup>2</sup> hot leg break

Table 1. The test matrix of Test Phase 1

#### 4. RESULTS OF TEST PHASE 1 EXPERIMENTS

Test Phase 1 of the experimental program started in December 1990 and ended in May 1992. In these experiments the behaviour of the ice condenser containment test facility was studied in detail; the effect of the ice condenser doors (the lower inlet doors, the intermediate and top deck doors), the effect ice condenser door by-passes and the effect of the amount of heat absorbed by the lower compartment structures on the ice melting and containment pressures, humidities, temperatures and upper compartment gas velocities were measured /6/.

##### Overall behaviour of the facility

In most of the experiments the overall behaviour of the facility was alike. After the initial pressurization the pressure increased slowly and at the end of the experiment the pressure in the facility had increased  $\approx 100$  mbar. During the first part of the experiment there was a strong temperature stratification in the lower compartment, at the inlet doors of the ice condenser and in sump water. The stratification in the lower compartment became smaller towards the end of the experiment. Temperatures increased slowly in the upper compartment during the experiments mainly due to heat transfer through the structures between the lower compartment and the upper compartment. The structures in the lower compartment were heated up to almost the lower compartment temperatures at the end of experiment.

Forcing the lower inlet doors open at the beginning of the experiment changed the overall behaviour of the facility dramatically. The final pressure increase was only  $\approx 75$  mbar. Temperature stratifications were stronger in the lower compartment and a great deal more ice was melted. Contrary to the base case the maximum surface temperatures in the lower compartment structures occurred soon after the maximum steam release rate, after which the temperatures started to decrease.

After half an hour from the initiation of the experiment, where all the ice condenser doors were forced open, the pressure started to increase rapidly due to the fact that the steam had penetrated the ice condenser, which was located near the release point. Also the temperatures in the dome part of the upper compartment increased rapidly. The increase in pressure was arrested by strong steam condensation in the upper compartment dome and by the large circulating flow, from the lower compartment through the ice condenser section closer to the release point into the upper compartment from where the flow was directed through the other ice condenser section back into the lower compartment. The stratification of temperature in the lower compartment was very strong and for the first time there was a clear temperature stratification in the upper compartment.

In the experiment, where the release rates into the facility were bigger by the factor of  $\sqrt{13}$  and the time shorter by the same factor, the final pressure was slightly bigger than in the base case. The lower compartment temperatures were higher, the sump water hotter, but the heat up of the lower compartment structures similar to the base case.

In experiments, where part of the lower compartment structures were insulated, the pressure difference between the upper compartment and environment increased first more rapidly than in the base case due to the smaller amount of condensation in the lower compartment. The pressure increase inside the facility at the end was only slightly higher than in the base case. At the

beginning of the experiment there was a small temperature stratification in the lower compartment, but after half an hour the whole atmosphere was quite uniform and remained such during most of the experiment. The insulated inner structures in the lower compartment did not heat up as fast as in the base case although the end temperatures in the structures were only  $\approx 5$  °C lower than in the base case. The thicker structures of the ice condenser floor heated up as in the base case. Those parts, which were not insulated heated up more and faster than in the base case due to the bigger increase in temperatures in the lower compartment.

### Ice melting and behaviour of ice condensers

In most of the experiments the basic ice melting behaviour was similar. Small releases of steam into the lower compartment caused only slow steam flow into the ice condenser. This flow created a channel (channels) through the ice bed near the inner wall of the ice bed. After penetrating the ice bed, the steam started to melt the ice from the top downwards. The location(s) of the steam channeling(s) depend on how uniformly the lower inlet doors operate. It seems obvious that, if one or two out of the 18 doors are for some reason more sensitive than the others, the channeling occurs above these doors, because more steam is flowing through them into the ice condenser. While the lighter gas mixture rose upwards near the inner wall of the ice bed, the colder and heavier gas mixture sank downwards in the outer part of the ice bed. These flows are the main driving forces of the natural circulation in the ice condenser. In cases, where there was only a little melting of ice, more ice was melted in the lowest level of the ice bed than in the upper levels and in cases, where the ice bed had melted significantly, most of the ice had been melted from the top part of the ice bed. In some cases there was ice left only in the lowest parts of the ice bed.

Large temperature differences between the upper and lower part of the lower inlet door opening ( $\approx 20 \dots 50$  °C) indicate that part of the cold gas mixtures that entered the bottom part of the ice condenser flowed out into the lower compartment through the lower inlet door openings. This "counter-current" flow of the lower inlet doors has a very important role in returning air back to the lower compartment making hydrogen combustion possible in the lower compartment atmosphere.

The amount of steam getting into and out of the ice condenser and the resulting degree of ice melt varied a lot ( $\approx 25 \dots 225$  kg) depending on the initial conditions of the experiment (see Figure 2). Important factors that influenced most are the behaviour of lower inlet doors, the intermediate and top deck doors, and the behaviour of the by-passes on the intermediate deck and the amount of steam released into the facility.

### Velocities in the upper compartment

Based on the LDA-measurements it can be concluded that the preheating system of the lower compartment and the subsequent temperature differences in the facility determine the flows in the upper compartment at the beginning of the experiments. The energy released into the lower compartment and the subsequent temperature increases in the facility only enhance the already existing flows in the upper compartment.

## AMOUNTS OF ICE MELTED

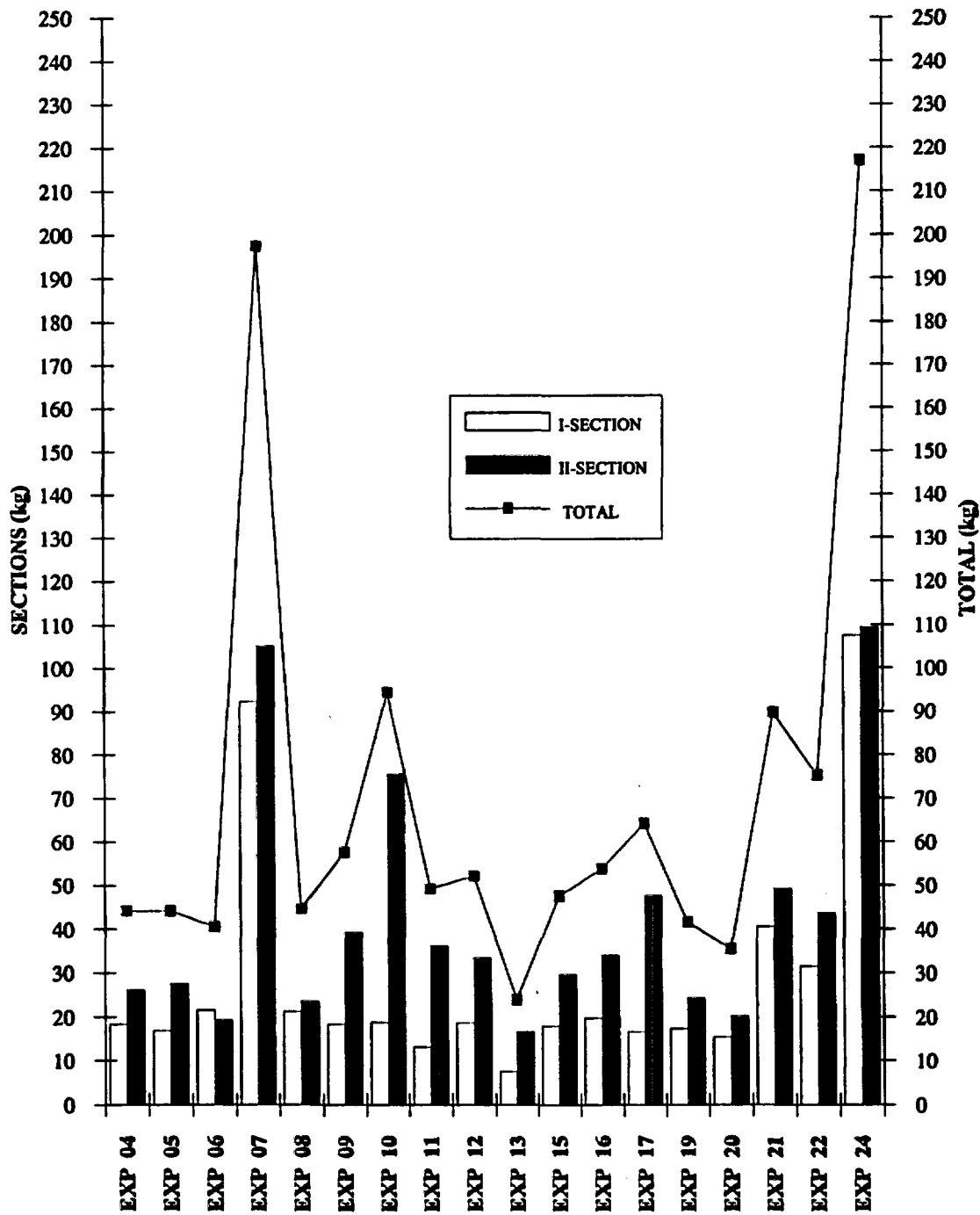


Figure 2. The amounts of ice melted in Test Phase 1 experiments

At the end part of the experiments the magnitudes of the velocities above the ice condensers were between 40 mm/s and 140 mm/s, below the top level of the ice condensers between 50 mm/s and 250 mm/s, and in the dome between 10 mm/s and 220 mm/s. The velocities in the upper compartment were much higher than expected. This gives an explanation to the fact that in most experiments the upper compartment was well mixed and there were no temperature stratifications present. The effect of these flows in the upper compartment has to be taken into careful consideration when the hydrogen mixing experiments are being conducted.

#### Heat transfer to lower compartment structures

A comparison, in which the heat transfer to the lower compartment concrete structures was calculated by several different methods found in the literature and based on the test results, was done in order to get more clear picture out of the different methods and their capability to calculate the heat transfer inside the facility. The comparison pointed out clearly that none of the heat transfer coefficient models alone seem to be suitable to be used in calculating the heat transfer to the structures in different locations through the whole experiment. Each different location and atmospheric condition, which was constantly changing during the transient, requires its own model in order to predict properly the heat transfer process /6/.

#### Distribution of energy in the facility

In the base case, where the energy into the facility was released in form of hot water and steam, the energy distribution after the experiment was such that  $\approx 50$  % of the energy was in the sump water,  $\approx 20$  % of the energy in the lower compartment structures and only  $\approx 5$  % has been used to melt the ice. In case, where the energy was released only in form of steam, the sump water contained  $\approx 25$  %, the structures in the lower compartment  $\approx 30$  % of the released energy and  $\approx 10$  % of the released energy was used in melting of the ice. These distribution factors will be quite different for the Loviisa containment itself, since the ratio of heat transfer area/volume in the facility is 15 times higher, and thinner walls absorb energy in much shorter time scale as the applied scaling presumes.

### **5. COMPARISON CALCULATIONS**

For interpretation and extrapolation of the experimental results the central role of a computer code as vital analytical tool has been emphasized. In Ref. 7 an attempt is made to identify areas of particular interest. For these great care should be exercised, when scaled experimental results are interpreted and extrapolated with the aid of dimensional analysis of a typical set of conservation equations normally used in the lumped parameter codes. Two basic assumptions have been made in the course of the dimensional analysis. These are the geometrical similarity of the test facility and the prototype plant and performing the experiments with the same fluid components, which are expected to dominate within the containment atmosphere of the prototype plant. Both of the two basic assumptions are valid in the VICTORIA test facility.

The scaling principle for the containment experiments can to a certain extent be compared to the idealized time preserving modelling approach which is based on the idealized assumption of an

equivalency of the analytical description for both the full-size prototype and the scaled test facility physical events. This means that the computer code to be employed for test planning and evaluation should itself fulfill the similarity requirements and should then be capable of predicting fluid-dynamic and heat transfer processes in both cases with the same degree of accuracy and reliability. At least these requirements are easier to fulfill, when the constructive details of the facility and nodalization are kept the same and adequately described by the code input.

The computer code that is being verified and developed with the use of the results from the VICTORIA experiments is RALOC MOD2.2, which belongs to the RALOC/FIPLOC code family /9/. The code can be applied to general containment problems (such as p-, T-calculations), special distribution considerations in subcompartmented geometries (for example H<sub>2</sub>, air, steam) and aerosol distribution. RALOC MOD2.2 is a typical lumped parameter containment code, in which temperature and pressure stand for the whole volume and the atmospheric flow leaving a node will be of the average temperature of this node. A containment is presented by numbers of nodes (up to 100) and junctions (up to 200 and 15 different types of junctions). A large compartment can be also subdivided into nodes (sump or atmosphere nodes). The nodalization of the VICTORIA facility is shown in Figure 3.

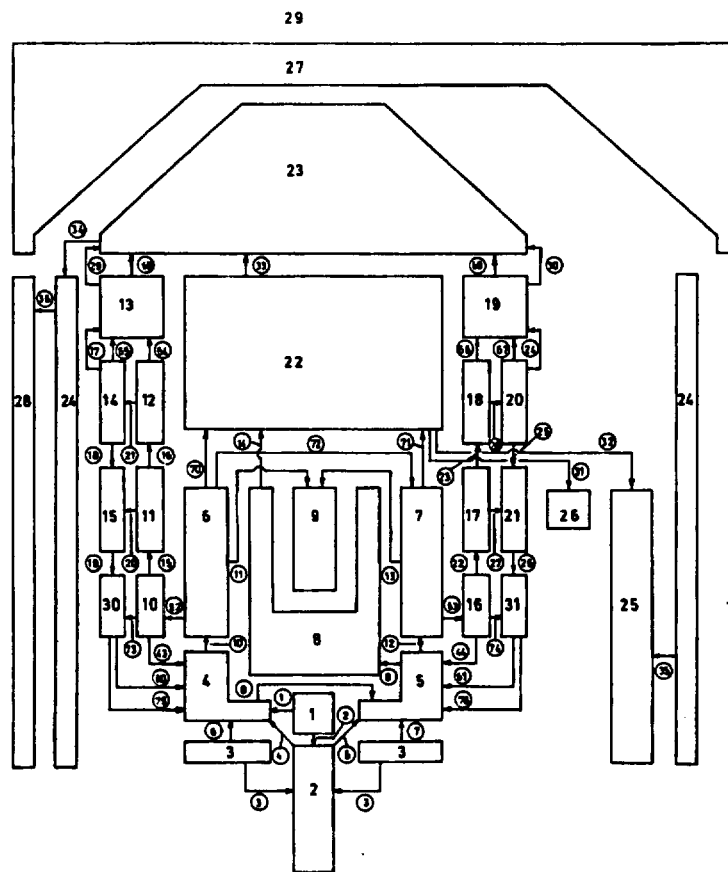


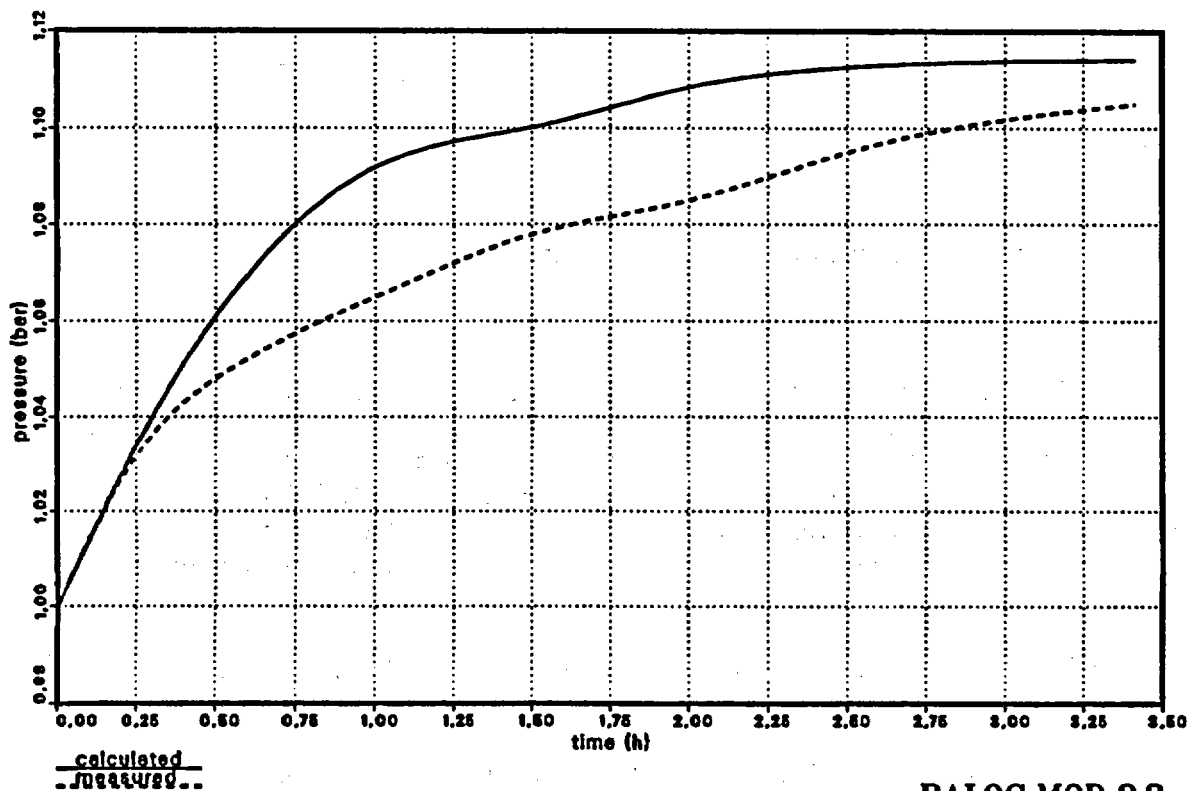
Figure 3. The nodalization of the VICTORIA facility in the RALOC-code

A simple ice condenser model has been added to RALOC-code. The behaviour of the lower inlet doors, the intermediate and top deck doors have been modelled into the code, too. In the VICTORIA facility there are 9 pairs of lower inlet doors in one ice condenser section, which have been replaced by one door in used nodalization. Besides this the lower inlet door flow area has been throttled to 23 % of the actual flow area and also all other junction have been throttled to  $\approx 25$  %. The modelling of "counter current" flow of the lower lower inlet door is not possible although the experiments indicate that this kind of flow may occur. For the Test Phases 2 and 3 the containment inside and external spray systems have also been included into the RALOC code.

The experiments numbers 07, 08 and 22 of Test Phase 1 have been used in the verification and development work of the RALOC-code. In the following text some examples of the comparison calculations (experiment 08) are shown and problems encountered are discussed.

Experiment 08 is the base case in Test Phase 1 with all ice condenser doors included. The calculated and measured pressure inside the facility is shown in Figure 4. The calculated values are about 0.02 bar higher than what was measured. Also the calculated temperatures inside the lower compartment were about 20 °C higher than in the experiment (see Figure 5). The amount of melted ice was also higher in the calculation.

Victoria  
test 08



RALOC MOD 2.2

Figure 4. The calculated and measured pressures inside the facility in experiment 08

Victoria  
test 08

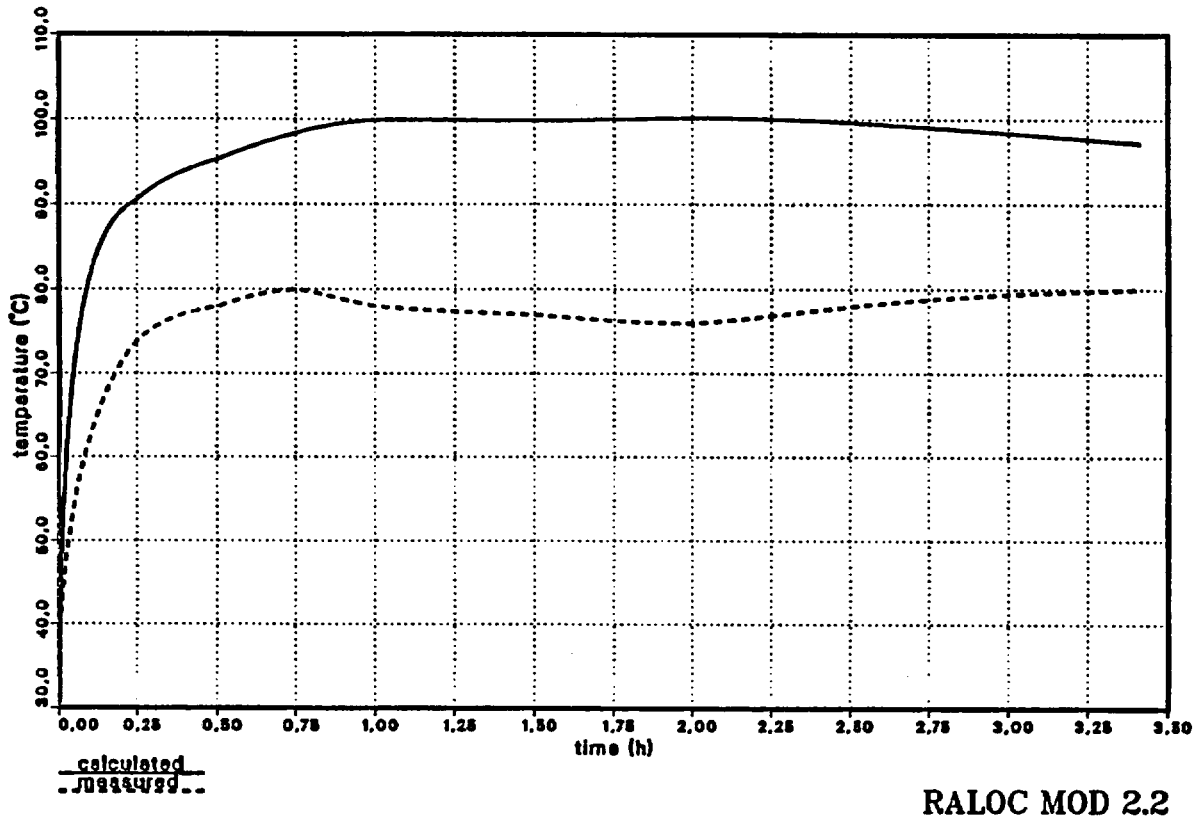


Figure 5. The calculated and measured maximum temperatures in the lower compartment in experiment 08

Because the code is a lumped parameter type, temperatures are always mean temperatures of the nodes. This means that the heat transfer to the walls and to the ice in the ice condenser are calculated using the average temperature of the node and the surface temperature of the heat structure. Temperature stratifications can not be taken into consideration in calculations. This causes unrealistic heat distribution in structures and influences on final temperatures and pressures. It is also questionable whether only one heat transfer correlation can be used from beginning to end in long calculations.

The sump water is hotter in calculation than in experiment, because in RALOC there is no heat transfer from water to the structures.

One of the main problems in the calculations is how to model the "counter current" flow from the lower part of the ice condenser into the lower compartment. The calculated pressures in the ice condenser are lower than in the lower compartment and the mass flow is always from the lower compartment into the ice condenser. At this moment there is no useful solution for this problem.

The lower inlet door area is also very sensitive to small pressure changes if pressures are low and therefore the mass flow through the doors may vary very rapidly. This causes some numerical problems to be solved.

If the real flow areas of the junctions are used in calculation, especially when pressure differences are small, there will be flow oscillation across the junctions. To prevent this the flow areas must be throttled to  $\approx 25\%$  in calculations. The question is whether this is appropriate or not. The throttling of the junctions have great effect on temperature stratification in lower compartments: the smaller the flow areas are, the larger temperature stratification is.

## 6. CONCLUDING REMARKS

Test Phase 1 of the VICTORIA experiments was carried out to study the behaviour of the Loviisa ice condenser containment and the influence of the ice condenser door operation on the ice melting process. The results indicate the importance of the ice condenser doors in the overall behaviour and the sensitivity to the door operation in ice melting process. Slow steam flow into ice condenser created channels through the ice bed and after penetrating the ice bed the steam started to melt the ice from the top downwards. The transfer of the test results to the Loviisa containment will necessitate careful consideration of the scaling. This includes also the use of RALOC containment code. The results of Test Phase 1 will be utilized in planning of the experiments, in which the long-term behaviour of the facility will be studied (Test Phase 2) and in hydrogen distribution experiments (Test Phase 3).

## ACKNOWLEDGMENT

The VICTORIA experiments are being carried out at the Hydraulic Laboratory of Imatran Voima Oy (IVO). The authors would like to thank the staff of the laboratory for their contribution and help. Particularly, the efforts of Pertti Mustonen who is responsible for conducting the experiments and processing the experimental data, Esa Pessa who is responsible for data acquisition and process control of the facility, Yrjö Tuokkola who is responsible for the facility construction and maintenance, are gratefully acknowledged.

## REFERENCES

1. REGNELL, B. and HELYNEN, S., "Analyses of the effects of hydrogen burning and measures taken for their mitigation at Loviisa Nuclear Power Plant", Proc. Spec. Mtg. on Hydrogen Behaviour and Control and Related Containment Loading Aspects, Suzdal, USSR, September 19-23, 1983, IAEA-TC-427.6 (TC-SR-2) 83-90.
2. TUOMISTO, H., "Overall Approach to Severe Accident Assessment of the Loviisa Containment Integrity", IAEA Technical Committee Meeting on Containment Loadings and Performance under Severe Accident Conditions, Vienna, Austria, May 21-24, 1990.

3. TUOMISTO, H. and THEOFANOUS, T.G., "A Consistent Approach to Severe Accident Management", Proc. of OECD CSNI Specialists Meeting on Severe Accident Management Programme Development, Rome, Italy, September 1991.
4. HONGISTO, O. AND TUOMISTO, H., "Experimental Verification of the Loviisa Ice Condenser Containment Transient Operation in Reactor Accidents", Proc. ANS International Topical Meeting on Safety of Thermal Reactors", Portland, Oregon, USA, July 21-25, 1991.
5. TUOMISTO, H. and HONGISTO, O., "Ice melting progress in a nonuniformly loaded ice condenser facility", Nucl.Eng. and Des. 120 (1990) 67-74.
6. HONGISTO, O., "The Results of Test Phase 1 of the VICTORIA Experiments", Imatran Voima Oy, Hydraulic Laboratory, Test Report, DLV1-G380-0374, August 1992.
7. H. KARWAT, "Scaling and extrapolation of hydrogen distribution experiments", Nucl.Eng. and Des. 104, (1987) 285-294.
8. JAHN, H., WEBER, G, PHAM, T.V., "Description of the MOD2/85 versions of the RALOC/FIPLOC family, Part 1: Code System", GRS-A-1315, (Dezember 1986).

# THE CALCULATION PROGRAMME TO PREPARE THE FIRST PHEBUS FP TEST

A. MAILLIAT and F. SERRE

CEA, NUCLEAR PROTECTION AND SAFETY INSTITUTE  
CADARACHE NUCLEAR CENTRE, FRANCE

A.V. JONES and I. SHEPHERD

JOINT RESEARCH CENTRE, ISPRA, ITALY

**Abstract** - The aim of the PHEBUS FP programme is to investigate in an pile test facility various phenomena governing the degradation of fuel and the release, transport and deposition of fission products in LWR severe accident conditions. This paper gives a summary of the preparation of the first test FPT0 expected to be performed in April 1993 and the associated experimental protocol.

## **1 TEST PREPARATION ORGANISATION**

### **1.1 BACKGROUND TO THE FIRST TEST**

In order to understand better the phenomenology of severe accidents the CEA/Safety institute and the Commission of European Communities have sponsored study of reactor severe accident sequence calculations in Europe through the CEC shared cost actions programme. Each organisation from five national teams was requested to assess the accident sequences which present the highest interest from the point of view of the risk to the population and of the relevance of the phenomena involved.

From the results a synthesis was made [1] which identified the most important aspects of such accidents ; these phenomena being the targets that the PHEBUS FP facility has to reach. The behaviour during core degradation (temperature heat up rates, gas mass flow rates...); the associated fission product and aerosol release rates ; the reactor components where the fission product trapping is the largest ; the main depletion mechanisms and their driving parameters.

Having defined the phenomenology to investigate, the verification of the experimental circuits devoted to reproducing such phenomena was started. It was done by the teams previously involved in the reactor sequences calculations using preliminary lay-outs of the experimental circuits derived from dimensional analyses and boundary conditions deduced from the synthesis of the reactor results. From this second step it was possible to derive important information on various dimensioning problems and to adjust the geometrical dimensions of some parts of the circuit [2,3].

As soon as the severe accident phenomenology was known, the European experts were asked to indicate the most interesting tests that should be performed. From this advice a provisional test matrix was drawn up jointly by CEA/IPSN and JRC/ISPRA and submitted for expert agreement. This test matrix is being periodically revised in order to integrate new knowledge.

### **1.2 PREPARATION OF THE FIRST TEST**

The tests of the PHEBUS programme are prepared by the Scientific Analysis Working Group (SAWG). Two groups of analysts, at CEA/Cadarache and at JRC/ISPRA propose for the SAWG approval an experimental protocol for each test. These proposals are based on joint calculations of tentative test protocols both by CEA and JRC teams and PHEBUS programme partners.

The test preparation starts 3 years before the test itself and is initiated by the test objective document issued by SAWG.

This document describes the test in terms of a fission product flow path and the reactor components to be simulated. During a one year period, both the CEA and JRC analysts and PHEBUS partners must define the geometrical characteristics and the operating specifications of the experimental components. The results of this work, after SAWG agreement, is included in a test geometry document which is released 15 months before the test.

A second period of 9 months is devoted to boundary and initial condition adjustments of each component of the experimental circuit in order to reach the objectives assigned to those components. At the end of this so called exploratory calculation period, a set of provisional test conditions, based on independent behaviour of the various components, is made available and released as the Provisional Test Protocol.

Finally, a third period of 12 months devoted to sensitivity calculations of the experimental circuit with coupled components including a 3 month synthesis is required to finalize the test protocol which is released as the Final Test Protocol. This self-standing document is issued 3 months before the test itself and must contain all the information needed to carry out the experiment.

Regarding the first test FPT0, this rather long procedure is at its ultimate state, the release of the Final Test Protocol being planned at the end of year 92. The test itself should take place by April 93.

### **1.3 OBJECTIVES OF THE FIRST TEST**

The first test FPT0 is devoted to study of the phenomenology of severe accident sequences for which the fission product flow path involves the primary side of the steam generator and the reactor containment building.

The objectives of FPT0 may be stated separately for the bundle, the circuit and the containment.

For the bundle, using PWR-typical fresh fuel with 9 days irradiation in the Phebus reactor, the first priority is to maximize the fission product release and the fuel rod degradation. A large degradation will be obtained by reaching the melting temperature of the fuel. Enhancement of the fission product release is obtained by fuel melting and also by a quick cooling of the bundle at the end of the transient.

It is required that the fission product emission takes place in a low pressure oxidizing gas steam with a fission product concentration inside the carrier gas

representative of the reactor core. Since the test will also provide information on rod bursting, the control rod internal pressure is similar to that of in the reactor and the fuel rod pressure adjusted to be representative of an irradiated BR3 rod, which will be used in subsequent tests under the same conditions.

The last boundary condition set for the bundle includes a first phase devoted to the thermal checking of the test train: 3 temperature plateaux will be performed. The following phase is a bundle heat up which leads to control rod relocation and almost complete clad oxidation with oxidation runaway. The next phase with temperature increase from the melting temperature of the zircaloy up to the fuel melting is devoted to fission product extraction. This third phase is followed by an increase of the nuclear power to produce a large amount of molten fuel and an important degradation of the bundle. Finally a rapid cooldown phase with steam flow ends the test since previous tests e.g. in PBF have shown surprisingly high amounts of fission product and aerosol release during cooldown.

Regarding the circuit, the main objective is to investigate fission product depletion inside a primary side of a steam generator at low pressure (around 0.2 MPa) in hot conditions. Secondary objectives are to explore phenomena in the section just above the bundle exit where sharp changes of the carrier gas temperature are expected and to provide data on fission product chemistry including interactions of these fission products with the pipe wall, under low pressure and high temperature conditions.

Preliminary boundary conditions involves a constant temperature of 700°C for the pipe internal liner from the bundle down to the steam generator entrance to minimize condensation onto the pipe wall of the main fission product species like CsOH, CsI and Te.

The steam generator secondary side is maintained at 150°C to avoid steam condensation. Fission product vapours condense both onto the steam generator pipe wall and the particles. Aerosol depletion through thermophoresis will be explored.

For the containment the objective is to study the fission product chemistry and especially iodine radiochemistry in the sump water and atmosphere and the effect of paints in the "dirty" chemical conditions of a reactor accident.

Tentative boundary conditions for the containment involve two successive phases. During the first one the containment has an atmosphere temperature around 110°C, a humidity ratio near 60 % and with steam condensation onto the condenser surfaces. For good scaling of the volume to surface ratio, the vessel walls are rendered "neutral", as far as condensation is concerned. Condensation, aerosol diffusiophoresis and FP-paint interaction take place on suspended structures called "condenser". When the bundle and circuit transient are over, the circuit is disconnected; aerosol deposition and subsequent operation of a washing system transfer FPs to the sump water. This second period duration is 3 days with an atmosphere temperature increase up to 150°C and superheated conditions. This period is devoted to Iodine radiochemistry.

This FPT0 test being the first test of the PHEBUS programme there are naturally some technological objectives also: to check out the instrumentation and its performance, to gain experience in operating the PHEBUS facility with a specified test procedure (including the pre-irradiation and the post test operations like e.g. decontamination).

## 2 BUNDLE STUDIES

The first point to note about the Phebus-FP bundle is that it has many features in common with the Phebus-SFD bundle, for which many calculations have been performed and checked against experiment. An international standard problem was based on one of these experiments [4]. The main differences are the power profile which is sharper for Phebus-FP, the much lower porosity of zirconia used for the shroud insulator in the new geometry, and the absence of a shroud zircaloy inner liner.

There is a major difference in the objectives of the two sets of experiments. The SFD experiments aimed to investigate the main core degradation processes in practically an analytical way. Phebus-FP, on the other hand, aims to observe the fission product release during core degradation with representative conditions of severe accidents for a given set of thermal hydraulics parameters; mostly flow rate and composition and temperatures.

Phebus FP is a harder problem to solve for the codes. The highest temperatures reached in the SFD series was in the order of 2700 K whereas the target in FPT0 is above 3000 K. The aim is to have up to 20 % of the uranium dioxide melted.

An added difficulty is that, at least for the first test, the oxidation reaction will be allowed to proceed in excess steam. It is thus clear that the calculations for the bundle will not be able to predict the precise degree of core degradation because computer codes are not totally assessed for these conditions. We hope to be able to show with the calculations that, even with this uncertainty, we can develop a test procedure that stands a good chance of achieving the objectives.

In addition to the base case calculations we can obtain an estimate for the uncertainty by performing the same calculation with many different codes and different users. The results are analyzed critically.

In this section we will describe the principal findings of these calculations.

### 2.1 SUMMARY OF INITIAL STUDIES

As mentioned in the introduction, following a phase A where a set of reactor sequence calculation were performed, the phase B consisted of a set of calculated scaled down sequences in the various Phebus geometries with the object of simulating as closely as possible the phase A phenomena.

Nine organizations from six countries took part in this phase B exercise using the codes ICARE-1, ATHLET-SA, KESS, MARCH3, BUTRAN and RELAP-SCDAP [5].

The conclusion was that Phebus FP was capable of simulating quite well the phenomena in a reactor but it is difficult to predict in advance the precise degree of degradation. This is partly because modelling degraded core is difficult and partly because there are

unresolvable difficulties in knowing the precise thermal properties of the shroud that surrounds the rod bundle. This last problem was also encountered in other experiment like PBF, Phébus-SFD and CORA. Sensitivity studies showed that the system pressure in a relatively unimportant parameter.

The next set of calculations, devoted to the dimensioning verifications phase to check the geometrical characteristics of the test components, was based firmly on the first Phebus-FP test FPT0 [6]. There were six participating organisations to this benchmark exercise ; six different codes were used : ICARE-1, ICARE-2, ATHLET-SA, KESS, CORMLT and BUTRAN. This time, everyone was using the same boundary conditions, so detailed comparison of the results was made. Some hydrogen was injected at the end of the transient in order to have a representative composition of the carrier gas for chemistry.

The predictions agreed well about certain basic points ; the proposed boundary conditions leads to high cladding oxidation but without steam starvation. There were, however, disagreements about the degree of core degradation to be expected. These disagreements were investigated and some found to arise from differences in choices in modelling made by the participants. Even in the period before large degradation there were important differences ; for instance, in the timing of the oxidation runaway. Although temperatures at the hottest part of the bundle showed some similarities the difference in temperature at the outlet was large due to different convective heat transfer correlations used. It was realised, at this stage, that the fission product releases were overestimated by the codes because the CORSOR type approach used by all the participants is not really valid for fresh fuel.

After this benchmark, codes capabilities were improved especially concerning the models for zircaloy oxidation, clad embrittlement, melting, eutectic formation and candling.

A new set of calculations, devoted to boundary and initial condition adjustment to define a preliminary test protocol, and called exploratory calculations, has been performed by four participants using three codes : ICARE2v1, ICARE2v2p and KESS [7], [8]. Agreement between the codes was generally better than before but outlet vapour temperature remained an unresolved issue. KESS predicted a much higher value than ICARE and sensitivity studies showed that the Nusselt number alone was not responsible. This temperature is important. If it is too cold, then fission product vapours will condense too soon. If it is too hot, then we risk burning out the heater elements in the vertical section above the core.

## 2.2 LATEST EXPLORATORY CALCULATIONS

Originally the objectives for the FPT0 test had included a low clad oxidation. This was shown to be impossible without steam starvation and so this objectives was dropped.

The following set of calculations [9,10] included the latest information from the experimental team concerning material properties. In particular, the recommended conductivity for the porous zirconia in the shroud has increased by a factor six in the high temperature region. This has necessitated a doubling of the nuclear heating in the bundle to balance the increased heat losses. In addition, the flow rates have been increased with respect to the previous values in order to reduce heat losses at the top of the bundle. The higher value of shroud conductivity would otherwise have led to unacceptable cold fission products at the bundle exit. The flow rate are now at the right side of the range considered representative of reactors. The boundary conditions are presented in figures (1) and (2).

The results of the seven calculations are presented below. These were performed by six organisations. The code used in each calculation is summarized in the table below. Each calculation is given a label which is used as an identifier on the overlay plots.

ORGANISATION	CODE LABEL
Centro de Investigaciones Energeticas, Medioambientales y Technologicas (CIEMAT), SPAIN	ICARE-2V 1 CIEMAT
Catedra D Tecnologia Nuclear, Universidad Politecnica De Madrid, Madrid, SPAIN	MELCOR Madrid
Joint Research Centre, Ispra, ITALY	ICARE-2V 2P JRC
Joint Research Centre, Ispra, ITALY	ICARE-2V 2P Grids
Institut de Protection et de Sûreté Nucléaire (IPSN) Cadarache, FRANCE	ICARE-2V 2mod0 CEA
Gesellschaft für Reaktorsicherheit (GRS), Garching, GERMANY	ATHLET SA GRS
Institut für Kernenergetik und Energiesysteme der Universität Stuttgart, GERMANY	KESS-III KESS III

There are three different ICARE versions used : the oldest version ICARE-2V1 and the most up to date is ICARE-2V2mod0. ICARE-2V2P, used was a preliminary version of the mod0 version and, since it was not an official version, was not fully quality controlled.

The 'grids' calculation, performed by JRC was the only ICARE calculation to include the spacer grids and stiffeners.

The fuel temperature halfway up the bundle is presented on the figure (3) ; Up to 2000 seconds there is a relatively high heat-up rate, caused by the exothermic chemical reaction between the zircaloy of the clad and steam. This is the first phase, the oxidation phase. At some time between 2000 and 3000 seconds most of the clad is oxidized so the reaction stops and the temperatures fall. The second phase of the transient then starts. The increasing nuclear power then leads to a slow heat-up till the fuel melting temperature around 3100 K is reached. Then the third phase, the cooldown, starts.

The oxidation phase is difficult to calculate and the results depend on the assumption used by the codes (figure 4). ICARE-2V2mod0 predicts that the rods burst at 1100 K and so oxidation can proceed on the inside of the cladding as well as the outside for some of its length and this effectively doubles the oxidation rate. On the contrary, ICARE-2V1 calculation does not allow oxidation after the rod burst on the inner surface of the cladding so the cladding can reach the melting temperature of zirconium before it is completely oxidized. Secondly, in the early version of ICARE-2V2P used for this calculation, oxidation stops once melting starts. Moreover, the GRS (ATHLET-SA) and CEA (ICARE-2V2mod0) calculations oxidise earlier. By 2000 seconds the central part of the bundle is fully oxidized. The standard JRC calculation (ICARE-2V2P) shows similar trends to the other two except it becomes fully oxidized a little later. During the oxidation runaway, the coolant never reaches 100 % hydrogen so the oxidation reaction is never steam-starved. This was intentional because an objective of the first test is that the coolant should always be oxidizing.

Afterwards, during the second phase of the transient, agreement between the different codes for the fuel is good.

Concerning the outlet vapour temperature shown on the figure (4), there is a peak between 1700 and 2500 seconds at the time of the oxidation runaway and a drop thereafter as the flow rate falls, the heat losses rise and the oxidation is nearly complete in the hottest zone. One noticeable difference from previous calculation exercises is the general agreement for outlet vapour temperature. The large differences between ATHLET-SA and ICARE showed in the previous calculations [6,7] have narrowed considerably. MELCOR, used here for the first time for Phebus-FP calculations shows a slightly different trend to the others but the difference is, at most, 300 K. Compared to previous efforts this is good agreement.

The core degradation starts at around 1400 seconds with the relocation of the molten control rod when the stainless steel guide tube fails. During the oxidation phase, calculations indicate that the cladding will remain in place and there is practically no eutectic formation due to the quick oxidation. Towards the end of the transient, the melting point of the clad zirconia and the fuel melting are reached more or less simultaneously so degradation and relocation occur. The flow area reduction inside the bundle according to the relocation is shown in figure (7) at the end of the heat-up phase.

This proposed scenario succeeded in producing a large amount of melted fuel (15 %, figure 6) and almost certainly a large fission product release (figure 8) in a oxidizing atmosphere which were the main objectives of the test.

Since the last benchmark calculation, due to safety and technological problems, the shroud design and the insulator used (less porous) have been changed ; also new wishes concerning the test conduct appear : it is necessary to check the thermal balance of the test train with steady states at the beginning of the transient. Therefore, a new scenario was proposed and a new set of calculations is presently under way. Preliminary results for the bundle are summarized below.

The scenario is now divided into 5 phases : the first phase with low vapour inlet flow rate and 3 temperature plateaux is devoted to the thermal checking ; then the following phase is a transition phase to increase the vapour flow rate before the oxidation runaway to avoid steam starvation. The following phases are identical to the previous presented scenario : oxidation phase, heat-up phase and cool-down phase. Objectives of this last phases are similar to the previous scenario so identical thermal behaviour was expected. The maximum of the driver-core power has been fixed to reach 15 % of molten fuel (figure 9) and the steam flow was adjusted in order to have oxidizing conditions throughout the transient and a correct temperature for the gases existing the bundle to avoid cold points or the burn-out of the heaters located above the bundle in the vertical section. In order to verify these objectives, the modelling of the test train has been done up to the top of the second heater, nearly 1 meter above the bundle exit. Also modelling of the grids and stiffeners was added (figure 11) in this latest scenario there is no more hydrogen injection.

Three temperature plateaux are performed at 720 K, 870 K, and 1170 K. During the two first plateaux, the bundle geometry is not modified : the test can be stopped if disagreement between calculation and experiment is found to be too large. A third plateau was necessary at higher temperature to obtain higher radiative heat transfer. During this last plateau, ballooning then burst of the clads are calculated ; but release of the fission product is negligible due to the use of a low irradiated fuel. Also molten material of the control rod remains in the clad. At the end of this phase, the cladding oxidation is low (13 %). As expected, the effect on the checking phase is small on the following phases.

For the last phases, the calculation shows similar trends to the previous scenario concerning temperatures (figure 10) and core degradation (figure 12), 15 % of molten UO<sub>2</sub>). The outlet vapour temperature is hot enough to avoid a cold point but not too hot to burn-out of the heaters (figure 13).

The fission product releases has been calculated with a CORSOR like correlation fitted on the PBF-SFD1.1 experiment where fresh fuel has been used [11]. Contrary to the CORSOR calculation, releases of the fission product occur quite late : 83 % of the volatile fission products are released (figure 14) instead of nearly 95 %. This results is confirmed by a more mechanistic calculation performed with the FREEDOM code [12].

### 2.3 MAIN PROBLEMS ENCOUNTERED

A precise knowledge of material properties (emissivities, conductivities and expansion coefficient for gap closing in the shroud) is of an extreme importance for having a good prediction of the thermal behaviour of the bundle. Different sensitivities studies have been performed to evaluate the effect of the uncertainties of each parameter on the test. Also the test conduct (plateau phase) can help to fulfil the test objectives.

Concerning the computer codes used, threshold effects affect the convergence of the results ; but the using of different codes by different people limits this last effect as well as the user effect (user parameters and user modelling). Differences can be explained by the analysis of the different results and often the differences can be narrowed after sensitivities calculations on user parameters or user modelling. Also, codes are often still under development and not always well assessed ; some phenomena modelling are still missing or too simple (debris bed formation, fission product release). So engineering judgment is often necessary. New codes are also under use to calculate the debris bed formation with SCDAP for instance or the fission product releases with FASTGRASS, VICTORIA and MITRA.

### 3 CIRCUIT STUDIES

By circuit we mean from the bundle exit to the containment entrance and, so far, these calculations have been performed in two phases ; first the thermal hydraulics then the fission product transport. In a reactor the decay heat of deposited aerosols would be expected to heat the pipe walls and thus feed back to the thermal hydraulics but this effect will be negligible in Phebus. It is therefore reasonable to perform the calculations uncoupled.

In Phebus, unlike in a reactor, most of the pipe walls are heated to a fixed temperature so the thermal hydraulic codes do not have to calculate them. The first exception is the part of the vertical line just above the bundle exit which is expected to be at such a high temperature that heater elements placed there would burn out.

The second exception is the steam generator entrance where the fluid temperature falls from 700 °C down to 150 °C on a length which varies with its mass flow rate.

Clearly having the wall temperatures defined makes the job easier for the thermal hydraulics codes. Furthermore, in FPT0, the coolant flow will always be single phase vapour. Originally, as we shall see, it had been proposed to allow condensation in the steam generator but this scenario has now been postponed to a later test.

As with the bundle calculations it has been a policy to perform calculations with as many codes and as many users as possible and to have a critical analysis of the results. Some of them will be presented below.

### 3.1 SUMMARY OF THE INITIAL STUDIES

In the Phase B exercise four different cases related to the conditions of ; TMLB', AB, S2D and Bypass sequences were calculated. Although none of these correspond precisely to the FPT0 test protocol which had not defined at that time, some of the conclusions are still valid.

There were six participants, from four countries, to the exercise. For the thermal hydraulics TRAC, ATHLET-SA and RELAP5 were used. Everybody used TRAPMELT for the fission product transport except for UKAEA who used VICTORIA. Although VICTORIA has the capability of calculating chemical equilibria this option was not used. These studies had put in light some trends.

The vertical line just above the bundle exit in Phebus FP is shorter and colder than would be expected in a reactor. The dominant retention mechanisms were therefore thermophoresis and wall condensation whereas gravitational settling would dominate in a reactor. Therefore it was decided to abandon the idea of representing the reactor upper plenum in PHEBUS.

Regarding the aerosol retention in the steam generator, Phase B calculation results have demonstrated that trapping is mainly located along the first metres of this component and a half height mock-up is sufficient in the PHEBUS facility.

All the results of this exercise have been summarized in [6].

After this first stage of the test preparation mainly devoted to appreciate the representativeness of the circuit, dimensioning of the actual components was initiated.

The participants to this dimensioning exercise are summarized in the table below. Generally primary circuit aerosol codes, unlike those that are used in the containment, do not model diffusiophoresis. During the "cold" steam generator phase this is expected to be a significant and dominant mechanism. CEA made a calculation including this process. None of the other codes modelled it. CEA was also the only group to include the feedback effect of the rising pressure in the containment [8].

ORGANIZATION	THERMAL HYDRAULIC CODE	DEPOSITION CODE
CIEMAT MADRID, SPAIN	TRAC	TRAPMELT
JRC ISPRA, ITALY	MERGE (modified for PHEBUS boundary conditions)	TRAPMELT
CEA/IPSN CADARACHE, FRANCE	CATHARE 2	TRAPMELT
CEA/IPSN CADARACHE, FRANCE	CATHARE 2	TRAPMELT with diffusio
EPRI USA	PSAAC	RAFT (version received from Argonne - January 1990)

The inlet conditions for these calculations were taken from the results for the bundle. As has been mentioned a scenario was proposed whereby 3000 seconds into the transient the steam generator secondary side was cooled down in order to provoke condensation of steam on the primary side.

The two areas of difficulty for these dimensioning studies related to the circuit components were the unheated part of the vertical line just above the bundle exit and the "cold" steam generator. Regarding the unheated part, it was found essential to nodalize this region rather finely and to take into account the radiative heat transfer.

During this exercise it was realized that none of the major thermal hydraulic codes had adequate models for wall condensation in the presence of hydrogen. This was one factor in the postponement of a cold steam generator till a later experiment. It is thought that advantage will be taken of such a delay to develop adequate models and to check them on a PHEBUS scale 1 companion facility.

Regarding aerosol trapping inside the circuit and the steam generator, it was seen that most of the fission products and the structure material released by the bundle arrive in the containment if the cold phase of the steam generator is disregarded.

All the results for this dimensioning verification exercise are summarized in [5].

### 3.2 EXPLORATORY CALCULATIONS

In the same way as for the bundle calculations, the analysts of CEA, JRC and PHEBUS partners are involved in the exploratory phase of the test preparation in order to define a test protocol for the circuit.

Exploratory calculation exercise for the fission product behaviour is at present ended with circuit input conditions, i.e carrier gas and F.P and aerosol mass flow rates from the bundle calculated by CEA using ICARE2V2 with CORSOR, and temperatures in the circuit deduced by CEA using CATHARE2.

A rather large number of contributions to these exploratory calculations were received from the PHEBUS FP programme partners. Some of these calculate chemical equilibrium as well as aerosol transport.

Some of the existing circuit calculation result will be presented here after. These results have allowed to define a Provisional Test Protocol [13] from which the Final Test Protocol will be issued at the end of the year 1992.

#### 3.2.1 THERMAL HYDRAULICS OF THE CIRCUIT

As mentioned previously, the main interests of the circuit thermal hydraulics are the thermal gradients both at the bundle exit and at the steam generator entrance.

Regarding the temperature of the pipe wall just before entering the heated pipe section, figure (15), the calculations from CATHARE2 code demonstrate that the provisional test protocol conditions are acceptable both for the technological constraints and scientific purpose of minimizing Cs, I, Te vapour condensation. The level of sleeve burn out (1100 °C) is never reached during the test and the wall temperature along the no heated length is practically always above 600 °C during the fission product emission period. Nonetheless this result has to be treated with caution as it is rather dependent on outlet gas temperature and axial conductivity both in the structures and the gas.

The variations of the carrier gas temperature and velocity can be found on the figures (16) and (17). The gas temperature first decreases down to 700 °C along the vertical line, then is maintained to such a level along the horizontal line. The step decrease down to 150 °C is obtained along the upwards part of the steam generator then this temperature level is maintained up to containment entrance along the downwards part of the steam generator and the so called cold line.

Regarding the carrier gas velocity field along the circuit, there is a velocity increase from 2 m/s up to 10 m/s related to the flow area variations along the vertical line followed by a small decrease associated to the gas temperature decrease. Then the carrier gas velocity is 9 m/s along the horizontal line. The flow area reduction at the steam generator produces a steepish increase of the velocity up to 20 m/s which is counterbalanced by the gas temperature decrease from 700 °C down to 150 °C. At the steam generator exit, the flow area increase produces a final velocity decrease down to 3.6 m/s approximately, this value being maintained up to containment entrance.

The location where thermal hydraulics is important is the steam generator entrance. As aerosol depletion through thermophoresis and F.P vapour condensations are driven by the temperature difference between the flow and the wall, a correct prediction of these processes requires a precise estimation of thermal hydraulic conditions. The figure (18) gives an example of the temperature and velocity variations of the carrier gas inside the steam generator.

### 3.2.2 FISSION PRODUCT RETENTION IN THE CIRCUIT

Retention in the primary circuit has been calculated by various codes at different organizations for an earlier specification of the circuit boundary conditions [14]. For the final specification of these conditions, the following codes were used: TRAPFRANCE for CEA/IPSN, RAFT and VICTORIA at JRC Ispra and at Sandia National Laboratories. Since the results obtained with the two versions of VICTORIA are very similar, only one will be presented here.

Input for primary circuit calculations was determined from the thermal hydraulic conditions provided by CATHARE2 and incoming fission product and aerosol mass flow rates deduced from the elemental release resulting of the ICARE2-CORSOR calculations. The chemical speciation of the elements that enter the circuit was defined according to the requirements of each code.

Since TRAPFRANCE does not consider chemical speciation, iodine was considered as CsI (total amount injected 64 mg), the remaining Cs as CsOH (total amount 127 mg), and Cadmium was considered as elemental vapour (total amount 10 g) at the circuit inlet section. Tellurium was assumed to have reacted with Tin from the fuel clad zirconium alloy to form SnTe (total amount 43 mg). The chemisorbtion of SnTe was not considered because the appropriate model is not yet available in the current version of TRAPFRANCE. Thus the results for this species concern its vapour condensation only.

RAFT and VICTORIA codes consider chemical speciation with a more extensive thermodynamic database for the last of them. The following elements were introduced as elemental vapours in the VICTORIA calculations: Cs, I, Te, Ba, Xe, Kr, Ag, In, Cd, Sn, Zr, Fe, Cr, Mn, Ni. The elemental vapours introduced in the RAFT calculations were: Cs, I, Te, Xe, Kr, Ag, In, Cd, Sn, Zr, Fe, Sr, Mo, Ru, Mn.

A total amount of 200 g of aerosol particles is emitted by the bundle. It was assumed that the initial aerosol distribution at the bundle exit was lognormal with a geometric mean radius of 0.1 micron and a geometrical standard deviation of 1.7 (1.6 for RAFT). Aerosol particle density is  $5 \text{ gr/cm}^3$  for TRAPFRANCE since  $\text{UO}_2$  release is vast by comparison with all but Cd vapour.

Figure (19) gives an illustration of the aerosol release from the bundle. It can be noticed that according to CORSOR the aerosol release rate decreases drastically as soon as the bundle temperature is reduced during the cooldown phase. It is thought that this behaviour is not representative of the expected emission during this phase. In fact it could be one of the important periods for the release during the test because the fuel pellets will fracture in response to thermal strain. To our knowledge there are no available models to estimate this specific emission of FPs and aerosols.

The deposition profiles at the end of the bundle transient (at 17,000 seconds) is shown for TRAPFRANCE results in figures (20) to (23). Twenty five volumes were used to represent the circuit with this code. The same circuit was divided into 30 cells for VICTORIA and 29 for RAFT.

Comparison of the results for the four major circuit components is shown in figure (24). It is apparent that the total deposition computed by RAFT is considerably higher, almost a factor of two, than the deposition predicted by VICTORIA and TRAPFRANCE. The VICTORIA results show slightly greater deposition than TRAPFRANCE. However, the dominant aerosol deposition mechanisms are the same for all three codes, as the location of most deposition. The deposition profiles and the dominant aerosol deposition processes are analyzed in terms of the four primary components in the circuit.

**1 Vertical hot line :** It consists of an unheated part of approximately 20 cm length and 7.3 cm inner diameter (first two volumes in figures 20 to 23). Along this part of the circuit, a large temperature difference between the wall of the pipe and the carrier gas enhances aerosol deposition by thermophoresis. The last part of the vertical line (the next three volumes) has a constant 700 °C wall temperature, the pipe has an inner diameter of 7.3 cm for 110 cm (volumes 3 and 4) then 4.8 cm for 110 cm (volume 5). Since the temperature difference between the carrier gas and the pipe wall decreases along this heated part, the thermophoretic deposition decreases also.

**2 Horizontal line :** It is an horizontal line with a length of 9 meters and 3 cm inner diameter (volume 6 for figures 20 to 23). As before the wall temperature is constant at 700 °C. In this region of the circuit, the dominant aerosol deposition is gravitational settling.

**3 Steam generator pipe :** It is preceded by two bends and a short contraction (nodalized by volume 7,8 and 9). The upward part of the 2 cm steam generator tube has a length of 4.5 meters (volumes 10 to 18). Along this length, the carrier gas temperature decreases from 700 °C down to 150 °C which is the temperature of the secondary side of the steam generator tube. This upward part is connected through a 180° bend (volume 19) to the downward section of the steam generator (volumes 20 and 21). A short vertical pipe section and a bend with a total length a 50 cm and 3 cm inner diameter (volume 22) connect the steam generator exit to the so called cold line.

All the codes show that most of the retention occurs along the upward part of the steam generator tube where the carrier gas temperature drops from 700 °C down to 150 °C, the wall temperature. According to TRAPFRANCE and RAFT the main deposition mechanisms are thermophoresis and FP vapour condensation. Whereas, according to VICTORIA, vapour condensation play a minor role. A correct estimation of these processes, which strongly depend of the temperature gradient, requires a fine nodalization of steam generator upward part. The TRAPFRANCE calculations uses nine volume for the first 4.5 m.

**4 Cold line :** This is the last part of the circuit from the steam generator to the containment entrance (volume 23 to 25). It is a 5 m pipe with an inner diameter of 3 cm. Its wall is maintained at 150 °C. Retention along the cold line is predicted to be small and associated to gravitational settling and bend impaction.

Consequently, all codes predict that the main location for retention is the steam generator tube and more specifically the upward part of this tube. Retention is driven by thermophoretic deposition of aerosol particles and wall condensation (the latter predicted only by RAFT and TRAPFRANCE). Typically 90 % of CsI, CsOH, SnTe and Cd depletions in the circuit are located in the steam generator tube.

The main differences between VICTORIA and RAFT predictions are attributable to [15] the Tellurium deposition profile. Neither VICTORIA nor VICTORIA contain a chemisorbtion model for tellurium species or SnTe, respectively. Further more the wall condensation is the dominant deposition mechanism according to RAFT and TRAPFRANCE, whereas VICTORIA predicts aerosol deposition as the main process. Finally the bend retention models are different in VICTORIA and RAFT.

The differences between RAFT and TRAPFRANCE are under investigation. The wall condensation models differ and the aerosol retention modelling in TRAPFRANCE are similar to those of VICTORIA.

### 3.2.3 CHEMISTRY INSIDE THE CIRCUIT

Both VICTORIA calculations show that deposition is time-dependent. The results suggest that revaporization becomes important after the final power reduction in the bundle, the total amount of deposited iodine decreases and the amount of hydrogen iodide that enters the containment increases.

### 3.4 MAIN PROBLEMS ENCOUNTERED

As it was said previously the thermal hydraulic calculations are not very complex. Nonetheless a precise determination of the thermal behaviour just above the bundle required a radiative heat transfer model including gas emissivity. The CATHARE2 model was change to better accommodate our physical conditions but, up to now it does not include the effect of the aerosol particles on the emission properties of the steam-hydrogen gas mixture.

Regarding aerosol and fission product transport results, one of the main problems is to have a relevant estimation of the release rates in the cooldown phase for which CORSOR predicts practically no release. Without such an estimation the present results have to be regarded as lower bounds of the deposited amounts in the circuit.

Large differences may be observed between the code results : quantities of FP deposited, location of maximum deposition and chemical speciation are all code-dependent. This makes calibration of instruments and planning of experimental sampling difficult. Dependency of deposition is seen with all codes on the aerosol particle spectrum, which is, in practice, largely unknown. This introduce another source of uncertainty.

## 4 CONTAINMENT STUDIES

### 4.1 SUMMARY OF THE INITIAL STUDIES

The initial information about the containment were obtained from the shared cost action phase B. There were six participants from four countries. Thermal hydraulic calculations used CONTAIN, COCMEL, RALOC, WAVCO, CONTEMPT4 and JERICH0. Aerosol calculations used CONTAIN, AEROSIM, NAUA, HAARM-DTM and AEROSOLS-B2. Some Iodine chemistry studies used IMPAIR-2. The principal results were summarized in [8]. The main findings were :

There was a large scatter in the thermal hydraulic code results. This was due partly to the codes themselves. Another reason was that the boundary conditions used by the code runners were not always exactly the same.

It was realized that there was no set of target thermal hydraulic conditions in the containment to aim for. A flexible approach was suggested instead whereby each test aimed for certain phenomena.

The dose rate in the sump was found to be too small compared to a reactor.

The thermal inertia of the vessel wall was found to be important.

The realization that the fission product inventory scaling factor was 5000 rather than 2000 led to the decision to reduce the containment volume from 25 m<sup>3</sup> to 10 m<sup>3</sup> in order to preserve chemical concentrations in the atmosphere. In addition the controversial results obtained from the shared cost action led CEA and JRC to set up a task force to look into this and other matters because the ordering of the vessel from the manufacturers was imminent. Many of the arguments used to define the geometry were either from technological constraints or from simple scaling laws but a large number of calculations were performed to check that they would work in practice. Some are reported in [16].

Apart from approving the volume change other major changes from the previous design were the sump design, the introduction of an internal condenser and wall heaters in order to have a better representation of the surface versus volume ratio and the correct amount of dry and wet surfaces. Condensation was then supposed to occur on the inner condenser rather than the outer walls which should remain dry, to easing the decontamination process.

### 4.2 EXPLORATORY CALCULATIONS

The containment thermal hydraulic behaviour is divided into four main periods. In the case of the FPT0 test (low humidity and consequently no condensation on aerosols), the first period, characterized by atmosphere temperature at 110 °C, an humidity ratio between 55 and 75 %, and no steam condensation on the walls, is the injection period (steam, hydrogen and material released from the degraded bundle enter the containment).

The second period of ten hours, with containment disconnected from circuit, is the aerosol deposition period. The atmosphere temperature is as previously 110 °C, no condensation on condenser should occur and the humidity ratio should be 60 %.

The third period is the chemistry period (3 days), with atmosphere temperature increased up to 150 °C and superheated conditions. The objective is to study the fission product chemistry and especially Iodine radiochemistry in the sump water, the atmosphere and the effect of paints in the "dirty" chemical conditions of a reactor accident.

The containment depressurization period is the fourth one.

#### 4.2.1 CONTAINMENT THERMAL HYDRAULICS

Containment calculations are only performed after bundle and circuit predictions which allow to define the carrier gas and aerosols mass flow rates to the containment.

The prediction of the thermal hydraulic behaviour of the containment is very sensitive to the heat and mass transfer correlations chosen for the calculations. Without a definitive and qualified set of such correlations it was decided to initiate scoping calculations to appreciate the uncertainties of the thermal hydraulic conditions of the containment. This exercise was related to the FPT1 test preparation, which provide more challenging boundary conditions than FPT0 test, the humidity ratio being near one. Some results of these scoping calculations are given below.

Four different codes were used with specified steam flow rate into the containment, figure (25), and heat flow onto condenser, figure (26). Heat transfer correlations were assumed laminar or turbulent ones see table below.

ORGANIZATION	CODE	WORD on GRAPHS
JRC	CONT	lami
JRC	CONT	turb
CIEMAT	CONTEMP T	CIEM
AEA, Winfrith	CONTAIN	Winf
NUPEC, Japan	MELCOR	Nupe

The results relative to the injection period are shown in figures (27) to (30). The better the heat transfer with the atmosphere is, the less the temperature rises. For example, the temperature in the Winfrith CONTAIN calculation rises less than the CONT calculation with a turbulent heat transfer correlation, the CONT result with laminar heat exchange rises most. The pressure in the containment cannot rise very much because it is already at the saturation pressure imposed by the wall temperature. The codes all agree about the pressure behaviour, so it is the difference in temperature that causes the differences in the results: the higher the temperature is, the lower the humidity ratio is estimated.

The CEA calculations related to the first three period of the FPT0 test were performed with a part of the ESCADRE code system; Namely JERICHO code for the containment thermal hydraulics, AEROSOL B2 for aerosol deposition and IODE for radiochemistry of iodine. In addition INSPECT code from AEA was used to provide an estimation of the

iodine chemistry result accuracy. Comparable calculations have been performed from JRC/ISPRA with CONT, CONTAIN and IODE codes.

The figures (37) gives the boundary conditions of the containment for the first period. In a pre-conditioning phase of one day duration, starting from an equilibrium initial state at 20 °C, the temperature of the vessel wall is increased up to 130 °C, the sump and condenser temperatures up to 90 °C within 12 hours then maintained at these temperatures for 12 other hours. At the end of this phase the bundle transient is initiated and steam, hydrogen and aerosols arrive in the containment.

This is the beginning of the 18,000 seconds of the containment period devoted to aerosol behaviour and specifically to diffusiophoresis onto the condenser structures. Figure (32) gives a comparison of the condensation rates onto the condenser structures, the sump water surface and the cold surface of the sump wall just above the water level. According to these JERICHO calculations, condensation on the vessel wall has been successfully avoided as requested both for test result analysis and containment decontamination eases. The mass of water in the sump is 88 Kg at the beginning of this period and increases according to the condensation above mentioned. The final mass of water is 122 Kg at the end of this phase, figure (33).

The humidity ratio behaviour is depicted as figure (34). At the end of the preconditioning phase and before arrival of steam from the bundle and the circuit, this ratio is around 50 %. As soon as steam is injected, the humidity varies according to the variations of steam mass flow rate but is maintained within the range 60-70 %.

After the first period of the transient, the containment is isolated from the bundle and the circuit and behaves as a closed system. Its atmosphere is driven to superheated conditions by increasing the temperatures of the vessel wall up to 150 °C and the condenser (which is now acting as an heater system) up to 130 °C. The objective of such a temperature difference between the containment wall and the condenser structures is to enhance natural convection to achieve a well mixed atmosphere inside the containment. Adjustment of the temperature difference was got from 3D calculations of the containment thermal hydraulic with the CEA code TRIO.

By this way the iodine species emitted by the sump water will be distributed all over the containment volume easing the measurements and the analyses of the iodine species concentrations. During this phase the sump water temperature is maintained at 90 °C.

#### 4.2.2 AEROSOLS INSIDE THE CONTAINMENT

The figure (35) gives an over all picture of the main depletion process for the containment transient. It will be noted no more that 25,000 seconds are required to extract the main part of the suspended mass from the atmosphere. This figure also provides an estimation of the ratio of the settling and diffusiophoresis processes. Aerosol settling is the main depletion process: 100 gr are deposited by this

process out of the 140 gr injected. The plated mass onto the condenser structures by diffusiophoresis is approximately a third of the injected mass.

### 4.2.3 IODINE CHEMISTRY INSIDE THE CONTAINMENT

The CEA results regarding the iodine behaviour in the containment has been computed with IODE code. These calculations integrate the thermal hydraulics and aerosol depletion rates previously described. The results take into account both the wet and dry surfaces of the condenser and the immersed painted surface in the sump.

The dose rate evaluation has been improved and the sump water pH is maintained at 5 by a buffer solution to be defined, in order to produce large quantities of gaseous iodine species.

For the present calculations the oxidation of iodine by O<sub>3</sub> and silver were not considered.

The distribution of the iodine mass in the various component of the containment system after 3 days are summarized on figure (36). The following trends are observed from IODE results : 77.1 % of iodine mass is in the water of the sump, 2.1 % is trapped in the paint of the painted surface immersed in the sump, 20.6 % is located in the paint of the dry condenser surfaces and only 0.2 % of the iodine mass is under gaseous species inside the containment atmosphere.

In addition to these iodine calculations directly related to the FPT0 test preparation, a benchmark exercise with several codes and participants is in progress to better define uncertainties in iodine partitions.

### 4.3 MAIN PROBLEMS ENCOUNTERED

Regarding the containment, the main problems are related to the thermal hydraulics even if the conditions of the first test FPT0 are less severe than those of FPT1 for which a high humidity ratio near 1 is requested. Any way, the control of the parameter is known to be very complex. Furthermore this quantity is highly dependent of local unhomogeneity in the vessel atmosphere or "cold points" on the vessel wall which might be associated with instrumentation penetrations. The present status of the codes does not allow to represent the containment behaviour with such a level of detail. Therefore we cannot be totally confident of our ability to obtain a correct control of the condensation rates and the humidity ratio. A preliminary programme of thermal hydraulics tests of the containment and its condenser device is planned both for appreciation of the technological constraints of these components and a correct appreciation of the code ability to compute their behaviour.

### 5 CONCLUSION

This paper has described a long programme of pre-test calculations involving many different organisations. All proposed sequences have been calculated by at least two different groups and two different computer codes. Mostly more than two have been used and this provides a quality check of the results. In the event very few input errors have been

detected and differences in results have been mostly attributed to alternative ways that complex physical and chemical phenomena can be modelled.

The first set of calculations, the "phase A" exercise, was for full-sized reactors and the results provided target phenomena that should be reproduced in Phebus. A test-circuit was then designed based on a scaling factor a 2000 and certain technical constraints. A set of scooping calculations on this geometry, the "phase B" exercise, checked this design for a number of simulated reactor sequences at high and low pressure. The conclusion was that Phebus could simulate most phenomena reasonably well but a number of design modifications would improve representativeness. The most important of these was that the circuit should be scaled by (1 : 5000 if similar aerosol and fission product concentrations to a reactor were to be reached because this is the ratio of the Phebus fission product inventory to the real case). High retention in certain pipes that were supposed to be neutral and non-representative behaviour in the containment led to separate studies of these two components.

Results from a horizontal line benchmark exercise recommended a larger diameter pipe than had been envisaged before and the containment task force looked into all aspects of the containment. They performed many calculations and examined closely the technical constraints before suggesting a smaller vessel, a sump that did not extend across the whole cross section of the vessel, an outer wall hot enough to discourage condensation and an inner structure, the "condenser", that would condense and collect water from the atmosphere.

The next set of calculations, the dimensioning verifications ("Benchmark exercise") concentrated on the first test FPT0 and calculations were sought for the whole sequence, from bundle to containment. This exercise was enthusiastically carried out by partners from many organisations. The circuit results indicated that objectives could be met apart from a phase when the secondary side of the steam generator was below the saturation temperature of the steam. This phase of the transient has now been dropped so the boundary conditions can be considered adequate. The bundle and the containment still posed problems. The trouble with the bundle was that it was found impossible to achieve an objective of low clad oxidation together with a low fraction of hydrogen in the coolant. Subsequent calculations confirmed the impossibility of this scenario in Phebus and the low clad oxidation requirement has now been dropped.

Armed with this knowledge a set of boundary conditions was proposed which offered more hope of success. Results using these from a new set of calculation showed that, although the test objectives were achievable, uncertainties in shroud properties would necessitate on line control of the power driven to the bundle. This control is based on the temperature measurements inside the bundle with thermocouples and ultrasonic thermometers and, after failure of these components, on estimated temperatures deduced from the shroud temperatures. High humidities in the containment were shown to be difficult to achieve without extensive thermal hydraulic testing of the containment vessel so it was decided to aim for a lower humidity in this

test. For the first time chemical equilibrium calculations were made in the primary circuit and, although results are available, they require more study before we can really assess the importance of chemistry in the test.

Due to the thermal uncertainties and a new shroud design to insure the safety of the test train, a new set of test conditions has been proposed : three plateaux steady states are foreseen in order to check the test train energy balance and surpass the thermal uncertainty difficulties ; the power driven to the bundle as the vapour inlet flow rate have been adjusted to recover the results obtains with the previous proposed scenario. A new calculation has been performed and the fission product releases calculated with a CORSOR like correlation fitted on the PBF SFD1.1 experiment to take into account the use of a low irradiated fuel.

Codes are being modified to predict the test better. Some of these modifications address problems that are not found in reactors such as the internal condenser in the containment ; other modifications will result in better reactor calculations as well [17].

A major sensitivity analysis was undertaken. This involved many codes and many organisations. It examined sensitivity to boundary conditions such as flow rates, sensitivity to physical properties such as shroud conductivity, sensitivity to different model for such phenomena as fission product release and core degradation, and sensitivity to numerical models, time step and spatial nodalization. The result of all these calculations were used to define a full Provisional Test Protocol [13] for the first test of the PHEBUS FP programme which is now approved by the Scientific Analysis Working group and submitted for approval to the Steering committee.

After such an extensive programme of preparatory calculations, the results of the first PHEBUS-FP test (expected to be performed in April 1993) are eagerly anticipated by all concerned. Meanwhile, preparation of the subsequent tests is also in progress.

#### Acknowledgements

The authors would also like to thank the following for their contributions to the preparation of this paper and to the corpus of Phebus pre-test calculations : Mrs Bonanni and Messrs Capita, Drossinos and Fermanjian (cea attaché at JRC) of the JRC Source term Analysis Group, Mr Herranz and colleagues of CIEMAT, Prof. Alonso and his group at University of Madrid, Mr Hocke of IKE Stuttgart, Mr Trambauer and co-workers at GRS, Messrs Powers, and Heames of Sandia, Mr Ellicot of AEA Winfrith, and last but no least Mr Akagane of NUPEC in Japan. Regarding the CEA/IPSN analyst team at Cadarache special thanks for numerous contributions to the work presented in this paper are due Mr Hidaka (JAERI attaché) for SCADP results, Mr Dumaz (CEA), Mr Kissane (former AEA attaché) and Fabre (CISI) for the CEA CATHARE calculations of the circuit thermal-hydraulics and the TRAPFRANCE aerosol transport results, Mlle Drosik (CEA) and Mr Carlucci (AECL attaché) for circuit calculations with RAFT, Mr Manet (CEA) for the chemistry calculations inside the circuit with GEMINI code, Mr Layly (CEA), Tirini (ENEA attaché) Mr Hueber (CEA), Mlle Dickinson (AEA attaché) and Mr Pignard

(CEA), for thermal-hydraulic, aerosol and chemistry results inside the containment with JERICHO, AEROSOLB2, IODE and INSPECT codes. We also thank Mss Mulet(cisi) for her contribution to the preparation of this paper.

## 6 REFERENCES

- [1] A. MARKOVINA, P. FASOLI-STELLA, A. MAILLIAT  
Review of the major predicted phenomena during FP transport and deposition in the RCS and containment building under severe accident conditions.  
International seminar on fission product transport processes in reactor accident.  
Dubrovnik, May 22-26, 1989
- [2] A. MARKOVINA, P. FASOLI-STELLA, A. MAILLIAT  
"Analytical assessment of the capability of a scaled down in pile for facility to simulate PWR phenomena under severe accident conditions".  
AAAR'89 Eight annual meeting Reno, Nevada, Oct. 10-13, 1989
- [3] A. MARKOVINA, A. MAILLIAT.  
"Scoping calculations in support of the PHEBUS FP experimental programme".  
Seminar on the commission contribution to the reactor safety research.  
Varese, Italy, Nov. 20-24, 1989
- [4] A. ADROGUER, A. COMMANDE, C. RONGIER  
"International Standard Problem ISP28, Phebus-SFD B9 + Experiment on the Degradation of a PWR Core Type".  
Note Phebus CSD 122/91 May 1991.
- [5] A. MARKOVINA and I. SHEPHERD.  
Summary of the dimensioning verification studies of the Phebus FP experiments (Phase B of the share cost actions : scoping calculations in support of the Phebus FP project) Volume 2 : The reactor coolant circuit.  
To appear as EUR report.
- [6] I. SHEPHERD, I. DROSIK, P. DUMAZ, B. FABRE, A. MAILLIAT, M. PIGNARD, A. BALL, K. TRAMBAUER, F. BARBERO, F. OLIVAR DOMINGUEZ, L. HERRANZ, L. BIASI, J. FERMANDJIAN, K. HOCKE.  
PHEBUS-FPT0. Benchmark Calculations.  
EUR 13698 EN (1991).
- [7] I. SHEPHERD, I. DROSIK, M.C. VICENTE and K. HOCKE.  
PHEBUS-FPT0. Pre-test calculations for the bundle.  
SAWG 91/019/0 (July 1991)
- [8] A. MAILLIAT and all  
Exploratory Calculations for FPT0.  
Note PHEBUS PF 91/07
- [9] I. SHEPHERD, F. SERRE, M.C. VICENTE, J.V. LOPEZ MONTERO, A. BALL, K. TRAMBAUER  
PHEBUS-FPT0. Calculations for the Reference Scenario Volume 1 : The bundle.  
EUR 14225 EN (1992).
- [10] I. SHEPHERD and F. SERRE  
Precalculations for the Bundle for the First Phebus-FP Test FPT0.  
IAEA Technical Committee Meeting, Behaviour of Core Materials and Fission Product Release in Accident Conditions in Light Water Reactors, Aix-en-Provence, France (16-19 March 1992).
- [11] D.A. PETTI  
Fission Gas Correlation  
DAP 43-91, (Nov. 1991)
- [12] B. CARLUCCI  
Phebus-FP Release Analysis Using a Microstructure Based Code  
IAEA Technical Committee Meeting, Behaviour of Core Materials and Fission Product Release in Accident Conditions in Light Water Reactors, Aix-en-Provence, France, (16-19 March 1992)
- [13] A. MAILLIAT - A. JONES  
Provisional test protocol for the Phebus FP Test FPT0.  
Note PHEBUS PF 92/32
- [14] J. FERMANDJIAN et Al  
Presentation of the results of the exploratory circuits calculations for Phebus FPT0.  
SAWG 92-035/2
- [15] J. CAPITAO and T. DROSSINOS  
Aerosol interactions and transport during the first PHEBUS experiment according to the VICTORIA and RAFT computer codes to be published, Journal of Aerosol sciences.
- [16] A.V. JONES, E. BONANNI and A. MARKOVINA.  
Principal results of the "Phase B" verifications studies in support of the Phebus FP project CSNI aerosol workshop, Fontenay-aux-Roses, September 1990.
- [17] G. HACHE, R. GONZALEZ, B. ADROGUER.  
Status of ICARE code development and assessment  
20th WRSM, Bethesda, October 1992

FIG. 1: Nuclear Power

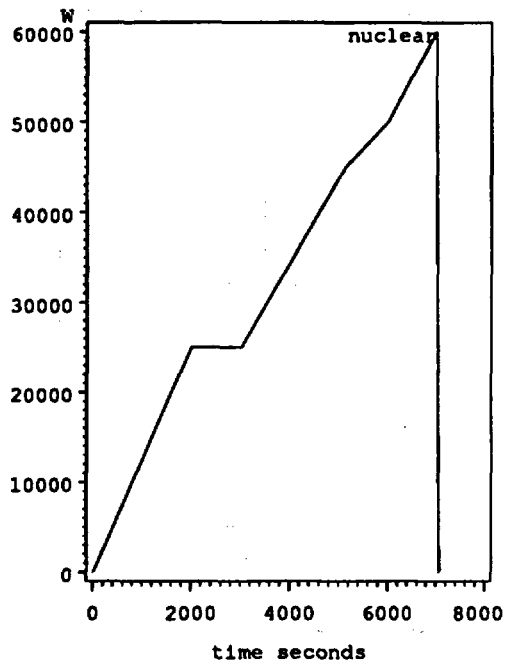


FIG. 2: H2O and H2 injection

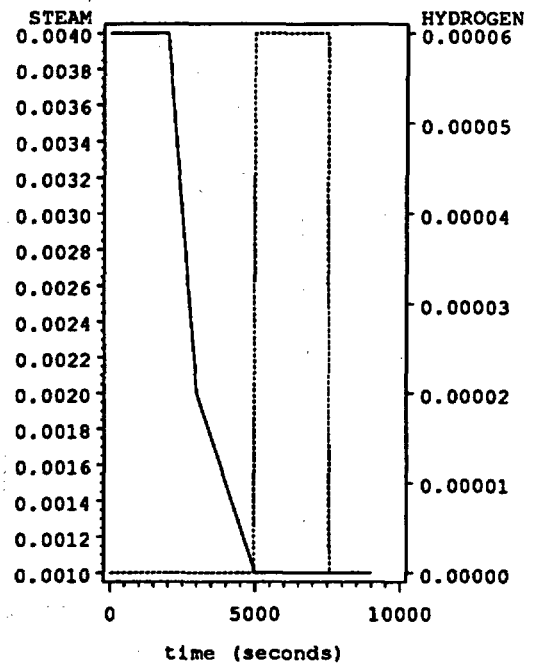


FIG. 3: Fuel temperature half way up the bundle

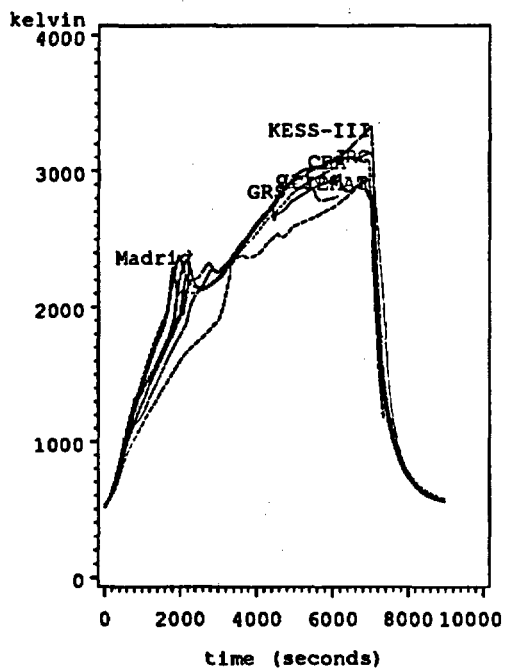


FIG. 4: Outlet vapour temperature

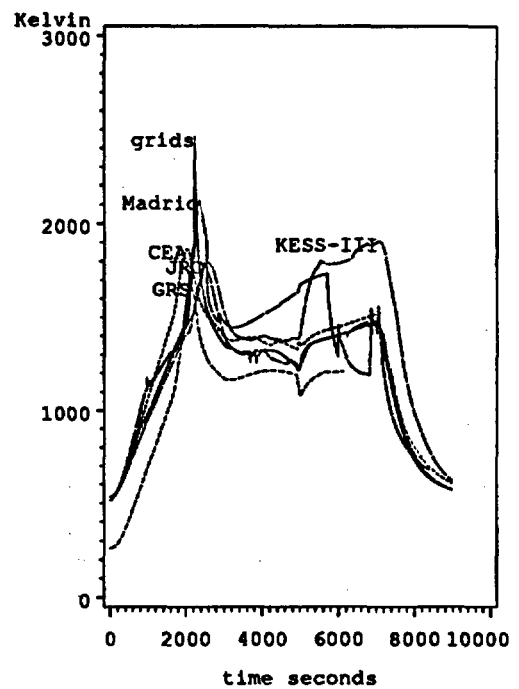


FIG. 5: Percentage of cladding oxidized

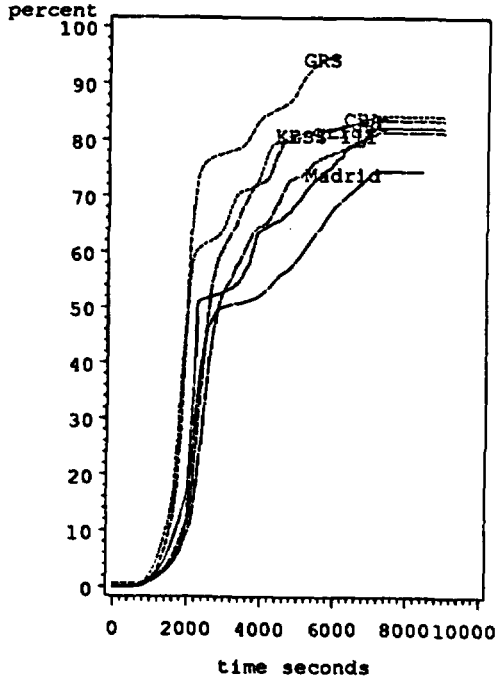


FIG. 6: UO<sub>2</sub> mass axial profile

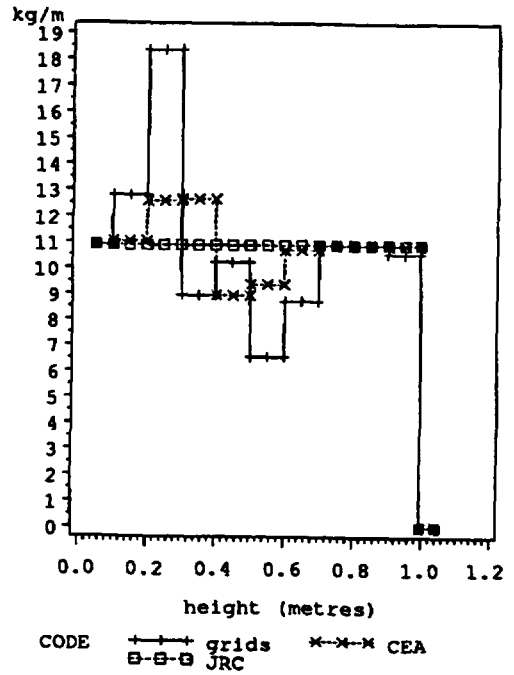


FIG. 7: Flow area axial profile

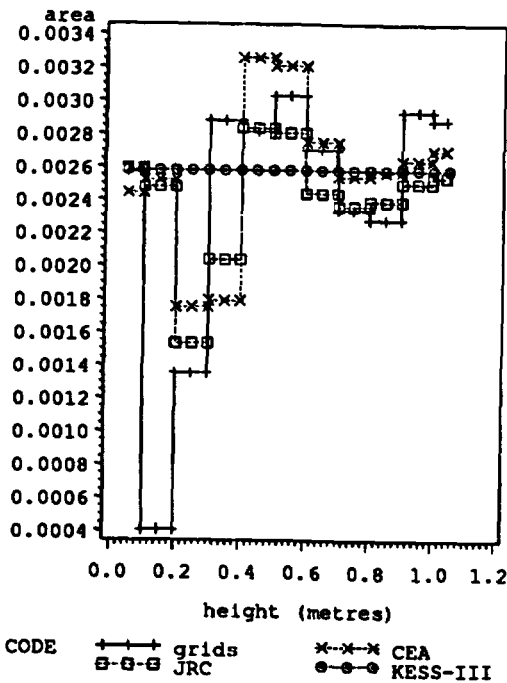


FIG. 8: Percentage of Iodine released

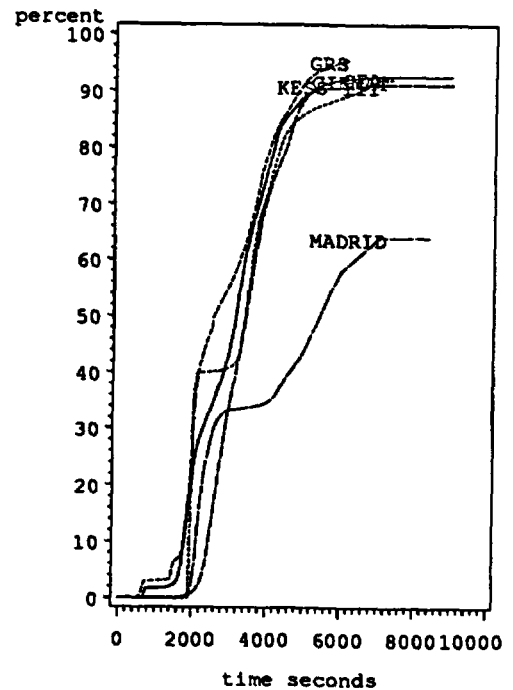


FIG. 9: Nuclear power and inlet flow rates

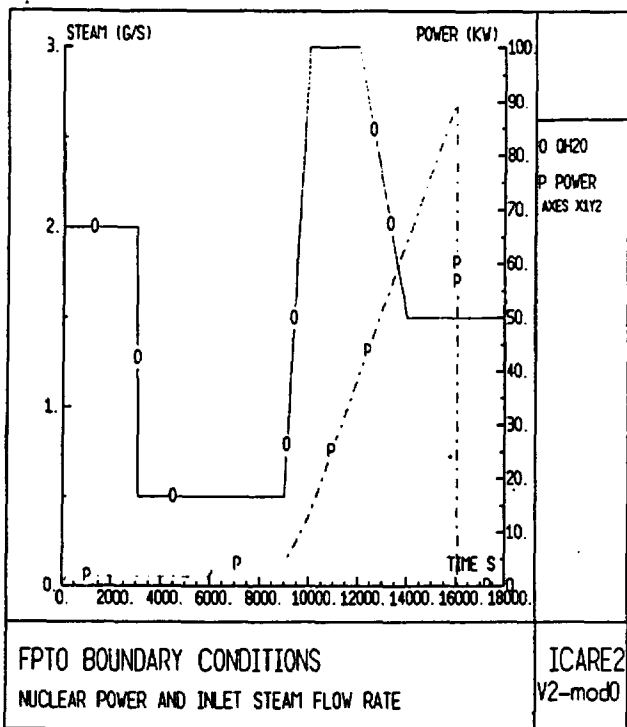


FIG. 10: Temperatures evolutions half way up the bundle

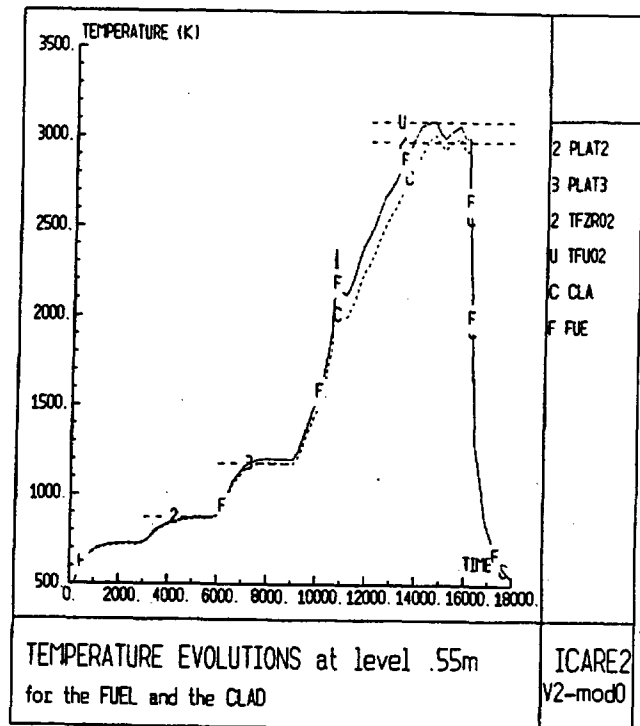


FIG. 11: Initial geometry

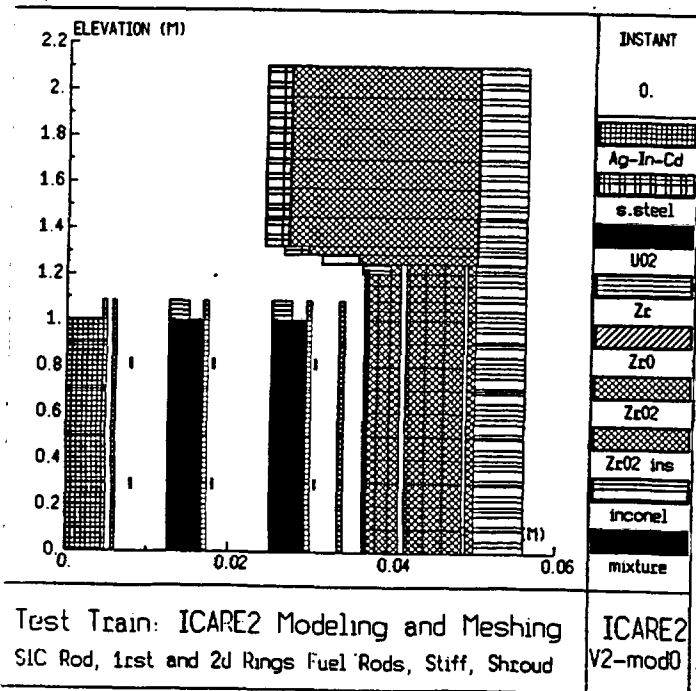


FIG. 12: Bundle geometry at the end of the transient

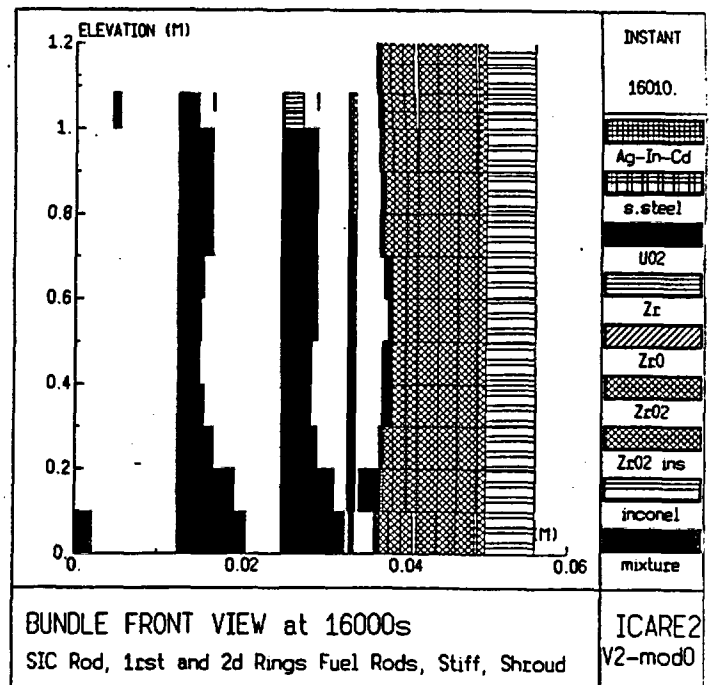


FIG. 13: Temperatures profiles above the bundle

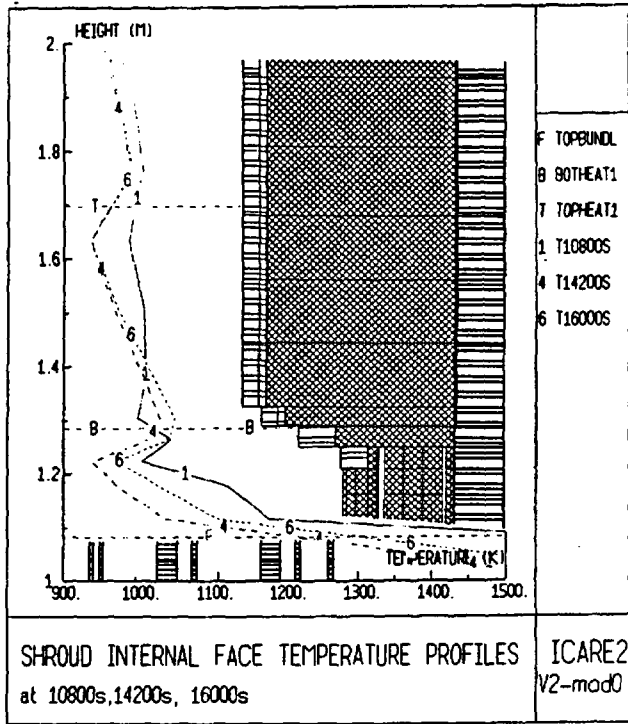


FIG. 14: FP releases

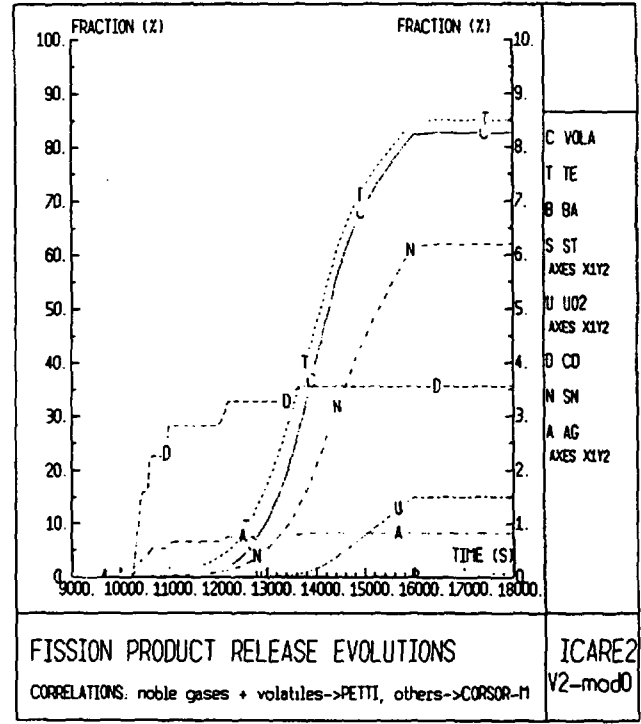


FIG. 15: Wall temperature above the bundle

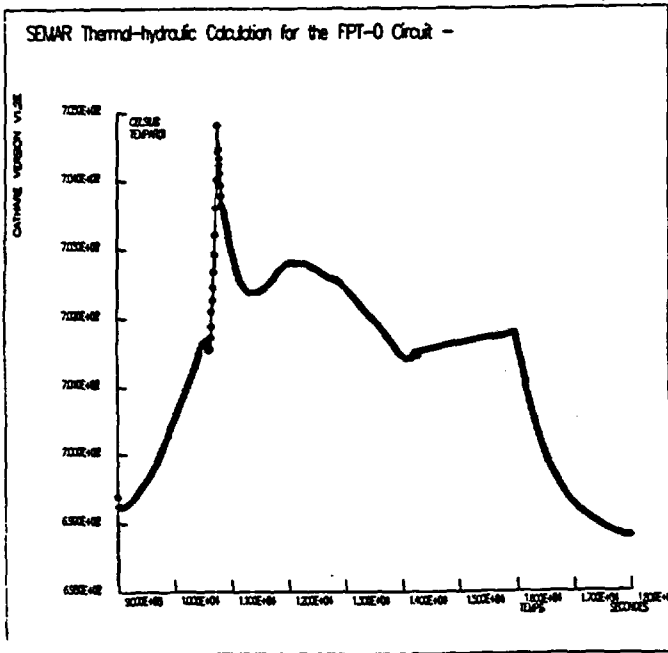


FIG. 16: Carrier gas temperature profile

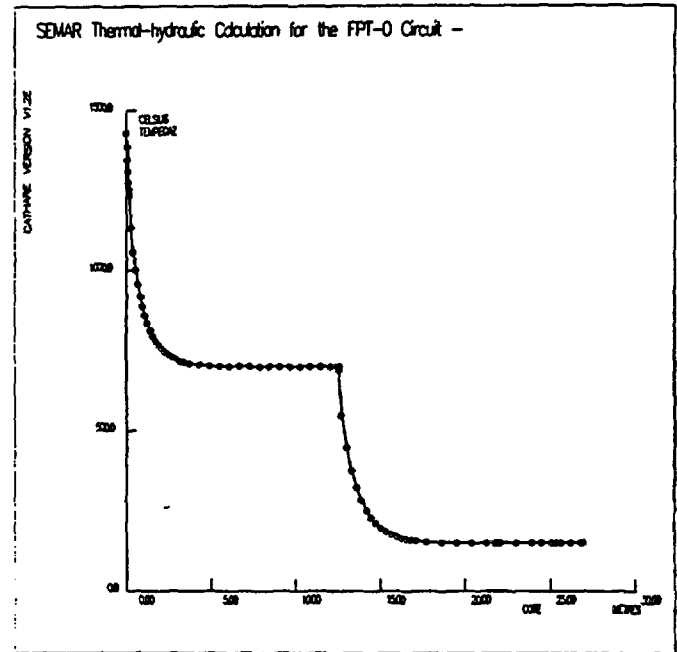


FIG. 17: Carrier gas velocity profile

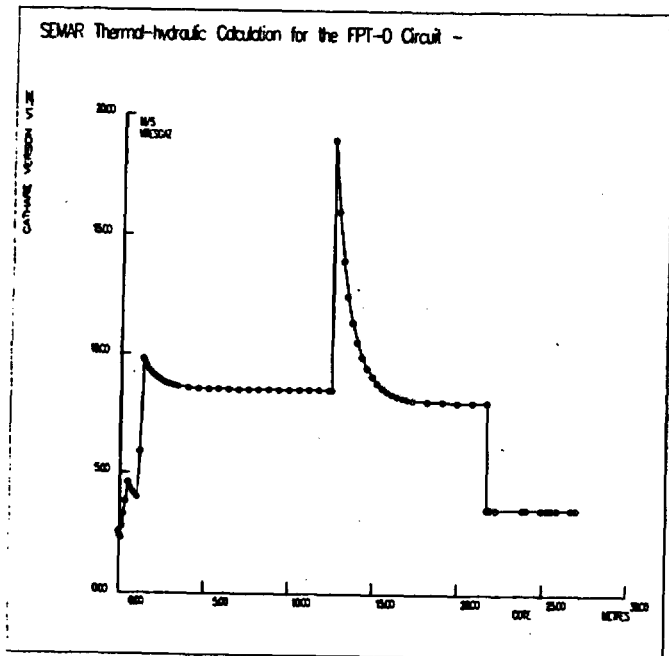


FIG. 18: Gas and Wall temperature in SG

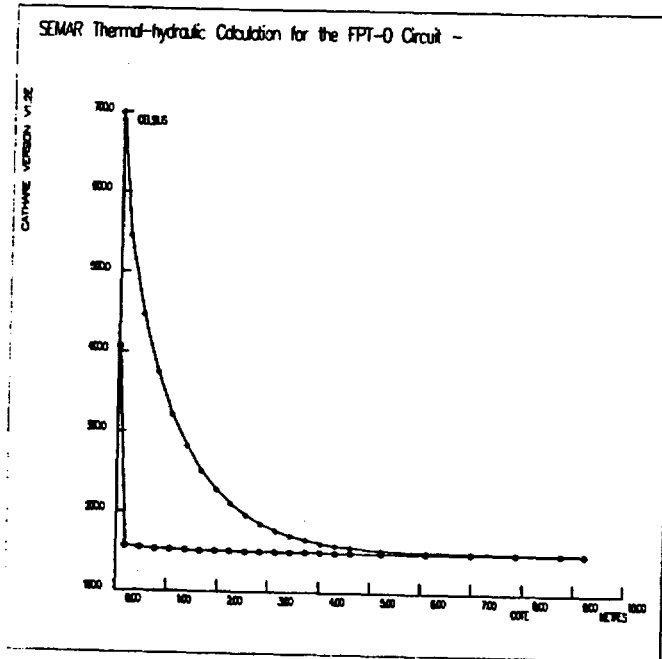


FIG. 19: Aerosol concentration at the circuit entrance

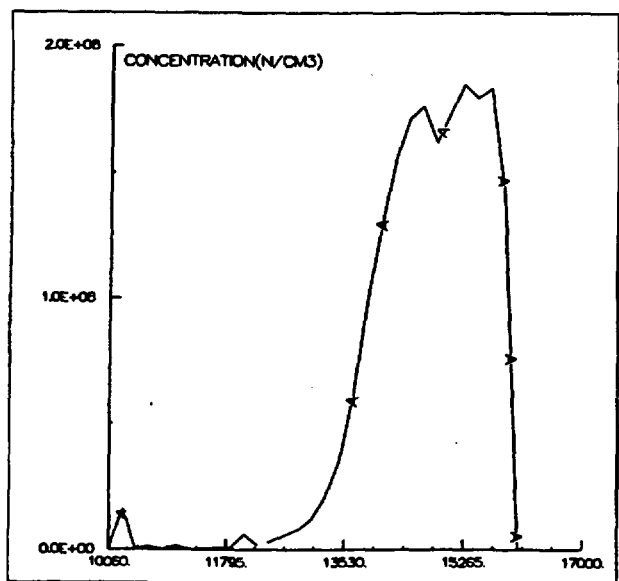


FIG. 20: Aerosol deposit profile

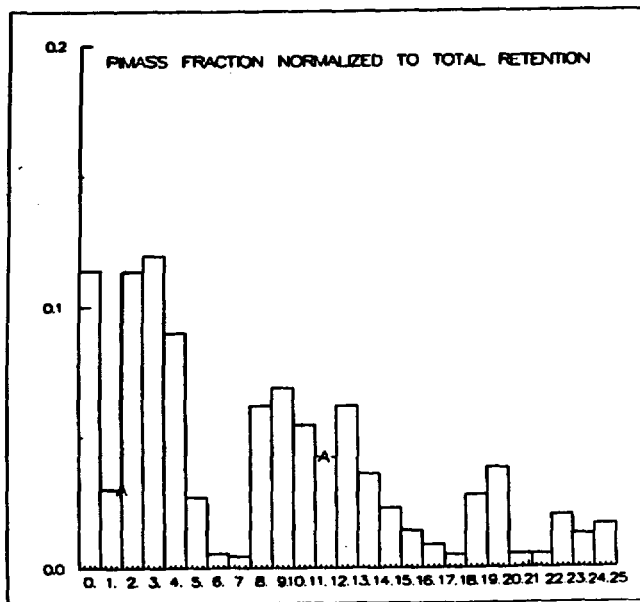


FIG. 21: CsI deposit profile

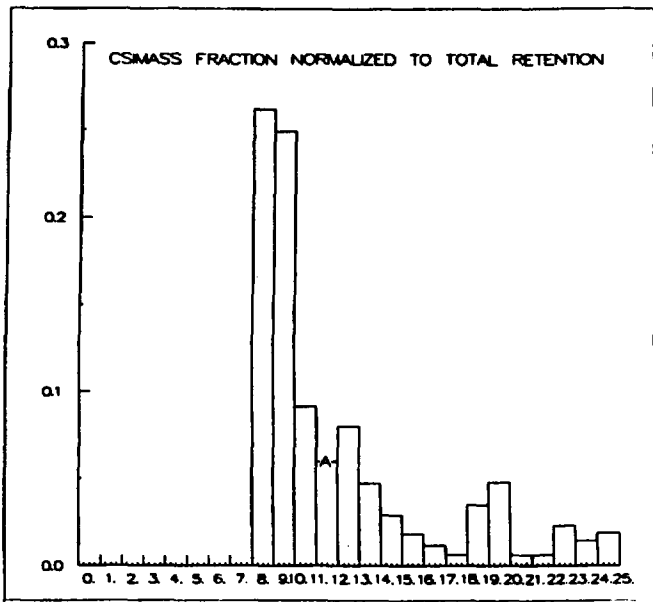


FIG. 22: CsOH deposit profile

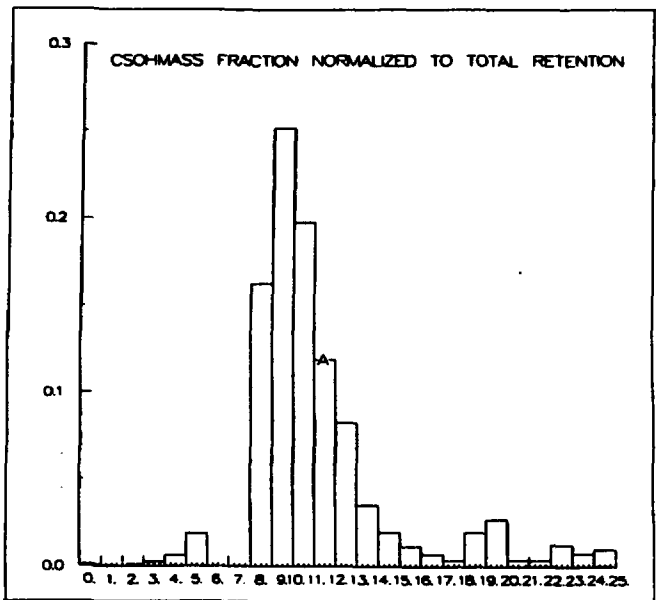
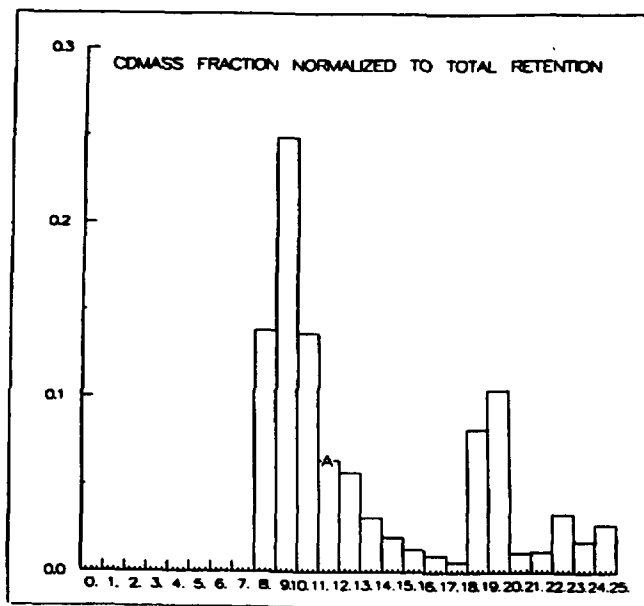
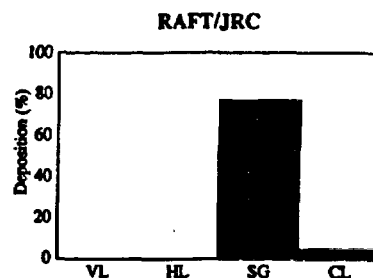
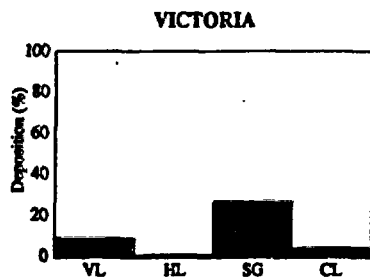
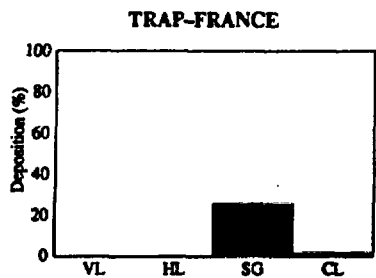


FIG. 23: Cd deposit profile

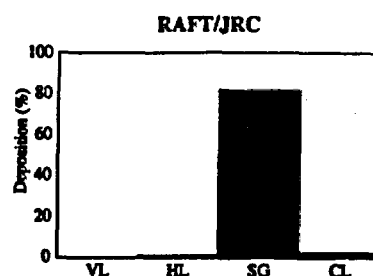
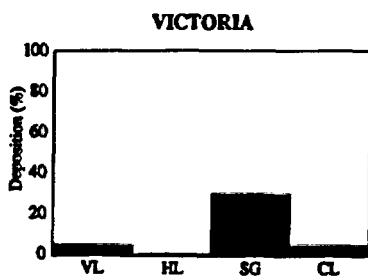
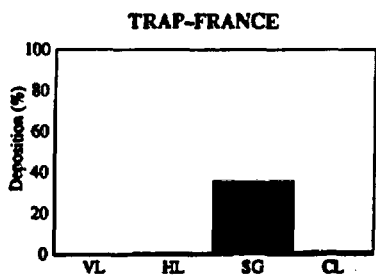


**FIG. 24: Code comparisons  
Circuit deposits**

**IODINE:**



**CAESIUM:**



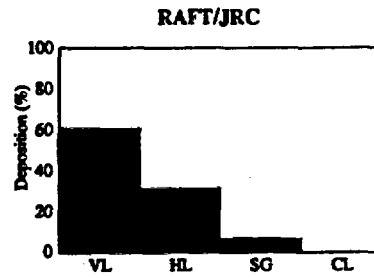
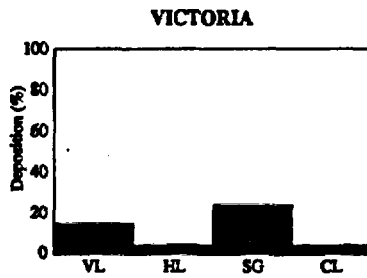
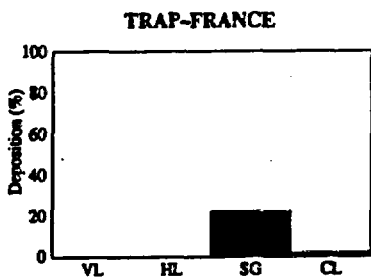
VL - vertical hot line

HL - horizontal hot line

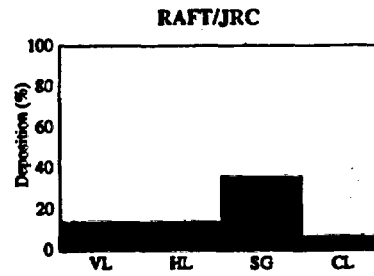
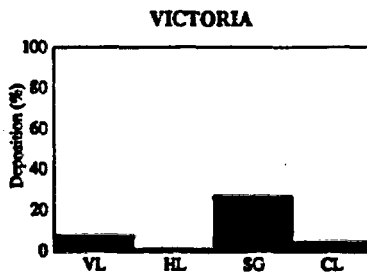
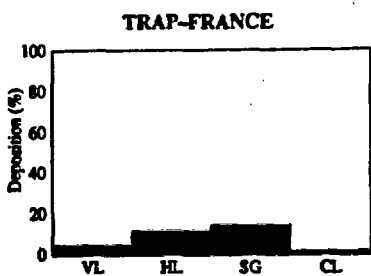
SG - steam generator

CL - cold line

**TELLURIUM:**



**AEROSOLS:**



VL - vertical hot line

HL - horizontal hot line

SG - steam generator

CL - cold line

FIG. 25: FPT1, flow rate into containment

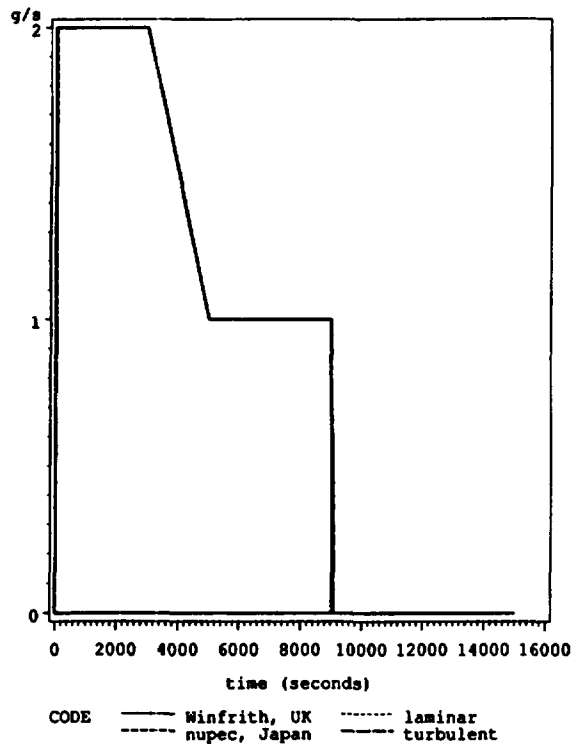


FIG. 26: FPT1, heat flow onto condenser

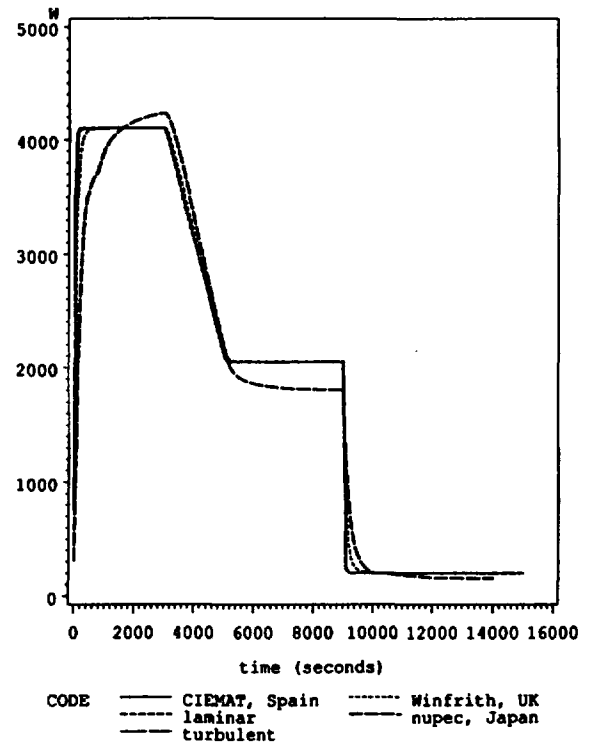


FIG. 27: FPT1, Atmosphere temperatures

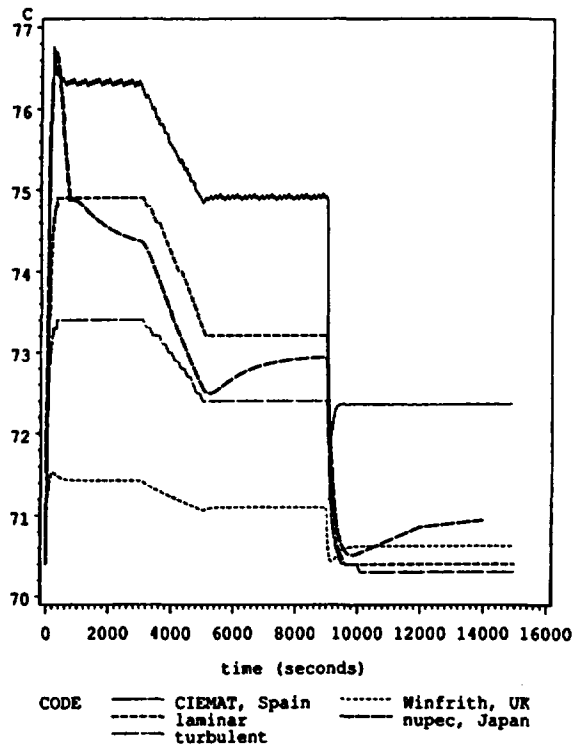


FIG. 28: FPT1, Atmosphere pressures

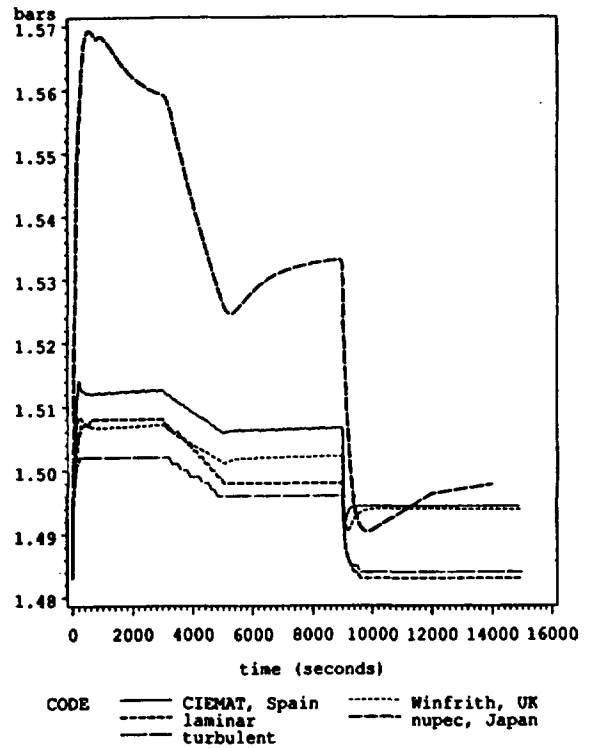


FIG. 29: FPT1, atmosphere humidity

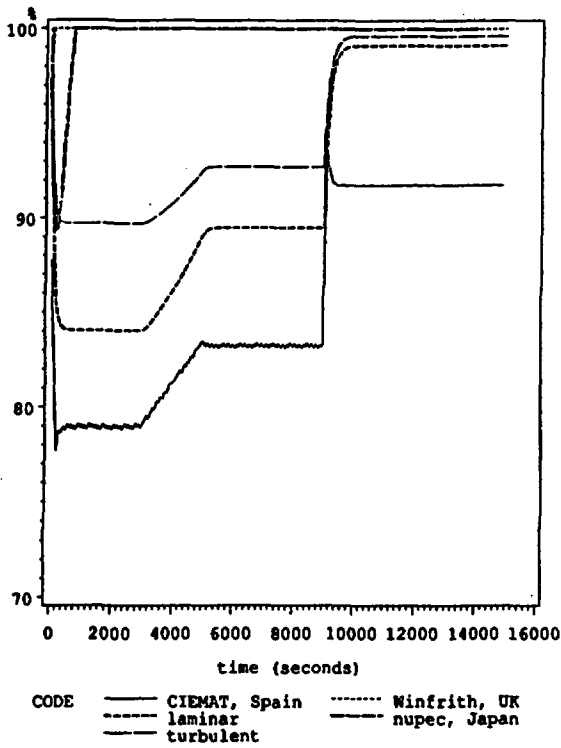


FIG. 30: FPT1, condenser temperatures

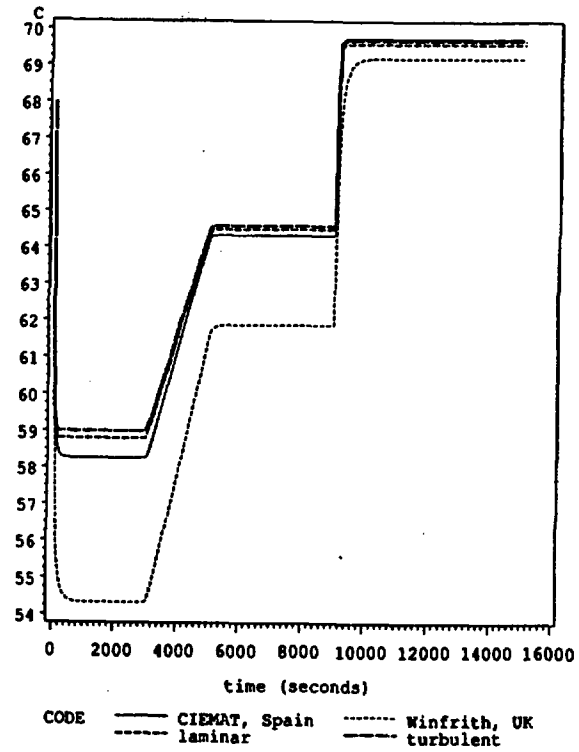


FIG. 31: Containment boundary conditions

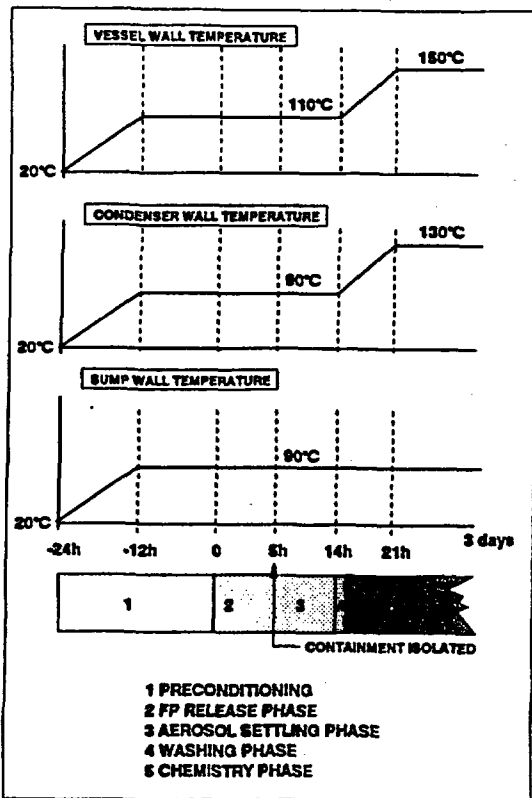


FIG. 32: Condensate in containment

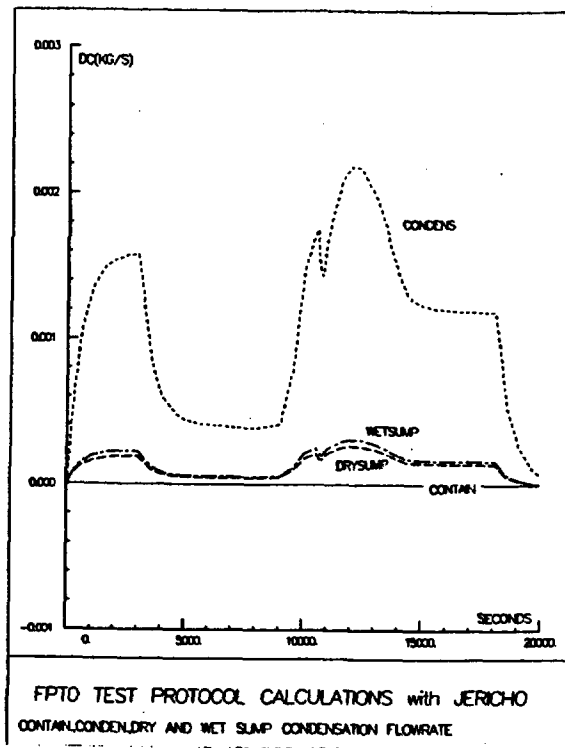


FIG. 33: Water mass in the sump

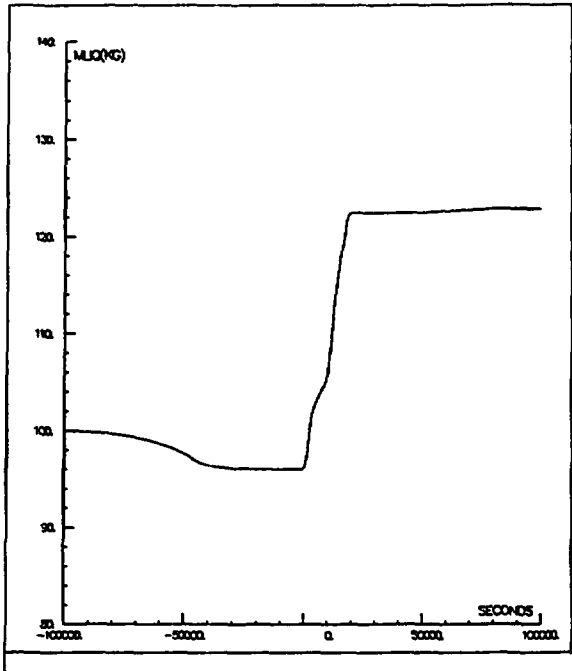


FIG. 34: Atmosphere humidity

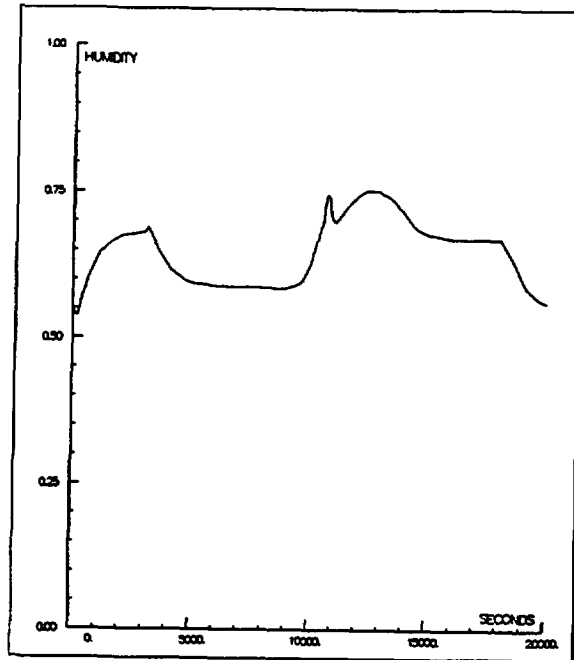


FIG. 35: Aerosol mass balance

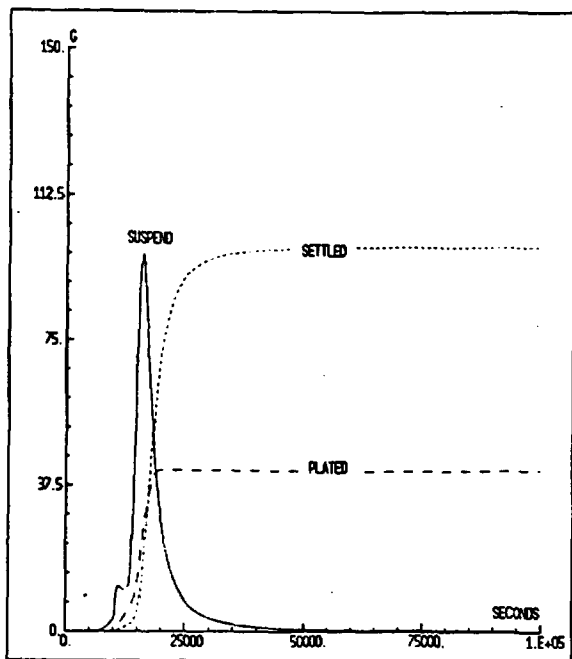
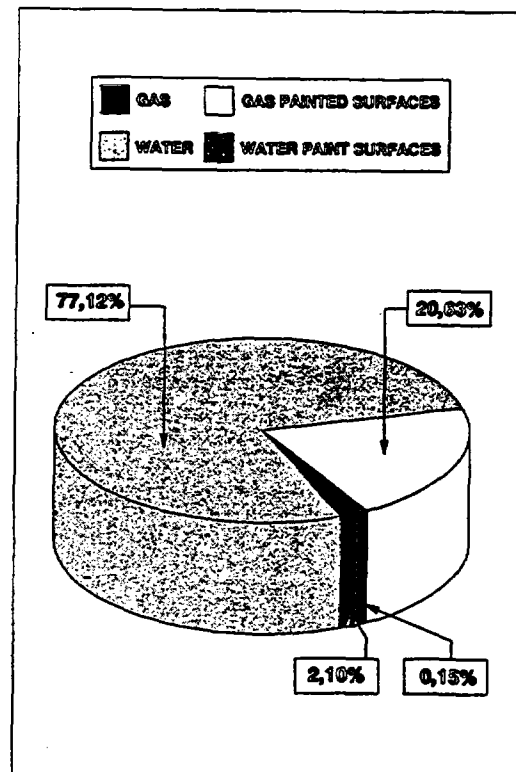


FIG. 36: Iodine mass distribution after 3 days



# COPO: EXPERIMENTS FOR HEAT FLUX DISTRIBUTION FROM A VOLUMETRICALLY HEATED CORIUM POOL

O.Kymäläinen, O.Hongisto, J.Antman, H.Tuomisto and  
T.G.Theofanous<sup>1</sup>

Imatran Voima Oy (IVO)  
P.O.Box 112, 01601 Vantaa, Finland

## ABSTRACT

An experimental facility, COPO, for studying the heat transfer from a molten corium pool has been constructed with emphasis on obtaining a detailed heat flux profile on the side and bottom boundaries. The facility is a Joule-heated, two-dimensional slice of the lower head of a VVER-440 reactor in a linear scale 1:2. In the first results the heat transfer coefficient on the upper boundary was slightly higher than that predicted from existing empirical correlations for cavities of rectangular cross section. No significant local peaking on the side boundary was observed.

## 1. INTRODUCTION

In a core melt accident of a LWR, a feasible option for arresting the progress of the accident, before the reactor pressure vessel (rpv) melt-through, is to provide cooling for the rpv bottom externally by submerging the lower part of the vessel in water. The effectiveness of the external cooling in such a case is determined by the volumetric power generation and the heat flux distribution from the corium on the rpv lower head on one hand, and by the capability to efficiently vent the steam produced from the reactor cavity to the upper compartments of the containment on the other hand.

The concept of external cooling is especially suitable for IVO's Loviisa plant (two VVER-440 units) which has a number of unique features advantageous for external cooling, like low power density in the core, no penetration in the rpv lower head, large water volumes in primary and secondary sides meaning long time delays and low decay power in case of an accident, and finally, an ice condenser containment which ensures a flooded cavity in most accident scenarios. Therefore, the external cooling of rpv is a cornerstone of the approach planned for the severe accident management of the Loviisa plant [1]. The venting of the steam, and the flow behavior outside the reactor vessel for the Loviisa case, has already been studied experimentally with promising results which indicate that a heat flux well in excess of  $1000 \text{ kW/m}^2$  would be needed in order to cause a heat transfer crisis on the outer surface of the vessel [2]. In this paper, the

---

<sup>1</sup> University of California, Santa Barbara

other key aspect of the issue, namely the heat flux distribution from the molten corium pool on the rpv lower head, is studied.

The average heat fluxes from a volumetrically heated pool with isothermal boundaries are relatively well known, at least if the Rayleigh number is low and the geometry of the pool is simple. Experimental data has been reported e.g. by Steinberner and Reineke [3] for a rectangular cavity with square cross section and with Rayleigh number up to  $3.7 \cdot 10^{13}$ , by Seiler [4] for a cylinder with aspect ratios (i.e. the ratio of height to width) 0.5 - 1.0 and Ra up to  $10^{16}$  and by Baker et al. [5] for rectangular cavities of aspect ratios 0.1 - 1.0 and Ra up to  $10^{11}$ . Numerical investigations have been done e.g. by Emara and Kulacki [6] and by Farouk [7]. For comparison, it has been estimated that the corium pool on the lower head of Loviisa reactor could have a Ra-number up to  $10^{14}$  -  $10^{15}$  and a small aspect ratio (down to 0.15 - 0.25). Furthermore, the shape of the corium pool, obviously, would not be rectangular.

Typically, the average heat transfer coefficients upwards, downwards and in the horizontal direction are correlated in terms of Rayleigh number. However, in order to assess the structural performance of a rpv wall during external cooling, the knowledge of the average heat flux alone is not enough, but also the heat flux profile and especially the peak heat flux on the side wall are needed. Unfortunately, only few experimental data on the heat flux profiles exist, those existing being for low Rayleigh numbers or for geometries different from a rpv lower head. For example, Steinberner and Reineke [3] measured the heat flux profile on the side wall of the square cavity and found significant peaking in the upper portion, but since the geometry in question differs essentially from our case, the results are not necessarily applicable here.

Therefore, in order to obtain detailed heat transfer data for a geometry similar to a corium pool on the lower head of the Loviisa rpv, a two-dimensional experimental facility COPO has been constructed at IVO's Hydraulic Laboratory.

## 2. THE COPO FACILITY

A schematic of the COPO facility is shown in Fig. 1. The basic idea is to simulate a corium pool on the lower head of a VVER-440 reactor with a two-dimensional slice of it in a linear scale 1:2. The 10 cm wide slice is bounded by two parallel polycarbonate plates. The height of the pool can be adjusted with the maximum of 80 cm. At the top, the facility spans 1.77 m. The simulant fluid is water, with some zinc sulfate added in order to adjust the electric conductivity for Joule heating. For the heating AC current is conducted through seven pairs of electrodes mounted on the surface of the polycarbonate walls. The maximum voltage used in the experiments is 30 V and the maximum power attainable, from the transformer currently in use, is 6 kW. The polycarbonate walls are covered with thick thermal insulation with peek holes for laser doppler (LDA) measurements. The facility is typically operated at maximum temperature of about 80°C.

The side and bottom walls are cooled by 56 separate cooling units, whereas on the top surface, the cooling is provided by two units. Location of the coolant units is illustrated in Fig. 2.

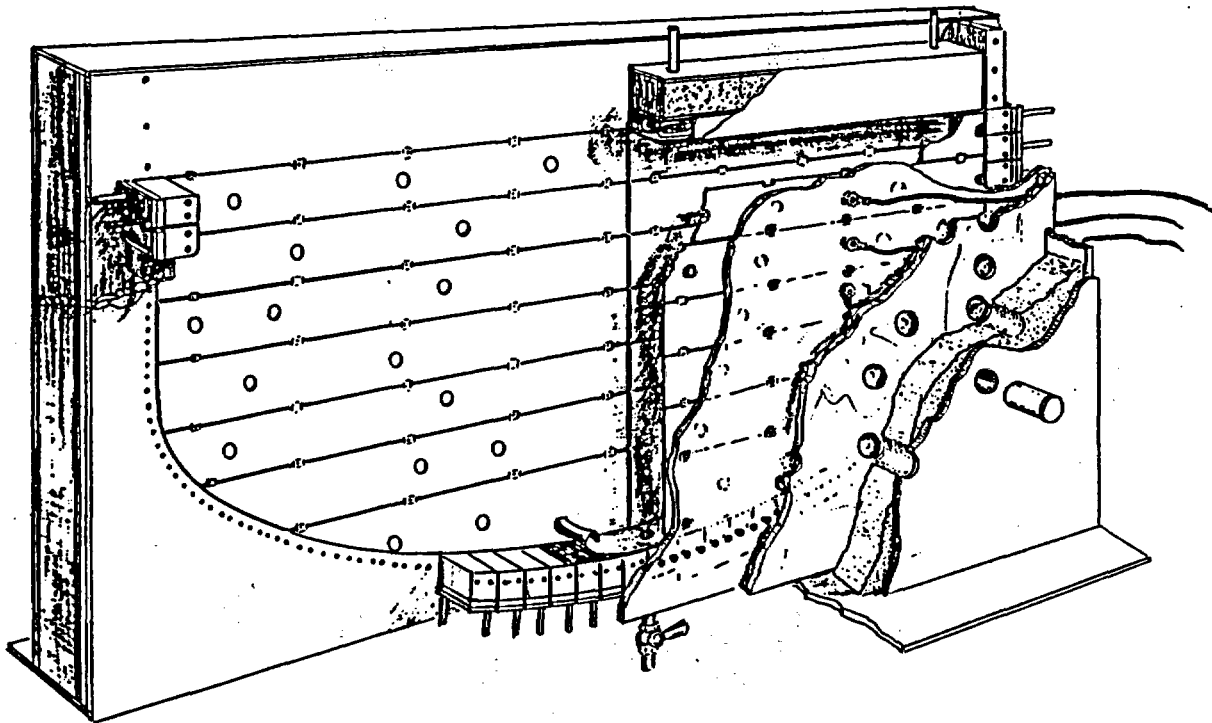


**Figure 1. Schematic of the COPO facility.**

The instrumentation of the facility consists of 260 thermocouples, coolant flow measurements, and a LDA facility to measure the local 2-D velocities inside the pool. The heat fluxes can be obtained by two independent means: first, by measuring the coolant flow together with coolant inlet and outlet temperatures of each cooling unit and second, at selected units by measuring the temperature gradient in the brass wall. The fluid temperatures inside the pool are measured with 38 stationary thermocouples.

The maximum power achievable from the facility is 6 kW which is enough in order to preserve the Rayleigh number ( $Ra = 10^{14} - 10^{15}$ ) from the full size corium pool. Depending on the assumptions used, the power of the corium pool on the rpv lower head of IVO's Loviisa plant is 11 - 13 MW, which corresponds to an accident scenario initiated by a large break LOCA and followed by a failure of the ECCS, i.e. a scenario with the shortest time delays.

### 3. RESULTS

#### 3.1. Average heat fluxes

Measured heat flux distributions upwards, sideways and downwards (denoted by "up", "h" and "dn", respectively) in the first complete runs fh1 through fh3 are summarized in Table 1. The 'sideways' (or 'horizontally') in this case was defined to comprise the cooling units 1 - 10 and 48 - 57 indicated in Fig. 2. Correspondingly, the cooling units 11 through 28 and 30 through 47 are included in the calculation of downwards heat transfer. There is no cooling in the unit

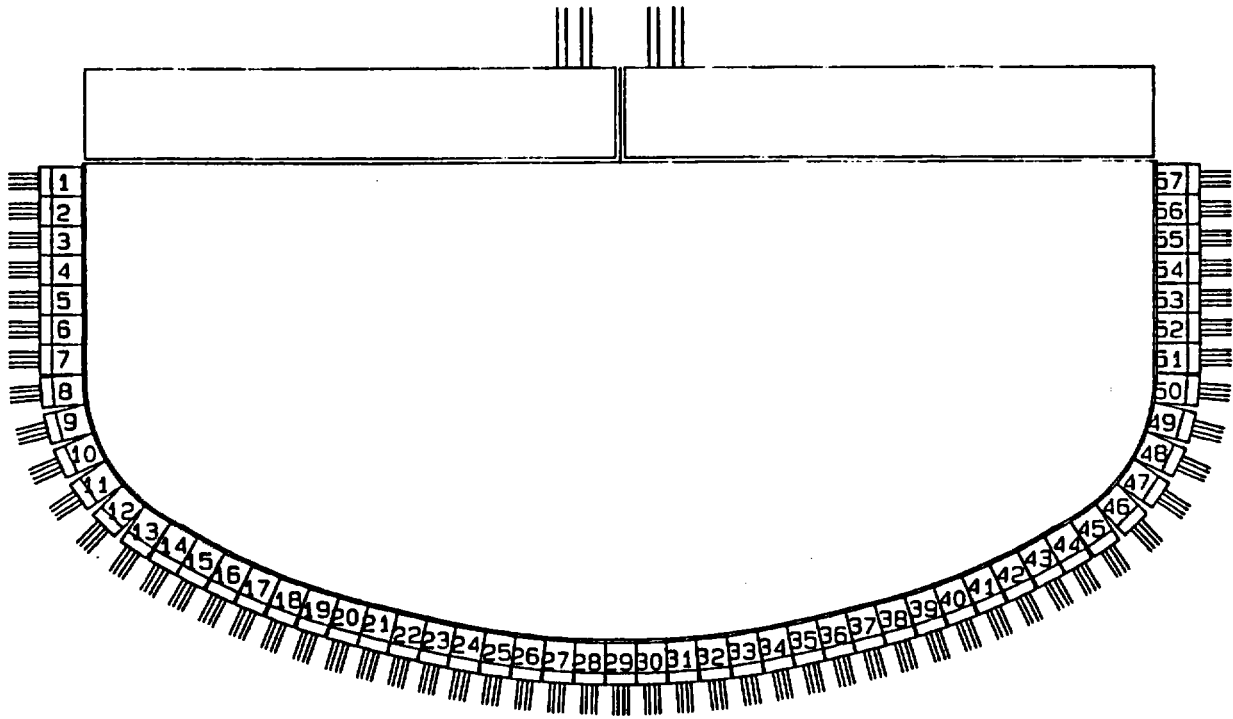


**Figure 2.** Side-wall cooling unit numbering of the COPO facility.

no. 29. The height of the pool was the full 80 cm in all the runs shown here.

$\Delta T$  in Table 1 refers to the difference between the maximum temperature of the pool and the temperature of the side wall. The upper surface was kept at the same temperature except in run fh1 where the upper surface was 2°C warmer.

The Rayleigh number in Table 1 is defined using the height of the pool  $H$ :

$$Ra = \frac{gQ\beta H^3}{\alpha\nu\lambda}, \quad (1)$$

where  $g$  = gravitational acceleration,  $Q$  = volumetric heat generation in pool,  $\beta$  = volumetric thermal expansion coefficient of the fluid,  $H$  = height of the pool,  $\alpha$  = thermal diffusivity of the fluid,  $\nu$  = viscosity of the fluid, and  $\lambda$  = thermal conductivity of the fluid. This definition of  $Ra$  (especially, the choice of the length scale) is similar to e.g. references [3],[4],[5]. For  $Ra$ , the water properties were evaluated at temperature obtained as an average between the maximum temperature of the pool and the boundary temperature.

The Nusselt number is defined as:

$$Nu = \frac{q H}{\Delta T \lambda}, \quad (2)$$

where  $q$  = heat flux,  $\Delta T$  = difference between the wall temperature and the maximum temperature of the pool.

**Table 1. Summary of the runs fh1 - fh3.**

run no.	P	T <sub>wall</sub>	ΔT	% of total power		
				up	hor.	down
fh1	4.6	59.3	14.0	70	16	14
fh2	5.2	63.7	12.6	76	13	11
fh3	1.9	55.0	5.9	71	16	13

run no.	Ra	q <sub>ave,up</sub>	q <sub>ave,h</sub>	q <sub>ave,dn</sub>	Nu <sub>up</sub>	Nu <sub>h</sub>	Nu <sub>dn</sub>
		kW/m <sup>2</sup>	kW/m <sup>2</sup>	kW/m <sup>2</sup>			
fh1	1.3·10 <sup>15</sup>	15.2	6.2	2.9	1600 (1100)	540 (630)	220 (38)
fh2	1.5·10 <sup>15</sup>	18.5	5.8	2.6	1800 (1200)	560 (650)	220 (38)
fh3	4.2·10 <sup>14</sup>	6.1	2.5	1.1	1200 (880)	440 (510)	160 (34)

The Nu numbers in parantheses are from correlations for rectangular cavities.

\* In run fh1 the upper boundary was 2°C warmer than the side boundary

For comparison, the Nusselt numbers predicted with correlations by Steinberner and Reineke [3] are given in parentheses in Table 1. In ref. [3] the heat fluxes were measured in a two-dimensional cavity of 800 mm x 800 mm x 35 mm. These empirical correlations for average upward, sideward and downward heat fluxes, written for turbulent flow in rectangular cavities, are:

$$Nu_{up} = 0.345 \cdot Ra^{0.233} \quad (3)$$

$$Nu_h = 0.85 \cdot Ra^{0.190} \quad (4)$$

$$Nu_{dn} = 1.389 \cdot Ra^{0.095} \quad (5)$$

Table 1 shows that in the present experiment the heat transfer upwards is clearly dominating.

When comparing the measured Nusselt numbers to those obtained from eqs. (3) through (5), it seems that the heat transfer up for this kind of geometry is more than for cavities of square cross-section. It could be speculated that the reason is the breaking up of the (two) large convective rolls in a case of a large aspect ratio cavity into several smaller ones in a shallower cavity. This assumption is supported by results of LDA measurements, which indicate the existence of at least four convective rolls.

There is a slight deviation also for  $Nu_d$  between the measured value and the value from the correlations (3) - (5). However, taking into account the uncertainties and the scarce data until now, it is too early to draw definite conclusions. More data on  $Nu_d$  will be obtained from the future runs.

The value of downwards Nusselt number for the present geometry obviously depends on the choice of the boundary between 'sideways' and 'downwards'. Therefore, the comparison between the measured value and that predicted from eq. (5) is not necessarily meaningful.

### 3.2. Heat flux profiles

Measured heat flux distributions to side and bottom walls in runs fh2 and fh3 are shown in Figs. 3 and 4 for  $Ra=1.8 \cdot 10^{15}$  and  $Ra = 5.1 \cdot 10^{14}$ , correspondingly. The numbers on the horizontal axis of the plots refer to the cooling unit numbers given in Fig. 2.

When comparing the curves to the average horizontal heat fluxes  $5.8 \text{ kW/m}^2$  for the run fh2 and  $2.5 \text{ kW/m}^2$  for fh3, there is no indication of such a strong peaking of the heat flux on the side wall as observed e.g. Steinberner and Reineke [3] for cavity of square cross section, where the maximum heat flux was about twice the average.

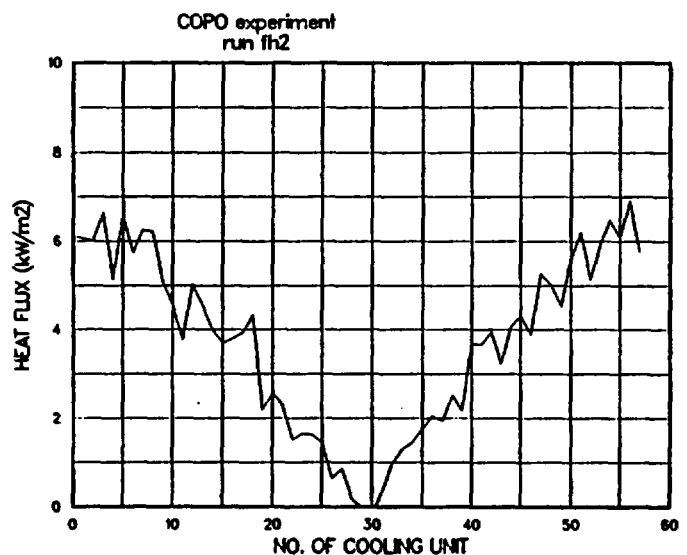


Figure 3. Heat flux profile in run fh2.

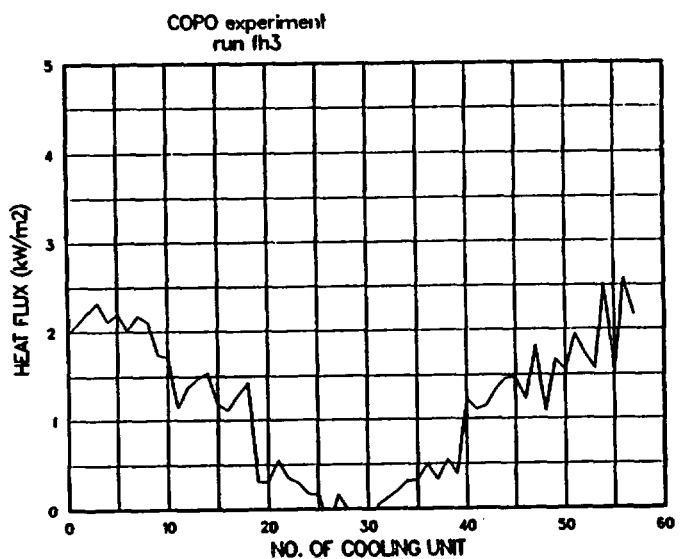


Figure 4. Heat flux profile in run fh3.

It can also be noticed that when the side wall starts to curve from vertical to horizontal, at cooling units 10 and 48, the heat flux decreases relatively smoothly without any abrupt change. This is important for the external coolability, i.e., the CHF is expected to also decrease as the slope of the downwards facing surface approaches that of horizontal.

The measured temperature fields inside the pool in runs fh1 and fh2 are shown in Figs. 5 and 6. In both cases, the pool is seen to be well mixed. Only at the very bottom of the pool, primarily in the run fh3 in which Ra is smaller, some stratification exists.

### 3.3. Velocities

Velocities in the pool were measured with an LDA. Some sample data near the wall, for run fh1, are shown in Figure 7. In this figure each velocity vector represents an average of the LDA measurement during a 30 s time period. All data in the figure were obtained within a time interval of ~1 hour.

The flow field was found to be continuously changing (unsteady). Thus, the data in Figure 7 are indicative of the general trend and they should not be interpreted as detailed velocity profiles. This trend indicates that the velocities increase along the wall reaching a maximum of ~50 mm/s. Work is continuing to more clearly characterize the the unsteadiness of the flow pattern near the wall.

Measurements in the bulk of the fluid indicate that this unsteadiness in the wall region is driven by continuously changing large scale convective rolls in the bulk. In particular, these LDA measurements suggest the existence of at least four convective rolls, the boundaries of which seem to be continuously moving. Investigation in this area is also continuing.

### 3.4. Numerical calculations

In order to support the experimental work, COPO experiments were simulated numerically with the PHOENICS code [8]. Since the main interest was in simulating the flow and heat transfer on the boundaries, a low-Reynolds number turbulence model by Lam and Bremhorst [9], instead of the standard k- $\epsilon$  model, was chosen as the turbulence model to be primarily used. In this model, some of the constants in the k- and

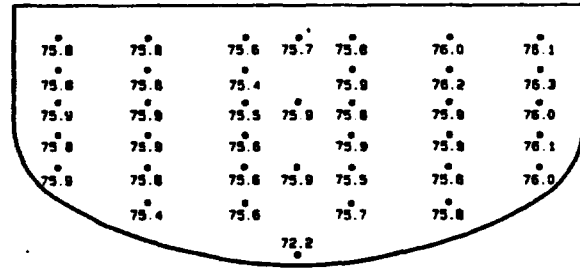


Figure 5. Measured pool temperatures (in °C) in the run fh2.

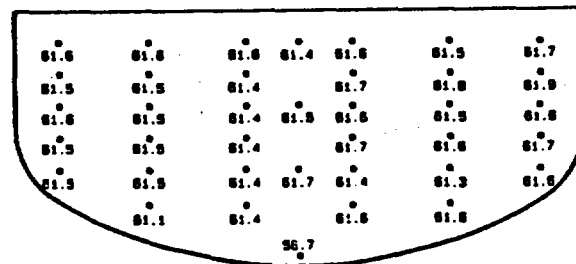


Figure 6. Measured pool temperatures (in °C) in the run fh3.

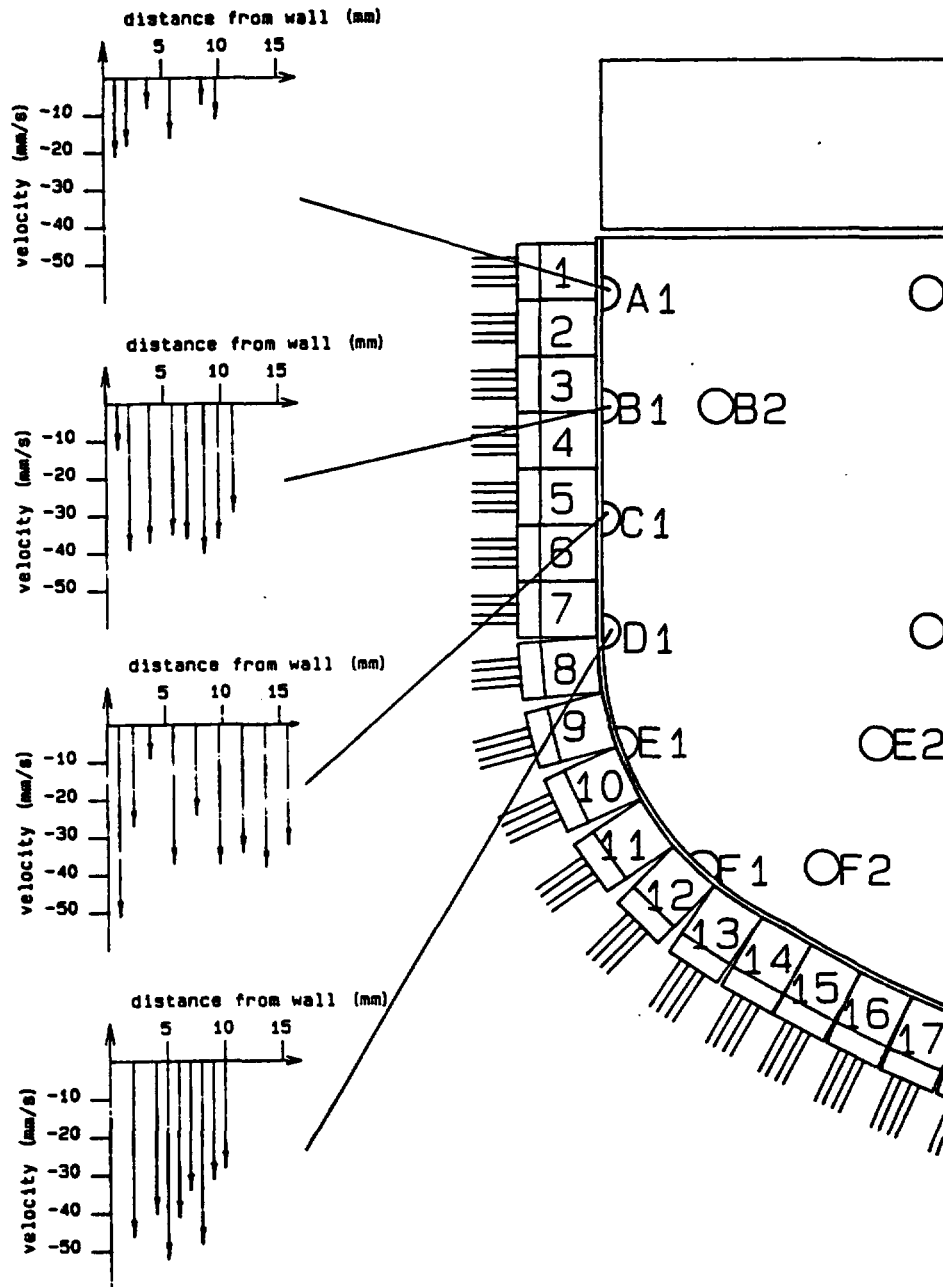


Figure 7. Velocity profiles measured with the LDA in the run fh1.

$\epsilon$ -equations of standard  $k$ - $\epsilon$  model are replaced by algebraic functions in order to allow the integration into the laminar sublayer of the flow. Therefore, laminar boundary conditions for temperature and velocity fields are used. Obviously, the nodalization close to the wall must be very dense.

For example, Chen et al. [10] obtained good results with this model for turbulent natural convection heat transfer in a closed cavity with air.

The COPO facility was modelled two-dimensionally using the body fitted coordinate option

available in PHOENICS, with 4900 control volumes. In simulation with  $Ra \approx 10^{15}$ , PHOENICS clearly overpredicted the heat transfer coefficient on the side walls and underpredicted it on the upper boundary. For example,  $Nu_w$  predicted by PHOENICS was as much as 1600, whereas the measured was 500, and that predicted by correlations (3) - (5), 600. At the wall, there was 30 grid points within 20 mm from the wall in such a way that the mesh size decreased towards the wall with a factor of 1.5. With even denser grid at the boundary, the solution failed to converge.

#### 4. CONCLUSIONS

The most important discovery in these initial tests with high Rayleigh numbers ( $\sim 10^{15}$ ) in small aspect ratio (shallow) volumetrically heated pools is that the convective currents are highly unsteady, and by breaking in to many rolls they favor heat rejections in the upward direction. In particular, the respective Nusselt number was found to be about 30% larger than the well known Steinberner-Reineke correlation which was based on work with a pool of aspect ratio of unity.

Further, these data provide evidence that the heat flux to the sidewalls is quite uniform. This again is in contrast to a factor of two (peak-to-average) non-uniformity found in an aspect-ratio-one pool by Steinberner and Reineke, even though their Nusselt number correlation, for the mean, was in reasonable agreement with the present data.

Both of these aspects have major implications for in-vessel core-melt retention in considerations of severe accident management for Loviisa, as well as other reactors with similar geometric features of a molten core pool in the lower head. Work in the COPO facility and related theoretical interpretations are continuing.

#### ACKNOWLEDGEMENTS

The experiments were carried out in the Hydraulic Laboratory of IVO. We thank the staff of the laboratory for their contribution and help. Especially, the efforts by Miss T.Kärkkäinen in carrying out the LDA measurements and by Mr. E.Pessa in designing the instrumentation are gratefully acknowledged.

#### REFERENCES

- [1] H.Tuomisto, T.G.Theofanous: A Consistent Approach to Severe Accident Management. Proceedings of the Specialist Meeting on Severe Accident Management Programme Development. CSNI/SESAM. Rome, Italy, September 23 - 25, 1991.
- [2] O.Kymäläinen, H.Tuomisto, T.G.Theofanous: Critical Heat Flux on Thick Walls of Large Naturally Convecting Loops. ANS Proceedings of the 1992 National Heat Transfer Conference. San Diego, CA, August 9 - 12, 1992. ANS HTC, Vol 6.

- [3] U.Steinberner, H.-H.Reineke: Turbulent Buoyancy Convection Heat Transfer with Internal Heat Sources. Proceedings of Sixth International Heat Transfer Conference. Toronto, Canada. August 7 - 11, 1978
- [4] J.M.Seiler: Cooling of Molten Material Liquid Pool Submitted to Heating. New Correlations for Various Cooling Conditions. Proceedings of NUCSAFE 88, International ENS/ANS Conference on Thermal Reactor Safety. Avignon, France, October 2 - 7, 1988.
- [5] L.Baker et al.: Heat Removal from Molten Corium Pools. Proceedings of the International Meeting on Fast Reactor Safety and Related Physics. Chicago, Illinois. October 5 - 8, 1976.
- [6] A.A.Emara, F.A.Kulacki: A Numerical Investigation of Thermal Convection in a Heat Generating Fluid Layer. Journal of Heat Transfer, 102 (1980) pp. 531 - 537.
- [7] B.Farouk: Turbulent Thermal Convection in an Enclosure with Internal Heat Generation. Journal of Heat Transfer, 110 (1988) pp. 126 - 132.
- [8] The PHOENICS Reference Manual. CHAM/TR200a. CHAM Ltd, London, 1991. .
- [9] C.K.G.Lam, K.Bremhorst: A Modified Form of the  $k-\epsilon$  Model for Predicting Wall Turbulence. J. Fluids Engineering. Transactions of ASME. 103 (1981) pp. 456 - 460.
- [10] Q.Chen, A.Moser, A.Huber: Prediction of Buoyant, Turbulent Flow by a Low-Reynolds-Number  $k-\epsilon$  Model. ASHRAE Transactions. pp. 564 - 573.

RESULTS FROM IN-REACTOR SEVERE FUEL DAMAGE TESTS  
THAT USED FULL-LENGTH FUEL RODS AND THE RELEVANCY  
TO LWR SEVERE ACCIDENT MELT PROGRESSION SAFETY ISSUES

F. E. Panisko and N. J. Lombardo  
Pacific Northwest Laboratory<sup>(a)</sup>  
Richland, Washington 99352

ABSTRACT

This paper presents results from four tests conducted to assess the behavior of full-length, light-water reactor fuel rods and the resulting damage in the event of a severe accident. The tests, identified as FLHT-1, -2, -4, and -5, were performed by Pacific Northwest Laboratory (PNL) in the National Research Universal reactor at Chalk River, Ontario, Canada, for the U.S. Nuclear Regulatory Commission. The findings revealed that the axial extent of the oxidation-induced damage increased with the length of time testing was conducted at high temperature; the region of rapid Zircaloy oxidation was confined to an axial length of 20 centimeters, which moved rapidly down the length of the bundle; only the Zircaloy below the coolant/steam interface would not be expected to participate in generating hydrogen; the relocation of molten materials was tied to the passage of the oxidation burn front; and cohesive blockages were not formed at the bottom of the fuel bundle as typically found in the short-length severe fuel damage tests.

---

(a) Operated for the U.S. Department of Energy by Battelle Memorial Institute under Contract DE-AC06-76RLO 1830.

## INTRODUCTION

Through the Cooperative Severe Accident Research Program (CSARP),<sup>(a)</sup> the U.S. Nuclear Regulatory Commission (NRC) is conducting or participating in numerous experiments to study the behavior of reactor core materials under severe accident conditions. As part of the CSARP, the NRC is sponsoring five experiments conducted by Pacific Northwest Laboratory (PNL).<sup>(b)</sup> In these experiments, instrumented, insulated assemblies of full-length (3.7 m) light-water reactor (LWR) fuel rods are subjected to coolant flow reductions while operating at low-fission heat ratings. This procedure simulates possible loss-of-coolant accident conditions in LWR cores. The consequent coolant boilaway, heatup of the exposed rods, and exothermic oxidation reaction of the hot Zircaloy cladding with steam result in hydrogen evolution, cladding melting, fuel liquefaction, material relocation, and fission product release.

A series of four tests identified as FLHT-1, -2, -4, and -5 began in 1985. These tests, designated as full-length, high-temperature (FLHT) experiments, featured a gradual increase in the severity of peak cladding temperatures, hydrogen generation rate, and length of time at maximum conditions. The major parameters associated with these tests are listed in Table 1.

### OBJECTIVES OF THE FLHT TESTS

The objectives of the tests were to 1) obtain well-characterized data for evaluating the effects of coolant boilaway and core melt progression in an LWR and 2) investigate integral severe accident phenomena in the full-length fuel bundle under prototypic conditions. The data are used to confirm the validity of results obtained from separate-effects tests sponsored by the NRC

- 
- (a) Partners in this program with NRC include nuclear organizations from the following countries: Belgium, Canada, England, Finland, Germany, Italy, Japan, the Netherlands, Republic of China (Taiwan), Republic of Korea, Spain, Sweden, Switzerland, France, and Russia.
  - (b) Operated for the U.S. Department of Energy by Battelle Memorial Institute under Contract DE-AC06-76RLO 1830.

**TABLE 1. Major Parameters for FLHT Severe Fuel Damage Tests in the National Research Universal (NRU) Reactor<sup>(d)</sup>**

Test Designation	Test Date	Nominal <sup>(b)</sup> Assembly Nuclear Power, kW	Number of Pre-irradiated Rods <sup>(c)</sup>	Peak Cladding <sup>(d)</sup> Temperature Achieved, K	Peak Hydrogen Production Rate, mg/s <sup>(e)</sup>	Approximate Pretest Fuel Preconditioning (Time at 670 kW Assembly Nuclear Power), h	Time at Peak Temperature, <sup>(f)</sup> min	Final Liquid Level, m	Average Heatup Rate, <sup>(g)</sup> K/s
FLHT-1	3/85	23	0	2300	140	0.0	<1	1.5	NM
FLHT-2	12/85	23	0	2500	210	0.0	4.5	0.9	3.1
FLHT-3 <sup>(h)</sup>									
FLHT-4	8/86	23	1	2600	174	1.0	30	0.86	2.6
FLHT-5	5/87	30	1	>2600	182	5.0	60	0.76	3.5

- (a) All tests to date have been conducted with a nominal bundle inlet flow of 1.3 g/s during the boilaway transient.
- (b) The fission power was confirmed by calorimetry of the water-filled bundle. The voided region of the bundle is estimated to have local power increased of 15% based on neutronics calculations.
- (c) Total rods per assembly as 12 (FLHT-1, -2) and (FLHT-4, -5). The preirradiated rods have a nominal burnup of 28 MWd/kgU and were discharged in May of 1975.
- (d) Best estimate values based on interpretation of thermocouple data.
- (e) Peak assembly heat generation rate due to oxidation (in kW) equals 0.15 times the peak hydrogen production rate in mg/h.
- (f) Time after onset of cladding melt temperatures (2100K).
- (g) Heatup rate at bundle midplane from saturation (467K) to 1700K. Not applicable for FLHT-1.
- (h) Conceptualized but not performed.

at PNL and other laboratories to reduce uncertainties in describing core melt progression by helping to validate computer models that describe reactor behavior during severe accidents.

### TEST DESCRIPTION

All the FLHT tests used hardware that is similar in design and followed similar test operations. Overall, the test hardware was designed to accomplish the following: 1) provide for a controlled coolant boilaway; 2) accommodate temperatures at least as high as 2500K within the fuel bundle; 3) measure and record key temperatures, flow rates, and pressures; 4) maintain control of pressures and flows; 5) sample the effluent; and 6) provide for operating safety throughout the course of tests.

The FLHT test hardware consists of the following four components plus the National Research Universal (NRU) reactor: test train assembly, steam closure cave (SCC), effluent control module (ECM), and a data acquisition and control system (DACS). The general arrangement of these components during a test in the NRU reactor is shown in Figure 1. During a boilaway transient two coolant systems are used. One system continuously circulates sub-cooled, pressurized water around a closed loop piping system. The water cools the external surfaces of the test train assembly. The second system is a once-through circuit that supplies sub-cooled, pressurized water from a storage tank to the fuel bundle inlet region. This water then flows up among the fuel rods, the upper plenum, through the closure, SCC, ECM, and finally into a storage tank. These coolant systems are also shown in Figure 1.

The test train assembly is about 9-m long and hangs inside a pressure tube in the NRU reactor and consists of almost equal lengths of upper plenum and reactor core sections. The upper plenum section connects the core section to a closure section. Figure 2 is a schematic of an axial view of the test train assembly.

The reactor core section of the test train assembly consists of a highly instrumented fuel bundle and thermally insulated shroud. A cross section of the fuel bundle and shroud is shown in Figure 3. The fuel bundle consists of

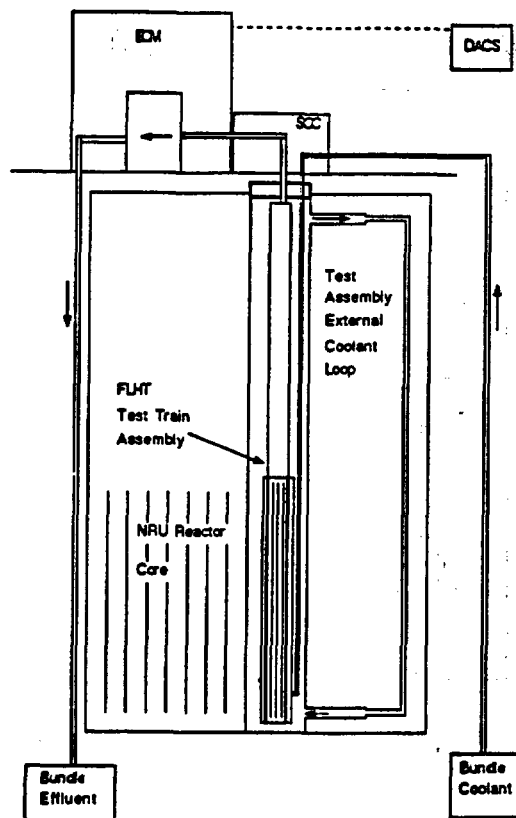


**FIGURE 1. FLHT Test General Hardware Arrangement**

a 4 x 4 square array with modified corners designed as a subsection of a 17 x 17 pressurized water reactor (PWR) assembly. The inlet section mechanically supports the fuel bundle, provides an entrance for bundle coolant, and is a pressure boundary for all bundle instrument lines.

Two structures are used in the FLHT tests to provide shielding and secondary confinement for the part of the effluent line that is exterior to the reactor. These two major components are interconnected as shown in Figure 4. As shown in the figure, the effluent line exits from the top of the test train then enters first the first structure called a steam closure cave, SCC, and then enters the second structure called an effluent control module, ECM, before terminating at an effluent catch tank.

The FLHT test operations include up to five phases:

1. Pretest installations and checks - reactor at zero power

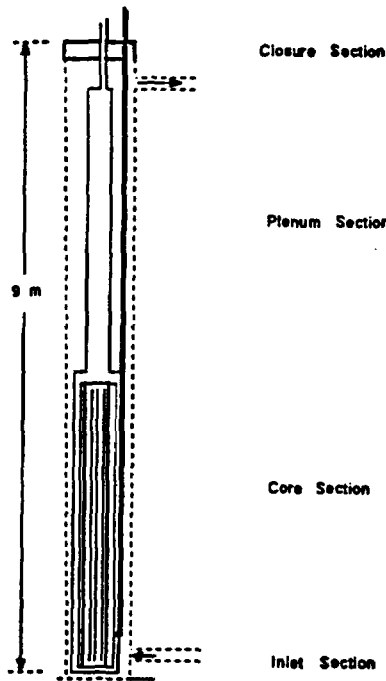


**FIGURE 2. FLHT Test Train Axial Schematic**

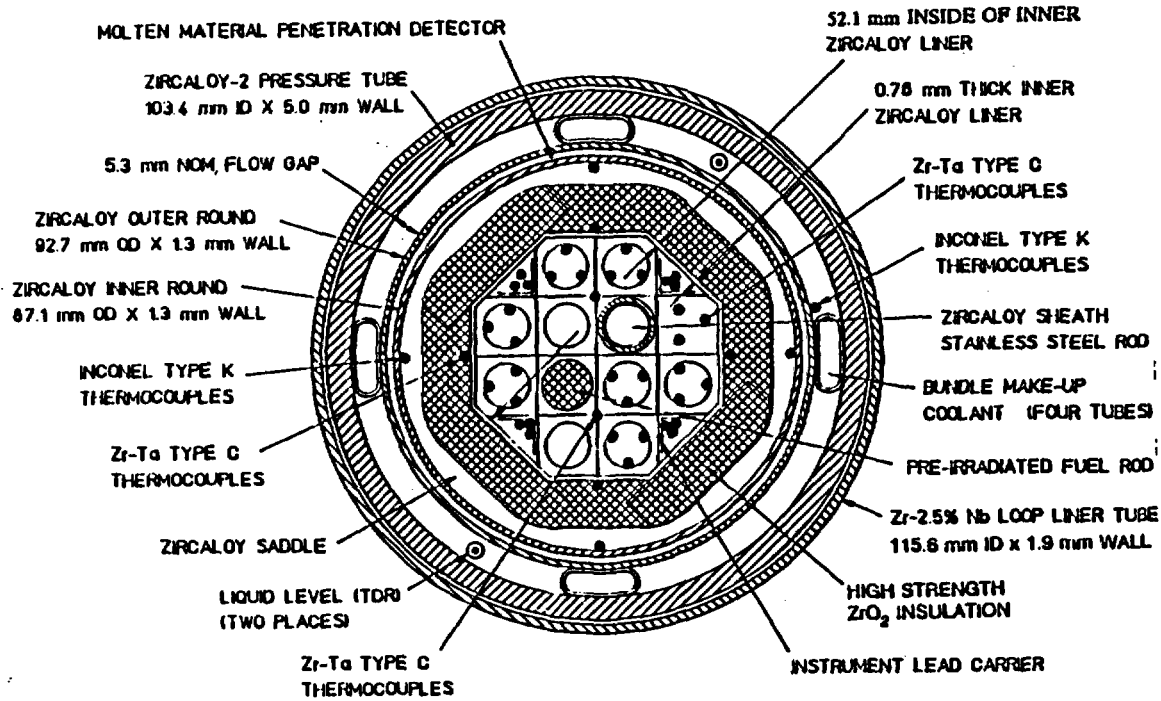


**FIGURE 3. Schematic of an FLHT Core Region Cross Section**

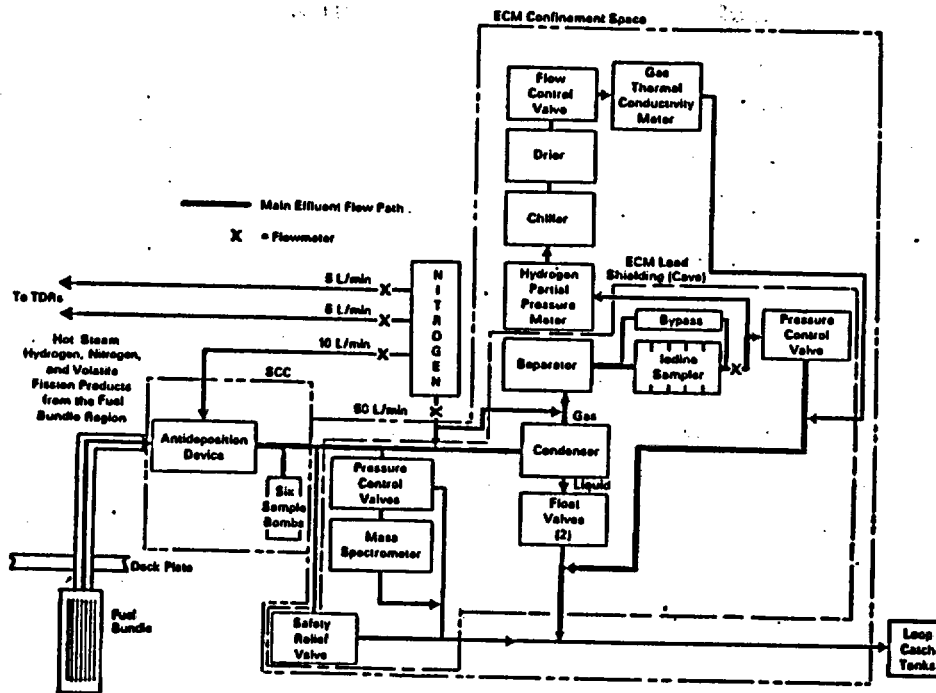


**FIGURE 4.** Flow Paths in the Steam Closure Cave and Effluent Control Module (specific to FLHT-5 but representative of all FLHT tests)

2. Commissioning and calibration - reactor at zero power
3. Preconditioning operation (FLHT-4 and -5 only) - reactor at full power
4. Coolant boilaway/severe damage transient - reactor at 5% of full power
5. Post-test examinations.

The fourth phase, the most important, is briefly described below.

The performance of the coolant boilaway/severe damage transient is initiated by bringing the NRU reactor to low power (~5% of full power) with 1-kg/s shroud coolant flow and 0.13-kg/s bundle coolant flow. After calorimetry and stabilization at 23-kW or 30-kW bundle nuclear power, the plenum section is drained and heated, and the assembly inlet flow is reduced to 9.4 g/s to arrive at a steady-state, dry-out front position ~0.7 m below the top of the fuel column.

Following the plenum heatup operation, the actual coolant boilaway is started by a rapid reduction of the bundle inlet flow to ~1.3 g/s. Less than

10 minutes after flow reduction, temperatures in the bundle increase rapidly as the exothermic oxidation reaction accelerates. The time from the first attainment of cladding melt temperatures (2100K) to the termination of the experiment varied from 4 minutes in FLHT-2 to 60 minutes in FLHT-5.

### KEY RESULTS

All the FLHT tests have resulted in extensive and severe fuel rod damage, with the severity and extent of the damage increasing with each subsequent test. The key results given that are relevant to melt progression safety issues are associated with oxidation-induced damage progression, hydrogen generation, and finally, material relocation and the associated coolant flow blockage.

#### Oxidation-Induced Damage Progression

In these integral tests it was not possible to separate the major chemical damage from the thermal damage. The oxidation behavior was inferred from temperature and flow measurements.

The initiating event for the FLHT-2, -4, and -5 tests was a step change in the bundle coolant flow rate while at constant power. Immediately following the flow reduction to 1.3 g/s, the coolant began to boil away as a result of the power/cooling mismatch. As the coolant level dropped and the cladding surfaces dried out, the cladding immediately began to heat up: at first almost adiabatically; then at a decreasing rate due to increased heat transfer; and, finally, at an increasing rate as oxidation heat generation began to increase. The heatup phase of the tests culminated near 1700K in a rapid temperature escalation, above 10K/s, signaling the onset of an autocatalytic oxidation reaction. The peak cladding temperatures attained during the escalation were not accurately determined because the cladding thermocouples failed near ~2400K. The peak cladding temperatures were, however, estimated to have been in the 2500K range for FLHT-2 and  $\geq 2600\text{K}$  for FLHT-4 and -5, based on behavior of the thermocouples on the liner and preliminary data from visual and metallurgical examinations.

A localized, rapidly downward-moving oxidation "burn front" developed at a non-dimensional elevation of approximately 0.7 (Level 100) as a result of the initial oxidation excursion; it progressed down past the midplane of the fuel assembly toward the steam-cooled region just above the coolant pool. Within the downward moving burnfront, cladding temperatures exceeded the oxygen-saturated Zircaloy [Zr(O)] melt temperature, resulting in local fuel dissolution and cladding and fuel material relocation. The axial extent of the burn front was relatively confined, generally within the 0.2-m axial distance between cladding thermocouples. The downward progression of the burn front occurred as a result of the developing axial temperature profiles and the decreasing coolant level, both of which together allowed progressively lower axial levels to reach oxidation excursion temperatures and consume the steam, thereby preventing Zircaloy at higher elevations from oxidizing.

During the tests, as the burn front reached the steam-cooled region above the coolant pool (e.g., Level 52 to Level 30 in FLHT-5),<sup>(a)</sup> temperatures were too low to initiate autocatalytic oxidation. Without the rapid oxidation that accompanies autocatalytic oxidation, steam was available for consumption in the upper elevations; this steam then fueled an upward-moving burn front. This front slowly moved up through the damaged bundle midsection and then along the relatively unoxidized upper section (above Level 100) toward the top of the bundle. The upward progression continued until the test was terminated.

The upward burn front progressed to the top of the fuel rods in FLHT-5, resulting in essentially complete consumption of the exposed Zircaloy and a significant reduction in the rate of hydrogen generation. The FLHT-5 test then continued operation for ~1000 seconds past the major reduction in bundle oxidation during which damage continued, primarily from the nuclear heating component. Thus, the FLHT-5 test investigated two distinct accident regimes-- one in which chemical power was the major contributor to damage progression and a second less vigorous regime in which damage was induced by a nuclear-dominated heating component.

---

(a) Level is defined as the elevation, in inches, above or below the bottom of the fuel stack.

The early temperature history during the FLHT-6 test of the cladding, liner, and saddle at Level 88 is shown in Figure 5. The heatup of the various components at this elevation typifies that of the FLHT tests.

The post-dryout cladding heatup rate ( $dT/dt$  averaged over 10-second intervals) is plotted for FLHT-4 and -5 at Level 96 in Figure 6. As expected, the heatup rate was slightly higher for the FLHT-5 test ( $\sim 0.5K/s$ ) due to the higher fission heat rate. Initially, on dryout, a step change increase in the cladding heatup rate occurred, reaching  $5K/s$  (i.e., adiabatic). The heatup rate then steadily decreased as a result of increasing convective and radiation heat transfer and fuel heat capacity before beginning a steady increase from the metal-water reaction energy release.

As observed from the cladding axial temperature profiles the oxidation power begins to increase the temperature rise rate when cladding temperatures exceed  $1400K$ , about 150 seconds before autocatalytic conditions are achieved.

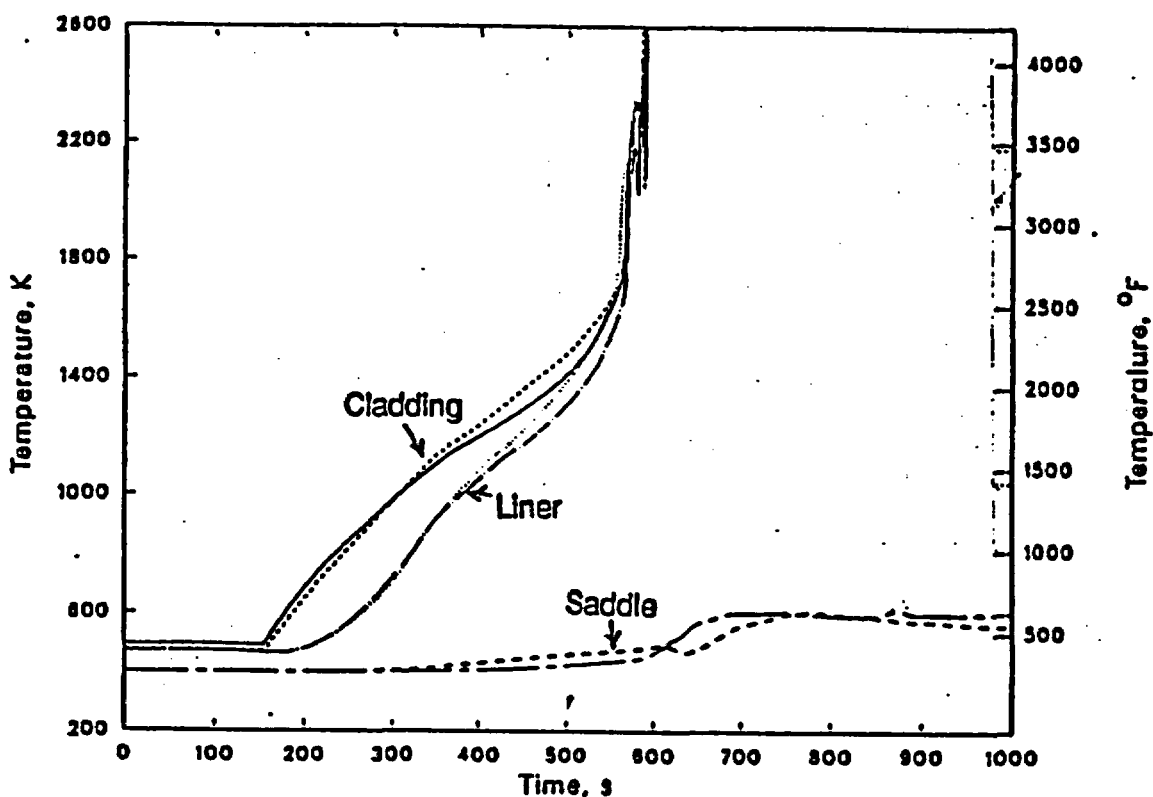


**FIGURE 5.** FLHT-5 Cladding, Liner, and Saddle Temperature Histories-Level 88

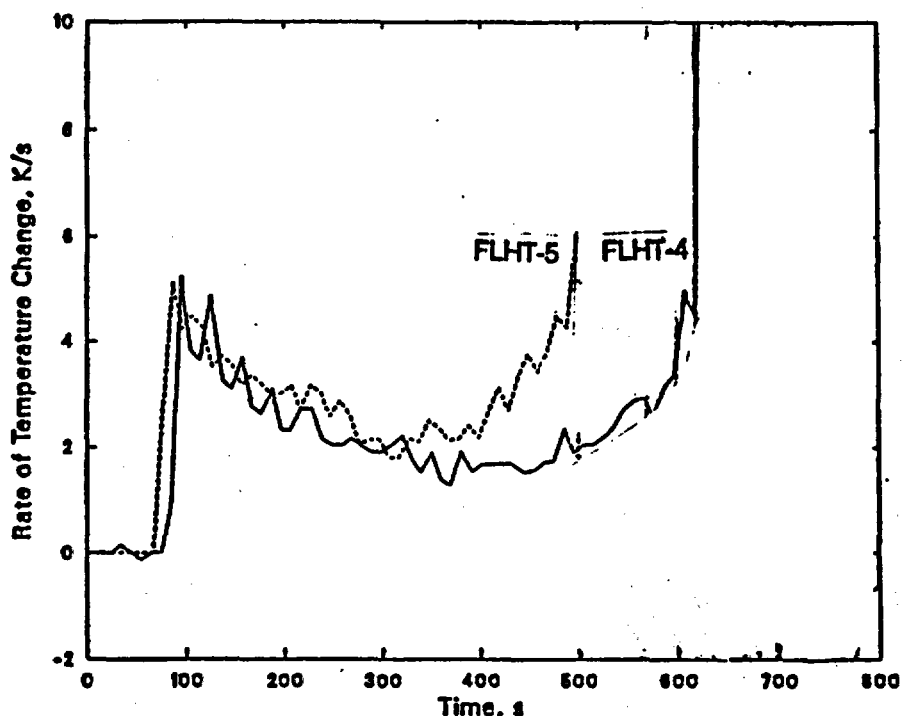


**FIGURE 6.** Level 96 Cladding Heatup Rates after Dryout for FLHT-4 and -5

The initial impact of the oxidation power was to offset the decrease in the cladding heatup rate. As the chemical power contribution increased further, however, the heatup rate was essentially doubled to 5K/s. Shortly after this time, at temperatures near 1700K autocatalytic oxidation behavior was recorded, with cladding thermocouple rise rates greater than 10K/s before failure of the thermocouples near 2400K.

The axial temperature gradients influence movement of both the chemical front and molten core materials. Cladding axial temperature gradients recorded during the FLHT-5 test from the initiating flow reduction to escalation are shown in Figure 7. In this figure, the cladding temperatures are plotted versus axial position at 50-second intervals, beginning with flow reduction (0 seconds) and ending with the initial onset of the rapid oxidation reaction (500 seconds).

A general steepening of the axial temperature gradient above the coolant pool is seen as the level of coolant decreases and approaches its steady-state

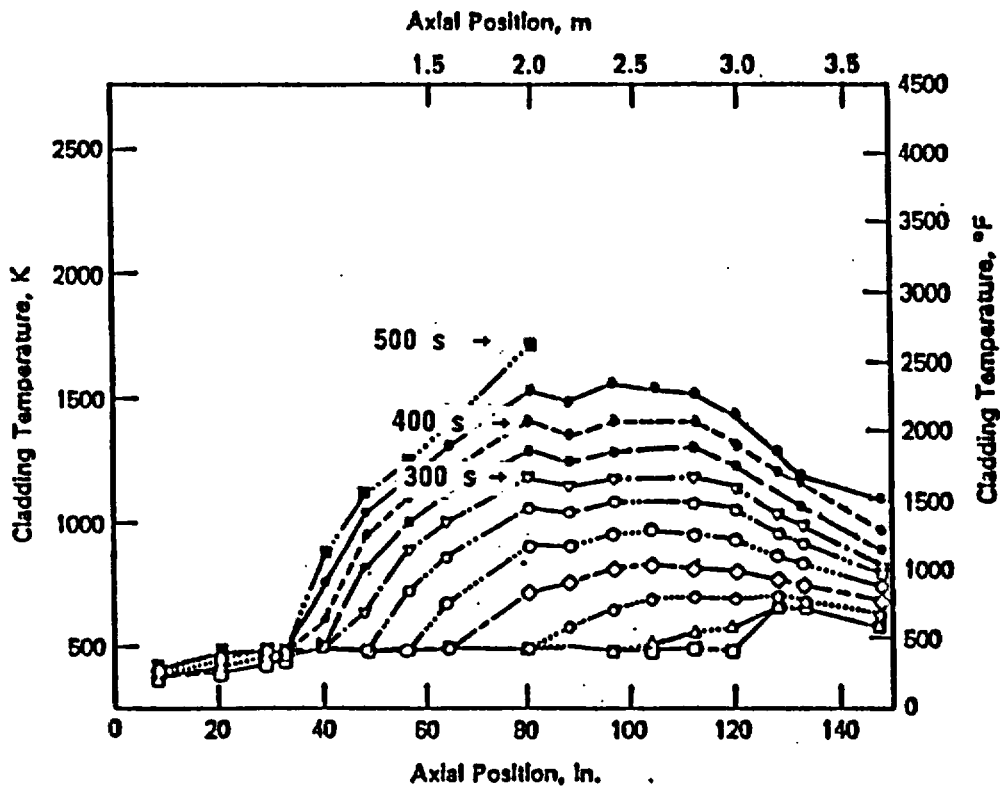


**FIGURE 7.** FLHT-5 Cladding Axial Temperature Profiles Prior to the Initial Oxidation Excursion (at 50-s intervals beginning with the flow reduction)

position. The larger gradient is a result of the decreasing steam flow and the increasing length of the fuel rods uncovered. During the time interval from 450 and 500 seconds, the axial gradient between Level 60 and Level 80 increased directly as a result of the oxidation energy release; this occurred between 1400 to 1500K, and is consistent among all the FLHT tests.

An overview of the oxidation and damage progression of the four FLHT tests is presented schematically in Figure 8. Illustrated in this figure is the relationship between the initial oxidation front location, the asymptotic or final coolant level, and the termination of the downward and upward burns. Also shown in this figure is the oxidation and steam-cooled regions; the damage in these regions is characterized, respectively, by white, highly-embrittled, oxidized cladding completely converted to  $ZrO_2$ , and undamaged cladding with a dark protective oxide layer.

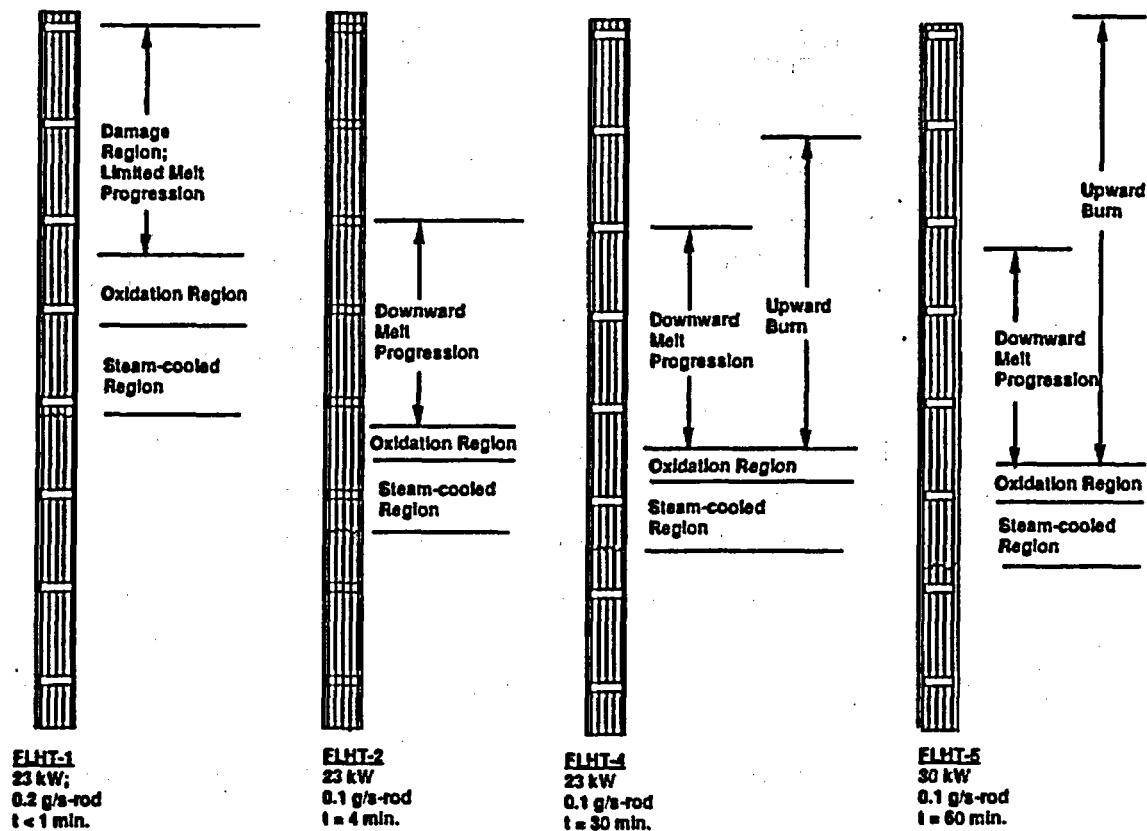


**FIGURE 8.** Overview of the FLHT Oxidation Progression

As shown in the figure, only a small fraction of the uncovered fuel remains undamaged, with this fraction being affected by the test time and the boilaway type. The damage that occurred was entirely oxidation induced; i.e., the simulated decay fission power levels and radial heat losses were such that Zircaloy melt temperatures could not be achieved in these tests without the local chemical power from oxidation. For the FLHT-1 extended boilaway, the length of the undamaged steam-cooled region was expanded and was located higher in the bundle. Coupled with the high coolant level and the short test time, the axial extent of the damage region is the smallest of the tests. Conversely, the oxidation-induced damage is greatest for the 1-hour-long FLHT-5 test.

## Hydrogen Generation

The results from the FLHT tests support the conclusion that no physical mechanisms exist that would terminate the hydrogen generation during severe accidents aside from complete consumption of the available Zircaloy. Although it did not terminate hydrogen production, the phenomenon of material relocation was found to cause a temporary reduction in the production rates. However, this temporary reduction has little influence on limiting the total hydrogen released. The mechanism for reducing hydrogen generation is the removal of hot materials from the high-temperature oxidation zone into a cooler zone. As the lower, and cooler, regions are heated as the oxidation excursion zone progresses downward, the hydrogen generation was found to return to fully-consumed conditions. During the tests, because little material relocated from the high-temperature region to the steam-cooled region above the coolant, hydrogen generation continued until either termination of the test or, as in the case of FLHT-5, complete consumption of the available Zircaloy. Thus, for severe accidents where steam production continues, only the Zircaloy below the coolant/steam interface would not be expected to participate in the production of hydrogen.

Hydrogen generation during the FLHT boilaway transients was measured by a combination of up to four different instruments--a mass spectrometer (MS), thermal conductivity meter (TCM), palladium hydrogen meter (PHM), and a non-condensable turbine flowmeter (NTF). The MS, TCM, and PHM essentially measured the percentage of hydrogen in the nitrogen carrier gas flow. The NTF provided a measurement of the hydrogen generation by measuring all the combined nitrogen/hydrogen mixture flows through the noncondensable flow meter, NTF and subtracting the nitrogen sweep gas flow. The NTF responded almost instantly (~5 s) to changes in hydrogen generation because it was located closest to the hydrogen source (<10 m) and on the main noncondensable gas line in the ECM. The MS and TCM had considerably longer delay times (3 to 8 min) because these two instruments were located further downstream from the hydrogen source and were located on the sample line. The lower gas velocity in the

sample line<sup>(a)</sup>, coupled with the increased distance from the hydrogen source, significantly increased the transit time to the mass spectrometer and TCM to 150 seconds and 420 seconds, respectively. (Longer transit times were noted for FLHT-4 and -5 than for FLHT-2 due to added components and piping in the ECM.) Because of the instantaneous response time, reliability, and demonstrated accuracy of the NTF, the discussions of hydrogen generation rate, total release, and timing will focus solely on the NTF measurements. A summary of the hydrogen release data and inferred oxidation behavior is presented in Table 2.

The real-time hydrogen generation rate during the FLHT-5 test as measured by the NTF is presented in Figure 9. Also plotted in this figure is the equivalent hydrogen generation represented by full conversion of the inlet makeup rate to hydrogen. The characteristics of hydrogen generation for each of the tests are compared and discussed below, and conclusions are made regarding the extent of steam consumption, the effects of material relocation, and the potential for long-term hydrogen release in severe accidents.

**TABLE 2. Hydrogen Generation and Oxidation Summary**

<u>Parameter</u>	<u>FLHT-1</u>	<u>FLHT-2</u>	<u>FLHT-4</u>	<u>FLHT-5</u>
Peak generation rate, mg/s	140	210	174	182
Average generation rate, mg/s	-	140	140	90
Total release, g	31	44	240	340
Percent of hydrogen released after 2100K	0	90	95	95
Percent of bundle Zircaloy consumed	8	12	61	86
Peak oxidation power, kW	21	32	26	27

---

(a) The sample line flow rate was limited to 250 cc/m by throttling valves in the sample line. The flow rate in the main noncondensable line in the ECM was ranged from 90 L/m to 240 L/m. Thus, the sample line flow rate was less than 1% of the main noncondensable effluent flow.

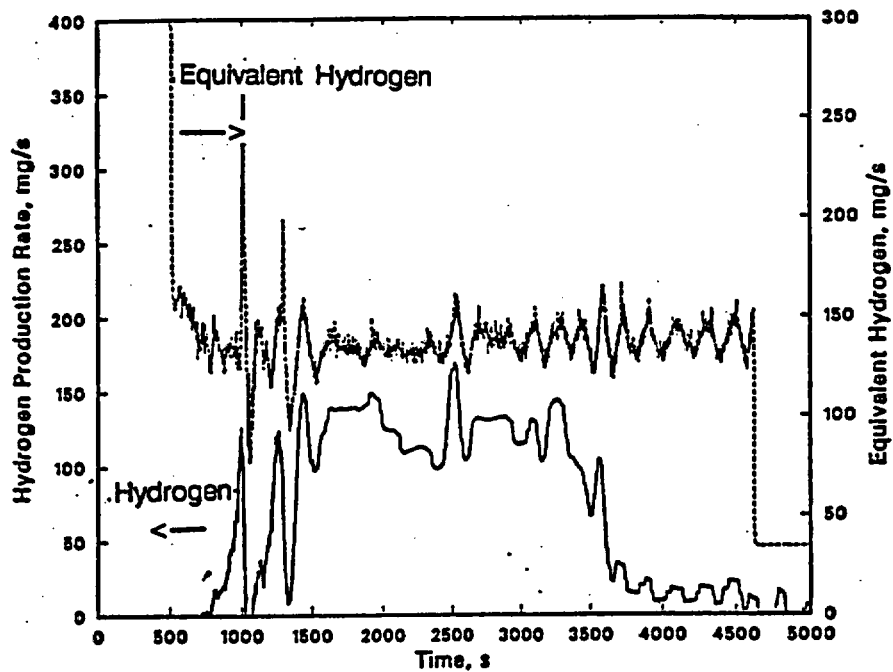


**FIGURE 9.** FLHT-5 Hydrogen Generation Rate Calculated from NTF and for Fully Converted Inlet Flow

Several consistent phenomena are observed in the generation of hydrogen during the FLHT tests. First, each of the tests operated under steam-starved conditions during the majority of the high-temperature transients, a condition that is not surprising given the steaming rate ( $\sim 0.1$  g/s-rod) and high temperatures recorded for the tests. As a result, fluctuations in the coolant makeup rate were therefore directly translated into the fluctuation in the hydrogen generation rate. Second, the onset of hydrogen generation is essentially coincident with the onset of autocatalytic oxidation. This conclusion is illustrated by a plot shown in Figure 10 of the FLHT-2 hydrogen generation versus the peak cladding temperature and is supported in an assessment of hydrogen generation behavior from in-pile test data by Cronenberg (1990). Third, all but a few percent of the total hydrogen generated during the course of the transients occurred before the onset of cladding melting; but more importantly, no physical mechanisms were found to limit hydrogen generation once the oxidation excursion started.

As indicated in Table 2 and Figure 10, >90% of the hydrogen was generated following the onset of cladding melt temperatures. This occurred because 1) the oxidation of the Zircaloy components continued uninterrupted with the steady supply of steam generated by the coolant boilaway and because 2) no physical mechanisms such as extensive material relocation occurred that moved material to low-temperature regions or formed a cohesive flow blockage, which would limit the availability of steam. In the FLHT-5 test, only complete oxidation of the exposed Zircaloy terminated hydrogen generation; however, this occurred after 80% of the available hydrogen was generated. Only the Zircaloy below the dryout front did not contribute to the production of hydrogen.

### Material Relocation

The relocation of molten materials was tied to the passage of the oxidation burn front. The material relocation behavior can be described as heterogeneous, with material melting, relocating, and reheating occurring as the

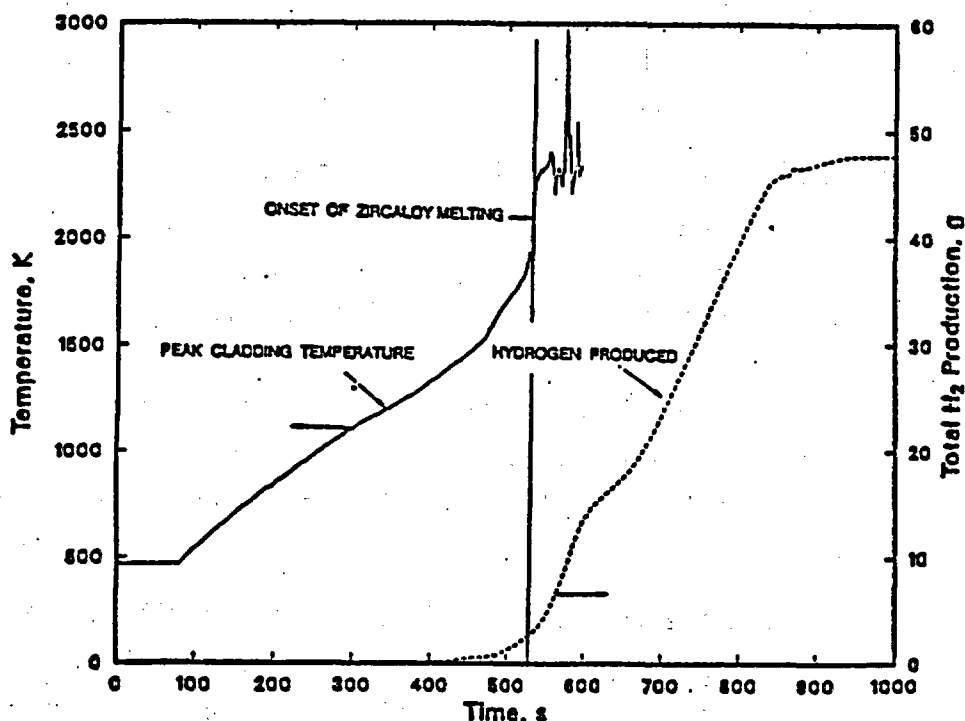


**FIGURE 10.** Partitioning of Hydrogen Production for the FLHT-5 Test

oxidation burn front moved downward. No information was obtained on the material relocation during the upward burn because of the loss of bundle region thermocouples. The axial extent of the material relocation was generally within the spacing of the grid spacers, e.g., <0.5 m. This relocation distance was not great enough to remove significant quantities of material from the high-temperature oxidation region to the steam-cooled region or the coolant pool; thus, oxidation and the accompanying hydrogen generation continued.

Cohesive blockages were not formed at the bottom of the fuel bundle as were typically found in the short-length, severe fuel damage (SFD) tests. The difference in the end-state blockage formation was attributed to differences in test design and operation. The short-length tests have intrinsic design and operational features that promote the formation of large cohesive blockages, particularly at the lower elevations. These features include large axial temperature gradients resulting from the short-length, high-fission power levels and the proximity of inlet region structures to the damage region. Conversely, the design and operational features of the full-length tests make the formation of large cohesive melts less likely, mainly the following: smaller fission power levels, relatively larger radial heat losses, and larger distances between the melt zone and inlet fixtures.

Following the oxidation excursion, local temperatures exceeded the Zircaloy melt temperature leading to the relocation of uranium, zirconium, and oxygen. That some of these materials relocated has been inferred from abrupt, coincident changes in the response of thermocouples at different axial levels and among different bundle components. From these coincidental changes in the response of thermocouples, conclusions have been made regarding the following: 1) the origin of relocated materials, 2) the relocation distance, 3) the effect of relocation on local temperatures, and 4) the velocity at which the molten material relocated.

In spite of the extensive thermocouple instrumentation within the bundle region of the FLHT tests, only a partial picture of material relocation behavior can be derived from the temperature data because of the discrete nature of the measurements. Therefore, real-time data on relocation must be correlated with the end-state picture provided by post-test visual and

metallographic examinations. To date, visual examinations through windows cut into the shroud have been performed on the fuel bundles from all the FLHT tests; detailed metallographic evaluations and gamma-tomography have been completed for the FLHT-2 and test bundle.

Of all the FLHT tests, FLHT-2 provided the best record of material relocation. This is because a greater number of thermocouples per plane were used in this test than were used in the other tests. During the 4 minutes that the FLHT-2 test was extended following attainment of 2100K cladding temperatures, a total of eight separate material relocation events have been inferred from the response of the thermocouples. An overview of these events for the FLHT-2 test is presented in Table 3; the thermocouple responses that identified five of these relocation events (A-E on Table 3) are displayed in Figure 11. Indicated in the table for the eight discrete relocation events are 1) the location of the thermocouple that indicated relocated materials, 2) the estimated origin of relocation, 3) the lowest axial level indicating a response, and 4) the local temperature increase.

The eight relocation events occurred over a 170-second period as the oxidation front progressed downward. The initial relocation occurred near the initial peak temperature location. Subsequently, fuel rod cladding and shroud liner temperatures at many locations responded with abrupt temperature increases, indicating extensive axial and radial relocation. The source of molten material for these eight events was estimated to range from Level 92 to Level 62, essentially the full extent of downward oxidation progression, i.e., the severe damage region.

Whereas molten material was estimated to have relocated as much as 0.7 m from the source, this distance was not sufficient to remove the material completely out of the high-temperature zone. Hydrogen generation, therefore, continued in all tests, although a temporary reduction in the generation rate in FLHT-2 was noted.

Because cladding melt temperatures were achieved as a result of the local oxidation power, the source of the relocated material was found to correlate well with the position of the oxidation excursion. Thus, the velocity of the oxidation front (a function of the rate of coolant level decrease), as

**TABLE 3. Overview of FLHT-2 Recorded Material Relocation Events<sup>(a)</sup>**

<u>Event</u>	<u>Time, s</u>	<u>Key Event Sensed by Thermocouples</u>	<u>Estimated Origin of Relocation, Level</u>	<u>Lowermost Level Thermocouple Showing Change</u>	<u>Distance Detected from Origin, m</u>	<u>Remarks</u>
A	594	Steam probe above grid Level 87.5	90	84.5	0.14	+580K increase steam probe temperature, Level 87.5; initial material relocation; start of hydrogen generation
B	600	Liner adjacent to grid Level 88	88	60	0.71	Hot material at Level 60
C	609	Steam probe below grid Level 84.5	86 <sup>(b)</sup>	76	0.25	+400K increase liner temperature, Level 88
D	614	Steam probe above grid Level 66	84	66	0.46	+270K increase in steam probe temperature, Level 66
E	623	Rod 2A cladding Level 76	82	72	0.25	+640K increase in cladding temperature; secondary heatup noted; minimum of hydrogen generation
F	654	Liner at Level 72	74	66.5	0.19	+700K increase in liner temperature; liner participation in bundle relocation behavior; hydrogen generation increasing
G	715	Steam probe below grid Level 63.5	66 <sup>(b)</sup>	48	0.46	Hot material into steam-cooled region (Level 48); fully consumed conditions restored <sup>(c)</sup>
--	765	Rods 1B, 2C, and 4C, Level 60	62	60	0.1	Coplanar indications of molten material.

(a) Source: Lombardo, N. J., and D. D. Lanning. 1988. FLHT-2 Data Report. Pacific Northwest Laboratory, Richland, Washington.

(b) Grid spacer location.

(c) Full conversion of bundle coolant flow to hydrogen.

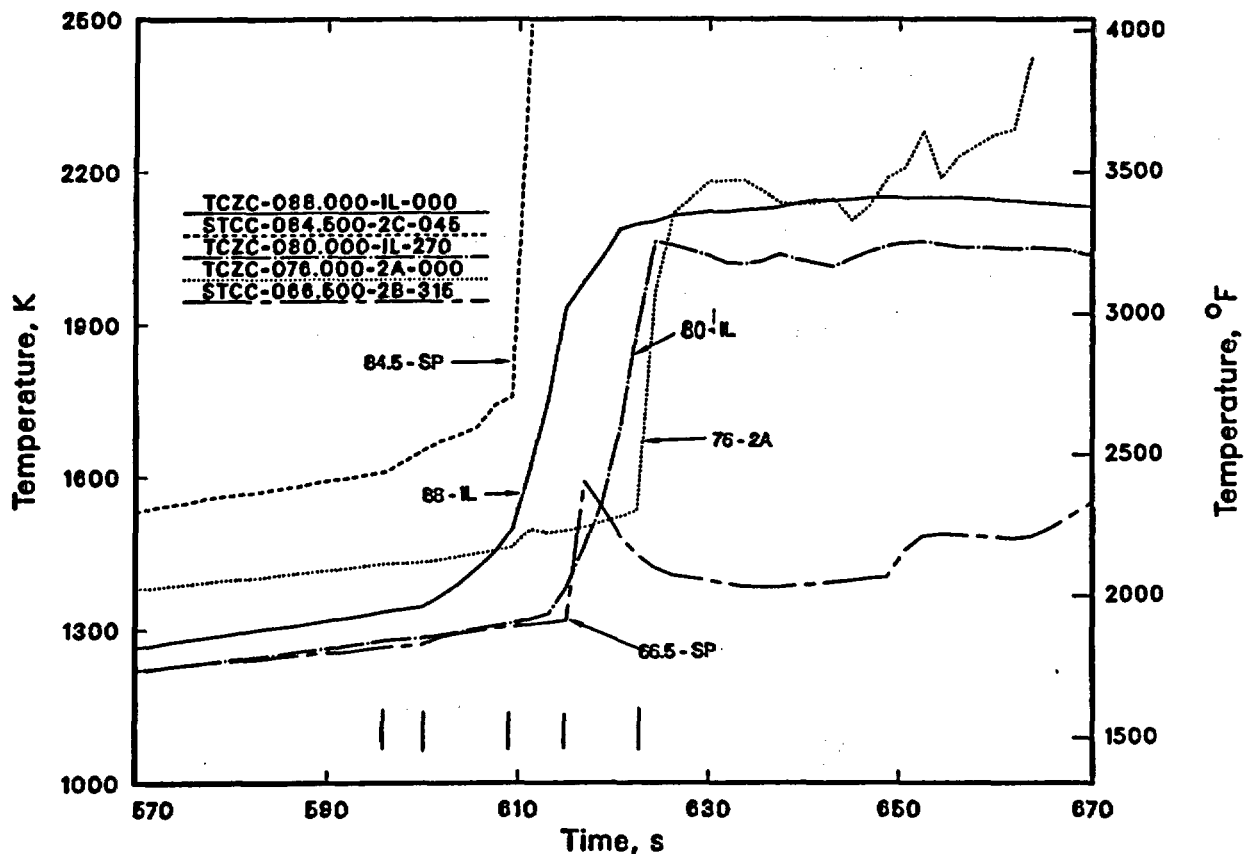


**FIGURE 11.** Thermocouple Responses Identifying FLHT-2 Material Relocation Events A-E Presented in Table 3

well as the length of the oxidation excursion zone (a function of the local steaming rate), affected the timing and amount of material that relocated and the distance it relocated. For the FLHT-2 test, a larger number of relocation events were recorded during the early phase of the burndown when the oxidation burn front velocity was greatest.

In instances where relocation occurred over a significant axial distance, e.g., the relocation distances at 600 seconds, 610 seconds, and 614 seconds, the change in the response of the thermocouples was instantaneous, indicating that the material flowed rapidly down the length of the bundle, a result of the low viscosity of molten Zircaloy. Additionally, the Inconel grid spacers appeared to have a dual role in the damage progression. They acted as molten material traps (as judged by the multiple excursions sensed at the spacer locations) and as sources of molten material (because of

eutectic formation). The behavior of the Inconel grid spacers noted in the FLHT tests is consistent with the behavior noted in the CORA out-of-pile experiments.<sup>(a)</sup>

An axial schematic of the relocation behavior in the bundle during FLHT-2 is presented in Figure 12. Illustrated in this figure are the relocation events presented in Table 3, except for the relocation event at 765 seconds. Also noted are the local interactions between materials in the

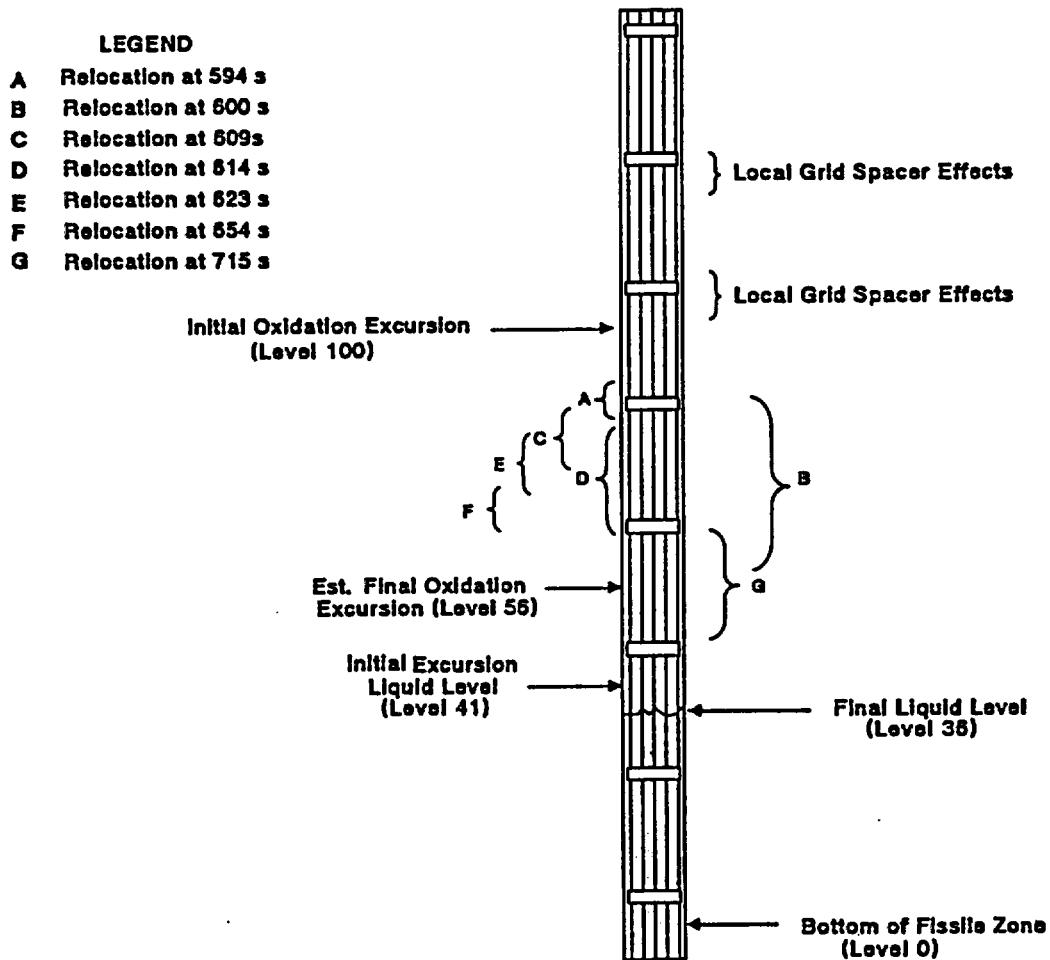


**FIGURE 12.** Axial Schematic of FLHT-2 Material Relocation Events

(a) Hagen, S., L. Sepold, P. Hofmann, and G. Schanz. 1987. "Recent Results of the KfK Severe Fuel Damage Experiments and Future Plans." Presentation/Handout at the CSARP Meeting, Silver Spring, Maryland.

cladding and materials in the grid spacer observed in the post-test visual examination but not recorded by the thermocouples. Note that the length of the brackets indicate the distances that molten material relocated. The heterogeneous nature of the relocation behavior and the potential for once-molten materials that have relocated to reheat and possibly relocate multiple times are evident in Figure 12. The axial extent of the relocation events are also indicated and are generally no longer than the axial distance between grid spacers (0.5 m).

Based on the on-line data collected during the FLHT tests and the currently available visual and metallographic results from the tests, the FLHT material relocation behavior is summarized as follows:

- The axial extent of material relocation is typically within the distance between grid spacers, i.e., <0.5 m. The relocation phenomenon is heterogeneous with the sources of molten material originating from different components within the oxidation burn front and freezing at different locations lower in the bundle elevations. Grid spacers act as both sources and sinks of molten metal.
- The extent of the axial relocation is such that once-molten materials can remelt and relocate as the oxidation excursion region proceeds downward.
- The tendency for relocation is greater early in the boiloff transient when the oxidation front velocity is highest and the amount of fresh metal the greatest. Once-molten materials have not been observed in the steam-cooled region above the coolant pool nor in the pool.

#### RELEVANCY

The FLHT tests provide data for assessing computer models that predict rapid oxidation, high temperatures, hydrogen generation, and material relocation that occur during the early phase of severe reactor accidents.

The four FLHT tests contribute data and insights unique to SFD behavior. This is because of the dynamically changing coolant level with full-length fuel rods and a constant low-fission power level that replicated decay heat

levels--parameters that lead to prototypic axial temperature profiles under coolant boilaway conditions and oxidation-induced damage progression.

The axial extent of damage increased with the length of time testing was conducted at high temperature. In the longer duration FLHT tests, an upward progression of the oxidation burn front was noted following the downward burn. Whereas the downward burn was driven by the rapidly changing axial temperature profiles, the upward burn was driven by the nearly complete oxidation of Zircaloy at lower elevations. As a result, the upward burn progressed at a slower rate, but occurred over a longer length of fuel. Downward burn occurred rapidly during a period of just a few minutes, whereas the upward burn progressed more slowly and encompassed a longer region of the fuel bundle and happened over a much longer time. Because of the disrupted geometry and oxidation that took place during the downward burn, the oxidation accompanying the upward burn in this previously oxidized region was less intense. However, in the steam-starved upper elevations above the initial oxidation excursion, the oxidation within the burn front appeared as vigorous as the downward burn. Although there existed a steam-cooled region just above the dryout front where temperatures remained below the oxidation excursion temperature and rapid oxidation did not take place, significant oxidation of the cladding took place. This resulted in highly embrittled cladding. Thus, essentially all of the exposed fuel rod cladding can be oxidized and damaged in a protracted coolant boilaway accident.

The results from the FLHT tests support the conclusion that no physical mechanisms exist that would terminate the hydrogen generation during severe accidents, aside from complete consumption of the available Zircaloy as demonstrated in the FLHT-5 test. The phenomena of material relocation, although it did not terminate hydrogen production, was found to cause a temporary reduction in the production rate; however, this temporary reduction has little influence on limiting the total hydrogen released. The mechanism for reducing hydrogen generation is the removal of hot materials from the high-temperature oxidation zone into a cooler zone. As the lower, and cooler, regions are heated as the oxidation excursion zone progresses downward, the hydrogen generation was found to return to fully-consumed conditions. During the tests,

because little material relocated from the high-temperature region to the steam-cooled region above the coolant, hydrogen generation continued until either termination of the test or, as in the case of FLHT-5, the available Zircaloy was completely consumed. Thus, for severe accidents where steam production continues, only the Zircaloy below the coolant/steam interface would not be expected to participate in the production of hydrogen.

The relocation of molten materials was tied to the passage of the oxidation burn front. The material relocation behavior can be described as heterogeneous, with material melting, relocating, and reheating as the oxidation burn front moved downward. No information was obtained on the material relocation during the upward burn because of the loss of bundle region thermocouples. The axial extent of the material relocation was generally within the spacing of the grid spacers, e.g., <0.5 m. This relocation distance was not great enough to remove significant quantities of material from the high-temperature oxidation region to the steam-cooled region or the coolant pool; thus, oxidation and the accompanying hydrogen generation continued.

Cohesive blockages were not formed at the bottom of the fuel bundle as were typically found in the short-length SFD tests. The difference in the end-state blockage formation was attributed to differences in test design and operation. The short-length tests have intrinsic design and operational features that promote the formation of large cohesive blockages, particularly at the lower elevations. These features include large axial temperature gradients resulting from the short-length, high-fission power levels and the proximity of inlet region structures to the damage region.

## REFERENCES

Cronenberg, A. W., et al. 1990. "Severe Accident Zircaloy Oxidation/Hydrogen Generation Behavior Noted from In-Pile Test Data." In Proceedings of the U.S. Nuclear Regulatory Commission: Seventeenth Water Reactor Safety Information Meeting. NUREG/CP-0105, Vol 2., U.S. Nuclear Regulatory Commission, Washington, D.C.

# STATUS OF ICARE CODE DEVELOPMENT AND ASSESSMENT

G. HACHE, R. GONZALEZ, B. ADROGUER.

Institute for Protection and Nuclear Safety  
Department of Safety Research  
Research Center of CADARACHE  
FRANCE

## ABSTRACT

An extensive programme including two series of in-pile PHEBUS-SFD and FP tests and the development of the ICARE2 code is presently being conducted in France in order to study Severe Fuel Damage phenomena occurring in PWRs. The ICARE2 code, designed to calculate reactor core damage progression, is based on the most reasonably mechanistic description of thermal hydraulics, thermal and mechanical behaviours of fuel rods as well as chemical interactions.

An overall description of the code is presented with planned future improvements and developments related to the early and late phases of core degradation : additional chemical interactions, coupling with advanced thermalhydraulics codes, debris beds and molten pools.

The development has been closely linked to the PHEBUS SFD Programme which constitutes a leading part of the assessment matrix of the code. Others available tests from the international data bank were also incorporated in order to take into account, as large as possible, a range of scales and degradation conditions. This matrix is now being extended to the PHEBUS FP Programme which will complete the data base as regards the late phase and high fuel burn-up.

Some examples of the validation work on selected PHEBUS SFD tests illustrate the current ability of the code to predict cladding oxidation, dissolution of  $UO_2$  and  $ZrO_2$  by molten Zr, failure of oxidized cladding and finally relocation of molten materials.

The simultaneous development and validation effort planned during the PHEBUS FP Programme will allow a larger and better applicability of the code for solving severe accident safety problems.

## 1 INTRODUCTION

A better understanding of in-vessel degraded core phenomena is fundamental for risk assessment and management measures. Degradation and melt progression entirely condition the crucial consequences of severe accidents such as fission product release, hydrogen production, failure of vessel and possibly failure of other parts of the primary circuit.

For these reasons, an extensive research programme is being carried out in the French Institute for Protection and Nuclear Safety (IPSN) including two series of in-pile PHEBUS-SFD and FP tests and the development of codes to predict Severe Fuel Damage phenomena occurring in PWRs.

This code programme includes the following key areas :

- physical modelling and model qualification using separate effect tests,
- development of the mechanistic computer code ICARE2 to assist with test design and applicable on a large variety of experiments,
- verification and validation by means of global experiments. The code assessment matrix includes all the PHEBUS-SFD tests and some available tests from the international data bank : PBF [1], CORA [2], FLHT. The future PHEBUS-FP Programme will complete this data base,
- plant calculations : this objective is covered by the TMI2 accident studies [3] and also by attempts to couple the ICARE2 code with fully complete system codes comprising thermalhydraulics, FP transport and chemistry.

This paper deals with the three first points of this analytical programme.

## **2 DESCRIPTION OF ICARE2 MODELS**

Among the computer codes developed at IPSN to deal with severe accident phenomenology, the ICARE2 code is especially devoted to compute -in a mechanistic way- the behaviour of a LWR core from its intact geometry up to its full destruction characterized by the appearance of debris beds evolving into molten pools.

This computer code is designed in such a way that it is able to treat both large reactor cores and smaller in-pile and out-of-pile bundles. Physical modelling is the same for both configurations except for heat transfer radiation exchanges since geometrical aspects are involved in the determination of view factors between structures and gas. Another phenomenon, not modelled at present, is only relevant for large core degradation. This concerns the axial nuclear power redistribution linked with liquefied fuel relocation. In small bundle experiments, the axial power profile is mainly dependent on the neutronic flux imposed by the surrounding driver core (PBF and PHEBUS for instance).

In the next sections, a brief description of the modelling approach applied in the ICARE2 code and an overview of planned future developments will be given.

### **2.1 COMPUTER MEMORY MANAGEMENT AND QUALITY ASSURANCE**

Several modelling aspects are difficult to deal with in the severe fuel damage field. For instance geometry changes and composition evolution due to chemical interactions. Another notable aspect is that the understanding and experimental data base in the severe accident field is in constant evolution. These conditions therefore necessitate building computer codes with great flexibility in order to be able to easily process adaptations or modifications of the computer tool according to further understanding of, or a new approach to physical phenomena. Due to the large uncertainties inherent in such physical phenomenology, several relevant modelling approaches to a given phenomenon are proposed.

Due to these requirements, the ICARE2 code is being made as modular as possible, whilst nevertheless retaining its numerical efficiency. The portability of the ICARE2 code in a large number of hardware systems has become necessary due to the large international cooperation involving the code. This requirement has been achieved using the

**FORTTRAN 77-ANSI standard (FT77) as the programming language.**

**Moreover, standard FT77 capabilities were considered to be insufficient to easily deal with large modifications in the number of problem unknowns during a transient (number of material layers in a wall mesh and number of wall meshes). Therefore, a tool package called SIGAL91, written in FT77, has been developed to extend the FT77 capabilities. This package, independent of the ICARE2 code, works on tree data base structures stored in the central computer memory which is managed dynamically. A reader and a powerful checker of input data is associated to this package as well as an analyser process able to modify, recover, add or delete any information stored in a SIGAL91-like data base.**

**With the help of SIGAL91, the development of the ICARE2 code has been widely made easier, increasing code legibility at the same time. However, efficient numerical methods must be applied in a computer code which intensively uses SIGAL91. The CPU time is indeed increased due to frequent access by this tool package to the data base stored in the central memory.**

**As regards the quality assurance, a frequent checking of the legibility and portability of the ICARE2 code is performed. The application of some programming rules, based on our code development experience, and the verification of the coherence between the coding and the physical documentation enhance the legibility. In addition, dynamic analysis tools exhibit the parts of the code which are not processed during the calculation of real case transients. Some programming errors could be detected by this means. Finally, a complete documentation is associated to a version of the code. It is composed of a user guide (pre and post processing), a physical models and numerics description report, an assessment document and a description of the tree data base of the code (coupling guide). Computer effects are avoided by checking, using different real transient cases, the portability of each version of the code with different computers.**

## **2.2 CODE DESIGN AND NUMERICS**

**The ICARE2 code is composed of a set of modules, each dealing with a specific physical model (chemical interactions, relocation of molten materials, thermal behaviour of walls, thermalhydraulics,...). There are therefore no specific modules concerning geometrical configurations such as fuel rods, absorber rods and shrouds for instance. These configurations are obtained by connecting simple objects such as hollow cylinders, grids and fluid channels.**

**The interactions between the objects are either of physical, chemical or mechanical type and they must be asked for in input data. Any interaction is facultative and, generally speaking, each could be applied in a restricted axial domain of an object and contains several options (model parameters, correlations or physical approach). This approach, leading to large input data files due to the definition of all the connections between objects, allows a large flexibility in sensitivity studies, code developments and new experimental test train modelling aspects.**

**Each module works on elementary cells generated by the intersection of the axial eulerian grid with all the studied objects. The cells are considered to be lagrangian since the geometry can evolve during the transient. A module solves a specific phenomenon assuming certain conditions and states to be constant during the global time step. For instance, the calculation of mass exchanges and chemical interactions are carried out**

assuming that the temperature of the cells involved in the process remain unchanged. The modules are processed during a time step one after the other, the final coupling between them is generally explicit in time with a few exceptions for which the explicit coupling mode could lead to unrealistic physical results. A module possibly works using a sub-cycling technique. It can modify the composition of a cell, linked with chemical reactions or flow-down of materials, but it never changes its temperature. Temperature updating is performed at the end of the time step by the thermal behaviour of walls module, coupled in an implicit way with the thermalhydraulics module.

Semi implicit coupling is applied between wall oxidation modules and the thermalhydraulics module. Thanks to this technique, complex numerical problems in the case of large consumption of steam are avoided. The numerical scheme consists in first processing the oxidation modules in order to estimate the oxygen mass required by the walls in no steam supply limitation conditions. During a second step, the solution of thermalhydraulics equations predicts possible starvation phenomena at some elevations (limitation of the oxygen flux required by oxidized walls). This solution is carried out assuming that all the interactions involving the fluid are explicit in time except the mass and energy exchanges with walls due to oxidation reactions. Finally, during a second call to the oxidation modules, the wall mesh composition are modified by fixing the real available oxygen.

## **2.3 PHYSICAL MODELS**

### **2.3.1 Thermalhydraulics**

The flowing gas is a mixture of steam with one non-condensable gas (generally Hydrogen but possibly Helium or Argon). Two mass balance equations, a momentum and an energy balance equations, completed by Dalton's law linking partial and total pressures, are solved using a one-dimensional staggered mesh fully implicit scheme. The geometry changes due to the relocation of molten materials are considered and parallel multi-channel modelling without a cross-flow is allowed. The steam mass flux available at a wall, and possibly consumed by oxidation, is estimated by applying the classic mass and heat transfer analogy (blanketing effect).

### **2.3.2 Thermal behaviour of walls**

The energy mass balance equation, written in a lumped form, is solved at the end of a time step when all the energy exchanges and heat transfer coefficients involving wall meshes have already being computed by specific modules. During the solution of coupled wall and fluid balance equations, only wall temperatures and main fluid variables are implicit in time. The energy contributions (chemical reaction heat, heat involved in mass exchanges, nuclear or electrical power) and the final mass and composition of walls are fixed.

### **2.3.3 Power generation**

Nuclear power is generated in each wall mesh according its content in  $\text{UO}_2$  (intact and relocated). The specific nuclear energy per unit mass of fuel is deduced from axial and radial power profiles provided in input data. These profiles can evolve during the transient (simulation of absorber rod relocation effect and water level decrease for instance). In the case of reactor calculations, the decay heat profile evolution linked with the

relocation of fission products is not considered.

Electrical heat generation in a set of parallel electrical rods is available (CORA facility). The heat is a function of the mesh composition and temperature. This last dependence leads to perform an implicit coupling between the thermal behaviour of walls module and the electrical resistance module.

#### 2.3.4 Conduction, convection and radiation exchanges

Conduction between two neighbouring wall meshes is modelled adding the thermal resistances associated to the mesh faces in contact. These thermal resistances are a function of the thermal conductivity of the materials in the mesh as well as of its geometry and the arrangement of the layers.

A large number of convective heat transfer correlations are available in both pipe and bundle geometries. Concerning the latter, correlations in parallel and perpendicular flow directions to a set of staggered cylinders in square or triangular (VVER type reactors) arrangement have been introduced. The perpendicular flow injection in the CORA bundle can be modelled.

The net radiation enclosure method is used to model the radiation heat transfer exchanges between grey wall surfaces and a homogeneous gas filling the enclosure. It is assumed that an enclosure corresponds to an axial mesh and therefore that no radiation exchanges take place between two axial neighbouring meshes. This two dimensional approach allows the calculation of view factors between the walls to be performed using Hottel's crossed string method. The steam is assumed to be participative. Its transmissivity is computed using classic methods and assuming that steam has five absorbent spectral bands. The radiative energy balance equation is solved in each enclosure in order to determine the total radiative flux between the walls, and between the walls and the gas (Hottel's concept of total interchange areas is used). This solution is carried out either in each transparent and absorbent spectral band characterizing the steam or in the overall spectrum if the steam is assumed to be a grey gas.

#### 2.3.5 Mechanical behaviour

A creep model allows calculation of cladding ballooning and burst. The evolution of the radius of the internally pressurized cladding is computed using a hoop creep velocity correlation established from the French EDGAR experiments. This velocity is a function of the cladding temperature and of the hoop stress. Cladding burst is declared when its temperature exceeds a burst temperature limit which is a function of both cladding temperature slope and hoop stress.

The creep module is the last module processed. A linear variation is assumed for cladding mesh characteristics (layer thickness, temperature), known at the beginning and at the end of the global time step. The sub-time step management is performed by verifying that the relative variation of the creep velocity and the absolute variation of the hoop strain, during a sub-time step, are lower than threshold values. This sub-cycling technique ensures accurate convergence in time of the ballooning calculation.

Each wall mesh layer is in one of the three following states : compact (generally the initial state), cracked or dislocated. The cracking of a layer is declared for instance after the cladding burst occurrence in a user specified axial zone near the burst elevation. A partially molten layer is automatically declared dislocated by the code. Both cracked and

dislocated states can also be imposed through the input data deck when some criteria are fulfilled (set of inequalities involving threshold values for some parameters such as temperature, layer thickness, temperature slope and time). This input data capability is used to simulate the loss of integrity of the cladding and shroud  $ZrO_2$  layers, as well as to take into account the dissolution of the Zr guide tube by the absorber rod materials. The cracked state allows the radial movement of possible enclosed molten materials towards the surface of a wall mesh, the internal oxidation of the mesh and finally the release of fission products. The dislocated state makes the axial movement of molten materials possible.

### 2.3.6 Relocation of molten materials

Only partially molten materials can flow down along the vertical surfaces and refreeze. This axial movement is achieved by solving a mass transport equation in which, at present, the candling velocity is assumed to be constant. A refreezing mass flow rate is applied in this balance equation at each elevation. This mass flow rate is estimated from the solution of a simplified energy balance equation. Only the heat exchange between the flowing melt and the contacting structure as well as the latent heat of freezing are considered to be dominant (other energy contributions are neglected). No chemical interaction is performed during the relocation process. The candling velocity is strongly reduced when mixtures flow through a spacer-grid.

A radial movement of molten materials from a structure to another neighbouring structure can be asked for in input data. So, deposition of molten absorber rod materials on the external surface of the guide tube is simulated by this means.

### 2.3.7 Fission product release models

The mass inventory evolution of 40 species of Fission Products (FP) located in the fuel or coming from the structural materials of absorber rods, is computed using 3 available models. These are the well known CORSOR-M model, the French EMIS module validated using the French HEVA experiments, and finally the German SASCHA module. All these models are based on the same simplified approach which assumes an exponential decay of each FP mass inventory. The fractional release rate coefficient associated with a specy (unit  $s^{-1}$ ) is temperature dependent. An Arrhenius formulation is applied in CORSOR-M for this coefficient.

The fuel rod cladding burst occurrence entails the sudden release of a fraction of the initial inventory of volatile fission products located in the gap. These fractions can be imposed in input data.

## **2.4 CHEMICAL INTERACTIONS**

### 2.4.1 Zr oxidation

The parabolic correlations of Urbanic, Cathcart or Prater are used to estimate the total oxygen mass gain of a Zr mesh and the  $ZrO_2$  layer thickness growth in unlimited steam conditions at a given temperature. The evolution of the  $\alpha$ -Zr(O) layer enclosed between the prior  $\beta$ -Zr and the  $ZrO_2$  oxide scale is computed assuming a constant oxygen mole fraction in this layer (generally 20 %).

Under limited steam conditions, the ICARE2 model assumes that the available oxygen mass preferentially supplies the  $\alpha$ -Zr(O) layer for its growth. Nevertheless, the oxygen

mass increase of the  $\alpha$ -Zr(O) layer cannot exceed the value calculated in unlimited steam conditions. If this condition is not fulfilled, then the oxygen excess is used to increase the oxide scale.

The same approach and correlations are applied to oxidize relocated mixtures containing Zr. A 3 layer configuration ( $\beta$ -Zr,  $\alpha$ -Zr(O), ZrO<sub>2</sub>) is artificially generated in the mixture in order to process the calculation as in the initial intact geometry of the cladding. Other materials composing the mixture are assumed to decrease the surface of the mesh in contact with the steam according to their volumetric fraction.

#### 2.4.2 Stainless steel oxidation

As regards Zr oxidation, parabolic correlations are used to compute the total oxygen mass gain of a stainless steel mesh. The oxide layer is composed of a mixture of iron, chromic and nickel oxides.

In both stainless steel and Zr oxidation reactions, the chemical heat generated is computed using the formation heat of the different oxides at the reaction temperature.

#### 2.4.3 UO<sub>2</sub> liquefaction by solid Zr

This interaction becomes significant above 1473K when the fuel pellet and the cladding are in contact. UO<sub>2</sub> is reduced in UO<sub>2-x</sub> by the prior  $\beta$ -Zr leading to the appearance of 2  $\alpha$ -Zr(O) layers enclosing a liquid U-Zr eutectic layer. This process has been demonstrated to be oxygen diffusion controlled by Hofmann [4]. The parabolic correlations deduced from this experimental work are used to compute the thickness increase of the 3 layers ( $\alpha$ -Zr(O), U-Zr,  $\alpha$ -Zr(O)) located between UO<sub>2</sub> and the prior  $\beta$ -Zr layer.

#### 2.4.4 UO<sub>2</sub> and ZrO<sub>2</sub> dissolution by molten Zr

A liquid mixture rich in Zr and enclosed between the fuel column and the external cladding ZrO<sub>2</sub> scale simultaneously dissolves both oxides. This interaction develops up to the saturation of the U-Zr-O melt in oxygen characterized by the precipitation of a solid phase (this means that the liquidus boundary is crossed). Therefore, dissolution of UO<sub>2</sub> is limited by the feeding of oxygen arising either from the dissolution of the ZrO<sub>2</sub> layer or from the oxygen of the fluid channel diffusing through the ZrO<sub>2</sub> scale. In addition, UO<sub>2</sub> dissolution can be stopped as soon as the U-Zr-O melt flow-down is allowed by the loss of mechanical integrity of the external ZrO<sub>2</sub> layer linked to its thickness decrease.

According to the experimental works of Kim-Olander and Hofmann [4], both dissolution processes can be modelled using parabolic kinetics correlations when they are oxygen diffusion controlled. However, a Uranium convection-controlled process explains the UO<sub>2</sub> dissolution according to Kim's experiments when the UO<sub>2</sub> surface is vertical and if the U-Zr-O mixture is sufficiently thick. In this case a transport equation providing the evolution of the U concentration in the melt is solved.

All these experiments have exhibited, at the beginning of the interaction, an incubation period characterized by a rapid dissolution of the oxides. This initial period is followed by the establishment of the diffusion process. Since the available experiments were carried out with initial oxygen-free Zr, some corrective factors have been introduced in the code modelling to try to extrapolate the experimental results to the case of Zr initially pre-loaded with oxygen. A more detailed description of this complex chemical interaction is provided in [5].

## **2.5 FUTURE DEVELOPMENTS**

In order to enlarge the scope of the code applicability to reactor cases, the implementation of a one-dimensional two-phase flow thermalhydraulics with 2 non-condensable gases is underway. The set of 8 balance equations (4 mass, 2 momentum and 2 energy equations) is completed by the physical grids of the French thermalhydraulics CATHARE 2 code. The introduction of this 2 phase flow model is carried out in such a way that the coupling between ICARE2 and CATHARE 2 codes will be possible.

A debris bed module dealing with a solid and a liquid phase in thermal equilibrium is under development. Darcy's law is used to compute molten material velocity in the debris bed taking into account capillarity and gravity effects. The steam flow through the debris bed is calculated by the thermal hydraulics module applying Darcy's law and assuming that the steam is in thermal equilibrium with the compounds of the debris bed.

The absorber rod model will be completed by introducing the voiding of molten columns above the break elevation of the guide tube, and the dissolution of Zr by the Ag-In-Cd absorber material.

At present, a spacer-grid acts during the relocation process of molten materials by reducing the candling velocity of the melt. The oxidation of a spacer-grid composed of Zr is also possible. To complete this spacer-grid modelling, the Zr/nickel interaction will be introduced.

An alternative approach to the parabolic kinetics correlations used to simulate UO<sub>2</sub>/cladding and cladding/steam interactions is being developed. In this new model, the diffusion equation of oxygen inside the cladding, due to external oxidation by steam and internal reduction of UO<sub>2</sub>, will be used in conjunction with oxygen concentrations at the phase boundaries provided by the U-Zr-O phase diagram.

A work is presently made in order to obtain more realistic modelling of the relocation process. A solution of the momentum equation of the molten materials flowing along vertical structures is being developed. Capillarity, viscosity and gravity effects will be considered.

Finally, the introduction of the mechanistic FASTGRASS code dealing with the release of Fission Products (FP) will complete the set of current simplified FP release correlations.

## **3 CODE ASSESSMENT**

### **3.1 ASSESSMENT MATRIX**

During the development of the code a systematic verification and validation process, mainly based on both code-to-data and code-to-code comparisons, was performed both by code developers and by PHEBUS analysts. The aim of this crucial work was to determine the technical adequacy of the code in different situations. In addition to the PHEBUS tests which are systematically analysed, others available tests have been chosen considering the following aspects.

- a) tests with different bundle geometries in order to check the convection and radiation models,
- b) separate effect tests so as to check particular chemical interactions between core materials,

Experiment or Accident	Thermal Response	Cladding Oxidation H2 release	Spacer Grid	UO2 dissolution by Zr	Absorber rods	Particulate debris formation	Blockage Formation	FP release
PHEBUS B9	Y (*)	H.ox(*)	Inc.	N	N	N	N	N
PHEBUS B9R-1	Y (*)	H.ox(*)	Inc.	N	N	N	N	N
PHEBUS B9R-2	Y (*)	H.ox(*)	Inc.	Few	N	Y (*)	Y (*)	N
PHEBUS C3	Y (*)	Lox	Inc. (*)	Y(solid Zr)	N	N	Y	N
PHEBUS C3+	Y (*)	Lox,H2	Inc. (*)	Y(solid Zr) Y(molten Zr)(*)	N	Y (*)	Y (*)	N
PHEBUS B9+	Y (*)	H.ox,H2(*)	Inc. (*)	Y(molten Zr)(*)	N	N	Y (*)	N
PHEBUS AIC	Y (*)	Lox,H2(*)	Zry	N	Y(SIC) (*)	N	Y (*)	N
CORA 5	Y (*)	H.ox	Inc., Zr(*)	Y	Y(SIC) (*)	N	Y (*)	N
CORA 13	Y (*)	H.ox,H2	Inc., Zr(*)	Y	Y(SIC) (*)	N	Y (*)	N
PBF SFD 6T	Y (*)	H.ox(*)	Inc.	Y	N	Y (*)	Y (*)	N
PBF SFD 1-4	Y (*)	H.ox	Inc.	Y	Y(SIC) (*)	Y (*)	Y (*)	Y (*)
FLHT-6	Y (*)	H.ox	Zry	Y	Y(B4C) (*)	N	Y (*)	Y
TMI-2	Y (*)	All the aspects of core degradation with crucible formation						
HEVA				N	N			Y (*)
S.E. TESTS			(*)	(*)	(*)	(*)		

TABLE 1: VALIDATION MATRIX OF ICARE 2. MAIN PHENOMENA EXHIBITED IN EXPERIMENTS  
Y:Yes, N:No, (\*) main phenomena,H.ox,I.ox,Lox: High,Intermediate,Low oxidation  
S.E.: Separate Effect, Inc.: Inconel, SIC: Silver Indium Cadmium

Experiment	Pressure (MPa)	TMAX	Flow Input	Spacer Grid	Bundle Nbr rod	Final cooling	Date of test	Fuel Burn-up MWd/tU
PHEBUS B9	1.9 to 0.5	2150 K	Steam,He	Inconel	21	S(He)	Dec. 3,1986	0
PHEBUS B9R-1	2.0 to 0.5	1800 K	Steam,He	Inconel	21	R(He)	Apr. 1,1988	0
PHEBUS B9R-2	0.5	2150 K	He,Steam	Inconel	21	R(Steam)	Apr.14,1988	0
PHEBUS C3	3.5	2050 K	He,H2,Steam	Inconel	21	S(He)	Oct.30,1987	0
PHEBUS C3+	3.5	2570 K	Steam,He	Inconel	21	S	Nov.24,1987	0
PHEBUS B9+	2.	2750 K	Steam,He	Inconel	21	S(He)	Jan.26,1989	0
AIC	0.6	2100 K	Steam,He	Zircaloy	20+1 (SIC)	S(He)	June 1,1989	0
PH-FP-FPT0	0.2	3100 K	Steam	Zircaloy	20+1 (SIC)	R(Steam)	Spring 1993	trace
PH-FP-FPT1	0.2	3100 K	Steam	Zircaloy	20+1 (SIC)	R(Steam)	Spring 1994	27
PH-FP-FPT2	0.2	3100 K	Steam/He + H2/Steam	Zircaloy	20+1 (SIC)	R(Steam)	Spring 1995	27

TABLE 2: PHEBUS SFD TEST SERIES - MAIN EXPERIMENTAL CONDITIONS  
SIC: Silver Indium Cadmium, S:Slow (S < 2K/S), R:Rapid

- c) tests focussing on additional conditions of core degradation (control rod behaviour, quenching),
- d) global tests at different scales in order to check overall core melting and relocation up to the crucible formation.

Following these principles, the code is being assessed on a test matrix (Table 1) which covers a wide range of scales and experimental conditions.

As regards the separate effect tests, the development and assessment of the code relies on some national results and mainly on international research data. For example, the cladding deformation model is based on the French EDGAR results, low temperature liquefaction processes due to chemical interactions between core structures are mainly based on the KfK data bank [4]- UO<sub>2</sub> dissolution by solid and molten Zr, ZrO<sub>2</sub> dissolution by molten Zr, Zr/Inconel interaction, chemical behaviour of (Ag, In, Cd) absorber rods - fission product release is based on the French HEVA and VERCORS results.

As regards the validation using global tests, efforts were focussed on the early phase of core degradation. In this area a large number of experimental data (PHEBUS-SFD, PBF-SFD, CORA, FLHT) allows a good understanding of the main core degradation phenomena which lead to the formation of a debris bed surrounded by a crust (TMI-2 end state). The main features of this early phase must at least be correctly calculated before making a prediction of the late phase. This final phase, for which a much poorer data bank exists, is mainly in a developmental stage and will be assessed using the future tests from the international SARP and PHEBUS FP Programmes.

The PHEBUS SFD tests represent a large part of the assessment matrix. Pre-test calculations served to design the experiments and understand the processes taking place during the experiment. Post-test simulations were performed including sensitivity calculations in order to complement the test analysis as well as to verify the code and improve the modelling of the physical and chemical processes.

Benchmarking activities using code-to-code comparisons are also currently being performed, particularly on the first PHEBUS FP experiment in the framework of the test design [6].

Some characteristics of the PHEBUS tests of the SFD and FP Programmes which were calculated with ICARE2 are given in Table 2.

### **3.2 POST-TEST ANALYSIS OF SOME PHEBUS-SFD TESTS**

In this section, the calculation results of selected tests of the PHEBUS-SFD Programme are assessed as to the extent and way in which some key degradation phenomena are simulated by ICARE2 V2. Additional examples of calculations performed on other experiment also illustrate current code performance [1,2,3].

The PHEBUS test facility and the bundle descriptions are provided in [7,8].

#### **3.2.1 PHEBUS B9 and B9R tests**

The main objective of these tests was to study cladding oxidation with different steam flow rates and in different cooling conditions.

The B9 test which was performed with a rich steam atmosphere and a low heat-up rate (0.2 K/s) was a first opportunity to check the initial versions of ICARE2 code, focussing mainly on the thermal exchanges and oxidation models up to 2150 K.

The analysis of this test enables the experimental uncertainties related to the heat losses through the porous  $ZrO_2$  layer of the surrounding shroud to be identified. Particularly evidence was found of the ingress of  $H_2$  from the liner oxidation into the porous  $ZrO_2$  which increased the conductivity of the shroud. After adjusting this parameter (see section 3.2.3.), a correct calculation of the thermal behaviour of the rods enabled the oxidation model of ICARE2 to be checked, based on a series of oxidation kinetics to be chosen by the user. The best global agreement was obtained with the Urbanic correlation which tends to underpredict the oxidation by up to 25 %. This tendency was confirmed by the first oxidation calculations of the B9+ test (see section 3.2.3) in which the final state of oxidation was similar to that observed in the B9 test (final escalation at the hot point with nearly complete oxidation).

Finally, considering that the  $ZrO_2$  thickness correlations are no longer valid in the case of complete consumption of the underlying metallic Zr, it was proposed to improve the calculation of the oxidation by estimating the  $ZrO_2$  layer increase from a ponderation between the total  $O_2$  consumption correlation and the  $O_2$  involved in the  $ZrO_2$  thickness correlation. A weighting factor equal to 0.5 was found to give the best results. This approximation was confirmed in comparing these oxidation predictions with the more mechanistic code PECLOX in which the oxidation is based on  $O_2$  diffusion [4]. With this approximation the current oxidation model of ICARE2 based on kinetics correlations predicts oxidation up to the melting of the Zr within the experimental uncertainty range.

Due to an operating incident, the B9R test was carried out in two parts : the first called B9R-1 was similar to the B9 test, the second called B9R-2 was performed with a first heating phase with pure Helium up to 1300 K and was followed by a pure steam phase. The test was finished by a rapid cooling-down (more than 10 K/s).

During the B9R-2 test, an unexpected strong escalation of the Zr-water reaction occurred at mid-bundle elevation during the steam injection. Considerable heat-up rates of 20 to 30 K/s were measured in this zone with steam starved conditions at upper levels. Post Irradiation Examinations (PIE) show cladding failures and considerable deformations (about 70 %). Unfortunately the  $H_2$  release related to this oxidation escalation could not be measured.

Sensitivity studies showed that a correct prediction of this escalation using the current oxidation model could not be obtained considering only the double-sided oxidation of the failed cladding tubes (as supposed from the PIE of B9 test and the actual considerable cladding deformations). An increased contact area between steam and Zr was also needed. This was confirmed by the PIE which show penetration of  $ZrO_2$  through cracks in the Zr sublayers. According to ICARE2 sensitivity calculations the Zr-steam contact surface should be increased by at least a factor 2 (Fig.1). No sufficient data are available to propose a general model taking into account this contact surface increase due to the cracking of the  $ZrO_2$  and underlying Zr layers. This cracking is supposed to have occurred during the cooling phase of the B9R-1 part of the experiment [8].

The final rapid cooling phase of the B9R-2 test was performed with a high steam flow rate. It was also characterized by a second oxidation escalation of the remaining non-oxidized Zr located at upper levels. As in the previous case, the current oxidation model does not

allow prediction of such an escalation. A solid debris bed was formed due to the rapid cooldown (10 K/s). These data are valuable to define general criteria for a loose rubble bed formation.

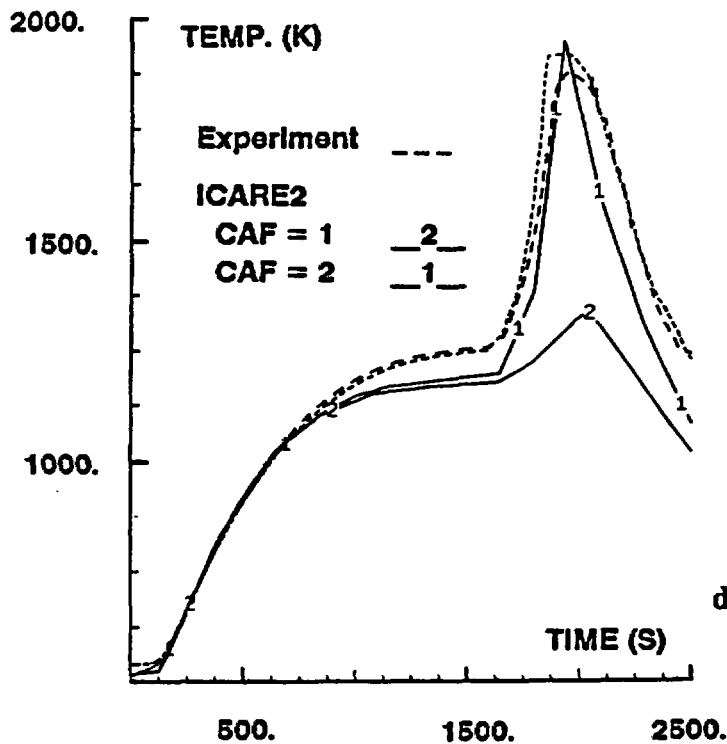


**Fig.1 :**  
Sensitivity calculation on the B9R test. Temperature escalation at the hot level (0.6 m) with different Contact Area Factors (CAF)

### 3.2.2 PHEBUS C3 + test

The main objective of this test was to study  $UO_2$  dissolution by chemical interaction with solid Zr in a first stage and with liquid Zr in a second stage in the case of limited cladding oxidation. The first low temperature oxidation phase was performed during 3000 s with pure steam at 0.6 MPa so as to reach a low cladding oxidation level. The second 11000 s phase long was performed in pure He at 3.5 MPa so as to obtain good  $UO_2$ -Zr contact inside the non-pressurized rods. The heat-up of the bundle was driven by several power step increases.

After adjusting the shroud heat losses in the first steam phase (see next section), the calculated and measured inner fuel rod temperatures at the 0.10, 0.40 and 0.60 m elevations agree well, until the thermocouple failures shown in Fig. 2 by arrows. Above 2200 K the calculation agrees with the fuel thermal behaviour estimated from the shroud measurements and PIEs. The calculated oxidation profile is shown in Fig. 3. A maximum of 18 % mean oxidation is predicted at the hot point (0.6 m from the bottom of the active length). The PIEs confirm a low level of oxidation but no significant measurement was performed due to the complete disappearance and relocation of the cladding between 0.05 and 0.60 m.

Fig. 4 shows two calculations of the  $UO_2$  dissolution. In the two cases the first stage of the  $UO_2$  dissolution by "Solid" Zr is calculated with the Hofmann (S) model but the second stage of  $UO_2$  dissolution by "Molten" Zr is calculated in one case with the Kim model and in the other with the Hofmann (M) model. In these two cases the same  $UO_2$  solubility limit

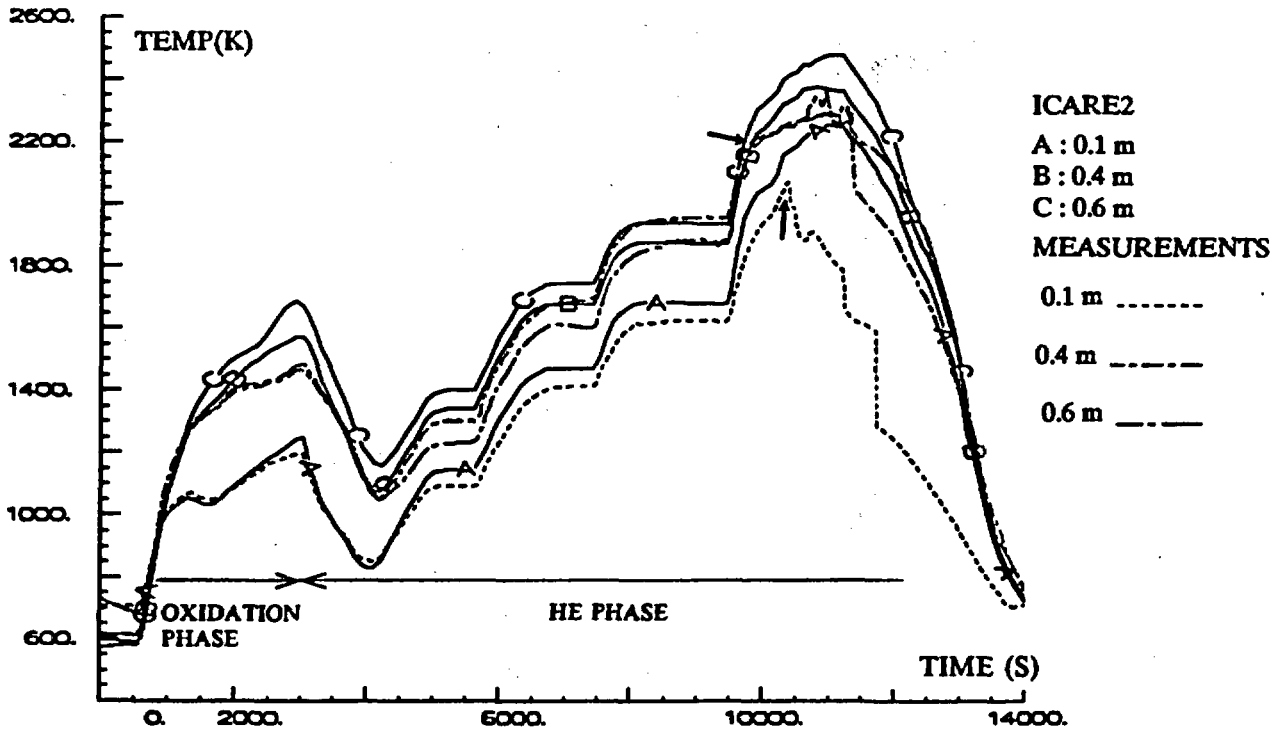


FIG. 2 PHEBUS SFD C3+ test. Fuel temperatures versus time at different elevations.

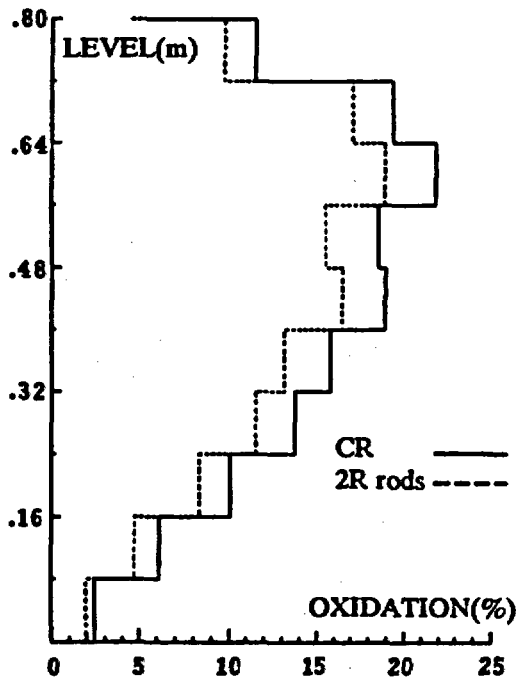


FIG. 3 : PHEBUS SFD C3+ test. Calculated oxidation profiles at 3000 s for Central Rod (CR) and 2nd Ring Rods (2R).

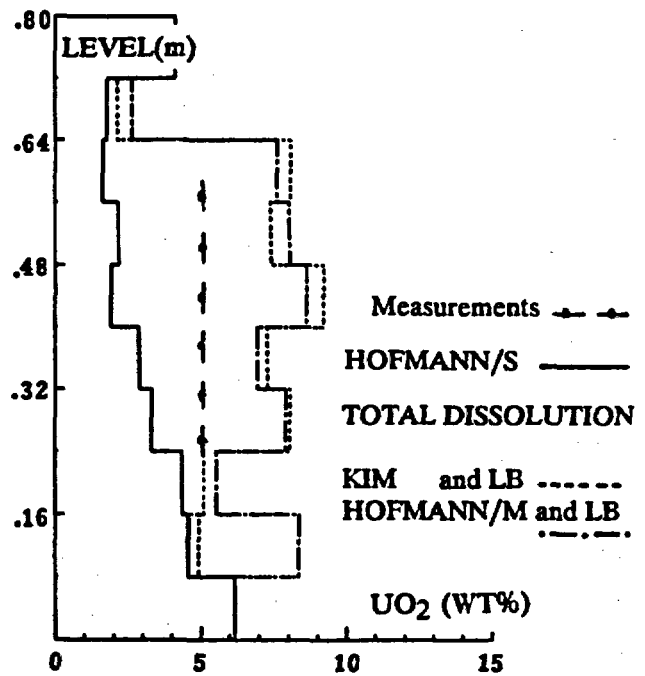


FIG. 4 : PHEBUS SFD C3+. Calculated UO<sub>2</sub> dissolution profiles with Kim and Hofmann Models.

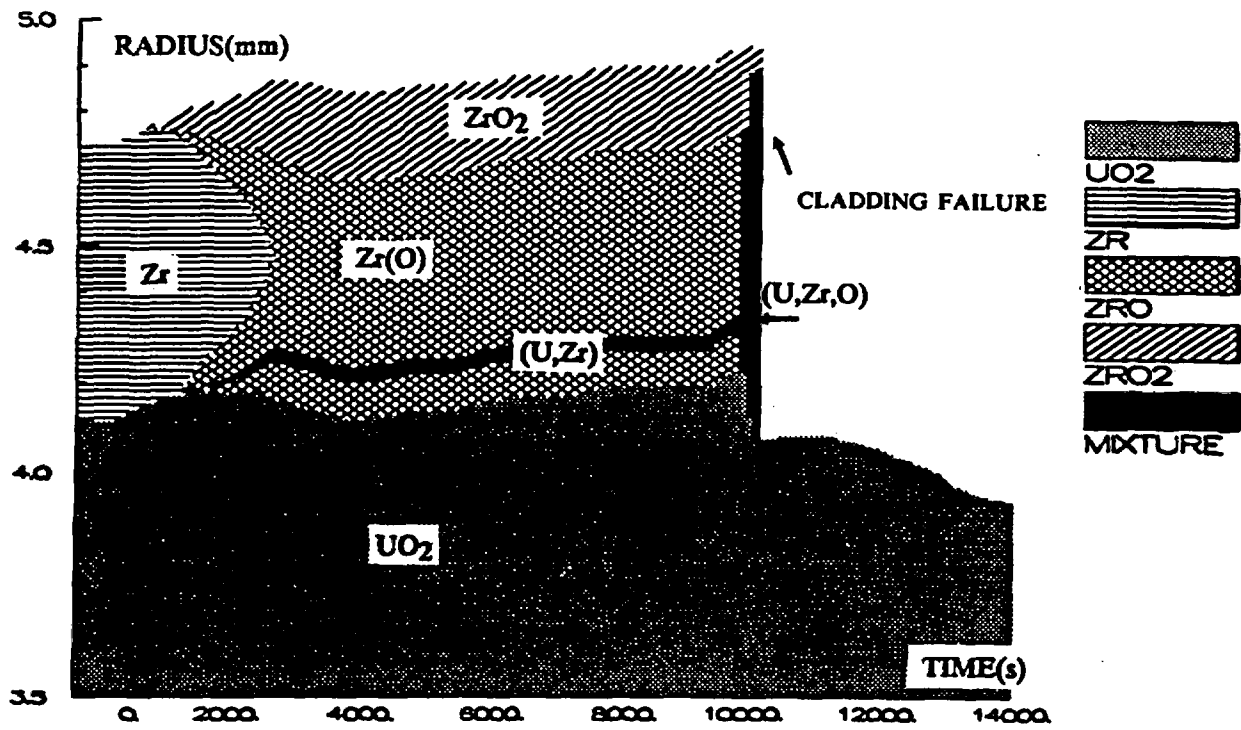


FIG. 5 PHEBUS SFD C3+. Cladding radius zones versus time at 0.6 m.

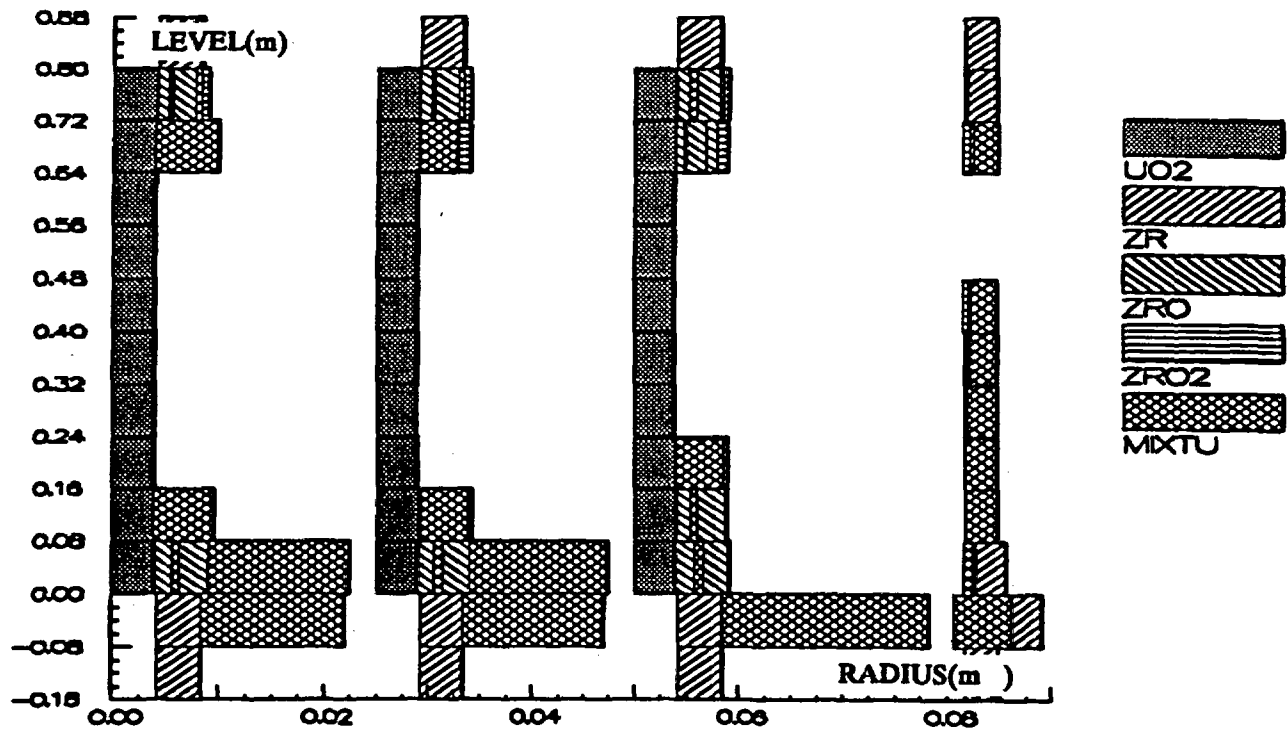


FIG. 6 : PHEBUS SFD C3+. Calculated final state of the bundle (3 kinds of rods and shroud liner). ICARE2 models : Kim UO<sub>2</sub> dissol model, UO<sub>2</sub> solubility limit equal to the liquidus temperature of the U-Zr-O mixture.

in the resulting U-Zr-O mixture is considered (liquidus temperature).

The first UO<sub>2</sub> dissolution by solid Zr was found as a weak effect with a UO<sub>2</sub> dissolution limited to about 2 to 3 wt % in the central zone and up to 6 wt % at 0.04 m. The end of this interaction, which corresponds to the complete transformation of  $\beta$ -Zr in  $\alpha$ -Zr (O), is reached sooner in the central zone than in the lower part where higher temperatures are reached during this interaction. This explains the greater UO<sub>2</sub> dissolution obtained in the lower part.

When the resulting two  $\alpha$ -Zr (O) layers melts, the UO<sub>2</sub> dissolution by molten Zr begins near 10000 s in the central zone and lasts less than 300 s because the outer ZrO<sub>2</sub> layer is not thick enough (max 150  $\mu$ m) to keep the molten Zr in place for a long time. The usual cladding failure criterion chosen ( $T^* > 2300$  K and  $e^* < 300$   $\mu$ m) stops the interaction on the temperature conditions (relocation of the U-Zr-O melt). Using the same UO<sub>2</sub> solubility limit in the U-Zr-O melt, the two models of UO<sub>2</sub> dissolution by molten Zr gave similar results with about 7 wt % of additional UO<sub>2</sub> dissolution in the hot zone (Fig. 4).

Finally the calculated 10 wt % total UO<sub>2</sub> dissolution by solid and liquid Zr is overestimated in comparison with the PIE which show a mean dissolution limited to about 5 wt %. As explained in [5], the choice of too high a failure temperature (user-specified parameter) explains this result. A calculation using a lower failure temperature  $T^*$  of 2260 K gives better results with more limited additional dissolution by molten Zr. This point illustrates the weakness of a parametric model which obliges the user to specify part of the degradation response in code input.

The behaviour of the different layers of the cladding at 0.6 m illustrates the different phenomena simulated (Fig. 5) : first UO<sub>2</sub> dissolution by solid Zr up to 3000 s, melting of the  $\alpha$ -Zr(O) layers and mixing with the U-Zr melt at  $\sim 10000$  s, the second short dissolution period by molten Zr, followed 300 s later by cladding failure and melt relocation.

The prediction of all these events is consistent with the current knowledge of the initial UO<sub>2</sub> cladding interactions in the case of good contact and low cladding oxidation.

The calculated final state of the bundle is shown in Fig. 6. This picture is in agreement with vertical and horizontal cross sections of the bundle which show complete decladding of the rods between 0.05 and 0.6 m and frozen mixtures located between - 0.075 and + 0.15 m. The upper plug in this zone (flow blockage of  $\sim 80$  %) is a ceramic mixture of (U,Zr) O<sub>2</sub> and  $\alpha$ -Zr(O) and the lower plug is a metallic mixture rich in Zr, Ni and U. The lower spacer-grid located at 0.14 m was melted and already relocated when the U-O-Zr melts flowed down later on. The predictions of the location and flow blockage (83 %) are correct. The lower plug could not be calculated because the provisional spacer-grid model was not used.

### 3.2.3 PHEBUS B9 + test

The main objective of this test was to study UO<sub>2</sub> and ZrO<sub>2</sub> dissolutions by molten Zr in the case of significant cladding oxidation. These rod degradation conditions enable the failure conditions of cladding tubes characterized by a deep axial ZrO<sub>2</sub> thickness profile to be studied. The test was performed in two phases as in the C3+ test but with a longer oxidation phase. The first process of UO<sub>2</sub> dissolution by interaction with solid Zr was minimized by avoiding an external pressure effect on the cladding. More details of this test are given in [7] and [9].

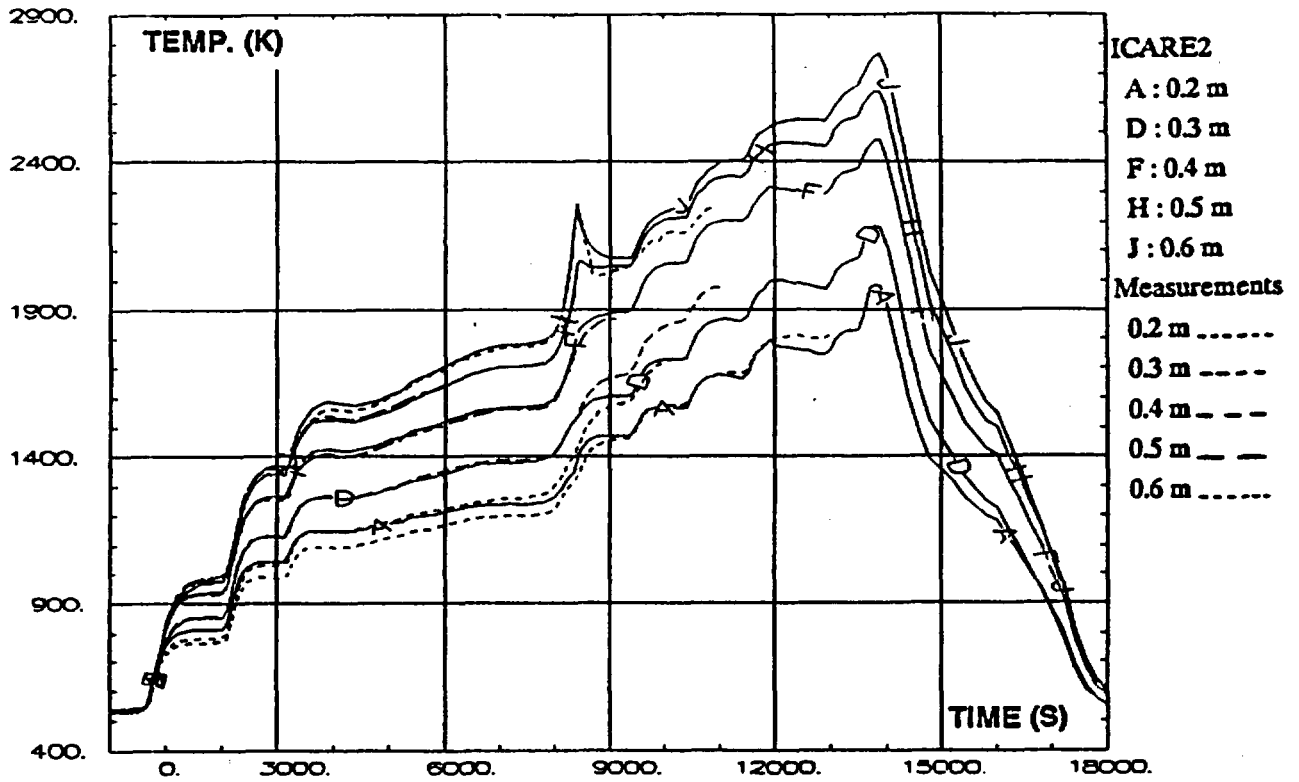


FIG. 7 : PHEBUS SFD B9+ test. Rod temperature versus time at different elevations. ICARE2 calculation with adjusted radial heat losses through the shroud.

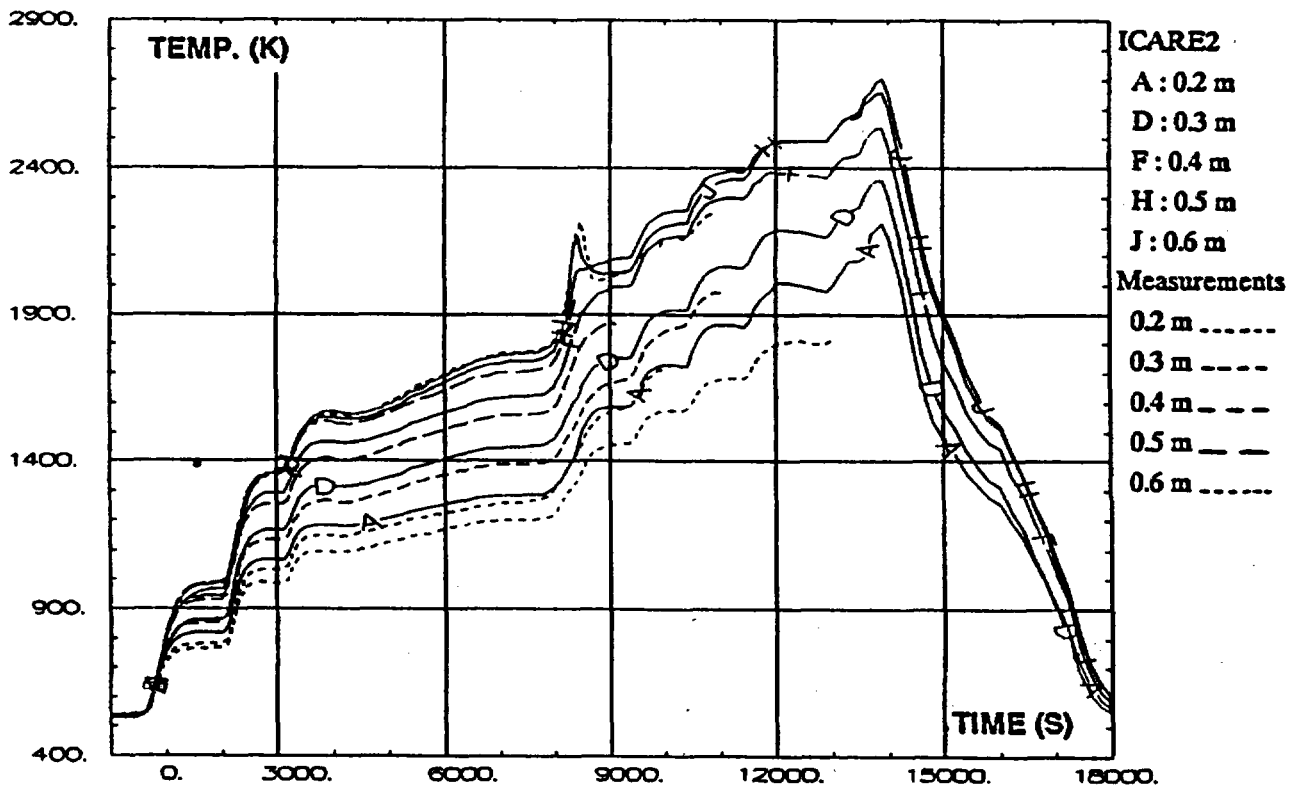


FIG. 8 : PHEBUS SFD B9+ test. Rod temperature versus time at different elevations. ICARE2 calculation without tuning of the radial heat losses through the shroud.

Comparisons of the thermal behaviour between the calculation and the measurements show a global satisfactory agreement when adequate adjustments have been made to cope with experimental uncertainties in the radial heat losses through the shroud. Figures 7 and 8 show comparisons of calculated and measured temperatures with and without tuning of the zirconia insulation around the bundle which is the dominant experimental uncertainty (deformation, failure, internal oxidation, conductivity and porosity evolutions at high temperature). The uncertainty related to the filling gas was avoided in this test by a continuous Helium injection into the shroud.

Sensitivity studies indicated that discrepancies between ICARE 2 calculations and experiments, due to these experimental uncertainties, are greater than those due to modelling uncertainties on the heat transfer models.

After adjustments of the radial heat losses a correct agreement was obtained as regards the radial temperature profile in the bundle, the rapid oxidation escalation which occurred in the hot zone - when the cladding temperature reached 1850 K just after 8000 s - and the peak temperature.

Fig. 10 shows the calculated axial oxidation profiles (Urbanic kinetics) of different rods within the bundle compared with the  $ZrO_2$  measurements on the outer and inner rods. These data, which are representative of oxidation at the end of the first steam phase, show large ranges of  $ZrO_2$  thickness measurements. These ranges are related to non-homogeneous cladding temperatures at one elevation and to uncertainties related to the identification of the  $ZrO_2$  thickness representative of oxidation at the end of the steam phase. The later reduction of the  $ZrO_2$  layer during the second Helium phase and the  $UO_2$  - cladding interactions tend to modify this state.

In spite of these measurement difficulties, comparisons between calculations and data were able to be made and they showed that oxidation prediction with the ICARE2 oxidation model is within the experimental measurement range.

Fig. 9 shows that there is a slight overprediction of  $H_2$  production which could result in part from a slight overprediction of the liner temperatures (~20 % of the total  $H_2$  is produced by the oxidation of the liner).

The second heat-up phase is characterized by extreme steam-starved conditions which facilitate simultaneous  $UO_2$  and  $ZrO_2$  dissolution by molten Zr. This phenomenon is very much a function of the temperature, and also of the oxidation profile which determines the mass of molten Zr available and its oxygen content.  $UO_2$  and  $ZrO_2$  dissolutions are limited by the temperature dependent  $UO_2$  saturation of the local U-Zr-O mixture or by the failure of the external  $ZrO_2$  layer which governs the flow-down of the mixture and the end of the dissolution.

Fig. 11 shows the mean axial profile of the  $UO_2$  dissolution calculated using the Hofmann (M) and Kim models applied with the same  $UO_2$  solubility limit (liquidus temperature of the U-Zr-O mixture). These two calculations give a correct prediction of  $UO_2$  dissolution. No dissolution was predicted near 0.7 m due to the prediction at this level of complete oxidation in agreement with the mean tendency observed in the test.

The high dissolution rates which characterize the Kim and Hofmann (M) models lead to a prediction of very rapid fuel dissolution up to either cladding failure or the  $UO_2$  solubility limit (60 % of the total fuel dissolution in less than 60 s). When this limit is reached the rate of the further  $UO_2$  dissolution becomes slower and is nearly only driven by the evolution of  $UO_2$  solubility with the temperature.

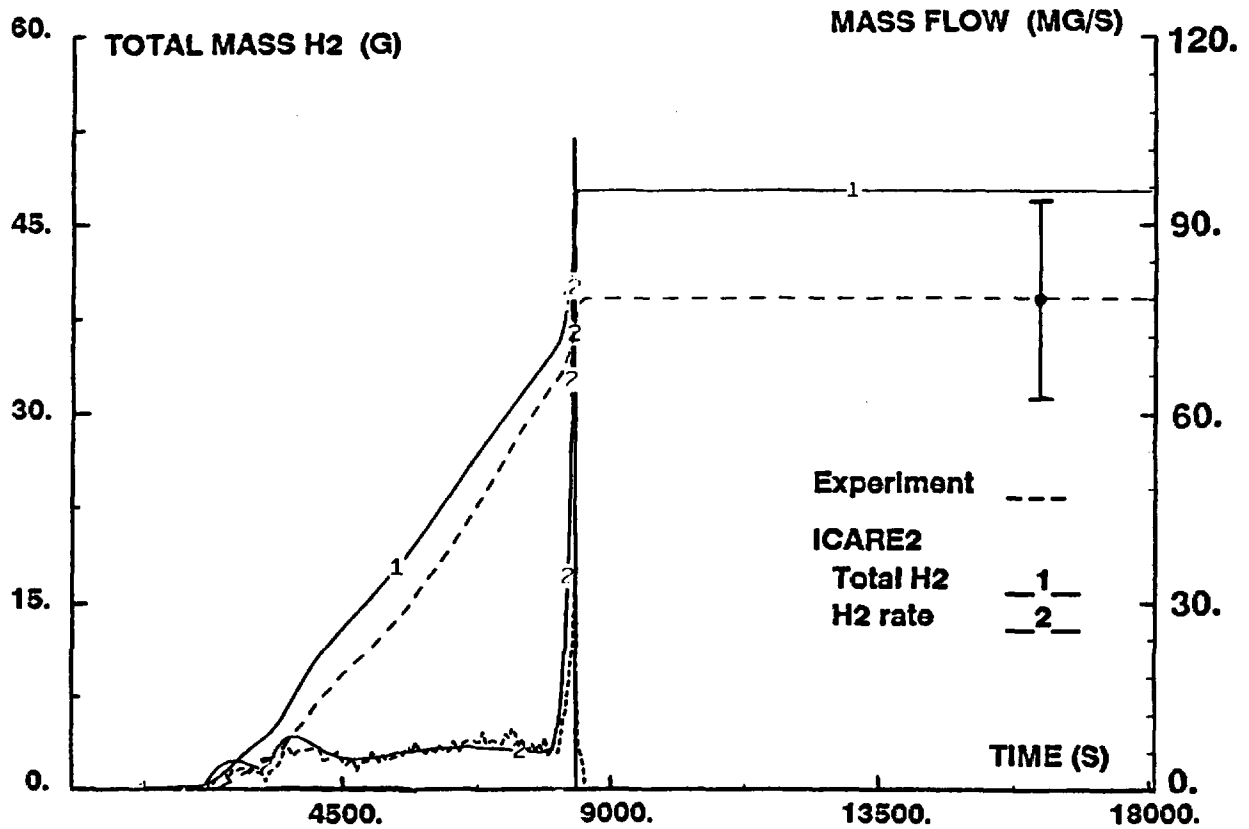


FIG. 9 : PHEBUS SFD B9+ test. Total H2 production versus time. Comparison between ICARE2 and measurement.

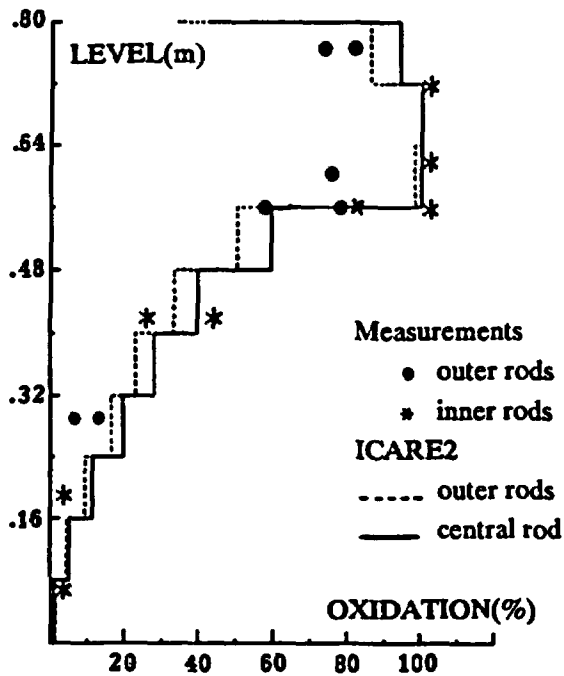


FIG. 10 : PHEBUS SFD B9+ test. Oxidation profiles at 9000 s. Comparison between ICARE2 and measurement.

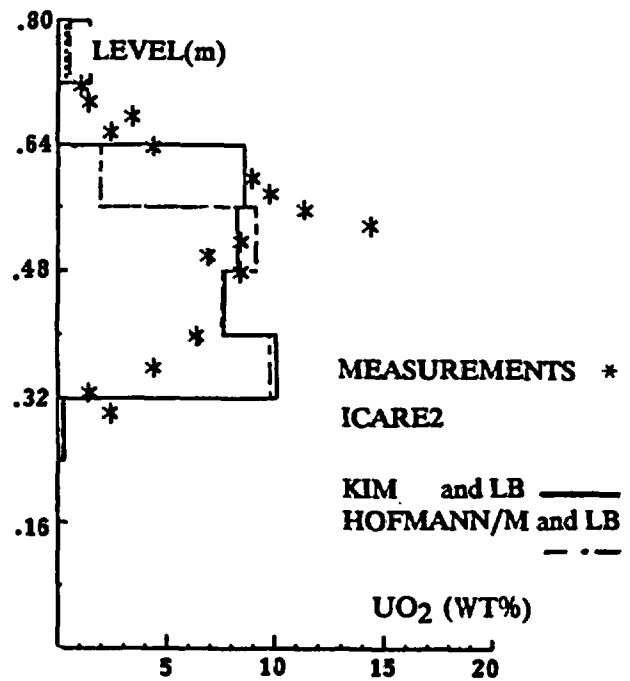


FIG. 11 : PHEBUS SFD B9+ test. UO<sub>2</sub> dissolution profiles calculated with Kim and Hofmann kinetics  
 UO<sub>2</sub> Solubility limit :  
 Liquidus Boundary (LB).

Using these two models and the same mechanical cladding failure criteria as those used for the C3+ test ( $T^* > 2300$  K and  $\epsilon^* < 300$   $\mu\text{m}$ ) the axial failure zones are predicted around the mid-bundle (0.4 m) as in the test. Predictions of these zones and of the final mixture relocation are summarized and compared with the PIE in Fig. 12. The molten Zr located between the fuel pellets and the external  $\text{ZrO}_2$  layer tends both to dissolve this layer (chemical effect modelled by the corresponding Hofmann kinetics) and to break it (mechanical effect). In the central zone of the bundle, significant  $\text{ZrO}_2$  dissolution was predicted which led to the chosen failure thickness limit (300  $\mu\text{m}$ ) being reached. Limited differences on the simultaneous  $\text{UO}_2$  and  $\text{ZrO}_2$  dissolutions between the Kim and Hofmann (M) models explain the differences of the prediction of the local  $\text{UO}_2$  dissolution observed at 0.5 m (Fig. 11) and of the calculation of the cladding failure zones (Fig. 12). Cladding failure is typically a threshold phenomenon whose calculation can lead to local differences between predictions performed in similar conditions.

The main ceramic plug observed in the test includes two  $\alpha\text{-Zr(O)}$  and  $(\text{U,Zr})\text{O}_{2-x}$  phases and is located between 0.16 and 0.28 m. The relocation distance is slightly overestimated and a flow channel blockage of 31 % is calculated instead of 23 % in the test. The second significant plug rich in Zr, Ni and U was found in the test around 0.05m (Fig. 12) but the provisional spacer-grid model was not used to predict its relocation.

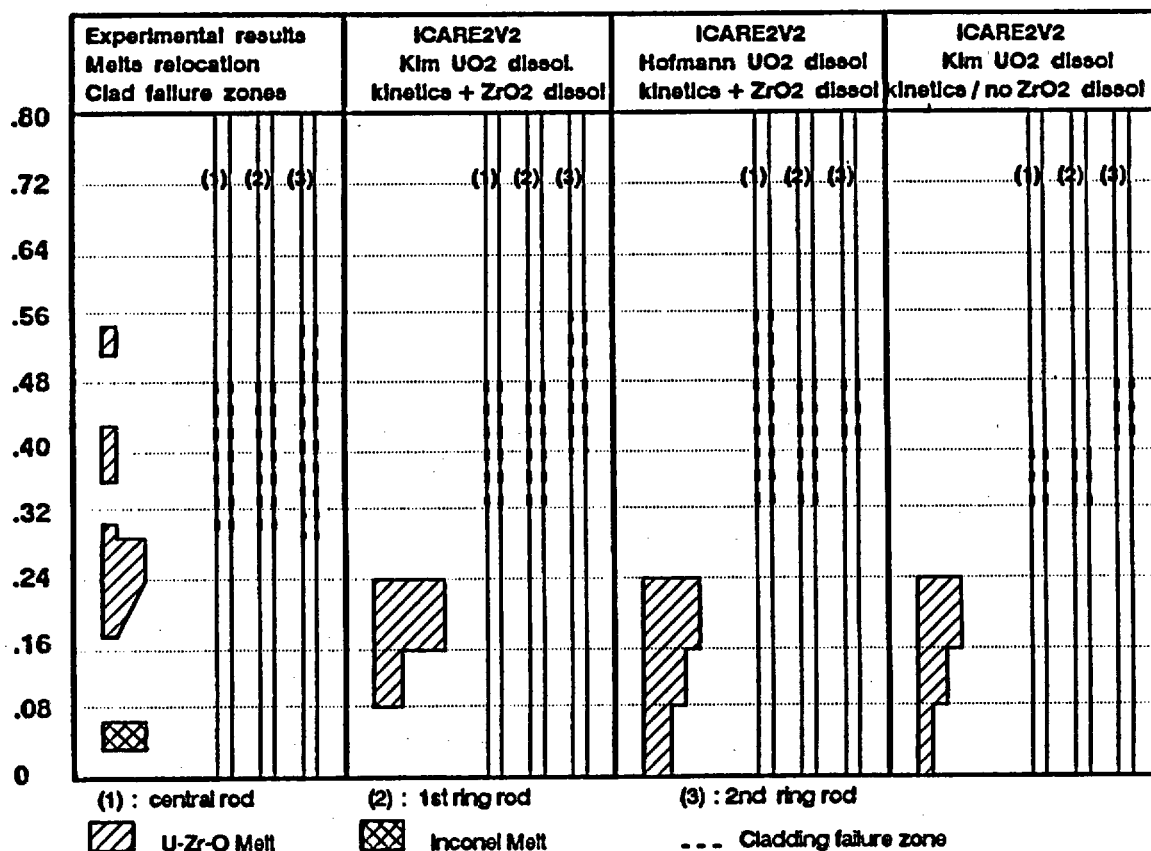


FIG. 12 PHEBUS SFD B9+ test. Cladding failure zones and melts relocation.

The ISP28 which was performed with this PHEBUS B9+ test showed that in spite of a large amount of available experimental data and relatively good knowledge of the main degradation phenomena of the early phase, current codes used in semi-blind conditions (only the thermal behaviour was known) gave incorrect predictions of the final state of the bundle [7]. Only the ICARE2 V2 calculation, carried out in open conditions, correctly predicted the UO<sub>2</sub> dissolution profile, the melt relocation distance and the bundle blockage.

The main reasons for the discrepancies observed for degradation, between the calculations and experimental data, were identified as being an incorrect prediction of rod temperatures, use of incorrect cladding failure conditions and lack of ZrO<sub>2</sub> dissolution models (except in ICARE2 V2).

The analysis of the B9+ results shows that the cladding failure occurred in a zone characterized by the following conditions at the end of the steam phase :

$$T_{\text{clad}} > 2300 \text{ K and } e(\text{oxide}) < 400 \text{ to } 500 \mu\text{m}$$

Two chemical and mechanical effects affect this cladding failure. ICARE2 calculations show that the first effect related to the ZrO<sub>2</sub> dissolution can significantly decrease the ZrO<sub>2</sub> thickness in the failure zone. This leads to a reduced 300 μm thickness limit related to the mechanical effect alone.

As shown by the ISP28 calculations, these failure conditions can significantly affect the local fuel dissolution. They determine both the axial extent of the failure zone and the duration -at each elevation- of the fuel dissolution. As illustrated by comparing failure conditions in C3+ and B9+ tests, simple criteria as those usually applied are not valid for all the oxidation conditions. There is a lack of data and a need of developing more general models in this field.

As regards the ZrO<sub>2</sub> dissolution, sensitivity studies performed with the ICARE2 V2 code show that this process also increases the O<sub>2</sub> content in the U-Zr-O melt resulting from the simultaneous UO<sub>2</sub> and ZrO<sub>2</sub> dissolution. This effect tends to limit the UO<sub>2</sub> solubility in the U-Zr-O melt and must be modelled in order to correctly calculate the UO<sub>2</sub> liquefaction [5].

#### 4 CONCLUSION

The ICARE2 code, designed to calculate reactor core damage progression occurring during a severe PWR reactor accident, is still in the development and validation stage. The current version is able to correctly calculate the main features of the early phase of core degradation and melt progression within the experimental uncertainty range. This was particularly demonstrated during the recent ISP28 organized on the PHEBUS SFD B9+ test.

More complete verification and validation of the models must be carried out on an extended test matrix comprising a wide range of scales and degradation conditions.

Development work is still necessary to complete the modelling of the early phase, particularly the addition of some chemical interactions - cladding/Inconel spacer-grids and Zircaloy/control rod material - and consideration of the effect of a fast cooldown or quenching on the oxidation and mechanical behaviour of degraded cores.

Future development and validation work will be focussed on reactor applications and on the later phase, taking into account the necessary experimental data expected in this field from future tests. This simultaneous work planned on ICARE2 during the PHEBUS FP Programme will enable a larger and better applicability of the code to be obtained for dealing with severe accident safety issues.

### **REFERENCES**

- [1] M. MEZZA, P. CHATELARD, R. GONZALEZ. "Validation Results of ICARE2 code on the PBF SFD 1.4 Experiment". IAEA Technical Committee Meeting - Aix-en Provence (FRANCE) - March 92.
- [2] R. GONZALEZ, M.C. VICENTE, S. HAGEN. "Results of ICARE2 code on the Severe Fuel Damage Test CORA-5". 1st JSME-ASME Joint International Conference on Nuclear Engineering (ICONE-1). Tokyo - JAPAN (November 92)
- [3] P. CHATELARD, R. GONZALEZ, A. PORRACCHIA. "Analysis of the TMI-2 Core Degradation using ICARE2 code". 27th ASME/AIChE/ANS-National Heat Transfer Conference, Minneapolis, July 91
- [4] P. HOFMANN and al. "Reactor core materials interaction at very high temperatures". Nuclear Technology, Vol. 87 (August 1989) - 146-186.
- [5] B. ADROGUER, S. BOURDON, R. GONZALEZ. "Analysis of the Fuel-Cladding Chemical Interaction in PHEBUS SFD Tests using ICARE2 Code". IAEA Technical Committee Meeting - Aix-en Provence (FRANCE) - March 92.
- [6] A. MAILLIAT, F. SERRE, A.V. JONES, I. SHEPHERD. "The calculation Programme to Prepare the First Phebus FP test". Twentieth water Reactor Safety Information Meeting - Bethesda - October 21-23, 1992.
- [7] B. ADROGUER, S. BOURDON, C. RONGIER. "Results of the International Standard Problem 28 on the PHEBUS SFD test B9+". 28th ASME/AIChE/ANS-National Heat Transfer Conference, San Diego, August 1992.
- [8] C. GONNIER, G. GEOFFROY, B. ADROGUER. "PHEBUS Severe Fuel Damage Programme. Main results". A.N.S. Meeting - Portland - July 1991.
- [9] S. BOURDON, P. VILLALIBRE, B. ADROGUER, G. GEOFFROY. "Analysis of the SFD test PHEBUS B9+ using ICARE2 code". 27th ASME/AIChE/ANS-National Heat Transfer Conference, Minneapolis, July 91.

# VICTORIA-92 AND ITS APPLICATION TO THE PHEBUS-FPT0 TEST

N. E. Bixler, T. J. Heames\*,  
Severe Accident Phenomenology Department 6422

and D. A. Powers  
Integration of NRC Work Program Support Department 6404

Sandia National Laboratories  
Albuquerque, New Mexico, 87185, USA

## ABSTRACT

VICTORIA-92 is a mechanistic computer code designed to analyze fission product behavior within the coolant system (RCS) during a severe nuclear reactor accident [1]. It provides detailed prediction of the release from the fuel and transport in the RCS of radionuclides and non-radioactive materials during core degradation. These predictions account for the chemical and aerosol processes that affect radionuclide behavior. Coupling of detailed chemistry and aerosol packages is a unique feature of VICTORIA: it allows exploration of issues involving deposition, revaporization, and re-entrainment that cannot be resolved with other codes.

A new version, VICTORIA-92, was recently released. New models account for the following effects: (1) decay-heat induced structural heat-up and its effect on revaporization and possible structure failure; (2) aerosol re-entrainment; (3) deposition of aerosols in sudden contractions, steam separators, and steam dryers; (4) uranium volatilization; (5) enhanced diffusion of fission products within the fuel due to oxidation; (6) permeable flow of fission products through the fuel pores, gap, and cladding breaches; (7) release of vapors and aerosols during rupture of control rods; (8) mechanisms within the fuel, such as grain-boundary sweeping and bubble formation, that affect release from intact fuel; (9) release from degraded fuel geometries, i.e., rubble beds and molten pools; and (10) kinetically limited surface reactions. In addition, other modifications and improvements have been made. These improvements include the following: (1) gas transport numerics have been made more robust and accurate; (2) calculation of diffusion rates through boundary layers has been improved; (3) chemical speciation is more inclusive; (4) chemistry package numerics have been improved; (5) chemistry in the fuel pores includes a layer of the fuel surface; and (6) volatilization of tin from the cladding is calculated.

The results are given for an analysis of fission-product transport and speciation in PHEBUS-FPT0, a test that is scheduled to be performed in France in 1993. In this test, fission products are generated and released in an in-pile fuel bundle, transported through a thermal gradient in an upper plenum region, then through an isothermal hot leg (at 700°C) with a number of bends, a simulated steam generator, a cold leg (at 150°C), and finally into a small containment. Pretest calculations are being done with VICTORIA to identify data from PHEBUS that should be useful to validate models for fission product and aerosol behavior in the reactor coolant system. This identification has also led to recommendations for on-line and post-test measurements. Results obtained to date indicate that PHEBUS data should provide a good test for VICTORIA transport and chemistry models.

\* Science Applications International Corporation, Albuquerque, New Mexico, 87106.

## **1. INTRODUCTION**

Release of radionuclides into the atmosphere is the main concern in the event of a nuclear reactor accident. The consequences of a severe reactor accident depend on the quantity, characteristics, and timing of the release of radionuclides from the reactor coolant system (RCS) into the containment, and finally into the atmosphere. The physical processes that influence the quantity and timing of a release are thought to be highly complex. In order to be able to predict the outcome of a nuclear accident, it is necessary to accurately model as many of the relevant physical processes as possible. VICTORIA-92 [1] is a mechanistic computer code designed to model such releases from the RCS during a severe reactor accident.

The purpose of VICTORIA is to enable the prediction of the magnitude, chemistry, physical properties, and timing of fission product release from the RCS of a nuclear reactor undergoing a severe accident. VICTORIA does not treat thermal-hydraulics, but requires such information as input. The heart of the code is in its mechanistic treatment of fission product release from fuel, chemistry, aerosol physics, transport, and decay heating. The coupled treatment of these phenomena make VICTORIA unique in its predictive capabilities. The ultimate goal is to identify, wherever possible, the essential physics and to develop simplified models that can be incorporated into system-level codes that can treat complete accident sequences.

The following paragraphs describe briefly the current capabilities of VICTORIA-92. Capabilities that have been added since the previous version of the code [2] are indicated as "new." The models and capabilities are described in more detail in the following sections.

VICTORIA-92 contains models for release of fission products from both intact and degraded fuel geometries, including rubble beds and molten pools. For intact fuel, release mechanisms within fuel grains are either strictly by diffusion [3,4] or, alternatively, may include new models for the effects of bubble formation, coalescence, and migration and the effect of grain boundary sweeping [5,6]. Transport through fuel pores is by surface and gaseous diffusion and by a new model for advection due to calculated pressure gradients [1]. Chemical speciation and interaction with surfaces is also an essential part of this calculation because chemical reactions and phase changes drive the concentration and pressure gradients that produce diffusion and advection. Only gaseous transport is considered in the gap between clad and fuel, but both diffusion and advection are treated. Chemical

speciation and interaction with the inner cladding surface are also modeled. Transport through a breached cladding is similar to that in fuel pores. From the cladding, fission products diffuse through a boundary layer and into the bulk gas.

The models for release of fission products from rubble beds are new [1]. For rubble beds, fission product release is modeled as a porous bed made up of fuel fragments. Diffusion, bubble growth and migration, and grain boundary sweeping are treated in the fuel fragments in the same way as they are for intact fuel. Once out of the fuel grains, advection and diffusion transport the fission products through the rubble bed and into the bulk gas. The model for release of fission products from molten pools accounts for molecular diffusion and buoyancy-driven bubble migration. Models and capabilities for radionuclide release from intact and degraded fuel geometries are described further in Section 2.

A new model for pressurized rupture and release from silver-indium-cadmium control rods has been added to VICTORIA-92. This model is based on the work of Powers [7], which defines the partial pressure of the vapor species above a molten alloy as a function of temperature and composition. This model also uses the experimental data of Bowsher et al. [8] to estimate the properties of the aerosol created during the burst. The models used to describe release from control rods are detailed further in Section 3.

The chemistry models used in VICTORIA-92 are largely based on thermodynamic equilibria; however, new models have introduced kinetically limited rates to several processes. These include oxidative volatilization of  $UO_2$ , tellurium-zircaloy interactions, and  $CsOH$  chemisorption onto structures. VICTORIA-92 now treats 288 chemical species composed of 26 elements. These models are described further in Section 4.

Bulk-gas processes include heterogeneous (with aerosol particles) chemical speciation, advection, diffusion, and aerosol formation, agglomeration, and deposition. Agglomeration and deposition mechanisms include Brownian motion, gravitational settling, turbulent shear, and turbulent inertia. Additional deposition mechanisms include thermophoresis and inertial deposition in pipe bends. In addition, new deposition models account for the following flow irregularities: sudden contractions, steam separators, and steam dryers [9]. A model for re-entrainment of deposited aerosols, based on the data of Wright et al. [10], has also been incorporated. These models are described further in Section 5.

A new model for radioactive decay heating has also been added to the code [11]. The model accounts for the heat-up of films and structures by decay heating from deposited radionuclides. The heat-up can induce revaporization of the deposited material and, in some cases, can cause the structure to fail. This model is described in more detail in Section 6.

Two additional models have been developed but not yet integrated into the code. The first is an aqueous chemistry model, which accounts for the effects of temperature and pH on aqueous speciation. This model is particularly important for understanding the behavior of iodine, which is quite soluble at high pH but tends to partition out of solution at low pH. The second model is a new multicomponent aerosol model that treats rate dependent condensation onto aerosol particles, allowing composition to vary with size distribution [12].

Section 7 below describes some of the results of recent calculations in support of PHEBUS-FPT0. These calculations illustrate the utility of a tool like VICTORIA for pretest identification of experimental parameters.

## **2. MODELS FOR RELEASE OF RADIONUCLIDES FROM FUEL**

Figure 1 shows schematically the problem domain for fission product release. The intact fuel rod configuration used in VICTORIA includes the fuel pellets, composed of fuel grains and pores, the gap between the fuel pellets and the cladding, and the cladding itself. The cladding may be intact or damaged, depending on whether a user-prescribed failure criterium on Zr-oxidation level or on cladding temperature has been reached. If the cladding becomes sufficiently oxidized, it is treated as a porous medium, with a user prescribed porosity, through which fission products can flow and diffuse. If failure has occurred, breaches exist through which fission products can easily flow and diffuse. When a user prescribed melting temperature is reached, the zirconium in the cladding is removed and the tin becomes available for oxidative volatilization.

Two options are available for modeling the processes within the fuel grains: (1) a Booth diffusion model in which the sole mechanism for transport is molecular diffusion [3,4] and (2) a diffusion model based on the work of Matthews and Woods [5] and models accounting for bubble formation and migration, grain growth, grain boundary sweeping, fuel liquefaction, and

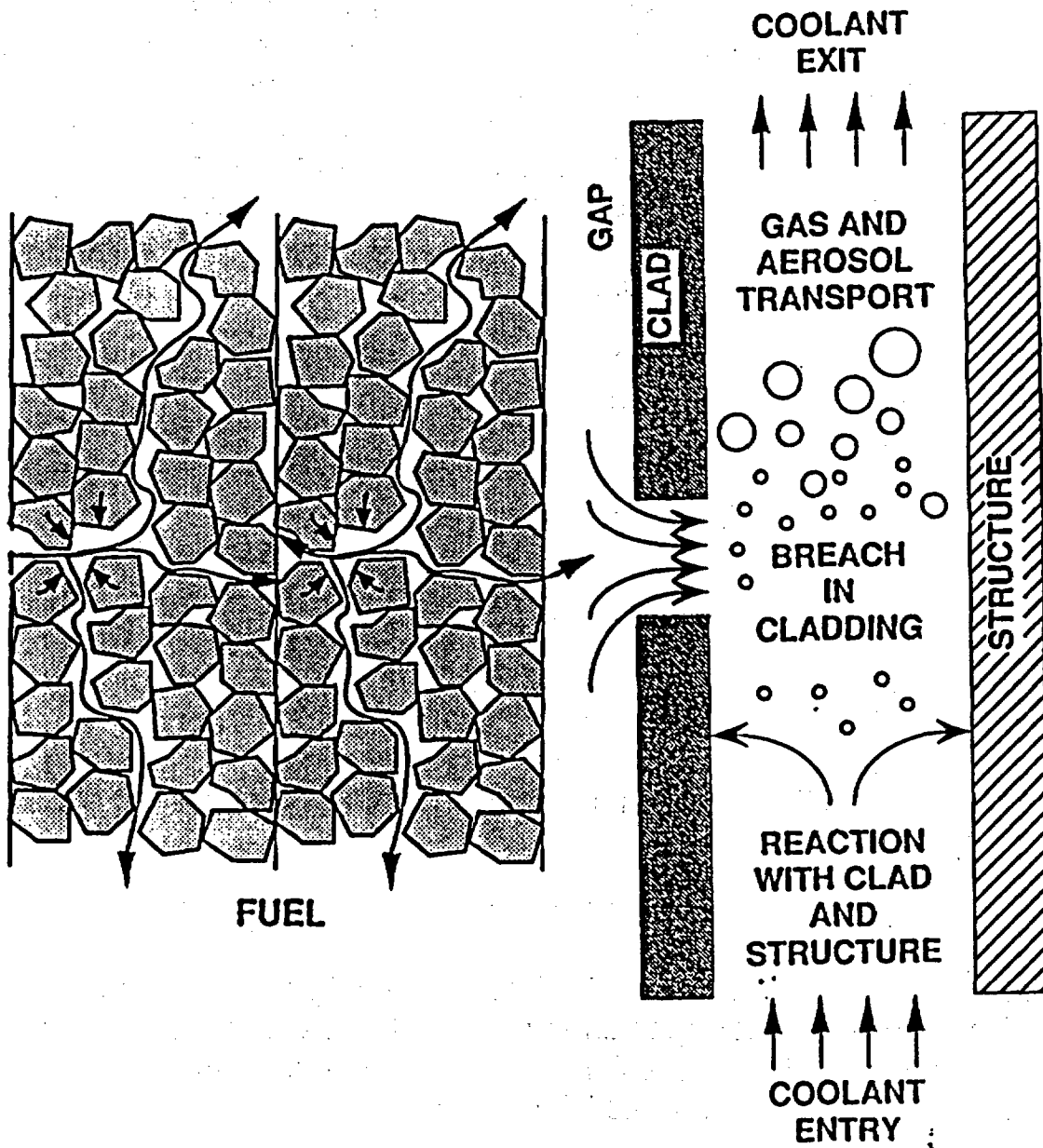


Figure 1. Schematic of domain for fission product release.

fuel dissolution [6]. In both options, the effect of fuel oxidation on diffusivity is treated [13].

Once fission products have diffused through fuel grains and have reached the interconnected fuel pores, the transport mechanisms considered are surface diffusion, gaseous diffusion, and advection by porous flow. Diffusion and advection rates depend on calculated concentration and pressure gradients, respectively. Pressure is calculated by summing up the partial pressures of each of the species. No surface diffusion is allowed in the fuel/clad gap, which by assumption is open rather than closed. Treated transport mechanisms in the damaged cladding are the same as in the fuel pores. From the cladding, fission products diffuse through a boundary layer, of which the thickness is computed according to local flow conditions and gas properties, and into the bulk gas.

Of course, chemistry plays an important role in determining the rates at which species are transported because, for example, partial vapor pressures and their gradients are, in part, determined by local thermodynamics. The chemistry model is described more fully in Section 4 below. Each of the models in VICTORIA-92 are describe in full detail in [1].

### **3. MODEL FOR BURST AND RELEASE FROM CONTROL RODS**

The model for release of control rod materials is based on a thermodynamic model [6] for the total vapor pressure inside the control rod, a burst criterion, and a model for the expulsion of gases and aerosols from the rod upon burst. In the thermodynamic model, the total vapor pressure inside the rod is approximated to be

$$P = P(\text{Ag}) + P(\text{In}) + P(\text{Cd}) + P(\text{AgIn}) + P(\text{Cd}_2) + P(\text{He}) \quad (1)$$

where  $P$  is the total pressure and  $P(i)$  is the partial pressure of species  $i$ . The partial pressure of other species is assumed to be negligible. Partial pressures are computed from equilibrium thermodynamics using the equation of Wilson et al. [14] to compute activity coefficients.

The failure criterion for control rods is that they fail as soon as the internal pressure exceeds the external pressure. This is a conservative criterion and should cause control rods to burst early.

The model for expulsion of control rod materials is based on the experimental data of Bowsher et al. [8]. Two percent of the mass of liquid alloy from the portion of the control rod above the failure point is ejected into the bulk gas as an aerosol with a specified particle size distribution. The remainder of the liquid is placed into the control rod surface film inventory, where it may later evaporate. Gases within the control rod are ejected directly into the bulk gas.

#### 4. CHEMISTRY MODEL

The chemical interactions between fission products can have an important effect on the timing, chemical form, and quantity of products that could be released from the RCS in the case of a severe reactor accident. Each of these factors affects the potential for release from containment into the environment. Two areas of particular importance are the chemical form of iodine (which affects its volatility) and the quantity and composition of deposited aerosols. The latter are important because of the possibility of re-entrainment or revaporization after vessel or RCS failure. An assessment of these areas of concern requires detailed consideration of chemical interactions within the fuel, within the gas, and between gas and vessel structures.

The current list of 26 chemical elements treated by VICTORIA includes not only the volatiles that are the primary concern in the event of an accident, but also those that may interact with the volatile species and inhibit their release, those that are easily measurable experimentally and so are beneficial for validation, and those that are important because of their quantity within the RCS. Chemical interaction of a set of 288 chemical species are analyzed by VICTORIA (condensed and vapor forms are regarded as separate species), which is given in Table 1. Both chemical equilibria and phase behavior are determined by minimization of Gibbs free energies. Chemical equilibria are imposed within the fuel grains, in the porosity of the fuel, within the fuel/clad gap, in the bulk gas, and in structural films. Within the fuel grains, either equilibrium chemistry using a small subset of the full species set (primarily  $\text{UO}_2$ , oxides, and uranates) is allowed or else no chemistry at all is performed.

In several cases, chemistry is taken to be kinetically limited rather than in equilibrium. The model of Urbanic and Heidrick [15] is used to determine the rate of zirconium oxidation. The rate dependent oxidative volatilization of  $\text{UO}_2$  is based on the data of Alexander and Ogden [16]. Tellurium-zircalloy

Table 1. VICTORIA Species Set. V - vapor, C - condensed.

Species	V	C	Species	V	C	Species	V	C	Species	V	C
Ag	x	x	CsH	x		IO	x		Sb <sub>4</sub>	x	
AgH <sub>2</sub> O <sub>2</sub>	x		CsI	x	x	I <sub>2</sub>	x		Sn	x	x
AgI	x	x	CsO	x		In	x	x	SnH <sub>2</sub> O <sub>2</sub>	x	
AgOH	x		CsOH	x	x	InH <sub>2</sub> O <sub>2</sub>	x		SnH <sub>4</sub>	x	
AgTe	x		Cs <sub>2</sub>	x		InI	x	x	SnI <sub>2</sub>	x	x
Ag <sub>2</sub> Te		x	Cs <sub>2</sub> CrO <sub>4</sub>	x	x	InOH	x		SnO	x	x
Ar	x		Cs <sub>2</sub> Cr <sub>2</sub> O <sub>7</sub>	x		InTe	x	x	SnOH	x	
B	x	x	Cs <sub>2</sub> I <sub>2</sub>	x		In <sub>2</sub> O <sub>3</sub>		x	SnO <sub>2</sub>	x	x
BH	x		Cs <sub>2</sub> MoO <sub>4</sub>	x	x	Kr	x		SnTe	x	x
BH <sub>2</sub>	x		Cs <sub>2</sub> O	x	x	Mn	x	x	SnTe <sub>2</sub>	x	
BH <sub>2</sub> O <sub>2</sub>	x		Cs <sub>2</sub> O <sub>2</sub>	x		MnO	x	x	Sn <sub>2</sub>	x	
BH <sub>3</sub>	x		Cs <sub>2</sub> O <sub>2</sub> H <sub>2</sub>	x		MnOH	x		Sn <sub>2</sub> Te <sub>2</sub>	x	
BI	x		Cs <sub>2</sub> Te		x	MnTe		x	Sr	x	x
BI <sub>2</sub>	x		Cs <sub>2</sub> TeO <sub>3</sub>		x	MnTe <sub>2</sub>		x	SrH <sub>2</sub>		x
BI <sub>3</sub>	x		Cs <sub>2</sub> TeO <sub>4</sub>		x	Mn <sub>3</sub> O <sub>4</sub>		x	SrI	x	
BO	x		Cs <sub>2</sub> Te <sub>2</sub> O <sub>5</sub>	x		Mo	x	x	SrI <sub>2</sub>	x	x
BOH	x		Cs <sub>2</sub> Te <sub>4</sub> O <sub>12</sub>	x		MoH <sub>2</sub> O <sub>2</sub>	x		SrMoO <sub>4</sub>		x
BO <sub>2</sub>	x		Cs <sub>2</sub> Te <sub>4</sub> O <sub>9</sub>	x		MoH <sub>2</sub> O <sub>4</sub>	x		SrO	x	x
BTe	x		Cs <sub>2</sub> UO <sub>4</sub>		x	Mol	x		SrOH	x	
B <sub>2</sub>	x		Cs <sub>2</sub> U <sub>2</sub> O <sub>7</sub>		x	Mol <sub>2</sub>	x	x	SrO <sub>2</sub> H <sub>2</sub>	x	x
B <sub>2</sub> H <sub>6</sub>	x		Cs <sub>2</sub> U <sub>4</sub> O <sub>12</sub>	x		Mol <sub>3</sub>	x	x	SrUO <sub>4</sub>		x
B <sub>2</sub> O <sub>3</sub>	x	x	Cs <sub>2</sub> ZrO <sub>3</sub>		x	Mol <sub>4</sub>	x	x	SrZrO <sub>3</sub>		x
Ba	x	x	Cs <sub>2</sub> Zr <sub>2</sub> O <sub>5</sub>	x		MoO	x		Sr <sub>2</sub>	x	
BaH	x		Cs <sub>2</sub> Zr <sub>3</sub> O <sub>7</sub>	x		MoOH	x		Te	x	x
BaH <sub>2</sub>		x	Cs <sub>3</sub> CrO <sub>4</sub>		x	MoO <sub>2</sub>	x	x	TeH <sub>2</sub> O <sub>2</sub>	x	
BaI	x		Cs <sub>4</sub> CrO <sub>4</sub>		x	MoO <sub>2</sub> I <sub>2</sub>	x		TeH <sub>2</sub> O <sub>4</sub>		x
BaI <sub>2</sub>	x	x	Eu	x	x	MoO <sub>3</sub>	x	x	TeI <sub>4</sub>	x	x
BaMoO <sub>4</sub>	x	x	EuH <sub>2</sub> O <sub>2</sub>	x		Mo <sub>2</sub>	x		TeO	x	
BaO	x	x	EuO	x	x	Mo <sub>2</sub> O <sub>6</sub>	x		TeOH	x	
BaOH	x		EuOH	x		Mo <sub>3</sub> O <sub>9</sub>	x		TeOI <sub>2</sub>	x	
BaO <sub>2</sub> H <sub>2</sub>	x	x	EuTe	x		Mo <sub>4</sub> O <sub>12</sub>	x		TeO <sub>2</sub>	x	x
BaTe		x	Eu <sub>2</sub> O	x		Mo <sub>5</sub> O <sub>15</sub>	x		TeO <sub>3</sub> H <sub>2</sub>	x	
BaUO <sub>4</sub>		x	Eu <sub>2</sub> O <sub>2</sub>	x		Ni	x	x	Te <sub>2</sub>	x	
BaZrO <sub>3</sub>		x	Eu <sub>2</sub> O <sub>3</sub>		x	NiH <sub>2</sub> O <sub>2</sub>	x		Te <sub>2</sub> O <sub>2</sub>	x	
Ba <sub>2</sub>	x		Fe	x	x	Nil <sub>2</sub>		x	U	x	x
Ba <sub>2</sub> O	x		FeI <sub>2</sub>	x	x	NiO	x	x	UH <sub>2</sub> O <sub>2</sub>	x	
Ba <sub>2</sub> O <sub>2</sub>	x		FeO	x	x	NiOH	x		UH <sub>4</sub> O <sub>5</sub>		x
Cd	x	x	FeOH	x		O	x		UO	x	
CdH <sub>2</sub> O <sub>2</sub>	x		FeO <sub>2</sub> H <sub>2</sub>	x	x	O <sub>2</sub>	x		UOH	x	
CdI	x		FeTe		x	Ru	x	x	UO <sub>2</sub>	x	x
CdI <sub>2</sub>	x	x	FeTe <sub>2</sub>		x	RuH <sub>2</sub> O <sub>2</sub>	x		UO <sub>3</sub>	x	x
CdO	x	x	Fe <sub>2</sub> I <sub>4</sub>	x		RuO	x		U <sub>3</sub> O <sub>8</sub>		x
CdOH	x		Fe <sub>2</sub> O <sub>3</sub>		x	RuOH	x		U <sub>4</sub> O <sub>9</sub>		x
CdTe	x	x	Fe <sub>3</sub> O <sub>4</sub>		x	RuO <sub>2</sub>	x	x	Xe	x	
Cr	x	x	H	x		RuO <sub>3</sub>	x		Zr	x	x
CrH <sub>2</sub> O <sub>2</sub>	x		HBO <sub>2</sub>	x	x	RuO <sub>4</sub>	x		ZrB <sub>2</sub>		x
CrI	x		HI	x		RuTe <sub>2</sub>		x	ZrH	x	
CrI <sub>2</sub>	x	x	HIO	x		Ru <sub>3</sub> U		x	ZrH <sub>2</sub> O <sub>2</sub>	x	
CrO	x		HO	x		Sb	x	x	ZrI	x	
CrOH	x		H <sub>2</sub>	x		SbH <sub>2</sub> O <sub>2</sub>	x		ZrI <sub>2</sub>	x	
CrO <sub>2</sub>	x		H <sub>2</sub> MoO <sub>4</sub>	x		SbH <sub>3</sub>	x		ZrI <sub>3</sub>	x	
CrO <sub>3</sub>	x		H <sub>2</sub> O	x		SbOH	x		ZrI <sub>4</sub>	x	x
CrTe		x	H <sub>2</sub> Te	x		SbTe	x		ZrO	x	
Cr <sub>2</sub> O <sub>3</sub>		x	H <sub>3</sub> BO <sub>3</sub>	x	x	Sb <sub>2</sub>	x		ZrOH	x	
Cs	x	x	He	x		Sb <sub>2</sub> O <sub>3</sub>		x	ZrO <sub>2</sub>	x	x
CsBO <sub>2</sub>	x	x	I	x		Sb <sub>2</sub> Te <sub>3</sub>		x	ZrTe <sub>2</sub>		x

interactions are based on the work of Bowsher and Jenkins [17]. Finally, a first-order rate expression, based on the work of Vine and Clough [18], is used to describe CsOH chemisorption onto structural materials. This model is in agreement with experimental data obtained by Elrick et al. [19]. All but the first of these models are new for VICTORIA-92.

A new model for aqueous chemistry has also been developed. This model is currently available in a stand-alone computer code. It might eventually be incorporated into VICTORIA if there is motivation to do so. This model accounts for the effects of temperature and pH on aqueous speciation. It could be especially useful for determining the partitioning of iodine.

## **5. AEROSOL PHYSICS AND TRANSPORT MODELS**

The aerosol model in VICTORIA is built upon the CHARM model developed by Wheatley [5]. The CHARM model treats aerosol behavior in a single computational cell, which is assumed to be well mixed. Time-varying external conditions are calculated in advance and supplied as data to the model. The implementation of CHARM in VICTORIA allows two options: (1) aerosol particle composition is independent of particle size or (2) aerosol particles are taken to be composed of a pure species, in which case a separate particle size distribution is calculated for each species that exists in the aerosol. In addition, the capability to account for the thickness of laminar or turbulent boundary layers and their effect on deposition rates has been added to the version of CHARM in VICTORIA.

The aerosol model in VICTORIA accounts for the following basic mechanisms: (1) condensation or evaporation from aerosol particle surfaces; (2) deposition onto structural surfaces; (3) agglomeration of aerosol particles; (4) and transport of aerosols from one cell to another by advection. The deposition mechanisms modeled are gravitational settling, laminar or turbulent deposition, Brownian motion, thermophoresis, diffusiophoresis, and inertial deposition in curved channels (bends). Agglomeration mechanisms include Brownian motion, relative gravitational motion, interactions in a shear field, and inertia in a turbulent field.

Several new aerosol physics mechanisms have been added to VICTORIA-92. A model for aerosol re-entrainment based on data from the ORNL ART facility [10] has been incorporated. Deposition models for sudden con-

tractions, steam dryers, and separators [9] have also been included in the code.

New transport models in VICTORIA-92 include calculation of diffusion coefficients in gaseous mixtures and of boundary layer thicknesses that depend on local flow conditions and gas mixture properties. These improvements allow better prediction of vapor/surface interactions.

## **6. RADIOACTIVE DECAY HEATING**

A new model for heat-up of structures due to radioactive decay heating caused by deposited fission products has been included in VICTORIA-92. Decay heating is calculated according to elemental mass distribution and time since reactor shutdown. Temperatures of the deposited film and structure are calculated. Radioactive decay heating can cause deposited materials to revaporize and migrate through the RCS. This process can affect the source term late in an accident sequence when the containment is likely to have failed. In some cases, decay heating may induce failure of the RCS.

## **7. PRETEST ANALYSIS OF THE PHEBUS-FPT0 PRIMARY CIRCUIT**

The PHEBUS-FP test series will be carried out in the PHEBUS reactor at Cadarache, France, beginning in 1992. The first in the series will be done with trace-irradiated fuel. Later tests will use relatively high burn-up fuel. These tests are integral in scope: the test apparatus includes an in-pile, 20-rod, fuel bundle, which may be instrumented, and one control rod; an upper plenum region; an Inconel hot leg that is maintained at 700°C; an optional steam generator; a cold leg that is maintained at 150°C; and a scaled containment with sump.

A schematic of the fuel bundle and primary circuit as it will be configured in FPT0, which includes a steam generator, is given in Figure 2. The region analyzed is the circuit beginning just above the fuel bundle and ending at the containment. The thermal-hydraulic data used in this calculation were generated using the computer code CATHARE; hydrogen generation and steam production were calculated using ICARE; and fission product release rates were predicted using CORSOR. The ICARE hydrogen release rate data and matching VICTORIA input data are shown in Figure 3; the fractional fission product releases predicted by CORSOR are shown in Figure 4.

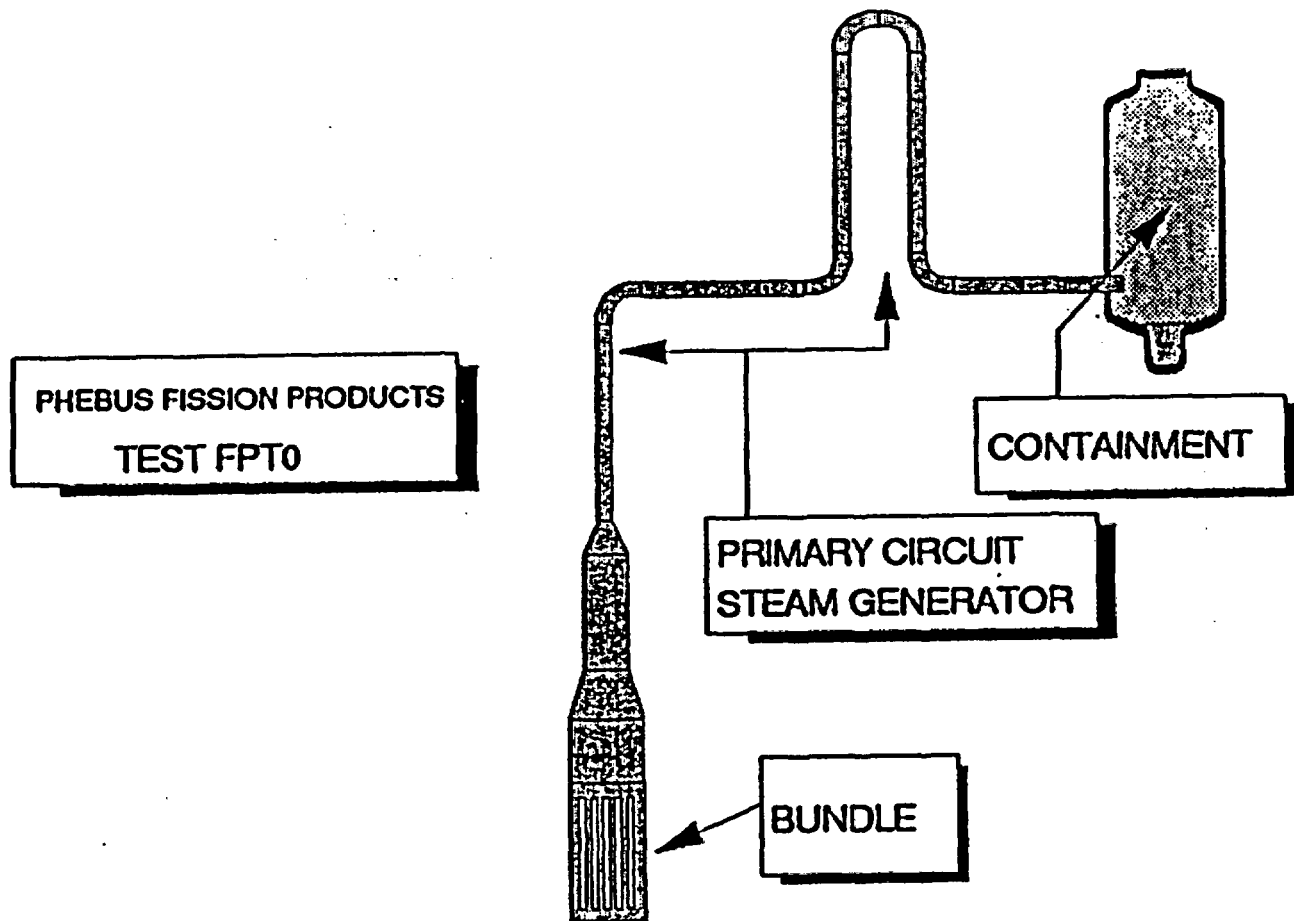


Figure 2. Schematic of the PHEBUS-FPT0 primary circuit.

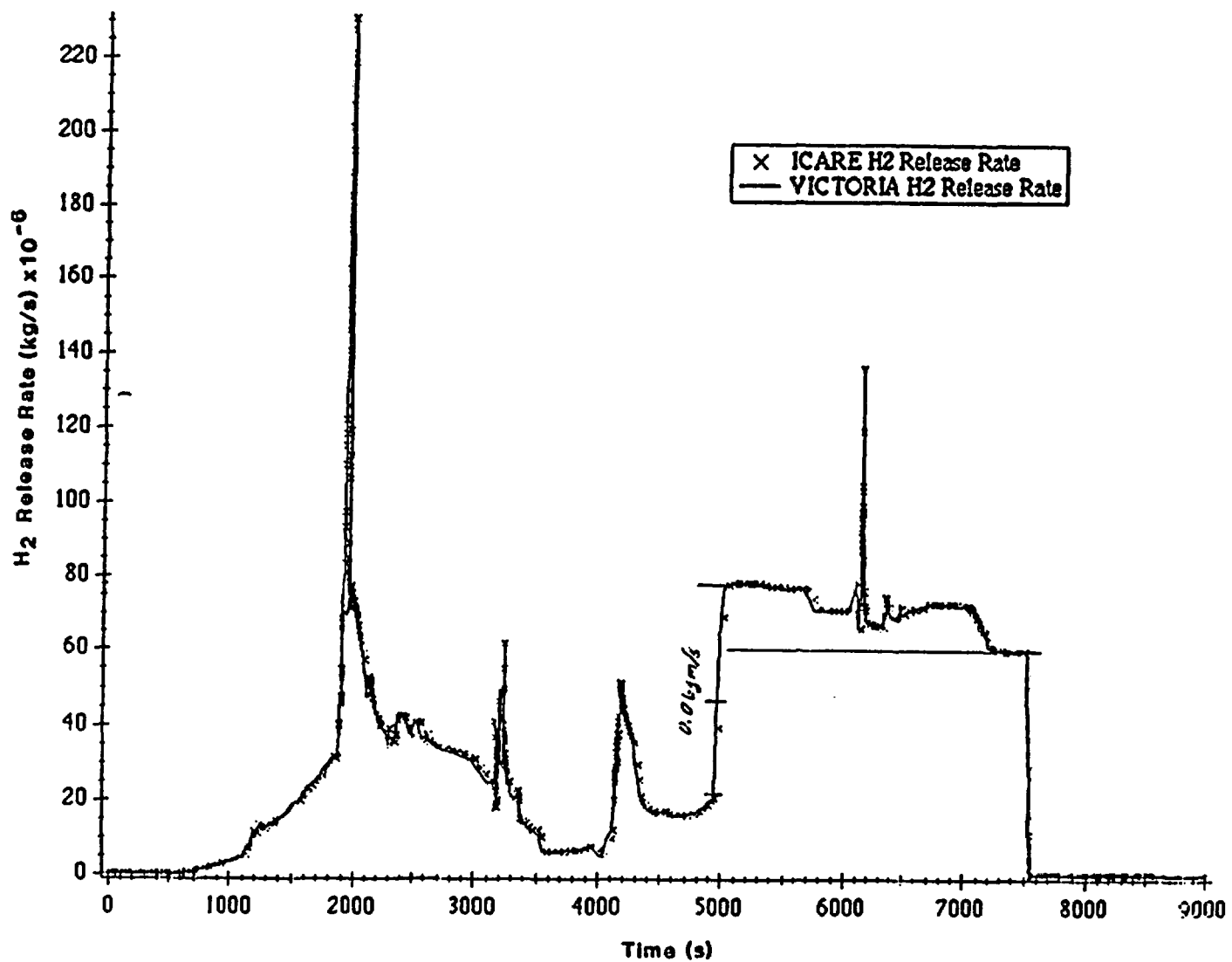


Figure 3. Hydrogen gas released into the PHEBUS-FPT0 circuit as calculated by ICARE and as input to VICTORIA.

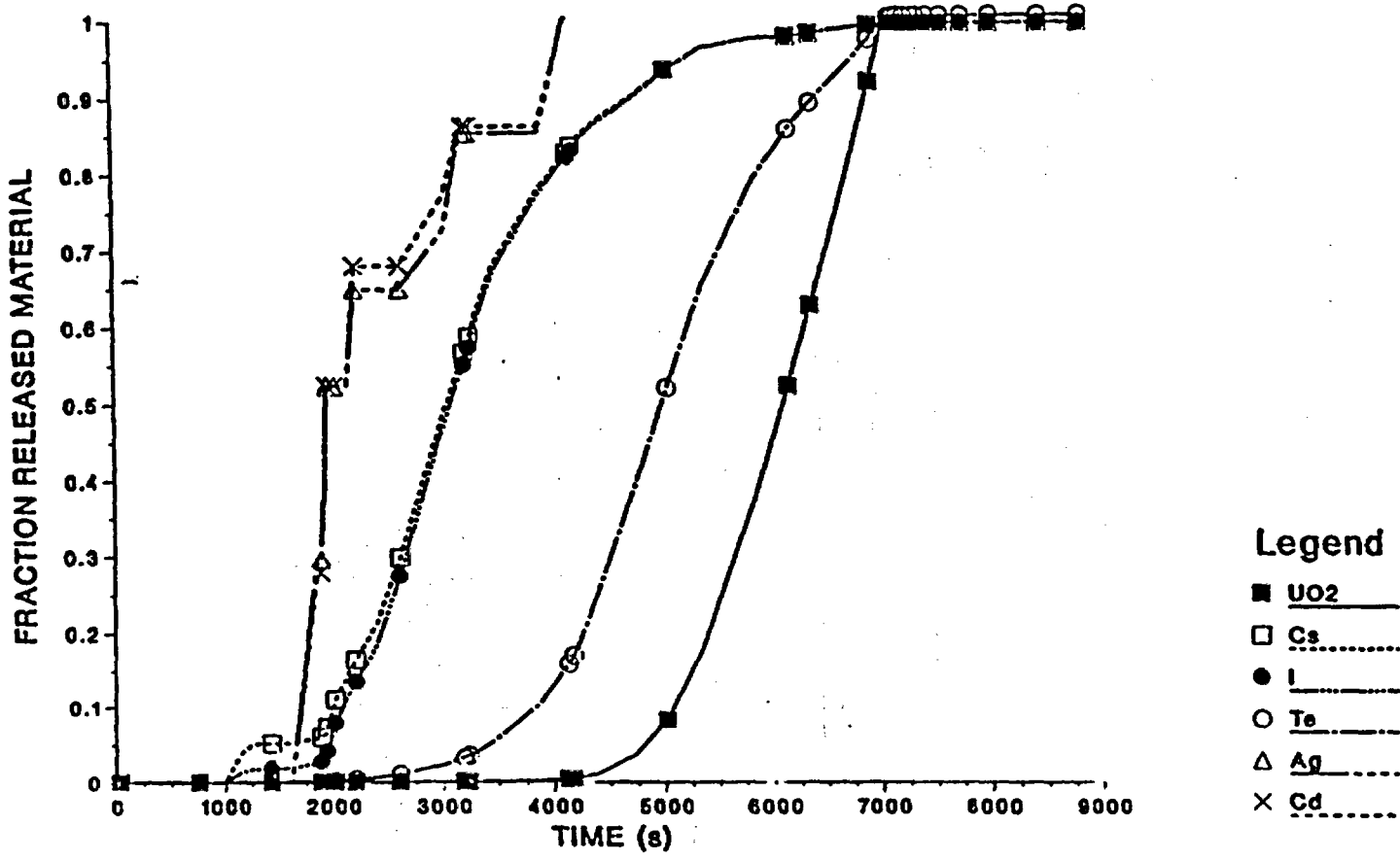


Figure 4. Normalized releases of fission products and control rod materials into the primary circuit as calculated by CORSOR.

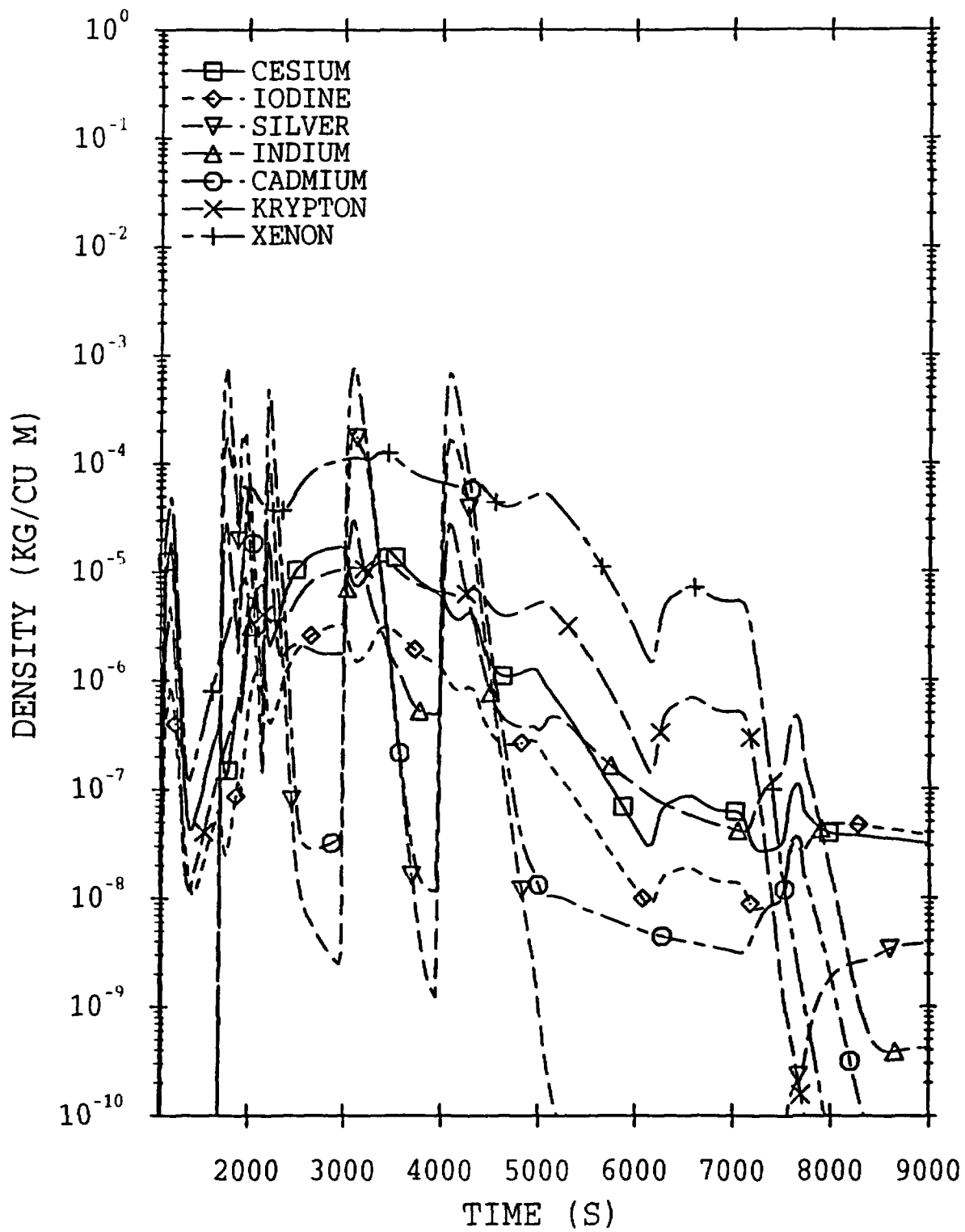


Figure 5. Fission product densities, by element, at the PHEBUS-FPT0 primary circuit exit.

Figure 5 shows the elemental fission product density histories at the exit of the circuit into the containment predicted by VICTORIA. Silver, indium, and cadmium releases have several peaks, which correspond to bursts of control rod segments predicted by CORSOR. Most of the fission product densities tail off at about 7000 s, which corresponds to shutdown of the reactor. However, cesium and iodine densities remain relatively high due to re-vaporization within the circuit.

Figure 6 shows the cesium speciation at the exit. Cesium iodide aerosol is the dominant species throughout the calculation; however, hydrogen iodide becomes significant at about 8000 s. This prediction indicates that instrumentation to detect the chemical form of iodine should continue to operate even after the reactor is shut down. The HI generation occurs shortly after the  $H_2/H_2O$  ratio drops nearly to zero (see Figure 3) and is driven by the following reaction:



This mechanism to form HI is an interesting process that could occur late in reactor accident sequences after zirconium oxidation is nearly complete and would likely affect the predicted source term after failure of containment.

The locations where aerosol deposition occurs are shown in Figure 7. In this calculation, deposition is primarily by thermophoresis in the steam generator and by deposition in bends. VICTORIA predicts that aerosols will also agglomerate as they pass the upper plenum and through the steam generator, two regions of high thermal gradient. These predictions provide guidance for aerosol sampling. They also show that PHEBUS-FPT0 should provide useful information for validating the deposition and agglomeration models in VICTORIA provided that adequate counting and sizing of particles deposited in the bends and in the steam generator are done.

## 8. SUMMARY

VICTORIA-92, a mechanistic computer code for analyzing severe nuclear reactor accidents, now contains models for release of fission products and control rod materials, chemical interactions (both equilibrium and non-equilibrium), aerosol physics, and transport. With the current suite of models, the code can be used to analyze a wide variety of accident scenarios. Validation studies to date have provided confidence in the current models.

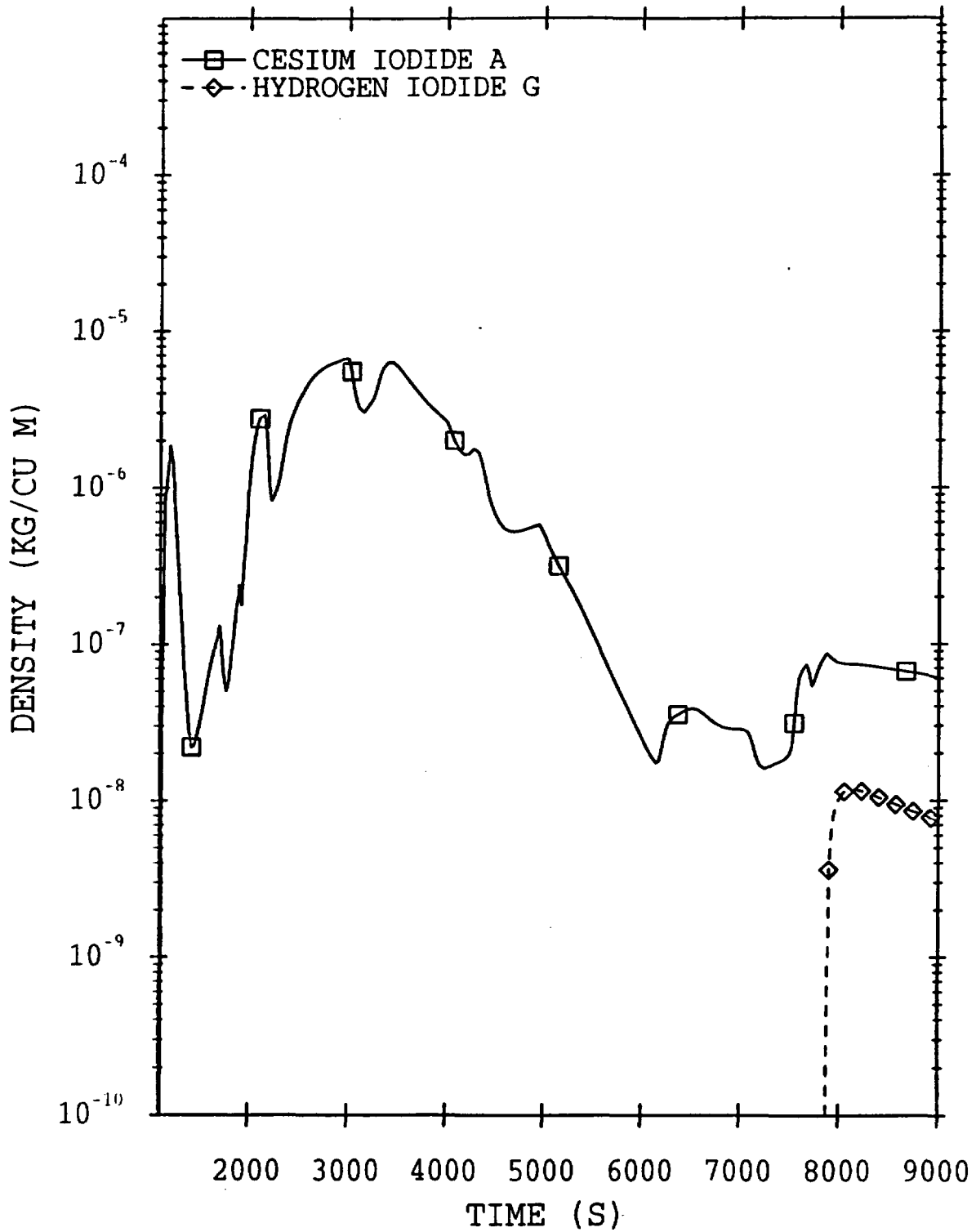


Figure 6. Iodine species densities at the PHEBUS-FPT0 primary circuit exit.

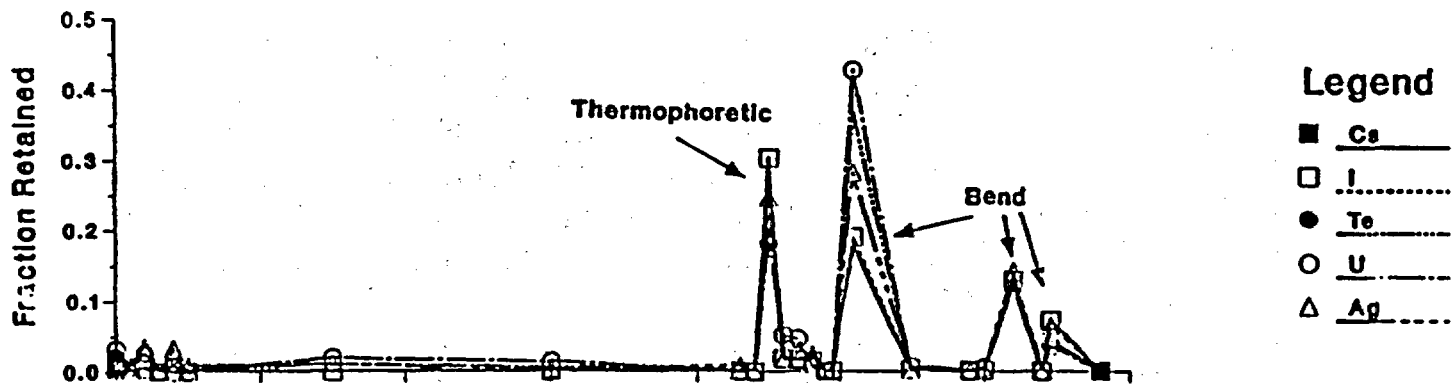
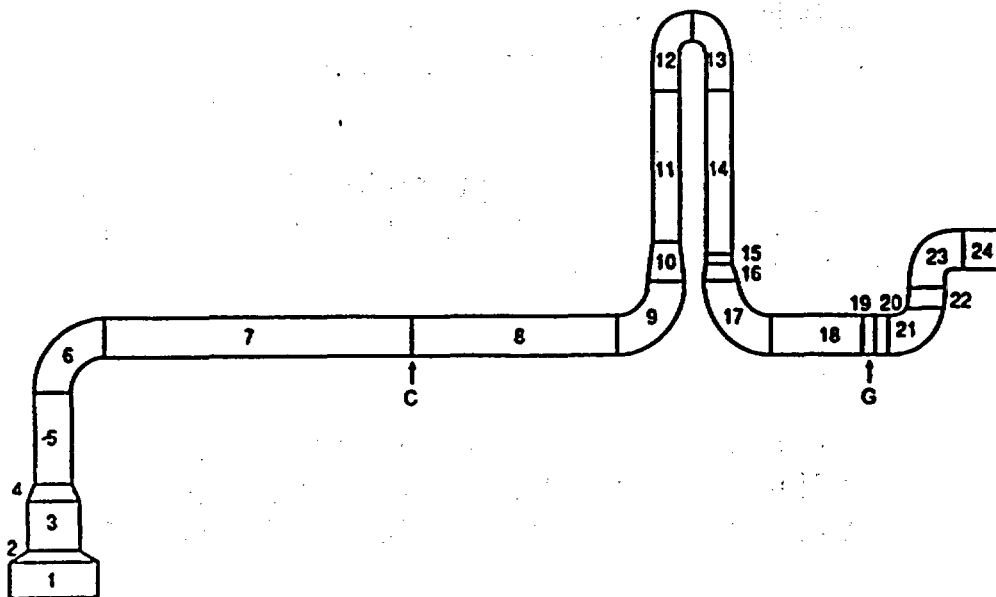


Figure 7. Distribution of aerosol deposition within the PHEBUS-FPT0 primary circuit.

The next stage of VICTORIA development is to perform further validation and assessment so that the models can be further refined and used to perform full plant studies.

PHEBUS-FPT0 analyses show that VICTORIA is a useful tool for judging what measurements are most useful for understanding significant phenomena. They also show that the PHEBUS-FP test series should provide useful information for validation of VICTORIA. Finally, predictions of HI formation within the circuit may have implications for many reactor accident sequences.

PHEBUS-FP is one of the test series being used to validate and assess the models in VICTORIA-92. Other validation is ongoing and is the main emphasis of the current development effort.

## **9. ACKNOWLEDGEMENT**

This work was supported by the US Nuclear Regulatory Commission and performed at Sandia National Laboratories, which is operated for the US Department of Energy under Contract Number DE-AC04-76DP00789.

## **10. REFERENCES**

1. T. J. Heames, D. A. Williams, N. E. Bixler, A. J. Grimley, C. J. Wheatley, N. A. Johns, and M. D. Vine, P. Domagala, L. W. Dickson, C. A. Alexander, I. Osborn-Lee, S. Zawadzki, J. Rest, and H. S. Bond, "VICTORIA: A Mechanistic Model of Radionuclide Behavior in the Reactor Coolant System Under Severe Accident Conditions, Revision 1" SAND90-0756, NUREG/CR-5545, Sandia National Laboratories, Albuquerque, New Mexico (1992).
2. T. J. Heames, D. A. Williams, N. E. Bixler, A. J. Grimley, C. J. Wheatley, N. A. Johns, and N. M Chown, "VICTORIA: A Mechanistic Model of Radionuclide Behavior in the Reactor Coolant System Under Severe Accident Conditions," SAND90-0756, NUREG/CR-5545, Sandia National Laboratories, Albuquerque, New Mexico (1990).
3. A. H. Booth, "A Method of Calculating Fission Gas Diffusion from UO<sub>2</sub> Fuel and Its Application to the X-2-f Loop Test," CRDC-721, AECL Chalk River, Canada (1957).
4. N. E. Bixler and T. J. Heames, "Status of VICTORIA Development and Assessment," *Proceedings of the Eighteenth Water Reactor Safety In-*

- formation Meeting, Rockville, Maryland, NUREG/CP-0114, Vol. 2, U.S. Nuclear Regulatory Commission, pp 271-282 (1990).
5. J. R. Matthews and M. H. Woods, "Modelling the Transient Behaviour of Fission Gas," *Journal of Nuclear Materials*, 84, pp 125-136 (1980).
  6. J. Rest and A. W. Cronenberg, "Modeling the Behavior of Xe, I, Cs, Te, Ba, and Sr in Solid and Liquefied Fuel During Severe Accidents," *Journal of Nuclear Materials*, 150, pp 203-225 (1987).
  7. D. A. Powers, "Behavior of Control Rods During Core Degradation: Pressurization of Silver-Indium-Cadmium Control Rods," NUREG/CR-4401, U.S. Nuclear Regulatory Commission (1985).
  8. B. R. Bowsher, R. A. Jenkins, A. L. Nichols, N. A. Rowe, and J. A. Simpson, "Silver-Indium-Cadmium Control Rod Behaviour During a Severe Accident," AEEW-R1991, UKAEA, Winfrith, UK (1986).
  9. K. H. Im, R. K. Ahluwalia, and H. C. Lin, "The RAFT Computer Code for Calculating Aerosol Formation and Transport in Severe LWR Accidents," NP-5287-CCM, Argonne National Laboratory, Argonne, Illinois (1987).
  10. A. L. Wright, W. L. Pattison, and J. Y. King, "'SERIES -2' Aerosol Resuspension Test Data Summary Report," Oak Ridge National Laboratory, Oak Ridge, Tennessee, unpublished.
  11. N. E. Bixler, "Model for Heat-Up of Structures in VICTORIA," SAND92-1506, Sandia National Laboratories, Albuquerque, New Mexico (1992).
  12. G. F. Holford and C. J. Wheatley, "VICTORIA Aerosol-Atmosphere Interaction Model Development," AEA RS 5226, AEA Technology, Risley, UK (1992).
  13. D. S. Cox, F. C. Iglesias, C. E. L. Hunt, N. A., Keller, R. D Barrand, J. R. Mitchell, and R. F. O'Connor, "Oxidation of UO<sub>2</sub> in Air and Steam with Relevance to Fission Product Releases," *Proceedings of the Symposium on Chemical Phenomenon Associated with Radioactivity During Severe Nuclear Plant Accidents*, Anaheim, California, NUREG/CP-0078, U.S. Nuclear Regulatory Commission, pp 2-35 (1986).
  14. R. J. Wilson, J. Araj, A. O. Allen, P. Auer, D. Boulware, F. Finlayson, S. Goren, and C. Ice, "Report to the American Physical Society by the Study Group on Radionuclide Release from Severe Accidents at Nuclear Power Plants," *Reviews of Modern Physics*, 57, No.3, Part II (1988).
  15. V. F. Urbanic and T. R. Heidrick, "High Temperature Oxidation of Zircaloy-2 and Zircaloy-4 in Steam," *Journal of Nuclear Materials*, 75, pp 251-261 (1978).

16. C. A. Alexander and J. S. Ogden, "Vaporization of  $\text{UO}_2$  at High Temperatures and High Pressures. A Generic Relation for Volatilization," *High Temperatures/High Pressures*, 21, p 149 (1990).
17. B. R. Bowsher and R. A. Jenkins, "High Temperature Studies of Simulant Fission Products: Part V, Temperature-Dependent Interaction of Tellurium Vapour with Zircaloy," AEEN-R1915, UKAEA, Winfrith, UK (1991).
18. M. D. Vine and P. N. Clough, "A Modelling Approach for Heterogeneous Chemistry in the VICTORIA Source Term Code," AEA TRS 5082, UKAEA, Culcheth, UK (1991).
19. R. M. Elrick, R. A. Sallach, A. L. Ouellette, and S. C. Douglas, "Reaction Between Some Cesium-Iodine Compounds and the Reactor Materials 304 Stainless Steel, Inconel 600 and Silver, Volume 1, Cesium Hydroxide Reactions," SAND83-0395, NUREG/CR-3197, 1 of 3, Sandia National Laboratories, Albuquerque, New Mexico (1984).

# SCDAP/RELAP5/MOD3 Code Development<sup>a</sup>

C. M. Allison, L. J. Siefken, E. W. Coryell  
Idaho National Engineering Laboratory

## ABSTRACT

The SCDAP/RELAP5/MOD3 computer code is designed to describe the overall reactor coolant system (RCS) thermal-hydraulic response, core damage progression, and fission product release and transport during severe accidents. The code is being developed at the Idaho National Engineering Laboratory (INEL) under the primary sponsorship of the Office of Nuclear Regulatory Research of the U.S. Nuclear Regulatory Commission (NRC). Code development activities are currently focused on three main areas - (a) code usability, (b) early phase melt progression model improvements, and (c) advanced reactor thermal-hydraulic model extensions. This paper describes the first two activities. A companion paper describes the advanced reactor model improvements being performed under RELAP5/MOD3 funding.

## Introduction

The SCDAP/RELAP5/MOD3 computer code is designed to describe the overall reactor coolant system (RCS) thermal-hydraulic response, core damage progression, and fission product release and transport during severe accidents up to the point of reactor vessel or system failure<sup>1,2</sup>. The code is being developed at the Idaho National Engineering Laboratory (INEL) under the primary sponsorship of the Office of Nuclear Regulatory Research of the U.S. Nuclear Regulatory Commission (NRC). The code also includes models developed by the U.S. Department of Energy.

SCDAP/RELAP5/MOD3[7x]<sup>b</sup>, created in January, 1991, represents a merger of

<sup>a</sup> Work supported by the U.S. Nuclear regulatory Commission, Office of Research, under DOE Contract No. DE-AC07-76ID01570.

<sup>b</sup> The number in brackets, [7x], represents the configuration control number assigned to each code version for quality assurance purposes.

the SCDAP/RELAP5/MOD2 damage progression and fission product transport and deposition models with RELAP/MOD3 thermal-hydraulics. A systematic code developmental assessment effort is now underway for both the RELAP5/MOD3 thermal-hydraulic models and the SCDAP early phase damage progression models<sup>3,4</sup>. As a result of the assessment completed thus far, SCDAP/RELAP5/MOD3[7x] was frozen in May and released to a limited number of organizations for beta testing and independent assessment. At that time, code improvement activities were also initiated to incorporate code improvements where the assessment had indicated that deficiencies existed. These development activities are currently focused on three main areas - (a) code usability, (b) early phase melt progression model improvements, and (c) advanced reactor thermal-hydraulic model extensions. This paper describes the results of the first two activities. A companion paper<sup>5</sup> describes the advanced reactor thermal-hydraulic model improvements.

### **Code Usability Improvements**

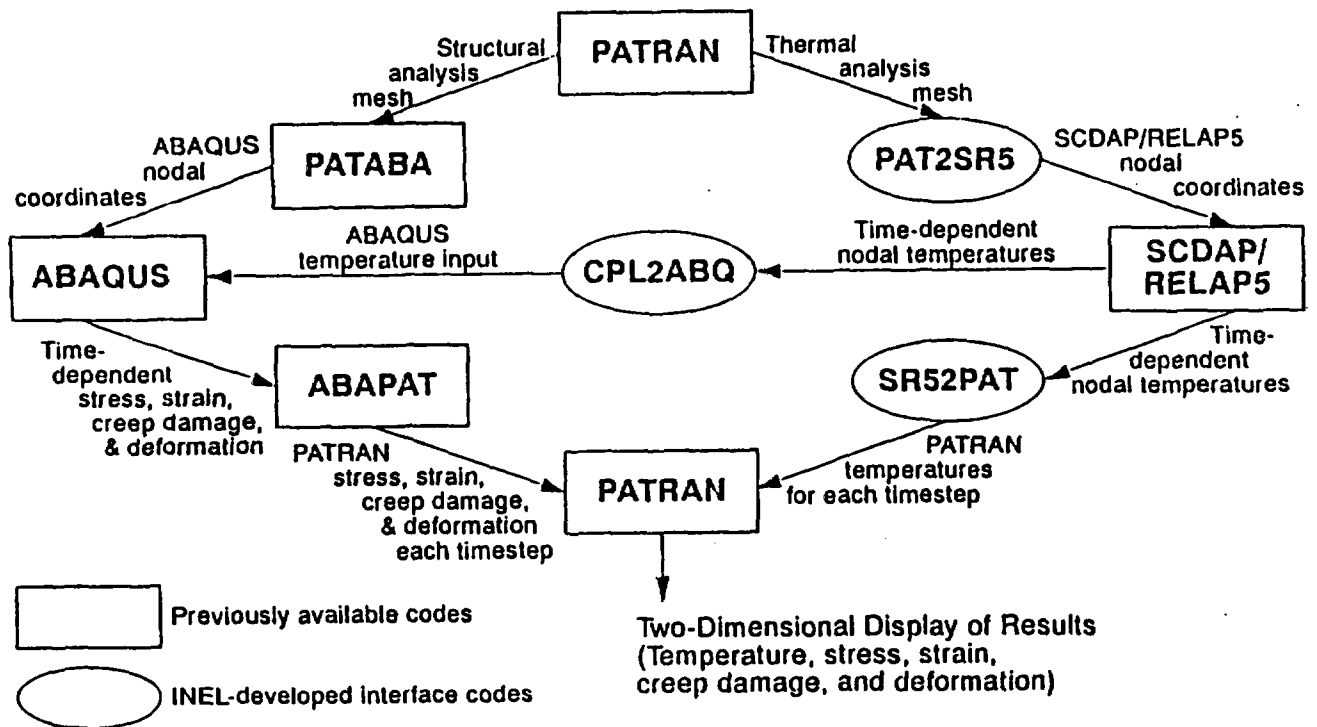
Specific requirements and priorities for code usability improvements were identified from a series of user surveys and the initial results of an independent peer review of the code. These improvements are focused primarily on the reduction of overall analysis costs associated with plant system analysis or the addition of specific user requested features. They include (a) changes to reduce numerical instabilities and water property or other state failures, (b) changes in input/output processing to reduce user errors and to compress output files, and (c) the addition of a data link between SCDAP/RELAP5/MOD3, PATRAN, and ABAQUS.

The changes in the code to reduce numerical instabilities and other code failures have dramatically improved the overall reliability of the code for many types of problems. In addition, in those problems where the code had previously reduced the time steps to unacceptable values to insure code stability, these changes have resulted in substantial reductions in overall run times. The most important changes in this category include (a) a better treatment of the influence of noncondensibles on phase appearance and disappearance, (b) time smoothing options for the explicit

coupling between radiation heat transfer and hydrodynamics models, and (c) elimination of the discontinuities in thermal-hydraulic constitutive models for many types of problems.

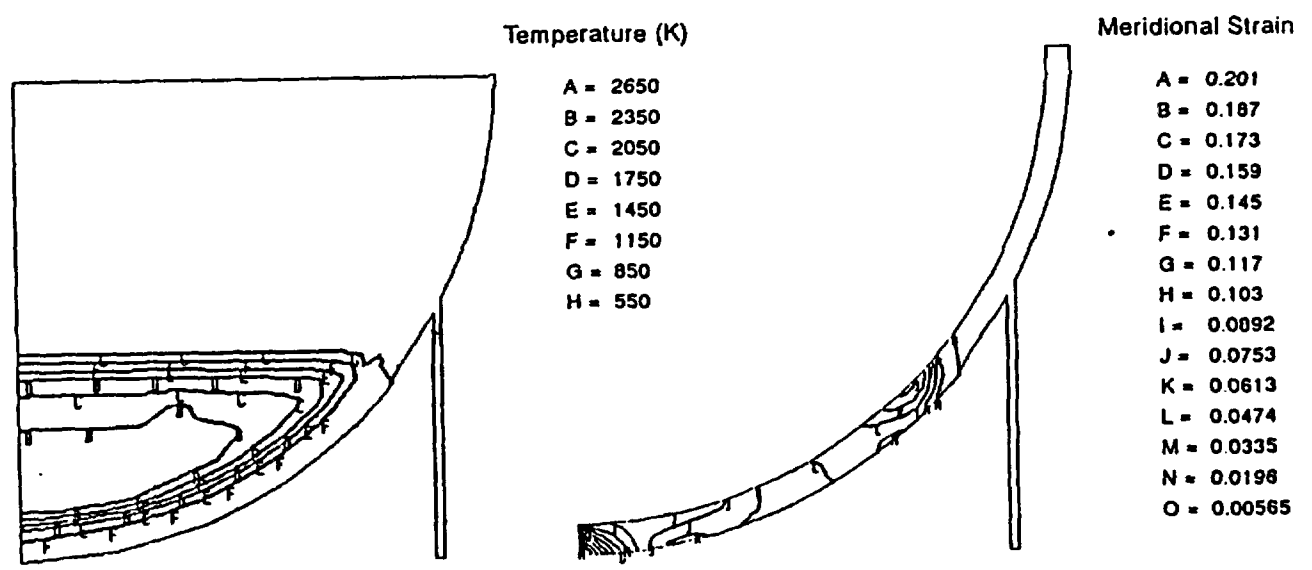
Changes in code input and output have included the (a) conversion of all the input to the RELAP5 free form, numbered card format, (b) addition of extensive input error checking, (c) addition of input range checking and best estimate defaults, (d) addition of options for automatic data compression for restart plot files, and (e) more descriptive output. As a result of the changes in code input, the time required to set up and qualify an input deck has been substantially reduced since a majority of actual and potential errors can be identified in a single input test run. In addition, the code will automatically substitute best estimate default values for selected model input based upon the results of code-to-data comparisons performed as part of the code assessment activities. However, the user can override the default values for sensitivity runs to evaluate the influence of modeling uncertainties on overall calculations. The addition of the restart plot compression options was the most notable change in the output process. These options can reduce the size of the output file and disk storage requirements substantially, in some cases by as much as a factor of 5.

The data link between SCDAP/RELAP5/MOD3, PATRAN, and ABAQUS has been added to the code as a user option. This option was developed to support the NRC's Lower Head Failure Program<sup>6</sup> and was intended primarily to allow the detailed thermal and structural analysis of the lower head. This option can be used to analyze structures throughout the system, however. An example of the possible application of this link is shown in Figures 1 and 2. In this example, the user uses the general purpose PATRAN code to build the thermal and structural meshes for a detailed 2D analysis of debris and associated lower head structures. The resulting thermal mesh is then used to create the input for the SCDAP/RELAP5/MOD3 detailed COUPLE model using the INEL-developed PAT2SR5 code while the structural mesh is processed for input into ABAQUS. The COUPLE model is then used to perform the detailed thermal analysis of the debris and lower head. This analysis can include (a) time dependent accumulation of debris, (b) 2D heat



MG25 05/02 2/31

Figure 1. Thermal and structural analysis performed using PATRAN-ABAQUS-SCDAP/RELAP5.



MG25 05/02 2/41a

Figure 2. Two-dimensional display of thermal and structural analysis results.

conduction within the debris bed and associated structures, (c) dryout or quench (rubble bed only), and (d) molten pool formation and growth. The resulting temperature response can then be used in the ABAQUS structural analysis. As shown in Figure 2, PATRAN can then be used to display the results from both the SCDAP/RELAP5 and ABAQUS.

### Early Phase Model Improvements

As described in a previous Water Reactor Safety Meeting paper[4] and subsequent report[7], a systematic assessment of the SCDAP/RELAP5 models has been underway since the summer of 1992. That assessment, which has included code-to-data comparisons for SCDAP/RELAP5/MOD3 and earlier versions of the code, has thus far focused upon the early phases of an accident where a wide range of experiment results are available. These early phase code-to-data comparisons have indicated that SCDAP/RELAP5 can describe many of the important features of the experiments. Specifically, it has been concluded that:

1. The thermal response of the early phase experiments, including variations in timing as well as magnitude, could typically be predicted within  $\pm 20\%$  with a few outliers in the  $\pm 40\%$  range. The ballooning and rupture could typically be predicted to a few percent. The hydrogen production had the worst overall agreement, particularly during bundle reflood, with a variation up to a factor of two. The general trends of the melt relocation, amount of material liquefied and location of the blockage regions, could be predicted but qualitative estimates were still limited by the availability of data.
2. Some features of the experiments could not be adequately predicted including (a) the renewed hydrogen production, heating and melting during reflood, (b) the influence of material interactions between the fuel rod, control rod/blade, and structural materials, (c) flow diversions due to changes in geometry, (d) rivulet and free droplet flow of liquefied fuel rod materials, (e) oxidation of the inside of unpressurized fuel rod

cladding, (f) the oxidation of relocating material or material that has formed a cohesive blockage, and (g) the porosity of frozen melt and the relocation of ceramic fuel rod material.

As a result of that assessment, work was started in improving the models where they were shown to be deficient. Of the seven areas noted above, model improvements have been completed for (a) renewed hydrogen production, heating, and melting during reflood, (b) interactions between Inconel spacer grids-Zircaloy cladding and BWR B<sub>4</sub>C, stainless steel control blade, Zircaloy channel boxes, and (c) the influence of cold walls upon the flow diversions associated with changes in geometry. Work was started on the interactions between (a) Ag-In-Cd control material, stainless steel, and Zircaloy and (b) rivulet and free droplet flow of liquefied fuel rod materials.

As shown on Figures 3 and 4, experiments performed in the CORA facility in Germany<sup>7,8,9</sup> have shown that the reflooding of a hot, damaged bundle can have a dramatic influence on the hydrogen production and heating of the bundle. Figure 3 shows the results from a PWR bundle test, CORA-12, while Figure 4 shows the results from two BWR bundle tests, CORA-16 and CORA-17. CORA-12 was an electrically heated bundle with a 25 rod array consisting of fuel rods, electrically heated fuel rod simulators, and Ag-In-Cd control rod. The power in the bundle was increased linearly with time until indicated temperatures exceeded the melting point of Zircaloy, at a time of ~4900 s, the power was then decreased, resulting in the initial cooling of the bundle. Then at ~5100 s, the bundle was quenched. The resulting spike in the hydrogen and temperatures at 50 and 1250 mm where bundle thermocouples were still operational is obvious. The same trend was shown in the CORA-17 experiment. In this case, the bundle was composed of BWR structures, fuel rods, electrically heated fuel rod simulators, Zircaloy channel, and B<sub>4</sub>C control blade segment. By way of contrast, the hydrogen production for the CORA-16 test is also shown. Both CORA-16 and CORA-17 were subjected to the same heatup and melting transient. However, the bundle in CORA-16 was slowly cooled while the CORA-17 bundle was quenched.

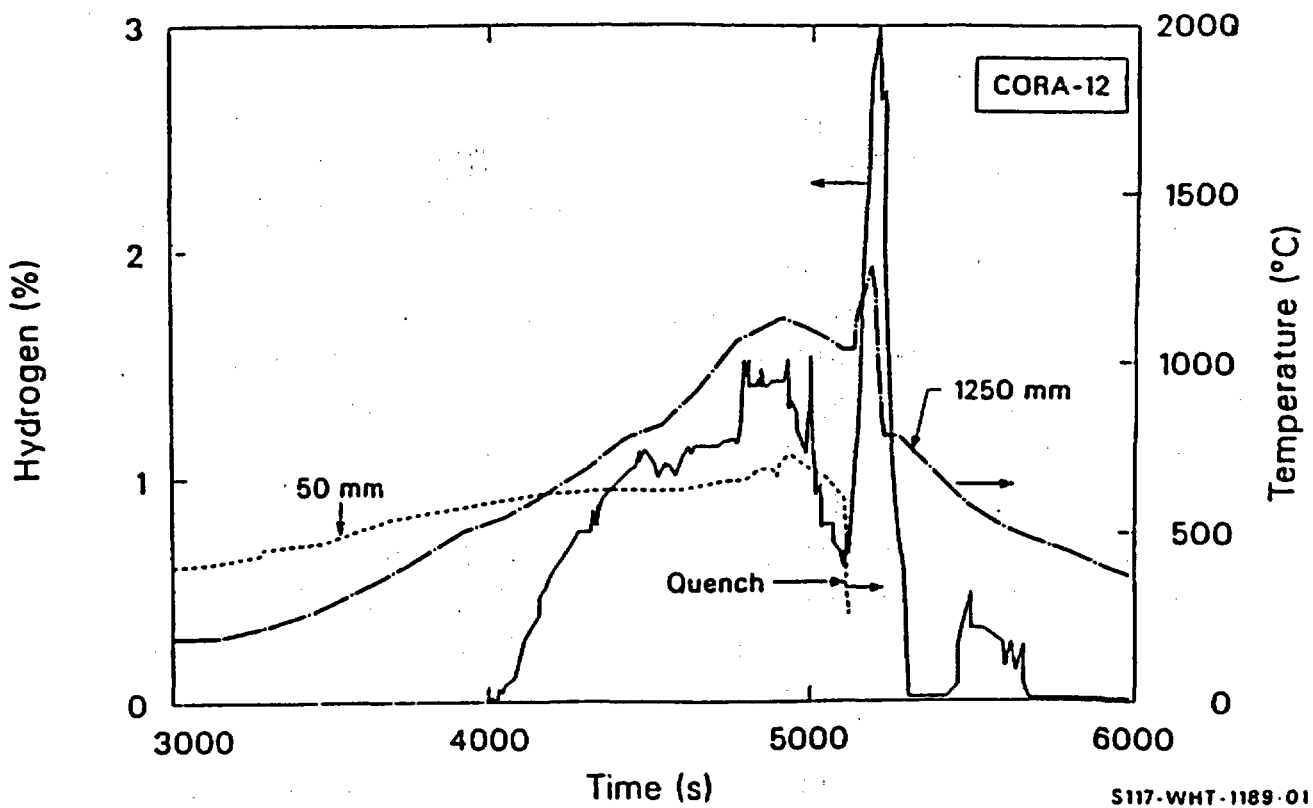


Figure 3. Measured CORA-12 PWR bundle test hydrogen generation rate and temperatures.

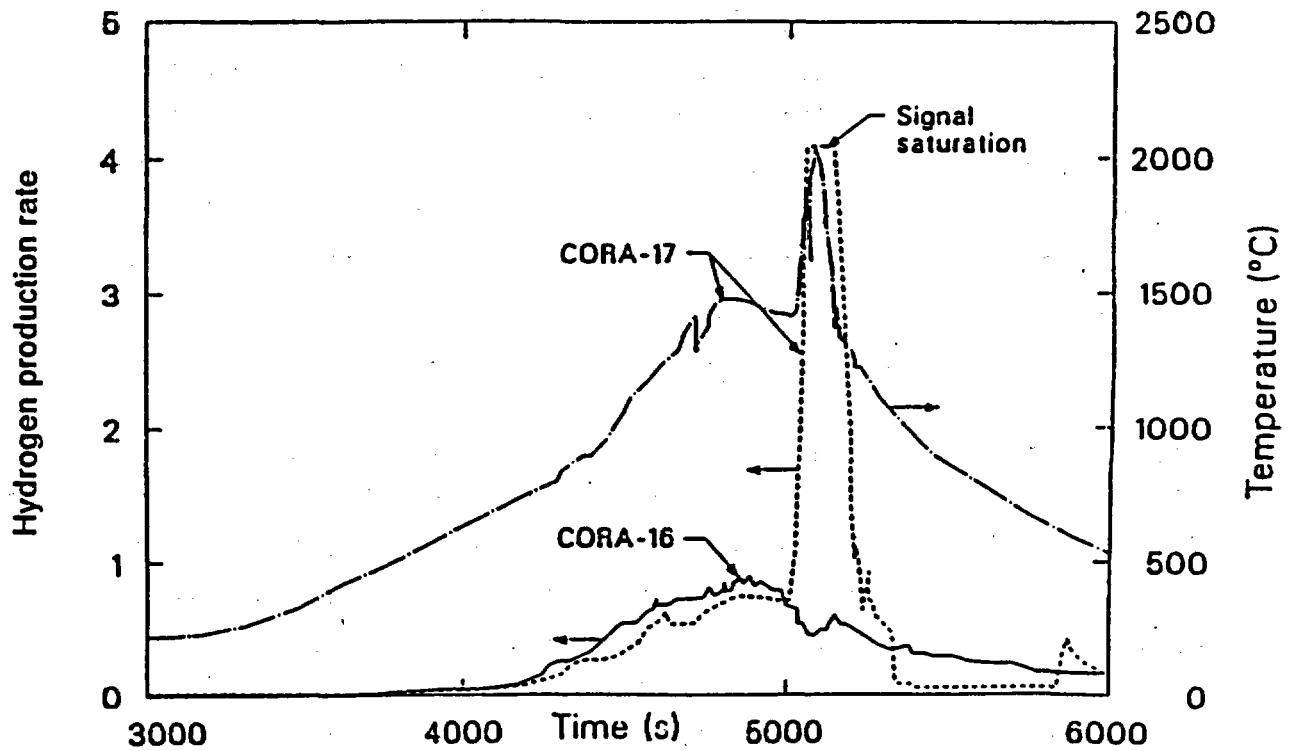
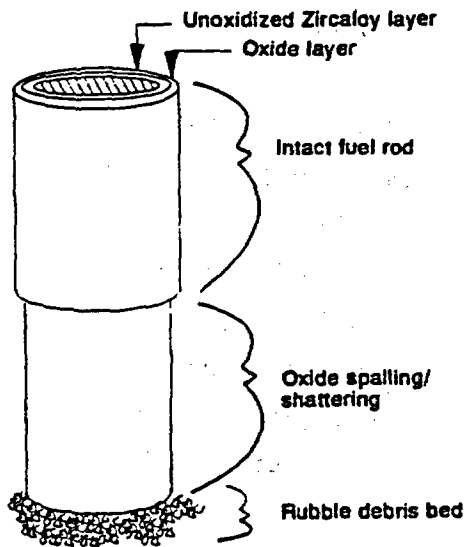


Figure 4. Comparison of measured CORA-16 and CORA-17 BWR bundle hydrogen generation rate and temperatures.

However, during the analysis of these experiments, it was found that the existing SCDAP/RELAP5 models could not predict such a rapid increase in oxidation during reflood. In fact, the models consistently underpredicted the oxidation during the reflood phase of the experiments by nearly a factor of two. In the original models, it was assumed that, during reflood, the fuel rods would shatter, exposing unoxidized Zircaloy and forming a loose rubble debris bed, if two basic criteria was satisfied. First, the cladding was sufficiently oxidized that the cladding had become embrittled using a criteria developed by Kassner and Chung<sup>10</sup>. That is, the remaining, relatively oxygen free (<0.9 wt %), beta layer of the Zircaloy cladding had a thickness less than 0.1 mm. Second, the fuel rods were cooled below 1270 K where it was expected that the oxide was no longer ductile due to a phase transition in the  $ZrO_2$ .

Consequently, the SCDAP/RELAP5 models were changed using the basic concepts illustrated in Figure 5. It was still assumed that the fuel rods would shatter using the same criteria as before. However, an additional region was added where the protective oxide could spall or shatter leaving a fresh unoxidized surface of metallic Zircaloy. The region would form, based upon an analysis of the available data, if the cooling rate was greater than 2 K/S and the temperature of the oxide fell below 1560 K. In addition, a vapor limited diffusion model was added using a heat/mass transfer analogy to limit the maximum rate of oxidation when the hot metallic surface was exposed to steam. Although a detailed assessment of this model has not been completed, results of verification testing<sup>11</sup> indicates that the predicted trends are correct.

The CORA, and other separate effects, experiments performed in Germany<sup>12</sup> also show that grid spacers have a pronounced impact on the relocation and freezing of liquefied material and relocation of loose debris. As shown in sketches of the end state of several CORA experiments, Figure 6, the grid spacers act as barriers to the relocation of liquefied material and loose debris. In addition, Inconel spacer grids can also chemically interact with the Zircaloy cladding to form relatively low melting temperature alloys. These interactions can occur quickly as the temperatures are increased with complete liquefaction of the material in



### Model Features

- Thermal hydraulics
  - RELAP5 reflood and quenching correlations used
- Vapor limited diffusion of steam to surface
  - Mass transfer coefficient calculated using heat/mass analogy
- Shattering of oxidized cladding
  - Cooling rate  $\geq 2$  K/s
  - $\beta$ -layer  $\leq 0.1$  mm
  - $T_{\text{debris}} \leq T_{\text{ox}} \leq 1560$  K

M155-EDR-1692-004

Figure 5. Features of the new reflood and oxide shattering model.

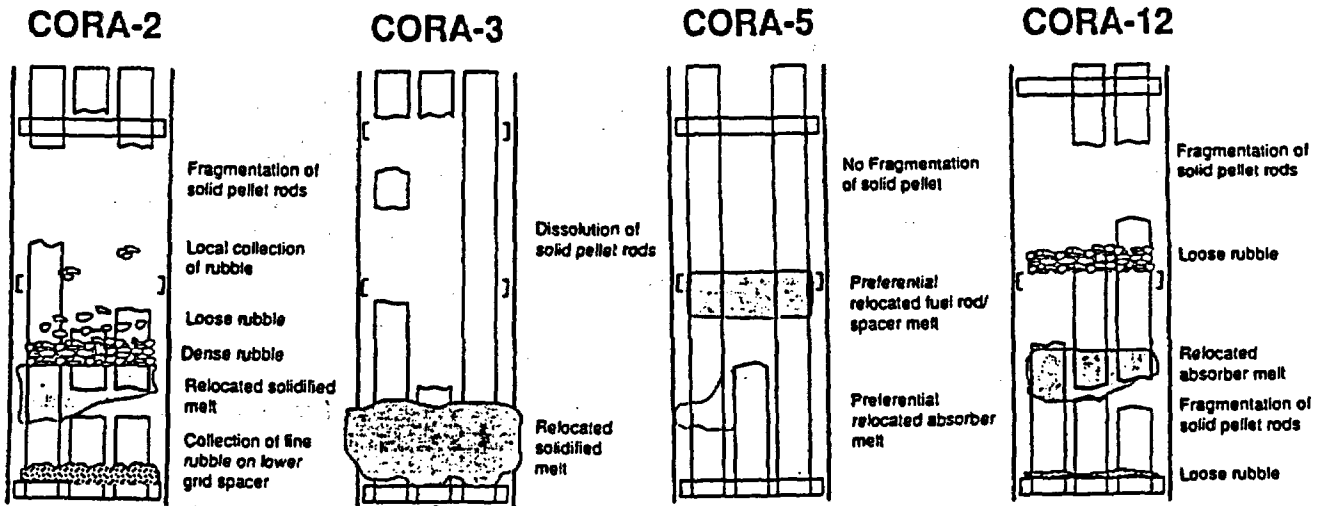


Figure 6. Influence of grid spacers in selected CORA experiments.

the location of the interactions at a temperature near 1500 K.

To account for these effects, the spacer grid models in SCDAP/RELAP5 were modified to account for the stored energy associated with the grid as well as the interactions between Inconel and Zircaloy. These models are described in detail by Siefken<sup>13</sup>. However, the key features of the models are shown on Figure 7. The Inconel spacer grid model is the most elaborate due to the incorporation of reaction kinetics correlations that define the rate of chemical interactions between the grid and the adjacent cladding. These correlations use a parabolic rate equation with exponential temperature dependence. These correlations also account for the rate limiting effect of an initial protective oxide layer. The interactions are assumed to proceed initially with the formation of a pin hole failure in the cladding at the point of contact between the spacer grid and cladding. The interactions will then spread from that point radially until the grid is completely liquefied. Both Zircaloy and Inconel spacer grids can also act as barriers to the downward relocation of liquefied debris. In this case, the thermal mass of the grid

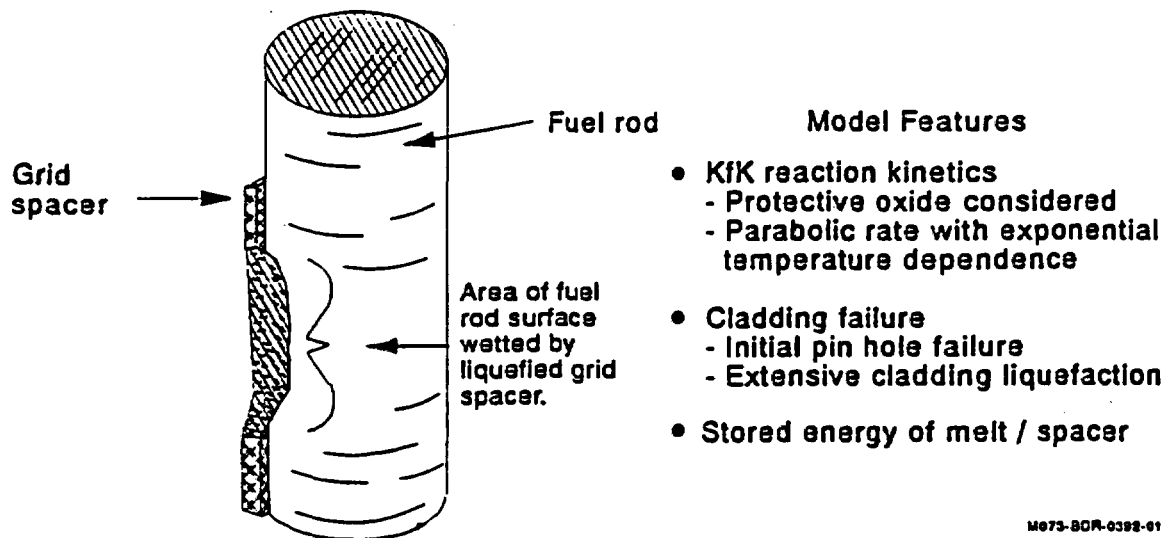


Figure 7. Features of the new Inconel spacer grid-Zircaloy cladding interaction model.

spacers are included in the event that the grid, adjacent cladding, and overlying debris or melt continue to heat up and eventually relocate downward. Initial assessment of the new model using the results from the CORA-7 experiment<sup>14</sup> indicates that the new model results in a prediction of melt relocation behavior in much better agreement with the test.

BWR heating and melting experiments in the Annular Core Research Reactor (ACRR)<sup>15,16</sup> and in the CORA facility<sup>7,8,9,17</sup> also showed that the interactions between the B<sub>4</sub>C control material, stainless steel cladding and sheath material, and the channel box Zircaloy dominated the initial liquefaction and relocation of the BWR control blade and channel box. However, these structures were originally modeled using two separate component models. A B<sub>4</sub>C/stainless steel control rod/blade component was used to represent the BWR control blade while a general slab model was used to represent the channel box. Because of this approach, the interactions between the control blade and adjacent channel box could not be properly addressed. To resolve this problem, a new component model has been added to the code which represents the BWR specific combined channel box and control blade geometry. This model was developed by Oak Ridge National Laboratory<sup>18</sup> and includes (a) a representation of the control blade and channel box segments adjacent to the control blade and open interstitial gap, (b) interactions between the B<sub>4</sub>C, stainless steel cladding and sheath, and the Zircaloy channel box, (c) oxidation of the stainless steel, Zircaloy, and B<sub>4</sub>C, and (d) liquefaction and relocation of the component structures. The model allows for different flow conditions in the interstitial region and fuel assembly using the RELAP5 thermal-hydraulics models and correlations.

The analysis of the LOFT FP-2 test with SCDAP/RELAP5<sup>19,20</sup> provided the first indication that the flow diversion due to changes in core geometry could be important even during the initial change in geometry due to fuel rod ballooning. As shown in Figure 8, which shows the calculated and measured temperatures in the central fuel assembly of the LOFT core, calculations either including or not including the influence of flow diversions due to fuel rod ballooning tended to bound the measured temperature response of the assembly, but resulted in a substantial change

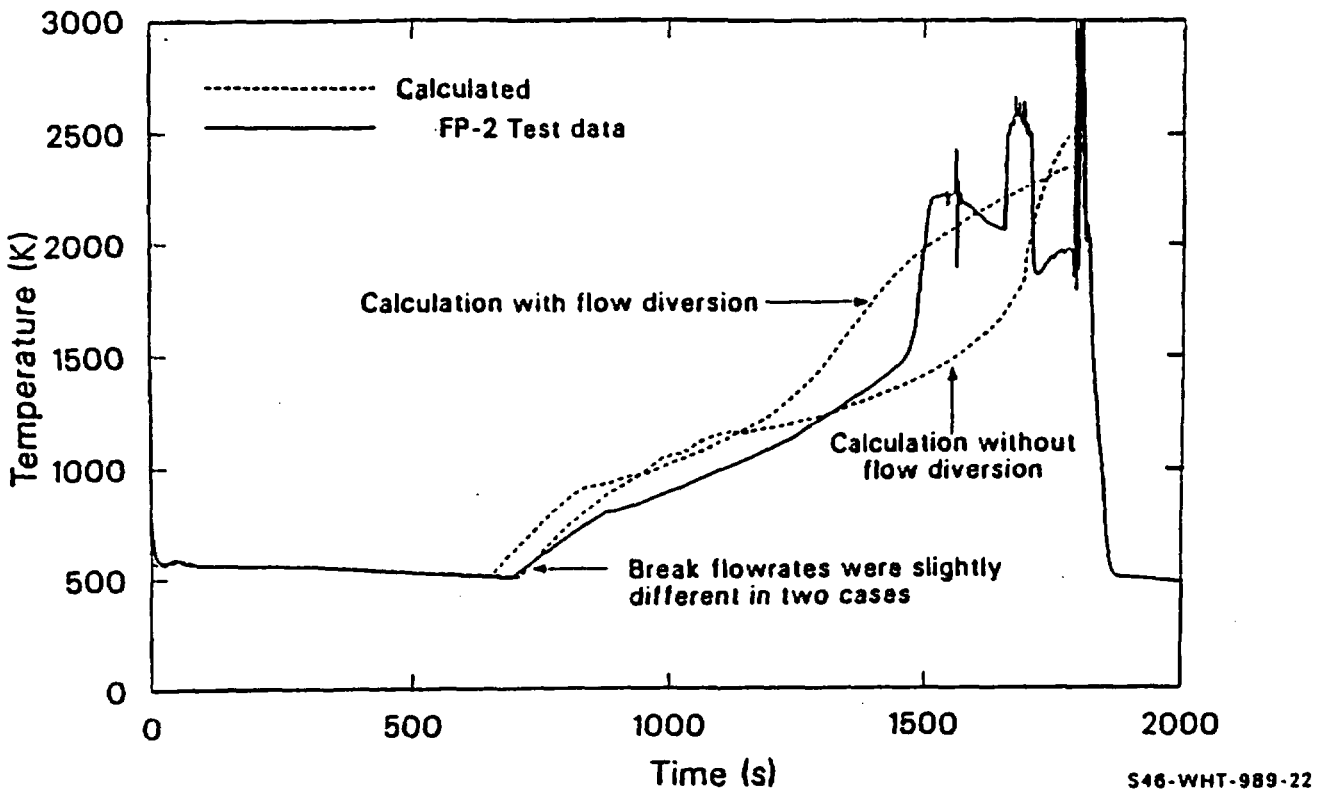
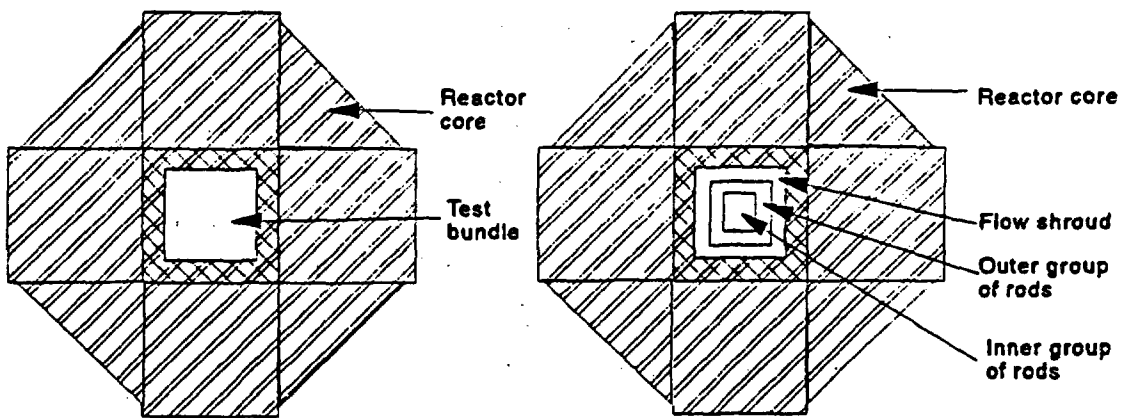


Figure 8. Calculated and measured temperatures for the LOFT FP-2 core central fuel assembly.

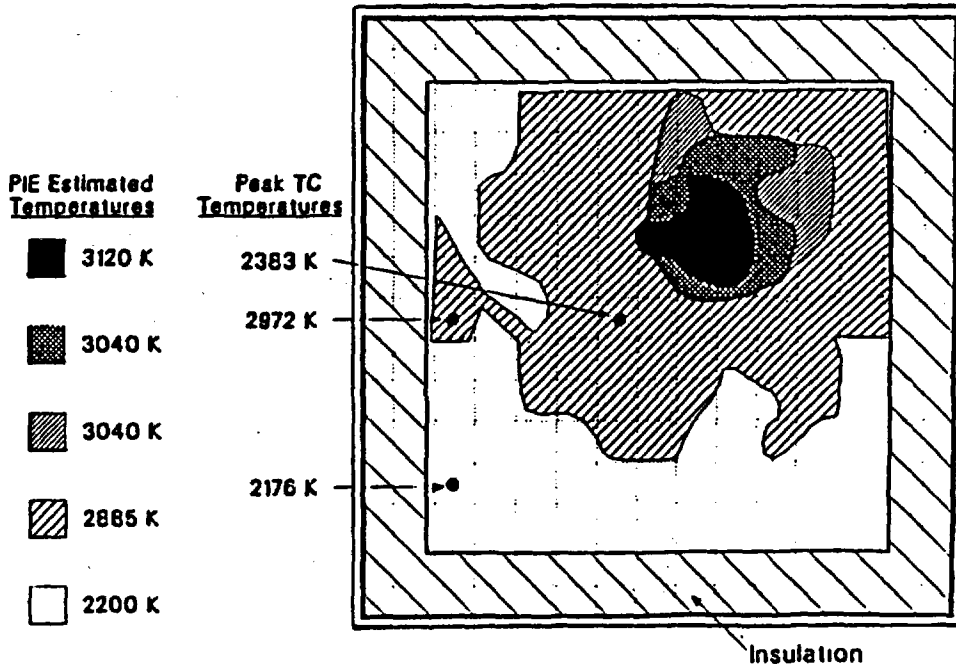
in the predicted temperatures. Further analysis indicated that the insulated shroud surrounding the central assembly had a substantial impact on the predicted behavior of the core. As shown in the schematic of the left hand side of Figure 9, the initial calculations were performed using a two flow channel core model due to limitations in coupling between the SCDAP/RELAP5 radiation heat transfer and hydrodynamics models. As a result, the radial temperatures in the central fuel assembly, fuel rod ballooning, and melt relocation were predicted to be relatively uniform across the assembly. The resulting predicted flow diversion was then from the central assembly to the outer assemblies. Yet, the experimental results showed that the fuel rod temperatures adjacent to the unheated shroud were significantly lower than those in the inner part of the assembly. As a result, as shown in Figure 10, the peak rod temperatures, and associated formation of blockages due to the melting of the assembly were concentrated in the center of the assembly.

Because of this result, the coupling between the radiation heat transfer



M101-BDR-1092-005

Figure 9. Flow channel representations used for the analysis of LOFT FP-2.



S46-WHT-989-10

Figure 10. Estimated peak bundle temperatures from LOFT FP-2.

and hydrodynamics models was modified to allow multiple flow channel within a single radiation enclosure. Initial analysis with these changes and using a more representative set of flow channels in the central assembly indicated that such a radial nodalization more accurately predicted the temperature distribution, fuel rod ballooning, and melting-induced blockage near a cold wall. In the case of the LOFT analysis, the more detailed representation of the flow channels and fuel rod behavior in the central fuel assembly resulted in a reduction in the average flow blockage and associated flow diversion to the outer assemblies as shown in the right hand schematic of Figure 9. Additional LOFT calculations are currently underway to better quantify the influence of the new modeling capability.

The CORA and earlier single rod heatup and melting experiments in the German NEILS facility<sup>21,22</sup> also clearly identified that the initial relocation of fuel rod materials associated with the dissolution of  $UO_2$  by molten Zircaloy occurs as rivulets and free falling droplets. Figure 11, taken from tests conducted in NEILS in Helium, shows the initial formation of rivulets of liquefied fuel rod material. Although the presence of steam, as shown in Figure 12, confused the image of the process, more recent CORA experiments also show the formation of rivulets and free falling drops in the presence of steam once significant amounts of liquefied material have been formed. This is shown in figure 13, which is a composite of data developed from videos taken for PWR and BWR experiments in CORA<sup>8</sup>. Because of the graphic evidence from recent CORA experiments, work has been started on modifying the existing film flow models that are used to treat the relocation of liquefied fuel rod material.

#### References

1. RELAP5/MOD3 Code Manual, Edited by C. M. Allison, C. S. Miller, N. L. Wade, Draft NUREG/CR-5535, EGG-2596, June 1990.
2. SCDAP/RELAP5/MOD3 Code Manual, Edited by C. M. Allison, E. C. Johnson, Draft NUREG/CR-5273, EGG-2555, September 1990.

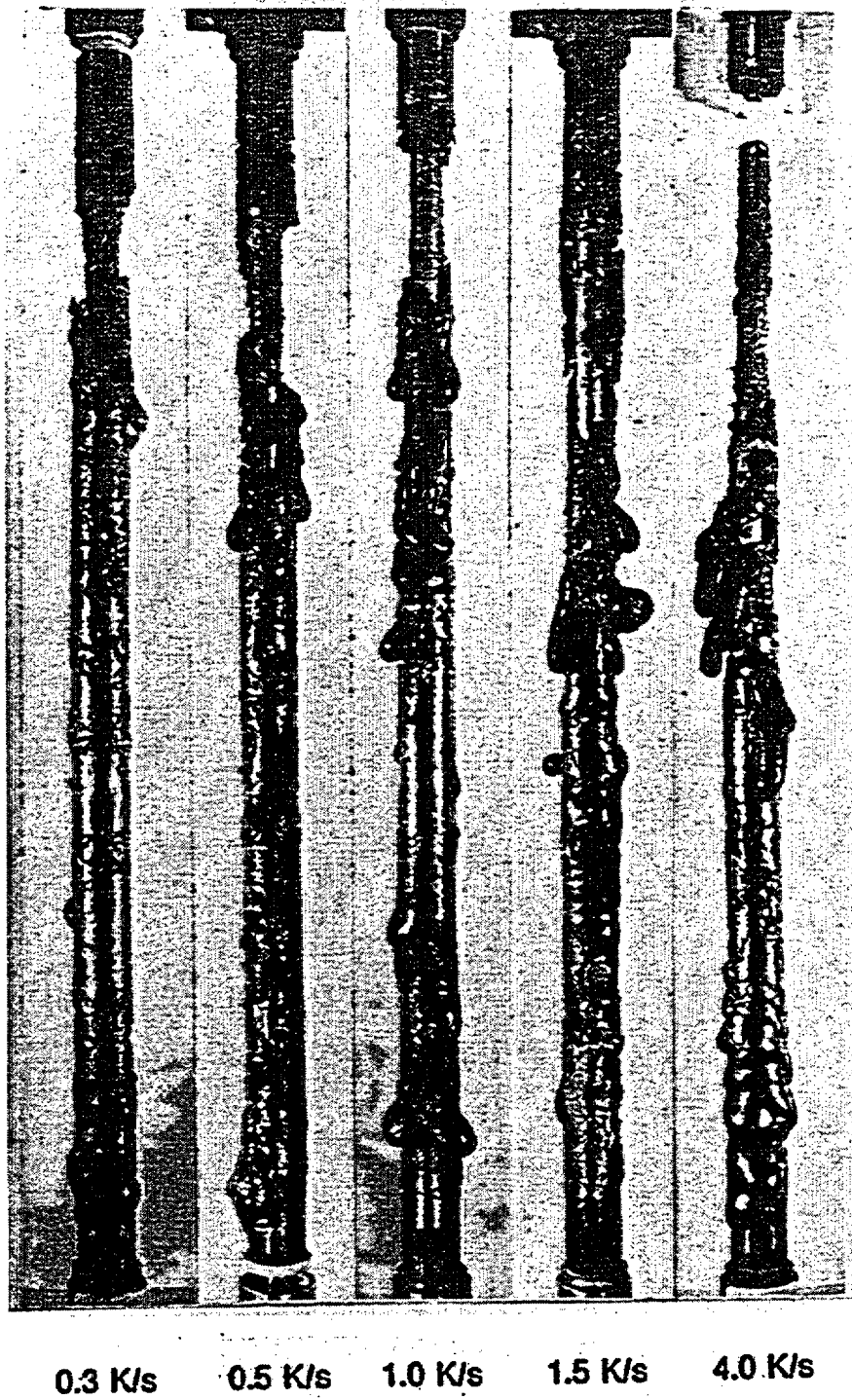


Figure 11. Fuel rod melting in single rod tests conducted in the German NEILS facility in helium.



Figure 12. Fuel rod melting in single rod tests conducted in the German NEILS facility in steam.

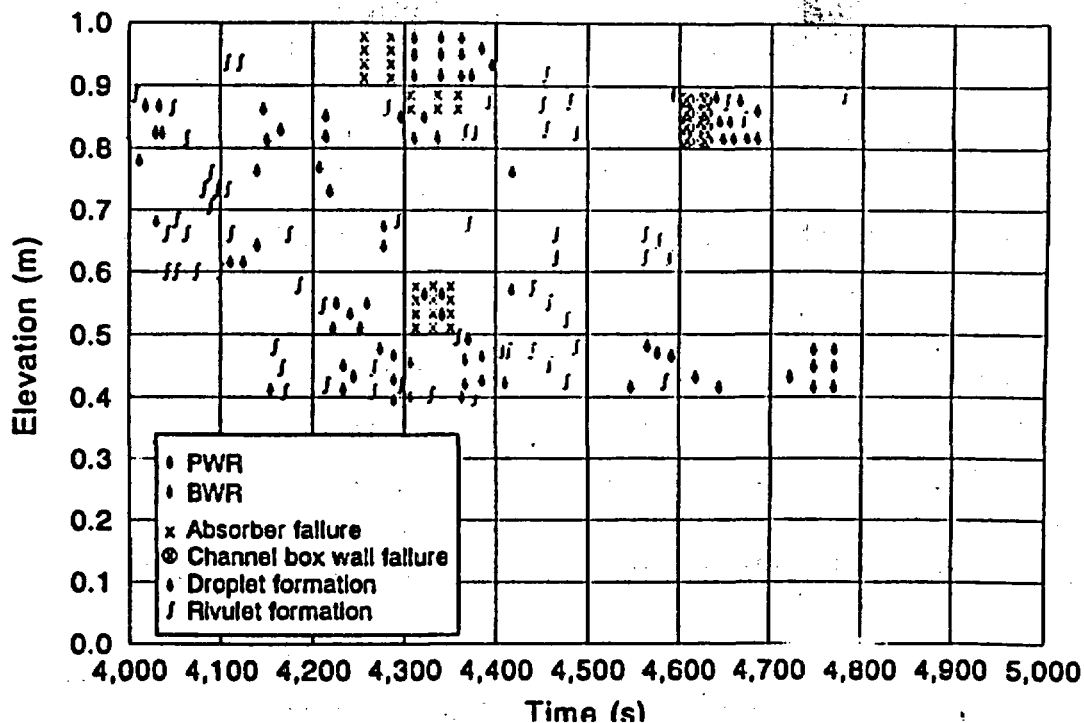


Figure 13. Composite of rivulet and free droplet melt relocation from CORA PWR and BWR tests.

3. C. M. Allison, et al., "SCDAP/RELAP5/MOD3 Code Development and Assessment", 19th Water Reactor Safety Meeting, Bethesda, October, 1991.
4. C. M. Allison, J. K. Hohorst, C. H. Heath, K. L. Davis, SCDAP/RELAP5/MOD3 ASSESSMENT: ASSESSMENT OF EARLY PHASE DAMAGE PROGRESSION MODELS, EGG-SSRE-10098, February, 1992.
5. G. W. Johnsen, "RELAP5 Improvement for Modeling Advanced Reactors", 20th Water Reactor Safety Information Meeting, Bethesda, October 21-23, 1992.
6. J. Rempe, et al., Light Water Reactor Lower Head Failure Analyses, NUREG/CR 5642, EGG-2618 (Draft), March 1992.
7. S. Hagen, et al., "CORA Experiments on the Materials Behavior of LWR Fuel Rod Bundles at High Temperatures", 19th Water reactor Safety Information Meeting, Bethesda, October 28-30, 1991.

8. J. K. Hohorst and C. M. Allison, "Interpretation of Experimental Results from the CORA Core Melt Progression Experiments", ANS Winter Meeting, San Francisco, November, 1991.
9. J. K. Hohorst, C. M. Allison, T. J. Haste, R. P. Hiles, S. Hagen, "Assessment of SCDAP/RELAP5 Using Data From the CORA Core Melt Progression Experiments", Fifth International Topical Meeting on Nuclear Reactor Thermal Hydraulics, Salt Lake City, September 21-24, 1992.
10. H. M. Chung and T. F. Kassner, Embrittlement Criteria for Zircaloy Fuel Cladding Applicable to Accident Situations in Light-Water Reactors; Summary Report, NUREG/CR-1344, ANL79-48, January 1980.
11. E. W. Coryell, S. A. Chavez, K. L. Davis, M. H. Mortensen, Design Report: SCDAP/RELAP5 Reflood Oxidation Model, EGG-SSRE-10307, (To be Published).
12. S. Hagen, et al., Interaction in Zircaloy UO<sub>2</sub> Fuel Rod Bundles with Inconel Spacers at Temperatures above 1200 °C (Posttest Results of Severe Fuel Damage Experiments CORA-2 and CORA-3), KfK-4378, September, 1990.
13. L. J. Siefken and M. V. Olsen, "Effect of Inconel Grid Spacers on Progression of Damage in Reactor Core", Fifth International Topical Meeting on Nuclear Reactor Thermal Hydraulics, Salt Lake City, September 21-24, 1992.
14. Personal communication to J. K. Hohorst
15. R. O. Gauntt, R. D. Gasser, and L. J. Ott, The DF-4 Fuel Damage Experiment in ACRR with a BWR Control Blade and Channel Box, NUREG/CR-4671, SAND86-1443, November 1989.
16. J. K. Hohorst and C. M. Allison, "DF-4 Analysis Using SCDAP/RELAP5", Nuclear Technology, Vol. 98, May 1992.
17. P. Hofmann, M. Markiewicz, and J. Spino, Reaction Behavior of B<sub>4</sub>C Absorber Material with Stainless Steel and Zircaloy in Severe LWR Accidents, KfK-4598, July, 1989.
18. F. P. Griffin, BWR Control Blade/Channel Box Interaction and Melt Relocation Models for SCDAP, ORNL/NRC/LTR-92/12, June, 1992.
19. E. W. Coryell, "Assessment of Core Damage Models in SCDAP/RELAP5 During OECD LOFT LP-FP-2", ANS Winter Meeting, San Francisco, November, 1991.

20. M. L. Carboneau et al., Experiment Analysis and Summary Report for OECD LOFT Project Fission Product Experiment LP-FP-2, OECD LOFT-T-3806, June 1989.
21. S. Hagen, et al., Experimental Investigation of the Melt-Down Phase of  $UO_2$ -Zircaloy Fuel Rods in the Event of Failure of the Emergency Cooling, PNS-4321, December 1978.
22. S. Hagen, Out-of-pile Experiments on the High Temperature Behavior of Zry-4 Clad Fuel Rods, KfK 3567, August 1983.

# **ESTER – a European Severe Accident Code System**

*A.V. Jones and I. Shepherd*

*(CEC Joint Research Centre, Safety Technology Institute)*

## **Abstract**

*The Commission of the European Communities has over the years supported considerable model development and code assessment in the area of LWR source term, and there have also been extensive efforts by individual member states in this direction. In an attempt to bring together the results and to exploit possible synergies JRC/STI has constructed a first version of ESTER, a portable software framework able to accommodate with minimal changes existing or newly developed modules for the various components and phenomena involved in a severe accident. A menu system allows the user to select the modules required for a particular calculation, after which information transfer between the various modules is handled automatically. ESTER also offers graphics facilities on various platforms, intermediate and final output to tape or disk etc. The core of ESTER is the database structure, with which each module is required to interface, and which assures simple and unambiguous data transfer between the modules. A comprehensive set of tools is offered for constructing the database within the computer memory, for manipulating it, for adding new branches to the structure, and for reclaiming unused memory. The first version of ESTER offers severe accident modules for core degradation (ICARE-2), for fission product release (FPRATE from the KESS system), for circuit thermal-hydraulics, for circuit fission product transport and deposition (VICTORIA), and for containment thermal-hydraulics, aerosol physics and chemistry (JERICHO, AEROSOLS and IODE respectively). Work is currently underway to extend the facilities of the ESTER structure, to incorporate alternative modules for core degradation, for two-phase flow in the core and circuit, and for containment phenomena, and to add new capabilities such as pool scrubbing and core-concrete interaction. Because of the advanced and flexible facilities which it offers it is hoped that ESTER will become the preferred framework for future European severe accident model and code development.*

## **1. Introduction**

In the course of the Phase B shared-cost action (SCAs) exercise for the dimensioning of Phebus-FP /1,2/ it became clear that while a wide variety of source term codes are in use in Europe, intercomparison of their predictions is rendered difficult by the different environments in which they run, meaning different computers, different operating systems, different input and output formats etc. The codes and modules nevertheless represent the state of the art in source term predictions, and

much could be learned from easier intercomparison. Furthermore, considerable effort is going into the development of source term modelling, but by different teams for different codes, leading both to some duplication and to difficulties in transferring improvements from one code to another. A third element in this picture is the CEC's own contribution to source term model development and validation through its SCAs and work in-house. The resulting developments, although worthwhile, have tended not to be used outside the team which originated them, partly because of the effort needed to transfer the models to a different code. The solution to all these problems proposed by the Commission was to develop a unique framework allowing the easy integration of new modules, and to urge European model developers to couple the best of existing codes or modules into it, and then make any further model improvements only in the context of the framework. In view of the traditional attachment of organisations and particularly developers to their own products this proposal might have seemed utopian, but a combination of funding restrictions across the entire nuclear scene and continued interest in severe accidents resulted in the idea of a code framework being welcomed, and in 1989 the JRC proposed a general architecture to a group of European experts, together with a name, ESTER. The architecture is presented in Section 2. Here we just emphasise that it is intended to eliminate direct communication between the various modules, and that systems with similar architecture are widely used in real-time control systems and other non-nuclear applications. The group approved both the name and the architecture, and stressed the importance of developing the framework with the utmost attention to QA (quality assurance). Thus encouraged the JRC launched a call for tender for an SCA to develop the ESTER framework. The contracts subsequently signed by CISI Ingenerie (principal developer and manager) and by IKE Stuttgart (developer) undertook to develop the framework, including two trial modules, by the end of 1991, and included a tight specification setting out the tasks to be achieved and the timetable. The ESTER development project was thus launched at the end of 1989.

## **2. What is ESTER?**

ESTER is simultaneously a framework, a set of tools and services, a group of coupled modules, a controller and a user interface, and a series of documents, all governed by QA procedures. ESTER is firstly a framework with a clear architecture, as shown in Fig.1 Probably the main obstacle to coupling together existing modules or codes is the difficulty in transmitting data between them through the mechanisms of FORTRAN such as argument lists or COMMON blocks. Experience shows that there is a strong risk that variables will be used before they have been defined, or that data will be "overwritten" i.e. accidentally replaced with other data by one of the modules of the system. Another difficulty with the traditional approach is encountered when due to a modification one routine needs to access certain data calculated in another routine; numerous other routines need to be modified in consequence just to transmit the required data. The architecture of ESTER is designed to overcome these problems by restricting communication between modules, structuring the data and controlling access to the data. Various modules are assumed to be available which can calculate aspects of a severe accident or an in-pile experiment e.g. fluid flow through the core, or clad

relocation and oxidation, so that a complete calculation can be performed by invoking them in sequence, perhaps several times. In an initial phase input data are prepared and stored on the central database by the controller. The controller then invokes the modules as required, adjusting the overall timestep to achieve stability. Each module naturally has an interface to the controller, to enable it to receive the message to begin work, and to pass back the message that work is complete and/or error diagnostics. Modules require data, which they obtain from the database via another interface. Results from the calculations of the module are returned to the database through the same interface. When required the controller can use the contents of the database to produce graphics, printout or messages to the user informing him of the progress of the calculation. Notice that for the introduction of a new module one need only supply two interfaces, and make some adjustments to the logic of the controller.

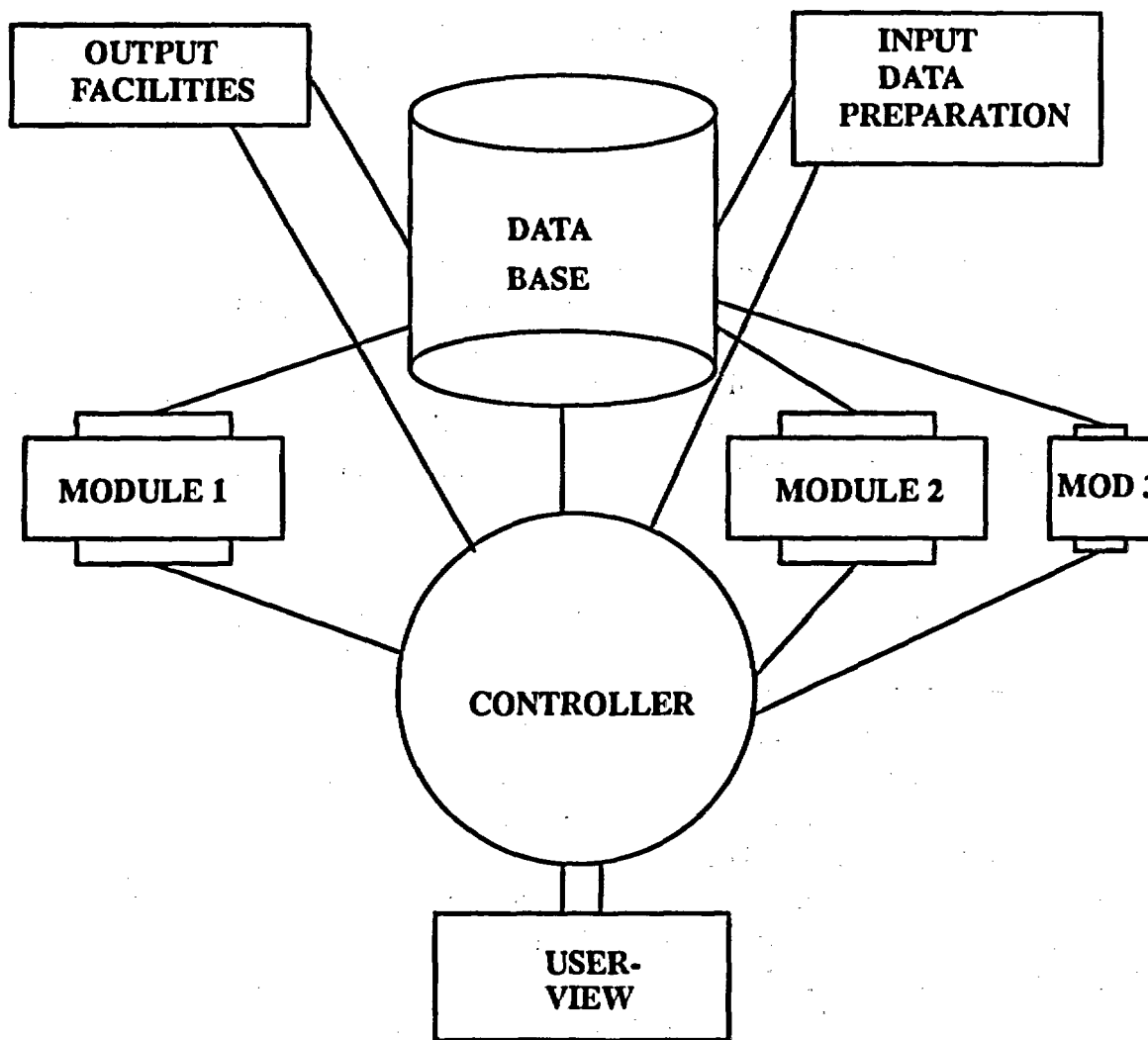


Fig. 1 - Structure of ESTER

ESTER is thus a framework. It is also a set of tools and services. These include graphics, menu management for the user interface, a data checker, systems for adding to and modifying the database etc. Section 5 contains a brief survey of the tools and services. From a third, practical point of view ESTER is primarily a set of calculational capabilities, contained in the modules. The philosophy of ESTER in this regard is that existing modules represent the state of the art, but that communication between them is often too poor (or even non-existent) to represent the physical coupling of phenomena and events which characterise a severe accident. ESTER is designed to "mix and match" existing modules so as to obtain previously unavailable calculational abilities e.g. circuit thermal-hydraulics coupled with fission product chemistry. The modules are under continual development in many national laboratories, and the results can be used to improve ESTER at low additional cost. Only as a last resort is it intended to develop new modules for ESTER from scratch. Fourthly, the user of ESTER sees not the individual modules but the user interface and through it the controller plus any on-line graphics, error messages, and other outputs channeled through the controller to the user interface. The interface includes facilities for preparing input data and guiding the course of the calculation. Hence the addition of a new module does not change the "look and feel" of ESTER, and no retraining is needed to use the system in its new and extended form.

Lastly ESTER is a set of documents which specifies the design choices, the quality assurance system, the potentialities of the tools and services, the user interface and the interfaces to modules. Also in preparation is a series of documents which will explain to code developers how to proceed when integrating an existing module into ESTER or writing a new module so that it can be integrated immediately into ESTER. There will also of course be a user manual, listings etc. for the complete system. The sections which follow look at some key ESTER documents as a way to illustrate the path taken by the development and to give a stronger feel for the scope of ESTER.

### **3. ESTER Specification**

A first specification of ESTER appeared in the contract, and it has been amplified and extended in successive iterations of the Specification Report. Key choices, apart from that of the architecture described above, were that where possible the same models should be used to describe the same phenomena wherever they might occur e.g. aerosol deposition in the RCS or the containment, and that modules should be incorporated from different sources, and might be in different languages. In practice all source term codes and modules of significance are written in FORTRAN77, and it was decided to use this language for ESTER and its tools also, because of its portability and ubiquity, unless there were special reasons to use another language e.g. in menu management. For the same reasons that Fortran was chosen as the programming language the operating system was chosen to be UNIX. It was required that ESTER should be proven to be portable across a wide range of machines with minimal effort, and provisions for parallel processing and networking should be included from the outset. Attention was drawn in the specifications to the importance of the database structure, and to the development and implementation of a Quality Plan (see next section). The specification report

also sets out the development and testing plan, which is given in Section 10 of this paper. In a nutshell the plan was that a preliminary version should be delivered to the JRC, which after optimisation

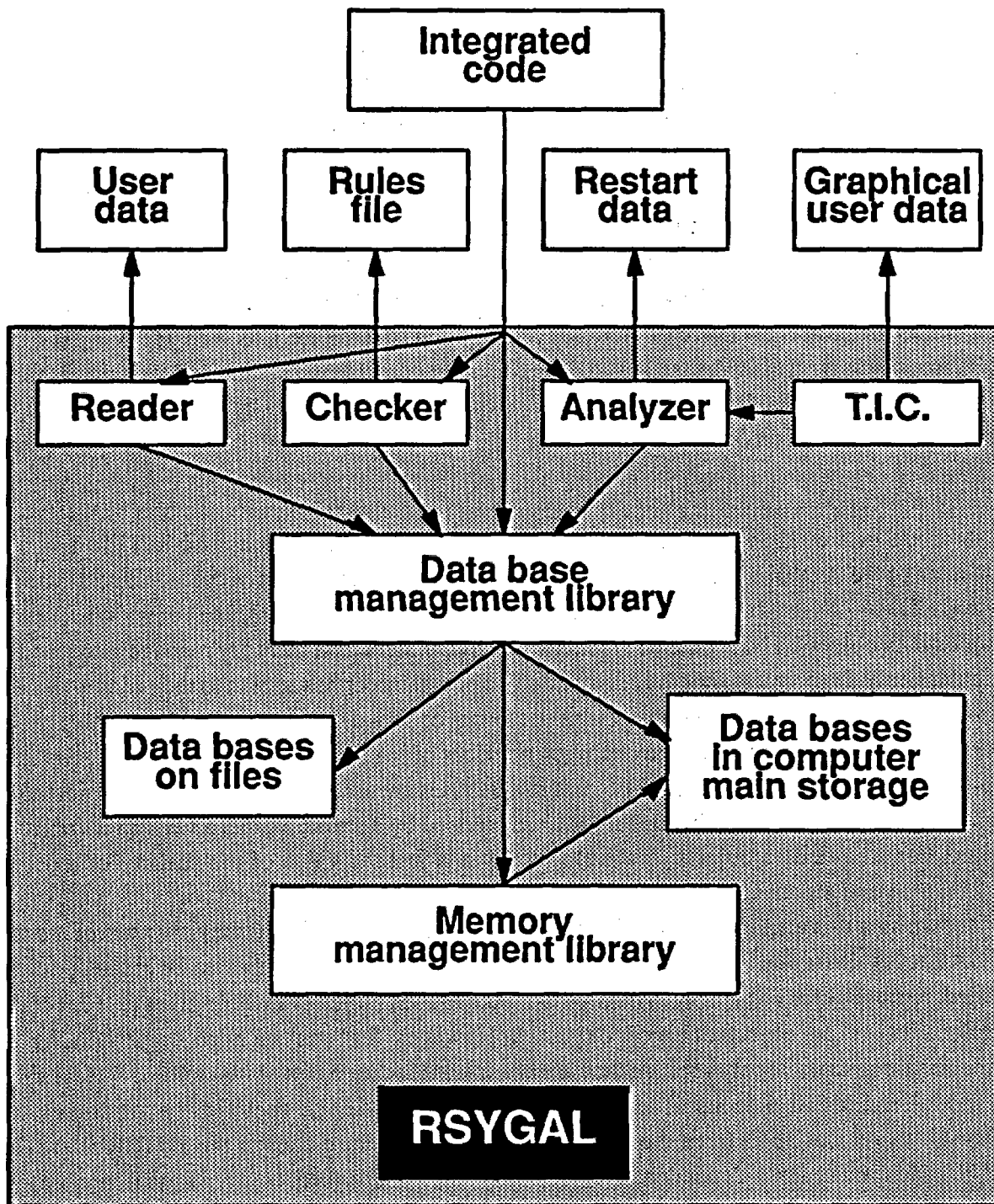


Fig. 2 - Functional view of ESTER

would form the basis of the final version to be delivered together with documentation at the end of the CISI-IKE contract.

A different view of the architecture of ESTER is shown in Fig.2, which omits the user interface, controller and modules to place more emphasis on the tools and database. The database is chosen for efficiency and portability reasons to reside not on disk as in the RSYST system of IKE/3/ but in the memory of the principal machine running ESTER. This choice has some consequences for parallelisation, as will be seen later. The database is created and manipulated by a set of tools and is provided with input and output services, tools and services together having the general name of RSYGAL, and developed by CISI from the smaller SIGAL set used e.g. in early versions of the CEA core degradation code ICARE-2. When running ESTER the user chooses the particular configuration desired (i.e. choice of modules , integration scheme etc.), as well as the input files to read in, from menus on his workstation. All the checking operations, reading and writing to the data base and storage on disk of restart files are then performed automatically by the controller, using the tools described in Section 5.

The structure of the database is obviously a key question for the success of ESTER The basic mechanism of the database is quite simple: RSYGAL takes a large section of the machine memory as a Fortran COMMON, and then divides it into segments (continuous areas), each of which contains a "complex data object". The segments are identified by pointers, and memory management modules manipulate only the pointers, not the segments. The programmer has access to the pointer value via the variable name. Complex data objects are databases or sub-databases and tables. Tables may be vectors of reals, integers or names/text strings, matrices of reals or integers or "couples", which are name-addressed reals or integers. All objects in databases are associated with semantic "attributes" (single-valued quantities). Each attribute is characterised by a name, a type, a version number, and its value. For simple data objects (scalars) this value is just the value of the scalar. For attributes which represent complex data objects the value is the pointer to the segment containing the object. Fig.3 shows how this arrangement can be used to produce a hierarchical (tree) structure of the data. RSYGAL tools allow one to create, delete and copy databases. Tables can also be created, deleted, modified, retrieved etc. The ability to manipulate databases or tables as a whole gives ESTER certain characteristics of an object-oriented database. However features such as encapsulation and inheritance are absent , largely because they are not present in the design philosophy of typical source term modules. Section 6 looks at the question of database design specifically for source term problems. Notice that apart from the particular database structure chosen the ESTER framework could be used for any time-dependent problems solved by interlinked computational modules. For example, RSYGAL-based code developments are in progress in France and in Germany in areas as diverse as forest fires and climate control for large buildings.

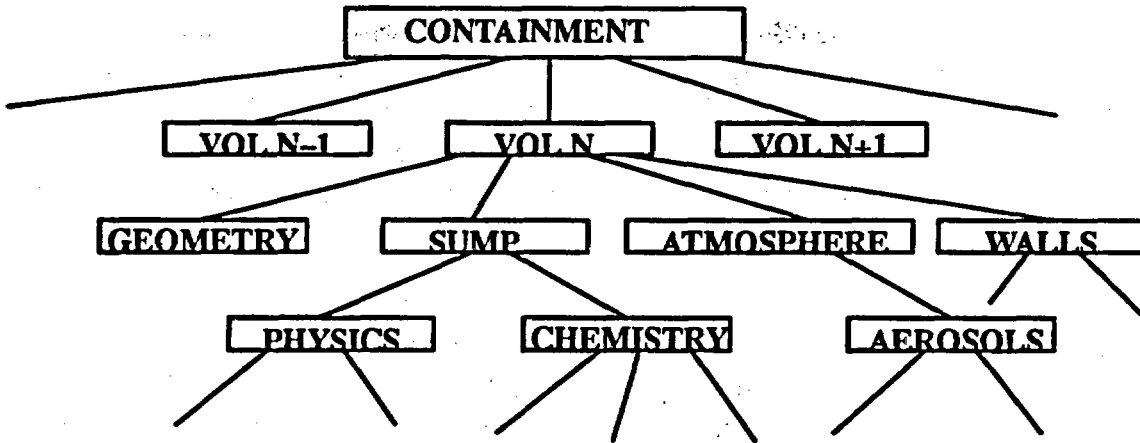


Fig. 3 - Volume-oriented data structure

Other major components of ESTER are the user interface and the driver. The user interface offers the user a succession of menus whereby he can (a) select the combination of codes/modules he wishes to use (b) choose to build up or modify data, run the job, or postprocess results, and (c) (depending on the choice made): construct or edit an input file; specify run parameters or select the file to be postprocessed and the tools to apply. The driver is responsible for memory initialisation, data reading and checking, sequential calling of the modules, management of the overall timestep, saving of databases for restarts or postprocessing, and the production of job-dependent printouts. A general technique for the determination of overall timesteps is included in ESTER, using whatever integration technique is provided within each module, an explicit time integration between modules, and a quadratic scheme for error control which has been applied with success in RSYST. More sophisticated overall timestep control may be implemented later. As well as the components already mentioned ESTER is accompanied by maintenance tools to allow the upkeep of libraries of module or data versions, and of a database recording the relationships between codes, modules, versions and the files which actually contain the libraries. The tools will be able to identify all the codes, files and directories affected by the modification of a given module. Note that the specifications were not fully defined at the outset. ESTER to some extent breaks new ground, and its specification is therefore a continuous learning process for all parties. Section 8 describes some of the changes made since the first draft specification in late 1989.

#### 4. The Quality Plan

One requirement of the specification was that the work should follow an approved quality plan, to be drawn up by CISI. The latest version was produced in November 1990. It begins by stating the contributions which each organisation will make to the development task, including the JRC and CEA (which contributes 40% of the costs of CISI). The Plan lists the staff, the codes and other tools they will employ, and the hardware upon which they will run. In essence CISI develops the RSYGAL tools and the UNIX operating environment, while IKE is responsible for developing

integration techniques, integrating ICARE and FPRATE, defining a common database, and developing time integration techniques. Each party is responsible for checking the work produced by the other, and for testing the portability of software by running it on their own machines under its own operating system. The JRC (with CEA) is responsible for the overall supervision of the development work, for acceptance of reports and software, and for testing portability on their own machines. The JRC may also execute a QA audit if so desired.

The work to be done is divided into a number of topics or "actions", and then each action is further split into a design phase, a development phase, and a testing phase. There is an acceptance procedure for each phase of each action, and a procedure to deal with any nonconformities. Report titles, layouts and groupings (for contractual purposes) are specified, as are test procedures for the contractors. Such tests include elementary tests (the routine must perform its function on a series of test cases); global tests (ditto, in the context of an overall code, as if it was in the hands of a final user); non-regression tests (a global test to check that performance is not degraded after a modification), and transfer tests (to be sure that the routine works on a new machine). The contractors routinely exchange documents and routines by electronic mail, and make use of standard forms for signalling errors and logging corrections. There is also the question of QA for the data used by ESTER modules, such as material properties and thermodynamic data. The quality of such data is the responsibility of their originators but also of the JRC, which will remain responsible for choosing which data to incorporate in ESTER. The SCAs of recent years reviewing and extending databases, particularly for chemical species, have been of great assistance here. In summary QA requires considerable time and care but is recognised by all concerned as essential if ESTER is to be reliable and well-qualified.

## **5. ESTER Tools and Services**

ESTER is provided with RSYGAL tools for memory management and data management, with more general tools like the reader, analyzer and checker, and with services such as a graphics package, a menu management tool, and a user interface. These go to make up the ESTER "environment" within which all further development will take place. The tools for memory management and data management have been reviewed briefly in Section 2. Here we examine the data reader, checker and analyzer, referring to Fig. 2, before going on to look at the services. The user interface and controller give the signal to read input data, which is done using the READER. The data reader is designed to read in the data of any module included in ESTER. The data are divided into blocks indicated by keywords; the reader recognises the keywords and constructs the appropriate databases to store the input data in the central memory. It also generates standard error messages if syntax errors are discovered in the data. The data CHECKER is a small expert system which checks the conformity of the input data against rules specified by the user and stored in a separate rule file. The rules may concern the presence of obligatory or optional keywords, the use of the correct data type, the sizes of arrays, that values lie within specified ranges, and that a keyword introducing a particular set of data

is followed by those data. The CHECKER thus replaces the long series of error traps to be found in the input routines of many codes. The ANALYZER is a restricted language interpreter which receives and executes user instructions to operate on the database e.g. extract information for post-processing, or add to or modify the database e.g. in preparation for a restart. The ANALYZER can also perform more complex data checks than the CHECKER. The database may produce graphical output using the graphics package, referred to in Fig.2 as TIC. Modules (not shown) accessing or writing to the database use a set of tools called the database management library, while at system level the computer memory is handled by the memory management library.

The tools described above are all written in Fortran and are fully portable. Portability considerations become more significant when one turns to the services provided with ESTER, particularly the graphics system and the menu management /user interface tools. This situation is not the fault of the ESTER developers; it merely reflects the current absence of standardisation in the area of graphics and on-screen displays. The more powerful graphics systems are either not portable or are discouragingly expensive or both, and for ESTER the choice was made to develop a series of graphics options based on a small number of library routines of primitive operations. There are three libraries: GKS, X11 and postscript. It is a reasonable assumption that most laboratories have access to at least one of these standards. The design of the graphics package consists of a common "core" plus sets of interface modules specific to the graphics system selected. When porting to a new system or new hardware only the interface set needs to be modified. The facilities offered include the ability to plot (in colour) a series of vectors e.g. in the familiar x-y plots, a matrix (2-d plots, contour plots), FE or FD meshes, and results on such meshes (isolines). More graphics facilities may be added later, as time permits.

The menu management system is designed to operate under X-windows, now to be found on all UNIX workstations and also available on PCs. The user interface is intended to be displayed on a workstation or PC; it is designed to be as "friendly" as possible without spending too much development time on fancy displays, and will offer choices to the user through a sequence of menus handled by the menu management system. Run-time messages and graphics will be returned in separate windows on the same screen. This is in accord with the general trend in interfaces to large codes. ESTER is not intended to be run interactively, but there is nothing in the overall architecture to prevent this way of working. It is more a question of how the individual physics and chemistry modules were designed (usually for batch operation), and the rather long running time of certain source term modules on current computers.

## 6. Data Structure

The importance of the data structure for the success of ESTER has been stressed earlier. The choice of database design essentially depends on the codes (modules) which will be incorporated. The preliminary version of ESTER includes the CEA core degradation code ICARE-2 v2 /4/ and the fission product release module FPRATE from the IKE core degradation system KESS/5/. ICARE

and KESS have quite different data structures, although both discretise the system into volumes. In ICARE all the data for a given volume are stored together, while KESS stores variables of like kind together e.g. all the pressures are stored in a single array. There are many other differences in data structure. ICARE being larger than FPRATE and constructed using RSYGAL, it was decided to use the data structure of ICARE for the core region in ESTER (it is sufficiently general to handle reactor cores as well as bundles), and to write an interface for FPRATE which converts that module's data into the same form as those of ICARE. The interface collects data of like kind from all the volumes, and returns them to the volumes after they have been updated. The interfacing system has been tested during the integration of FPRATE from KESS. The data structure of ICARE is worth a word of explanation, since it illustrates some possibilities of the RSYGAL database organisation. Physical objects (rods etc.) are associated with databases of axial meshes, each of which may contain several components e.g. layers of cladding. The components in turn have their own sub-databases corresponding to the different physical models e.g. geometric data, material, material properties, internal heat source and connections to other components. Knowing the overall data structure it is a simple matter to obtain e.g. the mass of the oxide layer on the cladding of a particular rod within a particular mesh, by proceeding down the tree structure to find the required elements. The choice of a volume-oriented data-structure is in some sense natural in a severe accident code, firstly because much of the physical interest is in phenomena such as aerosol agglomeration or chemical equilibrium which tend to be calculated one cell at a time, and secondly because in the core region at least the geometry changes with time so that control volumes can appear and disappear as the calculation progresses.

While the choice of data structure appears clear for the core or bundle there is more difficulty over the circuit. The obvious choice for the thermal-hydraulics of the circuit would be a two-phase "system code" such as CATHARE or ATHLET. In meetings between the developers of these codes, the JRC and the ESTER contractors some rather uncomfortable facts emerged however. Firstly, both codes are much larger than all the remaining possible component modules of ESTER put together. The data structure of the system thermal-hydraulics code would thus tend to dominate ESTER as a whole. Secondly, although they both chose finite volume treatments of the circuit CATHARE and ATHLET thereafter made such different choices and so many of them that adopting a common data structure would require re-writing one or both codes. This would be far too demanding a task, especially since thermal-hydraulics is not the main focus of ESTER. Thirdly, the specification and discretisation of components such as vessels and pumps in the two codes is so different that it is difficult to imagine even a common input data format and reader. Both codes are thus sufficiently large and sufficiently set in their ways that their adaptation to a newcomer like ESTER would require a great deal of work. Of course if a joint European system code is developed in the future it could be written to ESTER standards and conventions from the outset and the problem would disappear. For the calculation of Phebus-FP at least most tests require only single-phase fluid dynamics in the circuit. This can be calculated quite adequately by ICARE. The DEIMOS code developed for the

JRC by Matec/6/ is an alternative. Section 10 returns to the question of circuit thermal-hydraulics in the context of future development for ESTER.

Also associated with the circuit are fission product and vapour physics and chemistry. A discretisation into volumes as in the bundle is natural in the circuit, and matches the data structure of codes such as VICTORIA. A volume-oriented data structure as in ICARE thus seems suitable for the circuit FP transport as well as the thermal-hydraulics.

For the containment the natural discretisation is into interconnected subcompartments (unless a fully three-dimensional treatment is envisaged), as a discussion between experts on CONTAIN and JERICHO emphasised. Each volume may then have sub-databases describing the walls, internal structures, sump, and atmosphere. This last will have its own database including thermal-hydraulic variables plus an aerosols database and so on. The details will become clearer as code integration proceeds, but the overall philosophy is clear. The description for all systems (core, circuit, containment) is to be in terms of volumes, with a well-defined and natural tree structure being imposed on the data describing each volume. Database definitions are now available for the core/bundle, circuit and containment (including iodine chemistry), and are under development for core-concrete interaction.

## 7. Code Integration

An essential element in the ESTER documentation is the Integration Report. This not only describes how ICARE and FPRATE were integrated into ESTER but provides guidelines as to how to integrate existing modules, and how to write new modules so as to facilitate integration. For existing modules or codes the procedure is well-defined. The user manual or other input description should first be used to write the rule file for the data checker. The code should then be split into three parts: preparation (reading in user data and/or a restart file, initialisation, opening scratch and output files etc.), the calculation itself, and post-processing, including output printing and graphics. The preprocessing part should then be replaced by calls to the data reader and data checker. Interfaces should be provided between the code and the database and controller, and all post-processing operations should be left to the controller, calling on ESTER services as required.

Codes brought into ESTER in this way are not integrated on a fine scale. For instance, a code may contain a routine for calculating certain material properties which are also required by another ESTER module. At this level of integration that module could obtain the desired properties only by executing the entire code. If it is desired to break down a code or module into smaller modules individual interface routines must be created for them and the controller must be modified to access the module whenever its services are required, whether by the original code or by another module. The smaller modules thus become "functional modules", fulfilling a specified function for many other modules. How finely one should modularise in ESTER must be decided pragmatically, as a balance between redundancy of coding and run-time efficiency. To avoid confusion certain

conventions must be adhered to; the subroutine names must start with two significant letters characterising the module, as should the common blocks. Because the type of a Fortran function is determined by its first letter this letter is fixed, and the second and third letters of the function name then characterise the module. ESTER tools have been developed which allow the necessary name changes to be made automatically.

## **8. Review of Specifications**

At least four meetings per year have been arranged with the developers, and during the discussions on designing the data structure meetings were more frequent still. Such meetings reviewed the progress made but also looked again at the feasibility or advisability of some of the choices made in earlier drafts of the specification report. One example concerns "external" software. ESTER must rely to some extent on software not created by the developers; compilers for instance are assumed to be available on the users' systems. Graphics and menu management software is more problematical. To favour the portability and acceptance of ESTER cheaper and more readily available alternatives to e.g. MOTIF such as X-windows and GKS were selected, even if these are not the most advanced available. There was also considerable discussion on data structure before the philosophy outlined in the previous section was adopted. The most knotty problem of specification however proved to be that caused by the reference in the original specification to networking and parallel processing.

One paradigm of a general computing environment which is becoming more and more popular is that of distributed processing. In distributed processing the various modules (or processes) involved in the computation of a particular problem run on more than one machine, which may be of different types and at more than one location. Data needed during the computations may be obtained from still other machines, or possibly from large databases maintained by an outside organisation. With such an arrangement the processes could run in parallel most of the time, only being synchronised and exchanging messages and data at certain time points. The machines running the more computationally intensive processes could of course themselves be highly parallel internally. The AECL system of INTARES// is designed to run on a distributed processing system of the sort described, motivated by the consideration that if to solve a problem one needs codes X, Y and Z then the right versions of the codes to use are those resident in the home systems of the organisations which develop and maintain them. The INTARES approach is certainly more futuristic than that of ESTER, but has certain disadvantages in the current state of technology. Communication over networks can be slow and unreliable, strict standards for data and message interchange must be imposed on all the codes and machines in the distributed system, and there is a general difficulty in coordinating all the processes so as to ensure both numerical stability and efficiency. The choice made in ESTER of a central database in the memory of a single computer restricts its immediate adaptation to distributed systems to those with a shared memory architecture. If the memory is distributed, parts of the central database will need to be copied to the processes and machines which need them, and the updated versions copied back when the process is complete.

In fact work has started at IKE, Stuttgart, to do just this through remote procedure calls. The principal aim of this is not to parallelise ESTER but to enable certain modules or functions to be performed on the computers for which they are best suited. A certain module of ESTER might dominate the cpu usage so it may be advantageous to put this module on a special architecture computer. For instance modules from the fission product and aerosol transport code VICTORIA are notoriously slow running. Significant savings in cpu time have been achieved by putting these modules on a distributed memory parallel computer /8/ and this will be feasible with these new features of ESTER. Another task that is suitable for specialized computers is high speed graphics. A recent demonstration had ESTER bundle modules running on a CRAY while the graphical analysis was performed on a Silicon Graphics machine. The philosophy of remote procedure calls can be extended without difficulty to truly parallel computation. The constraints on parallelisation are not due to software but rather to the needs of the various modules to exchange updated information throughout the course of the calculation.

## 9. New Contributions to ESTER

The shared-cost action programme for 1989 included contracts for the development of ESTER, as described above. It also included the CEC's participation in the development of VICTORIA, a code from the USNRC which was originally part of MELPROG. VICTORIA calculates fission product release from the fuel and control rods, and its transport in dry conditions within the circuit as aerosols or vapours. The code models the aerosol transport and deposition mechanisms to be found e.g. in RAFT, but places much more emphasis on the chemistry. Two hundred chemical species or more can be considered in the equilibrium calculations, and the aerosols are treated as multicomponent i.e. aerosols of different chemical composition may have different size distributions. VICTORIA development for the CEC is undertaken by the UKAEA, and is part of a wider programme of development by laboratories in the US and Canada.

All these developments are leading to a much improved version of the code which will be incorporated in ESTER. An intermediate version of VICTORIA has already been coupled in, thus conferring on ESTER the ability to calculate release from the bundle, thermal-hydraulics in the bundle and circuit, and fission product transport and chemistry in the circuit all in the one code system, a capability not previously available in Europe.

Although ICARE is primarily considered as being a bundle code, it is perfectly adequate for calculating the thermalhydraulics of the primary circuit provided that there are no loops or branches. In fact it is capable of modelling the thermalhydraulics of all the proposed Phebus circuits and all the Falcon tests as well as a good number of reactor sequences. As such it is a perfect partner for VICTORIA whose use is at present restricted by the drudgery involved in obtaining thermalhydraulic boundary conditions from another code and arranging them in a form suitable for VICTORIA. Feedback from the aerosol and fission product vapours on the thermalhydraulics is small so an explicit coupling method was used. The ESTER coupling approach makes data transfer

easy and the programming involved writing interface routines; not changing ICARE or VICTORIA modules.

VICTORIA is a modular code and, as a first approach, only the modules concerned with fission product and aerosol transport were integrated into ESTER. Thus phenomena such as aerosol agglomeration and deposition and chemical equilibria are calculated but fission product release is not. There are three reasons for this. Firstly ICARE already has a number of fission product release models, based on CORSOR, secondly VICTORIA's fuel modelling is currently undergoing rapid development so it may be wise to see where these changes are leading before embarking on interface writing and, thirdly, coupling the fuel model is more difficult. The difficulties stem from the changing geometry of the fuel during degradation which may be described differently in VICTORIA and ICARE.

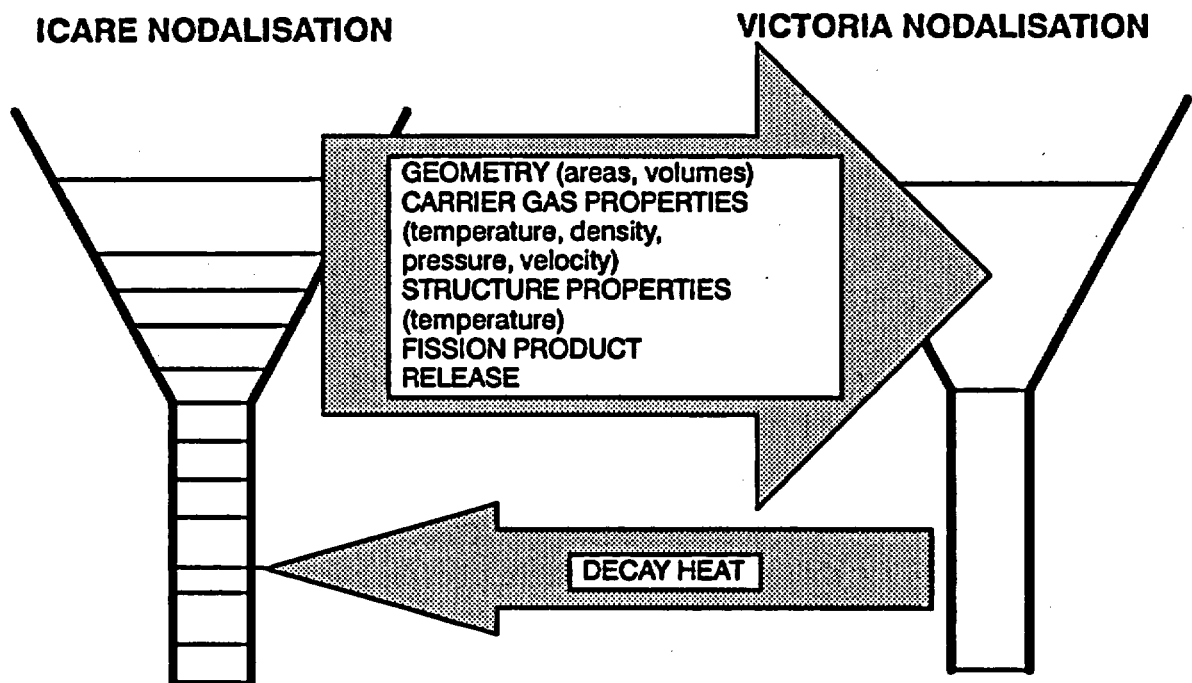


Fig. 4 - ICARE-VICTORIA information transfer

The figure above shows the information flow between ICARE and VICTORIA. ICARE is usually noded much more finely than VICTORIA. A typical Phebus FPT-0 calculation uses about 100 fluid cells for ICARE and about 15 for VICTORIA. Even so about 99% of the cpu time is taken up with VICTORIA.

Adaptation and improvement of codes and modules for ESTER was included in the 1990 and 1991 SCA programmes. Two successful tenderers were IKE, who are adapting significant parts of the KESS core degradation package to ESTER (as an alternative to ICARE), and the UKAEA, who are further developing the modelling of vapour–aerosol interaction using results from the FALCON and ACE experimental programmes, and incorporating the models in VICTORIA and in the containment iodine chemistry code INSPECT. The improved INSPECT has now been brought into the ESTER framework. A third contractor now at work on adapting codes to ESTER

is CEA, which has modernised and converted to ESTER standards the containment thermal–hydraulics code JERICHO, the code AEROSOLS–B2 which calculates aerosol physics in the containment, and the iodine chemistry code IODE. IODE is simpler and more pragmatic in spirit than INSPECT, so there is no duplication in having them both in ESTER. Indeed, ESTER should make it easier to compare the predictions of the two approaches for specific problems such as Phebus tests. CEA is also adapting to ESTER the core–concrete interaction code WECHSL, in collaboration with KfK.

An interesting contribution provided under SCA contract has come from Vincotte, the Belgian firm of consultants. Vincotte has been concerned with the quality of the modules included in ESTER. The concept of the quality of a physical module is somewhat hard to pin down, but a number of tools are now available to enable an expert assessor (who should preferably not be from the development team) to judge some measurable aspects of quality. Firstly, there is a static Fortran checker by which each statement can be labelled for conformity with Fortran77 standards, for the presence of header information in each routine, for correspondence with the documentation etc. It has been applied to ICARE and to VICTORIA and should lead to improved coding and documentation. A flow charter is also available, useful for revealing unintended loops and other structural errors. A third tool executes the standard test cases supplied with a module and flags which parts of the code have been executed (and so "tested"). This tool can help design better test cases, since it indicates which logic statements are responsible for the path taken through the code in a particular run, with an indication of how nearly a particular test was satisfied. It is intended to apply all these tools to each new module at the time of its integration into ESTER.

The SCA programme includes other model developments not tied to particular codes. The JRC in collaboration with the relevant contractors intends to integrate the most appropriate improvements into ESTER modules directly. These could include chemical data, chemical kinetics models, thermal resuspension models, and condensation and nucleation models.

Currently in progress is the integration of several more physical models into ESTER. For the bundle or core CISI (Aix–en–Provence) is coupling in CHIP, a module for two–phase flow including up to two non–condensable gases. The heat transfer and changes in geometry are supplied to this module by ICARE or perhaps KESS. For the circuit AEA is introducing the pool scrubbing module BUSCA, some improvements to which are being made by University of Madrid. Concerning the containment,

in addition to JERICHO/AEROSOLS ESTER will soon contain the German codes FIPLOC and RALOC from GRS. These will extend ESTER's capacity to treat hydrogen stratification and burns, and provide alternative models for multicompartment thermal-hydraulics and aerosol physics. The introduction of INSPECT as a mechanistic alternative to IODE and of WECHSL for core-concrete interaction has already been mentioned.

## **10. ESTER Development and Validation Plans**

The ESTER development plan in the short term is as follows. The contractors delivered to the JRC the first preliminary version ESTER-p1 at the beginning of 1992. This code consisted of the framework, tools and services, controller, and integrated versions of the modules ICARE-2v2 and FPRATE. The CEA containment codes JERICHO, AEROSOLS-B2 and IODE have been converted to run with RSYGAL and have been able to reproduce the results of their stand-alone versions. In fact comparisons of the coupling through ESTER compared to the old looser coupling showed significant advantages in the ESTER method. Similarly an RSYGAL KESS has been shown to give the same results as the old RSYST version.

The iodine chemistry model INSPECT and the aerosols/chemistry code VICTORIA have been inserted recently. We expect that ESTER-VICTORIA, because it is tightly coupled to the thermalhydraulics, will be easier to run than the old stand-alone version and, in some laboratories at least, may become the standard version. At this stage once the necessary drivers have been developed and tested it should be possible to calculate an entire Phebus test, from bundle to containment and ESTER will be the only European code able to do so. The JRC may then insert models for chemical kinetics and for nucleation developed under SCA, and possibly a special-purpose model for the difficult zone just above the bundle in Phebus.

Towards the end of 1992 the modules integrated in the last shared cost action should become available including some KESS modules, RALOC, FIPLOC, WECHSL and BUSCA. The careful selection of suitable codes or modules for incorporation in ESTER is essential for the quality of the system as a whole; it must take account of the standard of coding and documentation (where the QA tools developed by Vincotte are proving helpful), the effort being put into continued maintenance and development, and the validation status of the code. Such selection will continue in the future. An additional "Darwinian" factor tending to improve quality is that if more than one module with similar functions is included in ESTER it becomes simple for users to compare them and see which performs best on given problems. Unreliable, poorly documented or over-simplistic modules will tend to be rejected by users and so become "extinct", i.e. no longer supported in future versions of ESTER.

The JRC is committed to establishing ESTER as the natural framework for code integration and for future code development in Europe, and will devote effort on its own behalf to the maintenance of ESTER, eliminating defects and extending facilities. A small maintenance team is being set up

which will have the responsibilities of ensuring liaison with the Users' Club (see next section), of maintaining standardised updates and versions of ESTER, of archiving and updating the documentation, and most importantly, of creating the driver routines and other software which fully incorporate new modules in the ESTER structure. One should not underestimate the problems both of numerics and of data transfer and control associated with coupling together a variety of modules from many different sources, even in a purpose-designed structure like ESTER, but it is hoped that adequate manpower has been assigned to this task. Another important maintenance task is to test ESTER after each module integration or other major modification using a battery of test cases. In this way one can ensure good quality control of updates.

ESTER validation is clearly essential; the individual modules are assumed to be validated by their developers or in international programmes such as LACE or ACE and Phebus, but the possibility of unforeseen interaction between them cannot be ruled out, and ESTER must be put through a series of qualification tests whenever a new module is integrated. This kind of work too demands a commitment from the JRC. A third type of work which needs JRC effort is the incorporation of improvements to individual modules in the adapted versions which will be present in ESTER. It is hoped that in the long term developers will naturally tend to prefer the ESTER version for further improvements because of the additional facilities to which it has access, and hence that this problem of updating will not grow unmanageable as the number of modules incorporated continues to increase. Validation of ESTER against Phebus tests is naturally included in the JRC source term R&D plan for 1992-94. Validation against FALCON tests and against certain CSNI ISP exercises is also planned. There is a possibility that the further development and application of ESTER by the CEC will not have to rely entirely on the JRC's own resources once the SCA programme is terminated. A new programme of "reinforced concerted actions" (RCAs) has now been launched by the CEC with the object of favouring collaboration in severe accident studies. ESTER is highly suitable as a tool for facilitating collaboration on severe accident code development, and hence some support from RCA partners appears possible.

The overall ESTER development plan is as follows. The first preliminary version ESTER-p1 has been distributed to a small number of users, and is being tested largely for portability by them and at the JRC. The maintenance team is being set up and the User Club established. By the end of 1992 a number of new modules will have come in, and efforts in 1993 will be devoted to ensuring their full and properly qualified integration into ESTER (including user interfaces, graphics etc.), with accompanying documentation, supported by the compilation and execution of a battery of test cases. Some first validation against e.g. Phebus and Falcon results will be done. At the end of 1993 a second preliminary ESTER version, ESTER-p2, will be issued to the users, and their active participation in implementation, testing and validation will be solicited. 1994 will be a year of consolidation, in which the activities of maintenance, testing and validation will be in the foreground. Some optimisation of drivers and addition of new software features, e.g. graphics facilities, is expected. It will also be necessary to update the ESTER versions of modules

## Main ESTER Modules: Version p2

<u>Systems:</u>	<b>RSYGAL</b> <b>RPCs</b> <i>{GUI, better graphics, video}</i>
<u>Core/Bundle:</u>	<b>ICARE-2</b> <b>KESS modules incl. FPRATE</b> <b>CHIP</b> <i>{ORIGEN, FUTURE, FASTGRASS, Control release, quench, lower head relocation, penetration}</i>
<u>Circuit:</u>	<b>ICARE-2</b> <b>CHIP</b> <b>BUSCA</b> <b>VICTORIA</b> <i>{ATHLET, LOCA =&gt; severe accident}</i>
<u>Containment:</u>	<b>JERICH0, AEROSOLS</b> <b>RALOC, FIPLOC</b> <b>IODE, INSPECT</b> <b>WECHSL</b> <i>{DCH, MCCI aerosol, models for new cont. designs}</i>

**Fig. 5 – Configuration of ESTER by end 1993 (P2 version)**

which have been improved by their originators. Towards the end of 1994 the first official version of ESTER, ESTER-v1, will be released to all Users.

Fig. 5 shows the main modules included for the various components of the Phebus experiment or reactor system. At the same time, it is planned to present a strategic plan for further ESTER development for user comments, which will be pursued in the years which follow. It is certain that by that time trends in software and hardware development will be clearer. New modules will have

become available, and interests in severe accident phenomenology and applications will have evolved. At this point it seems likely that as the Phebus programme matures ESTER will become more oriented to reactor problems. The ability to use directly the databases of geometrical and other specifications for real plants built up for other codes e.g. system codes, would be a real plus, since these often represent a considerable investment on the part of their compilers. The studies now in course concerning the feasibility of coupling ESTER to the thermal-hydraulics "systems code" ATHLET are considering this aspect, and clearly ESTER will need to be able to calculate two-phase flow in the reactor vessel and circuit no matter whether it is coupled to a systems code or some other strategy is adopted. ESTER should also become able to handle accident management operations, more engineered safety features, and possibly phenomena associated with new reactor designs or with reactors of older design which may be operating in Eastern Europe. Some indications for possible ESTER modules are included in Fig.5 in italics.

## 11. The Availability of ESTER

The Commission of the European Communities has the right to distribute ESTER within the EC. The JRC intends to make the system freely available on condition that recipients join a Users' Club. A first presentation of ESTER with demonstrations took place in May this year and was followed by a constitutive meeting of the Users' Club. Membership of the club carries with it an obligation to inform the JRC of any errors discovered and of any improvements made, and to report the results of any calculations which could help validate the system. In return members receive not only the system but also updates and corrections or extensions to the documentation. The JRC intends to hold periodic Users' Club meetings and to circulate an ESTER newsletter. Training in ESTER fundamentals and more advanced features is also planned.

Property rights to the individual modules of course remain vested in their developers, but a condition of acceptance for the incorporation of a module in ESTER is that it should be available for distribution by the CEC within ESTER to members of the Users' Club, and this condition applies even to VICTORIA, which was not developed in Europe. This arrangement has a certain advantage for the code developer, as well as for the CEC and for Europe at large. A module inserted in ESTER is likely to be tested on a wider range of problems and by a wider clientele than the same module standing alone. The developer will naturally have access to the resulting error reports and other feedback regarding his module. If these lead him to improve the module and so improve ESTER the virtuous circle will be complete. Although ESTER will be free in Europe, its use outside the EC will require a licensing agreement reflecting the effort which is being put into its development. Some preliminary enquiries about such agreements have already been received.

In conclusion, ESTER has good prospects of fulfilling the CEC's hopes of creating a framework which will foster collaboration and synergy between groups developing and validating codes and models in the source term area. If the present spirit of cooperation is maintained it should rapidly

grow into the natural environment for future development efforts, to the benefit of severe accident studies in Europe as a whole.

### **Acknowledgements**

Our thanks go to Joaquim Areia Capitaó for his assistance in preparing this paper for presentation.

### **References**

/1/ Markovina,A.,Fasoli-Stella,P., Mailliat,A. Analytical Assessment of the Capability of a Scaled-down In-pile Facility to Simulate PWR Phenomena under Severe Accident Conditions. AAR '89, 8th Annual Meeting, Reno, NV (USA).

/2/ Jones, A.V.,Bonanni,E.,Markovina,A. Principal Results of the "Phase B" Verification Studies in Support of the Phebus-FP Project. CSNI Workshop on Aerosol Behaviour and Thermal-hydraulics in the Containment. Fontenay-aux-Roses (F), November 1990.

/3/ Ruehle,R. RSYST as a Software Framework for a Unitary System for Computer-aided Aerospace Analysis and Design. (in German); Rechenzentrum der Universitaet Stuttgart und Lehrstuhl fuer Anwendungen der Informatik im Maschinenwesen (1988).

/4/ Chatelard,P.,Gonzalez,R.,Jacq,F.,Porracchia,A. ICARE: A Computer Code for Severe Fuel damage Analysis. General Description of the Second Version ICARE2. IAEA Technical Committee Workshop on Computer-aided Safety Analysis. Berlin, April 1989.

/5/ Hocke,K-D.,Bisanz,R.,Schmidt,F.,Unger,H. Fission Product Release and Transport Modeling in KESS-2. KfK 3800/3. 5th Int Mtg. on Thermal Nuclear Reactor Safety. Karlsruhe, Sept. 1984.

/6/ Biasi,L. DEIMOS - A Fast-Running Circuit Thermal-hydraulics Model. Private Communication (January 1991)

/7/ McDonald,B.H.,Wallace,D.J.,Hanna,B.N.,Dormuth,D.W. INTARES - A Code for Integrated Thermal-hydraulics and Aerosol Safety Analysis. CSN Workshop on Aerosol Behaviour and Thermal-hydraulics in the Containment. Fontenay-aux-Roses (F), November 1990.

/8/ Tautges T.J. Modelling Fission Product Chemistry and Aerosol Physics on a Distributed Memory Parallel Computer: the P-VIC code. EUR report 14387EN (1992)

/9/ Jones,A.V., Shepherd, I.M. ESTER - a European Source Term Evaluation System. The Phebus Fission Product Project (ed. W. Krischer & M.C. Rubenstein) (Elsevier, London) (1992)

/10/ Jones, A.V., Shepherd, I.M. ESTER- a New Approach in Source Term Code Development. Jahrestagung Kerntechnik '92, Karlsruhe, May 1992.

# MELCOR VERIFICATION, BENCHMARKING, AND APPLICATIONS EXPERIENCE AT BNL

Imtiaz K. Madni  
Brookhaven National Laboratory  
Department of Nuclear Energy  
Upton, New York 11973

## ABSTRACT

This paper presents a summary of MELCOR Verification, Benchmarking and Applications experience at Brookhaven National Laboratory (BNL), sponsored by the U.S. Nuclear Regulatory Commission (NRC). Under MELCOR verification over the past several years, all released versions of the code were installed on BNL's computer system, verification exercises were performed, and defect investigation reports were sent to SNL. Benchmarking calculations of integral severe fuel damage tests performed at BNL have helped to identify areas of modeling strengths and weaknesses in MELCOR; the most appropriate choices for input parameters; selection of axial nodalization for core cells and heat structures; and workarounds that extend the capabilities of MELCOR. These insights are explored in greater detail in the paper, with the help of selected results and comparisons. Full plant applications calculations at BNL have helped to evaluate the ability of MELCOR to successfully simulate various accident sequences and calculate source terms to the environment for both BWRs and PWRs. A summary of results, including timing of key events, thermal-hydraulic response, and environmental releases of fission products are presented for selected calculations, along with comparisons with Source Term Code Package (STCP) calculations of the same sequences. Differences in results are explained on the basis of modeling differences between the two codes. The results of a sensitivity calculation are also shown. The paper concludes by highlighting some insights on bottomline issues, and the contribution of the BNL program to MELCOR development, assessment, and the identification of user needs for optimum use of the code.

## 1. INTRODUCTION

MELCOR is a fully integrated computer code that models all phases of the progression of severe accidents in light water reactor nuclear power plants [1]. It is being developed for the NRC by Sandia National Laboratories (SNL). BNL has a program with the NRC called "MELCOR Verification, Benchmarking, and Applications." Its aim is to provide independent assessment of MELCOR as a severe accident/source term analysis tool. The scope of this program is to perform quality control verification

on all released versions of MELCOR, to benchmark MELCOR against more mechanistic codes and experimental data from severe fuel damage tests, and to evaluate the ability of MELCOR to simulate long-term severe accident transients in commercial LWRs, by applying the code to model both BWRs and PWRs. This paper presents a summary of MELCOR experience gained under this program at BNL, which includes:

1. MELCOR verification over the past several years during which all released versions of the code were installed on BNL's computer system, verification exercises were performed, and defect investigation reports were sent to SNL;
2. MELCOR analyses of integral severe fuel damage tests PBF SFD 1-1, SFD 1-4, FLHT-2, and FLHT-4, and comparisons with experimental data and other calculations;
3. fully integrated applications calculations with MELCOR to simulate dominant accident sequences in Peach Bottom (a General Electric BWR with Mark I containment), Oconee (a Babcock & Wilcox PWR with large dry containment), ZION (a Westinghouse PWR with large dry containment), and current efforts at developing an input model for Calvert Cliffs (a Combustion Engineering PWR);
4. limited sensitivity studies which explore the impact of varying user input modeling and timestep control parameters on the calculated results for integral tests and full plant calculations; and
5. support to the NRC-sponsored MELCOR Peer Review Committee.

Over the past few years, all released versions of MELCOR have been installed and maintained on BNL's VAX mainframe, the latest released version at BNL being version 1.8.1. While BNL's main emphasis has been on VAX, the IBM 3090 mainframe computer has also been used. As part of verification, BNL has submitted 36 defect investigation reports (DIRs) to SNL thus far. These have served to identify code errors and deficiencies, and have recommended improvements.

## 2. BENCHMARKING

In accordance with an FY1988 study on experimental data alternatives for benchmarking MELCOR [2], which identified in-vessel phenomenology as an area in MELCOR that needed to be assessed, benchmarking analyses with MELCOR have been carried out for the following integral severe fuel damage tests:

1. Power Burst Facility (PBF) Severe Fuel Damage (SFD) Test 1-1 [3],
2. PBF SFD Test 1-4 [4],

3. National Research Universal (NRU) Full-Length High Temperature 2 (FLHT-2) Test [5], and
4. NRU FLHT-4 Test [6].

A typical MELCOR nodalization for the test simulations is shown in Figure 1 [5]. There are 4 control volumes (inlet, fuel bundle, plenum, and environment) and 3 flow paths interconnecting them. The environment is a contrived volume and is assumed very large, allowing the system pressure to stay nominally constant, as in the experiments. The fuel bundle active length is nodalized into several axial segments and 1 radial ring. The shroud is nodalized axially to match the core cells and radially into several layers.

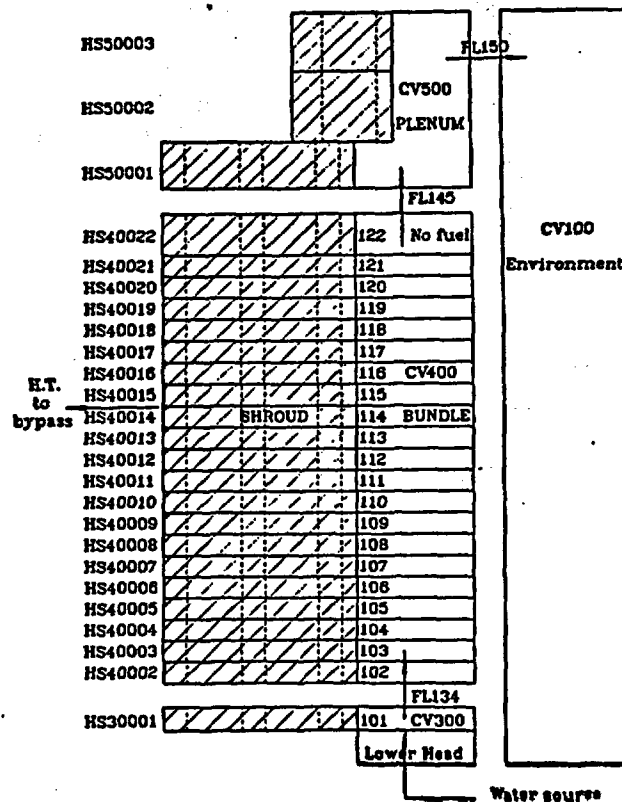


Figure 1. MELCOR Nodalization for FLHT-2 Test

The benchmarking calculations of integral severe fuel damage tests have helped to identify areas of modeling strengths and weaknesses in MELCOR (eg. oxidation and relocation of heat structures, two-sided clad oxidation, clad ballooning, fission product release, etc.); the most appropriate choices for input parameters (eg. candling heat transfer coefficient, radiation view factors, oxidation excursion temperature, holdup temperature for oxide shell, etc.); selection of axial nodalization for core cells and heat structures; and workarounds that extend the capabilities of MELCOR (eg. selection of a large environmental control volume to hold the test system pressure constant as in the experiment, replacing the bypass control volume by an external heat transfer coefficient to speed up calculations, etc.). These insights are explored in greater detail, with the help of selected results and comparisons from all four integral tests, as follows.

### Temperature Comparisons

Figure 2 [3] shows comparisons between measured clad temperatures at 0.5 m, and those calculated with MELCOR (1.7.1) and SCDAP for the PBF SFD1-1 test. Also included are the STCP calculated fuel average temperatures. For the first 2000 seconds, prior to thermocouple failure, MELCOR calculated temperatures lie within the uncertainty range of the measured values, and show slightly better agreement with data than SCDAP. Thereafter, MELCOR predictions continue to rise similar to SCDAP, but for  $t > 2500$  s, they drop slower than SCDAP calculations. STCP-calculated temperatures appear to underpredict the sharp temperature rise near thermocouple failure, and start dropping earlier than both SCDAP and MELCOR.

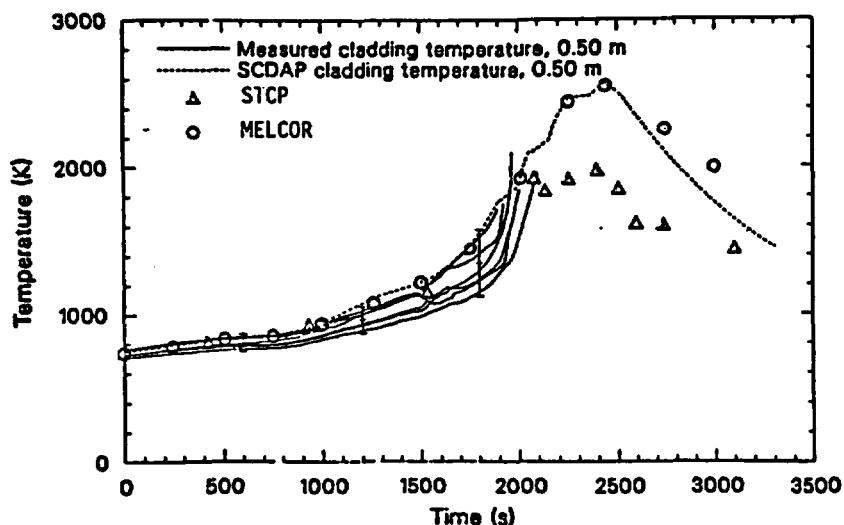


Figure 2. Comparison between measured and calculated clad temperatures, SFD1-1.

In Figure 3, for PBF SFD1-4, MELCOR calculated clad temperatures, while exhibiting the same trend, are higher than measured data and not as good as SCDAP/RELAP5 calculations. MELCOR predicts clad and fuel relocation to occur following the temperature peak, hence no calculated temperatures could be plotted thereafter. Figure 4 shows comparisons between measured and calculated shroud inner liner temperatures [4]. Thermocouples in both experiments could not survive beyond  $\approx 2000\text{K}$ .

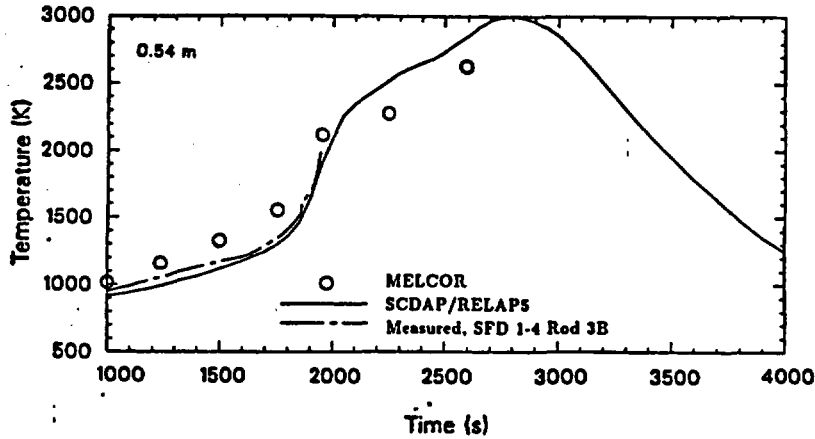


Figure 3. Comparison between measured and calculated clad temperatures, SFD1-4.

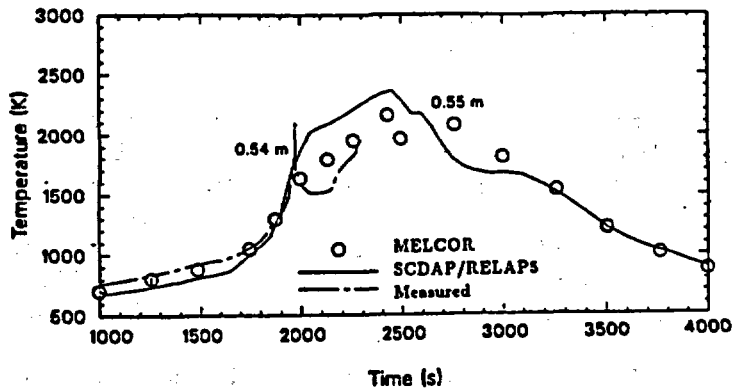


Figure 4. Comparisons between measured and calculated shroud inner liner temperatures.

Figure 5 shows a comparison between measured average cladding temperature and the calculated temperatures at a 2.3-m elevation for FLHT-2 [5]. The agreement between MELCOR and the test data appears to be very good in the heatup phase, prior to the onset of accelerated oxidation. However, both MELCOR and SCDAP appear to underpredict the sharp temperature rise due to accelerated Zircaloy oxidation. There is also a lag in the calculated temperature peak. The MELCOR-calculated cladding temperature shows better agreement, overall, with test data.

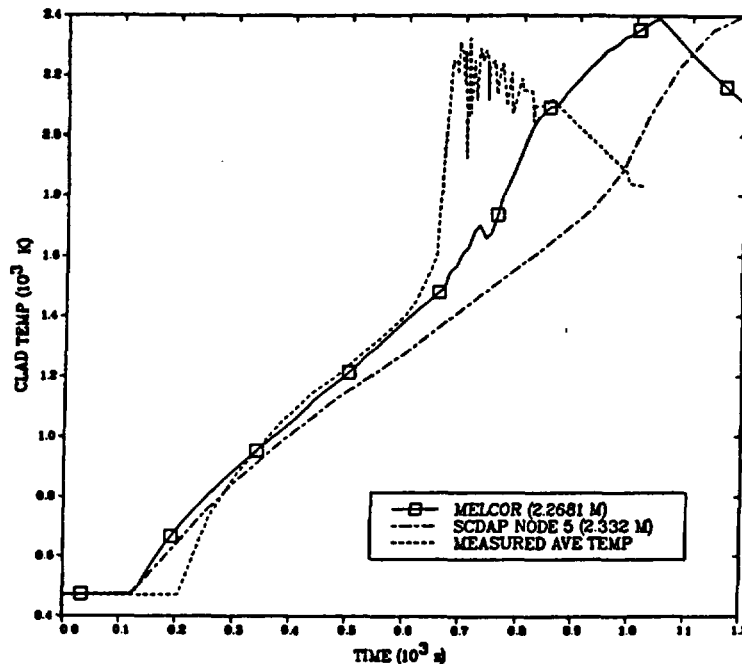


Figure 5. Comparison between measured and calculated clad temperatures, FLHT-2.

MELCOR generally fails to achieve the steep temperature rise observed in experimental data prior to thermocouple failure. This could be attributed to several causes. Firstly, following clad rupture, the inner clad surface also gets exposed to steam and hence subject to oxidation. This is not modeled in MELCOR. The effect may not be pronounced for steam-starved conditions, but there could nonetheless be local availability of steam close to the rupture opening. Secondly, the effect of clad ballooning (not modeled in MELCOR) could give rise to local flow reductions and temperature excursions. Finally, zircaloy present in the shroud inner liner, which can react with steam, is not currently allowed to oxidize in MELCOR as it is not a core component. This effect is not important for steam-starved conditions as in SFD 1-1. But where there is adequate steam supply, this may create divergence in predictions. A way to circumvent that may be to add more mass to clad, while remembering that this will affect the core degradation/relocation calculation since the shroud will not participate in relocation as the fuel cladding would.

The overall temperature behavior is strongly influenced by the calculated liquid level in the bundle region, and the converse is also true. A contributing factor to uncertainties in liquid level calculations is that the actual bundle flow was never constant, whereas MELCOR input (for convenience) assumed it to be constant.

Oxidation and Hydrogen Production

MELCOR calculates oxidation of both zircaloy and steel by solid-state diffusion through the oxide layer using standard parabolic kinetics, with appropriate rate constant expressions, and limited by steam availability. For zircaloy, the rate constant is evaluated from the correlation by Urbanic and Heidrick. The shift to rapid oxidation is modeled to occur at 1853K [1]. This temperature can be changed via sensitivity coefficient.

Table 1 shows comparisons between experimental and calculated values of total hydrogen production for PBF SFD1-1, SFD1-4, FLHT-2 and FLHT-4 experiments [3-6]. MELCOR calculations show good agreement with test data for all except FLHT-4, for which the poor agreement could be attributed to the following: (i) There was less zircaloy mass available for oxidation in MELCOR, since the liner, being a heat structure, was not allowed to oxidize; (ii) MELCOR does not model clad ballooning, and allows no oxidation on the inside of the clad after it fails, and (iii) MELCOR calculates more relocation than in the test, bringing zircaloy to cooler regions of the bundle, where oxidation is suppressed.

Table 1. Comparison of Calculated Total Hydrogen and Test Data

	HYDROGEN PRODUCED (g)			
	Experiment	MELCOR	SCDAP or SCDAP/RELAP5	STCP
PBF SFD 1-1	64 ± 7	67	89	60
PBF SFD 1-4	86 ± 12	86	87	--
FLHT-2	42 ± 2.5	43	39.7	--
FLHT-4	175 - 240	119	110/125	--

Changes in Bundle Geometry

The first indication of bundle geometry changes is clad ballooning. There is no explicit model for clad ballooning in MELCOR. Clad rupture is modeled to occur when the clad temperature at an axial cell exceeds a user-specified threshold temperature. This temperature has a default value of 1173K.

Table 2 [3] shows comparisons of measured (SFD 1-1) clad rupture times and location and MELCOR, SCDAP, and STCP predictions.

Table 2. Comparison of Calculated Clad Rupture and Test Data for PBF SFD Test 1-1

	Criterion	Rupture Time(s)	Axial Location (m)
Experiment		1538 - 1632	0.30 - 0.69
MELCOR	$T_{fail} = 1173K$	1370	0.46 - 0.57
SCDAP	Mechanistic	1290	0.46 - 0.55
STCP	$T_{fail} = 1173K$	1755	

Based on this comparison, the default value of 1173K, while not mechanistic, is adequate and need not be changed unless appropriate data is available for a given application.

Table 3 shows comparisons of bundle geometry changes observed in Test SFD 1-4 and the calculations of MELCOR and SCDAP/RELAP 5 [4].

Table 3. Comparison of Observed and Calculated Bundle Geometry Changes in Test SFD 1-4

	EXPT.	SCDAP/RELAP5	MELCOR	
Clad Ballooning		1050s (at 910K)	1166.5s (at 1173K)	No Explicit Model Default Clad Failure Temperature
Continuous FP Release	1750s	1750s	1750s	
Initial CR Failure	1928 - 1978s (at 1700K)	1950s (at 1700K)	1820s (at 1700K)	Higher T's
Relocation	2300 - 2600s (Eutectics & Ceramics)	2325s (Eutectics) at 2250 - 2680K and 2680s Ceramic at 2990K)	2460s (Zr at 2600K & UO <sub>2</sub> at 2650K)	No Eutectics

MELCOR calculates 40 percent of fuel relocated. This is a strong function of the assumed holdup temperature for the oxide shell in MELCOR (2600K in this case). An assumed holdup temperature of 2650K resulted in almost no relocation. The value of 2600K was selected based on observations by Osetek

[7]. This sensitivity to user-input quantities clearly demonstrates the need for the user to be knowledgeable about the modeled phenomena or gain the knowledge through reading and have experience in using the code.

#### Fission Product Release from Fuel

The release of fission products from fuel is modeled in MELCOR using either the original CORSOR or CORSOR-M formulation [1]. Depending on user choice, these release rates can be modified to be a function of the surface-to-volume ratio (S/V) of the material compared to the ratio in the CORSOR experiments. Both models are based on the same experimental data using irradiated fuel. It can be expected, therefore, that agreement with data for fresh fuel will be poor and much better for irradiated fuel. This was confirmed by comparisons of MELCOR calculations using CORSOR and data for test SFD 1-1 which used fresh fuel and test SFD 1-4 that used irradiated fuel. These are shown in Table 4 [3-6]. In FLHT-2, there were no measurements of fission product release. For FLHT-4, MELCOR (1.8.1) somewhat overpredicts and SCDAP somewhat underpredicts the noble gas release.

Table 4. Comparison of Measured and Calculated Release Fractions of Fission Products

Element	Experiment SFD 1-1	MELCOR (CORSOR)	SCDAP
Xe, Kr	0.06 ± 0.03	0.53	0.04
I	0.12 ± 0.02	0.53	
Cs	0.094 ± 0.014	0.53	
Element	Experiment SFD 1-4	MELCOR (CORSOR)	FASTGRASS
Noble Gas	0.23 - 0.52	0.57	0.63
I	0.24 ± 19%	0.57	
Cs	0.51 ± 15%	0.57	
Te	0.03	0.03	
Element	EXPT. FLHT-4	MELCOR (CORSOR)	SCDAP
Noble Gas	0.25 - 0.55	0.67	0.12

#### Effect of Axial Nodalization

In the MELCOR core model, the bundle region is divided into concentric radial rings and axial segments that define core cells. Each cell may contain one or more components such as fuel pellets, cladding, etc.; and a lumped parameter approach is used for each component within a cell. For the

FLHT-2 test simulation, besides the reference case with 20 axial segments in the bundle active region, three sensitivity cases with 5, 10, and 30 segments were also calculated. Comparisons of cladding temperatures are shown in Figure 6 and of hydrogen production are shown in Table 5. There are noticeable differences between different nodalizations, where the case with 20 segments appears to give predictions that are closer to experimental data, compared with the coarser nodalizations. The calculations with 30 segments gave results that were very close to the 20 segments case and are not shown here. Hence, the choice of 20 axial segments in the active length was justified for the reference case.

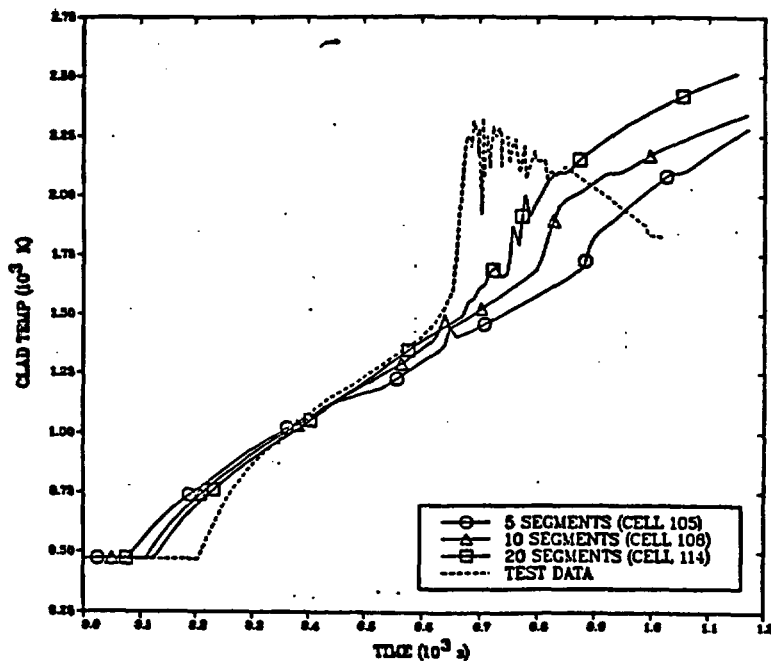


Figure 6. Impact of bundle nodalization on calculated clad temperatures, FLHT-2.

Table 5. Impact of Bundle Nodalization on Calculated Hydrogen Production

Test (g)	MELCOR		
	20 Segments (g)	10 Segments (g)	5 Segments (g)
42	41	27	26

## Workarounds

Experience with the code has allowed the use of several innovative inputs or "workarounds" that were successful in extending the capabilities of MELCOR [8]. Most of them were used during MELCOR benchmarking analyses. For example, one can sometimes speed up a calculation if a problem control volume is eliminated without loss of physics. Initially, the MELCOR input model for the PBF SFD 1-1 test had a bypass volume, which received heat from the bundle region via the insulating shroud. During MELCOR simulation of the test, the timestep was severely restricted by Courant stability limitations. This problem was traced to the bypass volume which had very high flow through it. To improve timestep behavior, the bypass volume was replaced by a user-specified heat transfer coefficient ( $H_{ext}$ ) on the outer surface of the shroud. The value of  $H_{ext}$  was selected based on actually calculated values of  $H_{ext}$  from the code. Sensitivity calculations showed the results to be insensitive to this parameter over a substantial range (5,000 - 15,000 W/m<sup>2</sup>-K). That was expected, since the insulating shroud constitutes the largest resistance to heat transfer. This workaround increased the calculational  $\Delta t$  by more than a factor of 50. A similar effect was also achieved in integral plant calculations by eliminating unimportant control volumes.

## 3. APPLICATIONS

The applications effort at BNL has helped in maturing of the code, by evaluating the ability of MELCOR to successfully simulate various accident sequences and calculate source terms to the environment from both BWRs and PWRs. While the different applications did lead MELCOR into uncharted territory where new code errors were uncovered, the code has shown overall robustness in calculating sequences to completion. Only a very few selected results will be shown to provide a flavor for the applications aspect.

### Peach Bottom

Table 6 compares MELCOR and STCP-predicted timing of key events for a Station Blackout event in Peach Bottom, a GE BWR with MkI containment [9,10]. While MELCOR and STCP [11] calculate similar overall timing of key events and similar peak core temperatures, the more sophisticated modeling in MELCOR allows it to calculate more gradual melting and relocation of core materials and failure of the reactor vessel that is staggered over a much longer time period. Failure of the reactor vessel leads to rapid pressurization of both the drywell and wetwell, but the pressure stays below the nominal failure level, and containment failure is calculated to occur late, due to the combination of an elevated suppression pool temperature and the buildup of non-condensable gas. STCP calculations show similar trends. Failure of the primary containment is followed shortly by several hydrogen burns in the reactor building and refueling bay. Their timings relative to containment failure are similar for both MELCOR and STCP. The predicted duration of deflagration is longer for MELCOR than for STCP, because the MELCOR plant

model considers many compartments in the reactor building, with delays in burn propagation from one compartment to the next, while STCP models the entire reactor building as one volume.

Table 6. MELCOR and STCP-Predicted Timing of Key Events for TMLB Peach Bottom.

Key Event	Time (min)	
	MELCOR	STCP
Core uncover	0.0	0.0
Start zircaloy oxidation	76.0	
First gap release of fission products	76.8	
Start melt and relocation	117.0	114.0
Core collapse	154.4 (partial) ring 1	166.8
Lower plenum dryout	206.3	176.3
Vessel failure (penetration Ring #1)	274.0	205.0
Reactor vessel depressurized	275.1	
Start debris ejection to cavity	341.2	205.1
Drywell failure	426.0	386.0
Start deflagrations in reactor building	426.4	386.5
End deflagrations in reactor building	427.6	386.9
Start deflagrations in refueling bay	429.4	390.6
End deflagrations in refueling bay	430.8	390.7

Table 7 shows the fractional distribution of fission products in various regions of the plant and the environment at the end of the calculation from both MELCOR and STCP. Note that the Cs fractions for MELCOR in the table were obtained by weighted addition of Cs fractions in CsI form (Class 16) and in CsOH form (Class 2), as follows:

$$f(\text{Cs}) = 0.92f(\text{Class 2}) + 0.08f(\text{Class 16}) \quad (1)$$

Table 7. Fractional Distribution of Fission Products by Group in Plant and Environment for TMLB in Peach Bottom.

Species	RCS		Wetwell		Drywell		Cavity		Reactor Building		Refueling Bay		Environment	
	MELCOR	STCP	MELCOR	STCP	MELCOR	STCP	MELCOR	STCP	MELCOR	STCP	MELCOR	STCP	MELCOR	STCP
I	0.404	0.67	0.146	0.23	0.325	7.8E-02	0.0	0.0	3.43E-02	4.2E-03	5.64E-03	5.8E-05	8.56E-02	7.8E-03
Cs	0.334	0.74	0.14	0.14	0.307	8.8E-02	0.0	0.0	4.36E-02	4.9E-03	9.49E-03	6.2E-04	0.164	9.0E-03
Te	2.6E-02	0.35	1.13E-02	3.6E-02	0.107	7.3E-02	0.797	0.23	3.01E-02	0.19	1.01E-02	1.1E-02	1.78E-02	0.10
Sr	5.29E-02	9.7E-04	9.88E-03	2.9E-02	8.48E-02	0.31	0.76	0.16	4.0E-02	0.26	1.12E-02	1.7E-02	4.13E-02	0.21
Ru	5.51E-03	1.3E-06	2.89E-04	3.3E-07	2.67E-04	1.1E-07	0.993	1.0	3.61E-04	5.3E-07	7.19E-05	4.8E-08	8.85E-04	3.2E-07
La	4.3E-03	1.3E-07	1.54E-05	4.1E-03	7.48E-03	1.2E-02	0.984	0.94	2.8E-03	2.4E-02	1.0E-03	1.4E-03	8.23E-04	1.7E-02
Ce	4.27E-03	0.0	6.05E-06	5.3E-03	7.4E-06	1.8E-02	0.996	0.91	7.89E-06	3.8E-02	1.69E-06	2.2E-03	1.88E-05	2.8E-02
Ba	5.29E-02	1.9E-02	9.88E-03	5.2E-02	8.48E-02	0.16	0.76	0.38	4.0E-02	0.22	1.12E-02	1.3E-02	4.13E-02	0.15

The coefficients, 0.92 and 0.08, in Eq. (1), were obtained from the distribution of Cs between the two classes. MELCOR-calculated I mass in the form of free Iodine (Class 4) was seen to be several orders of magnitude smaller than I mass in the form of CsI (Class 16). Hence, MELCOR-calculated I fractions in Table 3 were assumed equal to the fractions of CsI.

A comparison of environmental releases between MELCOR and STCP reveals significant differences. MELCOR predicts much lower release fractions of refractories such as Sr, La, Ce, and Ba, while predicting higher fractions of volatiles I and Cs. STCP predicts similar release and retention of I and Cs from the fuel during in-vessel core meltdown. However, MELCOR models late revaporization from the RCS after core debris penetrates the reactor vessel. This phenomenon is not modeled in STCP, and it represents an important advance for MELCOR. These fission products escape directly into the drywell without the benefit of suppression pool scrubbing, hence the higher release fractions from MELCOR. Note that since Te is mostly released during core/concrete interactions, the revaporization of Te from the RCS has no impact on its total release to the environment. The lower refractory releases is because MELCOR calculates debris ejection into the cavity over a much longer period of time, based on successive penetration failures in the three rings, while STCP assumes the release of all of the core at the time of vessel breach. The MELCOR meltdown model, therefore, results in less vigorous core concrete interactions than STCP, leading to lower release of the fission products associated with this phase of the accident.

Oconee

Table 8 compares MELCOR (1.8DN) and STCP-predicted timing of key events for a LOCA sequence (3-inch hot leg break) in Oconee, a B&W PWR with large dry containment [12].

Table 8. MELCOR and STCP-Predicted Timing of Key Events for LOCA (3-inch hot leg break in Oconee.)

Key Event	Time (min)	
	MELCOR	STCP
Core uncover	15.0	16.0
Accumulators empty	29.9	21.6
First gap release of fission products	27.3	--
Start melt and relocation	70.7	80.5
Core collapse	96.7(Ring 2) 98.8(Ring 1) 127.4(Ring 3)	107.1
Lower plenum dryout	108.3	124.5
Lower head failure	113.2(Ring 1) 123.1(Ring 2) 133.0(Ring 3)	164.4
Start concrete attack	120.0	164.4
Hydrogen burns begin	162.2	--
Containment failure	2720.8	1074.9
End calculation	3667.0	1366.0

MELCOR predicts melting and relocation of core material to start somewhat earlier than STCP, but the relocation is more gradual. MELCOR calculations assume vessel failure to occur when temperature of the penetrations reached 1273.15K (default value). The STCP calculation, on the other hand, assumes that gross failure of the lower head due to ablation would be the governing mode, based on depressurized conditions in the reactor vessel, and calculates vessel failure to occur much later. Thereafter, MELCOR calculates gradual release of core materials into the cavity, so that even after vessel failure in all 3 rings, there is a substantial amount of fuel still left in the core, whereas STCP essentially releases the entire core inventory at the time of vessel failure. This results in a less vigorous core-concrete interaction for MELCOR, and a more gradual pressurization of the containment, leading to containment failure much later than for STCP.

A comparison of environmental releases (Table 9) shows that MELCOR calculates lower release fractions of Sr, La, Ce, and Ba, while STCP calculates lower release fractions of I, Cs, and Te. The differences are small (less than a factor of 5) for Cs, Sr, and Ba. MELCOR predicts significantly higher release of I (order of magnitude), while STCP predicts significantly higher release of La and Ce (2 orders of magnitude). The lower refractory releases from MELCOR occur because MELCOR calculates debris ejection into the cavity over a much longer period of time, which results in less vigorous core-concrete interactions than STCP, and hence, larger retention of the refractory fission products in the cavity. This can be clearly seen from the table.

Table 9. Fractional Distribution of Fission Products in Plant and Environment for LOCA (3-inch hot leg break in Oconee).

Species	RCS		Containment		Cavity		Environment	
	MELCOR	STCP	MELCOR	STCP	MELCOR	STCP	MELCOR	STCP
I	9.92E-2	8.7E-2	0.840	0.9015	0.0	0.0	0.154	1.15E-2
Cs	6.73E-2	8.43E-2	0.887	0.9042	0.0	0.0	5.40E-2	1.15E-2
Te	1.95E-2	0.1808	0.966	0.4634	3.70E-3	0.3527	1.12E-2	3.1E-3
Sr	2.13E-2	1.5E-4	0.321	0.6153	0.658	0.3843	9.24E-5	2.4E-4
Ru	2.0E-2	0.0	1.16E-4	2.9E-6	0.98	1.0	3.25E-7	3.1E-9
La	2.01E-2	0.0	5.51E-2	0.1176	0.925	0.8824	4.40E-7	4.7E-5
Ce	2.0E-2	0.0	3.06E-5	0.1574	0.98	0.8425	4.85E-7	5.7E-5
Ba	2.13E-2	3.1E-3	0.321	0.3465	0.658	.6501	9.24E-5	3.2E-4

## Effect of Break Location

There were several sensitivity calculations performed as part of applications analyses. The results from one of them, i.e., the impact of break location for Oconee, will be highlighted here. Table 10 compares the radionuclide release fractions into the environment calculated by simulating a LOCA sequence initiated by a 3-inch diameter break in a hot-leg pipe and a cold-leg pipe.

Table 10. Impact of Break Location on Environmental Release Fractions - LOCA in Oconee.

Species	Break Location	
	Hot Leg	Cold Leg
I	0.154	6.56E-3
Cs	5.4E-2	4.01E-3
Te	1.12E-2	1.59E-3
Sr	9.24E-5	9.30E-5
Ru	3.25E-7	1.57E-11
La	4.40E-7	4.79E-7
Ce	4.85E-7	5.73E-7
Ba	9.24E-5	9.30E-5

The impact of break location is seen to be minimal for the refractory species. The lower release fraction of Ru could also be a result of round-off error, the number being so small. However, the volatile species I, Cs, Te all exhibit about an order of magnitude lower environmental release fractions, because of substantially greater retention in the RCS, for the break in a cold leg. This is expected since the pathway to the break for the fission products is via the steam generator, where substantial retention occurs. As far as timing of containment failure, for a break in a cold leg, there is greater loss of coolant out of the break. Boil-off of a larger mass of water in containment causes rapid pressurization leading to earlier containment failure.

#### 4. INSIGHTS ON BOTTOMLINE ISSUES

MELCOR is a versatile system code, with generalized architecture, and has demonstrated robustness in simulating a variety of systems and severe accident sequences to their completion. The code has several deficiencies, and the NRC-appointed Peer Review Committee has worked on identifying these

[13]. While the documentation is indispensable, there is a general lack of sufficient guidance for selection of input parameters, nodalization, and timestep size.

The selection of  $\Delta t_{max}$  (maximum timestep size) and its impact on the calculational behavior of MELCOR has been an area of lingering uncertainty in the use of MELCOR. Its significance was first realized when carrying out an investigation of the impact of maximum allowable timestep ( $\Delta t_{max}$ ) on observed machine dependencies in the sample problem of MELCOR Version 1.7.0 [14]. The impact of this parameter was also explored as part of a limited sensitivity analysis for the Station Blackout simulation in Peach Bottom using MELCOR Version 1.8BC and 1.8DN [9], which showed significant differences in timing of key events, and a lack of convergence of the solution with reduction of  $\Delta t_{max}$ . However, the development staff at SNL have re-examined the internal timestep algorithm, and it is expected that the latest version of the code, not yet released to BNL, would have made significant progress towards resolving this problem.

The user must be aware that MELCOR, as any other system code, has limitations in its modeling and numerics, and there will be a significant uncertainty associated with its calculation of accident progression and source terms to the environment. Furthermore, typical input size for a full-plant simulation would be a few thousand lines, with many input choices. Thus, the user shoulders a heavy responsibility for the correctness and appropriateness of the input model, and hence knowledge and experience are essential.

## 5. CONTRIBUTION OF BNL PROGRAM

This concluding section highlights the contribution of the BNL program to MELCOR development, assessment, and the identification of user needs for optimum use of the code.

Feedback from BNL to SNL and the NRC on code errors/deficiencies, has contributed significantly towards improving the code, and will hopefully continue to do so in the future. Feedback was also provided to the Peer Review Committee and the NRC on "Lessons Learned" with MELCOR. Finally, MELCOR Benchmarking and Applications at BNL have provided and will continue to provide a focus on code capabilities and limitations, user tricks and workarounds to extend the capabilities of the code, and user needs, i.e., what the code requires from a user, in order to be used in a meaningful way, and also, what the user needs from MELCOR to enable him to use the code effectively.

Such efforts will be able to guide MELCOR towards maturity as a severe accident/source term analysis tool for PRA studies of current LWR plant designs, which is one of the key targeted applications for MELCOR.

## 6. REFERENCES

1. R. M. Summers et al., "MELCOR 1.8.0: A Computer Code for Severe Nuclear Reactor Accident Source Term and Risk Assessment Analyses," NUREG/CR-5331, SAND90-0364, Sandia National Laboratories (Jan. 1991).
2. I. K. Madni, "Review of Experimental Data Alternatives for Benchmarking MELCOR," Brookhaven National Laboratory Technical Report A-3281, July 1988.
3. I. K. Madni, "MELCOR Simulation of the PBF Severe Fuel Damage Test 1-1," *Proc. 26th National Heat Transfer Conference*, Philadelphia, Pennsylvania, August 6-9, 1989, *AIChE Symp. Ser.*, 85, 269 (1989).
4. I. K. MADNI, "MELCOR Modeling of the PBF Severe Fuel Damage Test 1-4," *Proc. International Conference Probabilistic Safety Assessment and Management (PSAM)*, Beverly Hills, California, February 4-7, 1991, Elsevier Science (1991).
5. I. K. Madni and X. D. Guo, "MELCOR Modeling of the NRU Full-Length High-Temperature 2 Experiment," *Nuclear Technology*, Vol. 99, August 1992.
6. I. K. Madni and X. D. Guo, "MELCOR Simulation of the Full-Length High-Temperature 4 Experiment," Brookhaven National Laboratory Draft Technical Report A-3281, November 1991.
7. D. J. Osetek, "Results of the Four PBF Severe Fuel Damage Tests," *Transactions, 15th Water Reactor Safety Information Meeting*, NUREG/CP-0090, October 1987.
8. I. K. Madni, "MELCOR Lessons Learned: A User Perspective," Brookhaven National Laboratory Technical Report A-3281, January 1991.
9. I. K. Madni, "Analysis of Long-Term Station Blackout Without ADS at Peach Bottom Using MELCOR," NUREG/CR-5850, BNL-NUREG-52319, 1992 (to be published).
10. I. K. Madni, "MELCOR Simulation of Long-Term Station Blackout at Peach Bottom," *Proceedings of the 18th Water Reactor Safety Information Meeting*, NUREG/CP-0113, October 1990.
11. J. A. Gieseke et al., "Source Term Code Package: A User's Guide," NUREG/CR-4587, BMI-2138, Battelle Memorial Institute (April 1986).
12. I. K. Madni, "Analysis of Severe Accident Scenarios in Oconee Using MELCOR," Brookhaven National Laboratory Draft Technical Report, A-3281, December 1991.

13. B. E. Boyack, et al., "MELCOR Peer Review," Los Alamos National Laboratory, LA-12240, March 1992.
14. I. K. Madni and W. Bornstein to M. Khatib-Rahbar, "Impact of Timestep on MELCOR 1.7.0 Calculations," BNL Technical Memorandum, January 20, 1988.

#### ACKNOWLEDGEMENTS

The author acknowledges W. T. Pratt and J. Lehner of BNL for reviewing the manuscript; R. Foulds, C. Gingrich, A. Rubin, and F. Eltawila of the NRC for their continued support and guidance throughout this work. A special note of thanks is due A. Costantini for her excellent preparation of the manuscript.

This work was performed under the auspices of the NRC under contract DE-AC02-76CH00016.

ANALYSIS WITH MELCOR OF FPs AND CORE MATERIALS  
RELEASE AND TRANSPORT DURING THREE ACCIDENTS  
IN A PWR PLANT

A. Alonso, S. Aleza, J.A. Fernández, F.J. González, E. Hontañón,  
J.V. López, F. Martín-Fuertes, I. Más and J.M. Sánchez

Chair of Nuclear Technology  
School of Industrial Engineering  
Madrid Polytechnical University<sup>(\*)</sup>  
Madrid SPAIN

ABSTRACT

Results from MELCOR (Version 1.8.0) calculations of three accident sequences in a W-PWR 900 Mwe three loop plant are presented. The scenarios considered include an AB sequence and two V type events: a rupture of the Low Pressure Coolant Injection System in the auxiliary building, and the rupture of ten steam generator tubes; in all cases without the intervention of the active emergency core cooling systems. Emphasis is put on the release and transport of core materials. It has been found that deposition of vapors from the most volatile species is high within the core structures. Later in the accident, revaporization induced by decay heat takes place, at times in coincidence with the production of steam due to core slumping, what may change the nature and composition of source terms.

1.- INTRODUCCION.

The MELCOR code has been used within the Chair of Nuclear Technology (Polytechnical University of Madrid) to analyze three accident sequences in a typical W-PWR 900 Mwe 3 loop plant. The study includes: (1) An AB sequence initiated by the rupture of the loop including the pressurizer in the cold leg close to the vessel. (2) A V sequence initiated by the rupture, within the auxiliary building, of a low pressure injection pipe connected to the hot leg of the primary circuit. (3) A SGTR sequence initiated by the simultaneous rupture of ten inlet tubes close to the plate. In this presentation emphasis is put on release, transport and revaporization of FP's during the in-vessel phase of the accident up to pressure vessel rupture.

---

(\*) This work has been sponsored by the CEC. Contract 4189-90-12 EL ISP E.

A brief description of the studied sequences is first included, together with the basic thermalhydraulics dominating each particular situation. The most salient aspects in modeling material release and transport in MELCOR is next described, as the way to present the results. Emphasis is put on the timing of events, the characterization of the materials being released and transported, residence times along the transport paths and thermal resuspension of fission product species previously deposited on surfaces.

In all cases studied, MELCOR predicted very low releases of fuel, control rod, cladding and structural materials. Fission products are released in accordance with their volatilities. Fission product vapor deposition is predominant on in-vessel structures, steam generator inlet water boxes and pressurizer. Revaporization of the most volatile species is significant from the in-vessel structures when core support plates fail.

## **2.- BRIEF DESCRIPTION OF THE STUDIED ACCIDENT SEQUENCES.**

The accident sequences have been analyzed with the MELCOR code. A brief description of each one is next presented.

### **2.1.- THE AB SEQUENCE.**

The initiating event for this sequence is a large break (200% double-ended) in the cold leg of the loop containing the pressurizer, near the vessel. The worst variant case of this accident is the AB sequence, where the B stands for loss of all AC electric power. None of the emergency systems would be functional, except the accumulators. The reactor vessel blows down in matter of seconds, followed by the discharge of two of the three accumulators into the vessel. The third one is discharged to the containment through the broken loop.

Severe fuel damage starts soon after blowdown, and the vessel penetration and corium concrete interaction starts in about 2h 10' after the initial event. Containment fails late, in about five hours, by overpressurization produced by the noncondensable combustible gases released from the corium concrete attack.

### **2.2.- THE V SEQUENCE.**

The V-sequence refers to a Loss of Coolant Accident (LOCA) through the Low Pressure Coolant Injection System (LPIS), which in this type of nuclear power plants has a common part with the Residual Heat Removal System (RHRS). The suction pipe of the RHRS connects two of the three hot legs in the primary circuit with the RHRS pumps placed into the Auxiliary Building. It has been assumed that three isolation valves fail in one of these pipelines (two of them are motorized valves): a break near the RHR pump has been postulated as a result of the over-pressurization generated in the pipe.

This event originates an intermediate LOCA in the hot leg. The reactor coolant water is driven outside the containment, bypassing it to one of the RHR pump rooms. The RHR pipeline consists of a very long (61.34 m) pipe having two cross sectional area segments: the first, 38.14 m long, 10.5" inside diameter; the second, 23.2 m long, 12" inside diameter.

Core degradation is achieved as no credit is given to the high and low pressure injection systems. However, it has been assumed the successful operation of the three passive accumulators that discharge in the cold legs, near the vessel downcomer. Steam generator auxiliary feedwater has not been considered either.

### **2.3.- THE STEAM GENERATOR TUBE RUPTURE SEQUENCE.**

The initiating event for this sequence is the simultaneous 200% guillotine type rupture of ten steam generator tubes at the tube plate (total area 0.00446 m<sup>2</sup>). The failed steam generator is part of the loop containing the pressurizer. During tube rupture transients, radioactive superheated primary fluid enters the secondary side of the faulted steam generator and mixes with secondary fluid. This mixture finds its way into the steam line and eventually to the environment by way of the safety valves. Transients initiated by a steam generator tube rupture are relatively probable events during the normal life of a commercial PWR plant.

The reactor trips due to low pressure in the pressurizer. It is assumed that the emergency core coolant system does not operate during the transient. It is also assumed that there is not auxiliary feed water to the steam generators and no steam dump to the condenser. Only the accumulators participate in the sequence, since they are passive elements; their discharge is only produced when vessel breaches, as, until this moment, the primary pressure is over the setpoint of the accumulator valves. Under these conditions the transient leads to core damage and melt-down.

Fission products escape to the environment through the safety valves of the broken steam generator. The secondary side of the broken steam generator is not dry when fission product release begins. Therefore, radioactive aerosols could be retained in this pool. After pressure vessel breach the release of fission products go directly to the containment.

### **2.4.- PLANT NODALIZATION.**

Fig. 2.4.1 shows the basic plant nodalization used, which should be considered standard for these type of analyses. New elements have been added to cover the specific features of each sequence.

The pressure vessel is divided into six volumes: the downcomer, lower plenum, core, core-bypass, upper plenum and upper head, with the necessary communications among them. Different heat structures have been included inside these volumes or connected to them as appropriate. The core package



The steam generators are represented by three volumes. One represents the secondary side; the two volumes, representing the primary side, cover, respectively, the inlet plenum and upcoming tubes and the downcoming tubes and outlet plenum. A flow path connects these two volumes.

Numerous flow paths connect these volumes with others representing the primary system, safeguards systems and normal and auxiliary feed water systems. Likewise, a set of flow paths communicates the secondary side of steam generator with the environment representing the five relief valves. A number of heat structures have been incorporated representing walls, moisture separators and steam dryers.

The reactor cavity is represented by a single volume connected to the containment bottom. The containment space is divided into two volumes. The cylindrical part of the containment, enclosing the primary system, is separated from the hemispherical dome above it. A number of heat structures represent different walls and floors, as well as numerous concrete and metallic inner walls, have also been included.

### 3.- MODELING CORE MATERIAL RELEASE AND TRANSPORT IN MELCOR.

To simulate release of materials from the damaged core the model CORSOR-M, corrected by the surface to volume ratio, has been selected. Volatile fission products (Cs, I and Te) follow the same release pattern from the fuel; nevertheless, Te is retained by the non-oxidized zircalloy. Less volatile fission products (Ba, Sr) leave the fuel only at temperatures above 2200 K, while the fuel itself is only released at temperatures above 2400 K. Other materials, such as control rod neutron poisons (Ag, In, Cd), clad (Zr, Sn) and structural components (Fe, Cr, Ni) are also released at high temperatures.

MELCOR incorporates TRAPMELT models to treat the behavior of vapors released from the core. It includes nucleation in the gas volume; condensation onto surfaces, such as on suspended aerosols and structures. Retention by water pools is evaluated by SPARC. MELCOR considers surface heating by decay energy and revaporization of previously deposited materials. This phenomenon could be of importance later in the accident, when support plates degrade and collapse into the water pools present in the bottom of the vessel releasing steam.

Aerosol physics during transport is modeled in MELCOR by MAEROS, which includes particle agglomeration and different retention mechanisms including: thermophoresis, diffusiohoresis, brownian diffusion and gravitational deposition. Aerosol retention in water pools is of interest in the V-LPIS sequence, when water pools may exist above the ruptured pipe in the auxiliary building; it could also be of interest in the water present in the secondary side of steam generators in the SGTR sequence.

Chemical models in MELCOR are too simplistic; nevertheless, the user has the option of defining some chemical reactions. For this study it was assumed that all of the I released is converted into CsI, while the excess Cs is converted into Cs(OH). Te is assumed to be transported as TeO. Other

less volatile fission products, such as Ba, Sr and Sn retain their metallic form and U is transported as  $UO_2$ .

#### 4.- RESULTS.

In what follows, the most interesting results obtained in the analyses of the selected sequences are summarized.

##### 4.1.- TIMING OF EVENTS.

Table 4.1.1 gives the timing of key events for each one of the considered sequences. The table reflects the different loss of coolant rates.

For the AB sequence, events occur very fast. Clad oxidation starts at 344s into the accident, while gap release starts at 382 s and core degradation at 693 s. The whole process ends with the vessel lower head failure at 10121s.

Sequence V-LPIS is considered as an intermediate size break. Oxidation is retarded up to 2740 s, while gap release and core degradation start at 2842 and 3458 s respectively. Likewise, vessel lower head failure, occurring at 12631 s, is the end of the simulation.

The SGTR corresponds to a small size break reflecting itself in a slow degradation process at high pressure. In fact, the accumulators discharge water only after gross pressure vessel failure. At that time core degradation is well advanced. Oxidation starts at 8200 s into the accident, while gap release occurs at 8276 s and core degradation starts at 9201 s. The simulation ends with a gross vessel lower head failure at 18513 s.

System pressures and temperatures, together with gas and condensed phase compositions, are also calculated. The different values obtained will not be presented here, they will only be discussed later in relation to the release and transport of core materials, as this is the subject of interest to this presentation.

##### 4.2.- RELEASE OF CORE MATERIALS AND FISSION PRODUCTS.

MELCOR predicts that more than 70% of volatile fission products in the fuel will be released. The estimated amount of less volatile fission products, together with fuel, control, clad and structural materials is extremely low and dependent on the relocalization processes dominating any particular sequence. Table 4.2.1 gives element release fractions for the three sequences under consideration.

EVENT	SEQUENCE	SEQUENCE		
		AB	V-LPIS	SGTR
Reactor Shutdown		0.015	8.0	81.73
Core Uncovery		0.13	502.4	-
Accumulator Discharge		7.3	586.9	-
Core Recovery		50.0	760.3	-
Definitive Core Uncovery:	Starts	70.9	1411.1	260
	Ends	4100.1	4600.0	12200
Oxidation Starts		343.9	2740.0	8200
Gap Release		381.6	2840.2	8276
Core Degradation Starts		693.2	3457.6	9201
Lower Core Support Plate Failure		3420.3	6675.3	13200
Lower Barrel Support Failure		6487.7	8330.7	14404
Vessel Dryout		7601.4	9780.4	16800
First Penetration Failure		7888.8	10470.8	16194
Vessel Lower Head Failure		10121.5	12621.5	18513

Table 4.1.1.- Timing of Events (Time Given in Seconds).

ELEMENT	RELEASE FRACTION (%)		
	AB	V	SGTR
Cs	76	98	70
I	76	98	70
Te	73	98	66
Ba	5.1E-1	1.5	1.1E-1
Sn	5.1E-3	1.2	3.4E-3
U	1.0E-2	1.7E-2	3.3E-4

Table 4.2.1.- Release Fractions for Three Accident Sequences.

#### 4.3.- THERMAL RESUSPENSION.

The analyses of accidental sequences here described reveal that revolatilization of volatile FP species from deposits on the RCS surfaces could occur during the last period of the in-vessel phase. It has also been found that thermal revaporization of other core materials is negligible. At this time, favored by the thermal and hydrodynamic conditions of the carrier gas through the RCS, the revolatilized FP vapors could nucleate and/or condensate onto particles. Thus, aerosol transport mechanisms could determine the release of radioactivity to the correspondent atmosphere during this period. In connection with this phenomenon, results obtained for the V, SGTR and AB scenarios are summarized.

The results obtained prove that FP vapor deposition in the core region could significantly affect the radioactive source term. MELCOR predictions evidence that core baffles could melt and relocate quite early after core uncovering; core atmosphere would, then, become into direct contact with the bypass atmosphere; as a consequence, vapors and aerosols released from the core region could be retained on the inner wall of the core barrel. Thus, it was finally decided to consider this fact when modeling FP behavior and transport in the scenarios considered.

Assuming this, MELCOR predicts two clearly differentiated periods in the behavior and transport of FP species through the RCS during the in-vessel phase of the accidents: the first corresponds to the strong FP release directly from the fuel; whereas the second is related to the revolatilization of the FP species from superficial deposits at the time when the core debris slumps into the lower plenum.

MELCOR results reveal that most of FP vapors released until revolatilization occurs are retained in the core region by direct condensation on the inner barrel wall. The high temperatures of the carrier gas through the core inhibit nucleation of the highly volatile FP vapors and their condensation on aerosols composed of low volatile FPs, Ba and Sr, and other inert materials such as Sn (cladding), Ag-In (control rods), and UO<sub>2</sub> (fuel); as a consequence, the deposition of Cs(OH), CsI and TeO as aerosols on the barrel wall is negligible. However, in the upper plenum region, where gas temperatures are significantly lower, condensation onto the structures and aerosol depletion due to thermophoresis compete to remove FP species from bulk gas; the remaining vapors reach cooler regions downstream the vessel, where they could nucleate and/or condensate on suspended particles. Partition of FPs between vapor and aerosol phases, when they leave the RCS, depends on the specific features of the accident.

##### 4.3.1.- Containment Bypass Scenario: The V Sequence.

About an hour and a half after gap release, MELCOR predicts for the V sequence that nearly all Cs(OH), CsI and TeO condensed on the barrel wall revaporize, promoted by the high temperatures that this surface has

achieved due to the decay of the FP's there deposited (see fig. 4.3.1.1). At about the same time, the core debris slumps down into the lower plenum and evaporates the water there contained; the sudden flow of steam removes vapors and aerosols from the atmosphere of the reactor vessel. Given the low temperature of the steam passing through the vessel, revaporized species nucleate and/or condensate onto particles suspended in the core region; as a result, the deposition profile of radionuclides within the RCS changes completely and they, partially, escape to the atmosphere.

Revaporization is a transient period, whose extent and duration vary from one accident to another. For the V sequence, about 90% of the total Cs(OH), CsI and TeO released from the fuel before core slumping revolatilizes from the core barrel in less than 3 min; as a result, the mass of these species released to the auxiliary building increases significantly. Tabs. 4.3.1.1 and 4.3.1.2 show the material distribution in the plant at two different times: 2h 15', just before core slump; and 2h 55', when there appears the first failure of a vessel penetrations in the lower head.

SPECIE	RELEASED MASS (Kg)	RCS (%)				PUMP ROOM (%)				SOURCE TERM TO AUXILIARY BUILDING (%)
		ATM	POOL	HS	TOTAL	ATM	POOL	HS	TOTAL	
CsOH	151.4	0.0	0.0	93.0	93.0	0.0	0.0	1.4	1.4	6.0
CsI	23.0	0.0	0.0	94.0	94.0	0.0	0.0	2.0	2.0	3.8
TeO	25.5	0.0	0.0	94.0	94.0	0.0	0.0	1.3	1.3	4.7
Ba (Sr)	1.7	0.0	0.0	34.0	34.0	0.0	0.0	6.3	6.3	60.0
Sn (Ag)	31.1	0.0	0.0	34.0	34.0	0.0	0.0	6.5	6.5	59.5
UO <sub>2</sub>	13.1	0.0	0.0	35.0	35.0	0.0	0.0	6.6	6.6	58.5

Table 4.3.1.1.- Sequence V. Material Distribution at Time 2h 15', Before Core Slump.

SPECIES	RELEASED MASS (Kg)	RCS (%)				PUMP ROOM (%)				SOURCE TERM TO AUXILIARY BUILDING (%)
		ATM	POOL	HS	TOTAL	ATM	POOL	HS	TOTAL	
CsOH	154.4	0.0	0.0	34.7	34.7	0.0	0.0	2.3	2.3	63.0
CsI	23.4	0.0	1.0	76.5	77.5	0.0	0.0	9.5	9.5	13.0
TeO	26.1	0.0	1.0	70.2	71.2	0.0	0.0	5.0	5.0	24.0
Ba (Sr)	1.8	0.0	0.0	33.7	33.7	0.0	0.0	6.5	6.5	60.0
Sn (Ag)	31.1	0.0	0.0	34.1	34.1	0.0	0.0	6.5	6.5	59.5
UO <sub>2</sub>	13.1	0.0	0.0	35.2	35.2	0.0	0.0	6.6	6.6	58.5

Table 4.3.1.2.- Sequence V. Material Distribution at Time 2h 55'. After 1st Vessel Penetrations Failure.

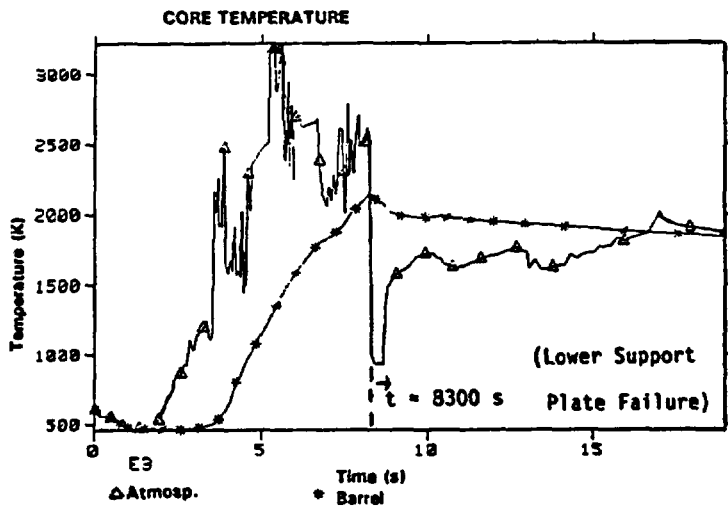


Fig. 4.3.1.1.- Sequence V. Time Evolution of Core Temperatures.

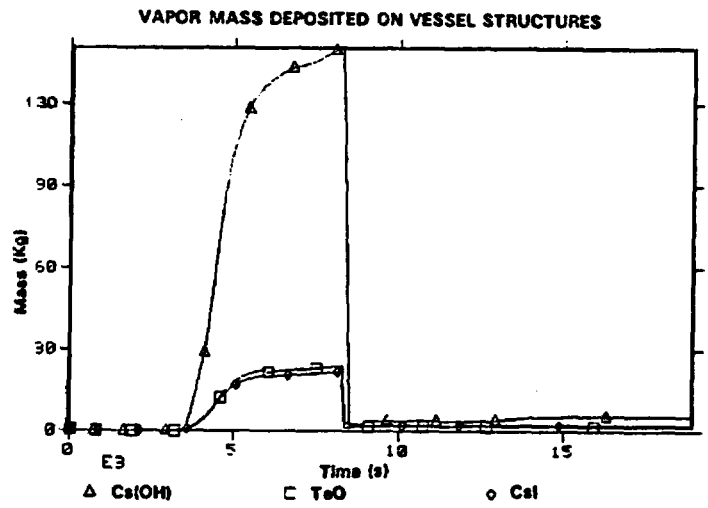


Fig. 4.3.1.2.- Sequence V. Time Evolution of Cs, I and Te Vapors Deposition on Vessel Structures (In-Vessel Phase).

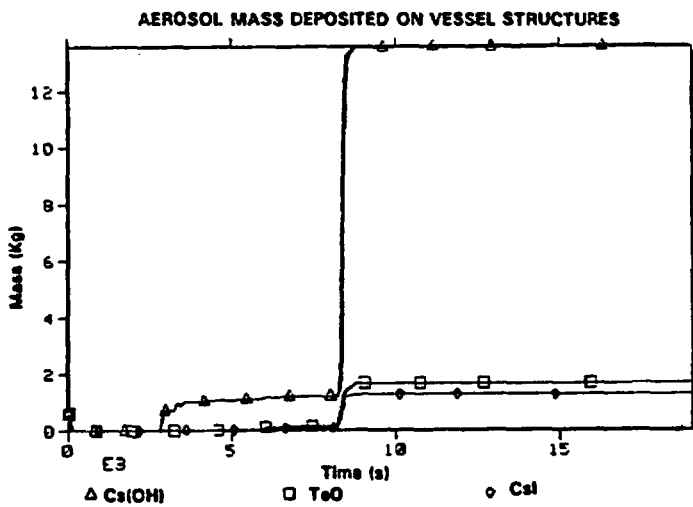


Fig. 4.3.1.3.- Sequence V. Time Evolution of Cs, I and Te Aerosols Deposition on Vessel Structures (In-Vessel Phase).

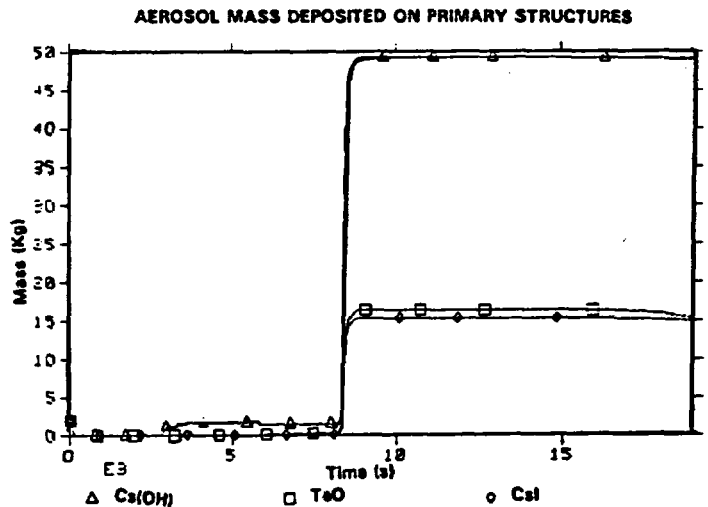


Fig. 4.3.1.4.- Sequence V. Time Evolution of Cs, I and Aerosols Deposition on RCS Structures (In-Vessel Phase).

The time evolution of the vapor and aerosol deposits on only vessel structures and onto all the RCS surfaces, including the vessel, are plotted in figs. 4.3.1.2 to 4.3.1.4.

As it can be seen, vapor depletion phenomena control FP retention before the failure of the core support plate, since temperatures of the RCS atmosphere are too high, what inhibits vapor nucleation and condensation onto inert aerosols. On the contrary, core slump at the same time that FP vapors revolatilize promotes their conversion into the condensed phase; therefore, aerosol generation and transport mechanisms determine the final escape of radioactivity to the auxiliary building atmosphere before vessel breach.

#### 4.3.2.- Containment Bypass Scenario: The SGTR Sequence.

For the SGTR scenario, MELCOR predicted a revaporization phase much slower than in the V case. At the time that penetrations fail first, a good amount of FPs still stay on the inner barrel wall; after their revolatilization in the vessel region, they escape directly to the containment atmosphere through the vessel breach.

Tabs. 4.3.2.1 and 4.3.2.2 show the material distribution in the plant at two different times into the accident: 4h 30', just before the first penetration breach in the lower head during the revaporization phase; and 5h 35, after the catastrophic failure of the vessel and when revolatilization is already completed. Table 4.3.2.1 gives the material distribution in % relative to the amount released up to the first failure of a vessel penetration, while Table 4.3.2.2 percentages are calculated with reference to the amounts released up to the catastrophic failure of the vessel.

SPECIES	RELEASED MASS (Kg)	RCS (%)						SG SECONDARY SIDE (%)						SOURCE TERM TO ENVIRONMENT (%)
		ATMOSPHER		POOL		RS	TOTAL	ATMOSPHER		POOL		RS	TOTAL	
		VAP	AER	VAP	AER			VAP	AER	VAP	AER			
CaOH	110.4	10.8	4.7	0.0	6.4	66.4	88.3	0.0	1.0	0.0	4.1	2.1	7.2	4.6
CsI	16.6	26.2	4.0	0.0	3.8	60.2	94.2	0.0	0.4	0.0	1.9	1.0	3.3	2.5
TeO	17.9	23.4	9.4	0.0	2.9	54.2	90.0	0.0	1.6	0.0	3.1	1.8	6.5	3.5
Ba(Sr)	0.12	-	11.5	-	2.7	81.2	95.4	-	0.5	-	1.4	1.0	2.9	2.0
Sr(Ag)	0.13	-	45.4	-	3.1	48.1	96.6	-	0.4	-	1.1	0.6	2.1	1.1
UO <sub>2</sub>	0.18	-	4.3	-	0.84	93.6	98.8	-	0.06	-	0.3	0.6	1.0	1.3

Table 4.3.2.1.- *Sequence SGTR: Material Distribution at Time 4h 30', Just Before 1st Vessel Penetrations Failure.*

SPECIES	RELEASED MASS (Kg)	RCS (%)				SG SECONDARY SIDE (%)				CONTAINMENT (%)				SOURCE TERM TO ENVIRONMENT (%)
		ATROSP	POOL	NS	TOTAL	ATROSP	POOL	NS	TOTAL	ATROSP	POOL	NS	TOTAL	
		AER	AER			AER	AER			AER	AER			
CsOH	137.8	0.0	0.07	25.0	25.0	0.0	0.0	1.8	1.8	49.1	8.1	12.0	69.2	3.6
CsI	17.4	0.02	0.04	57.4	57.5	0.0	0.0	1.0	1.0	19.8	1.5	18.0	39.3	2.3
TeO	18.9	0.02	0.07	56.9	57.0	0.0	0.0	1.8	1.8	26.3	2.7	8.6	37.6	3.4
Ba(Sr)	1.0	0.0	0.0	10.3	10.3	0.0	0.0	0.1	0.1	57.6	28.2	3.4	89.2	0.2
Sn(Ag)	0.18	0.5	0.02	41.3	41.8	0.0	0.0	0.4	0.4	43.7	3.2	10.0	57.9	0.8
UO <sub>2</sub>	0.22	0.0	0.0	80.5	80.5	0.0	0.0	0.5	0.5	12.0	5.0	1.2	18.2	1.0

Table 4.3.2.2.- Sequence SGTR. Material Distribution at Time 5h 35'. After Catastrophic Vessel Failure.

Tab. 4.3.2.1, shows the significant proportion of Cs(OH), CsI and TeO suspended in the RCS atmosphere in both phases, vapor and aerosol, while revaporization takes place; when vessel lower head breaks through, all this suspended material is swept out into the containment, as it can be seen in Tab. 4.3.2.2.

Pool scrubbing is produced in the secondary side of the broken steam generator, starting with the gap release, at 8276 s, and ending the dryout of the failed steam generator at 16401 s. During this time, 7.5 Kg of materials, most of it Cs(OH), are retained, as given in table 4.3.2.3. Nevertheless, it is considered that the SPARC model in MELCOR does not properly represent the complicated phenomena taken place under such accidental conditions.

	TOTAL AEROSOL INJECTION (Kg)	TOTAL AEROSOLS RETAINED (Kg)	DECONTAMINATION FACTOR
Cs(OH)	12.88	6.29	1.95
Ba	5.12E-3	2.4E-3	1.88
TeO	1.772	0.77	1.77
UO <sub>2</sub>	3.83E-3	0.86E-3	1.29
Sn	4.3E-3	2.1E-3	1.95
CsI	1.278	0.43	1.51
TOTAL	15.94	7.5	1.89

Table 4.3.2.3.- Pool Scrubbing in Broken Steam Generator.

#### 4.3.3.- Containment Scenario: The AB Sequence.

For the AB sequence, FP revolatilization from the RCS surfaces seems to have a minor effect. The high temperatures of the carrier gas prevent FP vapors conversion into the aerosol phase, therefore condensation onto surfaces controls their retention within the RCS during the whole accident. Tab. 4.3.3.1 shows the material distribution in the plant just before vessel failure, time 2h 11'; whereas time evolution of the vapor and aerosol deposits on the vessel structures and on the whole RCS surfaces, can be seen in Figs. 4.3.3.1 to 4.3.3.4.

SPECIES	RELEASED MASS (Kg)	RCS (%)						CONTAINMENT (%)					
		ATMOSPHERE		POOL		HS	TOTAL	ATMOSPHERE		POOL		HS	TOTAL
		VAP	AER	VAP	AER			VAP	AER	VAP	AER		
CsOH	155.1	0.0	0.1	0.0	3.2	51.5	54.8	0.4	35.8	0.0	2.5	6.1	44.8
CsI	23.7	0.0	0.2	0.0	1.1	58.4	59.7	0.4	35.2	0.0	1.1	3.4	40.1
TeO	26.5	0.0	0.3	0.0	0.4	37.8	38.5	0.4	53.0	0.0	1.7	5.5	60.6
Ba(Sr)	1.3	-	0.4	-	1.3	5.3	7.0	-	80.0	-	3.1	10.0	93.1
Sn(Ag)	23.1	-	0.3	-	1.3	5.4	7.0	-	79.4	-	2.7	10.7	92.8
UO <sub>2</sub>	7.0	-	0.07	-	0.3	5.6	6.0	-	79.5	-	3.2	12.0	94.7

Table 4.3.3.1.- Sequence AB. Material Distribution at time 2h 11' (Just Before Vessel Penetrations Failure).

Fig. 4.3.3.1 shows the evolution of Cs(OH), CsI and TeO deposited on the vessel structures during the in-vessel phase of the accident. A revaporization episode is apparent between 2000 and 3000 s, i.e. during the late phase of the core degradation process, but before core support plate failure. At that time, the CVH Package finds a core vapor temperature close to the temperature of the deposits, so revaporization is achieved. Other revaporization episodes are noticeable at 4776 and 5902, corresponding to failures of the second and third radial rings of the lower core support plate.

Fig. 4.3.3.2 gives a clearer picture of the situation. It represents the Cs(OH) vapor deposited inside the vessel. Total revaporization is achieved from the inner barrel wall between the said 2000 to 3000 s. Nevertheless, most of this vapor is later deposited on the cooler upper plenum surfaces.

Deposition in the hot legs is very significant, as given in fig. 4.3.3.3. An important revaporization episode takes place in coincidence with the failure of the lower barrel support plate at 6488 s. The study also shows that deposition on surge line and pressurizer, as well as on the cold legs, is negligible.

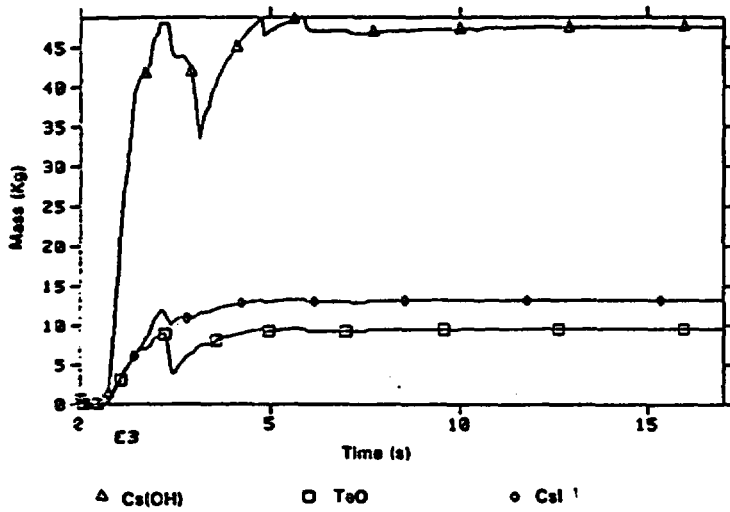


Fig. 4.3.3.1.- Sequence AB. Vapor Mass Deposited on Vessel Structures.

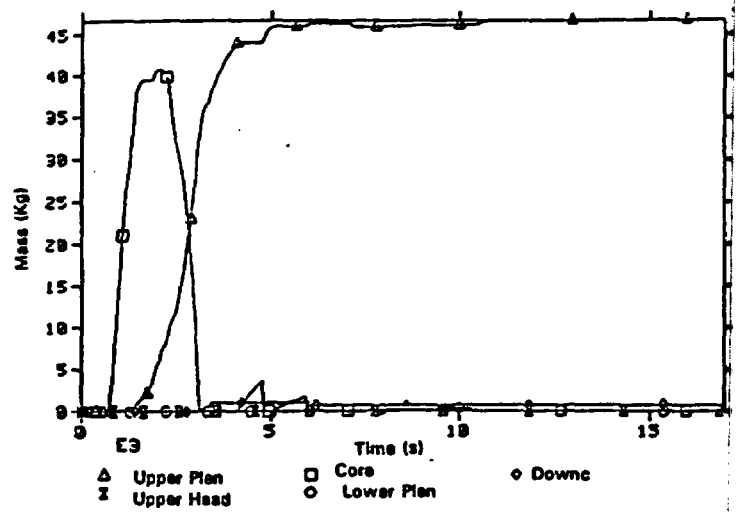


Fig. 4.3.3.2.- Sequence AB. Cs(OH) Vapor Deposited in Vessel Volumes.

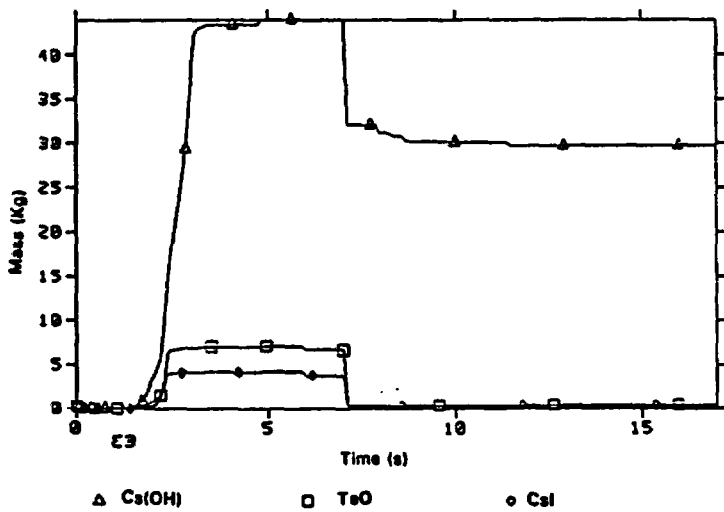


Fig. 4.3.3.3.- Sequence AB. Vapor Mass Deposited on Hot Legs.

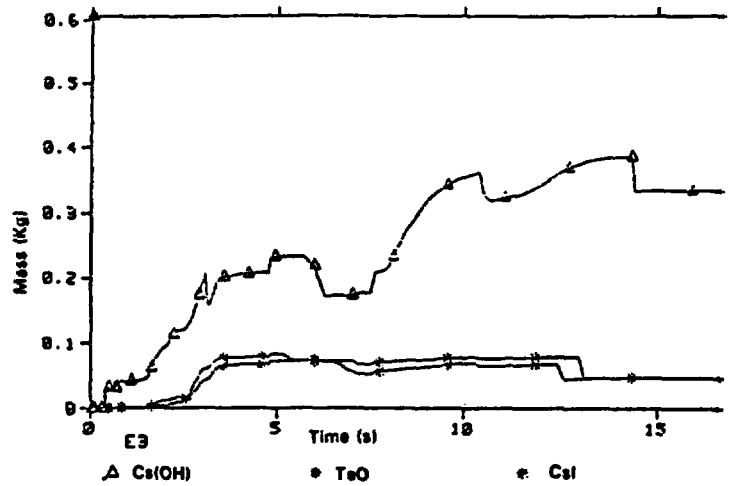


Fig. 4.3.3.4.- Sequence AB. Aerosol Mass Deposited on Vessel Structures.

The aerosols from the volatile species deposited on the vessel structures and in the hot legs also undergo revaporization processes. Revaporization of aerosols deposited on the vessel structures is clear in fig. 4.3.3.4 at different times, mainly in coincidence with the failure of the lower barrel support plate.

#### 4.4.- RESIDENCE TIMES.

Typical residence times and velocity ranges of the carrier gas within the RCS for the scenarios here described are compared in tabs. 4.4.1 to 4.4.3.

#### AB SEQUENCE

VOLUME	VELOCITY RANGE (m/s)	LENGTH (m)	RESIDENCE TIME (s)
CORE	0.5+10	4	8+0.4
UPPER PLENUM	0.5+10	3	6+0.3
HOT LEG	10+100	5.5	0.6+0.06
SG	5+50	20	1+0.4
COLD LEG	5+50	13	3.0+0.3
TOTAL (s)			22+1.5

Table 4.4.1.- Sequence AB. Carrier Gas Velocity Range and Residence Time.

#### V SEQUENCE

VOLUME	VELOCITY RANGE (m/s)		LENGTH (m)	RESIDENCE TIME (s)	
	FP Release	Core Slump		FP Release	Core Slump
CORE	0.5-1.0	3	4	8-4	1.5
UPPER PLENUM	0.5-1.0	3	3	6-3	1.0
HOT LEG	15-20	30	5.5	3.3-2.5	1.5
LPIS	60-80	80	60	1-0.5	1.0
TOTAL (s)				20-10	5

Table 4.4.2.- Sequence V. Carrier Gas Velocity Range and Residence Time.

## SGTR SEQUENCE

VOLUME	VELOCITY RANGE (m/s)		LENGTH (m)	RESIDENCE TIME (s)	
	FP Release	Core Slump		FP Release	Core Slump
CORE	0.01-0.1	0.1	4	400-40	40
UPPER PLENUM	0.01-0.1	0.1	3	300-30	30
HOT LEG	0.1-1.0	1.0	5.5	55-5.5	5.5
SG-Secondary	0.01-0.1	0.1	20	2000-200	200
			<b>TOTAL (min)</b>	<b>50-5</b>	<b>5</b>

Table 4.4.3.- Sequence SGTR. Carrier Gas Velocity Range and Residence Time.

Significantly different residence times can be observed in the three scenarios. For the AB sequence the residence times for the longest path vary between 1.5 s to 22 s. For the V case, a low pressure sequence at about  $10^5$  (Pa), they are in the order of 5 to 10 s; on the contrary, for the SGTR case, a high pressure accident at about  $8 \times 10^6$  (Pa), they are in the order of 5 to 50 min. In the three sequences, residence times within the RCS, during the core slump phase, when FP revolatilization occurs, become smaller. This means higher carrier gas velocities, which may produce aerosol mechanical resuspension, not considered in MELCOR.

### 5.- SUMMARY AND CONCLUSIONS.

The study of fission product behavior during accident sequences, as predicted by the MELCOR code, can give useful information to characterize the source term, despite MELCOR being simplistic on its treatment of chemistry effects. The basic facts deduced from any MELCOR simulation could be further explored with more detailed codes.

Three accident sequences have been assumed to occur in a W-PWR 900 Mwe, three loop NPP. Sequences AB, V-LPIS and SGTR have been analyzed with the MELCOR code. The attention has been focused on thermal reevaporation, and subsequent transport, of volatile fission product vapors (Cs(OH), CsI and TeO) condensed on surfaces.

For the three cases studied, it has been found that large amounts of Cs(OH), CsI and TeO deposit on the vessel structures, mainly on the inner barrel wall, during core degradation. This deposited materials reevaporize due to radioactive decay heat, these vapors can be swept out of the vessel and transported by the RCS by the sudden production of steam produced by

core slump into the water pool on the vessel bottom, modifying the nature of the source term.

It has been found that for the V-LPIS sequence revaporization within the vessel is practically complete at the time of core slump. The so transported materials increase the source term to the auxiliary building. The effect is less important for the other two sequences.

It has also been found that core slump could produce high velocities of the carrier steam inside pipes, making it possible the mechanical resuspension of deposited aerosols on surfaces from both volatile fission products and more refractory core materials. This phenomenon has not yet been considered in MELCOR.

Pool scrubbing may be particularly important in the secondary side of a broken steam generator, mainly if feed water is added to prevent its dryout. Nevertheless, the SPARC models included in MELCOR may not represent correctly the complicated phenomena taking place under such accidental circumstances.

# MELCOR Assessment at SNL

L. N. Kmetyk  
Thermal/Hydraulic Analysis Department  
Sandia National Laboratories  
Albuquerque, NM 87185-5800

## 1 Introduction

MELCOR [1] is a fully integrated, engineering-level computer code that models the progression of severe accidents in light water reactor (LWR) nuclear power plants, being developed at Sandia National Laboratories for the U. S. Nuclear Regulatory Commission (USNRC). The entire spectrum of severe accident phenomena, including reactor coolant system and containment thermal/hydraulic response, core heatup, degradation and relocation, and fission product release and transport, is treated in MELCOR in a unified framework for both boiling water reactors (BWRs) and pressurized water reactors (PWRs). The MELCOR computer code has been developed to the point that it is now being successfully applied in severe accident analyses, particularly in probabilistic risk assessment (PRA) studies.

MELCOR was the first of the severe accident analysis codes to undergo a formal peer review process. One of the major conclusions of the recent MELCOR Peer Review [2] was the need for a more comprehensive and more systematic program of MELCOR assessment. A systematic program of code assessment provides a number of benefits, including:

1. guidance to the code developers in identification of areas where code improvements are needed (such as coding implementation errors in models, inappropriate or deficient models, missing models, excessive numerical sensitivities),
2. documented evidence to external observers, users, reviewers and project management that the code is modelling required phenomena correctly, and
3. increased general public acceptance that the code adequately treats issues related to public safety concerns.

---

\* This work was supported by the U. S. Nuclear Regulatory Commission and performed at Sandia National Laboratories, which is operated by the U. S. Department of Energy under contract DE-AC04-76DP00789.

A MELCOR verification and validation ("V&V") program was funded at Sandia in 1985-1986 [3]. That limited effort primarily involved containment phenomena. Results from MELCOR 1.0, 1.5.0 and 1.6.0 were compared with experimental data, with more mechanistic codes and with analytical solutions for a number of problems. MELCOR has been used by Sandia to participate in the TMI-2 [4] plant accident, and HDR T31.5 (ISP-23) [5] hydrogen mixing and PHEBUS B9+ (ISP-28) [6, 7] and CORA 13 (ISP-31) [8] core damage standard problem exercises.

Because some assessment is available for MELCOR in the areas of containment thermal/hydraulics and core damage assessment, calculations done at Sandia since the Peer Review concentrate on primary system thermal/hydraulic response, on fission product and aerosol release, transport and deposition, and on integral severe-accident analysis, areas where little or no MELCOR assessment was previously available. Completed and ongoing MELCOR assessment analyses at Sandia, whose results are summarized in this paper, include:

1. the LACE LA4 containment-geometry aerosol deposition test [9],
2. the FLECHT SEASET natural circulation tests [10],
3. the ACRR ST-1/ST-2 in-pile source term experiments [11],
4. the OECD LOFT integral severe accident experiment LP-FP-2 [12],
5. the Marviken-V ATT-2b and ATT-2 aerosol transport and deposition tests in primary system geometries [13],
6. PNL ice condenser experiments 11-6 and 16-11 [14], and
7. PWR TMLB' calculations with and without DCH.

One of the major contributions of this assessment project to the MELCOR effort has been the systematic search for and identification of code features which lead to time step and other numerical dependencies, as summarized in the individual task reports. Nearly all major advances in elimination of these undesirable features during the last year are the result of these systematic studies. Many of the numeric sensitivities have been traced to code problems that would not be readily detected in the single, isolated calculations that are typical of many user applications.

In addition, a number of user guidelines on input modelling and on the adequacy and applicability of default parameter settings are being generated, with details contained in the individual assessment reports. In some cases, these will be included in the preliminary users' guide scheduled for next year. In other cases, the end result is a change in the code documentation or changes to the default variable setting in the code; this latter option seems more effective in the long term because it eliminates the need to document when and why the user should override default settings.

## 2 LACE LA4 Aerosol Transport and Deposition

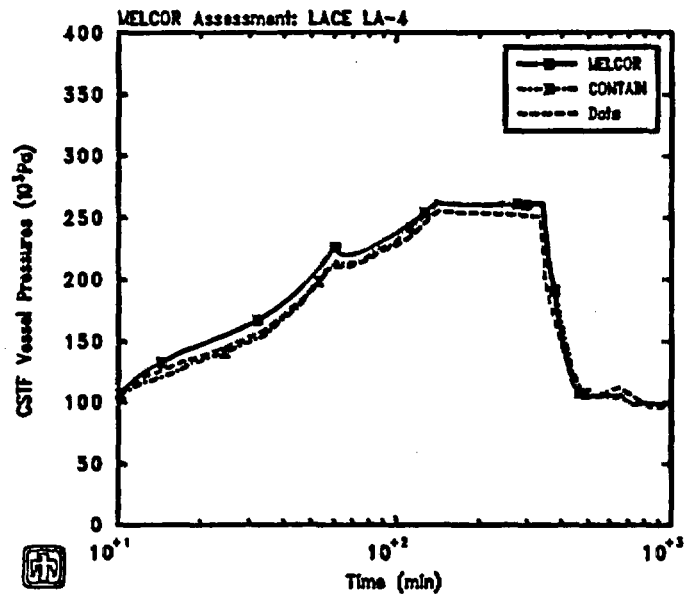
The LWR Aerosol Containment Experiments (LACE) program [15] was a cooperative effort to investigate inherent aerosol behavior for postulated accident situations for which high consequences are presently calculated in risk assessment studies because either the containment is bypassed altogether, the containment function is impaired early in the accident, or delayed containment failure occurs simultaneously with a large fission-product release. A series of six large-scale experiments has been conducted at the Containment Systems Test Facility (CSTF) at Hanford Engineering Development Laboratory (HEDL):

The MELCOR code has been used to simulate LACE experiment LA4 [9], an integral aerosol behavior test simulating late containment failure with overlapping aerosol injection periods [16]. In this test, the behavior of single- and double-component, hygroscopic and nonhygroscopic, aerosols in a condensing environment was monitored. Nonhygroscopic MELCOR results were compared to experimental data, and to CONTAIN hygroscopic calculations for LACE LA4 [18]. The reason for the difference in predicted suspended aerosol masses in the two codes is the larger aerosol particles calculated by MELCOR despite the lack of treatment for hygroscopic effects; the reason for the difference in aerosol particle sizes is primarily the larger agglomeration shape factors used in the MELCOR input.

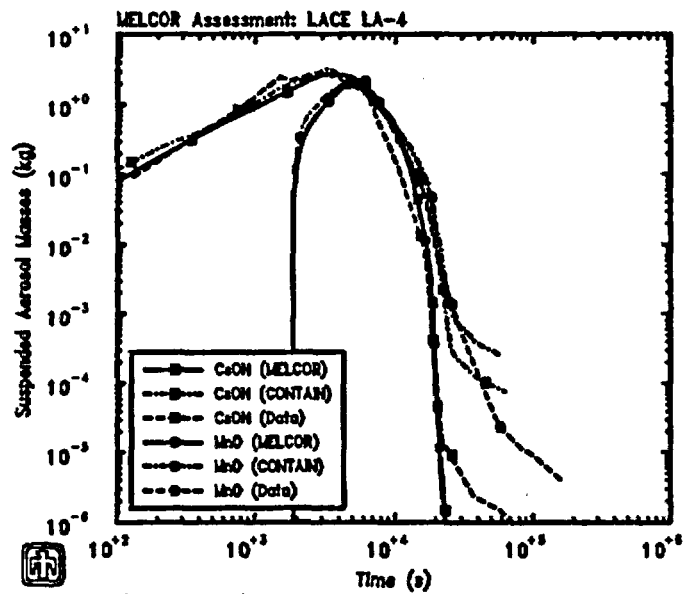
MELCOR calculated the thermal/hydraulic and aerosol response phenomena observed during the LACE LA4 experiment. Figure 2.1 shows the test vessel pressure and the suspended aerosol masses predicted by MELCOR and CONTAIN, compared to experimental data. The lack of any hygroscopic effects in the MELCOR aerosol treatment is visible mostly as the lack of any calculated difference in the behavior of the hygroscopic CsOH and the nonhygroscopic MnO aerosols. MELCOR predicted aerosol particles generally larger than measured, which then settled faster than observed, and consequently less suspended aerosols were leaked and/or plated in the calculation than in the experiment.

The MELCOR LA4 analysis included sensitivity studies on time step effects, wall and pool condensation, radiation heat transfer, number of aerosol components and sections, impact of non-default values of shape factors and diameter limits in the aerosol input, and the degree to which plated aerosols adhere to the walls or are washed off by draining liquid condensate films. The results showed that water should be modelled as a separate aerosol component in this problem, and that more sections (size bins) than the MELCOR default should be used. Including atmosphere-structure radiative heat transfer, even at the relatively low temperatures (300-400K) characteristic of this test, produced better agreement with data, as did using a detailed volume-altitude table reflecting the differences in sump pool liquid surface area with elevation in the elliptical lower head. There was a strong effect on amount of aerosol plated on walls of whether plated aerosol mass was allowed to wash off heat structures with condensate films draining down into the pool, as indicated in Table 2.1. The suspended aerosol results depended most strongly on the value used for the agglomeration shape factor, with a much weaker (but still visible) dependence upon the dynamic shape factor.

Although there has been a lot of discussion recently on numeric effects seen in other MELCOR calculations, no machine dependencies were seen in this problem, and smooth convergence in results with reduced time steps was demonstrated.



LACE LA-4 (2-component)  
 HOCKCUZKY 8/27/92 10:31:39 MELCOR



LACE LA-4 (2-component)  
 HOCKCUZKY 8/27/92 10:31:39 MELCOR

Figure 2.1. LACE LA4 CSTF Vessel Pressure and Suspended Aerosol Masses Predicted by MELCOR, Compared to Test Data and to CONTAIN Results

**Table 2.1. LACE LA4 Final Aerosol Deposition**

Aerosol Species	Location	Test Data (kg)	Code (kg)	
			Reference ("Sticky")	Default ("Nonsticky")
CsOH	Settled	2.563	2.615	2.841
	Plated	0.304	0.230	0.004
	Leaked	0.007	0.002	0.003
MnO	Settled	1.927	2.153	2.267
	Plated	0.228	0.117	0.002
	Leaked	0.101	0.001	0.002
Sum	Settled	4.490	4.768	5.108
	Plated	0.532	0.347	0.006
	Leaked	0.108	0.003	0.005

### 3 FLECHT SEASET Natural Circulation

The Full-Length Emergency Cooling Heat Transfer Separate Effects and Systems Effects Test (FLECHT SEASET) program was a cooperative NRC/EPRI/Westinghouse effort to investigate heat transfer and hydraulic phenomena in a Westinghouse PWR primary system. Part of this program [19, 20] consisted of a series of natural circulation tests in a 1:307-scale facility, with prototypic full lengths and full heights. Steady-state single-phase liquid, two-phase and reflux condensation modes of natural circulation cooling were established, and flow and heat transfer characteristics in the different cooling modes were identified. In addition, other tests studied the variation of single-phase liquid natural circulation with changing core power or with different secondary side heat removal capabilities, and the effect of noncondensables on two-phase natural circulation flows.

In our assessment [10], MELCOR correctly calculated the thermal/hydraulic phenomena observed during steady-state, single-phase liquid natural circulation, as summarized in Table 3.1. MELCOR predicted the correct total flow rate and the flow split between two unequal loops without any *ad hoc* adjustment of the input. The code could reproduce the major thermal/hydraulic response characteristics in two-phase natural circulation, after a number of non-standard input modelling modifications; MELCOR could not reproduce the requisite physical phenomena with "normal" input models. The natural circulation mass flows predicted in these two cases are shown in Figure 3.1.

One major input model change consisted of subdividing the steam generator U-tubes into stacks of multiple control volumes. The top elevations of the control volumes containing the U-tubes were adjusted to lie above the top of the connecting horizontal flow path opening heights, and small incremental volumes were added in the volume-altitude tables in those control volumes; this is an input trick to ensure that a minimal atmosphere is always present and the

**Table 3.1. FLECHT SEASET Single-Phase Liquid Natural Circulation**

Parameter	Measured	Calculated
Specified by Input:		
Core Power (kw)	222.4	222.4
Pressurizer Pressure (MPa)	0.930 ± 0.110	0.930
Pressurizer Liquid Subcooling (K)	409.0 ± 1.7	409.0
Pressurizer Liquid Level (m)	0.21 ± 0.50	0.21
SG Pressure (MPa)	0.260 ± 0.110	0.323
SG Collapsed Liquid Level (m)	7.62 ± 0.50	7.62
Calculated:		
Upper Plenum Pressure (MPa)	0.930 ± 0.115	0.932
Core Flow (kg/s)	1.47 ± 0.075	1.41
Upper Plenum Temperature (K)	442.0 ± 1.7	445.3
Lower Plenum Temperature (K)	408.0 ± 1.7	409.4
Intact Loop (IL) Flow (kg/s)	1.11 ± 0.075	1.07
IL Hot Leg Temperature (K)	439.0 ± 1.7	(416.4)†
IL Cold Leg Temperature (K)	408.0 ± 1.7	410.3
Broken Loop (BL) Flow (kg/s)	0.36 ± 0.075	0.34
BL Hot Leg Temperature (K)	437.0 ± 1.7	(417.1)†
BL Cold Leg Temperature (K)	410.0 ± 1.7	409.8

†for MELCOR volume which includes uphill leg of SG U-tubes

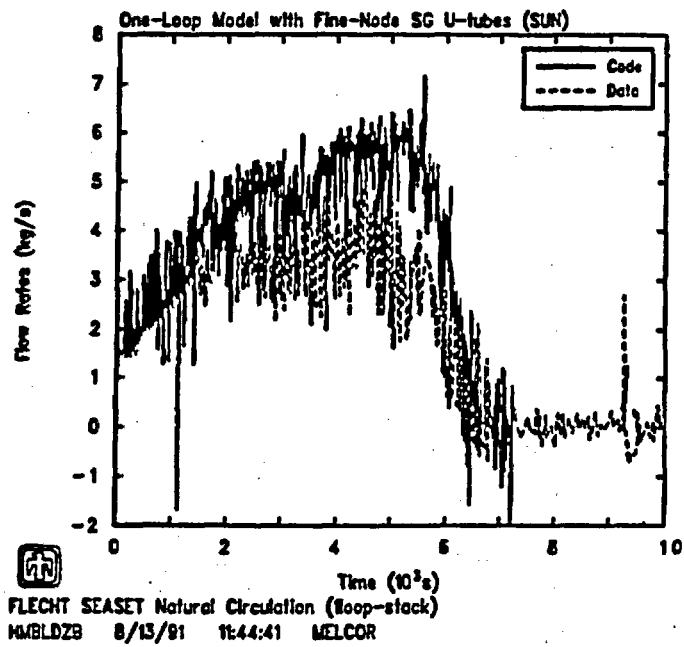
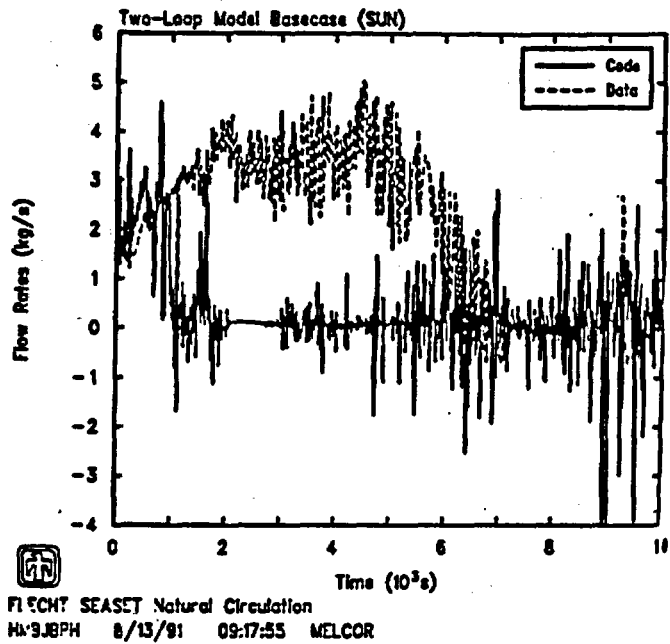


Figure 3.1. FLECHT SEASET Natural Circulation Mass Flows for Initial (top) and Final (bottom) MELCOR Calculations, Compared to Test Data

nonequilibrium physics model always used in the control volume. Other required input changes included enabling the nondefault bubble rise model to account for interactions of bubbles with the pool, and increasing the junction opening heights between vertically-stacked volumes.

With these various input modifications, the correct dependence of mass flow on system mass inventory was obtained; the pressure and temperatures were then calculated to be in good agreement with test data. However, even in this case, the two-phase flow was overpredicted by ~30%, possibly because of incorrect two-phase interface and/or wall friction code models. As in the single-phase liquid natural circulation calculations, the two-phase simulations experienced a lot of subcycling and repeated advancement attempts, and time step cycling.

No significant machine dependencies were seen in sensitivity studies for this problem; however, much smoother two-phase mass flow rates were calculated with a substantially reduced time step.

## 4 ACRR ST-1/ST-2 Source Term Experiments

The ACRR Source Term (ST) experiments [23, 24] provide time-resolved fission product release data to help validate models and to identify important release mechanisms. ST-1 and ST-2 were performed with the same temperature history, fuel characteristics, hardware configuration, sampling methods, and hydrogen partial pressure; the main difference in the experiment conditions was in the pressure and in the gas velocity through the fueled test section.

MELCOR has been used to simulate both the ST-1 and ST-2 experiments [11], using the CORSOR, CORSOR-M and CORSOR-Booth release models [21, 22]. Both release rates and total releases calculated by MELCOR generally agreed well with test data, as shown in Table 4.1. Both qualitative and quantitative differences between volatile and refractory species were correctly reproduced. The more volatile species (Xe, Cs, I and Kr) were released starting earlier and peaking earlier than the more refractory species (Ba, Sr and Te) and most of the initial inventories were released for the volatiles, while only part of the initial masses present were released for the more refractory species. Very low release fractions were predicted for the most refractory species (U and Zr) which agreed well with the limited test data.

None of the release model options produced consistently better agreement with test data for all species considered. The new CORSOR-Booth model matched the europium test data best, while CORSOR and CORSOR-M significantly underpredicted Eu release. CORSOR-Booth predicted less release of all volatiles than the nearly complete release calculated using either the CORSOR or CORSOR-M options; none of the models predicted the different release fractions measured for the various volatiles. CORSOR-Booth and CORSOR-M underpredicted the releases of refractory species such as Ba, Sr, Zr and U, while the CORSOR results for those species appear in good agreement with test data.

The MELCOR results also were compared directly to the release rate correlations as functions of temperature, using control functions, and to ST-1/ST-2 results obtained by Battelle using their standalone CORSOR code, to verify that the models have been implemented correctly within MELCOR.

Because the release is a very strong function of temperature, it was important to match the experimental temperature distribution as well as possible. Sensitivity studies showed no signifi-

cant temperature dependence on changes in power, pressure or gas flow (within the experimental uncertainties and variations), or on convective heat transfer coefficients; the temperatures calculated were sensitive to the insulation thermal conductivity and the view factors used in radiation heat transfer from the fuel to the shroud.

Sensitivity studies checking for time step and noding effects, and for machine dependencies, were done. The major problem identified was a machine dependency associated with exponentials and very small numbers; it resulted in significantly different releases being predicted on different machines for refractory species. Other problems associated with differences in round-off of small numbers were also found. All these problems were corrected immediately, and no machine dependencies were found in our final calculations.

## 5 LOFT LP-FP-2

MELCOR has been used to model experiment LP-FP-2 [25, 26, 27, 28, 29, 30, 31], which simulates many of the primary system and core thermal/hydraulic conditions that would be expected during a PWR V-sequence. The relatively large scale of the test and the extensive instrumentation used make the LP-FP-2 experiment an important integral source of data for qualifying severe accident code predictive capabilities.

Our MELCOR results [12] can be put into perspective best, perhaps, by examining them in relation to the performance of other codes in predicting this very challenging experiment [31]. MELCOR does at least as well as other "best-estimate" (*i.e.*, SCDAP/RELAP5) or integral (*i.e.*, MAAP) codes in predicting the thermal/hydraulic and core responses in this experiment, as shown in Figures 5.1 and 5.2; in fact, MELCOR and MAAP appear to give the best agreement with data, especially for clad temperature histories. Further, MELCOR does at least as well as "best-estimate" fission product codes in predicting the source term (with a number of such codes having to be run in tandem and driven by test data or other "best-estimate" thermal/hydraulic and code damage codes to provide results equivalent to a single, integrated MELCOR calculation), as shown in Table 5.1.

The predicted primary system pressure was generally lower than measured, while the predicted primary system mass inventory was generally higher than measured, but with a large uncertainty on the test data. The pressurizer was predicted to empty within 1min, in good agreement with test data, and the early-time intact-loop mass flow also was calculated in good agreement with measurement, despite the lack of a complicated pump coastdown model in MELCOR. Despite the differences in calculated and observed thermal/hydraulic response, the core uncover, dryout and onset of clad heatup were calculated in excellent agreement with thermocouple data.

Sensitivity studies on parameters which directly affect the thermal/hydraulic response showed a significant dependence on several break flow modelling parameters, including areas, discharge coefficients and loss coefficients used. Results showed little or no dependence on structural heat transfer, either on the magnitude of the convective heat transfer coefficients or on the correlation sets ("int" vs "ext") and characteristic lengths used, on the radiative heat transfer emissivity or path length used, or on the modelling of piping insulation, on bubble rise physics in flow paths, or on secondary system leakage. The sensitivity studies did find a strong dependence on the junction opening heights used in flow paths connecting vertical stacks of control volumes, particularly at the core inlet and outlet.

Table 4.1. Aerosol and Fission Product Vapors Released from Fuel in ST-1

Element	Test Data	Percent (%)						
		VICTORIA[24]	Standalone CORSOR[22]			MELCOR		
			CORSOR	CORSOR-M	CORSOR-Booth	CORSOR <sup>1</sup>	CORSOR-M <sup>1</sup>	CORSOR-Booth
Xe		100	100	100	58.5	98.1-99.3	98.8-99.6	55.6
Cs	71‡-56‡	94	100	100	58.5	98.1-99.3	98.8-99.6	55.6
Ba	8‡+3.2‡	27-39	16.75	0.88	4.1	11.0-14.0	0.48-0.63	4.30
I	38‡	81	100	100	58.5	98.1-99.3	98.8-99.6	55.6
Te	<0.2‡		19.1¶	100¶	2.0	0.31-0.40	15.2-19.2	2.18
Kr	100		100	100	58.5	98.1-99.3	98.8-99.6	55.6
Sr	5‡+ ≤0.43‡		16.75	0.88	4.1	4.07-5.25	0.48-0.63	4.30
Zr	≥0.034‡		0.016	0	0.0026	0.017-0.042	0.00001-0.0002	0.005
Eu	15‡-5‡		0.024	0	8.4	0.014-0.018	0	8.38
U	0.011‡		0.024	0.007	0.0088	0.014-0.018	0.003-0.004	0.009
Sn			49.03	7.18	4.1	32.9-39.9	4.45-5.73	4.30

<sup>1</sup> values without-with surface/volume correction term

¶ apparently not scaled by 1/40

‡ amount released (measured by gamma scans)

‡ amount collected (measured by filters)

‡ amount collected (measured in water leachates)

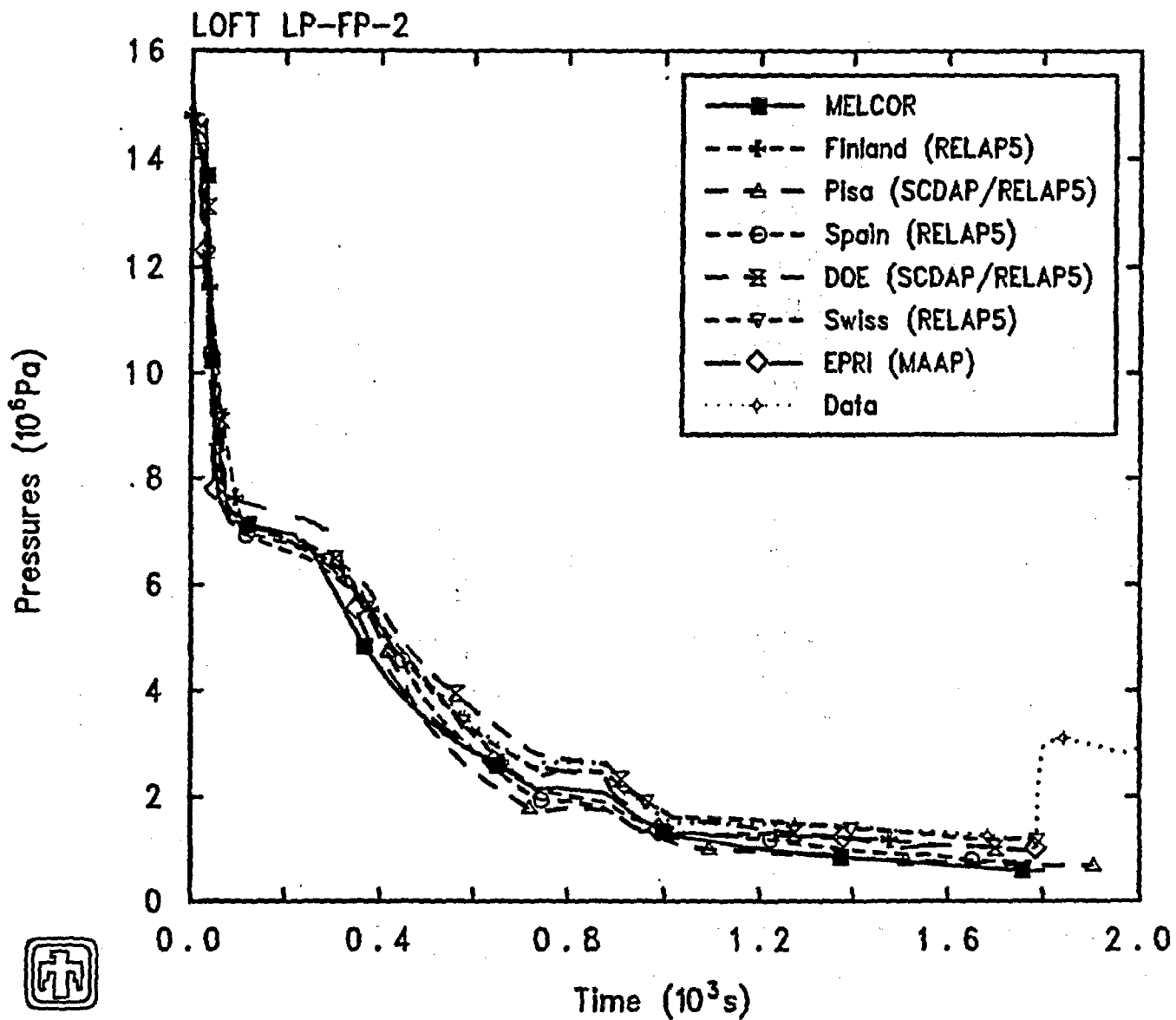
428

Table 5.1. LOFT LP-FP-2 Source Terms

Class	Data ([31])	CFM Radionuclide Release (% CFM Initial Inventory)					
		MELCOR			INEL		Spain
		CORSOR‡	CORSOR-M‡	CORSOR-Booth‡	CORSOR	FASTGRASS	
1 (Xe)	2.5-2.8	6.977/8.376	8.124/10.74	3.718/1.744	44.5	5.3	9.58
2 (Cs)	2.9	6.976/8.371	8.125/10.74	3.337/1.653	44.5	3.0	8.1
3 (Ba)		0.157/0.192	0.0058/0.0069	0.0150/0.0089	2.22		
4 (I)	5.2	6.973/8.372	8.120/10.73	3.715/1.739	44.5	3.0	8.1
5 (Te)	0.54	0.171/0.267	3.985/6.559	1.880/0.863	1.75	0.058	4.31

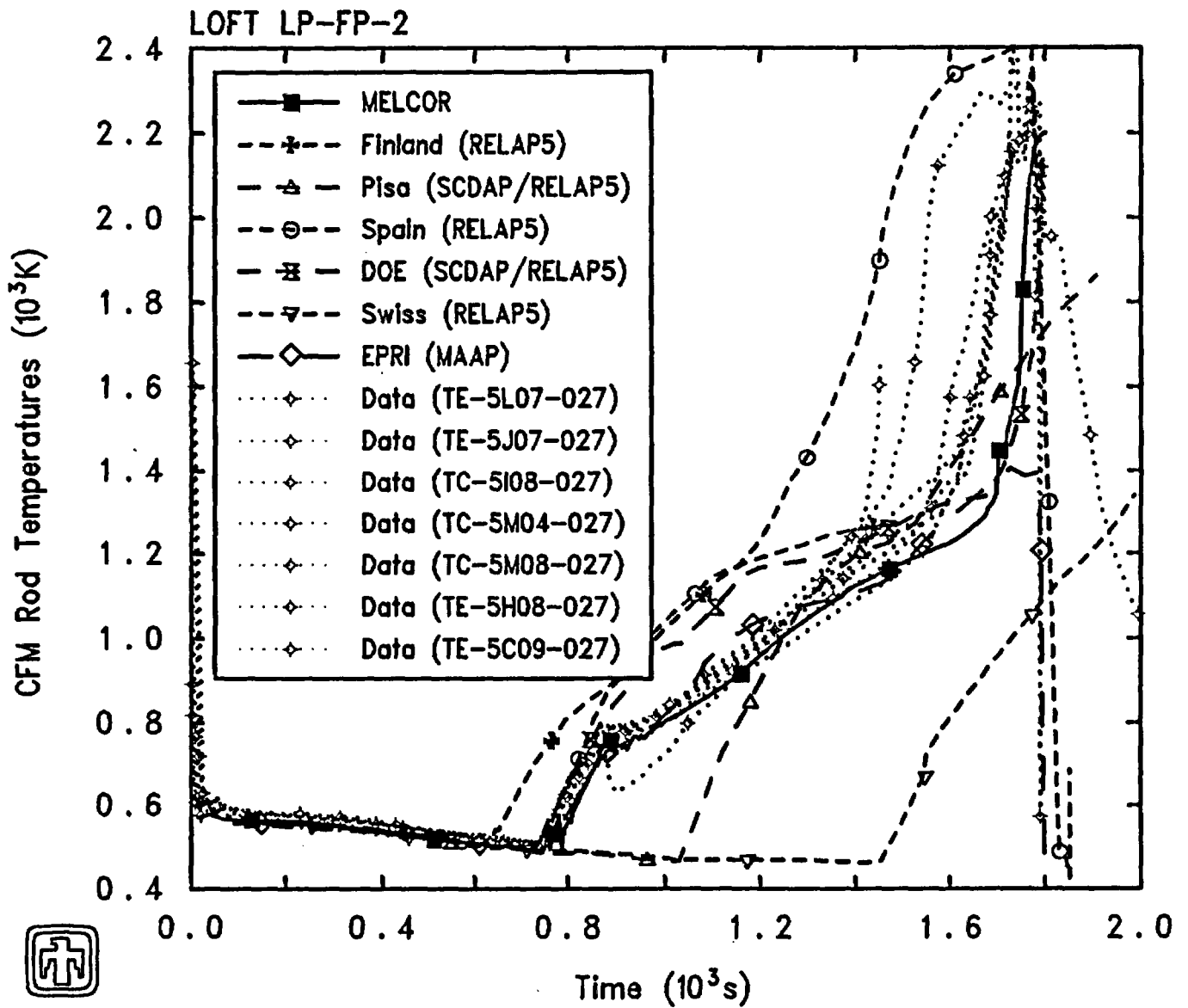
‡ values without/with surface-volume correction term

‡ values using low-burnup/high-burnup coefficients



LOFT LP-FP-2 (12level-core)  
 GYCUCTPKR 7/25/92 20:31:03 MELCOR

Figure 5.1. LOFT LP-FP-2 Primary System Pressure Predicted by MELCOR, Compared to Test Data and to Results from Other Code Calculations



LOFT LP-FP-2 (12level-core)  
 GYCUCTPKR 7/25/92 20:31:03 MELCOR

Figure 5.2. LOFT LP-FP-2 CFM Mid-Core Clad Temperature Predicted by MELCOR, Compared to Test Data and to Results from Other Code Calculations

The core heatup predicted was in very good agreement with test data (even to the effect of enhanced core cooling and a partial rewet soon after core dryout and uncover) until the onset of rapid metal-water reaction late in the transient. This behavior could not be predicted using the default models and parameters in MELCOR, but required changing the temperature switching from a low-temperature to a high-temperature set of Zircaloy oxidation rate constants.

Post-irradiation examination (PIE) of the central fuel module (CFM) [30] concluded that the material relocation and stratification in LP-FP-2 resulted in low-melting-point metallic melts near the bottom of the fuel bundle, a high-temperature (U,Zr)O<sub>2</sub> ceramic melt region above this, and a debris bed of fuel pellets near the top of the fuel bundle. The final material distribution in MELCOR is in reasonable qualitative agreement with the test results. A debris bed consisting mostly of solid UO<sub>2</sub> fragments overlies a central region where much of the oxidized and unoxidized Zircaloy clad has refrozen, with the steel in the other structure refreezing at a somewhat lower average elevation and the control rod poison material flowing down to the lower core and core support plate before refreezing. The PIE identified a 79-86% blockage due to material relocation and stratification in LP-FP-2. There is no internal blockage model in MELCOR. With flow blockage approximated *via* input at  $\geq 1400s$ , predicted clad temperatures are in better agreement with data; the agreement might be improved further if the blockage could be modelled as occurring at the "correct" (moving) core elevation, rather than simply at the CFM inlet.

The hydrogen generated in our MELCOR analyses is in good agreement with data. The reference MELCOR calculation, with the inner Zircaloy liner of the insulating shroud assumed to oxidize at the same temperature and rate as the adjacent clad, showed 267g of hydrogen in the BST, while a sensitivity study in which oxidation of the shroud inner liner was neglected gave 218g of hydrogen in the BST. Two experimental data sets are available for comparison. Grab samples from the suppression pool indicating  $205 \pm 11g$  reflect hydrogen generation during the transient because the tank was isolated just prior to reflood; the PIE indicated 63g and 118g of hydrogen, respectively, generated as a result of Zircaloy oxidation in cladding shells and in relocated material in the lower bundle, for a total of  $\sim 181g$ .

Modelling the CFM shroud proved important primarily because of its effect on preventing radiative heat transfer and coolant temperature equilibration in the two parallel, isolated core flow channels. Minor changes were noted as a result of varying Zircaloy melt temperature or core axial nodding resolution, eliminating a gaseous diffusion oxidation rate limit or axial conduction, or varying convective heat transfer in the core, refreezing heat transfer coefficient values, minimum oxide shell thicknesses for material holdup or other structure composition (*i.e.*, steel or Inconel).

Significant fractions of the most volatile species (Xe, Cs and I) were released using both the CORSOR and CORSOR-M expressions, with all three classes having nearly equal releases of  $\sim 7-11\%$  (with the test data in the lower half of this range, with more I found released than Cs, Xe and Kr). Only the gap inventories were released for the most highly refractory species (*e.g.*, Ce, La and U) for all options, and also for Ru, Mo and Cd in the CORSOR-M version. CORSOR gave higher releases for several classes (Ba, Mo, Cd and Sn, and - to a lesser degree - Ru), while CORSOR-M produced significantly higher release of Te (with data indicating a Te source term somewhere inbetween). CORSOR-Booth predicted significantly lower releases (2-4%) for the most volatile species (Xe, Cs and I) than either of the older CORSOR options, in very good agreement with test data, while the releases of other species (Ba, Te, Cd and Sn) were intermediate between the CORSOR and CORSOR-M predictions. Calculations were done

with both the low- and high-burnup CORSOR-Booth default constants, although the CFM fuel in the LP-FP-2 test would clearly lie on the low-burnup side of the expressions.

Different initial gap release times were calculated with the different CORSOR and CORSOR-Booth options in MELCOR, indicating that some differences existed in these source-term sensitivity study calculations prior to clad failure. MELCOR analyses using CORSOR-M (with and without using MELCOR's optional surface/volume correction term) showed identical results up to the time of first clad failure and gap release, but this was not the case in preliminary calculations; a number of code problems had to be identified and corrected to obtain this expected result. We also thought that no differences should exist in calculations varying assorted MAEROS parameters prior to clad failure and subsequent aerosol release, but found that small differences were caused by the effect of the MAEROS input parameter changes on water droplets present in control volume atmospheres during the first portion of the transient (confirmed in a sensitivity study with specification of zero fog density through sensitivity coefficient input.)

Both machine-dependency and time-step studies, and evaluation of the new heat transfer model for partially covered core cells, indicate strongly that additional time step controls must be developed in the COR and/or CVH packages to avoid what appear to be unphysical, numerically-driven liquid level oscillations during core uncover and dryout, and valve-setpoint over- and undershoots. The Cray, VAX, and SUN and IBM workstations gave very similar results, while the "same" analysis done on a 486-PC gave visibly different results throughout most of the latter half of the transient, primarily due to the increase in both number and magnitude of liquid level oscillations during core uncover. Increasing the time steps used generally resulted in progressively larger and more numerous liquid level oscillations.

Our results indicate that more separate-effects assessment of MELCOR is needed, particularly for break flow in the early-time thermal/hydraulics and for rapid metal-water reaction during core damage. Numerical effects were significant in both the COR and HS packages for heat transfer under two-phase conditions, in the COR and CVH packages for liquid level oscillations during core dryout, and in the CVH and FL packages for valve setpoint over- and undershoots. New time step control algorithms are now being developed to check and adjust for rapid liquid level changes in control volumes, and for valve setpoint over- and undershoots; preliminary results indicate that these will resolve many of the outstanding difficulties in these LOFT analyses.

This LOFT LP-FP-2 assessment analysis clearly demonstrates MELCOR's ability to fulfill a large portion of its primary intended use, the calculation of severe accidents from full-power steady-state initiation through primary-system thermal/hydraulic response and core damage to fission product release, transport and deposition. After a number of identified code errors were corrected, few nonstandard inputs and no code problem-specific modifications were needed to provide reasonable agreement with test data in all areas considered.

## **6 Marviken-V ATT-2b/ATT-4 Primary System Aerosol Transport and Deposition**

A series of five aerosol transport test (ATT) experiments were done in the large-scale Marviken facility investigating the behavior of vapors and aerosols under typical LWR primary system accident conditions.

MELCOR calculations have been completed for test ATT-2b and are currently underway for test ATT-4. In test ATT-2b [33], the system geometry consisted of a pressurizer and four pipe sections followed by a relief tank, which was used to scrub materials which would otherwise escape the system; the fission aerosol was injected horizontally, near the bottom of the pressurizer. In test ATT-4 [34], the aerosol was injected into a simulated reactor vessel containing internal structures, whose top was connected by piping to the pressurizer volume and the remainder of the fission transport system.

The results for test ATT-2b showed that MELCOR could match most of the pressurizer and piping gas and wall temperature histories, after an extra flow path representing internal circulation in the pressurizer was added. Sensitivity studies were done on thermal/hydraulic parameters, such as amount of internal recirculation and wall emissivity, and on aerosol modelling parameters, such as the number of MAEROS components and sections. Both the pressurizer and the downstream piping were subdivided into a number of control volumes as a "best-estimate" model of the facility, and nodding studies were done progressively combining volumes until a nodding typical of plant calculations was used. Because no data were given on the size of the aerosol particles injected, results have been compared for a range of initial aerosol average diameters; the aerosol deposition results were generally in reasonable agreement with test data when a relatively large initial diameter (5/*mum*) was assumed.

The MELCOR results for ATT-2b are compared to results from corresponding TRAPMELT2-UK [35, 36, 37], VICTORIA [38] and TRAP-MELT2 [39] analyses in Table 6.1.

Identical calculations for test ATT-2b were run on a Cray, SUN and IBM workstations, VAX and 486 PC, and otherwise identical calculations were run on the SUN using the code-selected time step (generally in the 0.7-0.9s range), and with the user-input maximum allowed time step progressively reduced to 0.5, 0.25, 0.1 and 0.01s. No machine dependencies or time step effects were seen, except for a 5-10% reduction in aerosol deposition using the smallest (0.01s) time step.

## 7 PNL Ice Condenser Tests 11-6 and 16-11

MELCOR has been used to simulate ice condenser tests 11-6 and 16-11, two of a series of large-scale experiments conducted at the High Bay Test Facility (HBTF) at Pacific Northwest Laboratories (PNL) to investigate the extent to which an ice condenser may capture and retain air-borne particles [40]. Experiment 11-6 was a low-flow test, while experiment 16-11 was a relatively high-flow test; in both tests, ZnS was used as the aerosol and temperatures and particle retention were monitored.

MELCOR results [14] have been compared to experimental data, and also to the results of CONTAIN calculations [41, 42] for these two tests. MELCOR version 1.8LF was used for the final calculations.

Agreement was very good between MELCOR predictions and PNL experimental data. MELCOR particle retention results agreed qualitatively with the data in that the value began at one and decreased quickly, levelled out during the time that the ice was melting, and then finally began decreasing again late in the experiment when the ice supply had been exhausted. Quantitative agreement with the experimental results was also excellent, based on the few values given for the experimental particle retention, as shown in Table 7.1. Agreement with

**Table 6.1. Cesium Retention in Primary System in Marviken-V Aerosol Transport Test ATT-2b**

Location	Data	Cesium Retention (% Total Cs Injected)			
		MELCOR†	TRAPMELT2-UK‡	TRAP-MELT2¶	VICTORIA§
<b>Pressurizer</b>					
Wall Runoff	1.09				
Bottom	35.04	6.0-37.5			
Lower Wall	3.30	2.1-1.2			
Middle Wall	0.61	2.7-1.6			
Upper Wall	0.60	1.2-0.6			
Top	0.58	0.1			
Total	41.22	12.1-40.8	10-70	87/25/34	27-35
<b>Piping</b>					
LOS4	0.30	0.2-0.1		0.29/0.10/0.11	
LOS5	3.93	12.2-22.1		1.60/0.86/0.94	
LOS6	0.27	1.5-0.6		0.04/0.08/0.05	
Total	4.50	13.9-22.7	10-15	1.9/1.0/1.1	5-10

†0.5-5.0 $\mu$ m range of initial AMMD  
‡1-35 $\mu$ m range of initial AMMD  
¶0.2/3.4/2.0 $\mu$ m range of initial AMMD  
§different pressurizer nodings

temperature data was also excellent, as shown in Figure 7.1, with MELCOR results usually falling within the low-temperature/high-temperature experimental data envelope; the time at which all of the ice in a region melted also was well-predicted by MELCOR.

The MELCOR results were in better agreement with experimental data for particle retention than the CONTAIN results, as indicated in Table 7.1. On average, MELCOR and CONTAIN results were quite similar for the diffuser inlet and outlet temperatures, although differences in nodalization complicate the comparison. Unfortunately, there was no CONTAIN data published or available for temperatures in the ice-condenser region, the region of most interest.

A number of sensitivity studies were performed for each experiment simulation, also. The results of a time step study showed a small time step dependency with the results clearly converging with reduced time steps. No machine dependencies were observed when running the same problems on a Cray-XMP/24, SUN Sparc2, IBM RISC-6000 Model 550, VAX 8650 and 486 PC.

Thermal/hydraulic sensitivity studies examined the effects of varying flow loss coefficients, equilibrium vs nonequilibrium thermodynamics, and including SPARC bubble rise physics. Parameters associated with the aerosol input examined through sensitivity studies included number of aerosol components, number of aerosol sections, aerosol particle density and aerosol particle size range. The last set of studies examined the effect of varying input parameters associated with the ice condenser model directly, and included varying the energy capacity of the ice, the ice heat transfer coefficient multiplier, the ice heat structure characteristic length, the number of nodes in the ice condenser heat structure, and radiation heat transfer for the ice condenser heat structure.

## 8 Surry TMLB' with and without DCH

As part of the MELCOR Peer Review process [43], Sandia performed and presented a demonstration calculation of a Surry station blackout (TMLB') accident with MELCOR. This was the first fully-integrated PWR severe accident calculation performed with the code (since the TMI analysis only included in-vessel phenomena).

That analysis is continuing, investigating problems identified by the Peer Review (e.g., lack of pressurizer draining prior to vessel breach), evaluating the impact on the results of

**Table 7.1. Aerosol Particle Retention in Ice Condenser Tests**

Time Period	Data	Aerosol Particle Retention (%)				
		Test 11-6		Test 16-11		
		MELCOR	CONTAIN	Data	MELCOR	CONTAIN
Initial	86	100	-	95.9	100	-
Average	78	80	67.7	93.7	94	89
Final	73	70	67.7	88	91	65

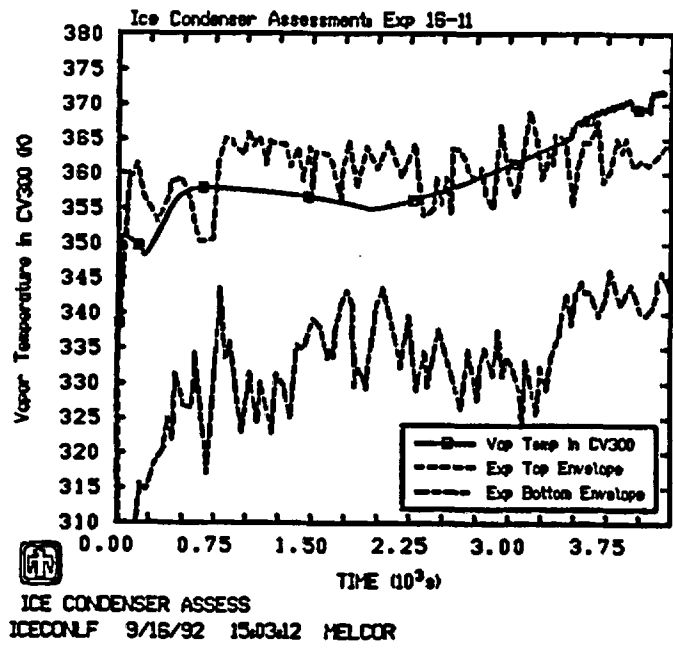
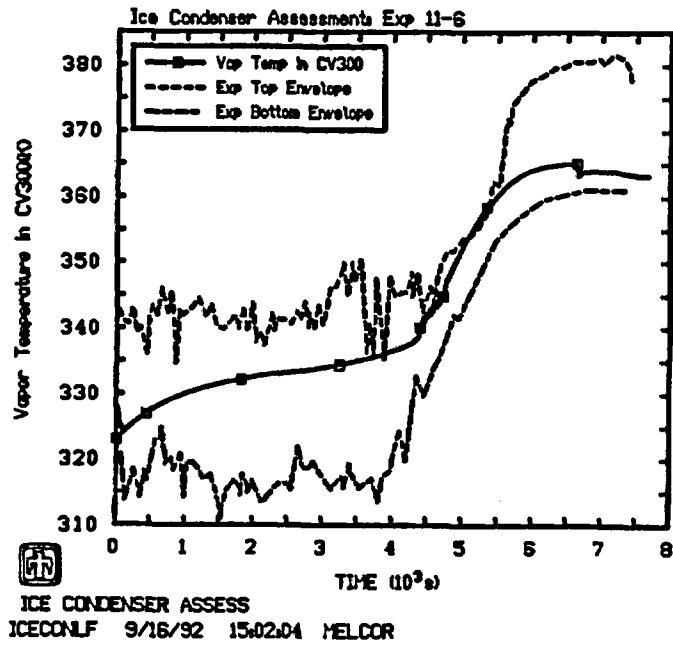


Figure 7.1. Temperatures in Lower Region of Ice Condenser Predicted by MELCOR for PNL Tests 11-6 (top) and 16-11 (bottom), Compared to Test Data Envelope

model improvements and of new models (such as radial debris relocation or direct containment heating due to high pressure melt ejection), and studying nodding and modelling sensitivities (for example, comparing releases predicted using the various CORSOR options).

Preliminary sensitivity studies have been done checking for time step and nodding effects, and for machine dependencies, and a number of numeric effects have been identified. The reference analysis has been run on a Cray, VAX, SUN and IBM workstations, and 486 PC, and with the code-selected time step and then the maximum allowable time step set by user input to 5, 2.5 and 1s.

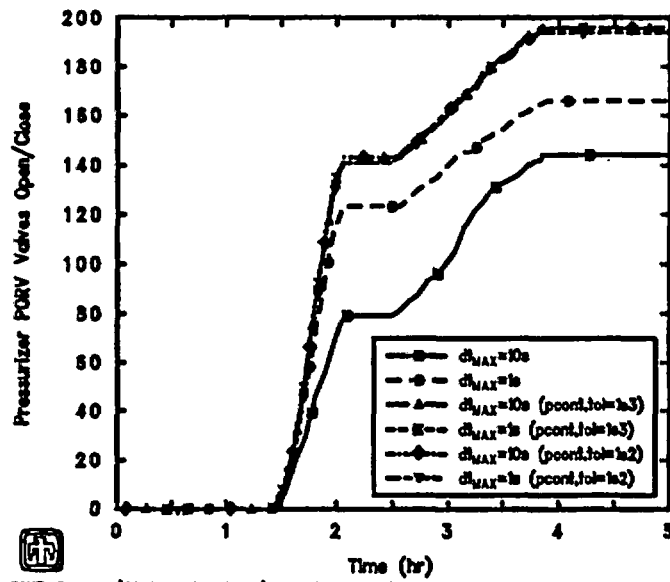
In both the machine-dependency and time-step studies, differences were noted early in the transient in the number of times that the steam generator secondary relief valve and, later, the pressurizer PORV cycled. Those differences were traced to differences in over- and undershooting the valve controller setpoint pressures with different time steps and/or different machine accuracies. The tabular function logic was modified to allow step function input, to minimize valves getting caught in a part-open state interpolating between table entries. A time-step controller is now being tested which is intended to limit the time step whenever a valve pressure setpoint is being approached in the control volume. Figure 8.1 shows that this addition to the code's time-step control algorithm significantly decreases the numeric sensitivity, but some small effect still remains to be identified.

The differences seen in timing of key events such as clad failure, core plate failure, lower head penetration failure, *etc.*, in these machine-dependency and time-step studies vary by much smaller times (on the order of 10-100s) than the timestep-variation results presented by BNL to the Peer Review for their Peach Bottom station blackout analysis (which often varied by 1,000-10,000s). A large part of this reduction in numeric sensitivity probably represents the significant efforts of the code developers since the Peer Review in identifying and eliminating numeric sensitivities in MELCOR. Unfortunately, we have no comparable results of time-step studies for the more recent BNL Oconee analyses.

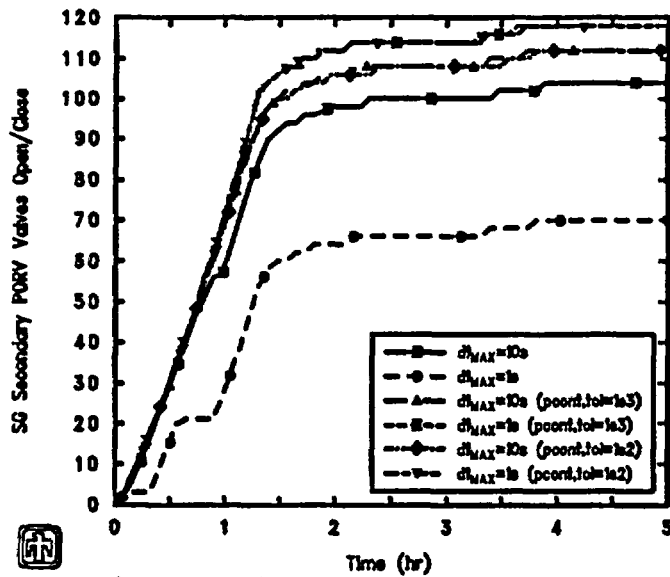
The times of lower core plate and lower head penetration failures are significantly affected by the new debris radial relocation model, with results showing material flowing from all core rings to and through the first core ring to fail the lower core support plate, and then to and through the first ring to fail the lower head. The new direct containment heating model in MELCOR, which models high pressure melt ejection from the vessel into containment, is being used in these PWR TMLB' analyses. Sensitivity studies have been done varying the relative amounts of melt deposited directly in the cavity, in the various containment volume atmospheres, and on various heat structures in the dome, basement and cavity.

A numeric effect recently identified in these PWR demonstration analyses is a big difference (up to 10,000s) in the time that hydrogen burns occur in containment, which in turn can significantly impact on containment failure times and releases to environment, on our machine-dependency and time-step sensitivity studies. This is currently being investigated.

We plan to use a new eutectics model for core material interactions and an in-vessel natural circulation model now being developed for these PWR TMLB' demonstration calculations as soon as available.



PWR Demo (Station Blockout) -  $dt_{max}=10s$   
 G2CODKXKT 7/29/92 14:38:23 MELCOR



PWR Demo (Station Blockout) -  $dt_{max}=10s$   
 G2CODKXKT 7/29/92 14:38:23 MELCOR

Figure 8.1. SG Secondary and Pressurizer Valve Cycling in PWR TMLB'

## 9 Summary and Recommendations

The MELCOR assessment program at Sandia is significantly expanding the available MELCOR validation database. A review of MELCOR verification, validation and assessment to date reveals that most of the severe accident phenomena modelled by MELCOR have received or are receiving some evaluation.

Figure 9.1 summarizes the available MELCOR assessment against experimental test data, for in-vessel and containment phenomenology, respectively. Only analyses that are completed or already underway are included; analyses scheduled but not yet begun are not included.

However, in many of these areas, the assessment to date does not cover all phenomena of interest, or is based on a limited number of experiments and analyses which may be insufficient to cover the scales of interest and which may be insufficient to allow identification of experiment-specific problems *vs* generic code problems and deficiencies. Furthermore, there has been no assessment at all of MELCOR for ex-vessel melt phenomena such as core-concrete interactions, debris bed coolability or direct containment heating (although some assessment of the new MELCOR DCH model is planned, and the core-concrete interaction model has had some inherited validation from the standalone CORCON assessment activities). And, although SNL has assessed the new ice condenser model, there has been no assessment against test data for hydrogen burns or for other engineered safety features such as containment sprays and/or fans.

There is no experiment (not even the TMI accident) which represents all features of a severe accident (*i.e.*, primary system thermal/hydraulics; in-vessel core damage; fission product and aerosol release, transport and deposition; ex-vessel core-concrete interaction; containment thermal/hydraulics; and hydrogen transport and combustion), and only the TMI accident is at full plant scale. It is therefore necessary for severe accident codes to supplement standard assessment against experiment (and against simple problems with analytic or otherwise obvious solutions) with plant calculations that cannot be fully verified, but that can be judged using expert opinion for reasonableness and internal self-consistency (particularly using sensitivity studies) and also can be compared to other code calculations for consistency.

## Bibliography

- [1] R. M. Summers *et al.*, "MELCOR 1.8.0: A Computer Code for Severe Nuclear Reactor Accident Source Term and Risk Assessment Analyses", NUREG/CR-5531, SAND90-0364, Sandia National Laboratories, January 1991.
- [2] B. E. Boyack, V. K. Dhir, J. A. Gieseke, T. J. Haste, M. A. Kenton, M. Khatib-Rahbar, M. T. Leonard, R. Viskanta, "MELCOR Peer Review", LA-12240, Los Alamos National Laboratory, March 1992.
- [3] C. D. Leigh, ed., "MELCOR Validation and Verification - 1986 Papers", NUREG/CR-4830, SAND86-2689, Sandia National Laboratories, March 1987.
- [4] E. A. Boucheron and J. E. Kelly, "MELCOR Analysis of the Three Mile Island Unit 2 Accident", Nuclear Technology 87, December 1989.

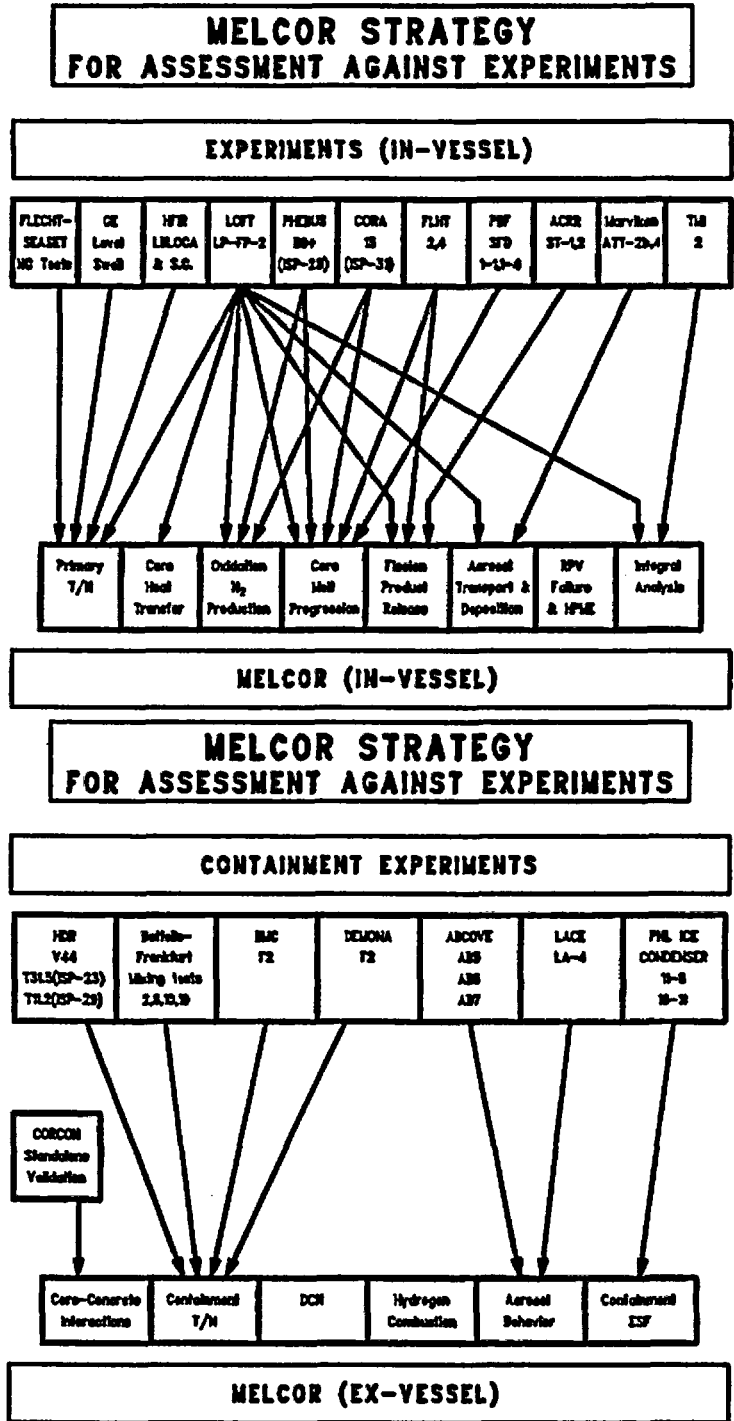


Figure 9.1. MELCOR Phenomena Assessment to Date

- [5] G. M. Martinez, "MELCOR Post-Test Calculations of the HDR Experiment", letter report to R. B. Foulds, NRC, September 29, 1989.
- [6] G. M. Martinez, "MELCOR Calculations of ISP28 SFD PHEBUS Test B9+", Letter report to B. Adroguer, CEN/Cadarache, France, dated December 14, 1990.
- [7] G. M. Martinez, "MELCOR Calculations of ISP28 SFD PHEBUS Test B9+", Letter report to F. Eltawila, NRC, dated December 20, 1991.
- [8] R. J. Gross, S. L. Thompson, G. M. Martinez, "MELCOR Simulation of the International Standard Problem ISP-31", Letter report to M. Firnhaber, GRS, March 6, 1992.
- [9] L. N. Kmetyk, "MELCOR 1.8.1 Assessment: LACE Aerosol Experiment LA4", SAND91-1532, Sandia National Laboratories, September 1991.
- [10] L. N. Kmetyk, "MELCOR 1.8.1 Assessment: FLECHT SEASET Natural Circulation Experiments", SAND91-2218, Sandia National Laboratories, December 1991.
- [11] L. N. Kmetyk, "MELCOR 1.8.1 Assessment: ACRR Source Term Experiments ST-1/ST-2", SAND91-2833, Sandia National Laboratories, April 1992.
- [12] L. N. Kmetyk, "MELCOR 1.8.1 Assessment: LOFT Integral Test LP-FP-2", SAND92-1373, Sandia National Laboratories, to be published.
- [13] L. N. Kmetyk, "MELCOR 1.8.1 Assessment: Marviken-V Aerosol Transport Tests ATT-2b/ATT-4", SAND92-2243, Sandia National Laboratories, to be published.
- [14] R. J. Gross, "MELCOR 1.8.1 Assessment: PNL Ice Condenser Tests 11-6 and 16-11", SAND92-2165, Sandia National Laboratories, to be published.
- [15] F. J. Rahn, "The LWR Aerosol Containment Experiments (LACE) Project Summary Report", EPRI NP-6094-D, LACE TR-012, Electric Power Research Institute, November 1988.
- [16] J. D. McCormack, *et al.*, "Final Report of Experimental Results of LACE Test LA4 - Late Containment Failure with Overlapping Aerosol Injection Periods", LACE TR-025, Westinghouse Hanford Company, October 1987.
- [17] K. K. Murata *et al.*, "User's Manual for CONTAIN 1.1: A Computer Code for Severe Nuclear Reactor Accident Containment Analysis", NUREG/CR-5026, SAND87-2309, Sandia National Laboratories, November 1989.
- [18] F. Gelbard, J. L. Tills, K. K. Murata, "CONTAIN Code Calculations for the LA-4 Experiment", Sandia National Laboratories, Proceedings, 2nd International Conference on Containment Design and Operation, Oct. 14-17, 1990, Vol. 2.
- [19] E. R. Rosal *et al.*, "PWR FLECHT SEASET Systems-Effects Natural Circulation and Reflux Condensation: Task Plan Report", NUREG/CR-2401, EPRI NP-2015, WCAP-9973, NRC/EPRI/Westinghouse Report No. 12, March 1983.
- [20] L. E. Hochreiter *et al.*, "PWR FLECHT SEASET Systems Effects Natural Circulation and Reflux Condensation: Data Evaluation and Analysis Report", NUREG/CR-3654, EPRI NP-3497, WCAP-10415, NRC/EPRI/Westinghouse Report No. 14, August 1984.

- [21] M. R. Kuhlman, D. J. Lehmicke, R. O. Meyer, "CORSOR User's Manual", NUREG/CR-4173, BMI-2122, Battelle Memorial Institute, March 1985.
- [22] M. Ramamurthi, M. R. Kuhlman, "Final Report on Refinement of CORSOR - An Empirical In-Vessel Fission Product Release Model", Battelle Memorial Institute, October 31, 1990.
- [23] M. D. Allen, H. W. Stockman, K. O. Reil, J. W. Fisk, "Fission Product Release and Fuel Behavior of Irradiated Light Water Reactor Fuel Under Severe Accident Conditions: The ACRR ST-1 Experiment", NUREG/CR-5345, SAND89-0308, Sandia National Laboratories, November 1991.
- [24] M. D. Allen, H. W. Stockman, K. O. Reil, A. J. Grimley, W. J. Camp, "ACRR Fission Product Release Tests: ST-1 and ST-2", SAND88-0597C, presented at the International Conference on Thermal Reactor Safety, Avignon, France, October 2-7, 1988.
- [25] J. P. Adams, J. C. Birchley, N. Newman, E. W. Coryell, M. L. Carboneau, S. Guntay, L. J. Siefken, "Quick-Look Report on OECD LOFT Experiment LP-FP-2", OECD LOFT-T-3804, EG&G Idaho, Idaho National Engineering Laboratory, September 1985.
- [26] M. L. Carboneau, R. L. Nitschke, D. C. Mecham, E. W. Coryell, J. A. Bagues, "OECD LOFT Fission Product Product Experiment LP-FP-2: Fission Product Data Report", OECD LOFT-T-3805, EG&G Idaho, Idaho National Engineering Laboratory, May 1987.
- [27] M. L. Carboneau, V. T. Berta, S. M. Modro, "Experiment Analysis and Summary Report for OECD LOFT Fission Product Experiment LP-FP-2", OECD LOFT-T-3806, EG&G Idaho, Idaho National Engineering Laboratory, June 1989.
- [28] J. J. Pena, S. Enciso, F. Reventòs, "Thermal-Hydraulic Post-Test Analysis of OECD LPFT LP-FP-2 Experiment", OECD LOFT-T-3807, OECD LOFT Spanish Consortium (CIEMAT, CSN, ENRESA, ENUSA, UNESA, UPM), March 1988. March 1988.
- [29] J. Blanco *et al.*, "OECD LOFT Experiment LP-FP-2 Fission Product Behavior Analysis", OECD LOFT-T-3809, EG&G Idaho, Idaho National Engineering Laboratory, September 1988.
- [30] S. M. Jensen, D. W. Akers, B. A. Pregger, "Postirradiation Examination Data and Analyses for OECD LOFT Fission Product Experiment LP-FP-2; Volumes 1 and 2", OECD LOFT-T-3810, EG&G Idaho, Idaho National Engineering Laboratory, December 1989.
- [31] "OECD LOFT Code Comparison Report; Volume 1: Thermal-Hydraulic Comparisons; Volume 2: Fission Product Comparisons", OECD LOFT-T-3811, EG&G Idaho, Idaho National Engineering Laboratory, February 1990.
- [32] A. Sharon, R. E. Henry, M. A. Kenton, "MAAP 3.0 Simulation of OECD LOFT Experiment LP-FP-2", EPRI NP-6178-L, Fauske & Associates for Electric Power Research Institute, March 1989.
- [33] J. Price, Ed., "MXE-202b Interim Report: Results from Test 2b, Studsvik - The Marviken Project", MXE-202b, Marviken, studsvik, April 1984.

- [34] A. Magnusson, Ed., "MXE-204 Interim Report: Results from Test 4, Studsvik - The Marviken Project", MXE-204, Marviken, studsvik, June 1986.
- [35] D. A. Williams, A. T. D. Butland, "Preliminary Analysis of the Marviken Aerosol Transport Tests 1, 2a and 2b using the TRAPMELT-2 Computer Code", AEEW-M2147, UKAEA Winfrith, October 1984.
- [36] D. A. Williams, "Further Analyses of the Marviken Aerosol Transport Tests 1, 2a and 2b using the TRAPMELT2-UK Computer Code", AEEW-M2298, UKAEA Winfrith, April 1986.
- [37] D. A. Williams, "Analyses of the Marviken Aerosol Transport Tests 4 and 7", AEEW-M2371, UKAEA Winfrith, December 1986.
- [38] D. A. Williams, "Nodalisation of the Marviken Pressuriser and Inter-Volume Gravitational Settling", UKAEA AEEW-R2499, April 1989.
- [39] M. R. Kuhlman, V. Kogan, P. M. Schumacher, "TRAP-MELT2 Code: Development and Improvement of Transport Modeling", NUREG/CR-4667, BMI-2141, Battelle Columbus, July 1986.
- [40] M. W. Ligothke, E. J. Eschbach, W. K. Winegardner, "Ice-Condenser Aerosol Tests", NUREG/CR-5768, PNL-7765, Pacific Northwest Laboratories, September 1991.
- [41] N. A. Russell, D. C. Williams, "Comparison of CONTAIN Code Simulations to Experimental Ice Condenser Data", SAND89-3096C, Sandia National Laboratories, 1989.
- [42] K. E. Washington, N. A. Russell, D. C. Williams, R. G. Gido, "Integrated Thermal/Hydraulic Analysis with the CONTAIN Code", SAND90-1382C, Sandia National Laboratories, 1990.
- [43] B. E. Boyack, V. K. Dhir, J. A. Gieseke, T. J. Haste, M. A. Kenton, M. Khatib-Rahbar, M. T. Leonard, R. Viskanta, "MELCOR Peer Review", LA-12240, Los Alamos National Laboratory, March 1992.

# Peak Cladding Temperature in LOFT Large Break Transients<sup>1</sup>

V. T. Berta  
R. G. Hanson  
G. W. Johnsen  
R. R. Schultz  
Idaho National Engineering Laboratory  
EG&G Idaho, Inc.

The fuel centerline temperature data in LOFT large break experiments LP-02-6 and LP-LB-1 were analyzed to determine the bias at peak cladding temperature (PCT) in the cladding exterior surface-mounted thermocouples and the effect of the thermocouple cable on the thermal behavior of the cladding. A statistically determined bias of  $11.4 \text{ K} \pm 16.2 \text{ K}$  was found in the cladding thermocouples (measured less than actual PCT). The fin effect of the thermocouple cable was determined to be small and within the uncertainty of the data in the blowdown phase of the transients in which PCT occurred. The PCT in LOFT experiments LP-02-6 and LP-LB-1 was determined to be 1104.8 K and 1284.0 K respectively.

## Introduction

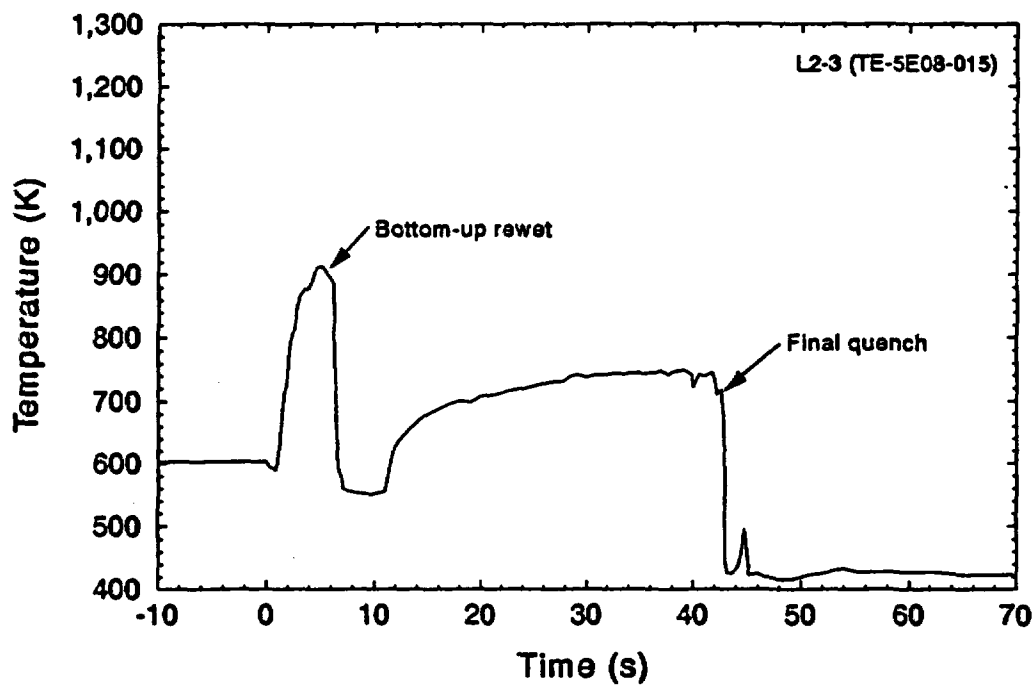
Data from the Loss-of-Fluid Test (LOFT) Program have been relied upon to quantify the margin of safety inherent in pressurized water reactors during postulated loss-of-coolant accidents (LOCAs). However, questions arose concerning the accuracy of LOFT fuel rod cladding temperature data following the first LOFT large break transient (L2-2)<sup>1</sup> with the core at power. This data was obtained from thermocouples laser welded to the outer surface of the fuel rod cladding. The origin of the concerns was the apparent large cooling of the cladding in the 5 - 15 s interval, during the blowdown phase of the transient, as indicated in the cladding thermocouple data shown in Figure 1. The interval of enhanced cooling subsequently was determined to be real phenomena based on analysis of coolant flow balances which showed that reestablishment of positive core flow can occur<sup>2,3</sup>. This phenomenon was verified through further analytical development and a large break transient (L2-5)<sup>4,5,6</sup> wherein boundary conditions were defined that would prevent the phenomenon from occurring. The cladding temperature in LOFT L2-5 is shown compared to the L2-3 cladding temperature in Figure 2.

The concerns about the cladding temperature data, then, consisted of the following questions:

1. Does a bias exist in the thermocouple measurement of cladding temperature in the thermal-hydraulic conditions of the large break blowdown phase?

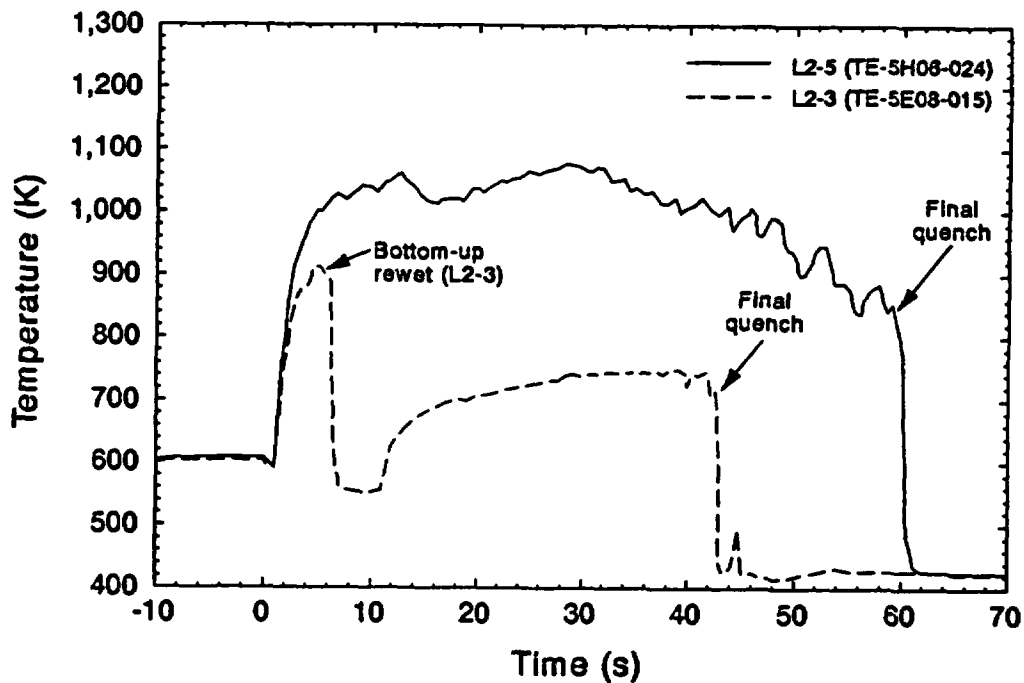
---

1. Prepared for the U. S. Nuclear Regulatory Commission, Office of Nuclear Regulatory Research/Reactor & Plant Systems Branch and for the U. S. Department of Energy under DOE Idaho Field Office Contract DE-AC07-76ID01570.



M722-WNF-1062-07

Figure 1. Cladding temperature in LOFT Experiment L2-3.



M722-WNF-1062-06

Figure 2. LOFT L2-3 and L2-5 cladding temperatures.

2. Does the presence of the thermocouple cable influence the thermal response of the cladding sufficiently (fin effects) such that the thermocouple data is not indicative of the thermal response of an uninstrumented fuel rod?

Additional instruments, consisting of fuel centerline thermocouples in specific fuel rods with and without thermocouples on the external surface of the cladding, were installed in fuel assemblies that were built following the first LOFT large break transients L2-2 and L2-3. The fuel centerline thermocouples would provide a measure of the thermal energy in the fuel rods and would not be influenced by coolant thermal-hydraulics. This paper deals with the analysis of fuel centerline thermocouple data in LOFT large break transients LP-02-6 and LP-LB-1 with the objective of determining the PCT. A more in-depth study of the phenomena occurring during the blowdown phase of the large break transient, and analyses of the experimental studies undertaken in separate effects facilities to answer the concerns about the LOFT cladding thermocouples are contained in another report<sup>7</sup>.

### LOFT Fuel Centerline Temperature Measurements

The instrumentation in the fuel assembly installed in the core center location for experiment LP-02-6 is shown in Figure 3. Of the five fuel centerline thermocouples, two, in fuel rods C7 and D6, had failed in LOFT experiments conducted prior to Experiment LP-02-6. Of the remaining three, fuel rod D7 also had four cladding thermocouples whereas, fuel rods D9 and D10 contained no cladding thermocouples. The data from these three fuel centerline thermocouples and the data from ten other cladding thermocouples, as summarized in Table 1, were used in the analysis to determine the PCT value in Experiment LP-02-6.

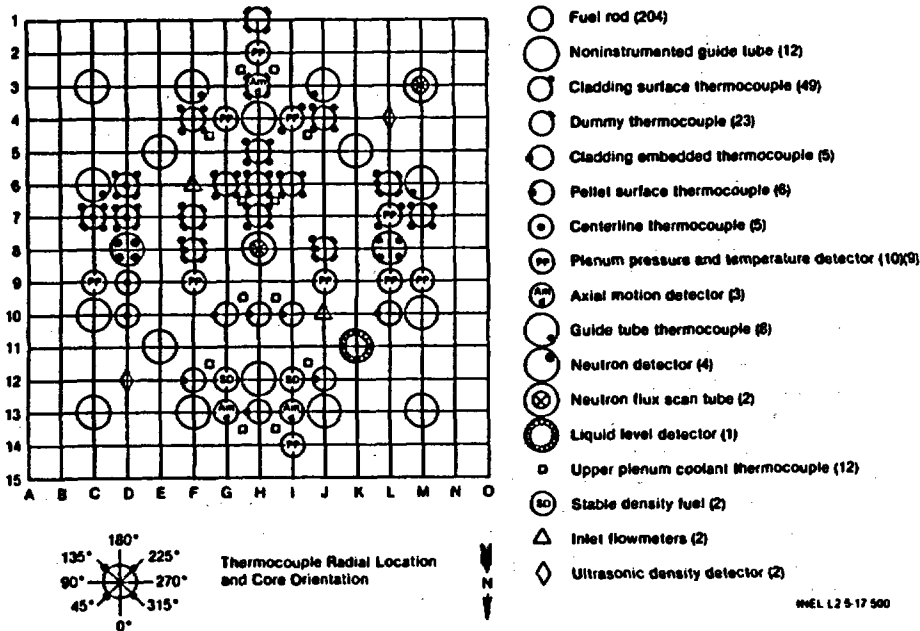


Figure 3. Instrumentation in the center fuel assembly in LOFT LP-02-6.

Table 1. LOFT LP-02-6 FUEL AND CLADDING TEMPERATURE INFORMATION

Fuel Rod	Fuel TC Axial Location <sup>a</sup>	Cladding TC Axial Location	Fuel temp. at t=0 (K) <sup>b</sup>	Fuel temp. at 5s (K)	Fuel temp. at 30s (K)	Cladding temp. at 5s (K) <sup>c</sup>
5D07	27"	27"	1769	1213	751	930.8
5D09	27"		1765	1233	756	
5D10	27"		1858	1393	823	
5F04		26"				1058.5
5F07		26"				1017.5
5F08		26"				1008.0
5H06		28"				1015.4
5H07		26"				1018.4
5I04		27"				1002.9
5J08		26"				1002.7
5L06		26"				1073.2
5M09		26"				1014.0

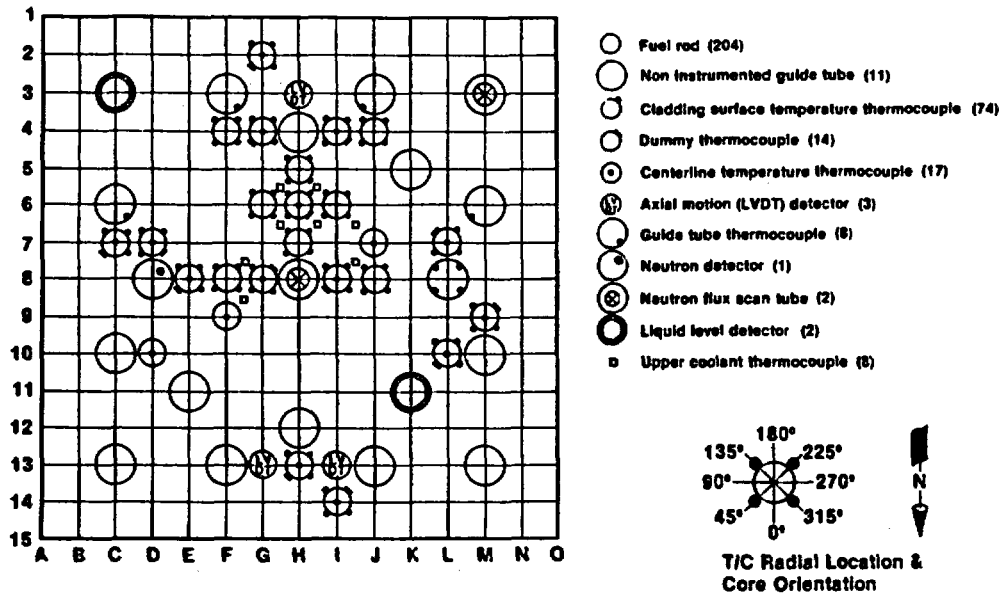
a. Relative to bottom of fuel rod.

b. Uncertainty in fuel thermocouple data is  $\pm 4.25$  K.

c. Uncertainty in cladding thermocouple data is  $\pm 3.9$  K.

The instrumentation in the fuel assembly installed in the core center location for experiment LP-LB-1 is shown in Figure 4. There are 17 fuel centerline thermocouples in this fuel assembly, eleven at the 27-inch elevation and six at the 43.8-inch elevation. The data from the fuel centerline thermocouples at the 27-inch elevation, ten of which were in rods that also contained cladding thermocouples, and from cladding thermocouples on ten other fuel rods that did not contain fuel centerline thermocouples, as summarized in Table 2, were used in the analysis to determine the PCT value in Experiment LP-LB-1.

The representative power distribution in the LOFT core for experiments LP-02-6 and LP-LB-1 is shown in Figure 5. The distribution is 1/8 sector symmetric. The location of the core relative to the reactor vessel is shown in Figure 6. Correlating the power distribution to the fuel centerline thermocouples in experiment LP-02-6 shows that fuel rods D7 and D9 are in symmetric locations and are expected to have the same power, and fuel rod D10 is in a high power location. Similarly for experiment LP-LB-1, among the ten fuel centerline thermocouples at the 27-inch elevation, fuel rods D7 and G4 are in symmetric locations and fuel rods C7 and M9 are in symmetric locations.



ORNL-4-33 002

Figure 4. Instrumentation in the center fuel assembly in LOFT LP-LB-1.

#### LOFT Large Break Experiments LP-02-6 and LP-LB-1

Experiment LP-02-6 simulated a double-ended offset shear of a commercial PWR main coolant inlet pipe<sup>8</sup>. The principal boundary conditions were (a) coincident loss of offsite power, (b) PWR nominal primary pump coastdown, (c) initial core power representative of USNRC licensing limits in a commercial PWR, and (d) US minimum emergency core coolant (ECC) injection. The cladding thermocouple temperature response was similar to that in LOFT L2-3 as shown in Figure 7. The early return to saturation conditions occurred at the same time, as had been expected.

Experiment LP-LB-1 also simulated a double-ended offset shear of a commercial PWR main coolant inlet pipe<sup>9</sup>. The principal boundary conditions were (a) coincident loss of offsite power, (b) an atypical fast primary pump coastdown (to suppress the blowdown phase cooling phenomena), (c) initial core power at maximum ( $49.3 \pm 1.2$  MW), and (d) United Kingdom minimum safeguard ECC injection. The cladding thermocouple temperature response was similar to that in LOFT L2-5, as shown in Figure 8, except that the magnitude was larger because of the higher initial core power.

Table 2. LOFT LP-LB-1 FUEL AND CLADDING TEMPERATURE INFORMATION

Fuel Rod	Fuel TC Axial Location <sup>a</sup>	Cladding TC Axial Location	Fuel temp at t=0 (K) <sup>b</sup>	Fuel temp at 5s (K)	Fuel temp 35-40s (K, max)	Cladding temp at 5s (K) <sup>c</sup>	Cladding temp 35-40s (K,max)
5D07	27"	27"	1933	1408	1141	1018.6	1118.6
5C07	27"	27"	1988	1410	1122	1050.6	1095.6
5H13	27"	27"	2060	1493	1239	1099.4	1198.6
5L10	27"	27"	2071	1464	1205	1064.4	1170.8
5M09	27"	27"	2049	1473	1207	1105.9	1178.0
5G04	27"	27"	2010	1442	1166	1019.7	1135.6
5G08	27"	27"	1999	1441	1196	1139.7	1190.1
5E08	27"	27"	1961	1430	1183	1077.1	1154.7
5H06	27"	27"	1903	1380	1218	1059.2	1196.1
5G02	27"	27"	1870	1348	1122	1010.8	1098.1
5F09	27"		1927	1393	1210		
5F04		26"				1134.8	1168.8
5F08		24"				1143.3	1223.2
5F08		28"				1124.7	1205.5
5G06		30"				1119.3	1201.8
5I06		21"				1180.5	1219.4
5J04		26"				1067.3	1185.0
5J04		30"				1139.6	1185.0
5J08		24"				1148.5	1252.5
5J08		28"				1163.4	1230.5

a. Relative to bottom of fuel rod.

b Fuel thermocouple uncertainty is  $\pm 4.25$  K.

c Cladding thermocouple uncertainty is  $\pm 3.9$  K.

Experiments LP-LB-1 and LP-02-6 provide bounding conditions for all other LOFT large break experiments. Therefore, the analysis of the cladding thermocouple data, and the fuel temperature data, which is available only in these two experiments, would apply in a conservative sense to the other LOFT large break experiments.



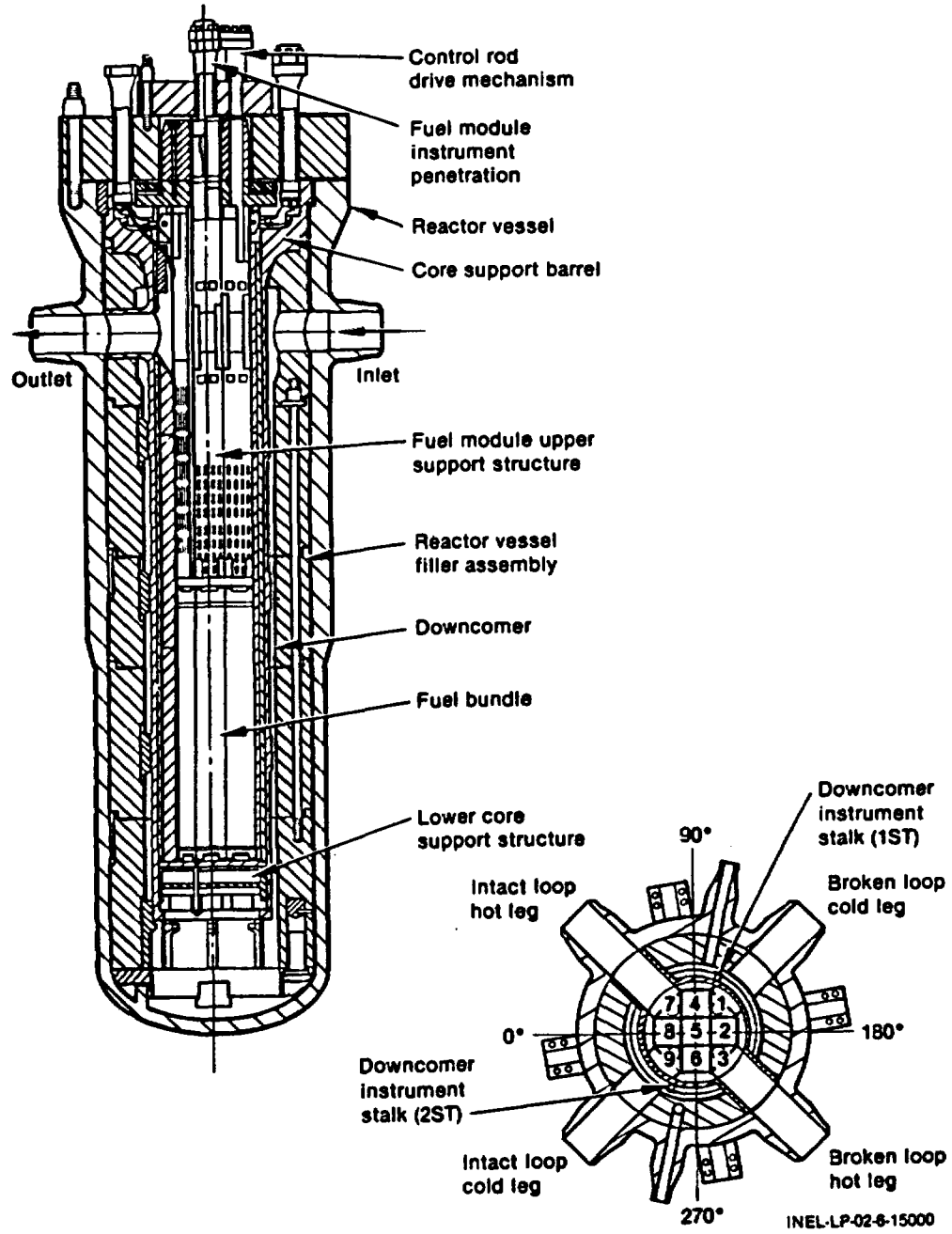


Figure 8. LOFT reactor vessel showing orientation of the core.

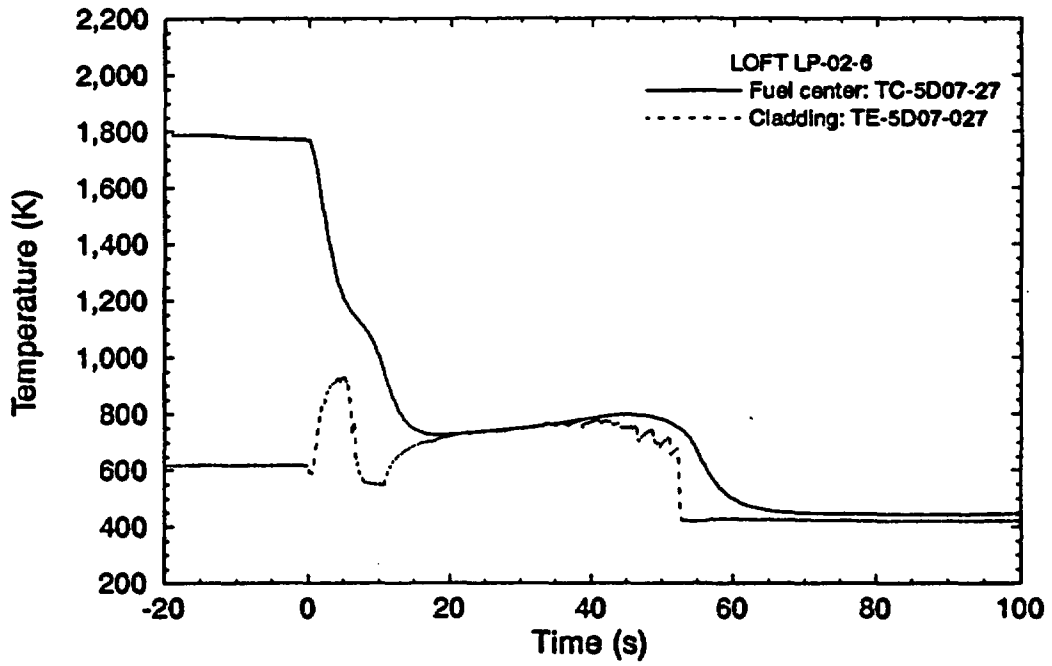
## Fuel and Cladding Temperature Analysis Methodology

The fuel temperature measurements provide a boundary condition for analysis of the thermal response of a fuel rod in a transient thermal-hydraulic condition. The uncertainty in the value of this boundary condition is the uncertainty in the fuel thermocouple. Thus, this boundary condition has much less uncertainty than the uncertainty in the thermal-hydraulic conditions at the surface of the fuel rod which, in the absence of temperature data inside of the fuel rod, must be used to determine heat transfer from the fuel rod.

The FRAP-T6 code<sup>10</sup>, a computer code for the transient analysis of oxide fuel rods, is applied to the analysis of the thermal response of the cladding in LOFT experiments LP-02-6 and LP-LB-1. The FRAP-T6 code has been assessed using the LOFT fuel rod as the assessment model<sup>11</sup>. The code contains the capability to model the presence of the thermocouple in the center of the fuel. The methodology consists of defining the heat transfer coefficient  $h(t)$  at the cladding surface as the independent variable. The cladding surface  $h(t)$  is adjusted by trial and error until agreement is reached between the FRAP-T6 calculated fuel centerline temperature and the measured fuel centerline temperature. Then, the FRAP-T6 calculated cladding temperature is compared to the measured cladding temperature to determine the degree to which the cladding thermocouple measures the cladding temperature. The uncertainties that must be accounted for in this methodology are (a) the fuel thermocouple uncertainty, (b) the cladding thermocouple uncertainty, and (c) the uncertainty in the FRAP-T6 code calculation. The single pair of fuel and cladding temperatures in LP-02-6 is shown in Figure 9. A representative pair of the ten fuel and cladding temperature pairs in LP-LB-1 is shown in Figure 10.

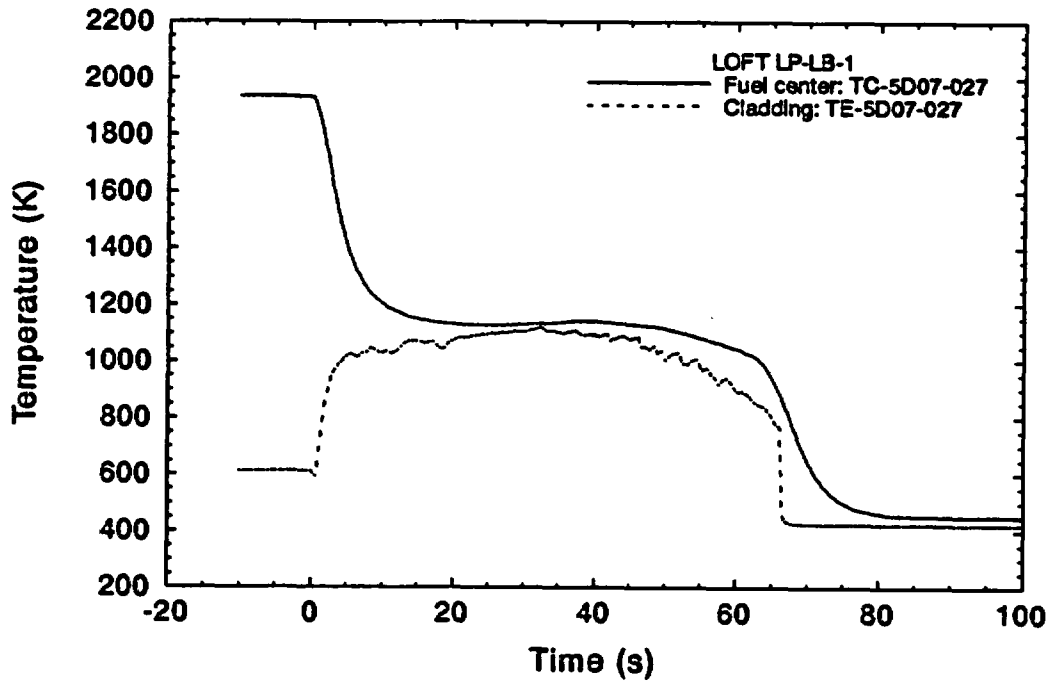
The objective of the analysis is the determination of the peak cladding temperature (PCT) in LP-02-6 and LP-LB-1. This is accomplished by applying the methodology using the FRAP-T6 code to determine if a bias exists in the LOFT cladding thermocouples at peak cladding temperature (PCT). This analysis, then, provides the resolution to the first question listed in the Introduction. The existence and the magnitude of the bias at PCT is determined by extending the analysis to include several calculations in each of the two experiments. Consequently, the bias is determined on a statistical basis wherein the uncertainty in the mean bias must also be accounted for as a source of uncertainty.

In order to utilize more of the cladding temperature measurements in the LP-02-6 experiment the analysis methodology is extended to the fuel rods without fuel centerline thermocouples. The thermocouple is removed from the FRAP-T6 fuel rod model. An assumption is made that the  $h(t)$  found for the single FRAP-T6 calculation in LP-02-6 does not change significantly over 11-inch from the 27-inch elevation where  $h(t)$  was determined. A FRAP-T6 code calculation is made that uses this  $h(t)$  as the cladding surface boundary condition. The calculation is made inclusive of the 26-, 27-, and 28-inch elevations corresponding to the elevations of the thermocouples shown in Table 1. Comparison of calculated and measured cladding temperatures provide an additional nine values of the bias at PCT in LP-02-6.



M722-WNF-1092-04

Figure 9. Fuel and cladding temperature in LOFT experiment LP-02-6.



M722-WNF-1092-08

Figure 10. Representative fuel and cladding temperature pair in LOFT experiment LP-LB-1.

The twenty bias values are combined into a single mean bias value with an uncertainty derived from the four sources of uncertainty involved in the analysis.

The second question listed in the Introduction, that of the possible fin effect of the thermocouple cable on the response of the cladding, is resolved by analysis of the fuel temperature data on the rods with and without cladding thermocouples in LP-02-6. A more extensive analysis of the data in LP-LB-1 on this question, which involves flow variations in the LOFT core, is contained in Reference 7.

#### Analysis Results

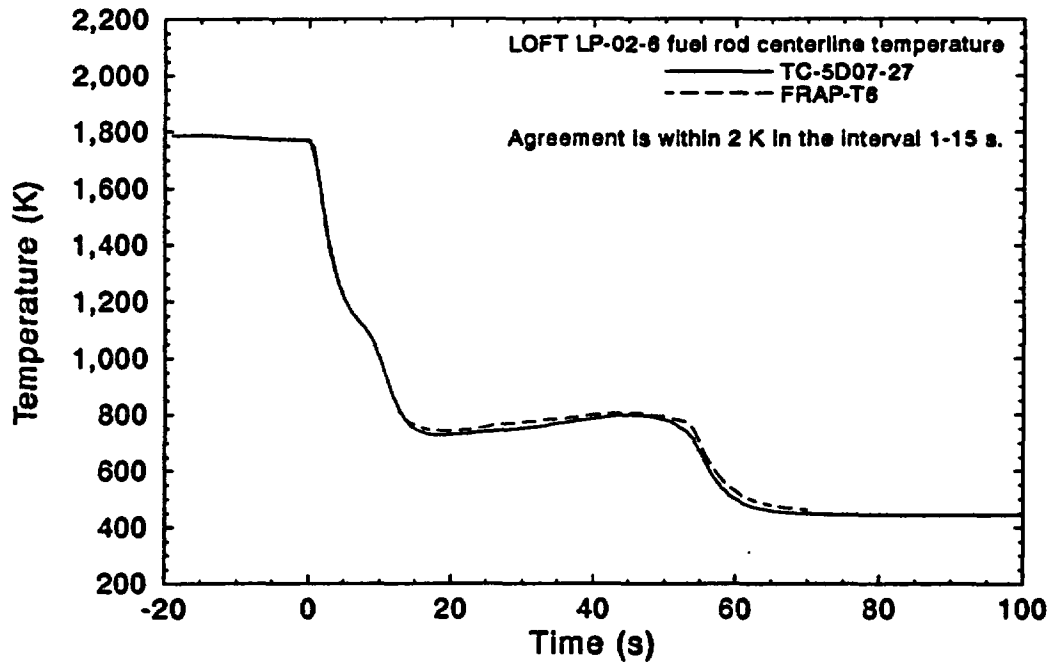
The heat transfer coefficient at the cladding surface was adjusted until the agreement between calculated and measured fuel centerline temperature on fuel rod 5D07 in LOFT LP-02-6 was within 2 K over the region of interest, as shown in Figure 11. The calculated cladding temperature is shown compared to the measured cladding temperature in Figure 12. The calculated temperature represents the average value around the circumference of the fuel rod since the FRAP-T6 code is one-dimensional. The comparison shows that the cladding temperature measurement is representative of the cladding cladding temperature except when the cladding temperature is undergoing a high rate of change. An example of this occurs in the interval of approximately 5 - 10s when the large cooling effect occurs. The heat transfer regime transitions from film boiling to nucleate boiling during this interval. The bias in this case is shown to exceed 100 K. However, in film boiling the bias in the measured temperature is small. At peak cladding temperature (PCT) the bias is 23.8 K for the case shown in Figure 12.

This procedure was followed for each of the ten fuel and cladding temperature pairs in LOFT LP-LB-1. The procedure of applying the FRAP-T6 code to fuel rods without fuel centerline thermocouples was applied to nine fuel rods in LOFT LP-02-6 which gave an additional nine bias values at PCT. The bias values from all calculations are listed in Table 3.

The differences in the bias values were expected and are attributed to the sources of uncertainty in the calculations and temperature measurements, and also to local and global variations in coolant flow in the core. The latter, discussed further in Reference 8, are accounted for in the analysis by including a statistical uncertainty in the mean bias value. The mean bias has a value of 11.4 K where the convention is chosen such that a positive bias corresponds to a calculated temperature greater than the measured temperature. The uncertainty in the bias is determined from the following four sources:

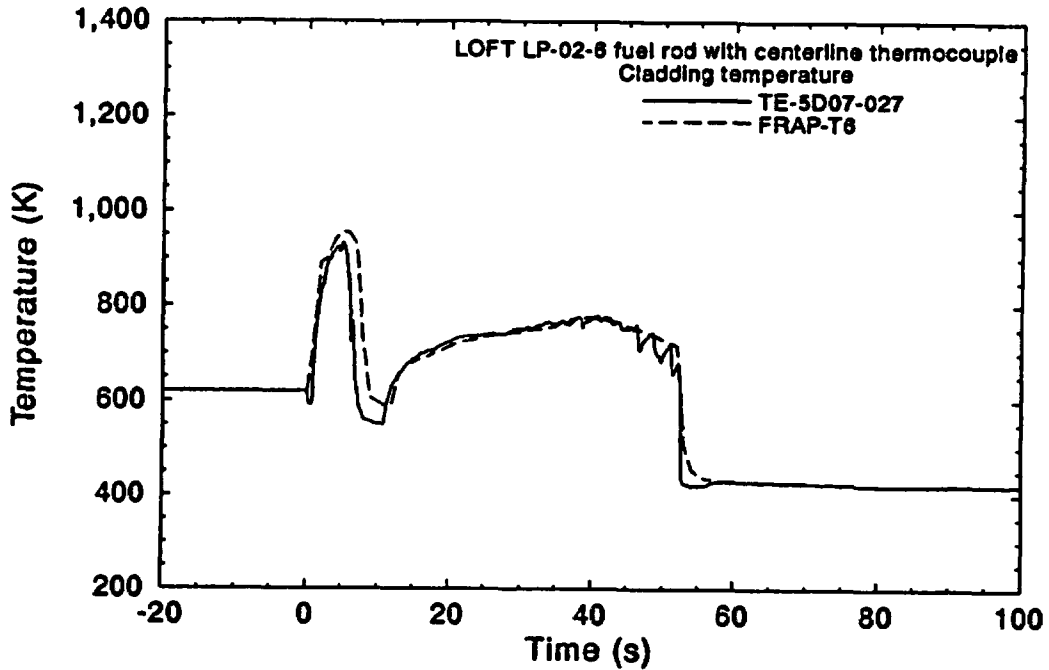
1. Uncertainty in the mean,  $2\sigma_1$
2. Uncertainty in the fuel centerline thermocouple,  $2\sigma_2$
3. Uncertainty in the cladding thermocouple,  $2\sigma_3$
4. Uncertainty in the FRAP-T6 calculation,  $2\sigma_4$

The uncertainty in the mean is determined from



M722-WHT-1092-00

Figure 11. Calculated and Measured Fuel Centerline Temperature in LP-02-6



M722-WHT-1092-00

Figure 12. Calculated and measured cladding temperature in LP-02-6.

Table 3. Cladding Thermocouple Bias Values in LP-02-6 and LP-LB-1.

Thermocouple	Calculated/Measured Temperature at 5s (K)	Bias at 5s (K)
LP-02-6		
5D07-27	954.6/930.8	23.8
5F04-26	1031.6/1058.5	-26.9
5F07-26	1031.6/1017.5	14.1
5F08-26	1031.6/1008.0	23.6
5H06-28	1031.6/1015.4	0.7
5H07-26	1031.6/1018.6	13.0
5I04-27	1029.9/1002.9	27.0
5J08-26	1031.6/1002.7	28.9
5L06-26	1031.6/1073.2	-41.6
5M07-26	1031.6/1014.0	17.6
	Average bias	8.2
LP-LB-1		
5D07-27	1050.5/1018.6	31.9
5C07-27	1056.9/1050.6	6.3
5H13-27	1123.6/1099.4	24.2
5L10-27	1120.7/1064.4	56.3
5M09-27	1117.3/1105.9	11.4
5G04-27	1065.7/1019.7	46.0
5G08-27	1117.9/1139.7	-21.8
5E08-27	1058.2/1077.1	-18.9
5H06-27	1067.7/1059.2	8.5
5G02-27	1013.8/1010.8	3.0
	Average bias	14.7
	Average bias in all values	11.4

$$2\sigma_1 = 2(\sigma^2/n)^{0.5} = 10.8 \text{ K}$$

where

n = number of values, (20)

$\sigma^2$  = variance of the population, (590.2).

The uncertainties in the cladding and fuel centerline thermocouples were determined from data taken during hot standby conditions. The reference temperature instruments have a 2-sigma uncertainty of 3.75 K<sup>12</sup>. All cladding and fuel centerline thermocouples were within this uncertainty. Inspection of the polynomial calibration equation for the cladding and fuel centerline thermocouples showed that in the region of 1200 K the calibration error is 2 K for the fuel centerline thermocouple and 1 K for the cladding thermocouple. The 2-sigma uncertainty, then, is 4.25 K for the fuel centerline thermocouple and 3.9 K for the cladding thermocouple. Thermocouple calibration drift was also investigated as a

possible source of uncertainty. The records of the LOFT data acquisition system were examined during power operation prior to experiment initiation. The results showed that from hot standby conditions to experiment initiation, several hours in duration, the drift was insignificant.

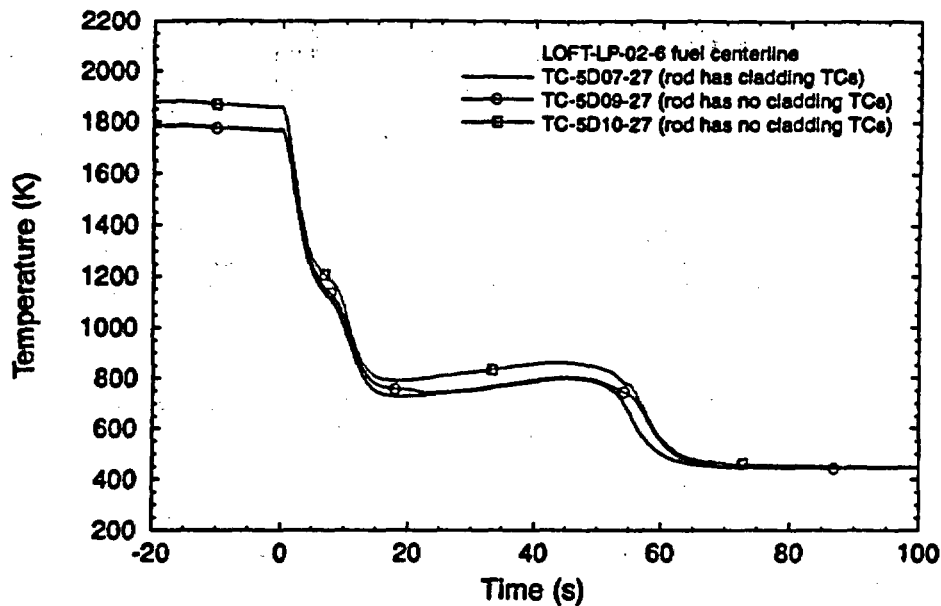
The 2-sigma uncertainty in the FRAP-T6 calculation was determined from the assessment of the code in Reference 11. All sources of uncertainty interior to the cladding in the FRAP-T6 model were included to give a 1-sigma uncertainty of 4.9 K in the calculated cladding temperature. The calculated fuel centerline temperature agreed with the measured data to within 2 K. The 1-sigma uncertainty in the FRAP-T6 code for this application, then, is statistically given as 5.3 K. The 2-sigma uncertainty is 10.6 K.

The 2-sigma uncertainty for the mean bias is calculated as follows:

$$\begin{aligned} 2\sigma &= (2\sigma_1^2 + 2\sigma_2^2 + 2\sigma_3^2 + 2\sigma_4^2)^{0.5} \\ &= 16.2 \text{ K} \\ 2\sigma_1 &= 10.8 \text{ K} \\ 2\sigma_2 &= 4.25 \text{ K} \\ 2\sigma_3 &= 3.9 \text{ K} \\ 2\sigma_4 &= 10.6 \text{ K} \end{aligned}$$

The bias in the LOFT cladding thermocouples at peak cladding temperature is  $11.4 \pm 16.2 \text{ K}$  ( $20.5 \pm 29.2 \text{ F}$ ). One way that this bias can be used to determine a PCT in the LOFT transients is to define the PCT to be the sum of the maximum measured cladding temperature plus the maximum bias value which would be  $27.6 \text{ K}$  ( $49.7 \text{ F}$ ). This would place PCT at  $1104.8 \text{ K}$  in LP-02-6 and  $1284.0 \text{ K}$  in LP-LB-1.

The effect of the thermocouple cables (fin effects) on the thermal behavior of the cladding is assessed by comparing the measured fuel centerline temperature data from fuel rods with and without cladding thermocouples. This comparison is shown in Figure 13 for the three rods with centerline thermocouples in LOFT LP-02-6. Fuel rods 5D07 and 5D09 are in symmetric power locations in the core as shown in Figure 5. Fuel rod 5D10 is in one of the high power locations and shows a higher initial operating temperature than the other two fuel rods. The comparison shows that rods 5D07 (with cladding thermocouples) and 5D09 (bare cladding) were very similar in thermal behavior out to the reflood cooling/quench. The thermal behavior in fuel rod 5D10 (bare cladding) was similar to the other rods except that the measured temperature stayed relatively uniformly higher. However, this means that the same relative amount of heat was removed from rod 5D10 as was removed from the other rods. The decrease in the fuel centerline temperature in the 0 - 15s interval, which can be taken as an indication of the heat removed from the fuel rods, is as follows for the three fuel rods:



M722-WHT-1000-04

Figure 13. Thermal behavior of fuel rods in LOFT LP-02-6.

Fuel Rod	Temperature Decrease (0 - 15s) (K)
5D07 (with cladding TCs)	1019 ± 8.5
5D09 (bare cladding)	1010 ± 8.5
5D10 (bare cladding)	1033 ± 8.5

The temperature decreased with the same time-wise functional behavior for all three rods. The conclusion from this is that the presence of the thermocouple cables did not cause significant fin effects in the blowdown phase of the large break transient. This statement applies only to the blowdown phase. These same thermocouples indicate the presence of significant fin effects in the reflood phase of the transient. The absence of significant fin effects in the blowdown phase is attributed to a very large convective heat transfer coefficient associated with the cooling that occurred after 5s. Analysis<sup>7</sup> of the coolant behavior showed that saturated coolant propagated upward through the core at a velocity approximately ten times greater than typical reflood rates. In this environment the presence of fins would be only a minor effect on a very large effective surface heat transfer coefficient.

#### Conclusions

The analysis methodology involving measured fuel centerline temperature as a boundary condition has shown that the thermocouples attached to the outer surface of the cladding have a small bias at peak cladding temperature (PCT). The mean bias was determined to be 11.4 ± 16.2 K (20.5 ± 29.2 F).

The cladding thermocouples are measuring a temperature that is representative of the actual cladding temperature. The bias in the measurement is small in the film boiling heat transfer regime. The bias can be large (>100 K) when the cladding temperature is undergoing high cooldown rates such as occur during the transition from film boiling to nucleate boiling.

The effects of thermocouple cables, attached to the exterior surface of fuel rod cladding, on the thermal behavior of the fuel rods is not significant in the blowdown phase of large break transients.

- 
1. M. L. McCormick-Barger, Experiment Data Report for LOFT Power Ascension Test L2-2. NUREG/CR-0492, TREE-1322, February 1979.
  2. W. H. Grush, "RELAP4 Posttest Analysis of LOFT Loss-of-Coolant Experiment L2-2", Proceedings of American Society of Mechanical Engineers Conference, San Francisco, California, June 25-29, 1979.
  3. J. H. Linebarger et al., "LOFT Experiment L2-2 Analysis of First Ten Seconds of Blowdown", Proceedings of American Society of Mechanical Engineers Conference, San Francisco, California, June 25-29, 1979.
  4. P. D. Bayless and J. M. Divine, Experiment Data Report for LOFT Large Break Loss-of-Coolant Experiment L2-5, NUREG/CR-2826, EGG-2210, August 1982.
  5. C. L. Nalezny, Summary of Nuclear Regulatory Commission's LOFT Program Experiments, NUREG/CR-3214, EGG-2248, July 1983.
  6. C. L. Nalezny, Summary of the Nuclear Regulatory Commission's LOFT Program Research Findings, NUREG/CR-3005, EGG-2231, April 1985.
  7. V. T. Berta et al., Determination of the Bias in LOFT Fuel Peak Cladding Temperature Data from the Blowdown Phase of Large-Break LOCA Experiments, NUREG/IA-0035, EGG-2610, (to be published).
  8. J. P. Adams et al., Quick-Look Report on OECD LOFT Experiment LP-02-6, OECD LOFT-T-3404, October 1983.
  9. J. P. Adams and J. C. Birchley, Quick-Look Report on OECD LOFT Experiment LP-LB-1, OECD LOFT-T-3504, February 1984.
  10. L. J. Siefken et al., FRAP-T6: A Computer code for the Transient Analysis of Oxide Fuel Rods, NUREG/CR-2148, EGG-2104, May 1981.
  11. R. Chambers et al., Assessment of FRAP-T6 Code Capabilities During Large-Break Loss-of-Coolant Accidents, EGG-CAAD-5829, March 1982.
  12. R. P. Evans and K. D. McKnight, LOFT Experimental Measurements Uncertainty Analysis, Volume XVII Process Instruments Recorded on DAVDS, NUREG/CR-0169, EGG-2037, Vol. XVII, September 1984.

# NATURAL CIRCULATION UNDER SEVERE ACCIDENT CONDITIONS<sup>a</sup>

D. J. Pafford            V. X. Tung<sup>b</sup>  
D. J. Hanson            S. V. Chmielewski<sup>c</sup>

Idaho National Engineering Laboratory  
EG&G Idaho Inc.

## ABSTRACT

Research is being conducted to better understand natural circulation phenomena in mixtures of steam and noncondensibles and its influence on the temperature of the vessel internals and the hot leg, pressurizer surge line, and steam generator tubes. The temperature of these structures is important because their failure prior to reactor vessel lower head failure could reduce the likelihood of containment failure as a result of direct containment heating. Computer code calculations (MELPROG, SCDAP/RELAP5/MOD3) predict high fluid temperatures in the upper plenum resulting from in-vessel natural circulation. Using a simple model for the guide tube phenomena, high upper plenum temperatures are shown to be consistent with the relatively low temperatures that were deduced metallurgically from leadscrews removed from the TMI-2 upper plenum. Evaluation of the capabilities of the RELAP5/MOD3 computer code to predict natural circulation behavior was also performed. The code was used to model the Westinghouse natural circulation experimental facility. Comparisons between code calculations and results from experiments show good agreement.

## 1. INTRODUCTION

During the latter stages of severe accidents in pressurized water reactors (PWRs), the inventory in the reactor coolant system may be significantly depleted and cells of natural circulation may be established in the reactor vessel, hot legs, and steam generators. In the hot leg, hot steam, or a mixture of steam and hydrogen, flows from the vessel along the upper portion of the pipe and cooler fluid is returned to the vessel along the lower portion. After some mixing in the steam generator inlet plenum, fluid enters the steam generator tubes and exchanges energy with the tubes and the secondary fluid before returning to the inlet plenum and hot leg. The net

- 
- a. Work supported by the U. S. Nuclear Regulatory Commission, Office of Nuclear Regulatory Research under DOE Idaho Field Office Contract No. DE-AC07-76ID01570
  - b. Currently at Aerospace Corporation, El Segundo, California
  - c. Currently at Detroit Edison, Detroit, Michigan

result of these natural circulation flows is to transport energy from the core and distribute it in the upper plenum and ex-vessel structures. Such natural circulation flows have been observed experimentally [1,2] and predicted by severe accident computer codes such as SCDAP/RELAP5 [3] and MELPROG [4].

The phenomena associated with natural circulation of mixtures of steam and noncondensibles is being evaluated to better understand their influence on the temperature of the vessel internals and the ex-vessel structures including the hot leg, pressurizer surge line, and steam generator tubes. High temperature creep rupture failure of the ex-vessel structures prior to failure of the reactor vessel lower head has the potential to reduce the likelihood of containment failure as a result of direct containment heating. This paper provides results from studies that have been completed in two areas:

- (a) The resolution of perceived inconsistencies between computerized code results and information on upper plenum temperatures obtained from the Three Mile Island, Unit 2 (TMI-2) accident
- (b) An assessment of the capability RELAP5/MOD3 to calculate natural circulation through a comparison of calculated results with natural circulation experimental data.

The following sections describe the analysis performed and results for these two areas.

## 2. TMI-2 UPPER PLENUM TEMPERATURE RESPONSE

Analyses of the TMI-2 accident [4] or similar scenarios [3] predict periods of natural circulation in the upper plenum with fluid temperatures as high as 1800K. Moreover, the predicted fluid temperature shows little variation in either the axial or the radial directions. However, these predicted temperatures appear to be incongruent with the temperatures deduced by a metallurgical examination of the B8 and H8 leadscrews recovered from the upper plenum of TMI-2 [5]. As shown in Figure 1, these temperatures ranged from 666K to 1255K with the bottom of the leadscrews experiencing a much higher temperature than the top. Not only are these temperatures much lower than those predicted by the codes, but they could also be interpreted as an indication of the existence of some stratification in the upper plenum. Such stratification, however, has been discounted by earlier work performed in this program [6] which indicated that long-term hydrogen stratification in the reactor vessel is not likely due to turbulent mixing associated with high Rayleigh number natural convection. Mixing time scales were predicted to be short (a few minutes), even when a fully stratified starting condition was assumed.

### Analysis Approach

An analysis was performed to examine inconsistencies between the leadscrew temperatures reported in Reference 5 and the fluid temperatures in the upper plenum reported in References 3 and 4. Several different mechanisms are examined to determine their influence on leadscrew temperatures. A bounding

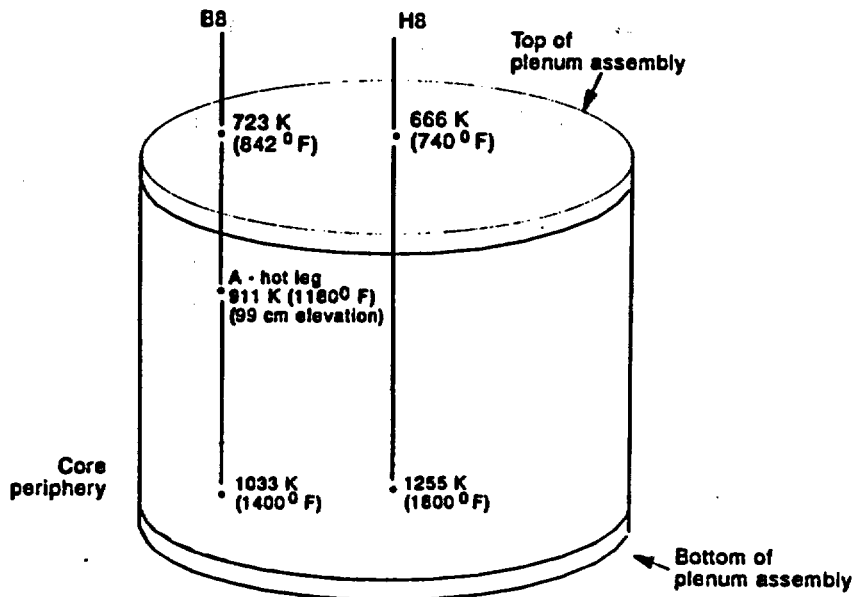


Figure 1. Results from metallurgical examination of TMI-2 leadscrews.

evaluation was performed initially to examine the influence of axial conduction along the lead screw and to assess the relative importance of radiation inside the tube. Results from these analyses indicated that axial conduction was not a significant influence, but radiation heat transfer must be considered in evaluating the leadscrew temperature. Based on these results, it was hypothesized that the guide tube provides an intervening shield between the leadscrew and the relatively hot fluid in the upper plenum. Initially, the outside surface of the guide tube was heated (via a combination of both radiation and convection) by the hot fluid in the upper plenum. Subsequently, the temperature difference between the guide tube and the leadscrew set up a convective current which serves as a heat transport mechanism from the guide tube to the leadscrew. Figure 2 shows a representation of these processes in a section of a guide tube. If such a transport mechanism is not very efficient, the shield provided by the guide tube can be effective and a large temperature difference between the leadscrew and the fluid temperatures in the upper plenum may exist. Further analyses were performed to test the hypothesis that the guide tube acts as a shield.

#### Guide Tube Model

To examine the potential shielding that the guide tube could provide, a simple model of the guide tube was developed. The model included the effects of convection and radiation heat transfer between the guide tube and the steam in the upper plenum. The model assumed the primary transport mechanism in the enclosure formed by the guide tube and the leadscrew is the recirculating flow set up by a temperature difference between these two components. The effects of radiation between the guide tube and leadscrew were also included. The following steps were used in the simple model to evaluate the temperature of

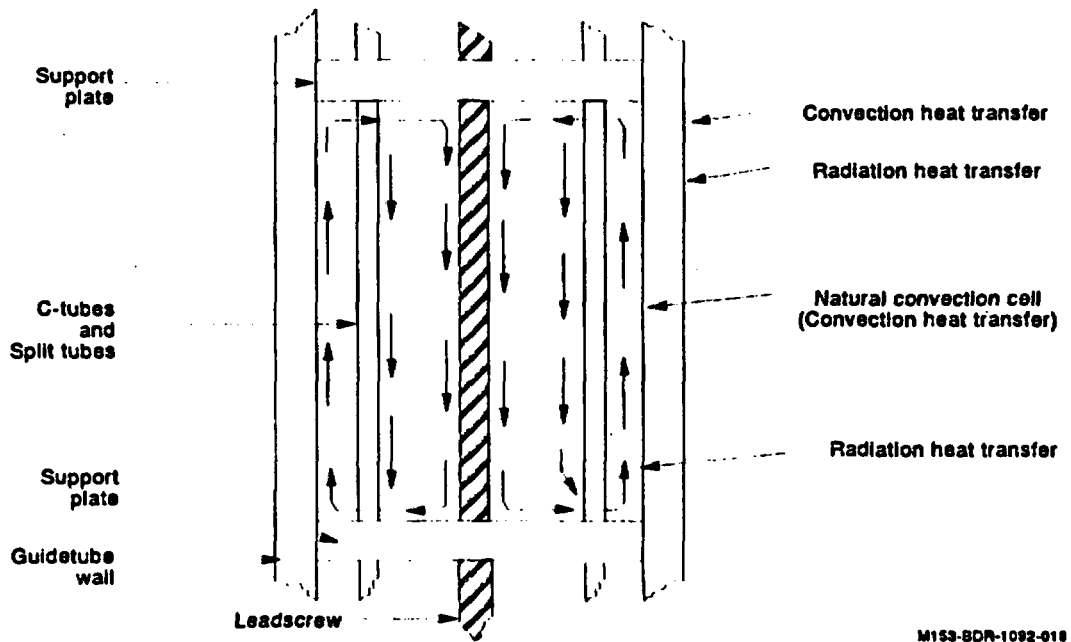


Figure 2. Guide tube representation showing heat transfer processes.

the leadscrew. It should be pointed out that the recirculating flow velocity within the cell, the fluid temperature, the leadscrew temperature, and the guide tube temperature are all known at the beginning of a time step.

- a) Heat Transfer Outside The Guide Tube: The model included convection between the high temperature gas in the upper plenum and the outer surface of the guide tube. Based on the upper plenum fluid conditions, the optically thick approximation for combining convection and radiation was found to be appropriate. Consequently, radiation was included through use of an effective Prandtl Number. Use of an effective Prandtl Number is recognized to only approximate the effects of radiation but is consistent with the lack of detailed information on the surface conditions, fluid temperatures, and fluid constituents. The natural circulation velocity in the upper plenum was calculated by SCDAP/RELAP5 [3] to be approximately 0.5 m/s upward flow near the H8 leadscrew and 0.2 m/s downward flow near the B8 leadscrew. Similar natural circulation velocities were also obtained in MELPROG and FLOW3D simulations of TMI-2 [4]. The vapor flow outside the guide tube was treated as flow over a flat plate at zero incidence. Reynolds numbers were calculated which showed that the flow can be considered laminar. The actual vapor temperatures at these locations are unknown, so these temperature were varied parametrically.

The average heat transfer coefficients (at 1000 psia) outside the guide tube were calculated over a range of temperatures and locations. Using the maximum heat transfer coefficient calculated, ( $117 \text{ W/m}^2 \text{ K}$ ), the Biot number based on the thickness of the guide tube can be found to be about 0.04. This Biot number is small enough such that the lumped capacity approximation can be applied to the guide tube wall.

- b) Heat Transfer Inside The Guide Tube: Given the recirculating flow velocity within the guide tube based on the previous time step, the heat transfer coefficient on any surface in the enclosure can be found by a procedure similar to that used for the outside of the guide tube. Convection was approximated as laminar flow over a flat plate. However, the heat transfer coefficient was averaged over the cell's height and the Prandtl Number dependence was doubled to reflect this averaging process. Radiation was included using the optically thick approximation.
- c) Heat Transfer To The C-Tubes, Slotted Tubes And Leadscrew: Heat transfer to the C-tubes and the slotted tubes is also similar to that between the recirculating steam and the leadscrew. The Biot number for these tubes is very small compared to unity and the maximum Biot number for the leadscrews is estimated to be about 0.10. Consequently, the lumped capacity approximation can also be applied to the C-tubes, the split tubes, and the leadscrew.
- d) Temperatures: Once all of the heat fluxes were known, the change in temperatures after a time step  $dt$  was found by an energy balance for each component using the lumped capacity approximation. Fluid temperatures at each point of the flow were also determined.
- e) Buoyancy Term: The buoyancy term in the momentum balance was calculated by an integration over the height of the cell.
- f) Friction Term: The total frictional resistance of the flow can be found by integrating the surface shear stress over the height of the cell. The terms containing friction can be calculated using the geometry of the guide tubes and leadscrew. The friction coefficient,  $c_f$ , is modeled as a function of the Reynolds Number ( $Re_H$ ) of the upflow and downflow by

$$\bar{c}_f = 1.328 / \sqrt{Re_H} \quad (1)$$

Such a friction coefficient accounts only for flow parallel to the inner tubes and lead screw. To account for the resistance caused by cross-flow at the top and bottom of the cell, the friction coefficient was determined by assuming that the cross-flow velocity at the top and bottom of the enclosure is the same as the recirculating velocity to yield

$$\bar{c}_f = \frac{1.328}{\sqrt{Re_H}} + \frac{32}{\pi} \frac{A_f D_k}{A_w D_i} \left[ 1 + \frac{10}{Re_{D_k}^{2/3}} \right] \quad (2)$$

Where  $A_f$  is the cross sectional flow area,  $A_w$  is the total wall surface area within the cell,  $D_k$  is the effective diameter of the C-tubes and split tubes,  $D_i$  is the inside diameter of the guide tube, and  $Re_{D_k}$  is the Reynolds number for the flow across the top and bottom of the cell. For the remainder of this paper, solutions obtained with the friction coefficient in Equation 1 will be referred to as the "low friction" cases while those obtained with Equation 2 will be referred to as the "high friction" cases. These "low" and "high" friction cases are estimates of lower and upper bounds of friction encountered by the recirculating flow in the enclosure.

- g) Flow Velocity: The flow velocity after a time step  $dt$  can then be found by applying the buoyancy force and friction force to the mass of recirculating fluid in the cell. Once this velocity has been updated, one can go back to step a) to begin a new time step.

### Calculations Performed

The following two approaches were taken in the application of the simple model for assessment of the shielding effect of the guide tube.

1. Parametric calculations were performed to examine the relationship between the steam temperature in the upper plenum and the leadscrew temperatures deduced from the TMI-2 leadscrew material samples as described in Reference 5. The steam temperature calculated in this fashion can be compared with that predicted by the codes to detect any inconsistency.
2. The upper plenum steam temperature that was calculated by MELPROG and FLOW3D (see Reference 4) is used to calculate the leadscrew temperature. The leadscrew temperatures calculated by the simple model were compared with those obtained by metallurgical examinations in Reference 5 to evaluate whether the large temperature difference between the upper plenum steam and the leadscrew is reasonable.

### Results

Prior to performing calculations with the simple model, sensitivity calculations were performed to examine the effects of various combinations of time step, spatial discretization and external steam temperature. An oscillating flow velocity which damped out after about 200 seconds was calculated inside the tube. The oscillations were determined not to be a result of numerical instability. Whether these oscillations actually occurred during the TMI-2 accident is not known, but in the calculation they are of short duration compared to the time frame of the accident and would not be

expected to significantly affect the calculated temperatures. The sensitivity calculations on friction factor effects showed the circulation velocity in the guide tube was about forty percent higher with the low friction case but the effect on temperature was not as large. For example, the time it took for the leadscrew to reach 800K was about 52 min. at low friction and 57 min. at high friction, a difference of only ten percent.

### Estimation of TMI-2 Upper Plenum Fluid Temperatures

The actual temporal variation of the steam temperature outside the guide tube is an unknown for the TMI-2 accident. A SCDAP/RELAP5 simulation of a Surry station blackout [3] indicated that, for a 40 minute period of natural circulation, the temperature of the fuel cladding at the top of the fuel assembly rises almost linearly. As an approximation, a linear variation of steam temperature outside the guide tube can also be assumed for TMI-2 during the period of natural circulation (139 min to 174 min). Between 110 and 139 minutes, however, the steam temperature near the top of the upper plenum is expected to rise more slowly because cladding oxidation has not begun and steam is escaping through the surge line and thus may not readily reach the top of the upper plenum. If we assume that the steam temperature near the top of the upper plenum varies parabolically with time from 110 min. to 139 min. and linearly from 139 min. to 174 min., only the maximum temperature at 174 min is needed to completely characterize the steam temperature over the excursion between 110 and 174 min.

$$\frac{T_s - 560K}{T_{max} - 560K} = \left\{ \begin{array}{ll} \frac{t'^2}{2871} & t' = t - 110 < 29 \text{ min} \\ \frac{2t' - 29}{99} & t' = t - 110 > 29 \text{ min} \end{array} \right\} \quad (3)$$

The assumed steam temperature's temporal variation shown in Equation 3 is only an approximation that does not account for large scale, rapid cladding oxidation. Another temporal distribution can be obtained by examining the maximum core temperature calculated for TMI-2 by SCDAP/RELAP5 [7]. Assuming that the steam temperature follows the same pattern it can be approximated by

$$\frac{T_s - 560K}{T_{max} - 560K} = \left\{ \begin{array}{ll} 7.532E-03 \cdot t' & 0 \text{ min} < t' < 47 \text{ min} \\ 6.460E-02 \cdot t' - 2.6822 & 47 \text{ min} < t' < 57 \text{ min} \\ 1.0 & 57 \text{ min} < t' < 64 \text{ min} \end{array} \right\} \quad (4)$$

Given a maximum steam temperature, either Equations 3 or 4 can be used to find the steam temperature as a function of time. This steam temperature then can be used to calculate the leadscrew temperature. A plot of the dimensionless steam temperatures defined by Equations 3 and 4 are shown in Figure 3.

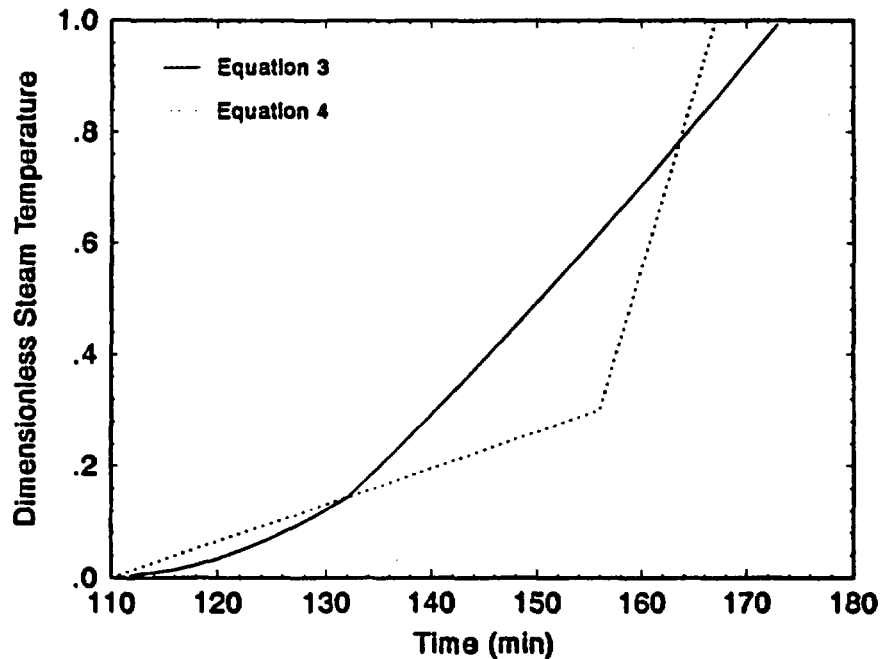


Figure 3. Assumed dimensionless steam temperatures in the upper plenum..

Equations 3 or 4 can be used as input to the simple model to calculate the leadscrew temperature as a function of time. The maximum leadscrew temperature will be the temperature calculated by the simple model at 174 min. Figure 4 shows the maximum B8 leadscrew temperature as a function of maximum steam temperature using both Equations 3 and 4. Using the maximum temperature experienced near the top of the B8 leadscrew ( $723\text{ K} \pm 28\text{ K}$ ) deduced in Reference 5, Figure 4 yields maximum steam temperatures of  $1289\text{ K} \pm 91\text{ K}$  and  $1424\text{ K} \pm 100\text{ K}$  using Equation 3 and 4 respectively. Using the same approach as was used for the B8 leadscrew, the maximum steam temperatures for the top of the H8 leadscrew were  $1385\text{ K} \pm 151\text{ K}$  and  $1528\text{ K} \pm 175\text{ K}$  using Equations 3 and 4 respectively.

Due to the uncertainty in the temporal variation of the steam temperature in the upper plenum, the calculated maximum steam temperatures may not represent the actual temperatures. However, they do indicate that the upper plenum steam temperature can be much higher than the maximum temperature experienced by the leadscrews. Even though the B8 leadscrew's temperature is higher than that of the H8 leadscrew ( $723\text{ K}$  vs  $666\text{ K}$ ) the steam temperature is found to be slightly lower. This is due to the higher heat transfer coefficient between the steam and the guide tube that exists for the B8 leadscrew. A point near the top part of the upper plenum in the center channel is at the trailing edge of the up flow while the same point in the outer channel will be near the leading edge of the returning down flow. This different relative location with respect to the flow results in a higher heat transfer coefficient for the outer channel (B8) compared to the center channel (H8). Moreover, a lower temperature in the outer channel is also consistent with the expected flow

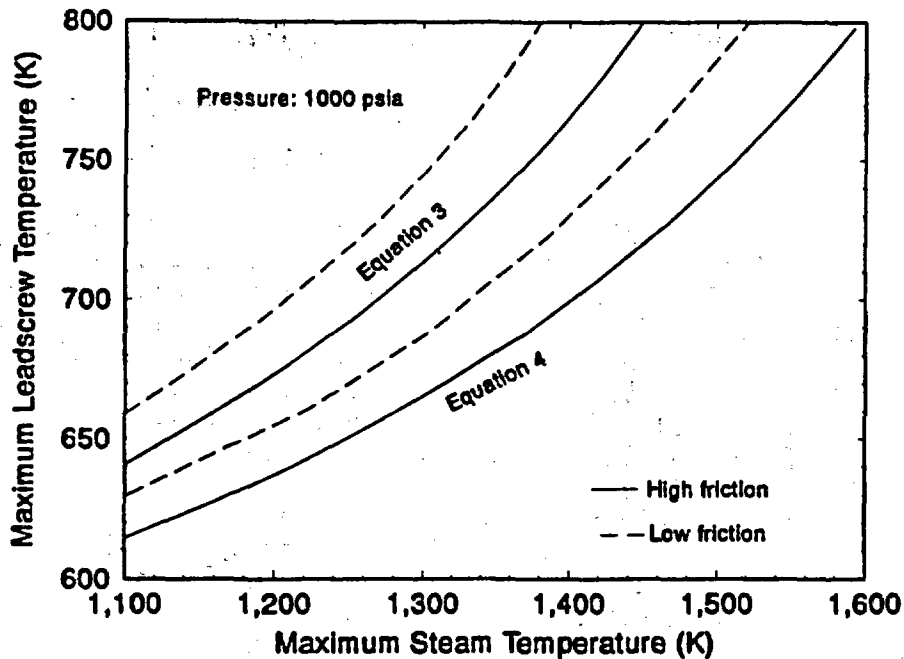


Figure 4. Maximum Leadscrew Temperature (B8).

pattern for natural circulation since the steam that goes up the center channel must lose heat to the upper head before returning to the upper plenum via the outer channel.

#### MELPROG and FLOW3D Temperature Profiles

Thermal-hydraulic calculations of TMI-2 using MELPROG and FLOW3D [4] indicate that the steam temperature near the top of the upper plenum is fairly uniform axially and radially. According to this calculation, the steam temperature remains at about 560K until 110 min. Thereafter, an approximately linear temperature rise is calculated until the temperature reaches about 1450K at 157 min. At this time a very steep rise brings the steam temperature to about 1800K (due to the Zirconium-Steam reaction). Because of calculational difficulties, the calculation in Reference 4 is terminated at 159 min. and further information on steam temperature in the upper plenum is unavailable after this time. However, the calculation does indicate a rate of decrease of about 1 K/s between 157 and 159 min. due to mixing with relatively cooler steam from below as the Zirconium-Steam reaction diminishes. Whether this decrease occurred during the TMI-2 accident is not known but it was included in the temperature profile. To extend the profile to 174 min., the temperature was assumed to increase with the same slope after 161.43 min. as it did prior to 157 min. Based on these assumptions, the following estimate of steam temperature was used.

$$T_s = \left\{ \begin{array}{ll} 560 + 18.94 \cdot t' & 0 \text{ min} \leq t' \leq 47 \text{ min} \\ 4620 - 60 \cdot t' & 47 \text{ min} < t' < 51.43 \text{ min} \\ 560 + 18.94 \cdot t' & 51.43 \text{ min} \leq t' \leq 64 \text{ min} \end{array} \right\} \quad (5)$$

A similar temperature variation was produced by with SCDAP/RELAP5 calculations of the TMI-2 accident [6]. Another complication is the flow velocity in the upper plenum after 157 min. The steep rise in temperature is a result of rapid oxidation of the fuel cladding which is expected to be accompanied by a partial relocation of the core. Thereafter, the flow velocity in the upper plenum may decrease due to a change in the geometry of the core (such as the formation of blockages) and by a reduction in the boil-off rate. Therefore, heat transfer from the steam in the upper plenum to the guide tube should be maximum prior to significant core relocation. Since information on flow velocity is not available in [4] after 157 min., a conservative estimate of the leadscrew temperature will be obtained here by assuming that there is no change in the flow velocity after this time. The leadscrew temperature thus obtained is plotted in Figure 5 as a function of time. The temperatures after 157 min. are shown as dashed lines since both the natural circulation velocity and the steam temperature are expected to be lower than the values used in the calculation. From Figure 5 the temperature of the H8 leadscrew is found to be about 950K at around 170 min. This is considerably higher than the temperature deduced from metallurgical samples of the leadscrews [5] (about 700K). However, due to uncertainties in the steam temperature and natural circulation flow rate mentioned earlier, the actual leadscrew temperature must be lower than the value of 950K predicted here.

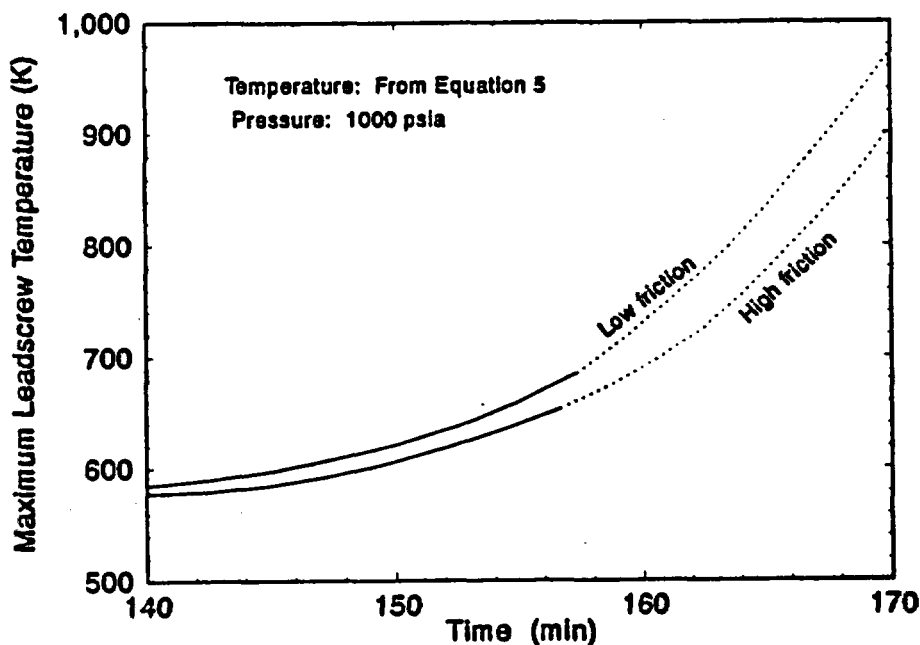


Figure 5. Leadscrew temperature - MELPROG result.

## Conclusions

The following conclusions were drawn from this study on the temperature of the leadscrew recovered from the upper plenum of TMI-2.

1. Even though the actual temporal variation of the steam temperature in the upper plenum is unknown for the TMI-2 accident, results obtained in this study indicate that the maximum steam temperature can be very high (on the order of 1300K to 1500K) compared to temperatures experienced by the leadscrews (666K to 723K).
2. Using an upper plenum steam temperature calculated for TMI-2 by MELPROG and FLOW3D produces maximum leadscrew temperatures which approximate those determined by metallurgical samples of the TMI-2 leadscrews.
3. It is likely that a gravity driven recirculating flow was set up in the enclosure bounded by the leadscrew and the guide tube during the TMI-2 accident. The buoyancy term for such a flow arises from the temperature difference between the guide tube and the leadscrew.
4. Radiative exchange between the guide tube and the leadscrew may be important and must be considered as a heat transfer mechanism.

### 3. RELAP5/MOD3 CALCULATION OF NATURAL CIRCULATION DATA

Calculating the effects of natural circulation in the vessel, hot legs, and steam generators is very complicated owing to the complex phenomena and the multidimensional nature of the flows during the latter stages of a severe accident. The SCDAP/RELAP5/MOD3 computer code has been used to model full scale PWRs and calculate the system response during severe accidents that include natural circulation. These calculations use a specially developed nodalization of the core, upper plenum, hot legs, and steam generator plenums and tubes to simulate the multidimensional natural circulation flow behavior. During their development, coefficients in these simulated components were adjusted to ensure that the results agreed with results from detailed multidimensional simulations of PWRs.

Results from the Westinghouse natural circulation experiment apparatus provide an alternate means of evaluating the capability of SCDAP/RELAP5/MOD3 to calculate natural circulation behavior. This evaluation was performed by nodalizing the components of the Westinghouse facility using the same approach as was used for the full scale plants. Steady state experiments were selected for comparison. Experimental boundary and initial conditions were defined and specified as inputs to the model. Code modifications were made to simulate SF<sub>6</sub> vapor, the experiment working fluid.

## Westinghouse Experiments

The objectives of the Westinghouse experiments (References 1 and 2) were to experimentally determine flow patterns, flow rates, and temperatures of natural circulation flows in PWRs during severe accidents such as a station blackout and small-break LOCA (TMLB' and S<sub>2</sub>D) events. These experiments were conducted with a 1/7 scale model of a Westinghouse four loop PWR. Sulfur hexafluoride (SF<sub>6</sub>) was used as the working fluid to emulate high pressure steam. Electric resistance heaters were used to simulate the core decay heat. Most of the experiments were conducted with steady cooling of the upper internals and steam generators provided by secondary side cooling water. These steady state tests allowed a more thorough investigation of the natural circulation flows. Transient tests were also conducted where the cooling was provided by the thermal storage in the model reactor structures.

### Steady State Experiments

Of the 14 steady-state natural circulation tests, Tests S-6 and S-7 were chosen for modeling with RELAP5/MOD3. These two test were chosen because they had representative system conditions, including upper plenum and steam generator cooling, and the experimental data indicated that the core heating was very closely balanced with the heat removal. For some other experiments, the core heating was not in balance with the heat removal due to experimental difficulties in maintaining the cooling water at a constant inlet temperature for the duration of the test. Tests S-6 and S-7 both had core powers of 20.5 kW, but different system pressures of 240 and 315 psia, respectively.

The experimental data reported includes the fluid temperatures in the reactor vessel, hot legs, and the left steam generator tube bundle. Also, the experimental thermal boundary conditions were adequately defined and included the heat removed by the upper internals (guide tubes, upper plenum wall, and upper head) and steam generators. SF<sub>6</sub> mass flow rates or velocities were not measured in the experiments. Instead, they were estimated using the experimental heat removal rates, and vapor temperatures. Derived experimental flow parameters in the hot legs and steam generators were obtained as part of this study using the analytical models, methodology, and experimental data presented in the Westinghouse report (Reference 2). The derivation of these flow parameters is summarized below.

### Derived Flow Parameters in the Hot Legs and Steam Generators

The experimental mass flow rate,  $\dot{m}_{HL}$ , in the hot leg was derived by equating the change in energy of fluid flowing through the hot leg with the heat rejected by the steam generator,  $q_{SG}$ :

$$\dot{m}_{HL} = \frac{q_{SG}}{\bar{c}_p (T_{HL,h} - T_{HL,c})} \quad (6)$$

where  $T_{HL,h}$  and  $T_{HL,c}$  are the average vapor outlet and inlet temperatures in the hot leg at the steam generator junction, respectively.

The derived flow parameters in the steam generators included the left steam generator tube bundle mass flow rate and average inlet and outlet temperatures; the number of tubes carrying hot and cold flow; the average temperature in the inlet plenum mixing volume; and the fraction of flow entering the inlet plenum that is mixed with flow returning to the hot leg. Note that the experimental flow parameters were only calculated for the left steam generator because vapor temperatures were not recorded in the right steam generator inlet plenum.

The left steam generator tube bundle mass flow rate,  $\dot{m}_{SG}$ , was derived by equating the change in energy of fluid flowing through the steam generator with the heat rejected by the steam generator:

$$\dot{m}_{SG} = \frac{q_{SG}}{\bar{c}_p (T_{SG,h} - T_{SG,c})} \quad (7)$$

where  $T_{SG,h}$  and  $T_{SG,c}$  are the average fluid temperature entering and leaving the tube bundle in the inlet plenum, respectively. As was done in the Westinghouse report, measured fluid temperatures in the tubes on the inlet plenum side were sorted to find those that had hot fluid entering the bundle and those that had cooled flow returning. For Test S-6, 64 'hot' steam generator tubes and 152 'cold' tubes were estimated. The average fluid temperatures entering and leaving the tube bundle,  $T_{SG,h}$  and  $T_{SG,c}$ , were calculated as the average temperature of the identified hot and cold thermocouple readings, respectively. The average temperature in the inlet plenum,  $T_{SG,m}$ , was derived using an analytical mixing model and experimental data. The mixing model results in the following expression for  $T_{SG,m}$ :

$$T_{SG,m} = \frac{T_{HL,h} + (\dot{m}_{SG}/\dot{m}_{HL})T_{SG,c}}{1 + (\dot{m}_{SG}/\dot{m}_{HL})} \quad (8)$$

The mixing model was also used to estimate the mixing fractions,  $f_1$  and  $f_2$ , which quantify the fraction of flow entering the inlet plenum from the hot leg and from the tube bundle, respectively. The flow mixing results in a lower inlet temperature to the tube bundle and raises the temperature of vapor returning to the hot leg. For symmetrical mixing,  $f_1 = f_2 = f$ , and the mixing fraction is defined as

$$f = 1 - (\dot{m}_{SG}/\dot{m}_{HL}) \frac{(T_{SG,h} - T_{SG,m})}{(T_{HL,h} - T_{SG,m})} \quad (9)$$

## RELAP5/MOD3 Model Description

The RELAP5/MOD3 model of the Westinghouse experimental apparatus included all of the major components necessary to perform the steady state analyses. The reactor vessel, two hot legs, and two steam generators were modeled. Also, thermodynamic and thermal hydraulic properties of SF<sub>6</sub> vapor were obtained. Figure 6 presents the RELAP5 nodalization of the Westinghouse apparatus.

### Reactor Pressure Vessel

The model of the Westinghouse experimental reactor vessel was developed analogous to that of the Surry vessel model used in earlier natural circulation analyses [3]. The core and upper plenum were divided into three radial regions. The core regions were selected so that similarly powered fuel assemblies were grouped together. The upper plenum regions were extensions of the core regions. Two-dimensional flows in the core and upper plenum were simulated by connecting the three channels at each elevation with crossflow junctions. Heat structures modeled include the reactor vessel walls, the fuel assemblies, the top nozzle assembly, the upper core plate, the upper plenum structures, and the upper head walls and internal structures. The lower plenum and upper head were also modeled. The upper head communicated with the lowest volumes in the upper plenum via the modeled communication tube flow paths. (In a reactor, this flow path is provided by the clearances in the control rod guide tubes.)

The core axial form pressure loss coefficients were calculated by the code for the specified geometry. The radial form loss coefficients could not be calculated explicitly by the code because the three channel radial nodalization oversimplified the crossflow geometry between adjacent fuel assemblies. Therefore, assumed radial form loss coefficients were specified as input. Also, the loss coefficients for the core/upper plenum junctions were not calculated with the code because the complex geometry of this junction was not characterized well enough to model accurately. (This junction includes the top nozzle assembly and the upper core plate.) Therefore, the assumed loss coefficients at the junction between the core and the upper plenum were specified.

The upper plenum's internal structures included the control rod guide tubes, communication tubes, and support columns. Additionally, the upper plenum wall enclosed these internal structures. The axial and crossflow loss coefficients for flow between adjoining upper plenum volumes were not known and assumed values were used for all these junctions. Also, during the experiments, cooling water flowed through tubing attached to the outside surface of the upper plenum wall and additional cooling water recirculated through tubing attached to the inside of the guide tubes. This cooling water entered the guide tubes through a manifold system located in the upper head. The heat removed by these cooled structures was modeled by specifying surface heat fluxes. The surface heat fluxes were determined by dividing the heat removed through the cooling systems by the structure's surface area.

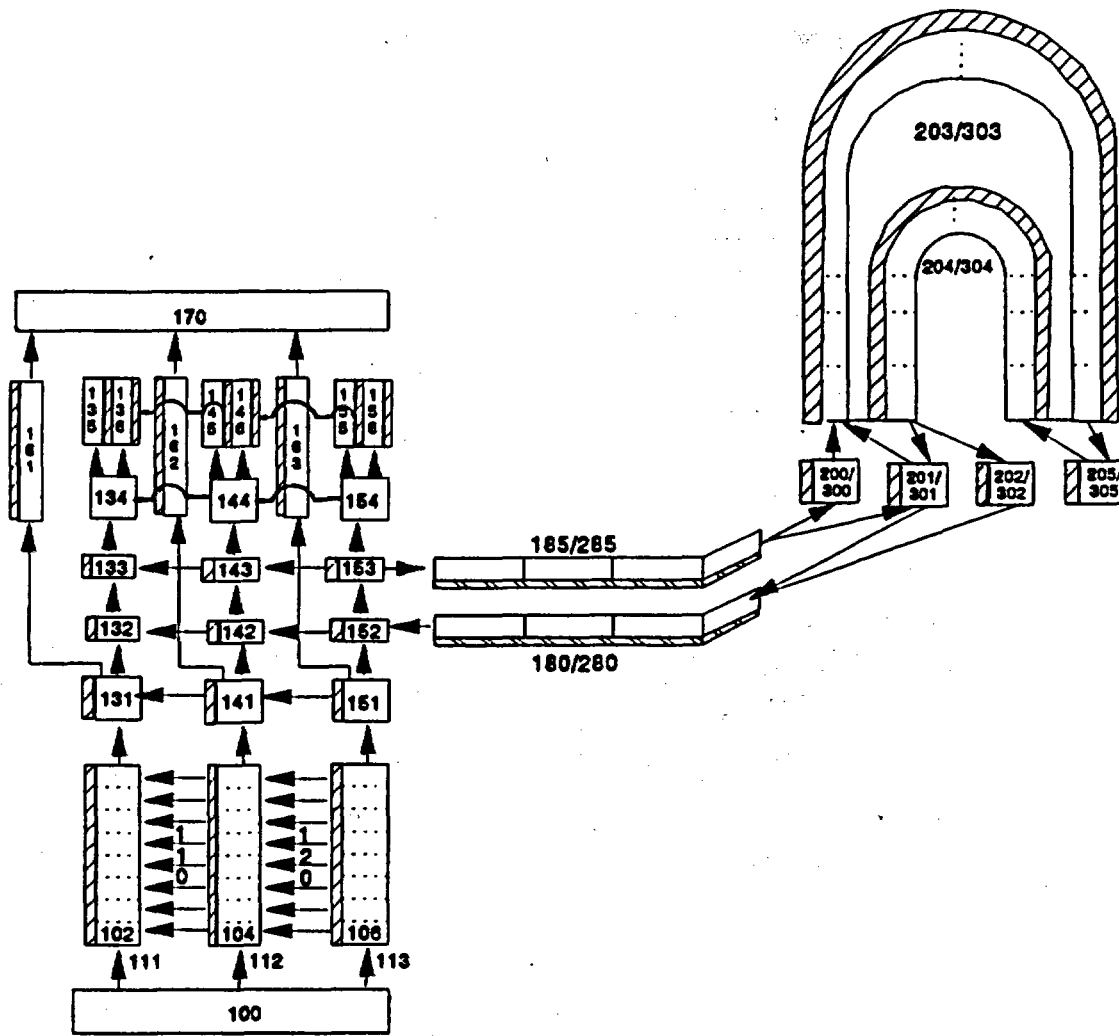


Figure 6. RELAP5 nodalization of the Westinghouse experimental natural circulation reactor pressure vessel, hot legs, and steam generators.

### Hot Legs

Both hot leg pipes were modeled. The hot leg models were identical and included both the fluid volume and the metal structures. The piping was assumed to be adiabatic on the outer surface. In order to model the countercurrent flow in the hot legs, the hot leg was divided into top and bottom flow paths. The shear loss at the countercurrent flow interface was approximated by assuming the interface acted as a very rough surface with a wall roughness of 9 mm. For comparison, the surface roughness of the pipe wall was specified as  $5 \times 10^{-6}$  m. An equivalent wall roughness for each hot leg volume was then defined as a surface area weighted average of the interface roughness and the pipe wall roughness.

## Steam Generators

The steam generator model included the tube bundle, the tube sheet, the inlet and outlet plena, the inlet channel head and flange, and the secondary side cooling water system. The left and right steam generators were modeled identically except for the secondary side cooling water inlet conditions. The metal masses associated with the steam generator walls and internals were modeled, with the outer surface of the steam generators assumed to be adiabatic. The steam generator inlet plenum was divided into three volumes. A mixing volume in the middle connected to the flows entering and leaving both the hot leg and the steam generator tubes. The volumes on either side of the mixing volume passed hot and cold vapor directly to the steam generator and hot legs, respectively, without mixing with the other fluid in the inlet plenum. Two sets of steam generator tubes connect the inlet and outlet plena. The number of tubes representing hot and cold flow tubes were derived from the Westinghouse experimental temperature data.

## SF<sub>6</sub> Vapor Properties

For the modeled high pressure Westinghouse experiments, the system conditions were such that the SF<sub>6</sub> vapor properties deviated a considerable amount from ideal gas property relations. Because of the ideal gas property inaccuracies, non-ideal gas property models for SF<sub>6</sub> vapor were developed and implemented in the RELAP5/MOD3 code calculations. These models were developed for the specific volume,  $v$ , the coefficient of thermal expansion,  $\beta$ , isothermal compressibility,  $\kappa$ , and heat capacity at constant pressure,  $C_p$ . The non-ideal property models were obtained using a five coefficient Martin-Hou type equation of state and thermodynamic relations [8].

## Analyses

An analytical simulation was performed for the Westinghouse steady state Test S-5 using the RELAP5/MOD3 computer code. Analytical results were obtained and are presented for the core and upper plenum, the two hot legs, and the two steam generators. These results include the SF<sub>6</sub> vapor temperatures, the mass flow rates, the heat added and removed, and the flow parameters derived in the Westinghouse experiments. Finally, some of the uncertainties and limitations of the analysis are described.

## Procedure

The analysis consisted of specifying the experimental boundary and initial conditions. The calculation was run for 10,000 seconds which assured steady state results. The form loss coefficients in the steam generator inlet plenums were obtained from a benchmark calculation using Test S-7 data. In that calculation, the junction loss coefficients and flow areas for the inlet plenum volumes were adjusted until the mass flow ratio and mixing fractions,  $f_1$  and  $f_2$ , matched the correlated experimental data for Test S-7.

## Natural Circulation Flow in the Core and Upper Plenum Results

The available experimental data for the core and upper plenum consisted of vapor temperatures, core power, upper plenum cooling rates, and system pressure. Vapor flow rates and velocities were not measured in the experiments. Nevertheless, an averaged temperature distribution in the core and upper plenum was derived from the recorded experimental vapor temperatures. Figure 7 presents the experimental average temperature distribution and the RELAP5 calculated temperature distribution for Test S-6. The experimental average temperatures were obtained by first locating the position of each thermocouple relative to the RELAP5/MOD3 defined control volumes. Then, an arithmetic average of the thermocouple readings assigned to each control volume was calculated. Control volumes that did not contain a thermocouples were left blank in the distribution diagram. The average vapor temperature in the left and right hot legs at the reactor vessel junction are also shown in this Figure. The upper temperatures are for the hot flow leaving the reactor vessel and the lower temperatures are for the returning cooled flow. In the experiments, the vapor temperatures in each stream changed along the length of the hot leg because of heat transfer and mixing of the two counterflowing streams. Recorded temperatures at the steam generator end of the hot leg are not depicted here but are presented later with the hot leg results.

The observed and calculated temperature distributions are the result of the recirculating flow in the core and upper plenum. In the core there is a radial temperature distribution with higher temperatures in the center and lower temperatures at the periphery. The axial distribution governs the recirculating flow. At the core periphery, the vapor temperature increases as the flow travels down through the core and is heated up. In the center channel, the vapor heatup continues and drives the flow up through the core. In the middle channel, the axial temperature distribution is somewhat more complicated due to the recirculating flow in the core. The maximum temperature is seen about half way up the channel with much cooler temperatures above this location. This is due to a combination of two phenomena. First, high temperatures occur half way up the channel because flow stagnated in the recirculating pattern is heated to higher temperatures. Secondly, lower temperatures occur at the top of the core due to cooler vapor in the upper plenum flowing into the core.

In the upper plenum, the radial temperature distribution is similar to that in the core with hotter vapor rising in the center channel and cooler fluid descending at the plenum periphery. The axial temperature distribution in the upper plenum is reversed to that in the core. As the fluid rises in the center channel, the vapor decreases in temperature as energy is transferred to the water cooled guide tube structures. The vapor temperature continues to decrease as it turns and descends down the periphery of the plenum.

A comparison of the calculated temperature distribution with the derived experimental average temperatures reveals that the model overpredicts the experimental values in the core region, underpredicts in the upper plenum and head, and yields mixed results in the communication tubes. Quantitatively,



core and upper plenum. The longer transit times in the core yields greater vapor temperatures and in the upper plenum results in lower vapor temperatures. The core/upper plenum junction loss coefficient was assumed to be 40.0 in the calculation. A theoretical evaluation of this loss coefficient was not made because the geometry of the upper core plate and top nozzle assembly was complex and not well characterized.

The upper head vapor temperature is underpredicted most likely due to an overestimation of the heat removed by the cooling water manifold. The vapor flow exiting the upper head and returning to the upper plenum via the outer channel communication tubes is also underestimated because of the underestimated upper head vapor temperature. The heat removed by the cooling water manifold was not reported explicitly in the experimental results, but was included in the total heat removed via the upper plenum guide tube cooling. The model assumed that the heat flux removed by the manifold and guide tubes was equal. However, the results indicate that this assumption is incorrect. A better comparison of the upper head results could be obtained by adjusting the specified heat flux. In any case, the vapor circulation through the upper head accounts for less than 5% of the heat removed from the core and does not significantly affect the overall problem.

**Flow Pattern Distributions.** The calculated average  $SF_0$  vapor mass flow rate and velocity vectors in the core and upper plenum for Test S-6 are presented in Figure 8. Comparison with experimental data was not possible because no mass flow rates or velocities were measured in the experiments. The core and upper plenum vector diagrams confirm the recirculation flows indicated by the temperature distribution. The recirculating mass flow rate in the upper plenum is approximately 2.6 times that in the core, with mass flow rates approximately, 0.54 and 0.20 kg/s, respectively. By comparison, the mass flow rate recirculating through the upper head is only 0.05 kg/s and that through each hot leg loop is 0.045 kg/s, on average.

The velocity vector diagram shows a flow pattern similar to that of the mass flow rate diagram. In the core, the maximum velocity occurs in the outer channel and is approximately 0.16 m/s. In the upper plenum, the maximum velocity occurs in the center channel and is 0.30 m/s. The velocity in the communication tubes is much higher than in other regions of the upper plenum because of the relatively small cross-sectional flow area of the tubes. The calculated velocity in the center channel communication tube was 1.5 m/s.

### **Countercurrent Hot Leg and Steam Generator Flow Results**

Derived flow parameters in the hot legs and steam generators are presented and compared with the experimental results in Table 1. The hot leg results include the vapor temperatures and mass flow rates. The hot and cold vapor temperatures are overpredicted, on average, by less than 4% and 5%, respectively. The hot leg temperature differences are overpredicted by 4%, on average, and the mass flow rates are underpredicted by approximately, 4%.

The steam generator heat removal rates compare quite well with the

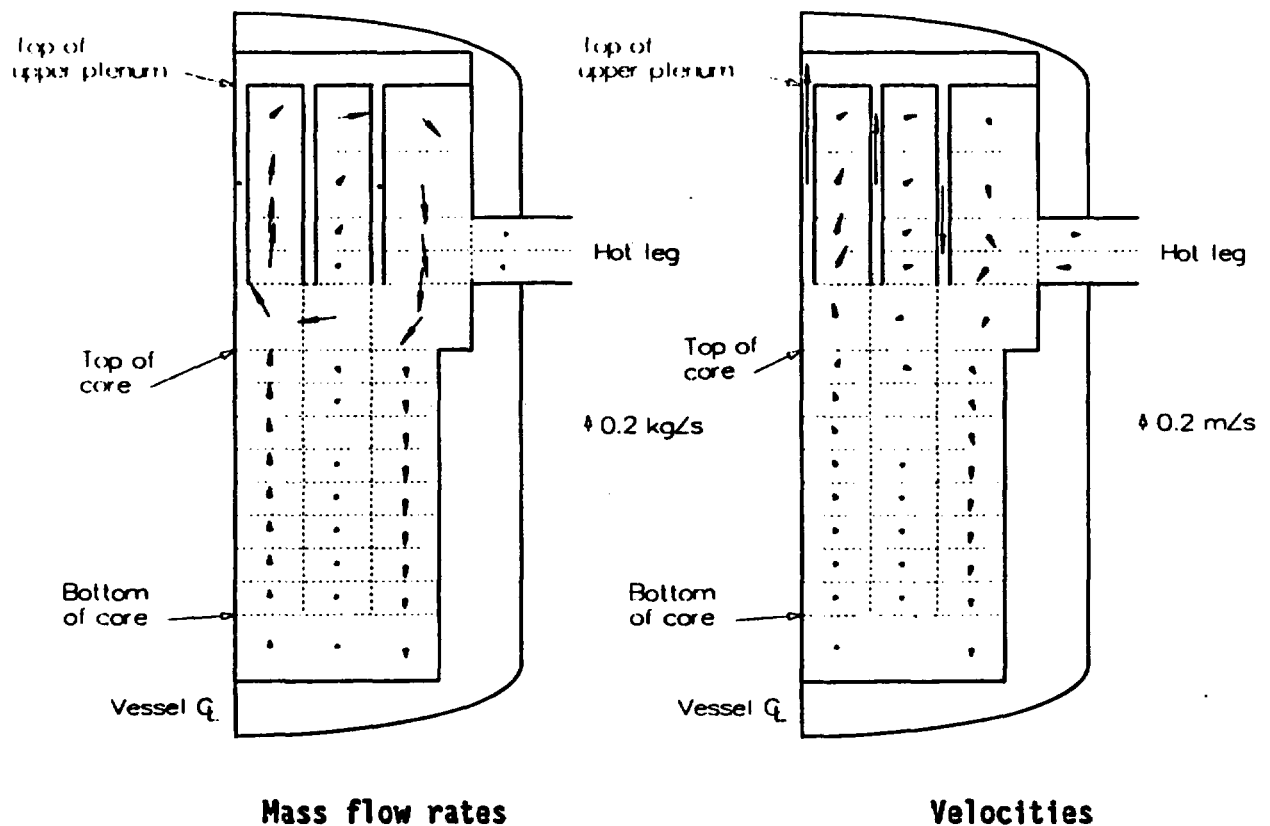


Figure 8. Calculated  $SF_6$  vapor mass flow rate and velocity vectors in the core and upper plenum for Test S-6.

experimental results and deviate by approximately 1%, on average. The tube bundle mass flow rate is underpredicted by approximately 1%. The tube bundle entrance and exit temperature are underpredicted by 1.4% and 3.8%, respectively, and the steam generator temperature difference is within 2% of the experimental value. Finally, the mixing volume temperature is within 2% of the experimental value.

While most of the hot leg and steam generator results are predicted to within -8% of the experimental data, whether this agreement is adequate or not depends upon how sensitive the core condition and reactor coolant system failure time and location are to the hot leg and steam generator flow parameters. Determination of the various system sensitivities is beyond the scope of this study and would be better suited to examination with a full plant sensitivity study. However, during the benchmarking of calculated the results with Test S-7 data it was observed that the mass flow rates and vapor temperatures in the hot legs are strongly dependent upon the steam generator flow parameters including the heat removed in the steam generator, the inlet plenum mixing fractions, and the ratio of the steam generator mass flow rate to the hot leg flow rate. It was also observed that changes in the core and upper plenum system modeling had only a small affect on the hot leg and steam

**Table 1. Experimental and RELAP5 calculated natural circulation flow parameters in the hot legs and steam generators for Test S-6.**

	<u>Experiment</u>		<u>Prediction</u>		<u>Percent Error</u>	
	Left	Right	Left	Right	Left	Right
Hot Leg						
$T_{HL,h}$ (°C)	129.7	134.9	137.3	137.3	5.9	1.8
$T_{HL,c}$ (°C)	65.5	63.4	67.7	66.8	3.4	5.4
$T_{HL,h} - T_{HL,c}$ (°C)	64.2	71.5	69.6	70.5	8.4	-1.4
$m_{HL}$ (kg/s)	0.0467	0.0461	0.0445	0.0451	-4.7	-2.2
Steam Generator						
$q_{SG}$ (kW)	2.43	2.67	2.49	2.55	2.5	-4.5
$m_{SG}$ (kg/s)	0.0919	NA	0.0907	0.0891	-1.3	
$f_1$	0.85	NA	0.89	0.89	4.7	
$f_2$	0.85	NA	0.89	0.89	4.7	
$T_{SG,h}$ (°C)	77.5	NA	76.4	75.9	-1.4	
$T_{SG,c}$ (°C)	44.5	NA	42.8	40.9	-3.8	
$T_{SG,h} - T_{SG,c}$ (°C)	33.0	NA	33.6	35.0	1.8	
$T_{SG,m}$ (°C)	73.2	NA	74.5	74.0	1.8	

NA Data was not obtained in the experiments.

generator flow parameters. For example, the temperature of the hot flow entering the top of the hot leg from the upper plenum is dependent upon the vapor temperature and mixing that occurs in the periphery of the upper plenum. However, changes in the upper plenum modeling had little affect on these. If it is desired to reduce the uncertainty in the hot leg and steam generator modeling, most likely enhanced modeling of the ex-vessel systems would be required. Possible enhancements would included increased nodalization, mechanistic models of the countercurrent hot leg flow that would include heat and mass transfer between the two streams, and three dimensional flow models of the steam generator inlet plenum.

### Uncertainties and Limitations

One uncertainty in the analysis that has not been addressed is what affect the model nodalization has on the results. Also, some of the model loss coefficients are uncertain. These include the crossflow loss coefficients in the upper plenum and core; the axial loss coefficients for the core/upper plenum junctions; and loss coefficients between the steam generator inlet plenum, hot leg, and steam generator tube volumes. Some of these loss coefficients, such as the crossflow losses in the core, could be determined explicitly by increased nodalization, but there is not sufficient information to quantify the others.

There is also uncertainty in the steam generator inlet plenum mixing model. Specifically, the derived mixing fractions assume perfect mixing and no heat transfer between the defined flow streams in the inlet plenum. The validity of this simplification and the sensitivity of the inlet plenum mixing to it are unknown. The experimental derived steam generator and hot leg mass flow rates also have unquantified uncertainties. These flow rates are derived from averaged hot leg and steam generator inlet and outlet temperatures. Deviations as high as 10% occur in the experimental temperatures used in calculating the averages.

Finally, the RELAP5 model can only simulate three-dimensional flows with a simplified two-dimensional approximation. Three-dimensional flows have been experimentally observed to occur in the core, upper plenum, hot legs, and steam generator inlet plena. Also, the hot leg model does not account for heat and mass transfer between the counter flowing streams. Experimentally, the top hot leg flow stream decreased in temperature as it traveled from the reactor vessel to the steam generator inlet plenum and the bottom flow stream increased in temperature as it returned to the reactor vessel. The temperature change was approximately 5 to 10°C in both directions. In the current hot leg model, the vapor temperature remains constant as it passes from the reactor to the steam generator and vice versa.

### Conclusions

This RELAP5/MOD3 model analysis of the Westinghouse natural circulation experiment system has demonstrated:

1. Predicted SF<sub>6</sub> vapor flow rates and temperatures in the hot legs and steam generators compare reasonably well with the experimental data. The code tended to overpredict hot leg vapor temperatures by up to 14% and underpredicted steam generator vapor temperatures by up to 4%.
2. Vapor temperatures in the core are overpredicted and in general are underpredicted in the upper plenum. Qualitatively the temperature distributions compare well with the experimental data. One possible explanation for the quantitative differences is due to an overestimated loss coefficient for the upper core plate and top nozzle assembly which separate the core from the upper plenum. This high resistance restricts the circulation between the two regions, increases the transit times in each region, and results in hotter vapor temperatures in the core and cooler temperatures in the upper plenum. An additional calculation is planned to evaluate the sensitivity of the temperature to this resistance. Another possible cause of errors is the three dimensional nature of the flows and the simplifications associated with simulating them with a one dimensional code.
3. The vapor flow rates and temperatures in the hot legs are strongly coupled with the steam generator tube flow rates and the steam generator inlet plenum mixing. However, the hot leg and steam generator natural circulation loops are weakly coupled with the core and upper plenum flow

conditions. Therefore, uncertainties in system modeling or calculated behavior in the core and upper plenum have only a small affect on the hot leg and steam generator results.

It would appear that the two pipe model of the hot leg adequately represents the simple countercurrent flow behavior. The coupling between the steam generator and the hot leg piping appears to be adequate. However, the effect of uncertainties in this coupling on full scale plant calculations was not investigated.

#### 4. REFERENCES

1. W. A. Stewart, A. T. Pieczynski, and V. Srinivas, "Experiments on Natural Circulation in a Pressurized Water Reactor Model for Degraded Core Accidents." Final Report, EPRI Project No. RP2177-5, 1990.
2. W. A. Stewart, A. T. Pieczynski, and V. Srinivas, "Experiments on Natural Circulation in a Pressurized Water Reactor Model With High Pressure SF<sub>6</sub>." Draft EPRI Report, 1990.
3. P. D. Bayless, "Analyses of Natural Circulation During a Surry Station Blackout Using SCDAP/RELAP5," NUREG/CR-5214, 1988.
4. J. N. Lillington, A. J. Lyons, I. M. Lovely, "Thermal-Hydraulic Calculation in TMI-2 Accident Analysis," Reactor Systems Analysis Division, AEE Winfrith, Report No. AEEW-R 2434, January 1989.
5. K. Vinjamuri, D. W. Akers and R. R. Hobbins, "Examination of H8 and B8 Leadscrews From Three Mile Island Unit 2," GEND-INF-052, Sept. 1985.
6. J. E. Obrien, "Effects of Hydrogen Generation on Severe Accident Natural Circulation", Proceedings of the Nineteenth Water Reactor Safety Information Meeting, NUREG/CP-0180, March 1992.
7. D. W. Golden and N. Ohnishi, "SCDAP/RELAP5 Demonstration Calculation of The TMI-2 Accident," EG&G Report, EGG-TMI-8473, March 1989.
8. W. H. Mears, E. Rosenthal, and J. V. Sinka, "Physical Properties and Virial Coefficients of Sulfur Hexafluoride," J. Phys. Chem., 73, 7, July 1969, pp. 2254-2261.

## PWR Depressurization Analyses<sup>a</sup>

D. A. Brownson  
C. A. Dobbe  
D. L. Knudson

Idaho National Engineering Laboratory  
Idaho Falls, ID 83415

### ABSTRACT

Early containment failure resulting from direct containment heating (DCH) has been identified as a potential contributor to the risk of operating a pressurized water reactor (PWR). One important factor needed to evaluate the contribution of DCH to risk is the conditional probability that, given a core melt, the primary system will be at high pressure when the reactor vessel lower head fails. Two mechanisms that could reduce the pressure during a station blackout core melt accident are discussed. First, natural circulation in the reactor coolant system (RCS) could cause a temperature-induced failure of the RCS pressure boundary, which could result in unintentional (without operator action) depressurization. Second, plant operators could open relief valves in an attempt to intentionally depressurize the RCS prior to lower head failure. Results from analytical studies of these two depressurization mechanisms for select PWRs are presented.

### INTRODUCTION

Depressurization of the reactor coolant system (RCS) prior to vessel breach has been proposed as a strategy to avoid high pressure melt ejection (HPME) during severe accidents in pressurized water reactors (PWRs). The strategy was proposed as a method to reduce the public risk associated with commercial operation of PWRs. Risk reduction is expected, since the potential for direct containment heating (DCH) and the associated challenge to containment integrity should be minimized if HPME can be avoided. Analyses are being performed at the Idaho National Engineering Laboratory (INEL) to evaluate the effects of RCS depressurization in commercial PWRs. The calculations, which extend from accident initiation to lower head failure, include evaluation of both intentional<sup>1</sup> and unintentional<sup>2</sup> depressurization during a TMLB' (station blackout) transient.

Reactor operators could be directed to take actions to depressurize the RCS if specific severe accident conditions occurred. However, intentional depressurization requires more than the overt actions of the reactor operators. Specifically, equipment availability and design features of a given PWR could influence the effectiveness of the operator actions. Previous calculations<sup>3</sup> indicated that a late depressurization strategy could be a viable option to avoid HPME in a Surry-type PWR. Additional calculations were needed to deter-

---

a. Work supported by the U. S. Nuclear Regulatory Commission, Office of Nuclear Regulatory Research under DOE Contract No. DE-AC07-76ID01570.

mine the effectiveness of the intentional depressurization strategy in other operating PWRs.

Calculations were required to evaluate PWR response if reactor operators do not take actions to depressurize. Without operator actions, natural circulation flow patterns could develop in the vessel and in the primary coolant loops. Full loop, in-vessel, and hot leg countercurrent natural circulation modes are possible. Under such conditions, ex-vessel RCS pressure boundaries could be heated to the point of failure prior to failure of the reactor vessel lower head. Under those conditions, unintentional RCS depressurization through the ex-vessel breach, independent of operator response and other plant-specific characteristics, could be sufficient to avoid HPME.

The objective of the assessments presented in this paper is to quantify the conditions that could occur following a severe reactor accident with and without operator response. Specifically, (a) the timing and location of the initial RCS pressure boundary failure and (b) the associated RCS and containment conditions at the time of pressure boundary failure are of interest. This information can then be used to assess the potential for HPME.

In these assessments, a TMLB' scenario (initiated by a loss of all ac power and a simultaneous loss of auxiliary feedwater) was selected as the subject core melt accident. For the intentional depressurization analyses, the RCS power-operated relief valve (PORV) was assumed to be latched open when the core exit thermocouple indicated superheated steam (922 K). The capability to simulate natural circulation in the RCS hot leg piping was incorporated into the calculations where no operator actions were assumed to appropriately represent the anticipated natural circulation flow patterns. The capability to simulate in-vessel natural circulation flow patterns was incorporated into all of the analyses. These models were based on previously reported work that investigated natural circulation cooling patterns in a Surry-type PWR under TMLB' accident conditions.<sup>4</sup> The calculations were performed using the SCDAP/RELAP5/MOD3<sup>5</sup> computer code to calculate the plant response associated with this accident and its progression.

The unintentional depressurization calculations (no operator actions) included assessment of the HPME potential for six different cases. In the Base Case, full loop, in-vessel, and hot leg countercurrent natural circulation flows were considered. This approach is consistent with flow conditions that could be expected following TMLB' initiation without operator interaction. Although hot leg countercurrent natural circulation is expected, uncertainties exist with respect to the effectiveness of heat transfer to ex-vessel structures. Based on these uncertainties, hot leg countercurrent natural circulation was eliminated in Case 2. As a result, Case 2 represents a bounding calculation where ex-vessel heat transfer is minimized and should reduce the time to reactor vessel failure. Cases 3 through 6 were designed to account for full loop, in-vessel, and hot leg countercurrent natural circulation, along with the effects of potential reactor coolant pump (RCP) seal leakages. Each case assumed an initial 21-gpm leakage per RCP (based on calculations for intact RCP seals subjected to normal RCS temperature and pressure<sup>6</sup>) up to the point where the RCP coolant saturated. The leakage rates were then increased to either 250 gpm (Case 3, highest probability leak rate) or 480 gpm (Case 4, catastrophic failure of all three RCP seal stages) per pump, based on expert opinion of RCP seal performance under severe accident conditions.<sup>7</sup>

Case 5 was identical to Case 3 except for the way heat transfer from molten materials was treated during relocation. In Case 3, it was assumed that molten materials would remain intact during relocation from the core to the reactor vessel lower head. This approach minimizes heat loss from the debris so that a relatively rapid thermal attack on the vessel follows. In contrast, it was assumed in Case 5 that molten materials would break up during relocation. This break-up could occur as a result of the pour interacting with vessel structures and with water below the core. However, the break-up of molten materials maximizes debris/coolant heat transfer, which delays the thermal attack on the reactor vessel until the debris has time to reheat.

Case 6 was identical to Case 4 except for the way cladding deformation was treated during core heatup. In Case 4, it was assumed that deformation was limited to 2% as a result of an oxide buildup on the outer surface of the cladding prior to the onset of ballooning. The oxide layer is relatively strong but less ductile than the underlying zircaloy. As a result, oxidized cladding tends to fracture at small deformations, leading to earlier oxidation of the inner cladding surfaces with the potential for earlier core heatup associated with the exothermic reaction. In contrast, cladding rupture was assumed at deformations of 15% in Case 6. That deformation provides a potential for larger in-core flow blockage, which could affect core heatup by reducing convective heat transfer to the steam flow (driven by natural circulation). In addition, core heat-up could increase, since the surface area available for oxidation increases with deformation.

The TMLB' sequence analyses with intentional depressurization were performed for four representative PWR geometries. The operating PWRs in the United States were separated into the four groups based on plant parameters deemed important to the capability of a PWR to successfully implement intentional depressurization. The four groups included one group for Combustion Engineering (CE) PWRs, one group for Babcock & Wilcox (B&W) PWRs, and two groups for Westinghouse (W) PWRs.<sup>8</sup> The calculations were performed using the late depressurization accident management strategy described in Reference 3. The Surry calculation performed in that reference was repeated for this study using the most current version of the SCDAP/RELAP5/MOD3 computer code. This version of the computer code incorporates improvements in the thermal-hydraulics and core melt progression models, as well as error corrections to code models used in the original calculation.

The first TMLB' analysis with intentional depressurization was performed for the Surry W 3-loop PWR, representative of the first group of W PWRs, repeating the calculation reported in Reference 3. The second analysis evaluated the capability of the Sequoyah W 4-loop PWR to successfully implement intentional depressurization. Sequoyah represents the worst-case PWR relative to the ability to successfully employ the intentional depressurization strategy in the second W group. Since no SCDAP/RELAP5 computer code model of Sequoyah currently exists, the analysis was performed by modifying the Surry PWR model parameters important to intentional depressurization to simulate the Sequoyah PWR. These parameters included initial core power level, initial steam generator liquid inventory, PORV relief capacity, and initial accumulator liquid volume and pressure. The changes were made using scaled values relative to Surry presented in Reference 8.

The third analysis was performed for the Calvert Cliffs PWR, a CE facility representative of all operating CE PWRs capable of implementing intentional depressurization. The last analysis was performed for the Oconee PWR, a B&W design representing the operating B&W PWRs. Sensitivity studies investigating the effect of the SCDAP/RELAP5 debris breakup model on RCS pressure and time to lower vessel head failure following core relocation were also performed for both Calvert Cliffs and Oconee. The effect of allowing debris breakup was evaluated for Surry in Cases 3 and 5 and, due to the similar analytical methodology employed, applied to the Sequoyah analysis.

This paper first provides an overview of the SCDAP/RELAP5/MOD3 computer code used for the analyses. Next, an overview of the Surry SCDAP/RELAP5 model is discussed, since the Surry model is representative of the models used for all the PWRs analyzed. The paper then provides a discussion of the no-operator-actions analyses results, preceded by an overview of the TMLB' transient using the sequence of events for the Surry PWR Base Case. The results for the intentional depressurization analyses are then presented. Finally, conclusions based on the analytical results are provided.

### SCDAP/RELAP5/MOD3 COMPUTER CODE DESCRIPTION

SCDAP/RELAP5/MOD3 was produced by incorporating models from the SCDAP,<sup>9</sup> TRAP-MELT,<sup>10,11</sup> and COUPLE<sup>12</sup> codes into the RELAP5/MOD3<sup>13</sup> code. SCDAP models provide coding for simulation of the reactor core. TRAP-MELT models serve as the basis for simulation of fission product transport and deposition. COUPLE models provide coding to allow two-dimensional finite-element heat conduction-convection calculations at user-specified locations. COUPLE detailed thermal simulations are typically used to represent molten regions in the core or lower head. And finally, RELAP5/MOD3 models allow simulation of the fluid behavior throughout the system, as well as the thermal behavior of structures outside the core. Feedbacks between the various parts of the code were developed to provide an integral analysis capability. For example, changes in coolant flow area associated with ballooning of fuel cladding or relocation are taken into consideration in the hydrodynamics.

SCDAP/RELAP5/MOD3 uses a one-dimensional, two-fluid, nonequilibrium, six-equation hydrodynamic model with a simplified capability to treat multidimensional flows. This model provides continuity, momentum, and energy equations for both the liquid and vapor phases within a control volume. The energy equation contains source terms that couple the hydrodynamic model to the heat structure conduction model by a convective heat transfer formulation. The code contains special process models for critical flow, abrupt area changes, branching, crossflow junctions, pumps, accumulators, valves, core neutronics, and control systems. A flooding model can be applied at vertical junctions. A generalized creep rupture model, which accounts for the cumulative effects of pressure- and temperature-induced stresses, is also included for prediction of pressure boundary failures. The creep rupture model can be applied to any RELAP5/MOD3 heat structure or to any structure represented by a finite-element COUPLE mesh.

SCDAP components simulate core disruption by modeling heatup, geometry changes, and material relocation. Detailed modeling of cylindrical and slab heat

structures is allowed. Thus, fuel rods, control rods and blades, instrument tubes, and flow shrouds can be represented. All structures of the same type, geometry, and power in a coolant channel are grouped together; and one set of input parameters is used for each of these groupings or components. Code input identifies the number of rods or tubes in each component and their relative positions for the purpose of radiation heat transfer calculations. Models in SCDAP calculate fuel and cladding temperatures, zircaloy oxidation, hydrogen generation, cladding ballooning and rupture, fuel and cladding liquefaction, flow and freezing of the liquified materials, and release of fission products. Oxidation of the inside surface of the fuel rod is calculated for ballooned and ruptured cladding. The code does not calculate oxidation of material (zircaloy) during or following relocation. Interactions between molten core material and the fluid below the core are explicitly modeled. Debris formation and behavior in the reactor vessel lower head and resultant thermal attack on the vessel lower head structure by the relocated core material are also treated.

### SCDAP/RELAP5/MOD3 INPUT MODEL DESCRIPTION

The PWR input models used for the analyses described in this paper utilized a common modeling philosophy. The following describes the Surry SCDAP/RELAP5 input model and, with the exception of component numbering and RCS coolant loop configuration, the following discussion applies to the CE and B&W input models as well.

The RELAP5 model was used to simulate the thermal-hydraulics of the reactor vessel, the piping in all three primary coolant loops, the pressurizer, all three steam generators, and selected parts of the secondary systems. Reactor vessel nodalization, as developed by Bayless,<sup>4</sup> is shown in Figure 1. As indicated, three parallel flow channels extend from the lower plenum through the core to the upper reactor vessel head. If the appropriate conditions exist, this arrangement will allow development of in-vessel natural circulation. Heat structures, which are shown as shaded areas, represent the structural mass of the reactor vessel walls, the core barrel and baffle, the thermal shield, the upper and lower core support plates, and structures in the upper and lower plena. External surfaces of all heat structures were assumed to be adiabatic.

Nodalizations of the primary coolant loop containing the pressurizer, as developed by Bayless,<sup>4</sup> is shown in Figure 2. With the exception of the pressurizer and associated surge line piping, similar nodalizations were included in the model to separately represent the other two primary coolant loops in the Surry PWR.

The nodalization shown in Figure 2 was used in conjunction with the reactor vessel nodalization from TMLB' initiation to core heatup. In this assessment, it was assumed that the onset of core heatup coincided with a core exit vapor superheat of 2.78 K. During this portion of the transient, full loop natural circulation of subcooled and saturated liquid can develop. As the core heats the primary coolant toward saturation, however, voids begin to form and collect at the top of the steam generator U-tubes. Once that occurs, full loop natural circulation of liquid is interrupted.

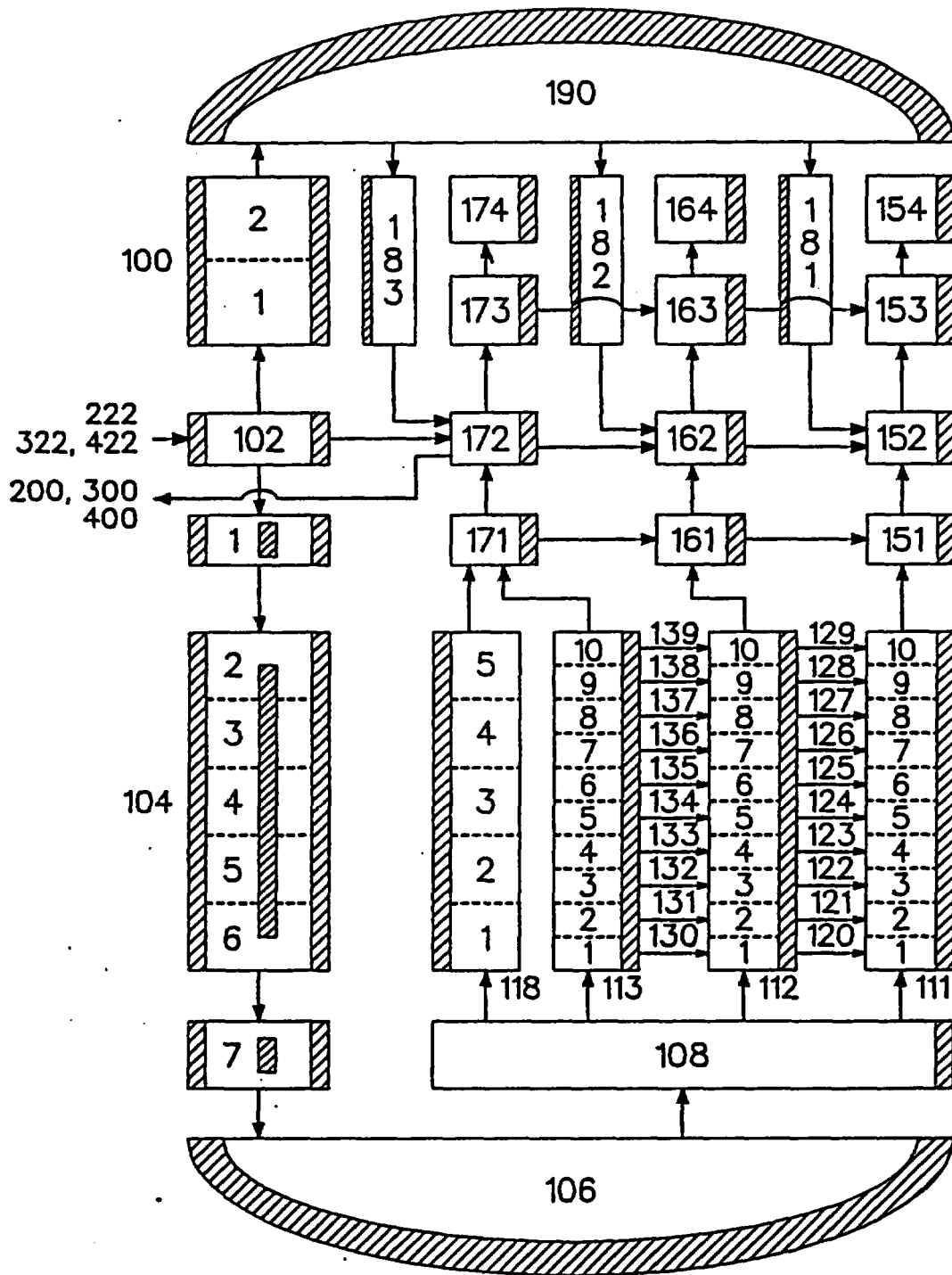


Figure 1. Surry NPP reactor vessel nodalization with provisions for in-vessel natural circulation.

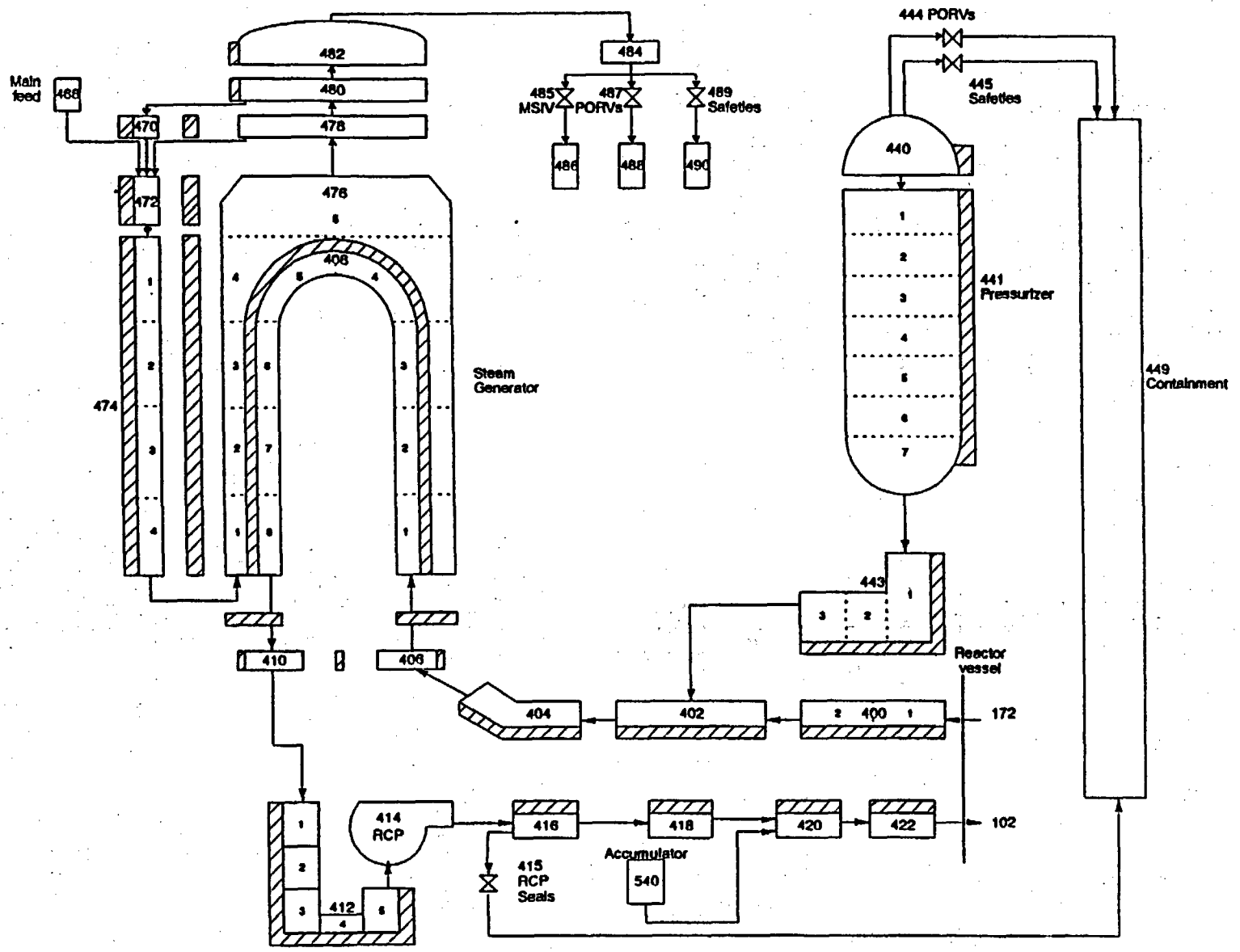


Figure 2. Pressurizer coolant loop nodalization for the Surry NPP without provisions for hot leg countercurrent natural circulation.

For the analyses assuming no operator actions, at the onset of core heatup, the Figure 2 nodalization was replaced by a more detailed representation in all calculations except those associated with Case 2. The more detailed nodalization provides the flow paths needed to represent hot leg countercurrent natural circulation. This nodalization was never used in Case 2, which was performed to evaluate conditions with minimum ex-vessel heat transfer, or in the intentional depressurization calculations, where the continued flow to the pressurizer PORV prevented hot leg countercurrent natural circulation patterns from developing. Hot leg countercurrent natural circulation becomes possible after saturated liquid in the hot legs drains to the vessel and/or flashes. At that time, temperature gradients from the core to the steam generator U-tubes can drive steam flow along the top half of the hot leg, through a portion of the steam generator U-tubes, and back to the vessel through a cooler portion of the steam generator U-tubes and the lower half of the hot leg. Note that if RCP loop seals clear, both nodalizations will allow full loop natural circulation of superheated steam. Flow areas and loss coefficients in the split hot legs, split U-tubes, and associated components were established to match experimental countercurrent flow data.<sup>4</sup>

The three core flow channels shown in Figure 1 were selected so that similarly powered fuel assemblies would be grouped together. A typical 15x15 fuel assembly used in Surry consists of fuel rods, control rods, and instrument tubes. In the SCDAP core models used for the subject analyses, control rods were combined with empty control rod guide tubes and instrument tubes in each core flow channel of the SCDAP/RELAP5/MOD3 model. This model simplification reduced the number of SCDAP components from nine to six by eliminating a separate component to simulate the instrument tubes and empty guide tubes in each channel.

SCDAP fuel rod components were linked to a table to provide an appropriate decay power curve for the Surry NPP following the loss of ac power (and associated reactor scram) in the analyses involving no operator actions. The decay power curve was based on an ORIGEN2 calculation used in the sensitivity calculations described by Bayless.<sup>4</sup> For the intentional depressurization analyses, the RELAP5 ANS79-3 kinetics model was used to allow plant-specific core parameters to be used consistently across the PWR models.

SCDAP input is required to define certain parameters that control severe core damage progression. In general, best-estimate parameters were selected where there are data or some basic understanding of the associated process. For parameters with higher degrees of uncertainty, values were selected to minimize the time to lower head failure in the analyses involving no operator actions. This approach provides the basis for a conservative evaluation of the potential for HPME, since the time available for generation of an ex-vessel failure by natural convection heating is also minimized. For the intentional depressurization analyses, the approach used was to select the best-estimate or recommended value for these parameters. Sensitivity calculations were performed for the subject analyses to ascertain the impact of the parameters on the results. A COUPLE mesh was used to represent the lower reactor vessel head in all the PWR models. The axisymmetric mesh includes elements that represent the lower vessel head structure and the lower vessel head volume that receives the relocated core debris. A layer of zero-width gap elements coincided with the inner surface of the lower head. These gap elements provide a way to model contact resistance between the debris and liner. In

all the analyses, a large conductance was used to simulate perfect debris/structure contact. This approach minimizes the time to lower head failure following relocation. The remaining elements are initially filled with primary coolant. During molten relocation, the coolant can boil-off and/or be displaced by debris.

Convection and radiation heat transfer were modeled at all interfaces between the coolant and debris. In addition, convection and radiation heat transfer were modeled along the vessel wall at all nodes that are not submerged by debris (those nodes exposed to primary coolant/steam). The external surface of the lower head was assumed to be adiabatic.

## UNINTENTIONAL DEPRESSURIZATION ANALYSES AND RESULTS

The sequence of events for the Base Case calculation is given in Table 1. Following transient initiation, decay heat was transported from the core to the steam generator secondaries by natural circulation of coolant in the primary coolant loops. As the liquid in the steam generators was boiled off, the energy being removed from the RCS by the steam generators dropped below the decay heat energy being added in the core and the RCS began to heat up and pressurize. The pressurizer PORVs controlled the RCS pressurization by cycling between the opening and closing setpoints of 16.2 and 15.7 MPa, respectively. The RCS reached saturation at 6,900 s, and boiling began in the core. Voiding in the steam generator tubes terminated full loop RCS natural circulation at 7,330 s. Venting of coolant by the pressurizer PORV reduced the RCS liquid inventory until the core was uncovered at 8,750 s, initiating core heatup and superheating of steam in the RCS. The core was completely uncovered by 10,560 s, with rapid oxidation of the fuel cladding commencing at 10,770 s.

Circulation of superheated steam in the core, upper plenum, and hot legs and cyclic flow through the pressurizer PORV to control RCS pressure removed core decay heat and caused a heatup of the hot legs and pressurizer surge line structures. The heatup resulted in a calculated creep rupture failure of the pressurizer surge line piping at 14,250 s. Assuming that the pressurizer surge line did not fail, creep rupture failure of the hot leg nozzles would be calculated to occur at 15,500 s. If none of the calculated creep rupture failures occurred, ceramic melting of core material at 16,700 s would have initiated the formation of a molten pool in the core supported by a metallic crust in the bottom of the core. The lower crust was calculated to fail at 28,850 s, causing a relocation of 66,990 kg of molten core material. The lower head was predicted to fail at 28,920 s, with an RCS pressure of 16.0 MPa and a containment pressure of 0.19 MPa. The RCS pressure response was predicated on the assumption that the RCS piping failures had not occurred.

Figure 3 shows the RCS pressure response to the Base Case TMLB' transient. The pressure initially decreased as the steam generators remove more energy than was being added by the core. The oscillations in the pressure prior to steam generator dryout at 4,700 s reflect the cycling of the steam generator secondary relief valves. Following steam generator dryout, the pressure increased to the PORV opening pressure. The pressure then cycled between the PORV opening and closing setpoint for the remainder of the transient. The

**Table 1. Sequence of events for the Surry TMLB' without intentional depressurization.**

Event	Event time by Case (s) <sup>a</sup>					
	Base	2	3	4	5	6
Accident initiation	0	0	0	0	0	0
Start of core uncover	8750	8750	8810	8490	8810	8490
Complete core uncover	10560	10640	11360	10060	11360	10060
Onset of oxidation	10770	10620	11040	10770	11040	10760
Surge line failure	14250	12930	20230	---	20230	---
First fuel clad failure	14500	12360	13230	11840	13230	12000
First hot leg failure	15500	14060	20090	---	20090	---
Beginning of accumulator injections	---	---	14280	12140	14280	12160
Initial formation of in-core molten pool	16700	15180	14510	14090	14510	20700
Accumulators empty	---	---	---	21970	28500	21790
Crust failure and core relocation	28850	15470	24200	25560	24200	23030
Lower head failure	28920	15610	24340	25980	28780	23390

a. Events marked '---' were not predicted during the calculation.

sustained pressure increase starting at 7,500 s was caused by the pressurizer becoming liquid-filled and the PORV venting liquid with a lower specific energy than steam. As noted earlier, an RCS boundary breach was not associated with the creep rupture failure of the surge line or hot legs. The effect of the breach would be a rapid reduction in RCS pressure starting at 14,250 s.

Figure 4 shows the temperature of the top of the pressurizer loop hot leg nozzle and the pressurizer surge line at the entrance to the hot leg. Due to its smaller thermal mass, the pressurizer surge line heated up faster and was predicted to fail earlier than the hot leg nozzle. Note that the hot leg nozzle failure prediction was based on the assumption that no RCS boundary failure was associated with the surge line creep rupture failure prediction.

The sequence of events for Case 2 are also given in Table 1. The Case 2 sensitivity calculation produced a more rapid progression of core damage than the Base Case. By eliminating the hot leg countercurrent flow, the only structures available to absorb core heat were in the upper plenum and along the

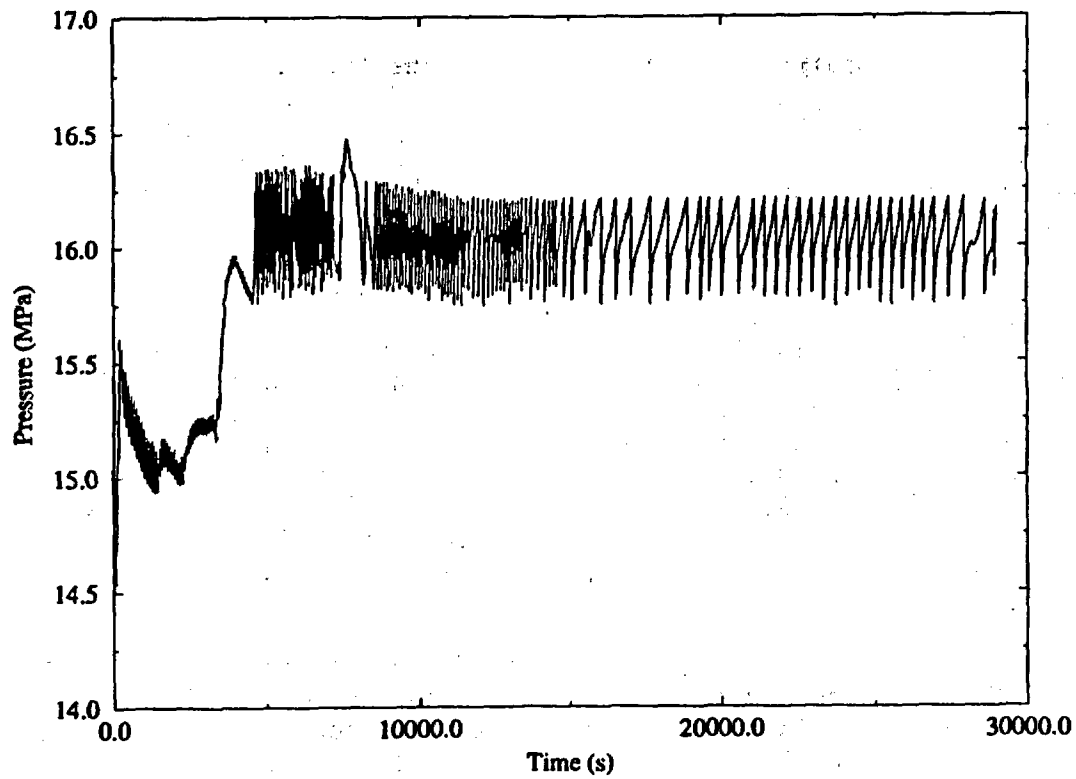


Figure 3. Reactor vessel lower head pressure vs. time for the Surry TMLB' Base Case.

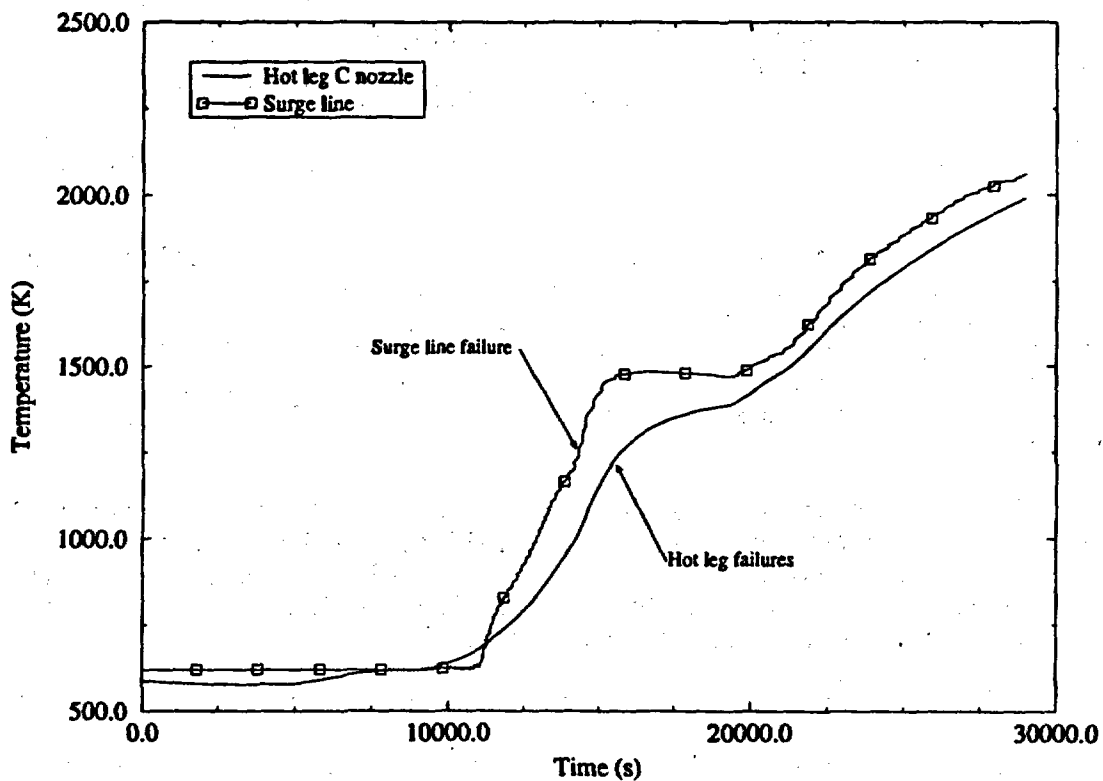


Figure 4. Hot leg and pressurizer surge line nozzle volume average structure temperature for the Surry TMLB' Base Case.

flow path from the upper plenum to the pressurizer (structure in the hot leg between the vessel and pressurizer surge line, and the pressurizer surge line). The faster core heatup produced a more rapid increase in steam temperatures than observed in the Base Case and resulted in a calculated creep rupture failure of the pressurizer surge line and the pressurizer loop hot leg nozzle 1,320 s and 1,440 s earlier than in the Base Case, respectively.

A major difference between the two calculations occurred in the core damage progression. For Case 2, the upper half of the core began meltdown at 15,180 s, 1,520 s earlier than in the Base Case. The resultant relocating Zr-UO<sub>2</sub> cooled and solidified at 1.10 m above the bottom of the core instead of at the core bottom, as observed in the Base Case. The initial melting of ceramic debris therefore occurred near the core midplane and had a higher heat generation rate than that formed in the Base Case. As a result, the bottom crust heated up and failed at 15,470 s; and 6,850 kg of molten core material relocated to the lower head. The massive relocation resulted in a creep rupture failure of the lower head at 15,610 s, 13,310 s earlier than in the Base Case calculation.

Case 3 was performed to evaluate the effect of RCP seal leakage on the potential for HPME through comparison to the Base Case. Before making that comparison, some details of this calculation need to be described to facilitate subsequent evaluation of the other RCP seal leak cases. The sequence of events from TMLB' initiation to creep rupture failure of the lower head for this calculation is summarized in Table 1.

Seal leaks of 21 gpm per RCP were introduced at TMLB' initiation to account for seal heating failure due to the loss of cooling water. Following RCP coast-down, decay heat was transported from the core and rejected to the steam generator secondaries by full loop natural circulation of subcooled and saturated liquid. At the same time, mass and energy were also removed by discharge through RCP seal leaks, leading to an RCS depressurization, as shown in Figure 5.

Following steam generator dryout, the energy removed by superheating vapor in the steam generator secondaries plus the energy discharged through the RCP seal leaks was less than the decay heat produced in the core. As a result, temperatures and pressures in the RCS began to increase. At 5,840 s, RCS pressure reached the opening setpoint of the pressurizer PORV. PORV cycling followed, which controlled RCS pressure between 15.7 and 16.2 MPa, as indicated in Figure 5.

In-core boiling and discharge through the PORV and the RCP seals reduced RCS inventory, with core uncover beginning at 8,810 s. By 9,680 s, core energy was absorbed by heat transfer to vessel and ex-vessel structures and by discharge through the RCP seals. At that point, PORV cycling ended and a second depressurization followed, as shown in Figure 5.

Cladding oxidation in the high-temperature steam environment began at 11,040 s and gradually increased as the core uncovered. Uncover was completed at 11,360 s. The exothermic oxidation reaction increased core temperatures, which led to fuel rod gas pressurization and the first clad rupture at 13,230 s. Clad rupture allowed double-sided oxidation, which produced an abrupt increase in core temperatures. Molten materials from the highest temperature

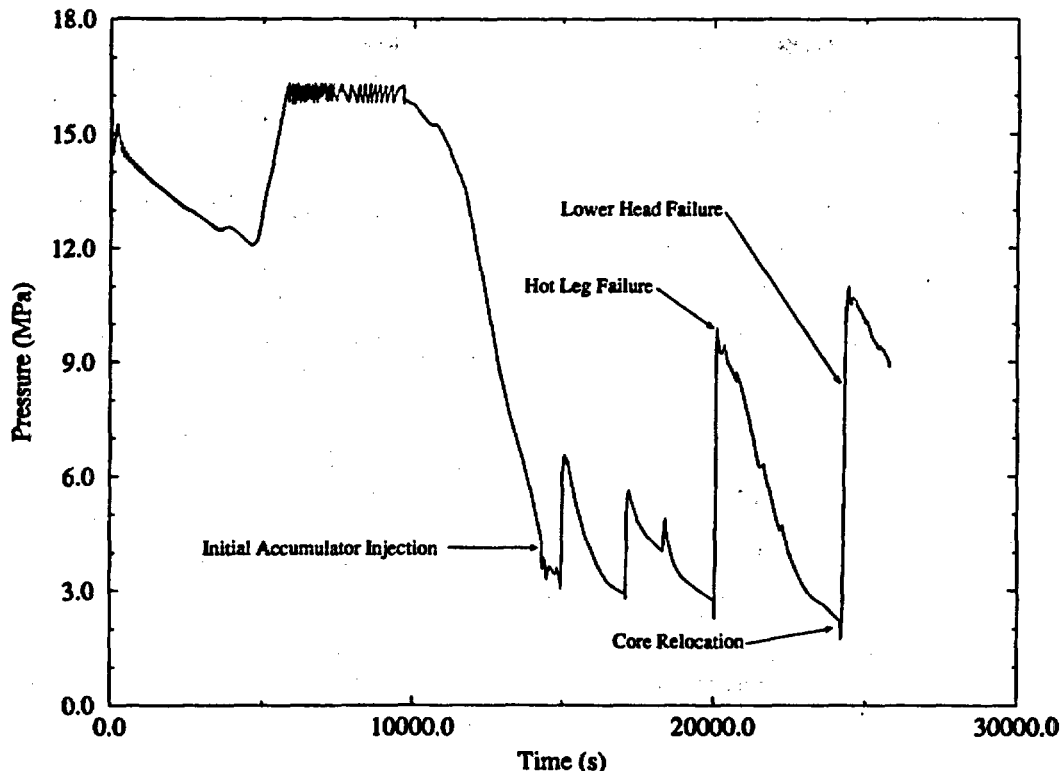


Figure 5. Reactor vessel lower head pressure vs. time for Surry TMLB' Case 3.

(highest power) regions near the center of the core began slumping shortly thereafter. A metallic crust was established as mixtures of cladding and dissolved fuel were frozen at an elevation 0.366 m above the bottom of the center channel. Meltdown in the center channel followed as a result of restricted cooling following crust formation.

RCS pressure was reduced to the initial accumulator pressure at 14,280 s by continued leakage through the RCP seals. Accumulator injection followed in four cycles. During each cycle, the RCS pressure dropped below the accumulator pressure and water was injected, cooling hot structures and core materials. Steam generated during the cooling increased RCS pressure to a point above the accumulator pressure, which terminated injection. The surge line piping was predicted to fail due to creep rupture at 20,230 s. Following the final injection cycle, a boil-off reduced crust heat transfer, leading to crust heatup and failure at 24,200 s. Crust failure allowed 12,370 kg of molten core material to relocate to the lower head. Thermal attack by the relocated core debris resulted in a creep rupture failure of the lower head at 24,340 s with an RCS pressure of 8.56 MPa and containment pressure of .16 MPa. Since creep rupture of the surge line occurred before this time, the potential for HPME should not exist under these conditions.

Case 4 was performed to evaluate the effect of depressurization rate on the potential for HPME through comparison to Case 3. This calculation was identical to Case 3 except that seal leakage was increased from 21 to 480 gpm per RCP at saturation. Thus, the sequence of events from TMLB' initiation to RCP saturation was identical to those listed for Case 3. Events from RCP saturation to creep rupture failure of the lower head are summarized in Table 1.

With respect to Case 3, the sequence of events in Case 4 is relatively early from RCP saturation to the first accumulator injection and relatively late thereafter. This relationship is consistent with the difference in RCP seal leak rates, as explained below.

Events from RCP saturation to the first accumulator injection occurred earlier in Case 4 because RCS coolant was depleted through RCP seal leaks at a faster rate. Since core uncover began sooner and progressed at a faster rate in Case 4, the onset of core damage (oxidation, ballooning) was also relatively early. Consistent with the difference in leak rates, depressurization to the initial accumulator pressure in Case 4 was 2,140 s earlier than in Case 3.

In addition to a relatively early start on accumulator cycling, the time lag between the onset of core damage and injection was shorter in Case 4. The initial accumulator pressure was reached 1,370 s after the onset of oxidation in Case 4, while 3,280 s elapsed in Case 3. As a result, reactor vessel liquid inventory was higher in Case 4 at the onset of core degradation, somewhat delaying core relocation and lower head failure relative to Case 3.

In this calculation, a lower crust failure at 24,200 s allowed relocation of 15,120 kg of molten core material to the lower head. The resultant failure of the lower head by creep rupture was predicted at 25,980 s, some 1,550 s after lower head failure in Case 3.

All ex-vessel RCS pressure boundaries were intact at the time of lower head failure in this calculation. With an RCS pressure of 1.36 MPa at the time of vessel failure, it is clear that a potential for HPME exists in this case.

Case 5 was performed to evaluate the effect of debris/coolant interaction on the potential for HPME through comparison to Case 3. Debris/coolant interaction was varied in this calculation by assuming that molten debris would break up during relocation to the lower head. Therefore, the sequence of events from TMLB' initiation up to the first molten relocation at lower crust failure was identical to that for Case 3. Case 5 events from accident initiation to creep rupture failure of the lower head are summarized in Table 1.

A pour of molten materials from the core is fragmented during relocation to the lower head if debris breakup is assumed (Case 5). The total heat transfer from the relocating materials is large because the surface area of the fragments exposed to the coolant is large. As a result, the pour is quenched before reaching the lower head. In contrast, molten materials pour from the core to the lower head in a coherent stream if an intact debris relocation is assumed (Case 3). Heat transfer from the molten materials is not calculated, since the exposed surface area is relatively small and the relocation period is (normally) short. The temperature of the relocated debris is initially much higher and the RCS pressure is much lower due to the lack of heat transfer to the coolant during relocation if debris breakup does not occur. The lower head was predicted to fail 4,480 s later with debris breakup (Case 5) than without (Case 3). The RCS pressure at vessel breach was 6.5 MPa. Due to earlier creep rupture failure of the RCS piping, the potential for HPME should not exist in this case (similar to Case 3).

Case 6 was performed to evaluate the effect of clad deformation on the potential for HPME through comparison to Case 4. The only difference between Cases

4 and 6 was in the specification of the maximum rupture strain, which controls the clad deformation associated with ballooning. Therefore, the sequence of events from TMLB' initiation to the first fuel cladding failure was identical in Cases 4 and 6. Case 6 events from the first fuel cladding failure to creep rupture failure of the lower head are summarized in Table 1.

Fuel pin pressure increases with core temperature. Ballooning begins when the difference between pin pressure and RCS pressure exceeds the clad strength, and deformation terminates when the clad ruptures. In Case 6, maximum deformations of 12.5% in the center and middle and 15 % in the outer channels were predicted to occur. Those deformations were larger than the 2% rupture deformations calculated in all flow channels in Case 4.

The coolant flow area through the core is reduced in proportion to the deformation as the cladding balloons. The higher core resistance resulted in longer accumulator injection cycles due to the longer time required for accumulator water to reach the hot core surfaces and flash. The longer accumulator injections produced an earlier emptying of the accumulators than observed in Case 4.

The core heatup proceeded more rapidly in Case 6 following the last accumulator injection. As a result of the faster core heatup, the crust in Case 6 reached a temperature of 2,200 K and failed at 23,030 s, 2,530 s before crust failure in Case 4. The resulting relocation of 52,350 kg of molten core material produced an associated creep rupture failure of the lower head at 23,390 s, 2,590 s earlier than observed for Case 4.

All ex-vessel RCS pressure boundaries were intact at the time of lower head failure in Case 6. With an RCS pressure of approximately 1.4 MPa at the time of failure, it is clear that a potential for HPME exists in this case.

## INTENTIONAL DEPRESSURIZATION ANALYSES AND RESULTS

This section of the paper describes the analytical results for a TMLB' sequence incorporating an intentional depressurization accident management strategy for the Surry, Sequoyah, Calvert Cliffs, and Oconee PWRs. The Surry results are presented first, through comparison to those results obtained in the Base Case calculation. The results for the other PWR intentional depressurization analyses are compared to the Surry intentional depressurization results.

The intentional depressurization strategy would be initiated by the operator when the core exit thermocouple temperature reached 922 K. The Surry results for the Base Case should be identical up to this point. However, replacing the ORIGEN2 decay heat tables with the ANS79-3 kinetics model produced a time shift of +190 s to the beginning of core uncovering. This time shift was not significant relative to the findings for the subject analyses.

One major model change made for the Surry intentional depressurization analysis compared to the Base Case was that relocating debris was assumed to break up. Since this assumption results in the maximum heat transfer between the relocating material and the liquid in the lower head, this assumption should

result in a higher RCS pressure increase than the Base Case during relocation. In addition, since the stored energy of the relocating material is transferred to the lower head liquid, additional time would be required for the debris to heat up sufficiently to fail the lower head. This assumption should result in a longer time to lower head failure than the Base Case.

The sequence of events for the Surry intentional depressurization analysis is given in Table 2. As stated above, the sequence was identical to that observed in the Base Case up to the start of core uncover. Due to differences in the steam generators for the PWRs analyzed, steam generator dryout time is included in the sequence of events. Steam generator dryout occurred at 4860 s. At this point, the RCS rapidly heated up and pressurized until the PORV setpoint pressure was reached at 4910 s, as shown in Figure 6. Since the RCS coolant inventory was continually being removed while the PORVs cycle, the core eventually begins to uncover at 8940 s. As the fuel cladding temperature increased, the steam became superheated. At 10,470 s, the core exit steam temperature reached 922 K and the PORVs were latched open, in accordance with the intentional depressurization strategy.

After the PORVs were latched open, the RCS pressure began to decrease until the accumulator setpoint pressure is reached. This occurs at 11,560 s, 1090 s after latching open the PORVs. This time was dependent upon three factors: (a) PORV setpoint pressure; (b) accumulator setpoint pressure; and (c) the PORV ratio.<sup>8</sup> The PORV setpoint pressure at Surry is typical of W nuclear power plants at 16.20 MPa. The accumulator setpoint pressure at 4.24 MPa is also typical of W plants. Finally, the PORV ratio for Surry is 1.00. Values for this ratio in other W plants range from 1.78 down to 0.75. The PORV ratio of Surry is the lowest value for W Group 1.

Once accumulator injection begins, injection cycles were predicted to continue until the accumulators empty. The RCS pressure increased following each injection due to vaporization of the accumulator liquid as it contacted hot core structures, halting the accumulator injection. The injection resumed when the RCS again depressurized via the PORVs to a point below the accumulator pressure. Between accumulator injections, the core structures began to heat up, and once the accumulator actuation pressure was reached for the next injection, this cycle was repeated. However, with each additional cycle, the core structure temperature increase was not as large and the RCS pressure increase following injection became less, as shown in Figure 6. From 16,500 s until the accumulators empty at 23,590 s, accumulator injections were smaller, maintaining a core liquid level about 1.3 m above the core inlet. The RCS pressure increase due to these smaller injections was minimal, resulting in a steady RCS pressure decrease as the accumulators emptied. Once the accumulators were completely empty, the RCS pressure smoothly decreased until core relocation began.

Because of the short time required to initially reach the accumulator setpoint pressure, only minimal core damage was predicted to occur before the first accumulator injection. Fuel rod cladding oxidation began at 10,750 s, the same time as in the Base Case, but was stopped by the accumulator injection cooling the core. Fuel cladding failure occurred at 11,220 s as a result of cladding ballooning and rupture, instead of the clad melting failure observed in the Base Case. Following accumulator injection, the center fuel channel melted and formed a molten pool starting at 27,230 s.

Table 2. Sequence of events for TMLB' with intentional depressurization for representative PWRs.

Event	Event time (s) <sup>a</sup>			
	Surry	Sequoyah	Calvert Cliffs	Oconee
Accident initiation	0	0	0	0
Steam generator dryout	4860	4560	3480	900
Start of core uncover	8940	8650	6100	1760
PORV latched open	10470	10090	9560	4570
Onset of oxidation	10750	10320	9860	4790
First fuel clad failure	11220	11080	10730	7190
Beginning of accumulator injections	11560	11530	12270	10120
Surge line failure	23580	23010	----	16940
Initial formation of in-core molten pool	27230	26700	15770	9930
Accumulators empty	23590	23772	----	----
Crust failure and core relocation	29010	30070	16990	19310
Lower head failure with/without debris breakup	29350	30390	29060/ 17740	19660/ 19820

a. Events marked with '----' were not predicted during the calculation.

Due to the low stresses in the surge line piping, the SCDAP/RELAP5 creep rupture model did not predict surge line failure. However, using the pressure-induced stress on the surge line in conjunction with the surge line temperature profile and ultimate strength data of the surge line material, an estimate can be made of the surge line failure time. Using this criteria, it was estimated that, at the latest, the surge line would fail at 23,580 s upon reaching an average structure temperature of 1530 K.

By 28,390 s, the entire center and middle fuel channels were molten in a manner similar to that observed in the Base Case. As in the Base Case, a crust of metallic material was formed at the bottom of the core that supports the pool of molten material. Failure of the bottom crust occurred at 29,010 s with 73,741 kg of molten core material relocating to the lower head, resulting in a creep rupture failure at 29,350 s.

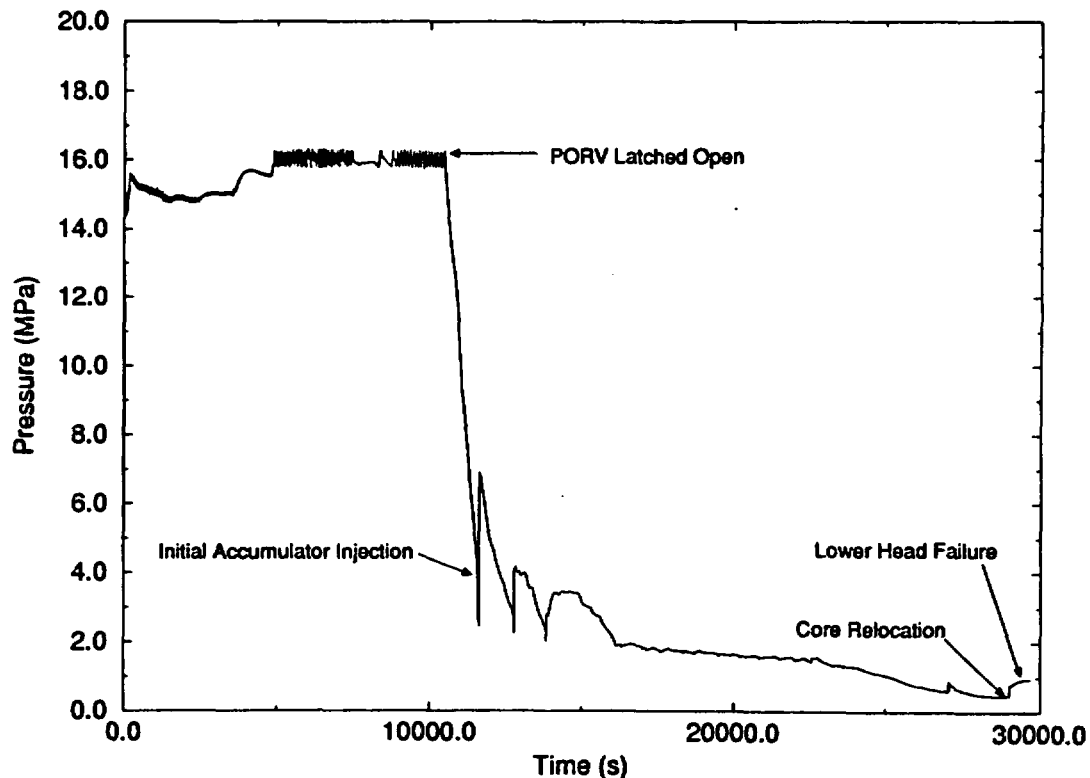


**Figure 6.** RCS pressure vs. time for the Surry TMLB' with intentional depressurization.

The debris breakup assumption for this case dictates that the relocating core material will be quenched due to contact with the liquid in the lower reactor vessel. Because the energy transfer occurred rapidly during relocation, lower head liquid was either vaporized or carried out by the high steam velocities. There was insufficient liquid in the lower head 0.7 s into the core relocation to quench the relocating material and the remainder of the relocation, roughly 99% of the total mass, relocated as a cohesive molten stream, as in the Base Case. Because the amount of mass relocated with debris breakup assumed was small, the RCS pressure increase associated with quenching was also small. The RCS pressure (Figure 6) during the entire relocation rose from 0.49 MPa to only 0.78 MPa. At the time of lower head failure, RCS pressure was 0.92 MPa, with a containment pressure of 0.16 MPa. Due to the low RCS pressure at lower head failure and the anticipated surge line creep rupture failure prior to lower head failure, the potential for HPME does not exist.

The second analysis evaluated was the TMLB' sequence with intentional depressurization for the Sequoyah PWR. As discussed earlier, the Sequoyah intentional depressurization analysis did not use a Sequoyah model; instead, the Surry model from the previous analysis was modified to simulate the Sequoyah PWR. The calculation was performed from transient initiation until lower head failure is predicted. The sequence of events is presented in Table 2.

The total secondary side water mass of the Sequoyah steam generators is smaller than Surry's (280,400 kg versus 291,000 kg); thus, as would be expected, the Sequoyah steam generators dried out earlier--in 4560 s, compared to 4860 s for Surry. Once the steam generators dried out, the RCS quickly heated up and

pressurized until the PORV setpoint pressure was reached at 4572 s. At 10,090 s, 380 s earlier than Surry, the core exit steam temperature reached 922 K and the PORVs were latched open.

Once the PORVs were latched open, the RCS pressure decreased to the accumulator setpoint pressure, as shown in Figure 7. This occurred at 11,530 s, 1440 s after latching open the PORVs. The time for RCS pressure reduction was one-third longer than was predicted for Surry. The accumulator setpoint pressure for Sequoyah is 4.65 MPa, slightly higher than the 4.24 MPa setpoint pressure of Surry. Also, the PORV ratio for Sequoyah is 0.75 compared to 1.00 for Surry. Based on these differences, it would be expected that Sequoyah would require more time to reduce the RCS pressure to the accumulator setpoint than Surry.

Once accumulator injection began, injection cycles were predicted to continue until the accumulators were empty at 23,772 s. From Figure 7, it is seen that the same pressure response during accumulator injection was observed for Sequoyah as was observed for Surry. The delay in emptying the accumulators relative to Surry is related to the smaller PORV in the Sequoyah analysis.

Because the time to reach the accumulator setpoint was longer than was predicted for Surry, more core damage was predicted to occur during this time period for Sequoyah. Fuel rod cladding oxidation was initiated at 10,320 s, and the initial fuel rod failure due to fuel rod cladding ballooning occurred at 11,080 s. Unlike the Surry calculation, the stresses in the surge line piping were sufficient to allow the SCDAP/RELAP5 creep rupture model to predict surge line failure at 23,010 s.

The center fuel channel began melting at 26,700 s. As in Surry, the molten core material was supported by a metallic crust at the bottom of the core. Failure of the bottom crust occurred at 30,070 s, with 73,828 kg of molten core material relocating to the lower head. The 1060 s delay relative to Surry was due to the protracted accumulator injection period discussed previously. The lower head was predicted to fail due to creep rupture at 30,390 s, with an RCS pressure of 0.98 MPa and a containment pressure of 0.16 MPa.

The third analysis evaluated the TMLB' sequence with intentional depressurization for the Calvert Cliffs PWR. The calculation was performed from transient initiation until lower head failure is predicted. The sequence of events for the transient is presented in Table 2.

The total secondary side water mass of the Calvert Cliffs steam generators is equivalent to that of Sequoyah (121,474 kg for Calvert Cliffs versus 127,189 kg for Sequoyah). Although both plants have an equivalent initial thermal power (2700 MW<sub>t</sub> for Calvert Cliffs versus 2715 MW<sub>t</sub> for Sequoyah), Calvert Cliffs' steam generators dried out at 3480 s, 1080 s earlier than Sequoyah's. This is a result of a much higher heat transfer rate brought about by a much higher natural circulation flow rate through the Calvert Cliffs steam generators. Once the RCS enters full loop natural circulation after the reactor coolant pumps coast down, the larger diameter of the Calvert Cliffs hot leg piping allows a mass flow rate approximately 35% higher than is calculated for Sequoyah. This allows heat to be transferred from the reactor core to the steam generators more quickly.

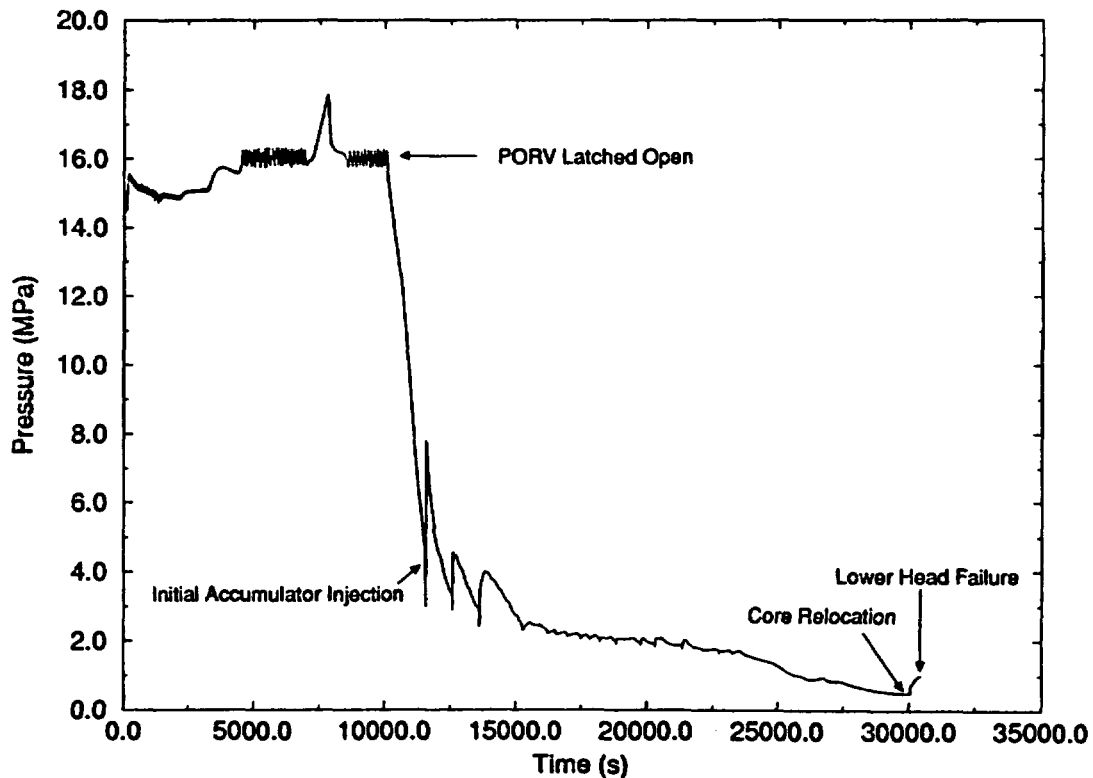


Figure 7. RCS pressure versus time for the Sequoyah TMLB' with intentional depressurization.

The PORV setpoint pressure was reached soon after steam generator dryout at 3738 s, as shown in Figure 8. The PORVs cycled to maintain RCS pressure until the core exit steam temperature reached 922 K; the PORVs were latched open at 9560 s. Once the PORVs were latched open, the RCS pressure began to decrease until the accumulator setpoint pressure was reached at 12,270 s. The RCS pressure reduction was over twice as long as predicted for Surry. The PORV setpoint pressure of 16.55 MPa for Calvert Cliffs is higher than other PWR types (16.20 MPa for W PWRs and 15.65 MPa for B&W PWRs). The accumulator setpoint pressure for CE PWRs was the lowest of any nuclear power plant type at 1.48 MPa compared to a typical value for other types of 4.24 MPa. Finally, the PORV ratio for Calvert Cliffs is 0.73 compared to Surry's value of 1.00. As a result of these factors, it would be anticipated that Calvert Cliffs would require more time to reduce the RCS pressure to the accumulator setpoint pressure.

Once accumulator injection began at 12,270 s, only three injection cycles were predicted to occur, with the last injection occurring at 20,778 s. A substantial volume of liquid was injected during each of these cycles, with 86.4% of the accumulator inventory injected prior to lower head failure. The large injections resulted from the low RCS pressure at the time of the injections. As the accumulator liquid enters the vessel, energy was removed from the vapor in the lower head to heat the injected fluid. At low pressures, the heat of vaporization is higher. As energy was removed from the vapor, it condensed; the RCS pressure decreased and more accumulator liquid was injected. This process continued until the liquid level reached the hot core structures and

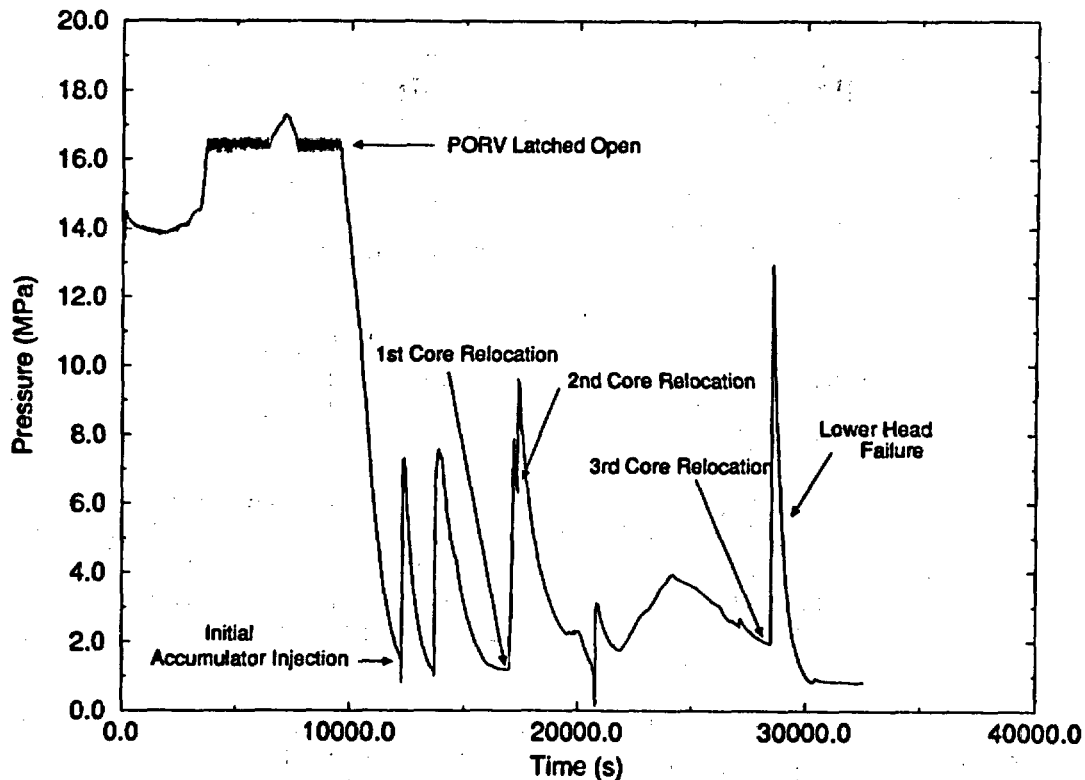


Figure 8. RCS pressure versus time for the Calvert Cliffs TMLB' with intentional depressurization.

flushed, causing the RCS pressure to increase rapidly and halting the accumulator injection.

The extended time required to reach the accumulator setpoint pressure relative to Surry resulted in more core damage before accumulator injection. Fuel rod cladding oxidation was initiated at 9860 s, and fuel rod failure due to cladding ballooning occurred at 10,730 s. The center fuel channel began melting at 15,770 s, 11,460 s earlier than Surry. This was the result of fuel rod fragmentation during the initial accumulator injection blocking flow to the center two core channels. The fragmentation resulted from the high fuel rod temperatures predicted for Calvert Cliffs. The early rod fragmentation limited the cladding oxidation to 24% of the cladding (compared to a value of 70% for Surry), since SCDAP/RELAP5 does not account for cladding oxidation after rod-like geometry is lost. The reduction in oxidation energy and core flow area reduced the core exit steam temperature and prevented the surge line piping from heating up and failing.

The molten core material was supported by a metallic crust as in the other analyses but located 1 m above the core inlet. The crust was predicted to fail at 16,990 s, with 13,087 kg of molten core material relocated. A second failure at 17,290 s relocated an additional 7,251 kg of molten core material. With the assumption that relocating debris would break up, the lower head failure time was 29,060 s, since there was sufficient liquid below the crust to quench the debris. The RCS pressure was 4.5 MPa, and the containment pressure was 0.30 MPa. With no RCS piping failures predicted, the potential for HPME exists.

A sensitivity calculation was performed to determine the effect of the debris breakup assumption. The result, as shown in Table 2, was a calculated lower head failure time of 17,740 s, 11,320 s earlier than the debris breakup case. Since the debris did not interact with the coolant in the lower head, the RCS pressure increase due to the relocation was only 1 MPa and the thermal attack on the lower head structure was much faster. The RCS pressure at lower head failure was 2.0 MPa, with an 0.24 MPa containment pressure. The potential for HPME still exists.

The final analysis evaluated the TMLB' sequence with intentional depressurization for the Oconee PWR. The calculation was performed from transient initiation until lower head failure was predicted. The sequence of events for the transient is presented in Table 2.

The total secondary side water mass of the Oconee once-through steam generators (OTSG) is 50% of that for the Surry steam generators (70,807 kg for Oconee compared to 131,998 kg for Surry). This resulted in the steam generators drying out 900 s after transient initiation. The rapid reduction in steam generator heat transfer early in the transient results in an RCS pressure increase to the PORV setpoint 192 s into the transient, as shown in Figure 9.

Once the PORV setpoint was reached, the PORV cycled to maintain RCS pressure; but, because of the relatively small relief capacity of the Oconee PORV (13.5 kg/s compared to 45.1 kg/s for Surry), it was impossible for the PORV to maintain RCS pressure. The pressurizer filled with liquid at 1190 s, and the RCS pressure continued to increase until the pressurizer safety relief valve (SRV) setpoint was reached at 2400 s. By 3000 s, the PORV and SRVs were again discharging steam; at 3720 s, the heat removal rate through the SRVs and PORV exceeded the decay heat generation rate in the core and the RCS pressure began to decrease.

Since the RCS coolant inventory was continually being removed during this period, the core eventually began to uncover at 2430 s. The core exit steam temperature reached 922 K at 4570 s, and the PORV was latched open in accordance with the intentional depressurization strategy. This occurred soon after the SRVs ceased operation, but before the RCS pressure had dropped below the PORV closure setpoint. Once the PORV was latched open, the RCS pressure decreased to the core flood tank (CFT) setpoint pressure at 10,120 s. The time for RCS pressure reduction was over five times longer than was predicted for Surry. The PORV setpoint pressure at Oconee and other B&W plants is lower than other plant types at 15.65 MPa. The CFT setpoint pressure of Oconee is typical of the accumulator setpoint pressure of W plants at 4.24 MPa, but higher than the CE value of 1.48 MPa. Finally, the PORV ratio for Oconee is 0.24, compared to Surry's value of 1.00. From the PORV ratio alone, it would be anticipated that Oconee would require more time than was predicted for Surry to reduce the RCS pressure to the CFT setpoint pressure.

Unlike the other PWR analyses, the higher decay heat levels and extended time required to reach the accumulator setpoint pressure resulted in significant core damage for Oconee before CFT injection began at 10,120 s. Fuel rod cladding oxidation was initiated at 4790 s, and fuel rod failure due to cladding ballooning occurred at 7190 s. Over 70% of the cladding in the core was oxidized before the initial CFT injection. The fuel in the center channel began melting at 9,930 s, effectively blocking that channel from CFT cooling.

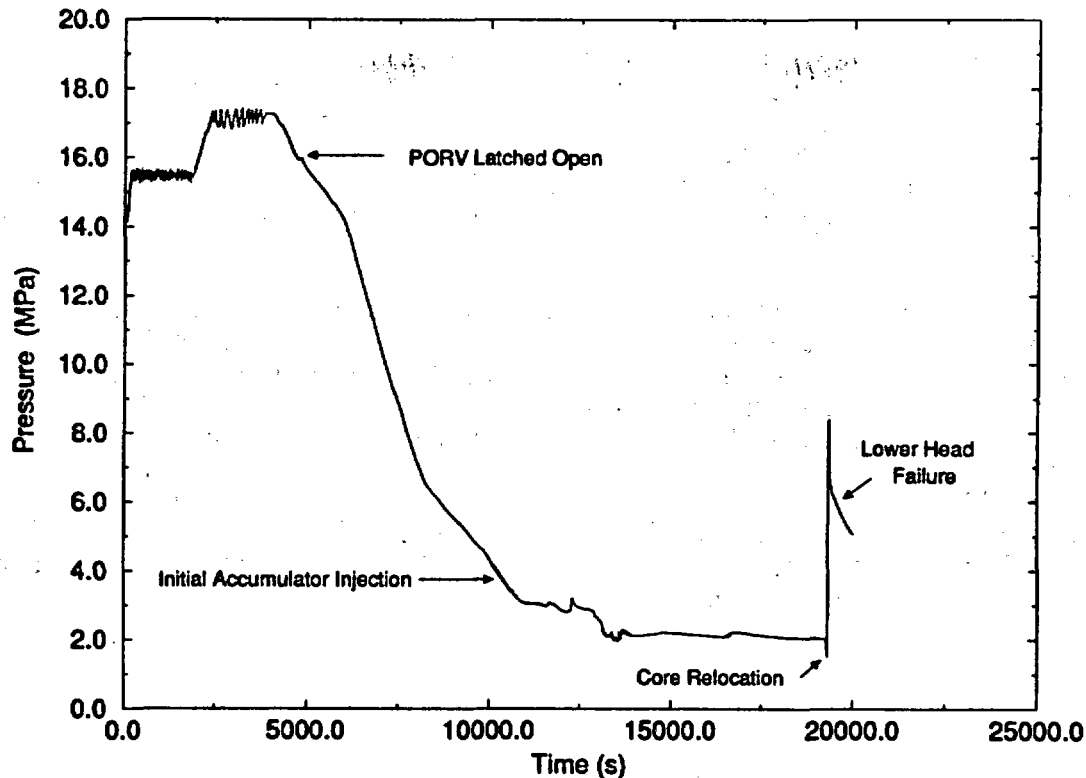


Figure 9. RCS pressure versus time for the Oconee TMLB' with intentional depressurization.

Once CFT injection began, all injection cycles have a short duration. (CFTs are equivalent to accumulators in CE and W PWRs except that CFTs inject directly into the reactor vessel instead of the cold leg piping.) This was because of the slow RCS pressure reduction caused by the small PORV capacity. The RCS pressure (Figure 9) barely decreased below the CFT setpoint before the injected liquid was vaporized, raising the RCS pressure above the CFT pressure and terminating the injection. The CFT injection period lasted 9180 s, with 54.6% of the CFT volume being injected.

Failure of the surge line was calculated to occur during the CFT injection portion of the transient. SCDAP/RELAP5 predicted creep rupture failure of the surge line at 16,800 s. An analysis of the surge line's ultimate strength was performed, using the pressure-induced stress on the surge line in conjunction with the surge line temperature profile and ultimate strength data of the surge line material (stainless steel). This analysis estimated that a surge line failure would occur at 16,940 s when the average structure temperature reached 1500 K, 138 s later than the SCDAP/RELAP5 prediction.

As the fuel channels continued to melt, a crust of metallic material was formed 0.4 m above the bottom of the core that supported the molten material. Failure of the bottom crust occurred at 19,310 s, with 99,141 kg of molten core material relocated. The relocating material was assumed to break up, and the relocating material was initially cooled by flashing coolant in the lower head to steam, shown by the rapid RCS pressure increase at this time (see Figure 9). After 24 s of relocation, there was insufficient liquid in the lower head to quench the relocating material; and the remainder of the core

material relocated over the next 192 s as a cohesive molten stream. As the molten core material relocated to the lower head in a cohesive stream, the lower head began to heat up dramatically. At 19,660 s, creep rupture failure of the lower head was predicted. The RCS pressure at the time of failure was 5.7 MPa, and the containment pressure was 0.19 MPa. If the surge line had failed as predicted, the RCS would probably have depressurized after the relocation and HPME would not be a concern.

A sensitivity analyses relative to the debris breakup assumption was performed for Oconee. If all of the relocating material was assumed to relocate as a cohesive stream, the increase in RCS pressure due to coolant flashing does not occur. The peak RCS pressure following relocation, assuming no debris breakup, was 1.7 MPa. The lower RCS pressure resulted in a predicted creep rupture failure of the lower head at 19,820 s, 160 s later than the debris breakup case. The RCS pressure at the time of failure was 1.7 MPa, and the containment pressure was 0.19 MPa. The heatup rate of the lower head was nearly the same in both calculations, since the majority of the relocation in the debris breakup calculation was in a cohesive stream.

## CONCLUSIONS

The unintentional depressurization analyses for a Surry TMLB' indicate that creep rupture failures of ex-vessel piping can be expected to occur before lower head failure if the RCS is not depressurized by leaks. Under those conditions, RCS pressure will be maintained by pressurizer PORV cycling. During each valve cycle, energy will be transferred from the core to the hot leg and surge line piping. Hot leg countercurrent natural circulation will also transfer core decay heat to the loop piping. A sensitivity study showed that ignoring hot leg countercurrent natural circulation changes event timing but not the conclusion relative to HPME. The analyses show that the surge line will be the first RCS piping structure to fail. It is anticipated that the surge line failure would depressurize the RCS and effectively eliminate the potential for HPME.

A potential for HPME exists if RCS pressure is reduced below the pressurizer PORV setpoint by leaks. RCP seal leakage could produce the required reduction in RCS pressure. Surge line heating decreases significantly when the RCS pressure falls below the setpoint and PORV cycling stops. Hot leg countercurrent flow does provide a mechanism for continued heating of the hot legs. For an RCP leak rate of 250 gpm, the hot leg was predicted to fail before lower head failure, effectively eliminating the HPME concern. For a leak rate of 480 gpm, the RCS pressure reduction is sufficient to allow the heated hot legs to remain intact while core degradation progresses and molten core materials are relocated to the lower head. A subsequent thermal attack can produce creep rupture failure of the lower head long before the hot legs are heated to failure temperatures (at the reduced pressure).

For the analyses where the intentional depressurization strategy was employed to mitigate HPME concerns, the W design PWRs could successfully depressurize. For the CE PWRs, the Calvert Cliffs analysis results showed lower head failure at elevated RCS pressures as the first pressure boundary failure even with the PORV latched open. As a consequence, HPME is a concern with the intentional

depressurization strategy implemented. No assessment has been done for Calvert Cliffs for unintentional depressurization (no operator actions). For the B&W PWRs, the Oconee analysis showed that intentional depressurization would result in surge line creep rupture failure prior to lower head failure. Again, no assessment was made relative to unintentional depressurization in Oconee.

The potential for HPME was not changed in any of the analyses by variation of the core damage parameters. The changes in cladding deformation limits and debris coolant interaction did have a significant effect on the ultimate timing of lower head failure.

#### REFERENCES

1. D. A. Brownson et al., *Intentional Depressurization Accident Management Strategy in PWRs*, NUREG/CR-5937, EGG-2688, October 1992.
2. D. L. Knudson et al., *Assessment of the Potential for High Pressure Melt Ejection Resulting from a Surry Station Blackout Transient*, NUREG/CR-5949, EGG-2689 (Draft), November 1992
3. D. J. Hanson et al., *Depressurization as an Accident Management Strategy to Minimize the Consequences of Direct Containment Heating*, NUREG/CR-5447, EGG-2574, October 1990.
4. P. D. Bayless, *Analyses of Natural Circulation During a Surry Station Blackout Using SCDAP/RELAP5*, NUREG/CR-5214, EGG-2547, 1988.
5. C. M. Allison et al., *SCDAP/RELAP5/MOD3 Code Manual*, NUREG/CR-5273, EGG-2555 (Draft), Revision 2, Volumes 1-4, September 1991.
6. T. Boardman et al., *Leak Rate Analysis of the W Reactor Cooling Pump*, NUREG/CR-4294, 85-ETEC-DRF-1714, 1985.
7. T. A. Wheeler et al., *Analysis of Core Damage Frequency From Internal Events: Expert Judgment Elicitation*, NUREG/CR-4550, SAND86-2084, Vol. 2, 1989.
8. D. A. Brownson, *Extension of Surry Late Depressurization Strategy Results to Commercially Operating Pressurized Water Reactors*, EGG-EAST-9717, October 1991.
9. G. A. Berna, C. M. Allison, and L. J. Siefken, *SCDAP/MOD1/VO: A Computer Code for the Analysis of LWR Vessel Behavior During Severe Accident Transients*, IS-SAAM-83-002, Revision 1, July 1984.
10. H. Jordon, J. A. Gieseke, and P. Baybutt, *TRAP-MELT User's Manual*, NUREG/CR-0632, BMI-2107, February 1979.
11. H. Jordan and M. R. Kuhlman, *TRAP-MELT2 User's Manual*, NUREG/CR-4205, BMI-2124, May 1985.

12. E. C. Lemmon, *COUPLE/FLUID: A Two-Dimensional Finite Element Thermal Conduction and Advection Code*, EGG-ISD-SCD-80-1, February 1980.
13. C. M. Allison et al., *RELAP5/MOD3 Code Manual*, NUREG/CR-5535, EGG-2596 (Draft), Volumes 1-5, June 1990.

#### NOTICE

This report was prepared as an account of work sponsored by an agency of the United States Government. Neither the United States Government nor any agency thereof, or any of their employees, makes any warranty, expressed or implied, or assumes any legal liability or responsibility for any third party's use, or the results of such use, of any information, apparatus, product or process disclosed in this report, or represents that its use by such third party would not infringe privately owned rights. The views expressed in this report are not necessarily those of the U.S. Nuclear Regulatory Commission.

## RISK IMPACT OF TWO ACCIDENT MANAGEMENT STRATEGIES\*

Susan Dingman  
Allen Camp

Sandia National Laboratories  
Albuquerque, NM 87185

Probabilistic Risk Assessment is used to evaluate two accident management strategies: intentionally depressurizing the reactor coolant system of a pressurized water reactor to prevent containment pressurization during high pressure melt ejection, and flooding the containment of a boiling water reactor to prevent or delay vessel breach. Sensitivity studies indicated that intentional depressurization would not provide a significant risk reduction at Surry. A preliminary evaluation of the containment flooding strategy indicated that it might prove beneficial for some plants, but that further strategy development would be needed to fully evaluate the strategy.

### INTRODUCTION

The Nuclear Regulatory Commission (NRC) has been developing accident management strategies with the potential for terminating or mitigating severe accidents at nuclear power plants. Because severe reactor accidents involve extremely complex system and phenomenological responses involving large uncertainty, it is not always intuitive whether or not a particular strategy will actually be beneficial. An action taken to alleviate the threat from some particular phenomenological concern might worsen the threat from some other phenomenon. Thus, to evaluate a particular strategy, a comprehensive view of the accident progression must be adopted.

Probabilistic Risk Assessment (PRA) provides the natural framework for such evaluations. Using the integrated framework of a PRA, operator actions that could mitigate or terminate a severe accident can be identified, and the impact of the action on risk can be quantified. In addition, such studies can be used to assist the NRC in prioritizing severe accident research such that detailed evaluations are performed for the operator actions that have the greatest potential for risk reduction.

---

\* This work was supported by the U.S. Nuclear Regulatory Commission and performed at Sandia National Laboratories, which is operated for the U.S. Department of Energy under Contract DE-AC04-76DP00789.

The PRA methods developed for NUREG-1150<sup>1</sup> provide an integrated analysis framework that can be used to evaluate the potential ramifications of a certain action over a wide range of possible outcomes. PRA techniques have been used to evaluate the risk impact of two accident management strategies: (1) intentional depressurization in pressurized water reactor (PWR) plants and (2) containment flooding in boiling water reactor (BWR) plants. The intentional depressurization strategy involves intentionally opening the power-operated relief valves (PORVs) after core uncover to lower the reactor vessel pressure at the time of vessel breach, and thus eliminate the threat of containment failure from containment pressurization during high pressure melt ejection. The risk measure considered for this strategy was the conditional containment failure probability. The containment flooding strategy involves injecting water into a BWR containment (using containment sprays) so that the reactor vessel would be partially submerged in water. The goal of this strategy is to prevent or delay vessel breach. In evaluating this strategy, the early fatality and latent cancer risk were considered in addition to the containment failure probability.

#### INTENTIONAL DEPRESSURIZATION STRATEGY

In the NUREG-1150 study, scenarios with loss of all coolant injection because of the loss of all offsite and onsite ac power (station blackout scenarios) were found to be important contributors to risk for the PWRs that were examined. In such scenarios there is the potential for vessel breach occurring with the reactor coolant system (RCS) at an elevated pressure. The pressurized blowdown of the RCS could sweep the molten material and gases exiting the RCS out of the reactor cavity and into the containment. This could lead to very rapid and efficient heat transfer to the atmosphere, possibly accompanied by oxidation reactions and hydrogen burning that further enhance the energy transfer. The pressurization accompanying this process, which is labeled direct containment heating (DCH), could potentially fail containment.

An accident management strategy has been proposed in which the operator would be directed to open the PORVs shortly after the core uncovers (as indicated by elevated core exit thermocouple readings). If this action were to succeed in reducing the RCS pressure, the driving force for DCH and the resultant containment threat would be eliminated. SCDAP/RELAP5 code evaluations<sup>2</sup> indicate that this strategy can reduce the pressure sufficiently to mitigate the DCH loads for a short-term station blackout sequence (immediate loss of all coolant injection when ac power is lost) at some plants, and is thus worthy of further evaluation.

To determine whether or not this strategy should be implemented, other factors need to be considered. The relative importance of DCH-induced containment failure and other threats must also be considered. For example, in the NUREG-1150 study, long- and short-term station blackout sequences were found to be the dominant contributors (56% and 13%, respectively) to core damage frequency for Surry, but were much less important (15% combined) than the containment bypass scenarios to the risk of early and latent cancer fatalities. Because of the dominance of bypass sequences to the risk at Surry, evaluation of the intentional depressurization strategy does not show a large effect in terms of overall risk reduction. It is possible that station blackout sequences will be

more important to risk at other plants because of differences among plants that will affect core damage frequencies, accident progression pathways, source terms, and consequences.

Although some station blackout sequences would be expected to proceed to vessel breach at high RCS pressure, there is a possibility of induced failures (stuck-open PORV, pump seal failure, hot leg failure, surge line failure) that could depressurize the RCS before vessel breach. If there is a sufficiently high probability that these failures occur, the intentional depressurization strategy would have minimal impact on the risk results. In addition, there is the possibility of recovering ac power before vessel breach and arresting core damage. These factors, combined with a relatively low estimate for DCH loads relative to the containment strength, resulted in a low probability of containment failure from DCH at Surry (less than 1% mean failure probability).

Sensitivity evaluations using the NUREG-1150 accident progression event trees (APETs) were performed in the NUREG-1150<sup>3</sup> and Containment Performance Improvement (CPI)<sup>4</sup> programs which provide some insights into the relative importance of some of these factors for the Surry plant. Uncertainties in temperature-induced hot leg and surge line failure prompted a sensitivity study for NUREG-1150 in which temperature-induced steam generator tube ruptures and hot leg or surge line breaks were not allowed. This resulted in slightly more containment failures occurring at vessel breach, but 99% of the station blackout sequences did not have containment failure before or at vessel breach. This indicated that other factors besides hot leg and surge line failure contributed significantly to the low containment failure probabilities estimated for Surry. A simplified evaluation of intentional depressurization was conducted for the CPI program in which intentional opening of the PORVs was assumed to always occur. A small benefit was predicted from the strategy, but the results were not largely impacted because of the large contribution of bypass sequences to the Surry risk.

Further thermal-hydraulic analyses of the potential for hot leg or surge line failure have been performed since the NUREG-1150 and CPI studies were completed. An evaluation of the risk impact of the intentional depressurization strategy at Surry is being performed using this updated information. The approach used and initial results are described in the following two sections.

#### Approach for Determining Risk Impact of Strategy

The PRA evaluation of intentional depressurization is being conducted in two phases: (1) examination of the sensitivity of the core damage progression to various accident progression uncertainties, and (2) updated evaluation using uncertainty distributions that reflect the current knowledge of the phenomena involved. The first phase has been completed and identifies the factors which have the greatest impact on the results. The second phase is in progress and will provide an updated evaluation with improved estimates of these most influential parameters when completed.

The first phase of the evaluation focused on the APET. The APET is a logical framework used to determine possible accident progressions for sequences that have proceeded to core damage, and the likelihood of each accident progression.

An evaluation was performed to determine which questions in the APET have the largest impact on the risk results, so that more emphasis can be directed at determining their uncertainty distributions during the second phase of the intentional depressurization evaluation.

The process being used to perform the evaluation of the intentional depressurization strategy is shown in Figure 1. The questions in the APET that are affected by depressurization and the questions that have the largest effect on the pressure at vessel breach were first identified. Both short-term (immediate loss of heat removal) and long-term (heat removal initially available, but failing about 7 hours after ac power loss) station blackout sequences were evaluated. Appropriate sensitivity studies to examine these parameters were then defined. The APETs for short-term and long-term station blackout sequences were modified to evaluate these sensitivities, computer calculations were performed to provide the quantification, and the results were evaluated.

When examining a particular issue, the PRA model can be expanded in key areas to provide a more realistic treatment. One concern about depressurization is the increased likelihood of energetic fuel-coolant interactions (FCIs). For the PWRs, NUREG-1150 only considered alpha mode FCIs, in which containment is failed following an in-vessel FCI that is large enough to fail the reactor upper head and launch it through containment. It is also possible that an energetic FCI could occur that would fail the vessel and then pressurize containment in a manner similar to a DCH load. No significant analysis has been performed for such FCIs, so to address the possibility, sensitivity studies were conducted.

### Results

Risk evaluations were performed for ten variations of the base NUREG-1150 evaluation for the long-term and short-term station blackout groups to determine the sensitivity of the risk results to key questions in the APET. Seven variations were examined in which the Surry NUREG-1150 treatment of FCIs was used. Next, the base NUREG-1150 results and two of the variations were re-examined with a modified treatment of in-vessel FCIs.

In Variation 1, all depressurization mechanisms in the APET were disabled, then in Variations 2, 3, 4 the single depressurization mechanisms of pump seal failure, stuck-open PORV, and hot leg/surge line failure, respectively were re-enabled, using the distributions for failure from NUREG-1150. In Variation 5, the PORVs were always assumed to be opened by the operator after core uncover. In Variation 6, all depressurization mechanisms were disabled, and ac power recovery before vessel breach was prohibited. Stuck-open PORVs that occur after core uncover were treated as leaks (S3 breaks) in Variation 7, rather than being fully open (S2 breaks) as in NUREG-1150.

As noted previously, the Surry APET used for NUREG-1150 considered alpha mode FCIs but not in-vessel FCIs that fail the vessel without generating a containment-failing missile. Such FCIs could also lead to containment failure, but by overpressurization instead of missile penetration. Unfortunately, practically no analyses have been performed to assess this potential. The limited current knowledge was reflected in the Grand Gulf APET used for

NUREG-1150, using the logic depicted in Figure 2. The Grand Gulf APET included the probabilities of an in-vessel FCI occurring, and of the FCI leading to various modes of vessel failure. The probabilities of each of the failure modes are also indicated in Figure 2. The containment loads for cases with in-vessel FCIs were the same as for cases without FCIs. That is, there was no extra pressurization considered from the FCI.

Variations 8 through 10 of the Surry sensitivity evaluation used the mean values that were used in the Grand Gulf APET for the probability of in-vessel FCIs occurring and the likelihood they would lead to vessel breach for the base NUREG-1150 results, and for Variations 1 (no depressurization) and 5 (PORVs always opened). However, for the Surry sensitivity evaluations, estimates for the containment loading were also included. Loads from in-vessel FCIs that failed the vessel were approximated by high pressure melt ejection (HPME) loads. The amount of material involved in the FCI is highly uncertain, and attempts to quantify it were beyond the scope of this project. Since this objective of this study was to identify the dominant parameters that influence the evaluation of the intentional depressurization strategy, we used a high fraction of material involvement (40% or more). The results of Variations 8 through 10 can then be used to determine if further research into FCIs would be needed to fully assess the intentional depressurization strategy.

Figure 3 shows the conditional probability of being at low pressure just before vessel breach for the NUREG-1150 evaluation and for Variations 1 through 7 for the long-term station blackout plant damage state. The mean, the median, and the 5th and 95th percentile of the distributions are indicated for each case. As noted previously, the NUREG-1150 evaluation had a relatively large conditional probability of being at low pressure at vessel breach (mean value of about 65%). The first case in Figure 3 shows the distribution of the probability about these mean values. The second case shows the result when all depressurization mechanisms are removed, and simply indicates the obvious result that the conditional probability of being at low pressure is exactly zero. The next three cases show the effect of pump seal failures, stuck-open PORVs, and hot leg/surge line failures. The hot leg/surge line failures have the largest probability of being at low pressure, followed by the stuck-open PORVs, and finally, the pump seal failures. This result is not solely due to the relative sizes of the RCS ruptures; the conditional probability of failure is largest for the hot leg/surge line failure, then stuck-open PORVs, then pump seal failures. The sixth case shows the probability of being at low pressure at vessel breach if the PORVs are always opened after core uncover. Note that all outcomes are not at low pressure at vessel breach for this variation; a small portion of the results for this case are at intermediate pressure because the pressure rise from steam generation during relocation of debris to the lower head does not decay completely before vessel breach. The next case on Figure 3 is for the variation that allowed neither depressurization nor ac power recovery before vessel breach. As for Variation 1, the obvious result of zero probability of being at low pressure is calculated. The final case reflects the impact of treating a stuck-open relief valve as a leak instead of being treated as fully open. The probability of being at low pressure at vessel breach is reduced considerably from the NUREG-1150 results.

Figure 4 shows the conditional probability that the loads generated near the time of vessel breach will fail the containment for the long-term station blackout plant damage state. The figure shows results for the base NUREG-1150 evaluation and Variations 1 through 7. Note that even in the variations that are always at system setpoint pressure at vessel breach, the conditional probability of containment failure at vessel breach is low. This results from two factors. First, the DCH loads used in NUREG-1150 do not provide a severe challenge to the Surry containment, and second, a large fraction of the sequences do not proceed to vessel breach because core damage is arrested by recovery of ac power and emergency core coolant (ECC) injection.

It is also interesting to note that the variations with high probability of being at low pressure before vessel breach did not see a large enough increase in containment failures from alpha mode FCIs to significantly affect the results. The conditional probability of this failure mode increases for the variations with higher likelihood of being at low pressure, but the likelihood is still relatively low. More of an impact was observed when non-alpha in-vessel FCIs were included, as will be discussed below.

Figure 5 shows the effect of including in-vessel FCIs on the conditional probability of early containment failure. Results for the base NUREG-1150 results, the variation without depressurization, and the variation with PORVs always opened are shown with and without in-vessel FCIs considered. As shown in this figure, including in-vessel FCIs had a large impact on the results. The distributions for early containment failure probability were higher for all cases when FCIs were included. The effect of FCIs was large enough to negate the beneficial reduction in DCH loads from depressurization as can be seen by comparing the distributions for Variations 8, 9, and 10. That is, when FCIs were included, the probability of early containment failure was higher for the cases with PORVs always opened than for the cases with no depressurization.

The FCIs had a larger impact on the sensitivity results than depressurization did. Although a conservative treatment of FCIs was used, the results indicate that it is necessary to obtain a better estimate of the impact of in-vessel FCIs before a final evaluation of intentional depressurization is made.

#### CONTAINMENT FLOODING STRATEGY

Several strategies have been identified as having the potential to mitigate the consequences of a severe accident in a BWR plant.<sup>5</sup> One of these strategies involves flooding the containment during a severe accident, such that the vessel lower head is submerged in water. A study was conducted at Oak Ridge National Laboratory (ORNL)<sup>6</sup> to evaluate the impact of this strategy. ORNL evaluated the strategy for a short-term station blackout accident at several BWR plants with Mark I containments. They found that containment flooding could not prevent vessel breach, but could delay vessel breach by several hours.

Although vessel breach would not be prevented by the strategy, several other mitigating factors would be introduced, which might make the strategy valuable. The delay in vessel failure would provide additional time for recovering ac power and ECC, and for evacuation. Although the phenomena accompanying ECC injection

with a degraded core are not well understood, there is a significant probability that the melt progression could be arrested. The large depth of water in containment would also reduce the threat from drywell liner meltthrough should vessel breach occur, and would provide additional scrubbing of radionuclide releases.

The strategy also has some potential for detrimental effects. ORNL identified the need to vent the containment for this strategy, which would give an early release of some radionuclides. ORNL also predicted a larger amount of molten debris in the lower head at vessel breach than predicted without containment flooding. In addition, the large depth of water would introduce the possibility of ex-vessel FCIs that might fail the containment wall. To assess the strategy, the integral effect of these aggravating and mitigating factors was determined.

PRA techniques were used to evaluate the risk impact of the containment flooding strategy at the Peach Bottom plant. The PRA framework accounts for the complex system and phenomenological responses and interactions, such that the overall merit of the strategy can be assessed. The uncertainty in the phenomenology, which yields a wide range of potential outcomes, is also considered.

#### Approach for Assessing Strategy

To assess the containment flooding strategy, the early and latent cancer fatality risks calculated using the NUREG-1150 models were compared to the results with the containment flooding strategy included for a long-term station blackout scenario. The NUREG-1150 models were used as a base for the containment flooding risk evaluation, with modifications made to reflect the effects of the strategy. Modifications were needed in the accident progression, source term, and consequence evaluations. The modifications for each of these steps in the risk evaluation are discussed in the following paragraphs.

The containment flooding strategy has only received a limited evaluation to date. The potential for preventing vessel breach has been addressed,<sup>6</sup> but other effects (such as venting strategy, effect of ECC restoration, loads at vessel breach, effect of opening the safety relief valve (SRV) with large head of water in the tailpipe, impact on in-vessel fission product release, etc.) have not yet been addressed. Because of the limited analysis performed to date, this risk evaluation included approximations which could be refined if further analyses become available. It should be considered a scoping evaluation to determine if further analysis of the strategy is appropriate.

This study did not consider the probability that the equipment would actually succeed in performing the required functions for containment flooding, but rather, the risk impact conditional on success of the equipment was evaluated. The probability that the containment flooding system components succeed would need to be considered in future analyses if this strategy is pursued further.

The risk impact was calculated for long-term station blackouts because this group of scenarios was found to dominate the risk from internal events at Peach Bottom in the NUREG-1150 study.<sup>7</sup> ORNL's evaluation addressed a short-term station

blackout because the higher decay heat in this scenario provides a more severe challenge to the strategy. ORNL evaluated a scenario in which the batteries were available so the reactor vessel could be depressurized through the SRVs. The scenario evaluated by ORNL is appropriate for the generic evaluation performed there. However, the specific short-term station blackout scenario studied was found to be improbable for Peach Bottom in the NUREG-1150 study. Although short term station blackout scenarios represent about 5% of the core damage frequency, most of these sequences will be at high pressure because of battery failure. Only 0.4% of the core damage frequency was represented by short term station blackout without battery failure. Although the ORNL evaluation did not directly apply for the scenario we evaluated, we were able to use the results to guide our selection of inputs for the long-term station blackout we evaluated.

#### Accident Progression Analysis

When water is introduced into containment in the containment flooding strategy, the free gas volume is reduced. Thus, venting is required to prevent an excessive pressure buildup. This was modeled in the APET by always considering the containment to be vented early (at core uncover) when the containment flooding strategy was evaluated. Reference 8 describes venting procedures late in a station blackout sequence, but does not fully address the concerns of venting during the particular strategy of containment flooding. If this strategy is pursued further, a detailed evaluation of the feasibility of accomplishing this venting would need to be performed. As described in Reference 6, the 18" vent lines in the drywell would be needed for this strategy because of their high elevation. The 18" lines connect to ductwork in the reactor building, which would be expected to fail with fairly small containment overpressure. Also, the valves on the 18" lines would have to be manually opened during a station blackout accident. Thus, unless venting could be initiated before there was much containment pressurization, the ducting in the reactor building would fail, exposing the personnel opening the valves to the blowdown, and possibly failing equipment located in the reactor building.

The additional heat removal from the reactor vessel when the containment is flooded with water delays vessel breach significantly. The ORNL evaluations have shown that vessel breach would be delayed about 9 hours for a short-term station blackout sequence in which the reactor vessel is maintained at low pressure by ADS actuation. ORNL also considered the possibility that ADS would fail during the core melt progression when the containment water level reaches the valves. For this case, the reactor vessel repressurized following ADS failure (and SRV reclosure) and the delay to vessel breach was found to be 7 hours rather than 9. As discussed previously, neither of these variations was found to be important for Peach Bottom in the NUREG-1150 study (but they could be important for other BWRs), so these specific variations were not be addressed in our risk evaluation. However, these results were used to guide our selection of the accident timing for the long-term station blackout.

Because the majority of the long-term station blackout cases are predicted to progress at high reactor vessel pressure, we conservatively used the 7-hour delay for the risk evaluation. It should be recognized that core damage would be delayed considerably in the long-term station blackout sequence so that decay

heat levels would be lower than for the short-term station blackout sequence. This would be expected to further delay the time to vessel breach. Because we did not have an analysis that was specific to the long-term station blackout scenario, we used the 7-hour value for this initial risk impact evaluation.

For cases in which ac power is recovered after core damage has occurred, there is considerable uncertainty about the impact of restoring the coolant on the core melt progression. The probability of arresting core damage (including the possibility of criticality if the control blades have relocated and the fuel is in a conducive geometry<sup>6</sup>) or triggering an in-vessel FCI have not been thoroughly examined to date. These uncertainties are present for both the cases with and without containment flooding. The core melt progression would be expected to be different with containment flooding, particularly conditions in the bottom head during the late phase of the in-vessel core melt progression. However, because there were no supporting analyses to quantify the impact, the probability of arresting core damage given ac recovery was treated the same as in the base NUREG-1150 evaluation. In addition, for cases with ac recovery but without core damage arrest, the subsequent accident progression was treated the same as in the NUREG-1150 study.

For cases without ac recovery, the debris was modeled to have a high mobility at vessel breach, based on the ORNL results. The analyses there indicated that a large molten pool would be formed in the bottom head, with an overlying crust. Consistent with this picture, we also treated the mode of vessel breach as being a large failure of the bottom head for these cases.

The large containment water inventory would be expected to prevent DCH, so the possibility of DCH was ruled out for this evaluation. However, the conditions are conducive to ex-vessel FCIs. Evaluations performed for NUREG-1150 indicated that when only a small amount of water is present on the drywell floor (a few feet), the FCI load would not be transmitted to the containment wall. However, the evaluations indicated that with a large water inventory present, the load could be transmitted to the containment wall and possibly fail it. The largest uncertainty for ex-vessel FCIs is the amount of debris that would actually be released at vessel breach. This uncertainty dominates the probability of containment failure from an ex-vessel FCI. We used the same probability for occurrence of an ex-vessel FCI as used for in-vessel FCIs, and considered containment failure to occur for cases with an ex-vessel FCI.

The flooded drywell floor affects the probability of drywell liner meltthrough. There is no consensus among experts in this area regarding the probability of averting drywell liner meltthrough under these conditions (large water depth, but also large debris pour). The values from the NUREG-1150 study for the probability of drywell liner meltthrough with water on the floor were also used in this evaluation.

The probability of forming a coolable debris bed and avoiding core-concrete attack is also higher with water on the drywell floor. The NUREG-1150 values for cases with a replenishable water supply were used to represent the case with a flooded drywell floor.

### Source Term Evaluation

Most of the effects of containment flooding on the source term were captured through the accident progression analysis. Examples include the type of containment failure and the availability of sprays early and late in the sequence. Minimal changes were required for the PBSOR code (which calculates the source term for each accident progression bin) and its input. These changes are described in this section.

The timing parameters were modified to reflect the 7-hour delay in vessel breach, which gives a 7-hour delay in containment failures that occur because of loads at vessel breach. No credit was given for reactor building decontamination because the vented releases were assumed to pass directly to the environment, rather than failing the ducting and passing through the reactor building. The suppression pool had been treated as saturated in the long-term station blackout scenarios in the NUREG-1150 study. This was modified for the containment flooding evaluation because containment flooding would bring the pool back to subcooled conditions. The decontamination factor of the suppression pool was also used for scrubbing releases from core-concrete attack (to approximate the greater water depth with containment flooding).

The radionuclide releases to the environment for Peach Bottom were described by two segments in the NUREG-1150 study. An initial, high energy release (puff) was used to describe the release at containment failure, and a release of longer duration was used to capture the continued radionuclide release after containment failure. Cases with containment venting are not fully represented by this framework. For example, in cases with venting and containment failure at vessel breach, there would actually be an initial lengthy release during the in-vessel melt progression, followed by a short high energy release at vessel breach, and then another period of long-term low energy releases. We adopted the approach used in the NUREG-1150 study to approximate radionuclide releases when the containment is vented early. Based on that logic, in cases with containment venting and either a late containment failure or no containment failure, the first release would be considered to occur before vessel breach. In cases with containment venting and containment failure at vessel breach, the first release would be considered to occur at vessel breach with the second release occurring immediately thereafter. This may underestimate the early fatalities because the release from venting may occur during evacuation.

### Consequence Evaluation

Since the NUREG-1150 study was completed, the process for partitioning (grouping) source terms has improved considerably. The improved process was developed in the PRUEP program,<sup>9</sup> and strives to create partitions with more-homogeneous characteristics. We used this improved partitioning for the containment flooding evaluation. We also re-evaluated the partitioning and consequences for the NUREG-1150 long-term station plant damage state. This was necessary to provide a common base for comparison, and to isolate the single plant damage state we are evaluating. (In NUREG-1150, all plant damage states were combined, then partitioned into groups, before performing the consequence calculations.)

To evaluate the consequences for each of the partitions, we used the same modeling assumptions as used in the NUREG-1150 study.

## Results

Using the modifications discussed previously, a risk evaluation was performed for the long-term station blackout plant damage state with containment flooding. For comparison, the NUREG-1150 models were re-evaluated for the single plant damage state using the improved partitioning scheme. The risk impact of the containment flooding strategy was then determined by comparing the accident progression and overall risk results for the two evaluations. The results are presented in this section.

The 7-hour delay to vessel breach significantly increased the probability of recovering ac power between core uncover and vessel breach. The mean value increased from 0.37 to 0.79. The reactor vessel was depressurized and ECC restored for most of these cases with ac recovery. However, the melt progression was only terminated in 8.5% of the cases in the NUREG-1150 study and 22% of the cases employing containment flooding. In the remaining cases with ac recovery, an in-vessel FCI fails the vessel.

With the flooded containment, the threat from DCH at vessel breach is eliminated, but the possibility of large-ex-vessel FCIs is introduced. The possibility of drywell liner meltthrough is not eliminated, but the probability is reduced considerably. The venting eliminates the threat from gradual overpressure before vessel breach. The net effect of these factors on the probability that the containment survives vessel breach is shown in Figure 6. The mean value increases from 0.34 to 0.58 when containment flooding is included.

The accident progression following vessel breach is also impacted by the containment flooding strategy. The mean value for the probability of forming a coolable debris bed increases from 0.23 to 0.45 when containment flooding is considered. The remaining cases have an overlying water pool for the containment flooding strategy, which scrubs much of the radionuclide release. Since the containment is vented for the containment flooding strategy, late containment overpressure failure is prevented. In the NUREG-1150 study, there was a mean probability of 0.14 that containment would fail late. These late failures are not important for the early fatality risk, but do impact the latent cancer fatality risk.

Figure 7 shows the early and latent cancer fatality risk results for the long-term station blackout plant damage state without and with containment flooding. The early fatality risk was decreased when containment flooding was included, but there was only a minimal impact on the latent cancer fatality risk.

## **SUMMARY AND CONCLUSIONS**

Based on the current state of knowledge, intentional depressurization would not give a significant reduction in overall risk at Surry because (1) in many cases depressurization will occur anyway because of stuck-open PORVs, failed pump

seals, or hot leg/surge line failure;; (2) a large fraction of the core melt sequences are terminated before vessel breach because of ac power recovery; and (3) those sequences that continue to vessel breach at high pressure do not usually result in sufficient loads at vessel breach to fail containment. In fact, when energetic FCIs are included, intentional depressurization could actually increase the conditional containment failure probability.

The delayed time to vessel breach with containment flooding resulted in a higher probability of recovering ac power, which reduced the probability of vessel breach. The probability of containment failure at vessel breach was also reduced. Since early venting is part of the strategy, there are radionuclide releases to the environment even for these cases. However, the large containment water pool and sprays reduce the source term for the releases.

The early fatality and latent cancer risk at Peach Bottom is low for the long-term station blackout plant damage state even without containment flooding. However, the containment flooding strategy reduced the early fatality risk by about a factor of two, with minimal impact on the latent cancer risk. The impact would likely be greater at plants in which short-term station blackout dominates the risk because there would be a greater impact on ac recovery and evacuation of the surrounding population. Key uncertainties in our risk evaluation are the consequences of ECC recovery to a damaged core, the venting/evacuation strategy to be employed, and the phenomena accompanying vessel breach.

These evaluations have demonstrated the usefulness of PRA in evaluating issues, determining key factors and searching for unexpected detrimental aspects of proposed actions.

#### REFERENCES

1. "Severe Accident Risks: An Assessment for Five U.S. Nuclear Power Plants," NUREG-1150, U.S. Nuclear Regulatory Commission, December 1990.
2. D. J. Hanson, et al., "Depressurization as an Accident Management Strategy to Minimize the Consequences of Direct Containment Heating," Idaho National Engineering Laboratory, NUREG/CR-5447, EGG-2574, October 1990.
3. R. J. Breeding, et al., "Evaluation of Severe Accident Risks: Surry Unit 1," Sandia National Laboratories, NUREG/CR-4551, SAND86-1309, Vol. 3, Rev. 1, Part 1, October 1990.
4. R. C. Gido, D. C. Williams, J. J. Gregory, "PWR Dry Containment Parametric Studies," Sandia National Laboratories, NUREG/CR-5630, SAND90-2339, April 1991.
5. S. A. Hodge, "BWR (In-Vessel) Late Accident Mitigation Strategies," letter report ORNL/NRC/LTR-90/18, September 1990.
6. S. A. Hodge, et al., "Identification and Assessment of BWR (In-Vessel) Severe Accident Mitigation Strategies," NUREG/CR-5869, In Preparation.

7. A. C. Payne, et al., "Evaluation of Severe Accident Risks: Peach Bottom, Unit 2," Sandia National Laboratories, NUREG/CR-4551, SAND86-1309, Vol. 4, Rev. 1, Part 1, December 1990.
8. D. J. Hanson, et al., "Containment Venting Analysis for the Peach Bottom Atomic Power Station," NUREG/CR-4696, December 1986.
9. T. D. Brown, et al., "Integrated Risk Assessment for the LaSalle Unit 2 Nuclear Power Plant: Phenomenology & Risk Uncertainty Evaluation Program (PRUEP)," NUREG/CR-5305, SAND90-2765, August 1992.

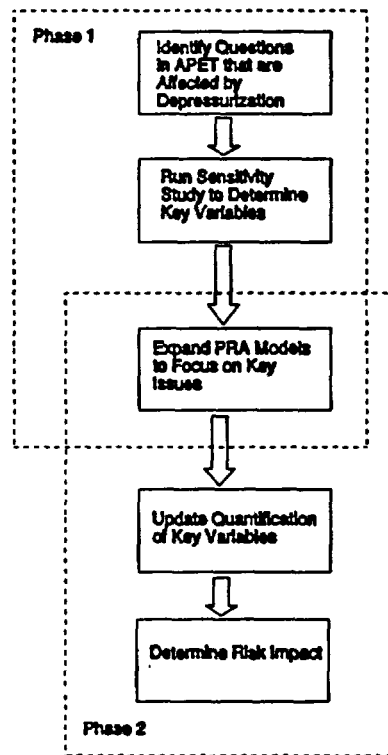


Figure 1. Evaluation Process

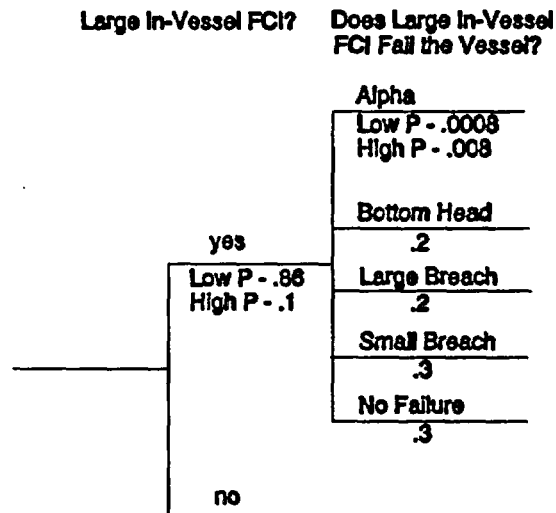


Figure 2. Logic for In-Vessel FCIs

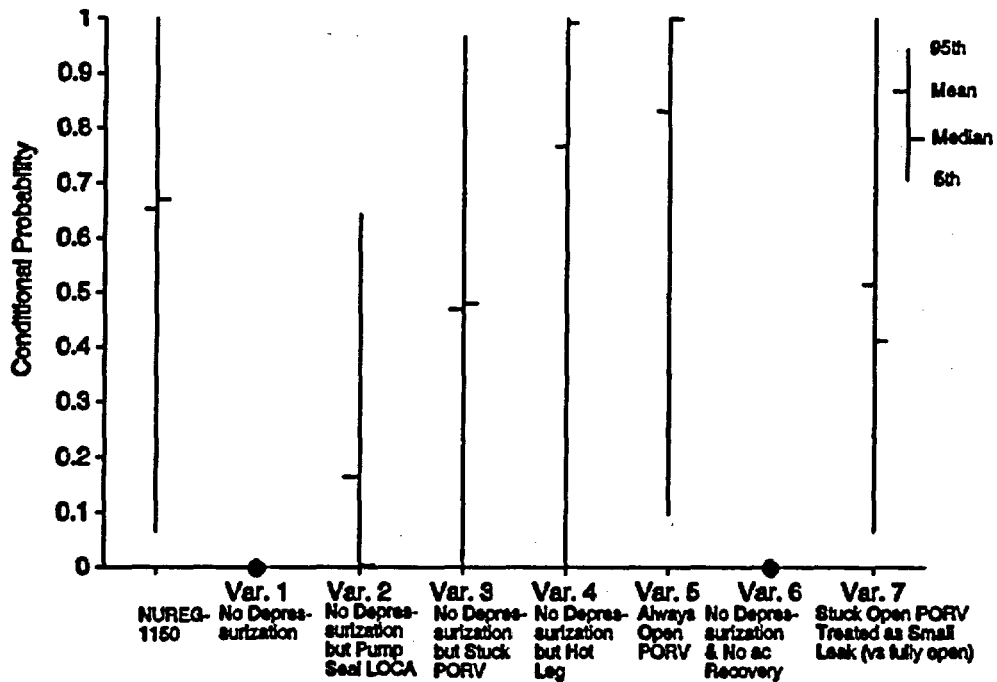


Figure 3. Conditional Probability of being at Low Pressure at Vessel Breach

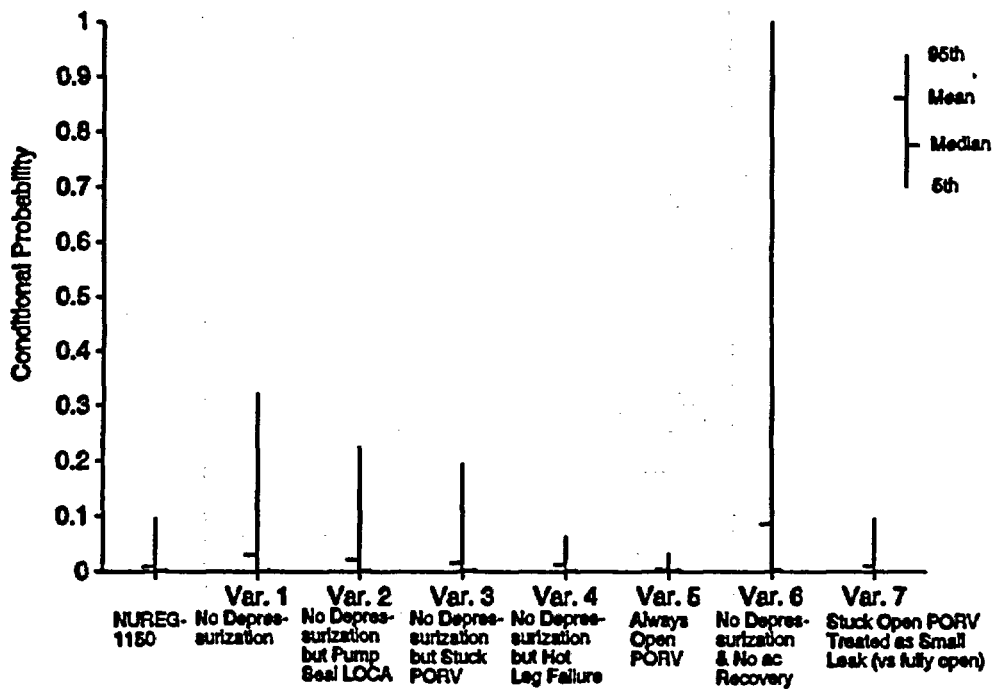


Figure 4. Conditional Probability of Containment Failure at Vessel Breach

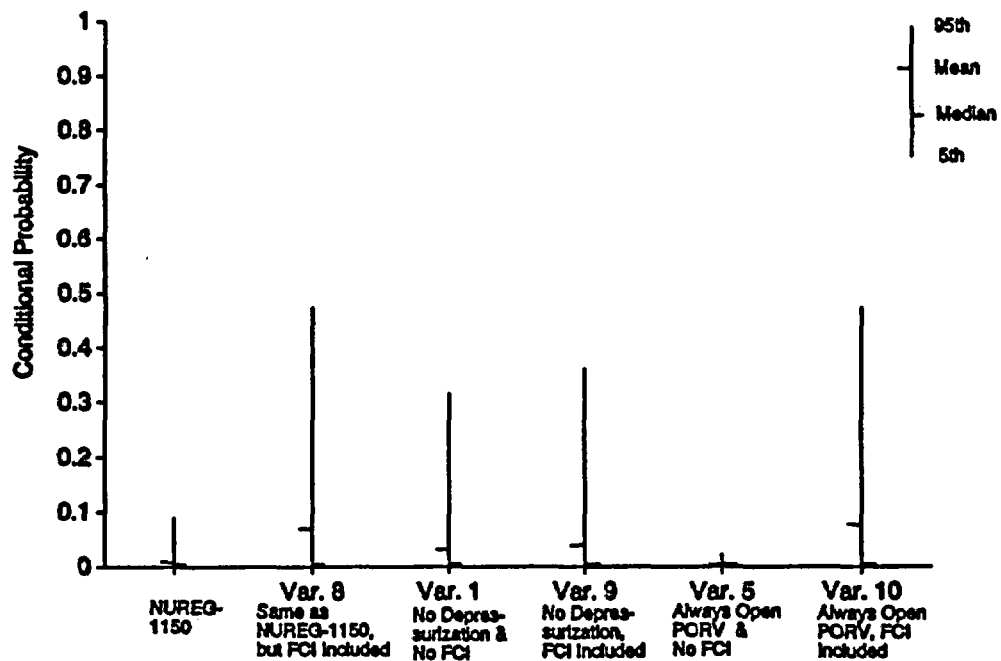


Figure 5. Conditional Probability of Containment Failure at Vessel Breach

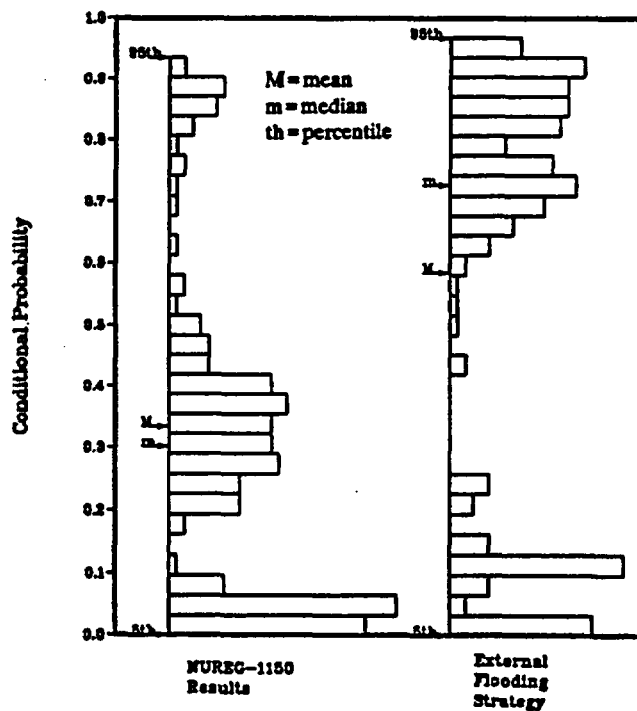
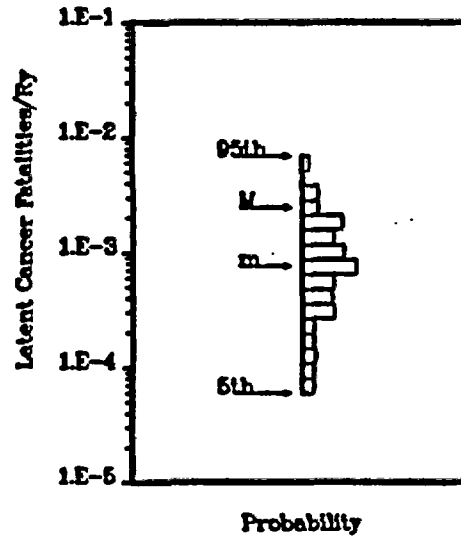
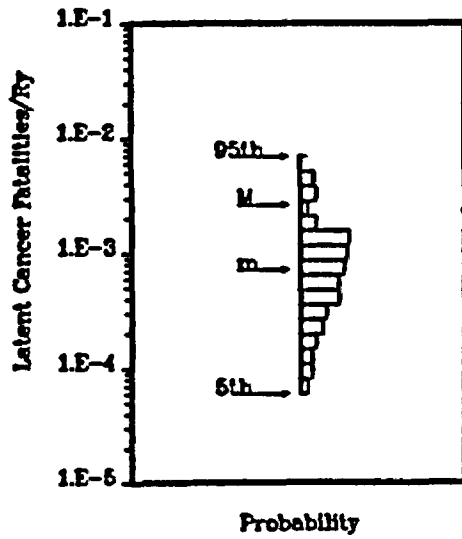
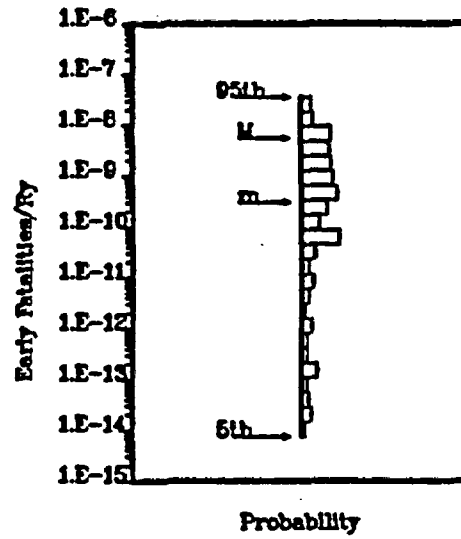
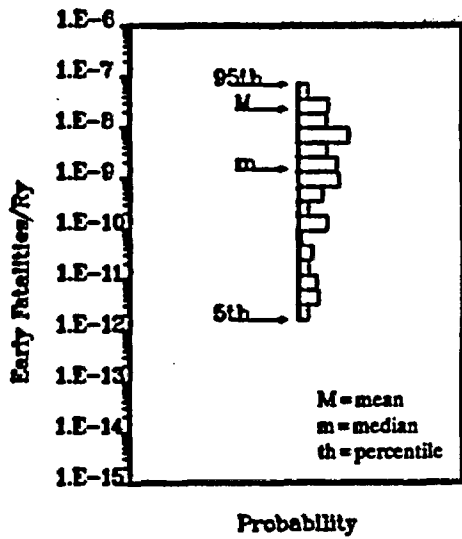


Figure 6. Conditional Probability of Preventing Early Containment Failure With and Without Containment Flooding



Without Containment Flooding

With Containment Flooding

Figure 7. Conditional Probability of Early and Latent Cancer Fatalities With and Without Containment Flooding

# IDENTIFICATION AND ASSESSMENT OF BWR IN-VESSEL SEVERE ACCIDENT MITIGATION STRATEGIES\*

Stephen A. Hodge      J. C. Cleveland  
T. S. Kress          M. Petek

Oak Ridge National Laboratory  
Oak Ridge, Tennessee 37831

## ABSTRACT

This paper briefly describes the results of work carried out in support of the U.S. Nuclear Regulatory Commission Accident Management Research Program to evaluate the effectiveness and feasibility of current and proposed strategies for BWR severe accident management. These results are described in detail in the just-released report *Identification and Assessment of BWR In-Vessel Severe Accident Mitigation Strategies*, NUREG/CR-5869, which comprises three categories of findings. First, an assessment of the current status of accident management strategies for the mitigation of in-vessel events for BWR severe accident sequences is combined with a review of the BWR Owners' Group Emergency Procedure Guidelines (EPGs) to determine the extent to which they currently address the characteristic events of an unmitigated severe accident. Second, where considered necessary, new candidate accident management strategies are proposed for mitigation of the late-phase (after core damage has occurred) events. Finally, two of the four candidate strategies identified by this effort are assessed in detail. These are (1) preparation of a boron solution for reactor vessel refill should control blade damage occur during a period of temporary core dryout and (2) containment flooding to maintain the core debris within the reactor vessel if the injection systems cannot be restored.

## 1. INTRODUCTION

Work sponsored by the Reactor and Plant Systems Branch of the Division of Systems Research, Office of Nuclear Regulatory Research, United States Nuclear Regulatory Commission (USNRC) to identify and assess BWR in-vessel accident management strategies was recently completed at Oak Ridge National Laboratory (ORNL). The purpose of this effort was the systematic development of new strategies for mitigation of the late phase events, that is, the events that would occur in-vessel after the onset of significant core damage. The methodology employed and the results of this effort are described in detail in the report *Identification and Assessment of BWR In-Vessel Severe Accident Mitigation Strategies*<sup>1</sup>, NUREG/CR-5869. This paper briefly describes the contents of this recently published report.

---

\* Research sponsored by the Office of Nuclear Regulatory Research, U.S. Nuclear Regulatory Commission under Interagency Agreement DOE 1886-8140-2L with the U.S. Department of Energy under contract DE-AC05-84OR21400 with the Martin Marietta Energy Systems, Inc.

NUREG/CR-5869 addresses the subject of BWR severe accident management for in-vessel events in three successive categories. First, the current status of BWR accident management procedures is assessed from the standpoint of effectiveness for application to the mitigation of critical (dominant) severe accident sequences. Second, where considered necessary, new candidate accident management strategies are proposed for mitigation of the late-phase events\* and briefly assessed. Third, for the two new candidate strategies for which the initial assessments are judged insufficient to adequately determine effectiveness and which are believed to have sufficient potential to justify additional consideration, detailed quantitative analyses are provided. The results and conclusions associated with each of these three topic categories are summarized in the following Sections of this paper.

## 2. EXISTING BWR ACCIDENT MANAGEMENT STRATEGIES

With respect to the current status of BWR accident management procedures, the BWR Owners' Group Emergency Procedure Guidelines<sup>2</sup> (EPGs) have been examined from the standpoint of their application to Station Blackout and Anticipated Transient Without Scram (ATWS). These accident sequences have been consistently identified by Probabilistic Risk Assessment (PRA) to be the predominant contributors to the overall calculated core damage frequency for BWR internally-initiated accidents. This examination was performed for two reasons. The first was to determine the extent to which the EPGs currently implement the intent of the BWR accident management strategies that have been suggested in the Brookhaven National Laboratory (BNL) report *Assessment of Candidate Accident Management Strategies*<sup>3</sup> (NUREG/CR-5474), published in March 1990. The second objective was to determine the extent to which the current operator actions specified by the EPGs would be effective in unmitigated severe accident situations. It was found that many of the candidate strategies discussed in NUREG/CR-5474 are included in the current version (Revision 4) of the EPGs and that with one exception, the remainder involve plant-specific considerations to the extent that they may be more appropriate for inclusion within local plant emergency procedures than within the generic symptom-oriented EPGs. The exception is a strategy for injection of boron following core damage and control blade relocation, which clearly is appropriate for the general applicability of the EPGs.

With respect to the second objective of this review, it has been determined that the EPGs do not provide guidelines for operator actions in response to the in-vessel events that would occur only after the onset of significant core damage. The general conclusion of this review is that additional guidance should be provided under these circumstances beyond the currently specified repetitive actions to restore reactor vessel injection capability, although restoration of vessel injection should retain first priority. Thus, the greatest potential for improvement of the existing BWR emergency procedure strategies lies in the area of severe accident management, both for determining the extent of ongoing damage to the in-vessel structures and for attempting to terminate the accident.

## 3. REQUIREMENT FOR ADDITIONAL STRATEGIES

The second main topic category of the recently published NUREG/CR-5869 addresses the identification of new candidate accident management strategies for mitigation of the late-phase in-vessel events of a BWR severe accident, including a discussion of the motivation for consideration

---

\* The late-phase events of a severe accident sequence are those events that would occur only after core damage including structural degradation and material relocation.

of these strategies and a general description of the methods by which they might be carried out. The identification of new candidate strategies was subject to the constraint that they should not require major equipment modifications or additions, but rather should be capable of implementation using only the existing equipment and water resources of the BWR facilities. Also, accident management strategies already included within the EPGs have not been addressed; the intention is to identify new candidate strategies that could enhance or extend the EPGs for the management of severe accidents.

In pursuing the goal of identifying strategies for coping with severe accidents, it is logical to first consider the vulnerabilities of the BWR to the challenges imposed. In general, BWRs are well protected against core damage because they have redundant reactor vessel injection systems to keep the core covered with water. Therefore, it is not surprising that probabilistic risk assessments have consistently identified the station blackout accident sequence as the leading contributor to the calculated core damage frequency for BWRs. The apparent vulnerability to Station Blackout arises simply because the majority of the reactor vessel injection systems are dependent upon the availability of AC power. While the detailed descriptions provided in the remainder of this paper are based upon the BWR-4 Mark I containment design, the associated conclusions are considered to have general applicability.

The steam turbine-driven reactor core isolation cooling (RCIC) and high pressure coolant injection (HPCI) systems can operate during Station Blackout, but do require DC power for valve operation and turbine governor control and are susceptible to mechanical failure. These systems would, therefore, be lost if AC power is not restored before the unit batteries become exhausted. Loss of reactor vessel injection capability in this manner defines the "long-term" station blackout accident sequence, since a significant period of time (typically six to eight hours) would elapse before battery exhaustion. "Short-term Station Blackout," on the other hand, denotes the station blackout accident sequence in which all reactor vessel injection capability is lost at the inception of the accident, most probably by a combination of loss of electrical power and HPCI/RCIC turbine mechanical failures. In either case, core degradation follows the uncovering of the core, which occurs as the reactor vessel water inventory is boiled away without replacement.

Other dominant core damage accident sequences also involve failure of reactor vessel injection, since the core must be at least partially uncovered in order for structural degradation and melting to occur. The ATWS accident sequence is consistently identified as second in order of calculated core melt frequency. With the core at power while the Main Steam Isolation Valves (MSIVs) are closed, the dominant form of this accident sequence tends to maintain the reactor vessel at pressures somewhat higher than normal, sufficient for steam release through the safety/relief valves (SRVs) to the pressure suppression pool. Since the rate of energy deposition into the pool can greatly exceed the capacity of the pool cooling equipment, the primary containment would become overheated and pressurized in an unmitigated ATWS accident sequence.

Containment events are the basic cause of the loss of reactor vessel injection systems for ATWS. However, the various injection systems would be lost in different ways. Most of the vessel injection systems are low-pressure systems, requiring that the reactor vessel be depressurized for performance of function. The turbine-driven HPCI and RCIC systems are capable of high pressure injection, but are susceptible to elevated pressure suppression pool temperatures when taking suction from this source since their lubricating oil is cooled by the water being pumped. In addition, both of these systems have high turbine exhaust pressure trips so that high primary containment pressure can defeat their function. Steam-driven feedwater pumps would be lost at the inception of the accident sequence when MSIV closure cuts off their steam supply.

Review of the results of probabilistic risk assessment for other important accident sequences demonstrates again that the postulated scenarios leading to core damage always include means for failure of function of the vessel injection systems. As defined, the various severe accident sequences involve different pathways to and timing of loss of vessel injection capability but, in every case, the core must become uncovered before core damage can occur. Nevertheless, the detailed means by which vessel injection capability might be lost are highly plant-specific; the detailed nature of the threats to the injection systems and the optimum measures that should be taken to cope with these threats depends upon the equipment characteristics of the individual plants. Extension of the methodology of the recent NRC-sponsored assessment of severe accident risks<sup>4</sup> (NUREG-1150) to take into consideration the plant-specific features of individual facilities is the responsibility of the plant operators as part of the individual plant examination (IPE) process.<sup>5,6</sup>

It is also desirable for defense-in-depth to develop mitigative strategies for coping with the late-phase severe accident events that would occur in the unlikely event that adequate reactor vessel injection cannot be maintained. Current accident management procedures are derived from the EPGs, which provide effective guidance for preventative measures to avoid core damage, including numerous diverse methods of maintaining reactor vessel injection capability with the provision of backup methods for use in abnormal circumstances. Some recommendations for improvement of the preventative guidelines of the EPGs can be offered, primarily in the realm of ATWS, where it is believed that the scrutability of the guidelines would be improved if distinctly separate procedures were provided for this accident sequence. Based upon the arguments that the signatures of ATWS are unmistakable so that operators would know when to invoke the ATWS procedures and that the operator actions required to deal with ATWS do not fit within the envelope of actions required to deal with other accident sequences<sup>7</sup>, it seems that the very complicated procedures required for coping with ATWS could be more concisely and effectively implemented as a separate document. This would also permit the remaining symptom-oriented guidelines to be greatly simplified.

Other recommendations with respect to the provisions of the EPGs from the standpoint of their application to ATWS are offered. These are first, that care be taken to avoid leading the operators to attempt manual depressurization of a critical reactor, second, that consideration be given to control the reactor vessel injection rate as a means for reduction of reactor power (as opposed to reactor vessel water level control as currently directed), and third, that removal of the rod sequence control system to facilitate the manual insertion of control blades under ATWS conditions be undertaken, as authorized by the NRC.

A final recommendation applicable to all accident sequences involving partial uncovering of the core has to do with the timing of opening of the automatic depressurization system valves for the steam cooling maneuver, which is intended to delay fuel heatup by cooling the uncovered upper regions of the core with a rapid flow of steam. It is believed that this maneuver would be more effective if performed at a lower reactor vessel water level, such as the level that was specified by Revision 3 of the EPGs. The current Revision 4 of the EPGs provides for steam cooling to be implemented with the water level near the top of the core; since the increase in temperature of the uncovered portion of the core would be small at this time, the amount of steam cooling achieved would be insignificant.

#### 4. AVAILABILITY OF PLANT INSTRUMENTS

In considering new candidate severe accident mitigation strategies for use with existing plant equipment, it is important to first recognize any limitations imposed upon the plant accident management team by lack of information with respect to the plant status. The most restrictive limitation as to plant instrumentation would occur as a result of loss of all electrical power, including that provided by the unit battery. This occurs after battery failure in the long-term station blackout accident sequence and in the (less-probable) version of the short-term station blackout accident sequence for which common-mode failure of the battery systems is an initiating event. For these accident sequences, loss of reactor vessel injection and the subsequent core degradation occur only after loss of DC power<sup>8,9</sup>.

For accident sequences such as Short-Term Station Blackout (with mechanical failure of HPCI and RCIC), ATWS, LOCA, or Loss of Decay Heat Removal, electrical power (DC and perhaps AC) is maintained after loss of reactor vessel injection capability. Therefore, the availability of information concerning plant status is much greater for these sequences. The more limiting case is that for which only DC power obtained directly from the installed batteries and the AC power indirectly obtained from these battery systems is available. The sources of AC power during Station Blackout include the feedwater inverter and the unit-preferred and plant-preferred systems for which single-phase 120-volt AC power is produced under emergency conditions by generators driven by battery-powered DC motors. Emergency control room lighting would be available.

#### 5. CANDIDATE SEVERE ACCIDENT MITIGATION STRATEGIES

With respect to application of the EPGs to the late phase of a severe accident sequence, these guidelines are not intended to propose actions in response to the accident symptoms that would be created by events occurring only after the onset of significant core damage. The final guidance to the operators, should an accident proceed into severe core damage and beyond, is that reactor vessel injection should be restored by any means possible and that the reactor vessel should be depressurized. While these are certainly important and worthwhile endeavors, additional guidance can and should be provided for the extremely unlikely, but possible severe accident situations where reactor vessel injection cannot be restored before significant core damage and structural relocation have occurred.

While recognizing that the probability of a BWR severe accident involving significant core damage is extremely low, it remains desirable to seek effective yet inexpensive mitigation measures that could be implemented employing the existing plant equipment and requiring only additions to the plant emergency procedures. Based upon the considered need for additional guidelines for BWR severe accident management for in-vessel events, four candidate late accident mitigation strategies are identified. These are:

1. Keep the Reactor Vessel Depressurized. Reactor vessel depressurization is important should an accident sequence progress to the point of vessel bottom head penetration failure because it would preclude direct containment heating (DCH) and thereby reduce the initial threat to containment integrity. This candidate strategy would provide an alternate means of reactor vessel venting should the SRVs become inoperable because of loss of control air or DC power. PRAs consistently include accident sequences involving loss of DC power and control air among the dominant sequences leading to core melt for BWRs.

2. **Restore Injection in a Controlled Manner.** Late accident mitigation implies actions to be taken after core melting, which requires at least partial uncovering of the core, which occurs because of loss of reactor vessel injection capability. BWRs have so many electric motor-driven injection systems that loss of injection capability implies loss of electrical power. (This is why Station Blackout is consistently identified by PRAs to be the dominant core melt precursor for BWRs.) If electric power is restored while core damage is in progress, then the automatic injection by the low-pressure, high-capacity pumping systems could be at a rate more than two hundred times greater than that necessary to remove the decay heat. This strategy would provide for controlled restoration of injection and is particularly important if the control blades have melted and relocated from the core.
3. **Inject Boron if Control Blade Damage has Occurred.** This strategy would provide that the water used to fill the reactor vessel after vessel injection capability was restored would contain a concentration of the boron-10 isotope sufficient to preclude criticality, even if none of the control blade neutron poison remained in the core region. This candidate strategy is closely related to the previous proposal for control of reactor vessel injection.
4. **Containment Flooding to Maintain Core and Structural Debris In-Vessel.** This candidate strategy is proposed as a means to maintain the core residue within the reactor vessel in the event that vessel injection cannot be restored as necessary to terminate the severe accident sequence. Containment flooding to above the level of the core is currently incorporated within the EPGs as an alternative method of providing a water source to the vessel in the event of design-basis LOCA (the water would flow into the vessel from the containment through the break). Here it is proposed that containment flooding might also be effective in preventing the release of molten materials from the reactor vessel for the risk-dominant non-LOCA accident sequences such as Station Blackout.

As explained in the Introduction, the third category of NUREG/CR-5869 derives from a reconsideration of these four candidate late-phase, in-vessel strategies for the purpose of identifying any that require (and have sufficient potential to justify) detailed quantitative assessment. The candidate strategy to keep the reactor vessel depressurized is not recommended for further assessment at this time because it is believed far more practical to improve the reliability of the control air and DC power supplies for the SRVs than to invent alternative methods for venting of the reactor vessel into the secondary containment under severe accident conditions. Nevertheless, consideration of the reliability of control air and DC power should be an important part of the IPE process since loss of these systems is involved in the risk-dominant sequences leading to core melt consistently identified for BWRs by PRAs such as the recent NRC-sponsored risk assessment (NUREG-1150).

The candidate strategies for restoration of injection in a controlled manner and injection of boron if control blade damage has occurred are recommended to be combined into a single concept for "Prevention of BWR Criticality as a Late Accident Mitigation Strategy." As described in the following Section, this would provide a sodium borate solution for the injected flow being used to recover the core, in sufficient concentration to preclude criticality as the water level rises within the reactor vessel. (The proposal for containment flooding will be addressed in Section 7.)

## 6. REFLOOD WITH BORATED WATER

This strategy for prevention of inadvertent criticality induced by severe accident recovery efforts could be implemented using only the existing plant equipment but employing a different chemical form for the boron poison. Available information concerning the poison concentration required is derived from the recent Pacific Northwest Laboratory (PNL) study, *Recriticality in a BWR Following a Core Damage Event*<sup>10</sup>, NUREG/CR-5653. This study indicates that much more boron would have to be injected than is available (as a solution of sodium pentaborate) in the Standby Liquid Control System (SLCS). Furthermore, the dominant BWR severe accident sequence is Station Blackout and without means for mechanical stirring or heating of the injection source, the question of being able to form the poisoned solution under accident conditions becomes of supreme importance. Hence the need for the alternate chemical form.

Polybor, produced by the U. S. Borax Company, seems to be an ideal means for creating the required sodium borate solution. It is formed of exactly the same chemical constituents (sodium, boron, oxygen, and water) as sodium pentaborate but has the advantages that for the same boron concentration, it requires about one-third less mass of powder addition and has a significantly greater solubility in water. Whereas sodium pentaborate solution is formed by adding Borax and boric acid crystals to water, which then react to form the sodium pentaborate, a solution of Polybor is formed simply by dissolving the Polybor powder in water. This attribute, that two separate compounds are not required to interact within the water, is a major reason for the greater solubility of Polybor.

The specific goal of the proposed strategy is to provide for the addition of the boron-10 isotope together with the flow being used to recover the core, in sufficient quantity to preclude criticality as the water level rises within the reactor vessel. NUREG/CR-5653 provides the estimate that a boron-10 concentration of between 700 and 1000 ppm would be required within the vessel to preclude criticality once control blade melting had occurred. This is much greater than the concentration (about 225 ppm) attainable by injection of the entire contents of the SLCS tank.

One means to achieve such a high reactor vessel boron concentration would be to mix the powder directly with the water in the plant condensate storage tank and then, upon restoration of electrical power, to take suction on this tank with the low-pressure system pump to be used for vessel injection. It is, however, not a simple matter to invoke this strategy and preplanning and training would be necessary.

During normal reactor operation, the condensate storage tank provides makeup flow to the main condenser hotwells via an internal tank standpipe, as illustrated in Figure 1. Any practical strategy for direct poisoning of the tank contents must provide for partial draining to reduce the initial water volume, particularly if boron-10 concentrations on the order of 700 ppm are to be achieved. The condensate storage tank could be gravity-drained through the standpipe to the main condenser hotwells under station blackout conditions.

Even with partial tank draining, however, the amount of powder required to obtain a boron-10 concentration of 700 ppm is large. Considering the Peach Bottom plant configuration, and assuming the use of Polybor to take advantage of its greater solubility, 19,300 lbs (8,750 kg) would have to be added to the partially drained tank. [If Borax/boric acid were used, the requirement would be 28,400 lbs (12,880 kg).] Clearly, this is too much to be manhandled [50-lb (23-kg) bags] to the top of the tank and poured in. The practical way to poison the tank contents would be to prepare a slurry of extremely high concentration in a smaller container at

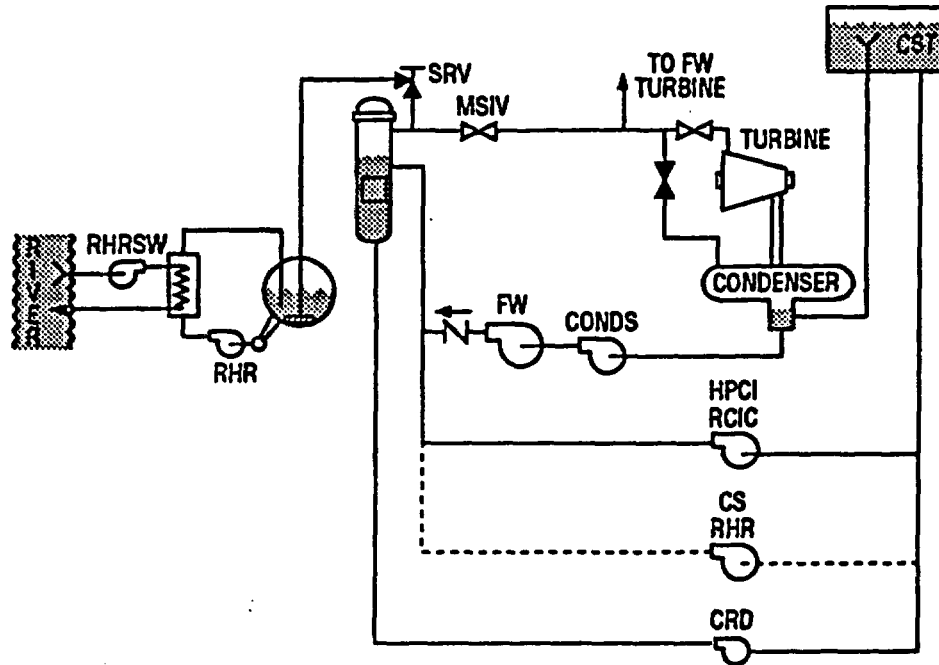


Fig. 1. Reactor vessel injection can be provided from the condensate storage tank by the motor-driven core spray (CS) or residual heat removal (RHR) system pumps.

ground level; then to pump the contents of this small container into the upper opening of the condensate storage tank. (Extremely high concentrations can be achieved with Polybor.) To avoid any requirement for procurement of additional plant equipment, a fire engine with its portable suction tank might be employed to perform the pumping function.

With the candidate accident management strategy identified, a simplified cost-benefit analysis was performed based upon the methodology described in NUREG-0933, *A Prioritization of Generic Safety Issues*<sup>11</sup> and following the guidelines of References 12 and 13. Implementation of the strategy was estimated to provide a reduction in the frequency of unmitigated core melting of  $1.19\text{E}-06$  per reactor-year (RY). The strategy proposed would, if implemented, affect the progression of severe accident events during the time window for recriticality, which is opened by the occasion of some core damage (the melting of the control blades). Thus, some core damage is associated even with successful implementation of the strategy. The goal of the strategy is to avert vessel breach and containment failure.

The estimated change in public risk associated with the proposed strategy is found to be 6.1 man-rem/RY. When applied to the present inventory of 38 BWR facilities with an average remaining lifetime of 21.1 years, the total potential risk reduction estimate is 4860 man-rem.

Implementation of the proposed strategy is estimated to involve per-plant expenditures (1982 dollars) of \$70,000 for engineering analysis, preparation of procedures, personnel training, management review, and acquisition of material (sodium borate powder in the form of Polybor). In addition, it is estimated that 20 man-hr/RY would be required for periodic procedure review and team training (including drills). With a cost of \$56.75 per man-hr (1982 dollars) and an average remaining plant life of 21.1 years, the average industry cost per reactor is estimated to be about \$93,950.

NRC costs for implementation of the proposed strategy would be small since the general approach has already been developed by the Office of Research as a candidate accident management procedure. It is anticipated that the strategy would be implemented on a voluntary, plant-specific basis by the industry. Therefore, no additional NRC development costs would be incurred. Allowance is made, however, for the costs associated with oversight of the associated plant procedures and of the general readiness (status of personnel training) to successfully execute the plant-specific actions. These oversight activities are estimated to require an average NRC cost per reactor of about \$7100.

Based upon an average industry cost of \$94,000 per reactor and an NRC oversight cost of \$7000 per reactor, the total cost (1982 dollars) associated with implementation of this strategy for the 38 BWR facilities is estimated to be \$3.84M.

The value/impact assessment consistent with the procedures of NUREG-0933 for the proposed strategy is

$$S = \frac{4860 \text{ man-rem}}{\$3.84\text{M}}$$
$$= 1266 \text{ man-rem}/\$M,$$

from which a priority ranking of **MEDIUM** is obtained for the proposed strategy.

Based upon this ranking, what further actions should be recommended? As pointed out in NUREG-0933, decisions should be tempered by the knowledge that the assessment uncertainties are generally large:

**"The criteria and estimating process on which the priority rankings are based are neither rigorous nor precise. Considerable application of professional judgment, sometimes guided by good information but often tenuously based, occurs at a number of stages in the process when numerical values are selected for use in the formula calculations and when other considerations are taken into account in corroborating or changing a priority ranking. What is important in the process is that it is systematic, that it is guided by analyses that are as quantitative as the situation reasonably permits, and that the bases and rationale are explicitly stated, providing a "visible" information base for decision. The impact of imprecision is blunted by the fact that only approximate rankings (in only four broad priority categories) are necessary and sought."**

With these considerations in mind, it is recommended that each plant assess its need for the proposed strategy based upon the results of its Individual Plant Examination (IPE). By far, the most important aspect of this recommended plant-specific assessment of the need for this strategy is the frequency of station blackout events predicted to progress through the first stages of core damage (the melting of control blades). In the generic analysis of public risk reduction reported here, the probability of a recriticality event was taken to be 1.25E-06/py, based upon the recent PNL study (NUREG/CR-5653).

The PNL study is based upon the NUREG-1150 results for Peach Bottom, which includes a core-melt frequency of about 4.5E-06 derived from station blackout events. If individual plants discover in their IPE process that a much lower station blackout core damage frequency applies,

then correspondingly lower recriticality potential would also apply and implementation of the proposed strategy would probably not be practical for their facility.

As a final note with respect to the question of boration under severe accident conditions, it is important to recognize that many of the BWR facilities are currently implementing accident management strategies, on a voluntary basis, to provide back-up capability for the SLCS. These back-up strategies invoke such methods as modification of the HPCI or RCIC system pump suction piping to permit connection to the SLCS tank, or poisoning of the condensate storage tank. In all known cases, however, the effect of these plant-specific strategies is to provide a means to obtain a reactor vessel concentration of the boron-10 isotope similar to that attainable by use of the SLCS system itself. It seems highly desirable that these facilities should include information within their training programs and procedural notes that according to the analyses reported by PNL (NUREG/CR-5653), this concentration would be insufficient to preclude criticality associated with vessel reflood after control blade melting.

## 7. DRYWELL FLOODING

The basis for this paper, the recently published NUREG/CR-5869, also provides a detailed assessment of the proposed strategy for containment flooding to maintain the core and structural debris within the reactor vessel. This strategy would be invoked in the event that vessel injection could not be restored to terminate a severe accident sequence. Geometric effects of reactor vessel size dictate that the effectiveness of external cooling of the vessel bottom head as a means to remove decay heat from an internal debris pool would be least for the largest vessels. Considering also that the motivation for maintaining any core and structural debris within the reactor vessel is greatest for the Mark I drywells, the primary focus of the detailed assessment is upon the largest BWR Mark I containment facilities such as Peach Bottom or Browns Ferry.

The immediate goal of the considered strategy for containment flooding would be to surround the lower portion of the reactor vessel with water, thereby protecting both the instrument guide tube penetration assemblies and the vessel bottom head itself from failure by overtemperature<sup>1, 14</sup>. (The concept is illustrated in Figure 2.) The threat would be provided by the increasing temperature of the lower plenum debris bed after dryout. First, molten liquids forming within the bed would relocate downward into the instrument guide tubes challenging their continued integrity<sup>15</sup>. Subsequently, heating of the vessel bottom head by conduction from the debris would threaten global failure of the wall by creep rupture.

Nevertheless, it seems beyond question that all portions of the reactor vessel pressure boundary (including the instrument guide tubes) that are in contact with and cooled by water on their outer surfaces would survive any challenge imposed by a lower plenum debris bed or its relocated liquids. There is a problem, however, in that most of the upper portion of the reactor vessel could not be covered by water and, more significant in the short term, much of the outer surface of the vessel bottom head would be dry as well.

That the upper portion of the reactor vessel could not be covered is due to the location within the containment of the drywell vents. Since low-pressure pumping systems would be used for flooding, the drywell would have to be vented during filling and the water level could not rise above the elevation of the vents, at about two-thirds vessel height. That much of the outer surface of the reactor vessel bottom head would be dry is due to the gas pocket that would be trapped within the vessel support skirt during the process of raising the water level within the drywell. The situation immediately after lower plenum dryout is illustrated in Figure 3.

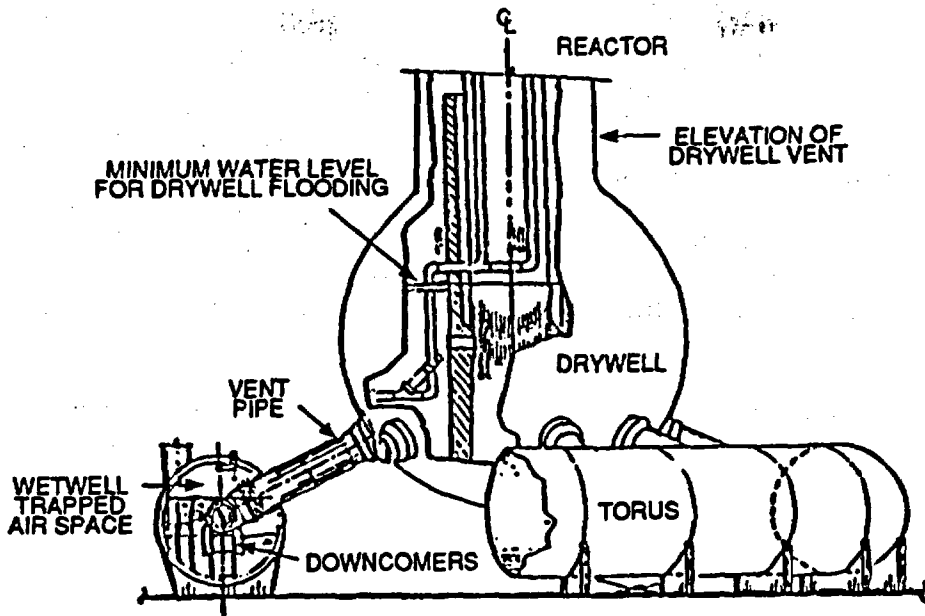


Fig. 2. Containment flooding to cover the reactor vessel bottom head in the BWR Mark I containment design.

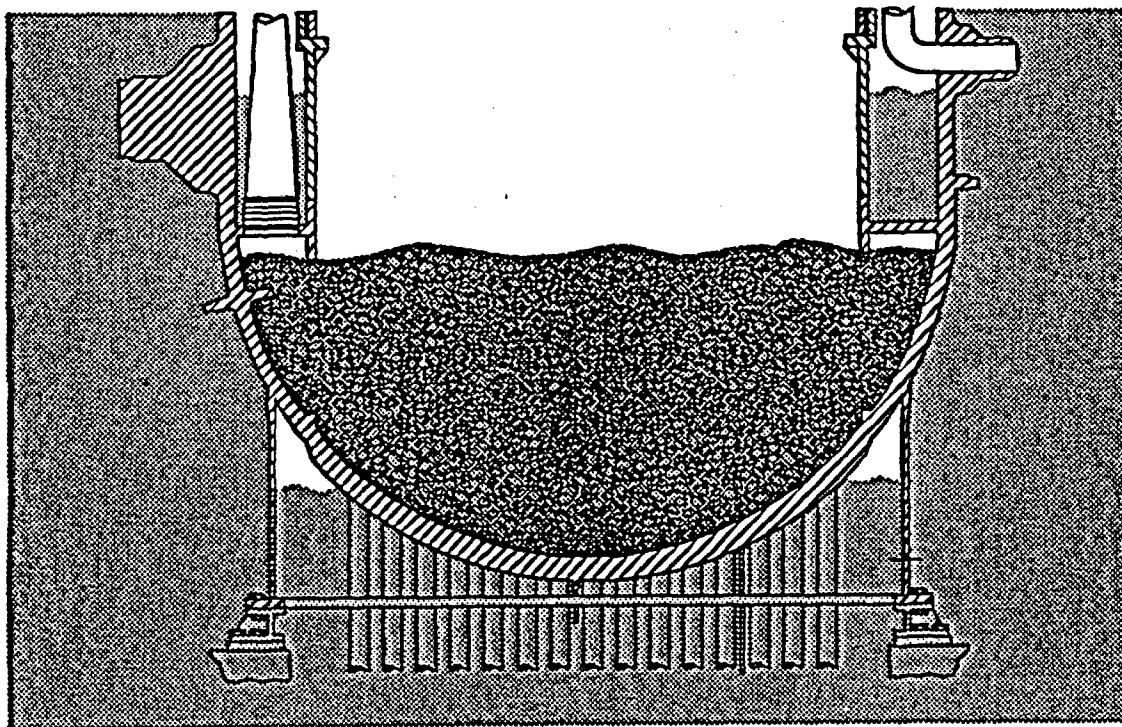


Fig. 3. An illustration of the quenched debris bed within the BWR lower plenum immediately after bed dryout.

The detailed assessment results demonstrate that the existence of a trapped gas pocket beneath the vessel skirt attachment would ultimately prove fatal to the integrity of the bottom head wall. Figure 4 illustrates the insulating crust of varying thickness that would remain adjacent to the wall after melting of the central portion of the debris. Nevertheless, the most important attribute of drywell flooding, that of preventing early failure of the instrument guide tube penetration assemblies, would be realized. These results are among those listed in Table 1 where it is shown (first entry) that in the absence of water, penetration assembly failures would be expected at about 250 minutes after scram. If penetration failures did not occur, then creep rupture of the bottom head would be expected after 10 hours if the bottom head is dry and after 13 hours if the drywell is flooded. The important contribution of drywell flooding is to shift the expected failure mode from penetration failures (Table 1 first entry) to bottom head creep rupture (Table 1 third entry).

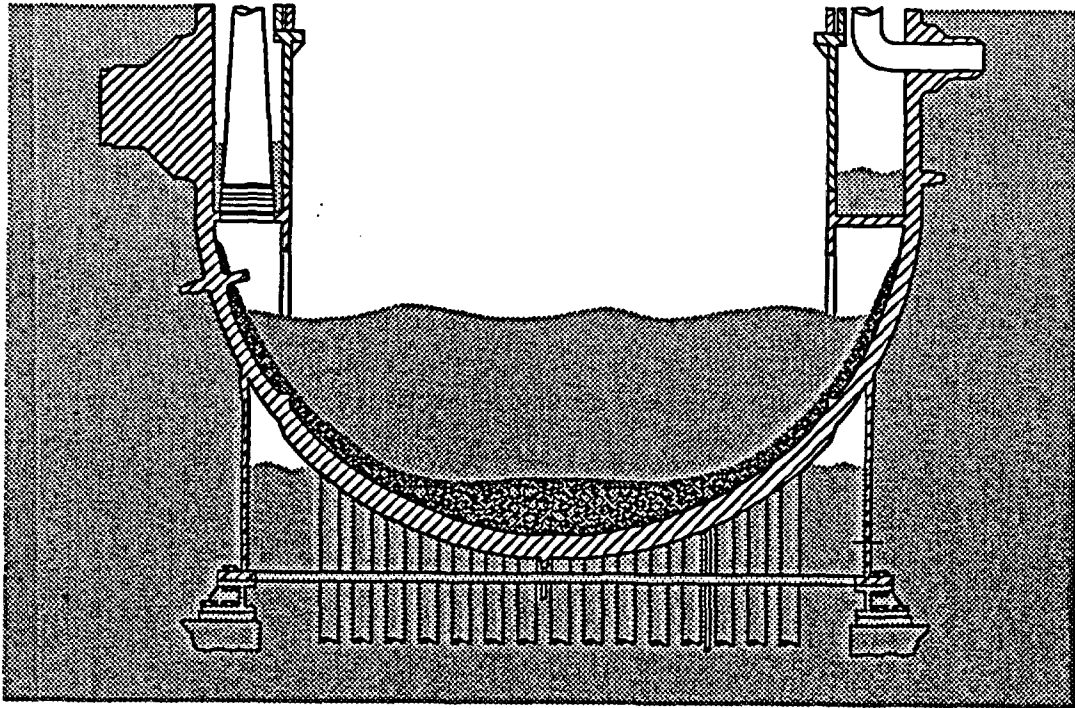


Fig. 4. A molten pool is predicted to form and spread radially from the upper center of the quenched debris.

Table 1. Estimated failure times for the reactor vessel bottom head pressure boundary for Peach Bottom/Browns Ferry short-term station blackout

Drywell Flooded	Failure Mechanism	Time to Failure	
		Minutes	Hours
No	Penetration Assemblies	250	4.2
No	Bottom Head Creep Rupture	600 - 640	10.0 - 10.7
Yes	Bottom Head Creep Rupture	780 - 840	13.0 - 14.0

The effectiveness of drywell flooding could be improved if the reactor vessel support skirt were vented in order to reduce the trapped gas volume and increase the fraction of bottom head surface area contacted by water. Partial venting could be achieved by loosening the cover on the support skirt manhole access hole. This would increase the wetted portion of the bottom head from 55% to 73% of the total outer surface area, which delays the predicted time of bottom head creep rupture by about one hour. The predicted failure times for the basic case without skirt venting and for the case of partial venting at the manhole access are indicated in the first two entries of Table 2.

**Table 2. Effect of skirt venting upon time to failure of the bottom head pressure boundary for Peach Bottom/Browns Ferry short-term station blackout with drywell flooding**

Skirt Vented	Failure Mechanism	Time to Failure	
		Minutes	Hours
No	Bottom Head Creep Rupture	780 - 840	13.0 - 14.0
Partial	Bottom Head Creep Rupture	840 - 900	14.0 - 15.0
Complete	Melting of Upper Vessel Wall	>1200	>20.0

Complete venting of the reactor vessel support skirt would provide 100% water coverage of the vessel bottom head but would require special measures such as provision of a siphon tube or the drilling of small holes at the upper end of the skirt, just below the attachment weld. Because of the associated personnel radiation exposure penalty and the predicted low core melt frequencies for the existing plants, this is not considered to be a practical suggestion for the existing BWR facilities, but provision for complete venting is inherent for the SBWR design. As indicated by the last entry in Table 2, 100% water coverage of the vessel bottom head would convert the failure mechanism from bottom head creep rupture to melting of the upper vessel wall and would delay the predicted time of failure to more than 20 hours after scram.

In summary, all portions of the reactor vessel wall that are covered by water would be adequately protected against failure by melting or creep rupture. For the cases with no venting or partial venting of the support skirt, the creep rupture failure is predicted to occur in the portion of the vessel wall adjacent to the trapped gas pocket beneath the skirt. Partial venting would reduce the size of the gas pocket and delay the predicted time of failure, but the failure mechanism would still be creep rupture beneath the skirt attachment weld. With complete venting, however, there would be no gas pocket and this failure mechanism would be eliminated.

What cannot be eliminated, however, is the radiative heat transfer upward within the reactor vessel from the surface of the lower plenum debris bed. About one-half to two-thirds of all energy release within the bed would be radiated upward after bottom head dryout. Initially, the primary heat sink for this radiation would be the water trapped in the downcomer region between the core shroud and the vessel wall above the debris bed. It is the heating of this water that creates the only steam source within the reactor vessel after lower plenum dryout.

After the water in the downcomer region became exhausted, the upward radiative heat transfer from the debris surface would serve to increase the temperature of the upper reactor vessel

internal structures. For calculations with the existence of a gas pocket beneath the skirt, bottom head creep rupture is predicted to occur while the temperature of these internal stainless steel heat sinks remains below the melting point. If bottom head creep rupture did not occur, however, the debris would remain within the vessel, the upward radiation would continue, and the upper internal structures would melt.

The mass of the BWR internal structures (core shroud, steam separators, dryers) is large. Melting of these stainless steel structures under the impetus of the upward debris pool radiation more than 14 hours after scram would occur over a long period of time. Nevertheless, decay heating of the debris pool and the associated upward radiation would be relentless and, after exhaustion of the stainless steel, the only remaining internal heat sink above the pool surface would be the carbon steel of the upper vessel wall. All portions of the wall cooled by water on their outer surfaces would remain intact, but unless the water height within the drywell extended well above the surface of the debris pool, upper portions of the vessel exposed to the drywell atmosphere would ultimately reach failure temperatures. The calculated minimum flooding height required to preclude inner wall melting for the Peach Bottom reactor vessel is illustrated in Figure 5.

It should be obvious from this discussion of the effect of water upon cooling of the vessel wall that it would be desirable to have a drywell flooding strategy that would completely submerge the reactor vessel and thereby eliminate questions concerning the required water level within the containment. This could not be achieved in existing facilities because of the limitation that the height of water within the drywell cannot exceed the elevation of the drywell vents. Future designs, however, might provide for complete coverage of the reactor vessel as a severe accident mitigation technique.

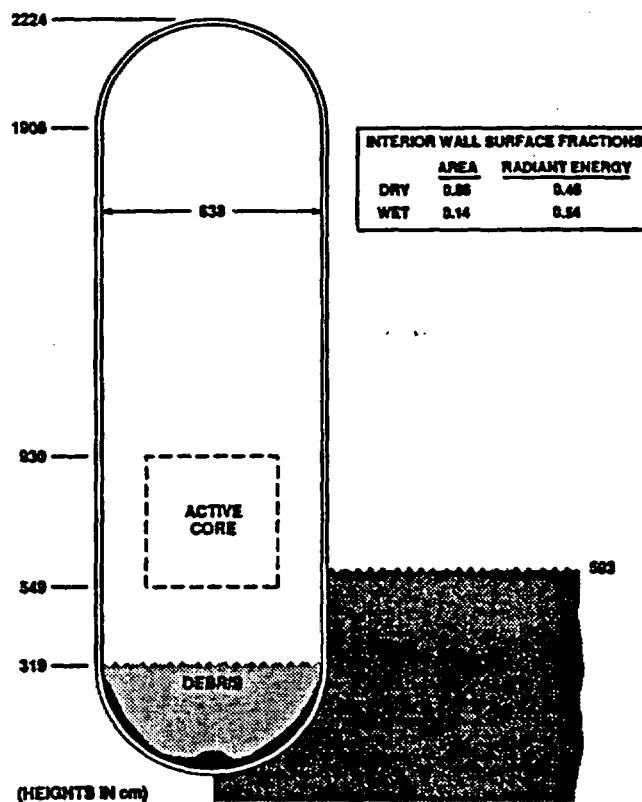


Fig. 5. The calculated minimum coverage of the upper reactor vessel necessary to preclude melting of the inner surface of the wall.

Table 3 provides a summary of the calculated failure times and release mechanisms for all of the cases considered in this study. These include the cases previously discussed in connection with Tables 1 and 2, plus one additional case (third entry) in which it is assumed that reactor vessel pressure control is lost at the time of drywell flooding, because of the submergence of the safety/relief valves. The increased wall tensile stress associated with this case would cause the wall creep rupture to occur at a lower temperature, advancing the time of failure by about two hours over the depressurized case (compare the third and fourth entries in Table 3).

**Table 3. Effect of drywell flooding upon time of debris release from the reactor vessel for the short-term station blackout accident sequence based upon Peach Bottom/Browns Ferry**

Drywell Flooded	Skirt Vented	Reactor Vessel Depressurized	Release Mechanism	Time to Failure	
				Minutes	Hours
No	—	Yes	Penetration Failures	250	4.2
No	—	Yes	Bottom Head Creep Rupture	600 – 640	10.0 – 10.7
Yes	No	No	Bottom Head Creep Rupture	660 – 700	11.0 – 11.7
Yes	No	Yes	Bottom Head Creep Rupture	780 – 840	13.0 – 14.0
Yes	Partial	Yes	Bottom Head Creep Rupture	840 – 900	14.0 – 15.0
Yes	Complete	Yes	Melting of Upper Vessel Wall	>1200	>20.0

The most important disadvantage of a drywell flooding strategy for existing plants is the requirement for venting to the external atmosphere<sup>16</sup> while the containment is being filled by the low-pressure pumping systems and during the subsequent steaming from the water surrounding the reactor vessel bottom head. Because of this, implementation of the drywell flooding strategy would initiate a noble gas release to the surrounding atmosphere as well as a limited escape of fission product particulates. All particulate matter released from the reactor vessel prior to failure of the vessel wall would enter the pressure suppression pool via the safety/relief valve T-quenchers and would be scrubbed by passage through the water in both the wetwell and drywell. Therefore, the concentration of particulates in the drywell atmosphere and any release through the drywell vents would remain small as long as the reactor vessel wall remained intact.

Creep rupture of the vessel bottom head beneath the support skirt attachment would release debris into the water-filled pedestal region to fall downward onto the drywell floor. Since containment flooding would provide a water depth of more than 30 feet (9.144 m) over the drywell floor, the particulate matter released from the debris mass should be adequately scrubbed provided, of course, that violent steam explosions do not occur. Furthermore, the large volume of water in the drywell would protect the drywell shell from late failure in Mark I containment

facilities, since the accumulating debris would never reach a height sufficient to break the water surface.

The advantages and disadvantages of a drywell flooding strategy for existing BWR facilities are summarized in Table 4. The listed advantages involve significant contributions to accident mitigation, which have previously been discussed. The listed disadvantages, however, are also important and will be discussed in the following paragraphs.

**Table 4. Advantages and disadvantages of a drywell flooding strategy for severe accident mitigation in existing BWR facilities**

<b>Advantages</b>	<ol style="list-style-type: none"> <li>1. Prevent failure of the bottom head penetrations and vessel drain</li> <li>2. Increased scrubbing of fission product particulate matter</li> <li>3. Delay creep rupture of the reactor vessel bottom head</li> <li>4. Prevent failure of the Mark I drywell shell when core debris does leave the vessel</li> </ol>
<b>Disadvantages</b>	<ol style="list-style-type: none"> <li>1. Requires availability of power source and pump capable of filling the drywell to the level of the vessel bottom head within 150 minutes under station blackout conditions.</li> <li>2. Requires that the drywell be vented.</li> </ol>

First, implementation of the proposed strategy would require equipment modifications and additions. Although there may be plant-specific exceptions, containment flooding with the existing pumping systems would require too much time; furthermore, the existing systems would not be available for the dominant station blackout accident sequences. What is needed is a reliable ability to sufficiently flood the drywell within a short period of time, since it would be unrealistic to expect that emergency procedures would call for containment flooding (and the associated undesirable effects upon installed drywell equipment) until after core degradation has begun. If the water did not reach the vessel bottom head until after lower plenum debris bed dryout and the initial heating of the vessel wall, it would be too late to prevent penetration assembly failures.

The second disadvantage, that the drywell vents would have to be opened early in the accident sequence to permit flooding of the containment, is particularly undesirable since this in turn involves early release of the fission product noble gases, beginning soon after the onset of core degradation. After the water had contacted the vessel bottom head, a continuous steam generation would begin within the drywell that would be released to the outside atmosphere by means of the open vents. This would tend to sweep any particulate matter from the drywell atmosphere through the vents. The amount of particulate matter reaching the drywell atmosphere would, however, be limited by water scrubbing as long as the reactor vessel wall remained intact above the water level in the drywell. This is expected to be the case for the existing BWR facilities where the ultimate failure of the wall would occur by creep rupture beneath the skirt attachment weld.

It is interesting, however, to briefly consider the potential benefits of application of a drywell flooding strategy to future BWR facilities, where the disadvantages listed in Table 4 might be avoided by appropriate plant design. Much less water would be required since the reactor vessel would be located in a cavity instead of suspended high above a flat drywell floor. Provision could be made for complete venting of the reactor vessel support skirt so that all of the bottom head would be in contact with water. This would preclude creep rupture of the vessel bottom head, shifting the potential failure mode to melting of the upper vessel wall, above the water level in the drywell.

For the existing BWR facilities, failure of the upper reactor vessel wall would provide a direct path from the upper surface of the debris pool to the open drywell vents without the benefit of water scrubbing.\* For future plant designs, this could be avoided in two ways. First, submergence of most, or all, of the reactor vessel wall above the debris pool surface would preclude failure of the upper vessel wall. Second, the requirement for containment venting could be eliminated by provision of an adequate water source within the containment and provision for condensation of the generated steam. Both of these approaches are within the scope of design features currently under consideration for the advanced passive design.

## 8. SUMMARY

The new report *Identification and Assessment of BWR In-Vessel Severe Accident Mitigation Strategies*<sup>1</sup> addresses the need for BWR accident management in the unlikely event that an accident sequence should proceed through core degradation into relocation of material debris into the reactor vessel lower plenum. Although the low predicted probability of such events does not demand remedial action for the existing BWR facilities, it seems that efficacious counter-measures might be established by a diligent utility on a cost-effective basis for (1) coping with vessel reflood after control blade melting and (2) maintaining core debris within the reactor vessel. The advanced SBWR equipment and structural design inherently supports implementation of both of these objectives.

## 9. REFERENCES

1. S. A. Hodge et al., Martin Marietta Energy Systems, Inc., Oak Ridge National Laboratory, *Identification and Assessment of BWR In-Vessel Severe Accident Mitigation Strategies*, USNRC Report, NUREG/CR-5869 (ORNL/TM-12080), October 1992.
2. *BWR Owner's Group Emergency Procedure Guidelines*, Revision 4, General Electric Topical Report NEDO-31331, March 1987.
3. W. J. Lucas, J. J. Vandenberg, and J. R. Lehner, Brookhaven National Laboratory, *Assessment of Candidate Accident Management Strategies*, USNRC Report, NUREG/CR-5474 (BNL-NUREG-52221), March 1990.
4. U. S. Nuclear Regulatory Commission, *Severe Accident Risks: An Assessment for Five U.S. Nuclear Power Plants*, USNRC Report, NUREG-1150, Vol. 1, Final Summary Report, December 1990.

---

\* This case corresponds to the last entry in Table 3. The reader is reminded that it is based upon complete venting of the vessel support skirt, which is not considered practical for the existing facilities.

5. U. S. Nuclear Regulatory Commission, *Individual Plant Examination: Submittal Guidance*, USNRC Report, NUREG-1335, August 1989.
6. U. S. Nuclear Regulatory Commission, *Individual Plant Examination for Severe Accident Vulnerabilities - 10CFR50.54(f)*, USNRC Generic Letter No. 88-20, November 23, 1988.
7. R. M. Harrington and S. A. Hodge, Martin Marietta Energy Systems, Inc., Oak Ridge National Laboratory, *ATWS at Browns Ferry Unit One - Accident Sequence Analysis*, USNRC Report, NUREG/CR-3470 (ORNL/TM-8902), July 1984.
8. D. H. Cook et al., Union Carbide Corporation Nuclear Division, Oak Ridge National Laboratory, *Station Blackout at Browns Ferry Unit One—Accident Sequence Analysis*, USNRC Report, NUREG/CR-2182 (ORNL/NUREG/TM-455/V1), Vol. 1, November 1981.
9. W. C. Arcieri and D. J. Hanson, EG&G Idaho, Inc., Idaho National Engineering Laboratory, *Instrumentation Availability During Severe Accidents for a Boiling Water Reactor with a Mark I Containment*, USNRC Report, NUREG/CR-5444 (EGG-2661), February 1992.
10. W. B. Scott, et al., Pacific Northwest Laboratory, *Recriticality in a BWR Following a Core Damage Event*, USNRC Report, NUREG/CR-5653 (PNL-7476), December 1990.
11. U.S. Nuclear Regulatory Commission, *A Prioritization of Generic Safety Issues*, USNRC Report, NUREG-0933, July 1991.
12. U. S. Nuclear Regulatory Commission, *Guidelines for Nuclear Power Plant Safety Issue Prioritization Information Development*, USNRC Report, NUREG/CR-2800, February 1983.
13. S. W. Heaberlin, et al., Pacific Northwest Laboratory, *A Handbook for Value-Impact Assessment*, USNRC Report, NUREG/CR-3568 (PNL-4646), December 1983.
14. R. E. Henry, et al., "Cooling of Core Debris Within the Reactor Vessel Lower Head," *paper presented at the Annual Meeting of the American Nuclear Society, Orlando, Florida, June 2-6, 1991, Section on Severe Accidents (June 4).*
15. G. W. Parker, L. J. Ott, and S. A. Hodge, "Small-Scale BWR Core Debris Eutectics Formation and Melting Experiment," *Nuclear Engineering and Design*, 121, 341-347, (1990).
16. D. J. Hanson, et al., EG&G Idaho, Inc., Idaho National Engineering Laboratory, *Containment Venting Analyses for the Peach Bottom Atomic Power Station*, USNRC Report, NUREG/CR-4696 (EGG-2464), December 1986.

**BIBLIOGRAPHIC DATA SHEET**

*(See instructions on the reverse)*

1. REPORT NUMBER  
(Assigned by NRC. Add Vol., Supp., Rev.,  
and Addendum Numbers, if any.)

NUREG/CP-0126

Vol. 2

3. DATE REPORT PUBLISHED

MONTH | YEAR  
March | 1993

4. FIN OR GRANT NUMBER

A-3988

6. TYPE OF REPORT

Proceedings of confer-  
ence on safety research

7. PERIOD COVERED (Inclusive Dates)

October 21-23, 1992

2. TITLE AND SUBTITLE

Proceedings of the Twentieth Water Reactor  
Safety Information Meeting

5. AUTHOR(S)

Compiled by Allen J. Weiss, BNL

8. PERFORMING ORGANIZATION - NAME AND ADDRESS (If NRC, provide Division, Office or Region, U.S. Nuclear Regulatory Commission, and mailing address; if contractor, provide name and mailing address.)

Office of Nuclear Regulatory Research  
U.S. Nuclear Regulatory Commission  
Washington, D.C. 20555

9. SPONSORING ORGANIZATION - NAME AND ADDRESS (If NRC, type "Same as above"; if contractor, provide NRC Division, Office or Region, U.S. Nuclear Regulatory Commission, and mailing address.)

Same as Item 8 above

10. SUPPLEMENTARY NOTES

Proceedings prepared by Brookhaven National Laboratory

11. ABSTRACT (200 words or less)

This three-volume report contains 93 papers out of the 108 that were presented at the Twentieth Water Reactor Safety Information Meeting held at the Bethesda Marriott Hotel, Bethesda, Maryland, during the week of October 21-23, 1992. The papers are printed in the order of their presentation in each session and describe progress and results of programs in nuclear safety research conducted in this country and abroad. Foreign participation in the meeting included 10 different papers presented by researchers from CEC, China, Finland, France, Germany, Japan, Spain and Taiwan. The titles of the papers and the names of the authors have been updated and may differ from those that appeared in the final program of the meeting.

12. KEY WORDS/DESCRIPTORS (List words or phrases that will assist researchers in locating the report.)

reactor safety - meetings, research programs - reviews, reactor accidents, reactor components, nuclear power plants - reliability, nuclear power plants - risk assessment, probabilistic estimation, loss of coolant, reactor accidents - management, human factors, systems analysis, leading abstract - proceedings, seismic effects, hydraulics - heat transfer, environmental engineering.

13. AVAILABILITY STATEMENT

Unlimited

14. SECURITY CLASSIFICATION

(This Page)

Unclassified

(This Report)

Unclassified

15. NUMBER OF PAGES

16. PRICE



**Federal Recycling Program**

**UNITED STATES  
NUCLEAR REGULATORY COMMISSION  
WASHINGTON, D.C. 20555-0001**

---

**OFFICIAL BUSINESS  
PENALTY FOR PRIVATE USE, \$300**

**SPECIAL FOURTH-CLASS RATE  
POSTAGE AND FEES PAID  
USNRC  
PERMIT NO. G-67**